



- Institute of Fundamental Technological Research •
 - Polish Academy of Sciences •
 - Warsaw • Poland •
-

LECTURE NOTES 6

Blood Flow Modelling and Diagnostics

edited by

Tomasz A. Kowalewski



Centre of Excellence for
Applied Biomedical Modelling
and Diagnostics



ERCOTAC SIG-37
Bio-Fluid Mechanics
and Heat Transfer

WARSAW 2005



- Institute of Fundamental Technological Research •
 - Polish Academy of Sciences •
 - Warsaw • Poland •
-

LECTURE NOTES 6

Blood Flow Modelling and Diagnostics

Advanced Course and Workshop—BF 2005

Warsaw, June 20–23, 2005

edited by

Tomasz A. Kowalewski



Centre of Excellence for
Applied Biomedical Modelling
and Diagnostics



ERCOTAC SIG-37
Bio-Fluid Mechanics
and Heat Transfer

WARSAW 2005

© Copyright by Institute of Fundamental Technological Research
Świętokrzyska 21, 00-049 Warsaw, Poland

ABIOMED LECTURE NOTES

Series Editors:

Executive Committee of ABIOMED:

Tomasz A. Kowalewski (*Scientific Coordinator*)
Tomasz Lekszycki
Andrzej Nowicki

Executive Editor:

Maciej Stańczyk

*Edition of this volume has been partially supported
by the European Commission*

*All Contributed Papers in this volume were reviewed
by anonymous referees prior to publication*

ISSN 1733-0874

Skład: Maciej Stańczyk, Tomasz Stańczyk

Papier offset. kl. III, 70 g, B1

Oddano do druku: XII 2005; druk ukończono: XII 2005

Druk i oprawa: Drukarnia Braci Grodzickich, Piaseczno, ul. Geodetów 47a

Contents

Invited Lectures	7
A. KUCABA-PIĘTAL, <i>Blood as Complex Fluid, Flow of Suspensions</i>	9
F. VAN DE VOSSE, <i>Pressure and Flow in the Cardiovascular System</i>	31
P. VENNEMANN and J. WESTERWEEL, <i>Full-Field Blood Velocity Measurement Techniques</i>	91
U. KERTZSCHER ET AL., <i>Experimental Assessment of Wall Shear Flow</i>	109
K. AFFELD ET AL., <i>Flow in Artificial Valves and Blood Pumps</i>	135
G.P. ROMANO, <i>Heart Valves: Modelling Experiments</i>	163
G.M.J. VAN LEEUWEN and A.A. VAN STEENHOVEN, <i>Heat Transfer in Humans—Local and Whole-Body</i>	205
A.P.G. HOEKS AND R.S. RENEMAN, <i>Do Doppler Systems Color Arteries Red?</i>	243
M. VOGT, <i>Concepts for High Resolution Blood Flow Imaging with High Frequency Ultrasound</i>	273
P. FIDANZATI ET AL., <i>Experimental Blood Flow Investigations in Large Human Arteries</i>	299
L. FORMAGGIA and A. VENEZIANI, <i>Geometrical Multiscale Models for the Cardiovascular System</i>	309
J. SZUMBARSKI and J.K. MIZERSKI, <i>Mathematical and Numerical Modelling of Cardiovascular Flows</i>	361

Contributed Papers	403
F.E.M. JANSSEN ET AL., <i>Biological and Physiological Mechanisms of the Hair Preservative Effect of Scalp Cooling in Chemotherapy-Induced Hair Loss</i>	405
G.PONTRELLI and A. TATONE, <i>Propagation of a Solute Wave in a Curved Vessel</i>	415
W. SECOMSKI ET AL., <i>Ultrasonic Doppler Measurement of the Attenuation, Scattering and Blood Hematocrit in the Human Artery</i>	427
N.M.W. SEVERENS ET AL., <i>Patient Temperature in Cardiac Surgery—Model Development and Experiments</i>	439
M. STAŃCZYK, <i>Vascular Model of Heat Transfer in Perfused Tissue</i>	451
P. STROEV ET AL., <i>Estimation of Wall Shear Stress Using a Multi-Branched Model of the Human Arterial System</i>	490
E.YU. TARAN AND O.O. MELNYK, <i>The Effect of Suspended Micro-spheres on Viscosity of Blood</i>	501

Preface

The rapid growth and development of the experimental methods in fluid mechanics, ultrasound systems for medicine and computational tools for flow modelling brought about the need for a closer exchange of knowledge used by people working in these areas. This aim encouraged us to organize in Warsaw a four days meeting on *Blood Flow—Modelling and Diagnostics* (BF 2005). It was prepared in the framework of the Center of Excellence ABIOMED (T. Kowalewski, A. Nowicki), conjoined with ERCOFTAC SIG-37: Bio-Fluid Mechanics and Heat Transfer Interest Group (A. van Steenhoven).

The main interest of today's research in haemodynamics is more and more dedicated to accurate modelling of blood flow characteristics. It became evident that blood is a complex fluid, with properties depending on many factors, not limited to shear rate and hematocrit. The cardiovascular tubing system is characterized by large variety of scales, shapes and wall properties. The fluid mechanics strongly varies inside different vascular regions, altering pressure drops and blood redistribution in a flexible way. Moreover, the heat and mass transfer within the system plays an important role. The pulsating flow characteristics and laminar to turbulent transitions introduce additional complications that are very difficult to deal with analytical and numerical tools. On the other hand, development of new diagnostic tools allows for more and more detailed verification and validation of the modelling attempts. The BF 2005 program made an effort to give a good overview of these problems. Generally, it consisted of three main parts: modelling of blood as a flow media, numerical modelling of the cardiovascular flow and experimental diagnostics by optical and acoustic means.

The present volume contains set of invited articles concerning the most recent advances in the above topics and selected research papers presented during the workshop as contributed papers. The lecture notes are ordered in the way facilitating understanding complexity of the cardio-vascular circulatory system. The book starts with a general description of blood properties, followed with an overview of peculiarities of the circulatory system and de-

scription of experimental methods used by fluid mechanicians to analyse the blood flow. Another view on the cardiovascular diagnostic is brought by the ultrasound technique (USD). Highlights of its recent advances offering high precision measurements are described in the book. The last two review papers demonstrate growing potential of the Computational Fluid Dynamics (CFD) in resolving extremely complex flow configurations of the cardiovascular systems. Seven contributed papers complete the book offering up to date research examples in the modelling and diagnostics of cardiovascular systems.

We hope that the book enables a wide range of researchers, with a different background (mechanical engineering, mathematics, electronics, acoustics and medicine) to find different experience and tools used in the area of cardiovascular fluid mechanics. It is especially interesting to find similarities and differences in optical and acoustic methods of the blood flow measurement, as well as to compare numerical modelling of cardiac surgery with practical experience of medical doctors. Experimental facts, computational results, and extensive bibliography following each article offer unique collection of information facilitating necessary efforts for merging these different fields of expertise.

Tomasz A. Kowalewski

Warsaw, November 2005

Invited Lectures

Blood as Complex Fluid, Flow of Suspensions

ANNA KUCABA-PIĘTAL

*Rzeszów University of Technology
Powstańców Warszawy 8,
35-959 Rzeszów, Poland
anpietal@prz.rzeszow.pl*

Blood is the most complicated fluid. While flowing, it interacts with vessel walls both mechanically and chemically. Still, however, descriptions of blood in the framework of suspensions theory is incomplete. In this paper current problems with blood modelling will be presented and the physiology of blood composition and hemorheology will be studied. Finally, the most popular constitutive models of blood and the range of their applicability will be discussed.

Key words: *Blood modelling, rheological parameters of blood, viscoelasticity of blood*

1. Introduction

Mathematical and numerical models together with computer simulations play an important role in biology and medicine. Research in blood flow has a direct impact on our improved understanding and management of human health.

Close examination of blood is supposed to become one of the major mathematical challenges of the next decade. Blood, like other biological fluids, is a “mysterious” one. It means that due to its vital functions in living organisms, blood has a highly complicated structure which changes depending on health and conditions of life. From the physical point of view, blood is a viscoelastic, complex fluid. The term “complex fluid” usually stands for a non-Newtonian fluid, which means that the shear stress and rate of strain are not directly proportional. Various cells in blood (typically making up 45% of the blood’s volume) make of it a suspension of particles [28, 31] what results in the non-Newtonian characteristic. When blood starts moving, the particles (or cells) interact with plasma and among one another.

Many fundamental issues concerning blood, like blood rheology and modelling, still need to be studied. The rheological parameters of blood can be used in diagnosis of clinical disorders, in maintaining nonbiological fluids which have rheological properties comparable to blood. What is more, the knowledge of the rheological parameters is necessary in mathematical modelling of blood circulation because of formulating blood flow equations.

Rheological analysis and modelling of blood is still incomplete. Blood is a highly concentrated, complex suspension of polydisperse cells. The cells are flexible, chemically and electrostatically active. They are suspended in an electrolyte fluid (plasma) of critical pH in which there are numerous active proteins and organic substances. The modelling of complex suspensions of flexible particles presents a difficult task for scientists and engineers. The boundaries determine the flow of homogeneous fluid, whereas the flow of a multi-component's fluid is additionally affected by individual, suspended particles interacting with one another and with the boundaries of the flow. To describe the rheology of a dilute suspension within the reach of analytical and computational methods there are already well established theories (derived from Einstein work [23]). Computations and analyses have shown that the response of a solitary liquid drop (in a dilute suspension) involves deformations in shape by stretching, contracting or shearing. The nature and extent of deformations can be determined by the intensity and type of the flow. The reaction of a drop depends on two parameters. The first is a measure of the balance between the shear force acting on a drop which tends to deform the drop and the tension on the surface of the drop, which keeps the drop together. The second parameter is the ratio between the viscosities of the drop and the suspending fluid.

The physical mechanisms which determine the dynamics of a concentrated suspension's flow are very complicated. It is known, for instance, that during a flow in a tube, the particles tend to migrate towards the centerline of a channel yielding the core annulus type of a flow with the majority of particles suspended in the fastest moving flow near the centerline.

Due to the complexity of a concentrated suspension's motions, no comprehensive theory has been developed to describe the flow of a general multi-component system, including blood. Furthermore, the convoluted and fragmented shapes of the fluid's interfaces prevent the application of classical numerical approaches, such as finite-difference or finite-element methods.

Therefore till now exact descriptions of blood using the concentrated suspension theory have not existed. The main difficulties in blood modelling as the frame of the theory can be summarized as follows:

- blood is a concentrated suspension, outside the range of applicability of theory of dilute suspensions [45, 23],
- in case of such a concentration, forces between particles should be taken under consideration,
- forces are not known; what is more, particles change their shape in reaction to the fluid's forces,
- the nature of red blood cells' membranes and their deformation in response to stress/strain interaction is much less established,
- red blood cells continuously deform.

For these reasons researchers are forced to seek simplified models to be able to construct constitutive relations for blood.

In this review, I shall discuss problems with blood modelling. First, blood composition and physiology will be discussed briefly. Next, we will go through hemorheology of blood and its determinants. Finally, the most popular constitutive models of blood will be shortly presented.

2. Blood Composition and Physiology

2.1. General Information

The first requirement in blood studying is gaining general information of its physiology. In this chapter a brief outline of blood's composition and circulatory system is presented.

Human blood is a liquid tissue which makes up about 1/13 of the total body mass and accounts for 5 to 6 litres in an average adult male [27, 29].

Blood performs two major functions:

1. transporting through the body:
 - oxygen and carbon dioxide,
 - food molecules (glucose, lipids, amino acids),
 - ions (e.g., Na^+ , Ca^{2+} , HCO_3^-),
 - wastes (e.g., urea),
 - hormones,
 - heat.

2. defending the body against infections and other foreign materials.

When blood is centrifuged, it separates into 2 portions (Fig. 1). Plasma is a fluid part of blood and it consists of about 90% of water, 7% of protein and small amounts of organic and inorganic molecules as well as dissolved gases. It behaves like a Newtonian, viscous fluid with viscosity of about 20% higher than that of water. The second phase consists of cells, primarily red blood cells, which make up over 50% of the volume of blood. Red cells, or erythrocytes, contain hemoglobin and carry oxygen throughout the body. Platelets are small cells that are involved in blood clotting. All of these cells have finite life spans ranging from 1 day to a month and are replenished by the bone marrow. Cells arise and die all the time, so their numbers vary constantly.

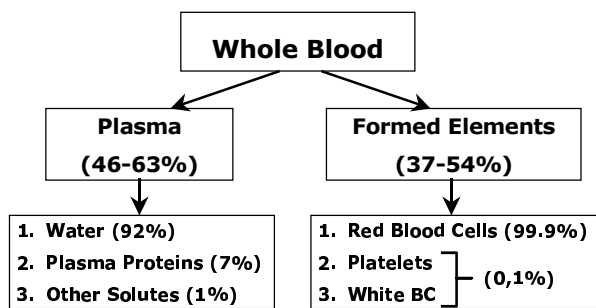


FIGURE 1. Scheme of blood composition

The blood is transported to all living cells in a body by a network of blood vessels. Their structure enables an exchange of blood plasma and dissolved molecules between blood and surrounding tissues. Blood flows away from the heart passing through a series of vessels progressively smaller in diameter: from arteries to arterioles and then to capillaries. Blood returns to the heart through a series of vessels progressively larger in diameter: from capillaries to venules and to veins. Capillaries are the simplest-structured vessels which permeate the entire body in a form of a fine mesh. The structure provides room for blood and allows the transfer of interstitial fluid.

The complex behaviour of blood and its interaction with the vascular walls play an important role in the physiology of blood circulation. Blood interacts both mechanically and chemically with the vessel walls which can get deformed under the blood pressure.

2.2. Composition of Blood

Blood is composed of fluid plasma, solids (erythrocytes, leukocytes, platelets), and other elements either carried to or away from cells. Microscopic view of blood and its solids is presented in Fig. 2.

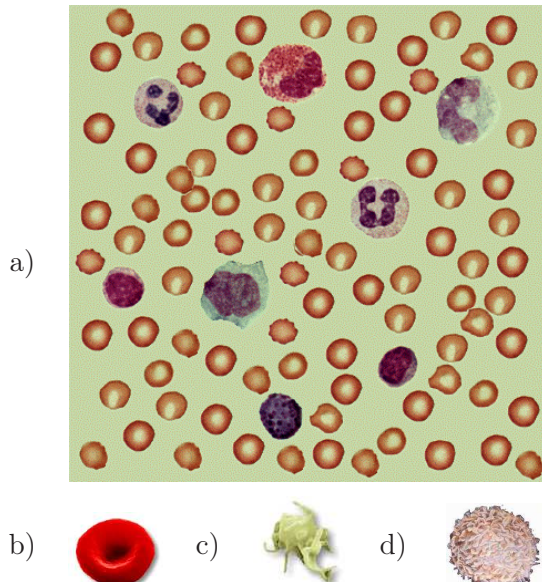


FIGURE 2. Microscopic view of a) whole blood, b) red blood cells c) platelet and d) white blood cell [68, 69, 70].

2.2.1. Plasma. Blood cells are suspended in straw-coloured plasma (liquid part of blood—Fig. 1). Plasma is a mixture of water, sugar, fat, protein, potassium and calcium salts. It contains also many chemicals which aid blood to form clots necessary to stop bleeding. Water makes up more than 92% of plasma. Water of plasma is freely exchangeable with that of body cells and other extra cellular fluids and is available to maintain the normal state of hydration in all body tissues.

Plasma is a complex solution which transports materials needed by cells and materials which must be removed from cells:

- various ions (Na^+ , Ca^{2+} , HCO_3^- , etc.),
- glucose and traces of other sugars,
- amino acids,

- other organic acids,
- cholesterol and other lipids,
- hormones,
- urea and other wastes.

Total volume and concentration of plasma is important in the regulation of blood pressure. Sodium ion is the major solute in plasma. Its concentration determines the amount of plasma water, and thus blood volume.

2.2.2. Red blood cells—erythrocytes. Red blood cells (RBCs), are the most abundant blood cells; 1 μL of male blood contains 4.5–6.3 million RBCs and 1 μL of female blood contains 4.2–5.5 million RBCs.

RBC it's a membrane filled with a solution of hemoglobin and various salts. It's shape is similar to flattened biconcave disc (closed torus) with a depressed center, about 2.5×10^{-6} m thick and 7.5×10^{-6} m in diameter, [6]. The depressed center provides increased surface area for the diffusion of gases. The membrane is composed of chemically complex lipids, proteins, and carbohydrates in a highly organized structure. RBCs carry the oxygen from the lungs to all parts of a body and then return carbon dioxide from our body to the lungs.

RBC creates hemoglobin until it accounts for some 90% of the dry weight of the cell. Hemoglobin is also responsible for making red blood cells red. The viscosity of RBC's interior fluid is five to ten times greater than that of exterior fluid. RBC in quiescent plasma tends to form aggregates known as rouleaux.

An extraordinary distortion of a red cell occurs in its passage through minute blood vessels, many of which have a diameter smaller than that of a red cell. When the deforming stress is removed, the cell springs back to its original shape. The red cell readily tolerates bending and folding, but, if an appreciable stretching of the membrane occurs, the cell is damaged or destroyed. Healthy red cells behave like liquid drops because membranes of red cells are equally elastic and flexible. Sick red cells, for example deformed ones in *sickle cell anemia* lose their elastic properties and may clog small blood vessels.

RBCs are produced continuously in our bone marrow from stem cells. They never divide. After ≈ 120 days, a RBC cell membrane ruptures, or the damage is detected by phagocytic cells in liver and spleen. Most of the iron in their hemoglobin is reclaimed for reuse.

2.2.3. White blood cells—lymphocytes. White blood cells (WBCs) are clear, round cells that are bigger than red blood cells. They have a nuclei and mitochondria which enable them to move around. WBCs are capable of squeezing through pores in capillary walls in order to reach sites of infection. This aids WBCs in their participation in the immune response of the body.

White blood cells produce proteins called antibodies that help our bodies fight infections caused by bacteria, viruses, and foreign proteins. A typical μL of blood contains 6000–9000 WBCs (1% volume). Most of the WBCs in a body at a given moment are in the connective tissue or in organs of the lymphatic system. They remain viable only during the last 18–36 hours before they also are removed.

WBCs can be classified on the basis of the appearance of granules when viewed under the light microscope (Fig. 3) and function as follows:

1. Granulocytes protect body from infection and are represented by:

- basophils,
- eosinophils,
- neutrophils.

2. Agranulocytes are a part of immune system and are represented by:

- lymphocytes,
- monocytes.

2.2.4. Platelets (thrombocytes). They are the smallest formed elements and actually are fragments of large bone marrow cells. Their shape is flat-

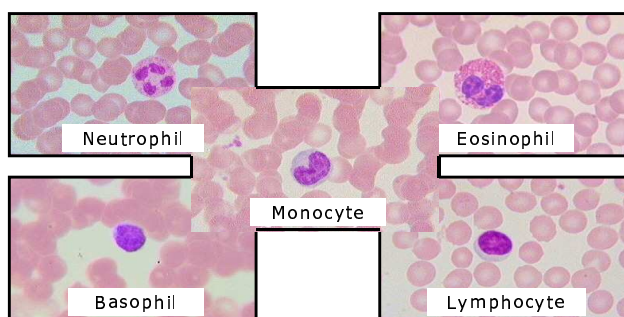


FIGURE 3. Microscopic view of various kind of white blood cells.

tened, disc-like, and the characteristic size of a cell is about $1\text{ }\mu\text{m}$ by $4\text{ }\mu\text{m}$ (1/3 size of RBC).

Platelets are continuously replaced. Each platelet circulates for 9–12 days before being removed by splenic phagocytes. They contain no nuclei but still are capable of moving and functioning in blood clotting. They act as a participant in the vascular clotting system.

When blood vessels are cut or damaged, the loss of blood from the system must be stopped before a shock or possible death. This is accomplished by solidification of blood, a process called coagulation or clotting.

3. Rheological Parameters of Blood

The heart pumps energy into the blood with each beat. Portions of this energy are either dissipated or stored as blood cells rearrange, orient and deform. This behavior is indirectly expressed by the rheological parameters of blood viscosity and elasticity coefficients.

The simplest physical interpretation of the rheological parameters can be as follows: viscosity is an assessment of the rate of energy dissipation due to cell deformation and sliding; elasticity is an assessment of the elastic storage of energy primarily in the kinetic deformability of the red blood cells.

The viscosity and elasticity determine the pressure required to produce blood flow. Due to correlations between the whole blood viscosity and arterial diseases, stroke, hypertension, diabetes, smoking and aging, the hemorheology has been of great interest in the fields of biomedical engineering and medical researches. Hemorheological properties of blood include the whole blood viscosity, plasma viscosity, hematocrit, RBC deformability and aggregation, and fibrinogen concentration in plasma.

3.1. Viscosity and Viscoelasticity

Viscosity is a measure of flow resistance depending on internal friction when one layer of fluid moves in relation to another layer. Viscoelasticity is the tendency to respond to stress as if the material were a combination of elastic solid and viscous fluid. This feature, possessed to some degree by all plastics, says that materials which have solid-like characteristics such as elasticity, strength and form stability also have liquid-like characteristics like flow depending on time, temperature, rate and amount of loading. The experimental value of the viscosity coefficient of a fluid is obtained from the

ratio of shearing stress to shearing rate. If the flow is constant in time, then the ratio of shear stress to shear rate is the viscosity of the fluid. When flows change in time, some liquids generally demonstrate both a viscous and an elastic effect; such liquids are called viscoelastic [25, 46, 58]. To determine the parameters of fluid, methods based on the relation between shear stress and time rate of shear strain (or shear rate) are employed [25, 46, 58].

Whole blood is both viscous and elastic while blood plasma normally exhibits viscosity only [38]. The viscoelasticity behavior of blood results mainly from red blood cells deformability and their ability to aggregate. The viscous and elastic properties of blood can be measured by use of standard rheometry or by using BioProfiler [64]. It should be noted, that the first who has measured the viscoelastic properties that control the pulsatile flow of blood was G.B. Thurston in 1972 [56].

3.2. Determinants of Whole Blood Viscosity

There are four main factors which influence the rheological parameters of blood: (1) plasma viscosity, (2) hematocrit, (3) RBC deformability and aggregation, and (4) temperature. Especially, the hematocrit and RBC aggregations, mainly contribute to the non-Newtonian characteristics of shear-thinning viscosity and yield stress. Below we describe them in detail.

3.2.1. Plasma Viscosity. Since blood is a suspension of various cells in plasma, the plasma viscosity affects blood viscosity and viscoelasticity, particularly at high shear rates. Studies have shown that normal plasma is a Newtonian fluid [28], Therefore, its viscosity is independent of shear rate [20, 21]. The viscosity coefficient of plasma is $\mu = 1.2 \times 10^{-3}$ Pa s.

3.2.2. Hematocrit. The rheological properties of suspensions highly correlate with concentrations of suspended particles. In blood, the most numerous suspended particles are red blood cells (RBC). Therefore hematocrit is the most important factor which effects the whole blood viscosity [7, 18, 28, 55].

Hematocrit is defined as a volume percentage of red blood cells in the whole blood. Hematocrit's average value is 46 (in the range of 40–54) for men and 42 (in the range of 37–47) for women. It can be determined by centrifuging a blood sample so that all formed elements come out of the suspension.

The effect of hematocrit in blood viscosities has been well documented in literature. In general, the higher the hematocrit, the greater the value of the whole blood viscosity [17, 20, 31]. Fig. 4 presents the influence of the hematocrit concentration on viscosity and viscoelasticity of blood.

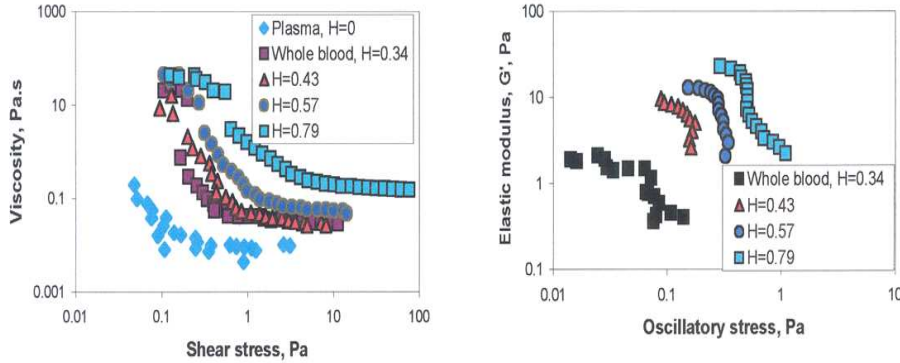


FIGURE 4. The influence of blood cell concentration (hematocrit H) on viscosity and viscoelasticity of blood (after [64]).

3.2.3. RBC Deformability. Deformability describes the structural response of a body or cell to applied forces. The effect of RBC deformability in influencing general fluidity of the whole blood is clearly revealed in Fig. 5. This figure shows the relative viscosity of blood at a shear rate $>100\text{ s}^{-1}$, at which particle aggregation is negligible, compared with that of suspensions with rigid spheres and oil-water emulsion.

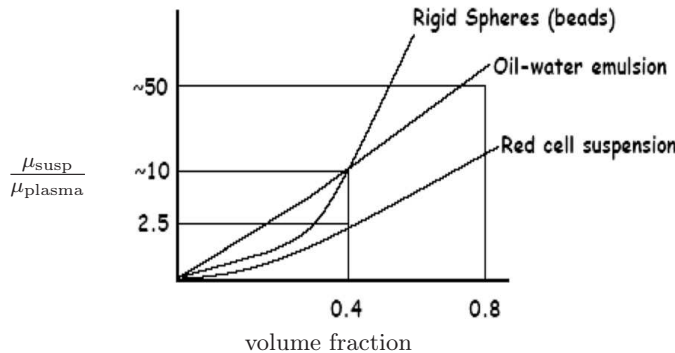


FIGURE 5. Variation of the relative viscosity of blood, oil-water emulsion and suspension with rigid spheres at a shear rate $> 100\text{ s}^{-1}$ after [30].

We can observe that at 50% concentration, the viscosity of a suspension of rigid spheres reaches almost infinity, so the suspension is not able to flow. On the contrary, normal blood remains fluid even at hematocrit's level of 98% on account of the deformability of its RBCs [28].

This blood fluidity is due to the special properties of red blood cells, particularly due to their shape and elastic properties of their membrane. These properties permit tremendous deformations of red cells and consequently blood can flow. In many small blood vessels, the capillary diameters are the same of even smaller than the one of a red cell. In such cases blood flow would be blocked if red cells were not so flexible.

3.2.4. RBC Aggregation. Since red cells do not have a nucleus, they behave like fluid drops [20]. Hence, when a number of red cells clusters together as in the flow of a low shear rate, they stack together, like coins, into aggregates called rouleaux. The extent of aggregation is strongly dependent on the shear rate; the aggregates will break up when the shear rate is increased, qualitatively explaining the decrease in viscosity at increasing shear rates shown in Fig. 6.

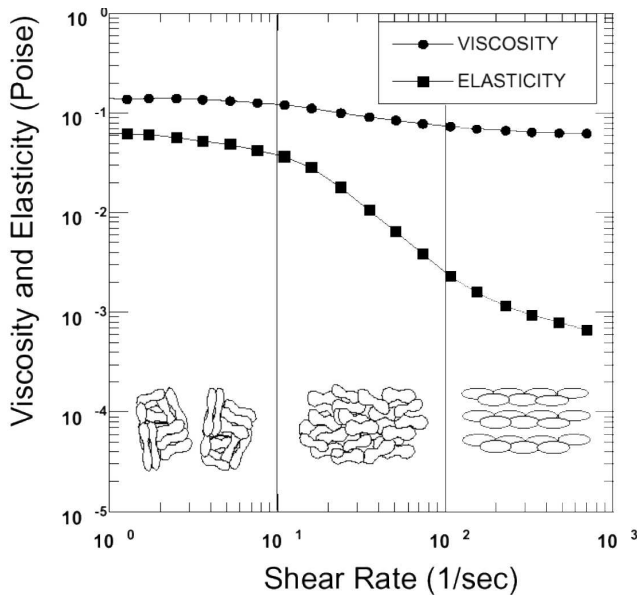


FIGURE 6. The shear rate dependence of normal human blood viscosity and elasticity at 2 Hz and 22°C, after [63].

Figure 6 shows the relationship between blood viscosity and elasticity and rouleaux formation, which can be divided into tree parts regardless of shear stresses [56, 64]. Rouleaux formation of healthy red cells decreases at increasing shear rates. As shear rate increases, blood aggregates tend to be broken up. The collapse disturbs the flow and requires the consumption of energy, which manifests itself in increasing blood viscosity at low shear rates [28]. So we can say that rouleaux formation increases blood viscosity, whereas breaking up rouleaux decreases blood viscosity.

Rouleaux formation is highly dependent on the concentration of fibrinogen and globulin in plasma. Note that bovine blood does not form rouleaux because of absence of fibrinogen and globulin in plasma [28].

It is important to point out, that forces which disaggregate the cells also produce elastic deformation and orientation of the cells, causing elastic energy to be stored in the cellular microstructure of the blood.

3.2.5. Temperature. As in most fluids, blood viscosity increases as temperature decreases [28, 31]. Typically, blood viscosity increases less than 2% for each °C decrease in temperature [4]. Precise control of the sample temperature is necessary to measure viscosity accurately in vitro.

In blood, reduced RBC deformability and increased plasma viscosity elevate particularly whole blood viscosity at low temperatures [4].

3.3. Yield Stress and Thixotropy

In addition to viscosity, blood also exhibits a yield stress [48, 49]. A fluid with no suspended particles starts moving as soon as an infinitely small amount of force is applied. Such a fluid is called a fluid without yield stress. Examples fluids with no yield stress include water, air, mineral oils, and vegetable oils.

The source of the yield stress in blood is the presence of cells in blood, particularly red cells. When such a huge amount (40–45% by volume) of red cells of 8–10 microns in diameter is suspended in plasma, cohesive forces among the cells are not negligible. The forces existing between particles are van der Waals-London forces and Coulomb forces [6, 44]. So the force needed to start the blood flow is large enough to break up particle-particle links among the cells.

The magnitude of the yield stress of human blood appears to be of the order of 0.05 dyne/cm² (or 5 mPa) [28, 51, 53, 61] and is almost independent of temperature in the range of 10–37°C [4].

The phenomenon of thixotropy in a liquid results from the microstructure of the liquid system. Thixotropy may be explained as a consequence of aggregation of suspended particles. If the suspension is at rest, the particle aggregation can form, whereas if the suspension is sheared, the weak physical bonds among particles are ruptured, and the network among them breaks down into separate aggregates, which can disintegrate further into smaller fragments [6]. This effect on blood viscosity has been studied in [34, 35, 55]. At high shear rates, structural change occurs more rapidly than that at low shear rates. Based on the results, it can be concluded that the recovery of quiescent structure requires approximately 50 seconds, while the high shear rate structure is attained in a few seconds. In other words, in order to minimize the effect of the thixotropic characteristic of blood on the viscosity measurement between the shear rates of 500 and 1 s⁻¹, at least 50 seconds should be allowed during the test to have the fully aggregated quiescent state at a shear rate near 1 s⁻¹.

3.4. Clinical Significance of Blood Viscosity and Viscoelasticity

A number of researchers who measured both blood and plasma viscosities, reported that both whole blood viscosity and plasma viscosity were significantly higher in patients with essential hypertension than in healthy people [52, 59, 60]. In the case of diabetics, whole blood viscosity, plasma viscosity, and hematocrit were elevated, whereas RBC deformability was decreased [21]. Other scientists conducted hemorheological studies to determine the relationships between whole blood viscosity and smoking, age, and gender [9, 36, 67]. They found that smoking and aging might cause the elevated blood viscosity. Variation in blood viscoelasticity in healthy population is very small. Thus, changes due to disease or surgical intervention can be readily identified, making blood viscoelasticity an useful clinical parameter.

Now extensive basic research on blood viscoelasticity and the factors affecting it have provided a firm foundation for the increasing interest in viscoelasticity among researchers in clinical medicine and physiology. It has been discovered that major shifts in the viscoelasticity of blood are associated with such pathologies as myocardial infarction, peripheral vascular disease, cancer and diabetes [14, 42].

4. Constitutive Models of Blood

For over four decades great attempts have been made to obtain a constitutive relation for blood. While some of these models are empirical, others involve rigorous mathematical derivations. Detailed review of these models can be found in [50, 57, 62, 69]. In this chapter some of the most popular constitutive models of blood: Newtonian, Casson, Herschel-Bulkley and micropolar model will be presented. The mathematical description will be given and range of applicability of the models will be discussed.

In general, viscous liquids can be divided in terms of rheological properties into Newtonian, general non-Newtonian, and viscoplastic fluids [54, 46]. The properties are expressed by constitutive equations. The Newtonian fluid model is the basis for classical fluid mechanics. Gases and liquids like water are Newtonian fluids. Blood, polymers, paint, and food are non-Newtonian.

Question about an appropriate constitutive model for blood is not trivial: it is a concentrated suspension of highly flexible particles in a complex aqueous polymer solution, the plasma, and exhibits a range of non-Newtonian properties. These properties, presented in the previous chapters, are mainly governed by the deformation and aggregation of red blood cells. Other important factors in determining an appropriate constitutive equation for blood—apart from the fluid properties—are the conditions of flow. Since the whole blood is non-Newtonian in nature, blood behaviour depends strongly on the size of blood vessels in relation to dimensions of red blood cells. The dimensions of vessels imply various shear conditions which affect blood viscosity. Therefore in order to apply the appropriate constitutive model for blood, the problem must be restricted to a specific flow area.

For instance, in capillaries where vessel diameters are comparable with that of red blood cells, blood behaves as a shear-thinning fluid and also exhibits viscoelastic properties that can be neglected in large and medium vessels flow. Such properties must be reflected in properly applied constitutive models.

The question of whether blood can be considered as a Newtonian fluid is still standing. The composition of blood would seem to indicate uncontestedly that it is indeed not a Newtonian fluid. However, in some situations it is sufficient to assume, that blood acts like a Newtonian fluid. So, Newtonian model of blood can be reckoned as the first approach in blood modelling. It is valid only when the dimension of flow is large enough—in large arteries. In capillary blood flow, the Newtonian fluid model breaks down.

It should be mentioned, that the constitutive models presented below are derived under assumption that blood is a continuum medium. That is, the elements of blood seem to be continuous with each other, with no empty spaces in between. The continuum hypothesis implies too, that every “point” in the fluid represents a fluid element, and that the properties at that point, represent the properties of that fluid element.

4.1. Newtonian Fluid Model

The simplest constitutive equation for the fluid is Newton's law of viscosity [46, 54].

$$\tau = \mu \dot{\gamma}$$

where μ is the Newtonian viscosity and $\dot{\gamma}$ is the shear rate or the rate of strain.

For Newtonian fluid model, when shear stress is plotted against shear rate at a given temperature, the plot shows a straight line with a constant slope that is independent of shear rate (see Fig. 7). This slope is called the viscosity coefficient of the fluid.

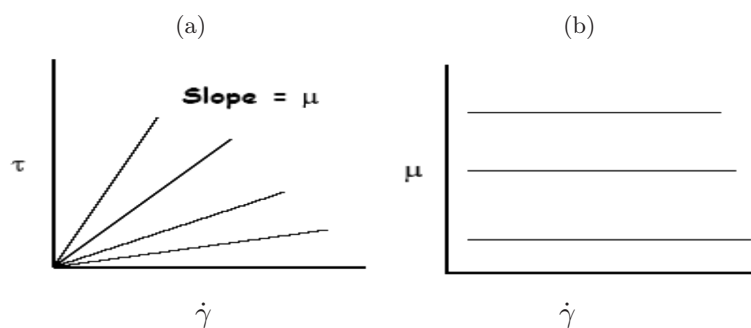


FIGURE 7. Newtonian fluids: a) shear stress vs. shear rate. b) viscosity vs. shear rate.

Plasma is Newtonian fluid with $\mu = 1.2 \times 10^{-3}$ Pa s. The viscosity of blood in Newtonian model is equal: $\mu = 3-4 \times 10^{-3}$ Pa s. This model is used for blood flow in arteries and large diameter vessels.

4.2. Non-Newtonian Fluid Models

In general, fluids that do not obey the Newtonian relationship between shear stress and shear rate are non-Newtonian [25]. Therefore for non-New-

tonian fluids, the slope of shear stress versus shear rate curve is not constant. The non-Newtonian models presented below can be used to describe blood flow in middle and small blood vessels. The constants which appeared in the models depend on hematocrit and their detailed form can be found in literature [49, 67, 60].

4.2.1. Power law model. One of the most popular is power law model, which can be described by the relation:

$$\tau = m\dot{\gamma}^n.$$

The constant, m , is a measure of the consistency of the fluid: n is a measure of the degree of non-Newtonian behaviour. It is well known that the power-law model does not have the capability to handle the yield stress [25].

4.2.2. Casson Model. The Casson model extends the simple power-law model and is based on a structure model of the interactive behaviour of solid and liquid phases of a two-phase suspension [8]. In contrary to the simple power law, the Casson model can handle both yield stress and shear-thinning characteristics of blood, and can be described as follows [8, 25, 41]:

$$\begin{aligned}\sqrt{\tau} &= \sqrt{\tau_y} + \sqrt{k}\sqrt{\dot{\gamma}}, & \tau \geq \tau_y, \\ \dot{\gamma} &= 0, & \tau \leq \tau_y.\end{aligned}$$

where k is a Casson model constant,

τ = shear stress,

$\dot{\gamma}$ = shear rate,

τ_y = a constant that is interpreted as yield stress.

4.2.3. Herschel-Bulkley model. The Herschel-Bulkley model extends the simple power-law model to include a yield stress as follows [32, 25]:

$$\begin{aligned}\tau &= m\dot{\gamma}^n + \tau_y, & \tau \geq \tau_y, \\ \dot{\gamma} &= 0, & \tau \leq \tau_y.\end{aligned}$$

τ = shear stress,

$\dot{\gamma}$ = shear rate,

τ_y = a constant that is interpreted as yield stress,

m and n = model constants.

The model is capable to describe both yield stress and shear-thinning of blood [25].

4.2.4. Comparison of the experimental data with the non-Newtonian models of blood. To compare the non-Newtonian models of blood an experiment was performed [51]. Viscosity of human blood and bovine blood were measured by using rheometry method. Then, the values were used to fit the coefficients of Casson, Power-law and Herschel-Bulkley models. All the constants which appeared in those constitutive models were determined by using curve fitting experimental data approach. Details of the experiment can be found in [51]. Below, in Table 1, the results of blood viscosity measurements with scanning capillary-tube rheometer (SCTR) are presented.

TABLE 1. Blood viscosity. Experimental data and theoretical prediction based on Power-law, Casson and H-B models, after [51].

Shear rate (s^{-1})	Viscosity (cP)	Viscosity (cP)		
		Power-law	Casson	H-B
300	4.43	4.39	4.49	4.28
150	4.78	4.75	4.84	4.71
90	5.11	5.03	5.18	5.09
45	5.75	5.44	5.85	5.71
30	6.25	5.7	6.38	6.2
13	8.81	6.16	7.7	7.21
7.5	17	6.67	9.7	8.9
3		7.4	14.5	12.8
Lower than 3		8.38 (at 1 s^{-1})	22.5 (at 1.35 s^{-1})	18.55 (at 1.55 s^{-1})

We can observe, that the biggest discrepancies between theoretical prediction and experimental data appeared in small shear rate. For high shear rates, experimental data and those predicted by theoretical models are very close.

4.3. Micropolar Fluid Model

The micropolar fluid model—proposed by Eringen in 1966 [3] is an extension of classical fluid dynamics model. It is based on the assumption of a continuous medium, but takes into account microrotation \mathbf{w} of the molecules, different from the local vorticity of the flow. The occurrence of the microrotation vector, which differs from the stream flow vorticity vector $\mathbf{w} \neq \text{rot} \mathbf{V}$

and from the angular velocity $\mathbf{w} \neq 1/2 \operatorname{rot} \mathbf{V}$ results in the formation of antisymmetric stresses and coupled stresses. Therefore in micropolar model of fluid description we need two constitutive equations: for shear stress—as in classical continuum medium, and the second—for couple stress, [3].

In last decades numerous papers appeared in which the blood has been modelled as micropolar fluid [35]. For instance steady and pulsatile blood flow was considered in [1], values for the micropolar material coefficients were determined in vitro for blood by Bugliarello and Sevilla [4], the phenomena of pulsatile blood flow were considered in [6] with respect to an investigation of the hydraulic impedance of blood vessels. The comparison of experimental data with the theoretical prediction for the blood flow parameters obtained by use of micropolar fluid shows, that this model is suitable for middle shear rates and small vessels flows.

5. Conclusions

Blood is a very complex fluid: homogeneous at macroscopic length scale but possesses a very complicated structure over a microscopic length scale. One of the primary difficulties in physical rather than empirical approach is the fact that blood is a highly complex and concentrated suspension the content of which varies each time and depends on living and health conditions.

The results presented above show how complex the blood structure is. They also indicate that blood modelling is far from being at a satisfactory level. Many open questions concerning blood modelling still arise. Current research shows that blood flow modelling in small vessels is a serious problem. The assumption that blood behaves like a Newtonian fluid fails in the case of small vessels. Mathematicians try to model blood flow in capillaries and small vessels by using non-Newtonian models. But there is still a gap in our understanding of all quantitative aspects of such flows.

Problems presented this review indicate main research directions on blood modelling in the near future. Obtained results can be helpful in our understanding of vascular diseases and in medical diagnosis and therapy.

References

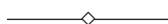
1. S.J. ALLEN, *Pulsatile blood flow; investigation of hydraulic impedance of blood vessels*, J. Biomechanics, **2**: 313–324, 1969.

2. T. ARIMAN, N.D. SYLVESTER, and M.A. TURK, *Microcontinuum fluid mechanics—a review*, Int. J. Engng. Sci., **11**: 905–909, 1973.
3. G. BUGLIARELLO and SEVILLA, *Velocity and Steady and pulsatile blood flow through a circular tube*, J. Biorheology, **7**: 85–95, 1970.
4. J.H. BARBEE, *The effect of temperature on the relative viscosity of human blood*, Biorheology, **10**: 1, 1973.
5. H.A. BARNES, *Thixotropy—a review*, J. Non-Newtonian Fluid Mech., **70**: 1–33, 1997.
6. H.A. BARNES, *The yield stress—a review—everything flows?*, J. Non-Newtonian Fluid Mech. **81**, 133, 1999.
7. A.M. BENIS, S. USAMI, and S. CHIEN, *Effect of hematocrit and inertial losses on pressure-flow relations in the isolated hind paw of the dog*, Circulation Res. **27**: 1047, 1970.
8. R.B. BIRD, R.C. ARMSTRONG, and O. HASSAGER, *Dynamics of Polymeric Liquids*, 1, Wiley, New York, 1987.
9. A.J. BOWDLER and A.M. FOSTER, *The effect of donor age on the flow properties of blood. Part I: Plasma and whole blood viscosity in adult males*, Exp Gerontol **22**: 155–164, 1987.
10. D.P. BRILEY, G.D. GIRAUD, N.B. BEAMER, ET AL., *Spontaneous echo contrast and hemorheologic abnormalities in cerebrovascular disease*, Stroke, **25**: 1564, 1994.
11. N. CASSON, *Rheology of Disperse System*, Pergamon, London, 1959.
12. S. CHAKRAVARTY and A. DATTA, *Dynamic Response of stenotic blood flow in vivo*, Mathl. Comput. Modelling, **16**: 3, 1992.
13. S. CHAKRAVARTY and A. DATTA, *Effects of stenosis on arterial rheology through a mathematical model*, Mathl. Comput. Modelling, **12**: 1601–1612, 1989.
14. H. CHMIEL, I. ANADERE, and E. WALITZA, *The determination of blood viscoelasticity in clinical hemorheology*, Clinical Hemorheology, **10**: 363–374, 1990.
15. H.Q. CHEN, L.L. ZHONG, X.Y. WANG, T. ZHOU, and Z.Y. CHEN, *Effects of gender and age on thixotropic properties of whole blood from healthy adult subjects*, Biorheology, **28**: 177–183, 1991.
16. D.C.H. CHENG and F. EVANS, *Phenomenological characterization of the rheological behavior of inelastic reversible thixotropic and antithixotropic fluids*, British J. Applied Physics, **16**: 1599–1617, 1965.
17. S. CHIEN, J. DORMANDY, E. ERNST, and A. MATRAI, *Clinical Hemorheology*, Martinus Nijhoff Publishers, Dordrecht, 1987.
18. Y. CINAR, G. DEMIR, M. PAC, and A.B. CINAR, *Effect of hematocrit on blood pressure via hyperviscoesity*, American Journal of Hypertension, **12**: 739–743, 1999.
19. B.M. COULL, N. BEAMER, P. GARMO, ET AL., *Chronic blood hyperviscosity in subjects with acute stroke, transient ischemic attack, and risk factors for stroke*, Stroke, **22**: 162, 1991.

20. U. DINNAR, *Cardiovascular Fluid mechanics*, CRC Press, Boca Raton, FL, 1981.
21. L. DINTENFASS, *Blood microrheology-Viscosity factors in blood flow, ischaemia and thrombosis*, Appleton-Century-Crofts, New York, 1971.
22. L. DINTENFASS, *Blood viscosity factors in severe non-diabetic and diabetic retinopathy*, *Biorheology*, **14**: 151–157, 1977.
23. A. EINSTEIN, *Eine neue Bestimmung der Moleküldimensionen*, *Ann. Physik.*, **19**: 289, 1906.
24. A.C. ERINGEN, *Theory of micropolar fluids*, *J. Math. Mech.* **16**(1) : 1–16, 1966.
25. J. FERGUSON and Z. KEMBLOWSKI, *Applied Fluid Rheology*, Elsevier Science, London and New York, 1991.
26. M. FISHER and H.J. MEISELMAN, *Hemorheological factors in cerebral ischemia*, *Stroke*, **22**: 1164, 1991.
27. Y.C. FUNG, *Biomechanics: Motion, Flow, Stress, and Growth*, Springer-Verlag, New York, 1990.
28. Y.C. FUNG, *Biomechanics: Mechanical Properties of Living Tissues*, Springer, New York, 1993.
29. Y.C. FUNG, *Biomechanics: Circulation*, Springer, New York, 1996.
30. H.L. GOLDSMITH, *The microrheology of human erythrocytes suspensions*. [in]: *Theoretical and Applied Mechanics*, [eds.] E. Becker and G.K. Mikhailov, Proc. 13th IUTAM Congress, Springer, New York, 1972.
31. A.C. GUYTON and J.E. HALL, *Textbook of Medical Physiology*, 9th edition, W.B. Sanders Company, Philadelphia, 1996.
32. W.H. HERSCHEL, and R. BULKLEY, *Measurement of consistency as applied to rubberbenzene solution*, *Proc. Am. Soc. Test. Matls.*, **26**: 621, 1926.
33. E.M. HOARE, A.J. BARNES, and J.A. DORMANDY, *Abnormal blood viscosity in diabetes and retinopathy*, *Biorheology*, **13**: 21–25, 1976.
34. T.V. HOW, *Advanced in Hemodynamics and Hemorheology*, Vol. 1, JAI Press, London, 1996.
35. A. KUCABA-PIĘTAL , *Aplication of Micropolar Fluid Model in Biomechanics*, Proceedings of ISC Mechanics **98**: 38–48 [ed.] Korzynski, RUT, Rzeszow, 1998.
36. J. LEVENSON, A.C. SIMON, F.A. CAMBIEN, and C. BERETTI, *Cigarette smoking and Hypertension*, *Arteriosclerosis*, **7**: 572, 1987.
37. D. LIEPSCH and S. MORAVEC, *Pulsatile flow of non-Newtonian fluids in distensible models of human arteries*, *Biorheology*, **21**: 571, 1984.
38. G.D.O. LOWE and J.C. BARBENEL, *Plasma and blood viscosity*, *Clinical Blood Rheology*, [ed.] G.D.O. Lowe, CRC Press, Boca Ration Florida, **1** : 11–44, 1988.
39. G.D.O. LOWE, M.M. DRUMMOND, A.R. LORIMER, ET AL., *Relation between extent of coronary artery disease and blood viscosity*, *British Medical Journal*, **8** : 673, 1980.

40. G.D.O. LOWE, F.G.R. FOWKES, J. DAWES, ET AL., *Blood viscosity, fibrinogen, and activation of coagulation and leukocytes in peripheral arterial disease and the normal population in the Edinburgh artery study*, Circulation, **87**:1915, 1993.
41. C.W. MACOSKO, *Rheology; Principles, Measurements, and Applications*, Wiley-VCH, New York, 1994.
42. Y. ISOGAI, S. IKEMOTO, K. KUCHIBA, J. OGAWA, and T. YOKOSE, *Abnormal blood viscoelasticity in diabetic microangiopathy*, Clinical Hemorheology, **11**:175–182, 1991.
43. J. MEWIS and A.J.B. SPAULL, *Rheology of concentrated dispersions*, Advances in Colloid and Interface Science, **6**:173–200, 1976.
44. S. MIDDLEMAN, *The Flow of High Polymers*, Interscience, New York, 1968.
45. B.R. MUNSON, D.F. YOUNG, and T.H. OKIISHI, *Fundamentals of Fluid Mechanics*, Wiley, New York, 1998.
46. M. NAKAMURA and T. SAWADA, *Numerical study on the flow of a non-Newtonian fluid through an axisymmetric stenosis*, ASME J. Biomech. Eng., **110**:137–143, 1988.
47. Q.D. NGUYEN and D.V. BOGER, *Yield stress measurement for concentrated suspensions*, J. Rheol., **27**:321, 1983.
48. Q.D. NGUYEN and D.V. BOGER, *Measuring the flow properties of yield stress fluids*, Annu. Rev. Fluid. Mech. **24**:47, 1992.
49. C.M. RODKIEWICZ, P. SINHA, and J.S. KENNEDY, *On the application of a constitutive equation for whole human blood*, Transactions of the ASME, **112**:198–206, 1990.
50. H. SCHMIDNBEIN and R.E. WELLS, *Rheological properties of human erythrocytes and their influence upon anomalous viscosity of blood*, Physiol. Rev., **63**:147–219, 1971.
51. K. SANGHO, *Study of Non-Newtonian Viscosity and Yield Stress of Blood in a Scanning Capillary-Tube Rheometer*, Ph.D. Thesis, Drexel University, 2002.
52. J.F. STOLTZ, M. SINGH, P. RIHA, *Hemorheology in Practice*, IOS Press, 1999.
53. R.I. TANNER, *Engineering rheology*, Oxford University Press, New York, 1985.
54. G.B. THURSTON, *Effect of hematocrit on blood viscoelasticity and in establishing normal values*, Biorheology, **15**:239–249, 1978.
55. G.B. THURSTON, *The viscoelasticity of human blood*, Biophysical Journal, **12**:1205–1249, 1972.
56. G.B. THURSTON, *Viscoelastic properties of blood and blood analogs: Advances in Haemodynamics and Haemorheology*, T.V. How [ed.], JAI Press Inc. 1996.
57. G.B. THURSTON, *Plasma release-cell layering theory for blood flow*, Biorheology, **26**:199–214, 1989.
58. K. TOTH, G. KESMARKY, J. VEKASI, J. NEMES, and L. CZOPF, *Hemorheological and hemodynamic parameters in patients with essential hypertension and their modification by alpha-1 inhibitor drug treatment*. Clin Hemorheol Microcirc. **21**:209–216, 1999.

59. Y. TSUDA, K. SATOH, M. KITADAI, Y. IZUMI, and T. TAKAHASHI, *Chronic hemorheological effects of the calcium antagonist nilvadipine in essential hypertension*. Arzneimittelforschung, **47**: 900–904, 1997.
60. W.P. WALAWENDER, T.Y. CHEN, D.F. CALA, *An approximate Casson fluid model for tube flow of blood*, Biorheol. **12**: 111, 1975.
61. F.J. WALBURN, D.J. SCHNECK, *A constitutive equation for whole human blood*, Biorheology, **13**: 201, 1976.
62. C.R. WILDEMUTH, M.C. WILLIAMS, *A new interpretation of viscosity and yield stress in dense slurries: coal and other irregular particles*, Rheol. Acta **24**: 75–91, 1985.
63. Vilastic Scientific, Inc. Austin, TX.
64. www.unisa.edu.au/iwri/research/sectors/blood.jpg
65. J.W.G. YARNELL, P.M. SWEETNAM, A. RUMLEY, and G.D.O. LOWE, *Lifestyle and hemostatic risk factors for ischemic heart disease: the Caerphilly Study*. Arterioscler Thromb Vasc Biol. **20**: 271–279, 2000.
66. D.M. YOUNG, R.T. GREGORY, *A Survey of Numerical Mathematics*, **1**, Dover, New York, 1988.
67. K.K. YALESWAPARU , *Evaluation of Continuum models fpr characterizing the constitutive behaviour of blood*. Ph.D. Thesis Dept. M. Engng. Pittsburgh University, 1996.
68. <http://www.gslc.genetics.utah.edu/units/basics/blood/blood.cfm>
69. <http://w3.ouhsc.edu/hemaonco/cases/pbs119.gif>
70. http://137.222.110.150/restricted/gallery/album86/Blood_film_human



Pressure and Flow in the Cardiovascular System

FRANS N. VAN DE VOSSE

*Department of Biomedical Engineering
Eindhoven University of Technology
The Netherlands*

In the introductory part of these notes a short overview of the circulatory system with respect to blood flow and pressure will be given. In section 1 a simple model of the vascular system will be presented despite the fact that the fluid mechanics of the cardiovascular system is complex due to the non-linear and non-homogeneous rheological properties of blood and arterial wall, the complex geometry and the pulsatile flow properties.

An important part, section 2, is dedicated to the description of Newtonian flow in straight, curved and bifurcating, rigid tubes. With the aid of characteristic dimensionless parameters the flow phenomena will be classified and related to specific physiological phenomena in the cardiovascular system. In this way difference between flow in the large arteries and flow in the micro-circulation and veins and the difference between flow in straight and curved arteries will be elucidated. It will be shown that the flow in branched tubes shows a strong resemblance to the flow in curved tubes.

Although flow patterns as derived from rigid tube models do give a good approximation of those that can be found in the vascular system, they will not provide information on pressure pulses and wall motion. In order to obtain this information a short introduction to vessel wall mechanics will be given and models for wall motion of distensible tubes as a function of a time dependent pressure load will be derived. The flow in distensible tubes is determined by wave propagation of the pressure pulse. The main characteristics of the wave propagation including attenuation and reflection of waves at geometrical transitions are treated in section 3, using a one-dimensional wave propagation model.

Key words: *hemodynamics, curved tube flow, vascular biomechanics, wave propagation, wave reflection*

1. The Cardiovascular System

1.1. Introduction

The study of cardiovascular fluid mechanics is only possible with some knowledge of cardiovascular physiology. In this section a brief introduction to cardiovascular physiology will be given. Some general aspects of the fluid mechanics of the heart, the arterial system, the micro-circulation and the venous system as well as the most important properties of the vascular tree that determine the pressure and flow characteristics in the cardiovascular system will be dealt with. Although the fluid mechanics of the vascular system is complex due to complexity of geometry and pulsatility of the flow, a simple linear model of this system will be derived.

1.2. Short Overview of the Cardiovascular System

The cardiovascular system takes care of convective transport of blood between the organs of the mammalian body in order to enable diffusive transport of oxygen, carbon oxide, nutrients and other solutes at cellular level in the tissues. Without this convective transport an appropriate exchange of these solutes would be impossible because of a too large diffusional resistance. An extended overview of physiological processes that are enabled by virtue of the cardiovascular system can be found in standard text books on physiology like [3].

The circulatory system can be divided into two parts in series, the pulmonary circulation and the systemic circulation (see Fig. 1). Blood received by the right atrium (RA) from the vena cavae is pumped from the right ventricle (RV) of the heart into the pulmonary artery which strongly bifurcates in pulmonary arterioles transporting the blood to the lungs. The left atrium (LA) receives the oxygenated blood back from the pulmonary veins. Then the blood is pumped via the left ventricle (LV) into the systemic circulation. As from fluid mechanical point of view the main flow phenomena in the pulmonary circulation match the phenomena in the systemic circulation, in the sequel of this course only the systemic circulation will be considered.

1.2.1. The heart. The forces needed for the motion of the blood are provided by the heart, which serves as a four-chambered pump that propels blood around the circulatory system (see Fig. 1). Since the mean pressure in

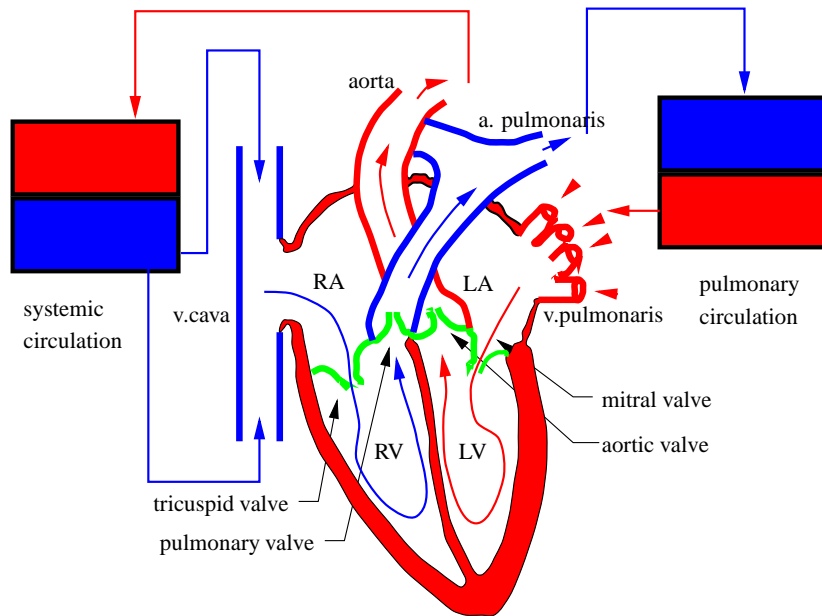


FIGURE 1. Schematic representation of the heart and the circulatory system.

RA = right atrium, LA = left atrium, RV = right ventricle, LV = left ventricle.

the systemic circulation is approximately 13 kPa, which is more than three times the pressure in the pulmonary system ($\approx 4 \text{ kPa}$), the thickness of the left ventricular muscle is much larger than that of the right ventricle.

The ventricular and aortic pressure and aortic flow during the cardiac cycle are given in Fig. 2. Atrial contraction, induced by a stimulus for muscle contraction of the sinoatrial node, causes a filling of the ventricles with hardly any increase of the ventricular pressure. In the left heart the mitral valve is opened and offers very low resistance. The aortic valve is closed. Shortly after this, at the onset of systole the two ventricles contract simultaneously controlled by a stimulus generated by the atrioventricular node. At the same time the mitral valve closes (mc) and a sharp pressure rise in the left ventricle occurs. At the moment that this ventricular pressure exceeds the pressure in the aorta, the aortic valve opens (ao) and blood is ejected into the aorta. The ventricular and aortic pressure first rise and then fall as a result of a combined action of ventricular contraction forces and the resistance and compliance of the systemic circulation. Due to this pressure fall (or actually the corresponding flow deceleration) the aortic valve closes (ac) and the pressure in the ventricle drops rapidly, the mitral valve opens (mo), while the heart muscle relaxes (diastole).

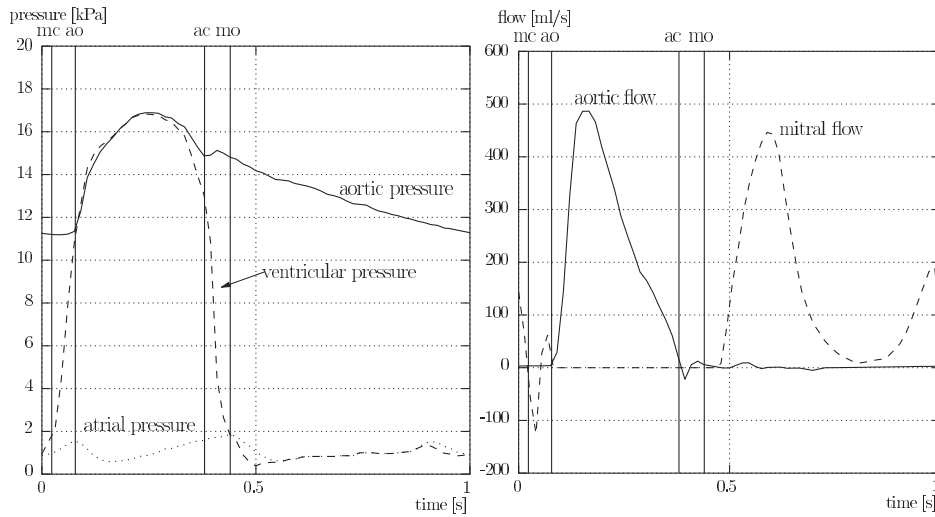


FIGURE 2. Pressure in the left atrium, left ventricle and the aorta (left) and flow through the mitral valve and the aorta (right) as a function of time during one cardiac cycle, after [4]. With times: mc = mitral valve closes, ao = aortic valve opens, ac = aortic valve closes and mo = mitral valve opens.

Since, in the heart, both the blood flow velocities as well as the geometrical length scales are relatively large, the fluid mechanics of the heart is strongly determined by inertial forces which are in equilibrium with pressure forces.

1.2.2. The systemic circulation. The systemic circulation can be divided into three parts: the arterial system, the capillary system and the venous system. The main characteristics of the systemic circulation are depicted schematically in Fig. 3.

From Fig. 3 it can be seen that the diameter of the blood vessels strongly decrease from the order of 0.5–20 mm in the arterial system to 5–500 μm in the capillary system. The diameters of the vessels in the venous system in general are slightly larger than those in the arterial system. The length of the vessels also strongly decreases and increases going from the arterial system to the venous system but only changes in two decades. Most dramatic changes can be found in the number of vessels that belong to the different compartments of the vascular system. The number of vessels in the capillary system is of order $O(10^6)$ larger than in the arterial and venous system. As a consequence, the total cross section in the capillary system is about 1000 times larger than in the arterial and the venous system, enabling an

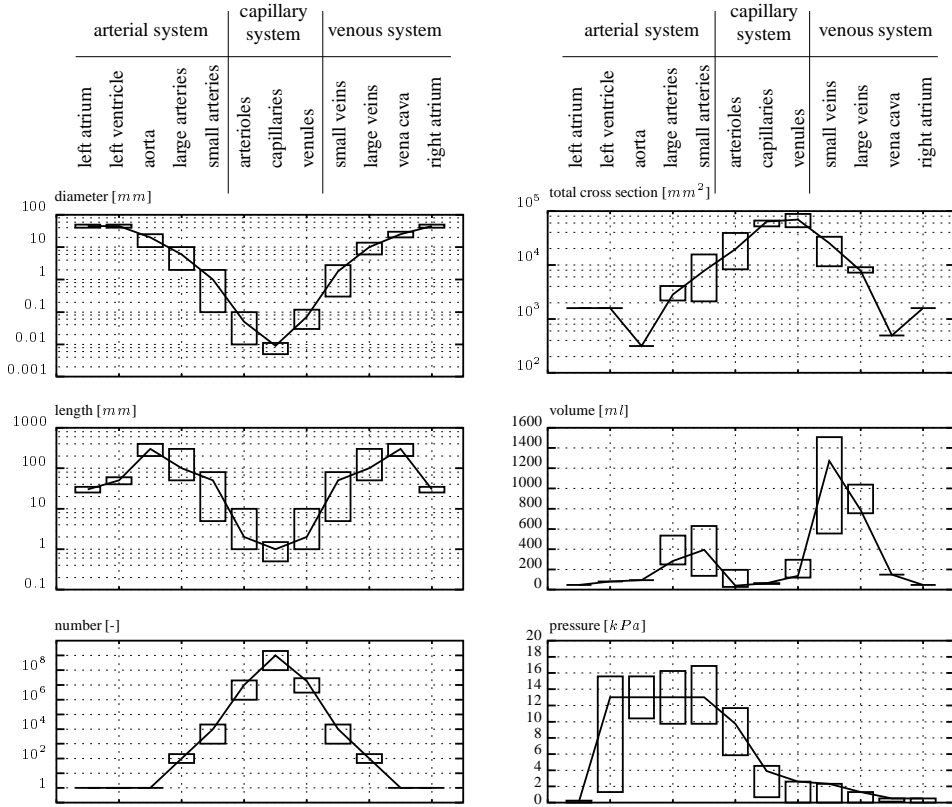


FIGURE 3. Rough estimates of the diameter, length and number of vessels, their total cross-section and volume and the pressure in the vascular system.

efficient exchange of solutes in the tissues by diffusion. Combination of the different dimensions mentioned above shows that the total volume of the venous system is about 2 times larger than the volume of the arterial system and much larger than the total volume of the capillary system. As can be seen from the last figure, the mean pressure falls gradually as blood flows into the systemic circulation. The pressure amplitude, however, shows a slight increase in the proximal part of the arterial system.

The *arterial system* is responsible for the transport of blood to the tissues. Besides the transport function of the arterial system the pulsating flow produced by the heart is also transformed to a more-or-less steady flow in the smaller arteries. Another important function of the arterial system is to maintain a relatively high arterial pressure. This is of importance for a proper functioning of the brain and kidneys. This pressure can be kept

at this relatively high value because the distal end of the arterial system strongly bifurcates into vessels with small diameters (arterioles) and hereby forms a large peripheral resistance. The smooth muscle cells in the walls are able to change the diameter and hereby the resistance of the arterioles. In this way the circulatory system can adopt the blood flow to specific parts in accordance to momentary needs (vasoconstriction and vasodilatation). Normally the heart pumps about 5 liters of blood per minute but during exercise the heart minute volume can increase to 25 liters. This is partly achieved by an increase of the heart frequency but is mainly made possible by local regulation of blood flow by vasoconstriction and vasodilatation of the distal arteries (arterioles). Unlike the situation in the heart, in the arterial system, also viscous forces may become of significant importance as a result of a decrease in characteristic velocity and length scales (diameters of the arteries).

Leaving the arterioles the blood flows into the *capillary system*, a network of small vessels. The walls consist of a single layer of endothelial cells lying on a basement membrane. Here an exchange of nutrients with the interstitial liquid in the tissues takes place. In physiology, capillary blood flow is mostly referred to as micro circulation. The diameter of the capillaries is so small that the whole blood may not be considered as a homogeneous fluid anymore. The blood cells are moving in a single file (train) and strongly deform. The plasma acts as a lubrication layer. The fluid mechanics of the capillary system hereby strongly differs from that of the arterial system and viscous forces dominate over inertia forces in their equilibrium with the driving pressure forces.

Finally the blood is collected in the *venous system* (vessels and veins) in which the vessels rapidly merge into larger vessels transporting the blood back to the heart. The total volume of the venous system is much larger than the volume of the arterial system. The venous system provides a storage function which can be controlled by constriction of the veins (venoconstriction) that enables the heart to increase the arterial blood volume. As the diameters in the venous system are of the same order of magnitude as in the arterial system, inertia forces may become influential again. Both characteristic velocities and pressure amplitudes, however, are lower than in the arterial system. As a consequence, in the venous system, instationary inertia forces will be of less importance than in the arterial system. Moreover, the pressure in the venous system is so low that gravitational forces become of importance.

The geometrical dimensions referred to above and summarized in Fig. 3 show that the vascular tree is highly bifurcating and will be geometrically complex. Flow phenomena related with curvature and bifurcation of the vessels (see Sec. 2) can not be neglected. As in many cases the length of the vessels is small compared to the length needed for fully developed flow, also entrance flow must be included in studies of cardiovascular fluid mechanics.

1.3. Pressure and Flow in the Cardiovascular System

1.3.1. Pressure and flow waves in arteries. The pressure in the aorta significantly changes with increasing distance from the heart. The peak of the pressure pulse delays downstream indicating wave propagation along the aorta with a certain wave speed. Moreover, the shape of the pressure pulse changes and shows an increase in amplitude, a steepening of the front and only a moderate fall of the mean pressure (see Fig. 4).

This wave phenomenon is a direct consequence of the distensibility of the arterial wall, allowing a partial storage of the blood injected from the heart due to an increase of the pressure and the elastic response of the vessel walls. The cross-sectional area of the vessels depends on the pressure difference

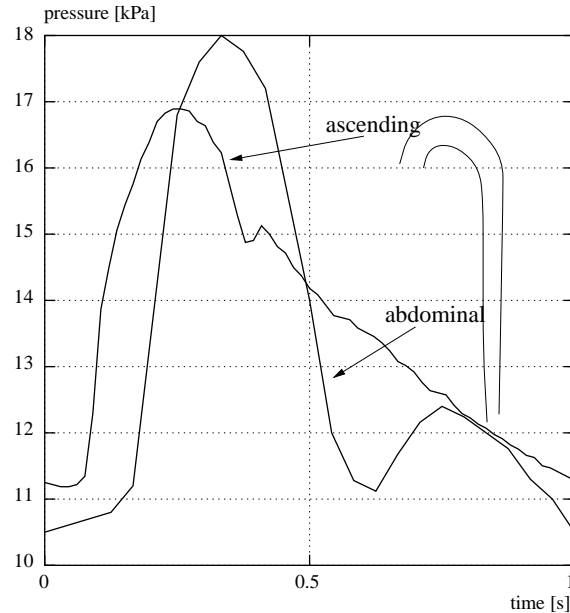


FIGURE 4. Typical pressure waves at two different sites in the aorta

over the wall. This pressure difference is called the transmural pressure and is denoted by p_{tr} . This transmural pressure consists of several parts. First, there exists a hydrostatic part proportional to the density of the blood inside ρ , the gravity force g and the height h . This hydrostatic part is a result of the fact that the pressure outside the vessels is closely to atmospheric. Next, the pressure is composed of a time independent part p_0 and a periodic, time dependent part p . So the transmural pressure can be written as:

$$p_{tr} = \rho q h + p_0 + p. \quad (1.1)$$

Due to the complex nonlinear anisotropic and viscoelastic properties of the arterial wall, the relation between the transmural pressure and the cross sectional area A of the vessel is mostly nonlinear and can be rather complicated. Moreover it varies from one vessel to the other. Important quantities with respect to this relation, used in physiology, are the compliance or alternatively the distensibility of the vessel. The compliance C is defined as:

$$C = \frac{\partial A}{\partial p}. \quad (1.2)$$

For thin wall tubes the following relation can be derived:

$$C = \frac{\partial A}{\partial p} = \frac{2\pi a_0^3 (1 - \mu^2)}{h E}. \quad (1.3)$$

The distensibility D is defined by the ratio of the compliance and the cross sectional area and hereby is given by:

$$D = \frac{1}{A} \frac{\partial A}{\partial p} = \frac{C}{A}. \quad (1.4)$$

In the sequel of this course these quantities will be related to the material properties of the arterial wall. For thin walled tubes, with radius a and wall thickness h , without longitudinal strain, e.g., it can be derived that:

$$D = \frac{2a}{h} \frac{1 - \mu^2}{E}. \quad (1.5)$$

Here μ denotes Poisson's ratio and E Young's modulus. From this we can see that besides the properties of the material of the vessel (E, μ) also geometrical properties (a, h) play an important role.

The value of the ratio a/h varies strongly along the arterial tree. The veins are more distensible than the arteries. Mostly, in some way, the pressure-area

relationship, i.e. the compliance or distensibility, of the arteries or veins that are considered, have to be determined from experimental data. A typical example of such data is given in Fig. 5 where the relative transmural pressure p/p_0 is given as a function of the relative cross-sectional area A/A_0 . As depicted in this figure, the compliance changes with the pressure load since at relatively high transmural pressure, the collagen fibres in the vessel wall become stretched and prevent the artery from further increase of the circumferential strain.

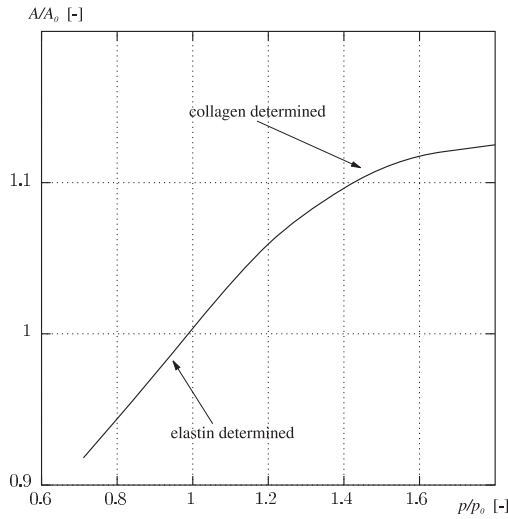


FIGURE 5. Typical relation between the relative transmural pressure p/p_0 and the relative cross-sectional area A/A_0 of an artery.

The flow is driven by the gradient of the pressure and hereby determined by the propagation of the pressure wave. Normally the pressure wave will have a pulsating periodic character. In order to describe the flow phenomena we distinguish between steady and unsteady part of this pulse. Often it is assumed that the unsteady part can be described by means of a linear theory, so that we can introduce the concept of pressure and flow waves which be superpositions of several harmonics:

$$p = \sum_{n=1}^N p_n e^{ni\omega t} \quad q = \sum_{n=1}^N q_n e^{ni\omega t} \quad (1.6)$$

Here p_n and q_n are the complex Fourier coefficients and hereby p and q are the complex pressure and the complex flow, ω denotes the angular frequency of the basic harmonic. Actual pressure and flow can be obtained by taking

the real part of these complex functions. Normally spoken 6 to 10 harmonics are sufficient to describe the most important features of the pressure wave. Table 1 is adopted from [4] and represents the modulus and phase of the first 10 harmonics of the pressure and flow in the aorta. The corresponding pressure and flow are given in Fig. 6.

TABLE 1. First 10 harmonics of the pressure and flow in the aorta, from [4].

harmonic	q in ml/s		p in mm Hg	
	modulus	phase	modulus	phase
0	110	0	85	0
1	202	-0.78	18.6	-1.67
2	157	-1.50	8.6	-2.25
3	103	-2.11	5.1	-2.61
4	62	-2.46	2.9	-3.12
5	47	-2.59	1.3	-2.91
6	42	-2.91	1.4	-2.81
7	31	+2.92	1.2	+2.93
8	19	+2.66	0.4	-2.54
9	15	+2.73	0.6	-2.87
10	15	+2.42	0.6	+2.87

1.3.2. Pressure and flow in the micro-circulation. The micro-circulation is a strongly bifurcating network of small vessels and is responsible for the exchange of nutrients and gases between the blood and the tissues. Mostly blood can leave the arterioles in two ways. The first way is to follow a metarteriole towards a specific part of the tissue and enter the capillary system. This second way is to bypass the tissue by entering an arterio venous anastomosis that shortcuts the arterioles and the venules. Smooth muscle cells in the walls of the metarterioles, precapillary sphincters at the entrance of the capillaries and glomus bodies in the anastomoses regulate the local distribution of the flow. In contrast with the arteries the pressure in the micro-vessels is more or less constant in time yielding an almost steady flow. This steadiness, however, is strongly disturbed by the ‘control actions’ of the regulatory system of the micro-circulation. As the dimensions of the blood cells are of the same order as the diameter of the micro-vessels the flow and deformation properties of the red cells must be taken into account in the modeling of the flow in the micro-circulation (see Sec. 2).

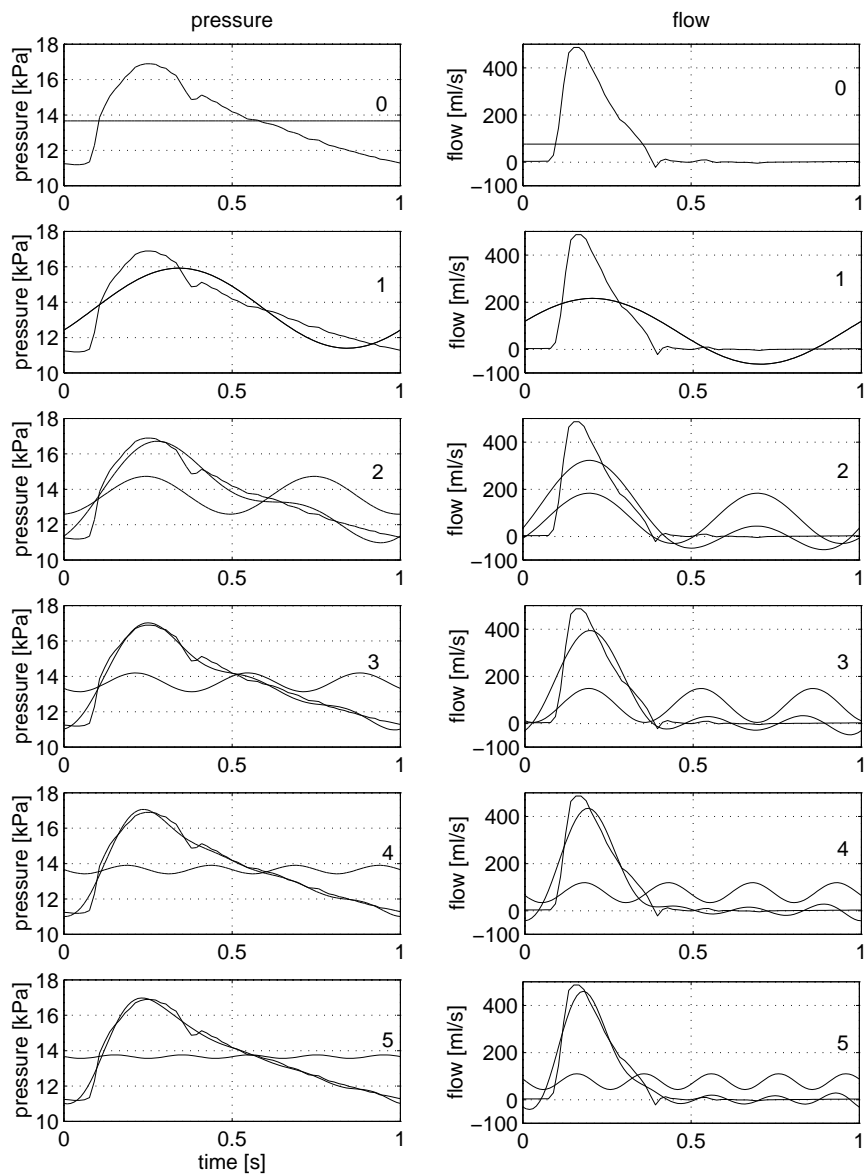


FIGURE 6. Pressure and flow in the aorta based on the data given in Table 1

1.3.3. Pressure and flow in the venous system. The morphology of the systemic veins resemble arteries. The wall however is not as thick as in the arteries of the same diameter. Also the pressure in a vein is much lower than the pressure in an artery of the same size. In certain situations the pressure can be so low that in normal functioning the vein will have an elliptic cross-sectional area or even will be collapsed for some time. Apart from its different wall thickness and the relatively low pressures, the veins distinguish from arteries by the presence of valves to prevent back flow.

1.4. Simple Model of the Vascular System

1.4.1. Periodic deformation and flow. In cardiovascular fluid dynamics the flow often may be considered as periodic if we assume a constant duration of each cardiac cycle. In many cases, i.e. if the deformation and the flow can be described by a linear theory, the displacements and velocity can be decomposed in a number of harmonics using a Fourier transform:

$$v = \sum_{n=0}^N \hat{v}_n e^{in\omega t}. \quad (1.7)$$

Here \hat{v}_n are the complex Fourier coefficients, ω denotes the angular frequency of the basic harmonic. Note that a complex notation of the velocity is used exploiting the relation:

$$e^{i\omega t} = \cos(\omega t) + i \sin(\omega t) \quad (1.8)$$

with $i = \sqrt{-1}$. The actual velocity can be obtained by taking the real part of the complex velocity. By substitution of relation (1.7) in the governing equations that describe the flow, often an analytical solution can be derived for each harmonic. Superposition of these solution then will give a solution for any periodic flow as long as the equations are linear in the solution v .

1.4.2. The windkessel model. Incorporating some of the physiological properties described above several models for the cardiovascular system has been derived in the past. The most simple model is the one that is known as the *windkessel* model. In this model the aorta is represented by a simple compliance C (elastic chamber) and the peripheral blood vessels are assumed to behave as a rigid tube with a constant resistance (R_p) (see top of Fig. 7).

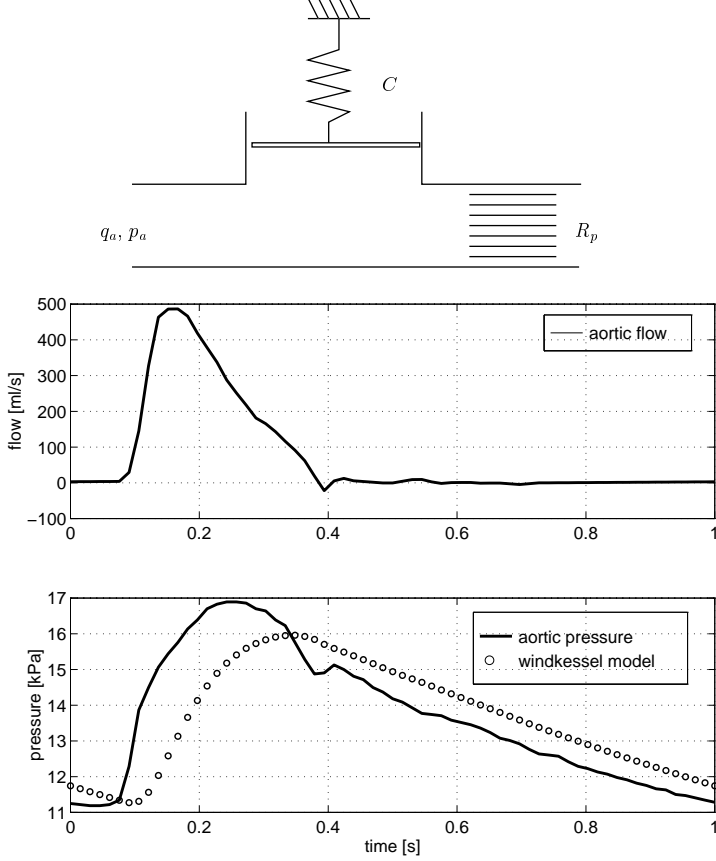


FIGURE 7. Windkessel model of the cardiovascular system (top). Aortic flow and pressure, data from [4] as function of time with pressure obtained from the windkessel model indicated with the dotted line (bottom).

The pressure p_a in the aorta as a function of the left ventricular flow q_a then is given by:

$$q_a = C \frac{\partial p_a}{\partial t} + \frac{p_a}{R_p} \quad (1.9)$$

or after Fourier transformation:

$$\hat{q}_a = (i\omega C + \frac{1}{R_p})\hat{p}_a. \quad (1.10)$$

In the bottom two charts of Fig. 7 experimental data [4] of the flow in the aorta (upper chart) is plotted as a function of time. This flow is used as input for the computation of the pressure from Eq. (1.9) and compared with experimental data (dotted resp. solid line in Fig. 7). The resistance R_p

and compliance C were obtained from a least square fit and turned out to be $R_p = 0.18 \text{ kPa}\cdot\text{s}/\text{ml}$ and $C = 11.5 \text{ ml}/\text{kPa}$.

During the diastolic phase of the cardiac cycle the aortic flow is relatively low and Eq. (1.9) can be approximated by:

$$\frac{\partial p_a}{\partial t} \approx \frac{1}{R_p C} p_a \quad \text{during diastole} \quad (1.11)$$

with solution $p_a \approx p_{as} e^{-t/R_p C}$ with p_{as} peak systolic pressure. This approximate solution reasonably corresponds with experimental data.

During the systolic phase of the flow the aortic flow is much larger than the peripheral flow ($q_a \gg p_a/R_p$) yielding:

$$\frac{\partial p_a}{\partial t} \approx \frac{1}{C} q_a \quad \text{during systole} \quad (1.12)$$

with solution $p_a \approx p_{ad} + (1/C) \int q_a dt$ with p_{ad} the diastolic pressure. Consequently a phase difference between pressure and flow is expected. Experimental data, however, show $p_a \approx p_{ad} + k q_a$, so pressure and flow are more or less in-phase (see Fig. 7). Notwithstanding the significant phase error in the systolic phase, this simple windkessel model is often used to derive the cardiac work at given flow. Note that for linear time-periodic systems, better fits can be obtained using the complex notation (1.10) with frequency dependent resistance ($R_p(\omega)$) and compliance $C(\omega)$).

In Sec. 3 of this course we will show that this model has strong limitations and is in contradiction with important features of the vascular system.

1.4.3. Vascular impedance. As mentioned before the flow of blood is driven by the force acting on the blood induced by the gradient of the pressure. The relation of these forces to the resulting motion of blood is expressed in the longitudinal impedance:

$$Z_L = \frac{\partial \hat{p}}{\partial z} / \hat{q}. \quad (1.13)$$

The longitudinal impedance is a complex number defined by complex pressures and complex flows. It can be calculated by frequency analysis of the pressure gradient and the flow that have been recorded simultaneously. As it expresses the flow induced by a local pressure gradient, it is a property of a small (infinitesimal) segment of the vascular system and depends on local properties of the vessel. The longitudinal impedance plays an important role in the characterization of vascular segments. It can be measured

by a simultaneous determination of the pulsatile pressure at two points in the vessel with a known small longitudinal distance apart from each other together with the pulsatile flow. In Sec. 3 the longitudinal impedance will be derived mathematically using a linear theory for pulsatile flow in rigid and distensible tubes. A second important quantity is the input impedance defined as the ratio of the pressure and the flow at a specific cross-section of the vessel:

$$Z_i = \hat{p}/\hat{q}. \quad (1.14)$$

The input impedance is not a local property of the vessel but a property of a specific site in the vascular system. If some input condition is imposed on a certain site in the system, than the input impedance only depends on the properties of the entire vascular tree distal to the cross-section where it is measured. In general the input impedance at a certain site depends on both the proximal and distal vascular tree. The compliance of an arterial segment is characterized by the transverse impedance defined by:

$$Z_T = \hat{p}/\frac{\partial \hat{q}}{\partial z} \approx -\hat{p}/i\omega \hat{A}. \quad (1.15)$$

This relation expresses the flow drop due to the storage of the vessel caused by the radial motion of its wall (A being the cross-sectional area) at a given pressure (note that $i\omega \hat{A}$ represents the partial time derivative $\partial A/\partial t$). In Sec. 3 it will be shown that the impedance-functions as defined here can be very useful in the analysis of wave propagation and reflection of pressure and flow pulses traveling through the arterial system.

2. Newtonian Flow in Blood Vessels

2.1. Steady and Pulsatile Newtonian Flow in Straight Tubes

In this section the flow patterns in rigid straight, curved and branching tubes will be considered. First, fully developed flow in straight tubes will be dealt with and it will be shown that this uni-axial flow is characterized by two dimensionless parameters, the Reynolds number Re and the Womersley number α , that distinguish between flow in large and small vessels. Also derived quantities, like wall shear stress and vascular impedance, can be expressed as a function of these parameters.

For smaller tube diameters (micro-circulation), however, the fluid can not be taken to be homogeneous anymore and the dimensions of the red blood

cells must be taken into account. In the entrance regions of straight tubes, the flow is more complicated. Estimates of the length of these regions will be derived for steady and pulsatile flow.

The flow in curved tubes is not uni-axial but exhibits secondary flow patterns perpendicular to the axis of the tube. The strength of this secondary flow field depends on the curvature of the tube which is expressed in another dimensionless parameter: the Dean number. Finally it will be shown that the flow in branched tubes shows a strong resemblance to the flow in curved tubes.

2.1.1. Fully Developed Flow

Governing equations

To analyze fully developed Newtonian flow in rigid tubes consider the Navier-Stokes equations in a cylindrical coordinate system:

$$\left\{ \begin{array}{l} \frac{\partial v_r}{\partial t} + v_r \frac{\partial v_r}{\partial r} + v_z \frac{\partial v_r}{\partial z} = -\frac{1}{\rho} \frac{\partial p}{\partial r} + \nu \left(\frac{\partial}{\partial r} \left(\frac{1}{r} \frac{\partial}{\partial r} (rv_r) \right) + \frac{\partial^2 v_r}{\partial z^2} \right), \\ \frac{\partial v_z}{\partial t} + v_r \frac{\partial v_z}{\partial r} + v_z \frac{\partial v_z}{\partial z} = -\frac{1}{\rho} \frac{\partial p}{\partial z} + \nu \left(\frac{1}{r} \frac{\partial}{\partial r} \left(r \frac{\partial}{\partial r} (v_z) \right) + \frac{\partial^2 v_z}{\partial z^2} \right), \\ \frac{1}{r} \frac{\partial}{\partial r} (rv_r) + \frac{\partial v_z}{\partial z} = 0. \end{array} \right. \quad (2.1)$$

Since the velocity in circumferential direction equals zero ($v_\phi = 0$), the momentum equation and all derivatives in ϕ -direction are omitted. For fully developed flow the derivatives of the velocity in axial direction $\frac{\partial}{\partial z}$ and the velocity component in radial direction v_r are zero and Eqs. (2.1) simplify to:

$$\frac{\partial v_z}{\partial t} = -\frac{1}{\rho} \frac{\partial p}{\partial z} + \frac{\nu}{r} \frac{\partial}{\partial r} \left(r \frac{\partial v_z}{\partial r} \right). \quad (2.2)$$

Now a dimensionless velocity can be defined as $v_z^* = v_z/V$, the coordinates can be made dimensionless using the radius of the tube, i.e. $r^* = r/a$ and $z^* = z/a$, the pressure can be scaled as $p^* = p/\rho V^2$ and the time can be scaled using $t^* = \omega t$. Dropping the asterisk, the equation of motion reads:

$$\alpha^2 \frac{\partial v_z}{\partial t} = -\text{Re} \frac{\partial p}{\partial z} + \frac{1}{r} \frac{\partial}{\partial r} \left(r \frac{\partial v_z}{\partial r} \right) \quad (2.3)$$

with Re the Reynolds number given by

$$\text{Re} = \frac{aV}{\nu} \quad (2.4)$$

and α the Womersley number defined as:

$$\alpha = a \sqrt{\frac{\omega}{\nu}}. \quad (2.5)$$

So two dimensionless parameters are involved: the Womersley number α defining the ratio of the non-stationary inertia forces and the viscous forces and the Reynolds number Re that is in this case nothing more than a scaling factor for the pressure gradient. The pressure could also be scaled according to $p^* = p/(a^2/\eta V)$ yielding one single parameter α .

In Table 2 the Womersley numbers for several sites in the arterial system are given. These values show that in the aorta and in the largest arteries inertia dominated flow and in arterioles and capillaries friction dominated flow may be expected. In most part of the arteries an intermediate value of α is found and both inertia and viscous friction are important.

TABLE 2. Estimated Womersley number at several sites of the arterial system based on the first harmonic of the flow. A kinematic viscosity of 5×10^{-3} Pa·s, a density of 10^3 kg·m $^{-3}$ and a frequency of 1 Hz are assumed.

	a [mm]	$\alpha [-]$
aorta	10	10
large arteries	4	4
small arteries	1	1
arterioles	0.1	0.1
capillaries	0.01	0.01

For the venous system a similar dependence of the Womersley number is found but it must be noted that inertia is less important due to the low amplitude of the first and higher harmonics with respect to the mean flow.

Velocity profiles

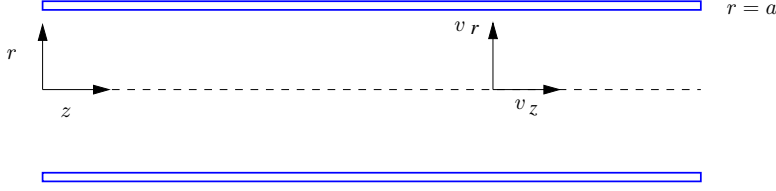
For flow in a rigid tube (see Fig. 8) with radius a the boundary condition $v(a, t) = 0$ is used to impose a no slip condition.

We will assume a harmonic pressure gradient and will search for harmonic solutions:

$$\frac{\partial p}{\partial z} = \frac{\partial \hat{p}}{\partial z} e^{i\omega t} \quad (2.6)$$

and

$$v_z = \hat{v}_z(r) e^{i\omega t}. \quad (2.7)$$

FIGURE 8. Rigid tube with radius a

The solution of an arbitrary periodic function then can be constructed by superposition of its harmonics. This is allowed because the equation to solve (2.3) is linear in v_z .

Now two asymptotic cases can be defined. For small Womersley numbers there is an equilibrium of viscous forces and the driving pressure gradient. For large Womersley numbers, however, the viscous forces are small compared to the instationary inertia forces and there will be an equilibrium between the inertia forces and the driving pressure gradient. Both cases will be considered in more detail.

Small Womersley number flow. If $\alpha \ll 1$ Eq. (2.3) (again in dimension-full form) yields:

$$0 = -\frac{1}{\rho} \frac{\partial p}{\partial z} + \frac{\nu}{r} \frac{\partial}{\partial r} \left(r \frac{\partial v_z}{\partial r} \right). \quad (2.8)$$

Substitution of Eq. (2.6) and (2.7) yields:

$$\nu \frac{\partial^2 \hat{v}_z(r)}{\partial r^2} + \frac{\nu}{r} \frac{\partial \hat{v}_z(r)}{\partial r} = \frac{1}{\rho} \frac{\partial \hat{p}}{\partial z} \quad (2.9)$$

with solution:

$$v_z(r, t) = -\frac{1}{4\eta} \frac{\partial \hat{p}}{\partial z} (a^2 - r^2) e^{i\omega t}. \quad (2.10)$$

So, for low values of the Womersley number a quasi-static Poiseuille profile is found. It oscillates 180° out of phase with the pressure gradient. The shape of the velocity profiles is depicted in the left graph of Fig. 9.

Large Womersley number flow. If the $\alpha \gg 1$ Eq. (2.3) yields:

$$\frac{\partial v_z}{\partial t} = -\frac{1}{\rho} \frac{\partial p}{\partial z}. \quad (2.11)$$

Substitution of Eq. (2.6) and (2.7) yields:

$$i\omega \hat{v}_z(r) = -\frac{1}{\rho} \frac{\partial \hat{p}}{\partial z} \quad (2.12)$$

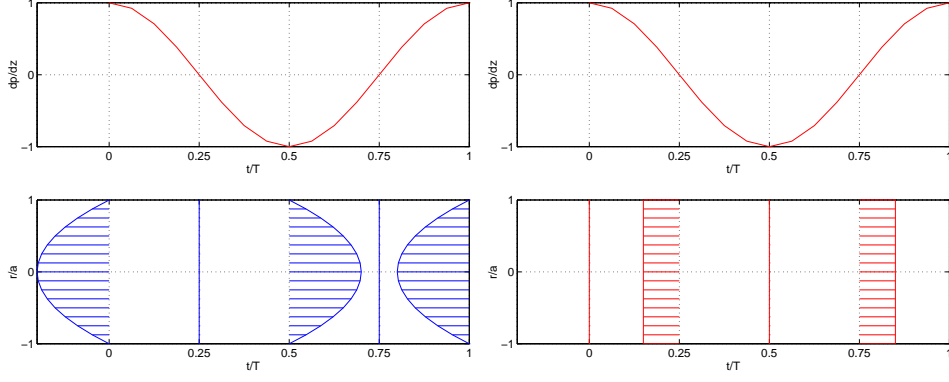


FIGURE 9. Pressure gradient (top) and corresponding velocity profiles (bottom) as a function of time for small (left) and large (right) Womersley numbers.

with solution:

$$v_z(r, t) = \frac{i}{\rho\omega} \frac{\partial \hat{p}}{\partial z} e^{i\omega t}. \quad (2.13)$$

Now, for high values of the Womersley number, an oscillating plug flow is found which is 90° out of phase with the pressure gradient (right graph of Fig. 9). The flow is dominated by inertia.

Arbitrary Womersley number flow. Substitution of Eq. (2.6) and (2.7) in Eq. (2.2) yields:

$$\nu \frac{\partial^2 \hat{v}_z(r)}{\partial r^2} + \frac{\nu}{r} \frac{\partial \hat{v}_z(r)}{\partial r} - i\omega \hat{v}_z(r) = \frac{1}{\rho} \frac{\partial \hat{p}}{\partial z}. \quad (2.14)$$

Substitution of

$$s = i^{3/2} \alpha r/a \quad (2.15)$$

in the homogeneous part of this equation yields the equation of Bessel for $n = 0$:

$$\frac{\partial^2 \hat{v}_z}{\partial s^2} + \frac{1}{s} \frac{\partial \hat{v}_z}{\partial s} + \left(1 - \frac{n^2}{s^2}\right) \hat{v}_z = 0 \quad (2.16)$$

with solution given by the Bessel functions of the first kind:

$$J_n(s) = \sum_{k=0}^{\infty} \frac{(-1)^k}{k!(n+k)!} \left(\frac{s}{2}\right)^{2k+n} \quad (2.17)$$

so:

$$J_0(s) = \sum_{k=0}^{\infty} \frac{(-1)^k}{k!k!} \left(\frac{s}{2}\right)^{2k} = 1 - \left(\frac{s}{2}\right)^2 + \frac{1}{1^2 2^2} \left(\frac{s}{2}\right)^4 - \frac{1}{1^2 2^2 3^2} \left(\frac{s}{2}\right)^6 + \dots \quad (2.18)$$

see also [1]. Together with the particular solution:

$$\hat{v}_z^p = \frac{i}{\rho\omega} \frac{\partial \hat{p}}{\partial z} \quad (2.19)$$

we have:

$$\hat{v}_z(s) = K J_0(s) + \hat{v}_z^p. \quad (2.20)$$

Using the boundary condition $\hat{v}_z(a) = 0$ then yields:

$$K = -\frac{\hat{v}_z^p}{J_0(\alpha i^{3/2})} \quad (2.21)$$

and finally:

$$\hat{v}_z(r) = \frac{i}{\rho\omega} \frac{\partial \hat{p}}{\partial z} \left[1 - \frac{J_0(i^{3/2}\alpha r/a)}{J_0(i^{3/2}\alpha)} \right]. \quad (2.22)$$

These are the well known Womersley profiles, [8] displayed in Fig. 10. As can be seen from this figure, the Womersley profiles for intermediate

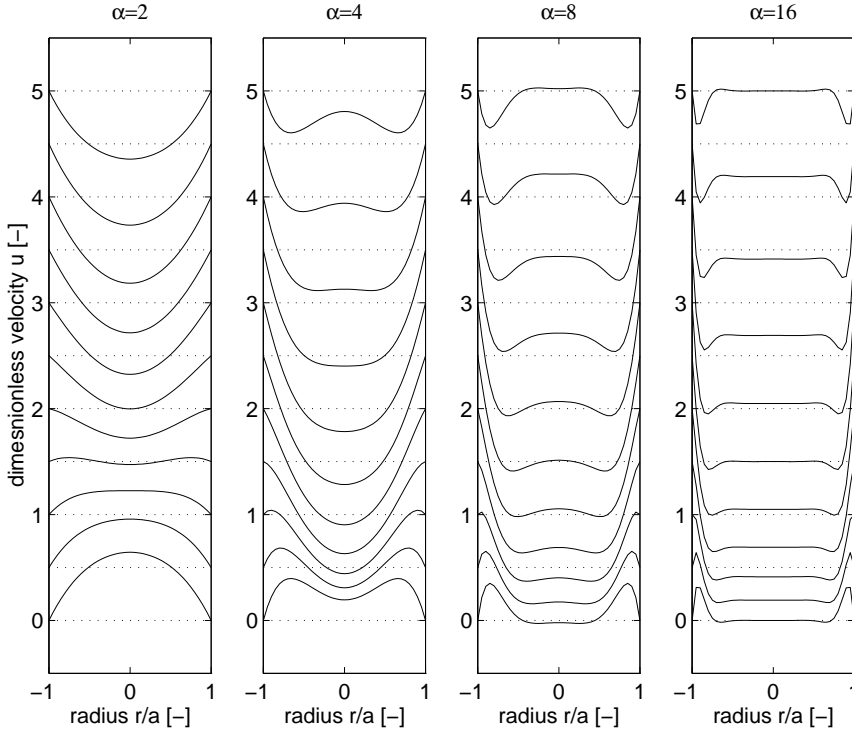


FIGURE 10. Womersley profiles for different Womersley numbers ($\alpha = 2, 4, 8, 16$)

Womersley numbers are characterized by a phase-shift between the flow in the boundary layer and the flow in the central core of the tube. Actually, in the boundary layer viscous forces dominate the inertia forces and the flow behaves like the flow for small Womersley numbers. For high enough Womersley numbers, in the central core, inertia forces are dominant and flattened profiles that are shifted in phase are found. The thickness of the non-stationary boundary layer is determined by the Womersley number. This will be discussed in more detail in Sec. 2.1.2.

Wall shear stress

Using the property of Bessel functions, see [1]

$$\frac{\partial J_0(s)}{\partial s} = -J_1(s) \quad (2.23)$$

and the definition of the Womersley function

$$F_{10}(\alpha) = \frac{2J_1(i^{3/2}\alpha)}{i^{3/2}\alpha J_0(i^{3/2}\alpha)} \quad (2.24)$$

the wall shear stress defined as:

$$\tau_w = -\eta \left. \frac{\partial v_z}{\partial r} \right|_{r=a} \quad (2.25)$$

can be derived as:

$$\tau_w = -\frac{a}{2} F_{10}(\alpha) \frac{\partial p}{\partial z} = F_{10}(\alpha) \tau_w^p \quad (2.26)$$

with τ_w^p the wall shear stress for Poiseuille flow. In Fig. 11 the function $F_{10}(\alpha)$ and thus a dimensionless wall shear stress τ_w/τ_w^p is given as a function of α .

Remark 1.

$$J_1(s) = \sum_{k=0}^{\infty} \frac{(-1)^k}{k!(1+k)!} \left(\frac{s}{2}\right)^{2k+1} = \left(\frac{s}{2}\right) - \frac{1}{1^2 2} \left(\frac{s}{2}\right)^3 + \frac{1}{1^2 2^2 3} \left(\frac{s}{2}\right)^5 + \dots \quad (2.27)$$

In many cases, for instance to investigate limiting values for small and large values of α , it is convenient to approximate the Womersley function with:

$$F_{10}(\alpha) \approx \frac{(1+\beta)^{1/2}}{(1+\beta)^{1/2} + 2\beta} \quad \text{with} \quad \beta = \frac{i\alpha^2}{16}. \quad (2.28)$$

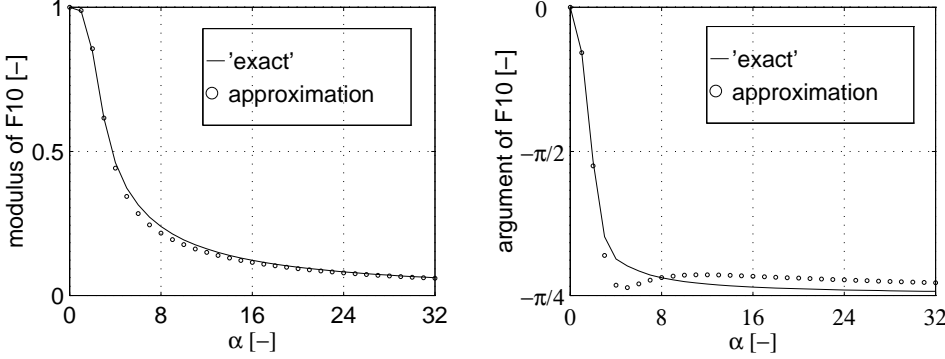


FIGURE 11. Modulus (left) and argument (right) of the function $F_{10}(\alpha)$ or τ_w/τ_w^p as a function of α . The approximations are indicated with dotted and dashed lines.

This approximation is plotted with dotted lines in Fig. 11. For small values of the Womersley number ($\alpha < 3$) the following approximation derived from Eq. (2.28) can be used:

$$F_{10}(\alpha) \approx \frac{1}{1 + 2\beta} = \frac{1}{1 + i\alpha^2/8} \quad (2.29)$$

whereas for large values ($\alpha > 15$) one may use:

$$F_{10}(\alpha) \approx \frac{1}{2}\beta^{-1/2} = \frac{(1 - i)\sqrt{2}}{\alpha}. \quad (2.30)$$

These two approximations are plotted with dashed lines in Fig. 11. Note that the dimensionless wall shear stress for large values of α approximates zero and not ∞ that one could conclude from the steep gradients in the velocity profiles in Fig. 10.

The mean flow q can be derived using the property, see [1]:

$$s \frac{\partial J_n(s)}{\partial s} = -n J_n(s) + s J_{n-1}(s). \quad (2.31)$$

For $n = 1$ it follows that:

$$s J_0(s) ds = d(s J_1(s)) \quad (2.32)$$

and together with $J_1(0) = 0$ the flow becomes:

$$\begin{aligned} q &= \int_0^a \hat{v}_z 2\pi r dr = i \frac{\pi a^2}{\rho \omega} [1 - F_{10}(\alpha)] \frac{\partial p}{\partial z} = [1 - F_{10}(\alpha)] \hat{q}_\infty \\ &\quad = \frac{8i}{\alpha^2} [1 - F_{10}(\alpha)] \hat{q}_p \quad (2.33) \end{aligned}$$

with

$$\hat{q}_\infty = \frac{i\pi a^2}{\rho \omega} \frac{\partial \hat{p}}{\partial z} \quad \text{and} \quad \hat{q}_p = \frac{\pi a^4}{8\eta} \frac{\partial \hat{p}}{\partial z}. \quad (2.34)$$

Combining Eq. (2.26) with Eq. (2.33) by elimination of $\partial p / \partial z$ finally yields:

$$\tau_w = \frac{a}{2A} i\omega \rho \frac{F_{10}(\alpha)}{1 - F_{10}(\alpha)} q. \quad (2.35)$$

With $A = \pi a^2$ the cross-sectional area of the tube. In the next section this expression for the wall shear stress will be used to approximate the shear forces that the fluid exerts on the wall of the vessel.

Vascular impedance

The longitudinal impedance defined as:

$$Z_L = - \frac{\partial p}{\partial z} \frac{1}{q} \quad (2.36)$$

can be derived directly from Eq. (2.33) and reads:

$$Z_L = i\omega \frac{\rho}{\pi a^2} \frac{1}{1 - F_{10}(\alpha)}. \quad (2.37)$$

For a Poiseuille profile the longitudinal impedance is defined by integration of Eq. (2.10) and is given by:

$$Z_p = \frac{8\eta}{\pi a^4}. \quad (2.38)$$

From this it can be derived that the impedance of a rigid tube for oscillating flow related to the impedance for steady flow (Poiseuille resistance) is given by the following equation:

$$\frac{Z_L}{Z_p} = \frac{i\alpha^2}{8} \frac{1}{1 - F_{10}(\alpha)}. \quad (2.39)$$

In Fig. 12 the relative impedance is plotted as a function of the Womersley number α . The relative longitudinal impedance is real for $\alpha \ll 1$ and becomes imaginary for $\alpha \rightarrow \infty$. This expresses the fact that for low frequencies (or small diameters) the viscous forces are dominant, whereas for high frequencies (or large diameters) inertia is dominant and the flow behaves as an inviscid flow.

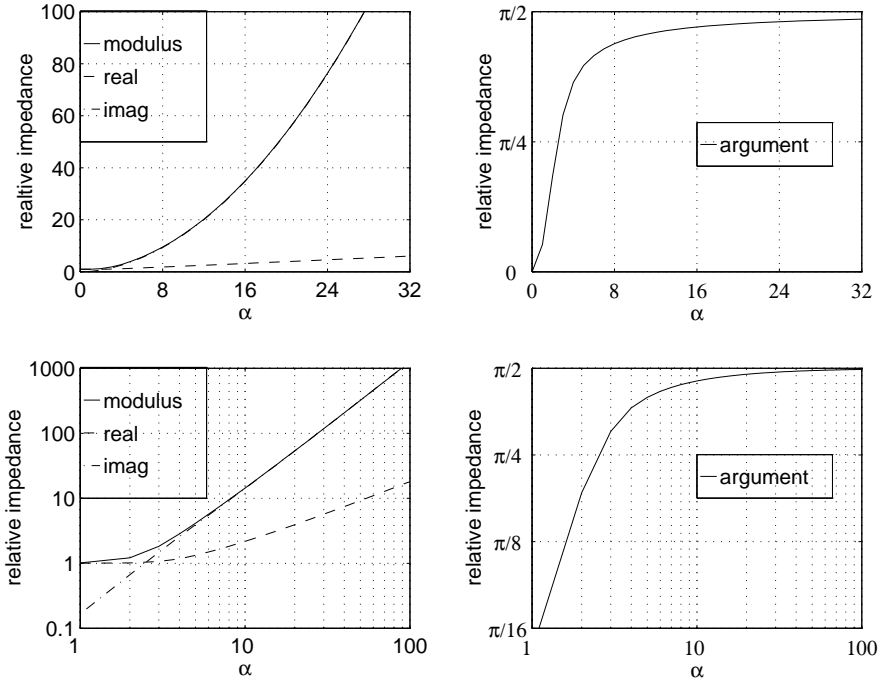


FIGURE 12. The relative impedance for oscillating flow in a tube (linear scale at the top and logarithmic scale at the bottom) as a function of α .

For small values of α the relative impedance results in (see 2.29):

$$\frac{Z_L(\alpha < 3)}{Z_p} \approx 1 + \frac{i\alpha^2}{8}. \quad (2.40)$$

Viscous forces then dominate and the pressure gradient is in phase with the flow and does not (strongly) depend on alpha. For large values of α Eq. (2.30) gives:

$$\frac{Z_L(\alpha > 15)}{Z_p} \approx \frac{i\alpha^2}{8} \quad (2.41)$$

indicating that the pressure gradient is out of phase with the flow and increases quadratically with α .

2.1.2. Entrance flow. In general the flow in blood vessels is not fully developed. Due to transitions and bifurcations the velocity profile has to develop from a certain profile at the entrance of the tube (see Fig. 13).

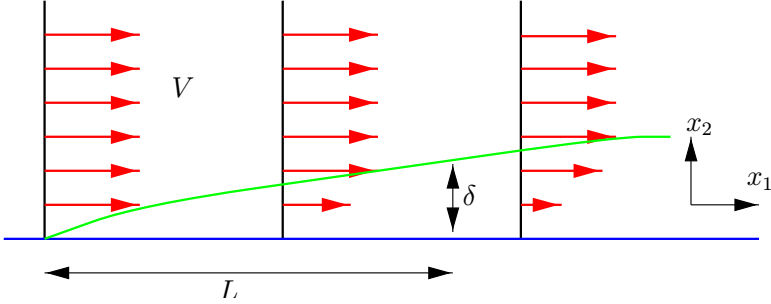


FIGURE 13. Development of a boundary layer

In order to obtain an idea of the length needed for the flow to develop, the flow with a characteristic velocity V along a smooth boundary with characteristic length L is considered. Viscous forces only play an important role in the small boundary layer with thickness δ . Outside the boundary layer the flow is assumed to be inviscid so that Bernoulli's law can be applied. From this configuration simplified Navier-Stokes equations can be derived by assuming that $\delta \ll L$ and the order of magnitude of its terms can be estimated:

$$\left\{ \begin{array}{l} \frac{\partial v_1}{\partial x_1} + \frac{\partial v_2}{\partial x_2} = 0, \\ O\left(\frac{V}{L}\right) \quad O\left(\frac{v}{\delta}\right), \\ \rho \frac{\partial v_1}{\partial t} + \rho v_1 \frac{\partial v_1}{\partial x_1} + \rho v_2 \frac{\partial v_1}{\partial x_2} = -\frac{\partial p}{\partial x_1} + \eta \frac{\partial^2 v_1}{\partial x_1^2} + \eta \frac{\partial^2 v_1}{\partial x_2^2}, \\ O(\omega V) \quad O\left(\frac{V^2}{L}\right) \quad O\left(\frac{V^2}{L}\right) \quad O\left(\frac{1}{\rho} \frac{\partial p}{\partial x}\right) \quad O\left(\frac{\nu V}{L^2}\right) \quad O\left(\nu V/\delta^2\right). \end{array} \right. \quad (2.42)$$

This shows clearly that the diffusive forces are determined by second order derivatives of the velocity normal to the boundary. Moreover it can be seen that the stationary inertia forces are of the same order of magnitude as the viscous forces (which is the case at the boundary layer $x_2 = \delta$) as long as:

$$O\left(\frac{\nu V}{\delta^2}\right) = O\left(\frac{V^2}{L}\right). \quad (2.43)$$

Steady flow

If the entrance length of the flow in a tube is defined as the length needed for the boundary layer to contain the complete cross section, i.e. $\delta = a$, then the ratio of the entrance length and the radius of the tube follows from the equation above as:

$$\frac{L_e}{a} = O\left(\frac{aV}{\nu}\right), \quad (2.44)$$

or with the definition of the Reynolds number $Re = 2aV/\nu$ the dimensionless entrance length $L_e/2a$ is found to be proportional to the Reynolds number:

$$\frac{L_e}{2a} = O(Re). \quad (2.45)$$

In [6] one can find that for laminar flow, for $L_e : v(L_e, 0) = 0.99 \cdot 2V$:

$$\frac{L_e}{2a} = 0.056Re. \quad (2.46)$$

For steady flow in the carotid artery, for instance, $Re = 300$, and thus $L_e \approx 40a$. This means that the flow will never become fully developed since the length of the carotid artery is much less than 40 times its radius. In arterioles and smaller vessels, however, $Re < 10$ and hereby $L_e < a$, so fully developed flow will be found in many cases.

Oscillating flow

For oscillating flow the inlet length is smaller as compared to the inlet length for steady flow. This can be seen from the following. The unsteady inertia forces are of the same magnitude as the viscous forces when:

$$O(V\omega) = O\left(\frac{\nu V}{\delta^2}\right) \quad (2.47)$$

and thus:

$$\delta = O\left(\sqrt{\frac{\nu}{\omega}}\right). \quad (2.48)$$

This means that for fully developed oscillating flow a boundary layer exists with a relative thickness of:

$$\frac{\delta}{a} = O(\alpha^{-1}). \quad (2.49)$$

If, for oscillating flow, the inlet length is defined as the length for which the viscous forces still are of the same magnitude as the stationary inertia forces, i.e.:

$$O\left(\frac{\nu V}{\delta^2}\right) = O\left(\frac{V^2}{L_e}\right) \quad (2.50)$$

then together with Eq. (2.49) the inlet length is of the order

$$L_e = O\left(\frac{V\delta^2}{\nu}\right) = O\left(\frac{a}{\alpha^2 \text{Re}}\right). \quad (2.51)$$

Note that this holds only for $\alpha > 1$. For $\alpha < 1$ the boundary layer thickness is restricted to the radius of the tube and we obtain an inlet length of the same magnitude as for steady flow.

2.2. Steady and Pulsating Flow in Curved and Branched Tubes

2.2.1. Steady flow in a curved tube

Steady entrance flow in a curved tube

The flow in a curved tube is determined by an equilibrium of convective forces, pressure forces and viscous forces. Consider, the entrance flow in a curved tube with radius a and a radius of curvature R_0 . With respect to the origin O we can define a cylindrical coordinate system (R, z, ϕ) . At the entrance (A: $R_0 - a < R < R_0 + a$, $-a < z < a$, $\phi = 0$) a uniformly distributed irrotational (plug) flow $v_\phi = V$ (see Fig. 14) is assumed. As long as the boundary layer has not yet developed ($R_0\phi \ll 0.1a \text{Re}$) the viscous forces are restricted to a very thin boundary layer and the velocity is restricted to one component, v_ϕ . The other components (v_R and v_z) are small compared to v_ϕ . In the core the flow is inviscid so Bernoulli's law can be applied:

$$p + \frac{1}{2}\rho v_\phi^2 = \text{constant}. \quad (2.52)$$

With p the pressure, and ρ the density of the fluid. The momentum equation in R -direction shows an equilibrium of pressure forces and centrifugal forces:

$$\frac{\partial p}{\partial R} = \frac{\rho v_\phi^2}{R}. \quad (2.53)$$

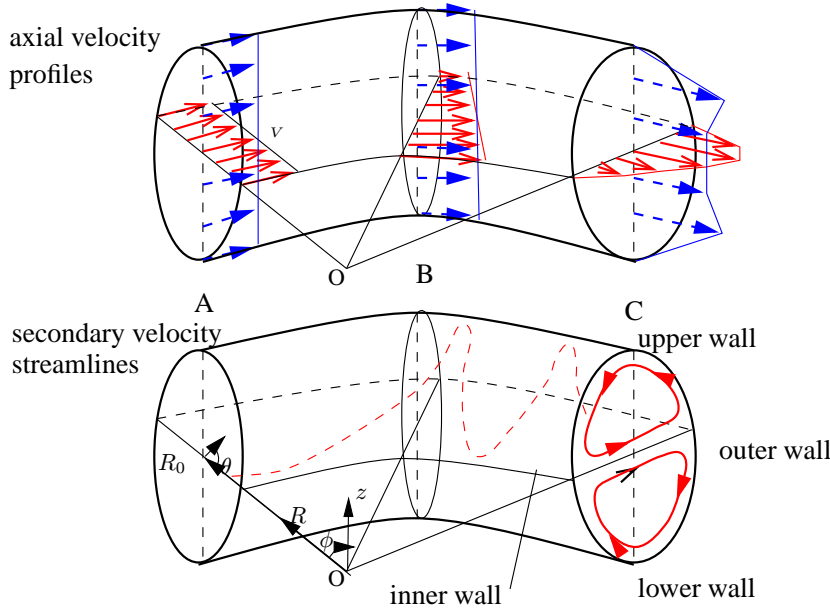


FIGURE 14. Axial velocity profiles, secondary velocity streamlines and helical motion of particles for entrance flow in a curved tube.

As a consequence, the pressure is largest at the outer wall and smallest at the inner wall. Together with Bernoulli's law it follows that the velocity will become largest at the inner wall and lowest at the outer wall of the tube (see Fig. 14 location (B)). Indeed, elimination of the pressure from Eq. (2.52) and Eq. (2.53) yields:

$$\frac{\partial v_\phi}{\partial R} = -\frac{v_\phi}{R} \quad (2.54)$$

and thus:

$$v_\phi = \frac{k_1}{R}. \quad (2.55)$$

The constant k_1 can be determined from the conservation of mass in the plane of symmetry ($z = 0$):

$$2aV = \int_{R_0-a}^{R_0+a} v_\phi(R')dR' = k_1 \ln \frac{R_0 + a}{R_0 - a} \quad (2.56)$$

and thus:

$$k_1 = \frac{2aV}{\ln \frac{1+\delta}{1-\delta}} \quad (2.57)$$

with $\delta = a/R_0$. So in the entrance region ($\phi \ll 0.1\delta \text{Re}$) initially the following velocity profile will develop:

$$v_\phi(R) = \frac{2aV}{R \ln \frac{1+\delta}{1-\delta}}. \quad (2.58)$$

It is easy to derive that for small values of δ this reduces to $v_\phi(R) = (R_0/R)V$.

Note that the velocity profile does only depend on R and does not depend on the azimuthal position θ in the tube. In terms of the toroidal coordinate system (r, θ, ϕ) we have:

$$R(r, \theta) = R_0 - r \cos \theta \quad (2.59)$$

and the velocity profile given in Eq. (2.58) is:

$$v_\phi(r, \theta) = \frac{2aV}{(R_0 - r \cos \theta) \ln \frac{1+\delta}{1-\delta}} = \frac{2\delta V}{(1 - \delta(r/a) \cos \theta) \ln \frac{1+\delta}{1-\delta}}. \quad (2.60)$$

Again for small values of δ this reduces to

$$v_\phi(r, \theta) = \frac{V}{1 - \delta(r/a) \cos \theta}.$$

Going more downstream, due to viscous forces a boundary layer will develop along the walls of the tube and will influence the complete velocity distribution. Finally the velocity profile will look like the one that is sketched at position C. This profile does depend on the azimuthal position. In the plane of symmetry it will have a maximum that is shifted to the outer wall. In the direction perpendicular to the plane of symmetry an M-shaped profile will be found (see Fig. 14). This velocity distribution can only be explained if we also consider the secondary flow field, i.e. the velocity components in the plane of a cross-section ($\phi = \text{const.}$) of the tube perpendicular to the axis.

Viscous forces will diminish the axial velocity in the boundary layer along the wall of the curved tube. As a result, the equilibrium between the pressure gradient in R -direction and the centrifugal forces will be disturbed. In the boundary layers we will have $\rho V^2/R < \partial p / \partial R$ and in the central core $\rho V^2/R > \partial p / \partial R$. Consequently the fluid particles in the central core will accelerate towards the outer wall, whereas fluid particles in the boundary layer will accelerate in opposite direction. In this way a secondary vortex will develop as indicated in Fig. 14. This motion of fluid particles from the inner wall towards the outer wall in the core and along the upper and lower

walls back to the inner wall will have consequences for the axial velocity distribution. Particles with a relatively large axial velocity will move to the outer wall and due to convective forces, the maximum of the axial velocity will shift in the same direction. On the other hand, particles in the boundary layer at the upper and lower walls will be transported towards the inner wall and will convect a relatively low axial velocity. In this way in the plane of symmetry an axial velocity profile will develop with a maximum at the outer wall, and a minimum at the inner wall. For large curvatures or large Reynolds numbers even negative axial velocity at the inner wall can occur due to boundary layer separation.

Once the maximum of the axial velocity is located near the outer wall, the secondary flow will transport particles with a relatively large axial velocity along the upper and lower walls and a C-shaped axial velocity contour will develop. This can clearly be seen in Fig. 15 where for different curvatures of the tube contour plots of the axial velocity and streamlines of the secondary velocity are given. Note that the combination of the axial and secondary flow results in a helical movement of the fluid particles (see Fig. 14). While moving in downstream direction the particles move from the inner wall towards the outer wall and back to the inner wall along the upper (or lower) wall.

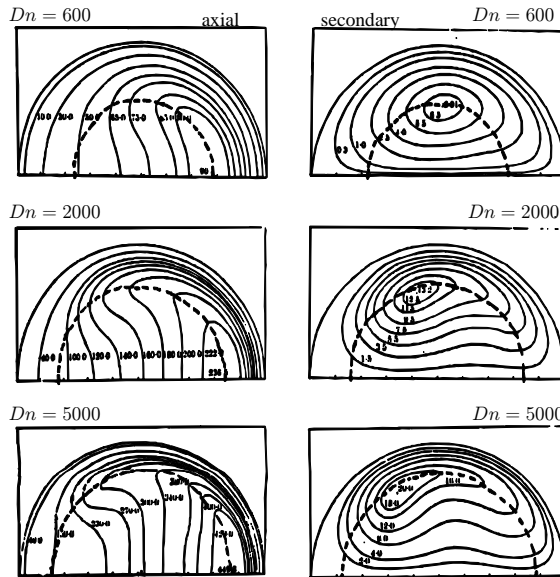


FIGURE 15. Contour plots of axial (left) and streamline plots of secondary (right) fully developed steady flow in a curved tube for Dean numbers of 600 (top), 2000 (middle) and 5000 (bottom) as computed by Collins and Dennis in [2].

Steady fully developed flow in a curved tube

In order to obtain a more quantitative description of the flow phenomena it is convenient to use the toroidal coordinate system (r, θ, ϕ) as is depicted in Fig. 14. The corresponding velocity components are v_r , v_θ and v_ϕ . The Navier-Stokes equations in toroidal coordinates read [7]:

- in r -direction:

$$\begin{aligned} \frac{\partial v_r}{\partial t} + \frac{1}{rB} \left[\frac{\partial}{\partial r} (rBv_r^2) + \frac{\partial}{\partial \theta} (Bv_r v_\theta) + \frac{\partial}{\partial \phi} (\delta r v_\phi v_r) - Bv_\theta^2 - \delta r \cos \theta v_\phi^2 \right] \\ = -\frac{\partial p}{\partial r} + \frac{1}{Re} \left\{ \frac{1}{rB} \left[\frac{\partial}{\partial r} \left(rB \frac{\partial v_r}{\partial r} \right) + \frac{\partial}{\partial \theta} \left(\frac{B}{r} \frac{\partial v_r}{\partial \theta} \right) + \frac{\partial}{\partial \phi} \left(\frac{\delta^2 r}{B} \frac{\partial v_r}{\partial \phi} \right) \right] \right. \\ \left. - \frac{1}{r^2} \left(2 \frac{\partial v_\theta}{\partial \theta} + v_r \right) + \frac{\delta \sin \theta v_\theta}{rB} + \frac{\delta^2 \cos \theta}{B^2} \left(v_\theta \sin \theta - v_r \cos \theta - 2 \frac{\partial v_\phi}{\partial \phi} \right) \right\}, \end{aligned} \quad (2.61)$$

- in θ -direction:

$$\begin{aligned} \frac{\partial v_\theta}{\partial t} + \frac{1}{rB} \left[\frac{\partial}{\partial r} (rBv_r v_\theta) + \frac{\partial}{\partial \theta} (Bv_\theta^2) + \frac{\partial}{\partial \phi} (\delta r v_\phi v_\theta) + Bv_r v_\theta + \delta r \sin \theta v_\phi^2 \right] \\ = -\frac{\partial p}{\partial \theta} + \frac{1}{Re} \left\{ \frac{1}{rB} \left[\frac{\partial}{\partial r} \left(rB \frac{\partial v_\theta}{\partial r} \right) + \frac{\partial}{\partial \theta} \left(\frac{B}{r} \frac{\partial v_\theta}{\partial \theta} \right) + \frac{\partial}{\partial \phi} \left(\frac{\delta^2 r}{B} \frac{\partial v_\theta}{\partial \phi} \right) \right] \right. \\ \left. + \frac{1}{r^2} \left(2 \frac{\partial v_r}{\partial \theta} - v_\theta \right) - \frac{\delta \sin \theta v_r}{rB} - \frac{\delta^2 \sin \theta}{B^2} \left(v_\theta \sin \theta - v_r \cos \theta - 2 \frac{\partial v_\phi}{\partial \phi} \right) \right\}, \end{aligned} \quad (2.62)$$

- in ϕ -direction:

$$\begin{aligned} \frac{\partial v_\phi}{\partial t} + \frac{1}{rB} \left[\frac{\partial}{\partial r} (rBv_\phi v_r) + \frac{\partial}{\partial \theta} (Bv_\phi v_\theta) + \frac{\partial}{\partial \phi} (\delta r v_\phi^2) \right. \\ \left. + \delta r v_\phi (v_r \cos \theta - v_\theta \sin \theta) \right] = -\frac{\delta}{B} \frac{\partial p}{\partial \phi} \\ + \frac{1}{Re} \left\{ \frac{1}{rB} \left[\frac{\partial}{\partial r} \left(rB \frac{\partial v_\phi}{\partial r} \right) + \frac{\partial}{\partial \theta} \left(\frac{B}{r} \frac{\partial v_\phi}{\partial \theta} \right) + \frac{\partial}{\partial \phi} \left(\frac{\delta^2 r}{B} \frac{\partial v_\phi}{\partial \phi} \right) \right] \right. \\ \left. + \frac{2\delta^2}{B^2} \left(\frac{\partial v_r}{\partial \phi} \cos \theta - \frac{\partial v_\theta}{\partial \phi} \sin \theta - \frac{v_\phi}{2} \right) \right\}, \quad (2.63) \end{aligned}$$

continuity:

$$\frac{\partial}{\partial r}(rBv_r) + \frac{\partial}{\partial \theta}(Bv_\theta) + \frac{\partial}{\partial \phi}(\delta rv_\phi) = 0 \quad (2.64)$$

with

$$\delta = \frac{a}{R_0} \quad \text{and} \quad B = 1 + \delta r \cos \theta.$$

For fully developed flow all derivatives in ϕ direction are zero ($\partial/\partial\phi = 0$). This of course does not hold for the driving force $\partial p/\partial\phi$. If we scale according to:

$$r^* = \frac{r}{a}, \quad p^* = \frac{p}{\rho V^2}, \quad v_r^* = \frac{v_r}{V}, \quad v_\theta^* = \frac{v_\theta}{V}, \quad v_\phi^* = \frac{v_\phi}{V} \quad (2.65)$$

the continuity equation and the momentum equation in r -direction read, after dropping the asterisk:

$$\frac{\partial v_r}{\partial r} + \frac{v_r}{r} \left[\frac{1 + 2\delta r \cos \theta}{1 + \delta r \cos \theta} \right] + \frac{1}{r} \frac{\partial v_\theta}{\partial \theta} - \frac{\delta v_\theta \sin \theta}{1 + \delta r \cos \theta} = 0 \quad (2.66)$$

and

$$\begin{aligned} v_r \frac{\partial v_r}{\partial r} + \frac{v_\theta}{r} \frac{\partial v_r}{\partial \theta} - \frac{v_\theta^2}{r} - \delta \frac{v_\phi^2 \cos \theta}{1 + \delta r \cos \theta} \\ = -\frac{\partial p}{\partial r} + \frac{1}{Re} \left[\left(\frac{1}{r} \frac{\partial}{\partial \theta} - \frac{\delta \sin \theta}{1 + \delta r \cos \theta} \right) \left(\frac{1}{r} \frac{\partial v_r}{\partial \theta} - \frac{\partial v_\theta}{\partial r} - \frac{v_\theta}{r} \right) \right]. \end{aligned} \quad (2.67)$$

The two important dimensionless parameters that appear are the curvature ratio δ and the Reynolds number Re defined as:

$$\delta = \frac{a}{R_0} \quad \text{and} \quad Re = \frac{2aV}{\nu} \quad (2.68)$$

with a the radius and R_0 the curvature of the tube. If we restrict ourselves to the plane of symmetry ($\theta = 0, \pi$, $\cos \theta = \pm 1$ and $v_\theta = 0$) we have for the momentum equation:

$$v_r \frac{\partial v_r}{\partial r} - \delta \frac{\pm v_\phi^2}{1 \pm \delta r} = -\frac{\partial p}{\partial r} + \frac{1}{Re} \left[\left(\frac{1}{r} \frac{\partial}{\partial \theta} \right) \left(\frac{1}{r} \frac{\partial v_r}{\partial \theta} - \frac{\partial v_\theta}{\partial r} \right) \right]. \quad (2.69)$$

If we consider small curvatures ($\delta \ll 1$) only, knowing that $v_\phi = O(1)$ and r is already scaled and in the interval $[0, 1]$, the momentum equation yields

$$v_r \frac{\partial v_r}{\partial r} = O(\delta v_\phi^2) = O(\delta)$$

and thus $O(v_r) = \delta^{1/2}$. From the continuity equation Eq. (2.66) it can be seen that v_r and v_θ scale in the same way, i.e. $O(v_r) = O(v_\theta)$, and thus also $O(v_\theta) = \delta^{1/2}$. If instead of using Eq. (2.65) we would use:

$$r^* = \frac{r}{a}, \quad p^* = \frac{p}{\delta\rho V^2}, \quad v_r^* = \frac{v_r}{\delta^{1/2}V}, \quad v_\theta^* = \frac{v_\theta}{\delta^{1/2}V}, \quad v_\phi^* = \frac{v_\phi}{V} \quad (2.70)$$

the continuity equation and momentum equation in r -direction for $\delta \ll 1$ would be (again after dropping the asterisk):

$$\frac{\partial v_r}{\partial r} + \frac{v_r}{r} + \frac{1}{r} \frac{\partial v_\theta}{\partial \theta} = 0 \quad (2.71)$$

and

$$v_r \frac{\partial v_r}{\partial r} + \frac{v_\theta}{r} \frac{\partial v_r}{\partial \theta} - \frac{v_\theta^2}{r} - v_\phi^2 \cos \theta \\ = -\frac{\partial p}{\partial r} + \frac{1}{\delta^{1/2} \text{Re}} \left[\frac{1}{r} \frac{\partial}{\partial \theta} \left(\frac{1}{r} \frac{\partial v_r}{\partial \theta} - \frac{\partial v_\theta}{\partial r} - \frac{v_\theta}{r} \right) \right]. \quad (2.72)$$

From this we can see that for small curvature another dimensionless parameter, the Dean number, can be defined as:

$$\text{Dn} = \delta^{1/2} \text{Re}. \quad (2.73)$$

The secondary flow depends on two important parameters, the Reynolds number Re and the curvature δ or the Dean number Dn and the curvature δ . The last combination is often used because for small curvature only the Dean number is of importance.

For large Dean numbers the viscous term in Eq. (2.72) can be neglected in the core of the secondary flow field and one can talk about a boundary layer of the secondary flow. The thickness δ_s of this boundary layer can be derived from the momentum equation in θ -direction:

$$v_r \frac{\partial v_\theta}{\partial r} + \frac{v_\theta}{r} \frac{\partial v_\theta}{\partial \theta} - \frac{v_r v_\theta}{r} + \delta \frac{v_\phi^2 \sin \theta}{1 + \delta r \cos \theta} \\ = -\frac{1}{r} \frac{\partial p}{\partial \theta} + \frac{1}{\delta^{1/2} \text{Re}} \left[\left(\frac{\partial}{\partial r} + \frac{\delta \cos \theta}{1 + \delta r \cos \theta} \right) \left(\frac{\partial v_\theta}{\partial r} + \frac{v_\theta}{r} - \frac{1}{r} \frac{\partial v_r}{\partial r} \right) \right]. \quad (2.74)$$

If we assume that at $r = a - \delta_s$ the viscous and inertia forces are of the same order of magnitude we have:

$$\frac{\delta_s}{a} = O(\text{Dn}^{-1/2}). \quad (2.75)$$

In Fig. 15 the boundary layer of the secondary flow is indicated with a dashed line and indeed decreases with increasing Dean numbers.

2.2.2. Unsteady fully developed flow in a curved tube. In unsteady flow in a curved tube the secondary flow will have the same orientation as in stationary flow. The reason for this is that the centrifugal forces are not sensitive for the direction of the axial velocity ($f_c \propto v_\phi^2$). For high frequencies, or better large Womersley numbers, like in the case for straight tubes an nonstationary boundary layer will develop such that in the central core the flow will behave more or less inviscid whereas at the boundary viscous forces are dominant. For oscillatory flow this may lead to a secondary flow field as is depicted in Fig. 16. In the core the secondary vortex will have an opposite direction as in the boundary layer where the direction corresponds with the one in steady flow. In contradiction to the flow in a straight tube, however, for flow in a curved tube the superposition of several harmonics is not allowed because the governing equations are strongly non-linear.

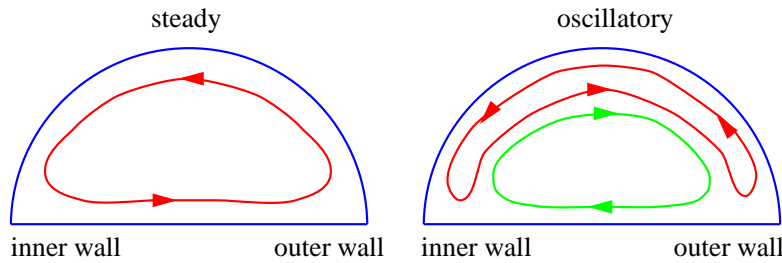


FIGURE 16. Streamline patterns of fully developed secondary flow in steady (left) and oscillatory (right) flow in a curved tube.

In pulsating flow this second vortex will not be that pronounced as in oscillating flow but some influence can be depicted. This is shown in the Fig. 17 where the results of a finite element computation of pulsating flow in a curved tube are given together with experimental (laser Doppler) data.

2.2.3. Flow in branched tubes. The flow in branched tubes (bifurcations) shows the same phenomena as in curved tubes. Actually the bifurcation can be considered as a two joined curved tubes. Of course there are also differences with curved tube flow due to the bifurcation point (apex) which will induce an extra asymmetry (see Fig. 18).

Detailed knowledge about the flow phenomena in curved and branched tubes is of great physiological and clinical importance. The prediction of areas of high and low shear rates and wall shear stress, the prediction of

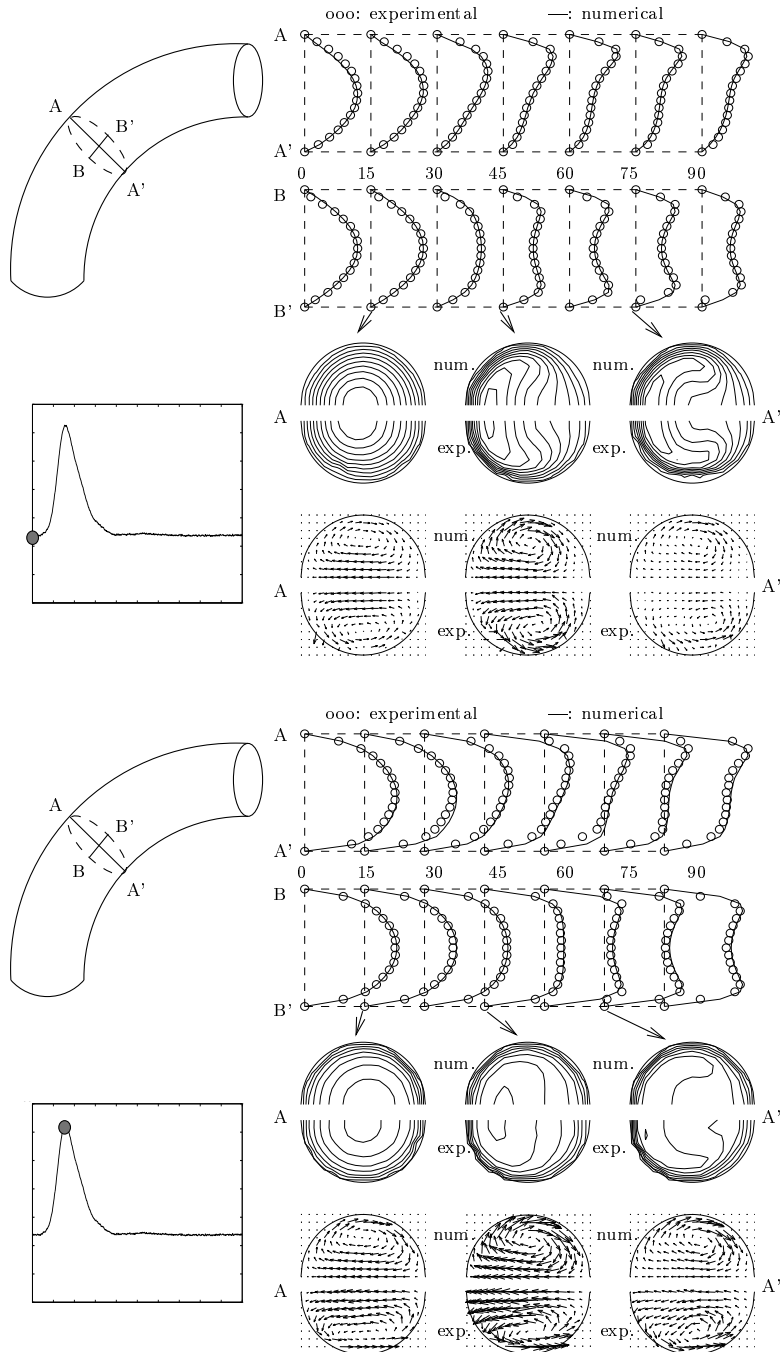


FIGURE 17. Computational (FEM) and experimental (LDA) results of pulsatile flow in a curved tube: end diastolic (top), peak systolic (bottom).

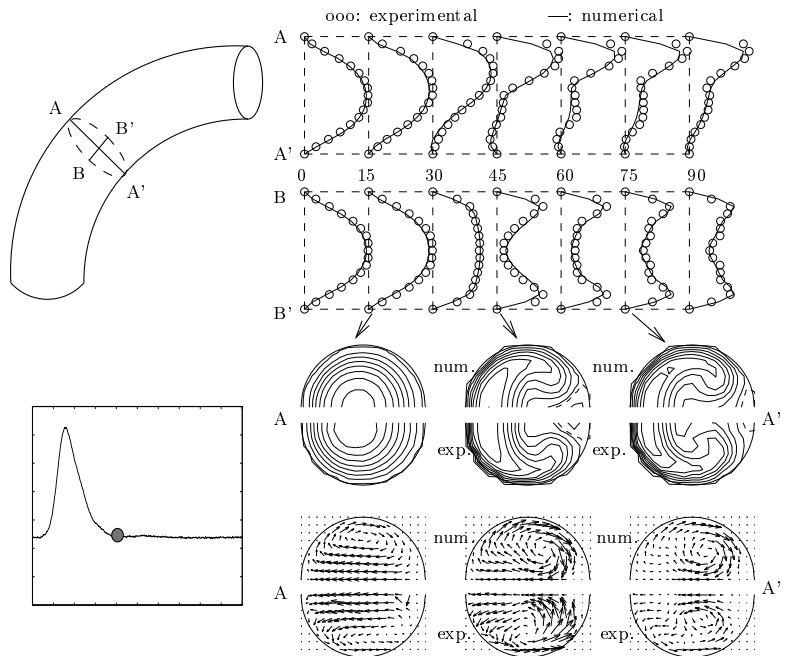


FIGURE 17. Continuation: Computational (FEM) and experimental (LDA) results of pulsatile flow in a curved tube: end systolic.

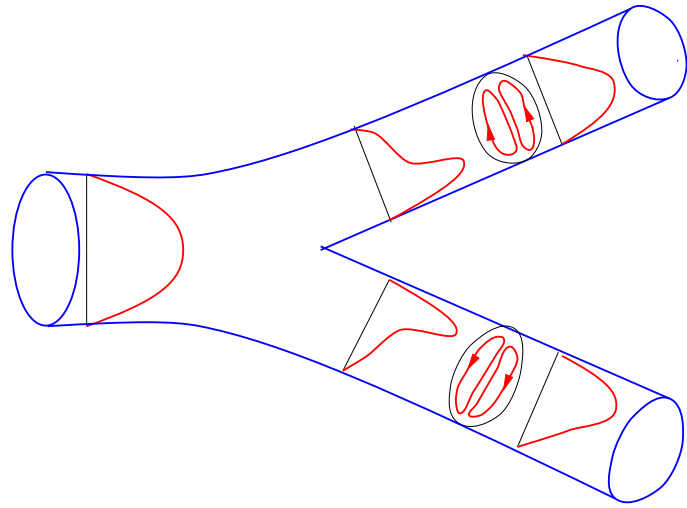


FIGURE 18. Axial velocity and streamline patterns of flow in a bifurcation.

flow instabilities related to high shear rates as occur at the interface between the areas with high and low axial velocity can help to interpret clinical data from ultra-sound Doppler measurements and MRI images and can help to get insight in the development of atherosclerosis. In many case advanced methods in computational fluid dynamics (CFD) are needed to obtain more than the qualitative information as is given in this section. An example of this is given in Fig. 19 where the results of computations of the flow in the internal carotid artery is given together with experimental results obtained with laser Doppler anemometry.

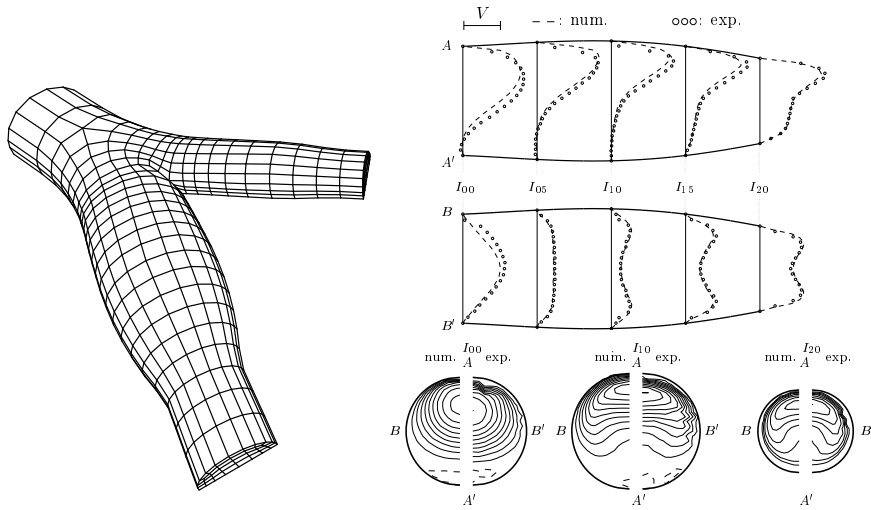


FIGURE 19. Computational (FEM) and experimental (LDA) velocity distributions of a steady flow in a model of the carotid artery bifurcation.

3. Wave Phenomena in Blood Vessels

3.1. Introduction

In this section we will show that traveling pressure and flow waves are the result of the distensibility (or compliance) of the arteries and the pulsatile character of the pressure. A typical relation between the pressure and cross-sectional area of an artery is given in Fig. 5 and shows that the compliance normally does not have a constant value but strongly depends on the pressure. In this section, however, only small area variations will be considered and a linear relation between the pressure amplitude and the vessel diameter

will be assumed. Apart from wave propagation and the importance of viscous forces expressed in the value of the Womersley number α , also wave reflection from arterial bifurcations or transitions in mechanical or geometrical properties will be dealt with. Moreover, attenuation of waves as a result of fluid viscosity and wall visco-elasticity will be discussed.

3.2. Pressure and Flow

In the physiological introduction of this course (Sec. 2) it is mentioned that the heart is a four-chambered pump that generates a pulsating pressure and flow (see Fig. 2). The frequency contents of the pressure and flow in the aorta is given in Table 1 and shows that the pulsatile character of the pressure and flow can be described very well with the first 8 to 10 harmonics (see also Fig. 6). Moreover, in Sec. 2 a simple (windkessel) model was introduced to describe the pressure/flow relation or impedance of the arterial system using the compliance $C_e = dV/dp$ of the elastic arteries and the resistance R_p of the peripheral arteries (see also equation 1.9):

$$q_a = C_e \frac{\partial p_a}{\partial t} + \frac{p_a}{R_p} \quad (3.1)$$

and with $p_a = \hat{p}_a e^{i\omega t}$, $q_a = \hat{q}_a e^{i\omega t}$:

$$Z = \frac{p_a}{q_a} = \frac{R_p(1 - i\omega R_p C_e)}{1 + \omega^2 R_p^2 C_e^2}. \quad (3.2)$$

In Fig. 20 the absolute value and argument of the impedance given by Eq. (3.2) is shown as a function of the harmonics. Experimental data (indicated with lines [4]) show that the windkessel model does not predict accurate results especially for the phase of the higher harmonics. Moreover, as illustrated in Fig. 4, the pressure and flow waves change their shape with increasing distance from the heart. This is a result of traveling waves and never can be described by the windkessel model.

In order to describe the pressure and flow in terms of traveling waves (i.e. $p = p(z, t)$ and $q = q(z, t)$) the following complex notation will be used:

$$p(z, t) = \hat{p} e^{i(\omega t - kz)} \quad \text{and} \quad q(z, t) = \hat{q} e^{i(\omega t - kz)} \quad (3.3)$$

where ω is the angular frequency, $k = k_r + ik_i$ is the complex wave number and $\hat{p} = |\hat{p}|e^{i\phi}$ denotes the complex amplitude. The actual pressure (c.q. flow)

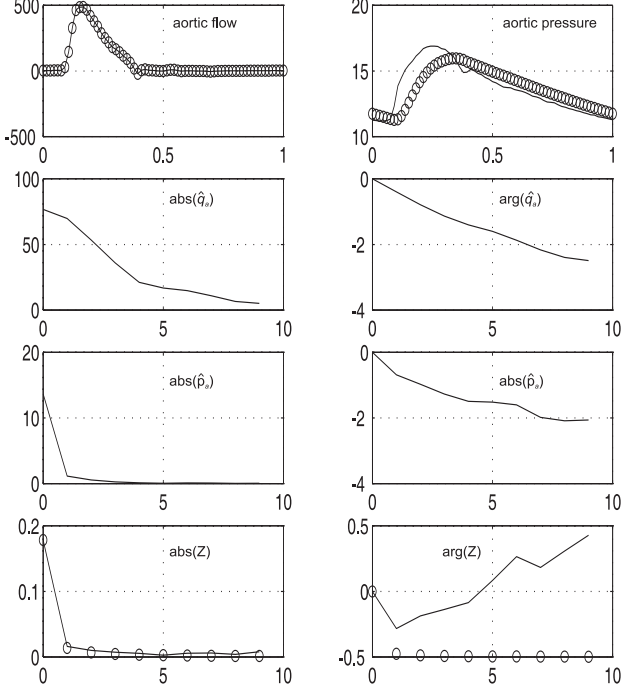


FIGURE 20. Absolute value and argument of the arterial impedance as computed with a windkessel model (o) and from experimental data (-).

is defined as the real part of Eq. (3.3):

$$\text{Re}[p(z, t)] = |\hat{p}| e^{k_i z} \cos(\omega t - k_r z + \phi) \quad (3.4)$$

It will be clear that $(-k_i)$ is a measure for the attenuation of the wave and that $k_r = 2\pi/\lambda$ with λ the wavelength.

3.3. Fluid Flow

To analyze fully developed Newtonian flow in distensible tubes we consider the Navier-Stokes equations in a cylindrical coordinate system:

$$\left\{ \begin{array}{l} \frac{\partial v_r}{\partial t} + v_r \frac{\partial v_r}{\partial r} + v_z \frac{\partial v_r}{\partial z} = -\frac{1}{\rho} \frac{\partial p}{\partial r} + \nu \left(\frac{\partial}{\partial r} \left(\frac{1}{r} \frac{\partial}{\partial r} (r v_r) \right) + \frac{\partial^2 v_r}{\partial z^2} \right), \\ \frac{\partial v_z}{\partial t} + v_r \frac{\partial v_z}{\partial r} + v_z \frac{\partial v_z}{\partial z} = -\frac{1}{\rho} \frac{\partial p}{\partial z} + \nu \left(\frac{1}{r} \frac{\partial}{\partial r} \left(r \frac{\partial}{\partial r} (v_z) \right) + \frac{\partial^2 v_z}{\partial z^2} \right), \\ \frac{1}{r} \frac{\partial}{\partial r} (r v_r) + \frac{\partial v_z}{\partial z} = 0. \end{array} \right. \quad (3.5)$$

Since the velocity in circumferential direction equals zero ($v_\phi = 0$), the momentum equation and all derivatives in ϕ -direction are omitted. Due to the distensibility of the tube, pressure and flow waves will propagate with a finite wave speed $c = \omega/k_r$ and a typical wavelength $\lambda = 2\pi/k_r$. First a properly scaled dimensionless form of the Navier-Stokes equations will be derived. To this end the radial coordinates are made dimensionless using the mean radius of the tube, i.e. $r' = r/a_0$. The axial coordinates, however, must be scaled with the real part of the wave number k_r : $z' = zk_r$ (see Eq. (3.3)). The axial velocity is made dimensionless with its characteristic value over a cross-section: $v'_z = v_z/V$. From the continuity equation it can be derived that the radial velocity then must be made dimensionless as: $v'_r = (v_r/V)(1/k_r a)$. The characteristic time $t' = \omega t$ can be written as $t' = (k_r c)t$ with c the wave speed. Together with a dimensionless pressure $p' = p/(\rho V c)$ the dimensionless Navier-Stokes equations read:

$$\left\{ \begin{array}{l} \frac{\partial v'_r}{\partial t'} + \frac{V}{c} \left(v'_r \frac{\partial v'_r}{\partial r'} + v'_z \frac{\partial v'_r}{\partial z'} \right) \\ = -\frac{1}{k_r^2 a_0^2} \frac{\partial p'}{\partial r'} + \frac{1}{\alpha^2} \left(\frac{\partial}{\partial r'} \left(\frac{1}{r'} \frac{\partial}{\partial r'} (r' v'_r) \right) + a_0^2 k_r^2 \frac{\partial^2 v'_r}{\partial z'^2} \right), \\ \frac{\partial v'_z}{\partial t'} + \frac{V}{c} \left(v'_r \frac{\partial v'_z}{\partial r'} + v'_z \frac{\partial v'_z}{\partial z'} \right) \\ = -\frac{\partial p'}{\partial z'} + \frac{1}{\alpha^2} \left(\frac{1}{r'} \frac{\partial}{\partial r'} \left(r' \frac{\partial}{\partial r'} (v'_z) \right) + a_0^2 k_r^2 \frac{\partial^2 v'_z}{\partial z'^2} \right), \\ \frac{1}{r'} \frac{\partial}{\partial r'} (r' v'_r) + \frac{\partial v'_z}{\partial z'} = 0. \end{array} \right. \quad (3.6)$$

Besides the Womersley parameter $\alpha = a_0 \sqrt{\omega/\nu}$ the dimensionless parameters that play a role in this equation are the speed ratio $S = V/c$ and the circumference-to-wavelength ratio $G = a_0 k_r = 2\pi a_0 / \lambda$. Under the assumptions that the wave velocity c is much larger then the fluid velocity V , the wavelength λ is much larger then the tube radius a_0 , i.e.:

$$S = \frac{V}{c} \ll 1, \quad G^2 = (k_r a_0)^2 = \left(\frac{2\pi a_0}{\lambda} \right)^2 \ll 1. \quad (3.7)$$

It can readily be shown that the equations of motion reduce to:

$$\begin{cases} \frac{\partial p}{\partial r} = 0, \\ \frac{\partial v_z}{\partial t} = -\frac{1}{\rho} \frac{\partial p}{\partial z} + \nu \frac{1}{r} \frac{\partial}{\partial r} \left(r \frac{\partial v_z}{\partial r} \right), \\ \frac{1}{r} \frac{\partial}{\partial r} (r v_r) + \frac{\partial v_z}{\partial z} = 0. \end{cases} \quad (3.8)$$

If we search for harmonic solutions with angular frequency ω and wave number k :

$$p = \hat{p} e^{i(\omega t - kz)} \quad (3.9)$$

and

$$v_z = \hat{v}_z(r) e^{i(\omega t - kz)} \quad (3.10)$$

substitution in Eq. (3.8) yields exactly the same differential equation for \hat{v}_z as in the case of a rigid tube given in Eq. (2.22). If we further assume that the wall motion is axially restrained, which is thought to be relevant *in vivo* [5], also the boundary condition for \hat{v}_z is not different from the one in rigid tubes but now must be applied in a linearized way at $r = a_0$. It will be clear that in that case we obtain exactly the same Womersley solution given by Eq. (2.22). Substitution of:

$$\frac{\partial \hat{p}}{\partial z} = -ik\hat{p} \quad (3.11)$$

yields:

$$\hat{v}_z(r) = \frac{k}{\rho\omega} \left[1 - \frac{J_0(i^{3/2}\alpha r/a_0)}{J_0(i^{3/2}\alpha)} \right] \hat{p}. \quad (3.12)$$

In [8] a relation similar to Eq. (3.12) is derived, however without the assumption of axial constraint. In that case the second term in the brackets is multiplied by an extra parameter that only slightly differs from unity. The wall shear stress is equal to the wall shear stress for rigid tubes and is defined by Eq. (2.35). The wave number k still has to be determined and depends on the properties of the arterial wall. In the next section the wall motion will be analyzed, again assuming axial restraint.

3.4. Wave Propagation

3.4.1. Derivation of a quasi one-dimensional model. In order to obtain an expression for the wave number introduced in the previous section,

a quasi one-dimensional wave propagation model for pressure and flow waves will be derived. To this end the Leibnitz formulae (or Reynolds transport theorem) will be used to integrate the equations of motion given in Eq. (3.8). A suitable form for the application in this section is (see also Fig. 21):

$$\frac{d}{dz} \int_0^{a(z)} s(r, z) dr = \int_0^{a(z)} \frac{\partial s(r, z)}{\partial z} dr + s(a, z) \left. \frac{\partial a}{\partial z} \right|_a . \quad (3.13)$$

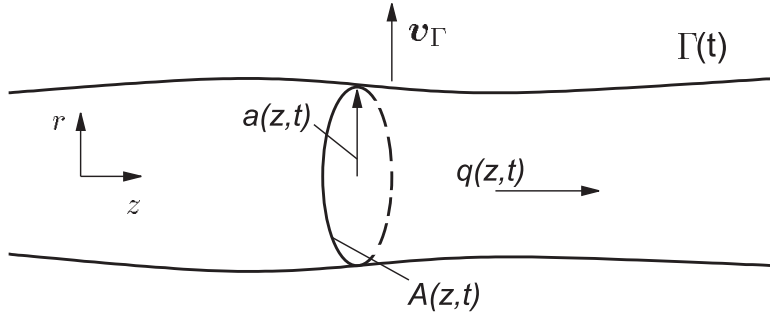


FIGURE 21. Flow $q(z, t)$ in a distensible tube with moving wall $\Gamma(t)$ and cross-sectional area $A(z, t)$.

Application to the second term of the continuity equation in Eq. (3.8) integrated over the radius:

$$2\pi \left[\int_0^{a(z)} \frac{1}{r} \frac{\partial}{\partial r} (rv_r) r dr + \int_0^{a(z)} \frac{\partial v_z}{\partial z} r dr \right] = 0 \quad (3.14)$$

yields:

$$2\pi \int_0^{a(z)} \frac{\partial rv_r}{\partial r} dr + 2\pi \frac{\partial}{\partial z} \int_0^{a(z)} v_z r dr - 2\pi v_z r \left. \frac{\partial a}{\partial z} \right|_a = 0 \quad (3.15)$$

or:

$$2\pi r v_r \Big|_0^a + \frac{\partial q}{\partial z} - 2\pi v_z (a, t) a \left. \frac{\partial a}{\partial z} \right|_a = 0 \quad (3.16)$$

and thus:

$$2\pi a \left(v_r(a, t) - v_z(a, t) \left. \frac{\partial a}{\partial z} \right|_a \right) + \frac{\partial q}{\partial z} = 0 \quad (3.17)$$

with $q = q(z, t)$ the flow through the cross-section. Rewriting the first term in terms of the cross-sectional area $A(z, t) = \pi a^2(z, t)$, finally the integrated continuity equation reads:

$$\frac{\partial A}{\partial t} + \frac{\partial q}{\partial z} = 0. \quad (3.18)$$

This equation is formally derived but will be clear immediately from Fig. 21 if we write $[A(z, t + dt) - A(z, t)]dz + [q(z + dz, t) - q(z, t)]dt = 0$.

In a similar way the momentum equation in axial direction can be integrated:

$$2\pi \int_0^{a(z,t)} \frac{\partial v_z}{\partial t} r dr = -2\pi \int_0^{a(z,t)} \frac{1}{\rho} \frac{\partial p}{\partial z} r dr + 2\pi\nu \int_0^{a(z,t)} \frac{\partial}{\partial r} \left(r \frac{\partial v_z}{\partial r} \right) dr. \quad (3.19)$$

Application of the Leibnitz formulae to the first term yields:

$$2\pi \frac{\partial}{\partial t} \int_0^{a(z,t)} v_z r dr - 2\pi v_z v_r r \Big|_0^a = -\frac{A}{\rho} \frac{\partial p}{\partial z} + 2\pi\nu r \frac{\partial v_z}{\partial r} \Big|_0^a. \quad (3.20)$$

The second term in the left hand side of this equation vanishes if a longitudinal restraint of the wall motion ($v_z(a) = 0$) is assumed. The second term in the right hand side can be written in terms of the wall shear stress defined in Eq. (2.25). The integrated momentum equation then reads:

$$\rho \frac{\partial q}{\partial t} + A \frac{\partial p}{\partial z} = -\frac{2A\tau}{a}. \quad (3.21)$$

Together with the expression for the wall shear stress given in Eq. (2.35) and linearisation of the $A \frac{\partial p}{\partial z}$ term we finally obtain:

$$\rho \frac{\partial q}{\partial t} + A_0 \frac{\partial p}{\partial z} = -f_0 q \quad (3.22)$$

with f_0 a friction function defined as:

$$f_0(\omega) = i\omega\rho \frac{F_{10}(\omega)}{1 - F_{10}(\omega)}. \quad (3.23)$$

The linearized one-dimensional equations that describe the pressure and flow in distensible tubes under the assumption that $V/c \ll 1$, $(2\pi a/\lambda)^2 \ll 1$

and under the assumption that the wall motion is longitudinally constrained thus are given by:

$$\begin{cases} C_0 \frac{\partial p}{\partial t} + \frac{\partial q}{\partial z} = 0, \\ \rho \frac{\partial q}{\partial t} + A_0 \frac{\partial p}{\partial z} = -f_0 q, \end{cases} \quad (3.24)$$

with C_0 the linearized compliance given by:

$$C_0 = \left(\frac{\partial A}{\partial p} \right)_{p=p_0} \quad (3.25)$$

Alternatively using the mean velocity \bar{v} instead of the flow $q = A\bar{v}$:

$$\begin{cases} D_0 \frac{\partial p}{\partial t} + \frac{\partial \bar{v}}{\partial z} = 0, \\ \rho \frac{\partial \bar{v}}{\partial t} + \frac{\partial p}{\partial z} = -f_0 \bar{v}, \end{cases} \quad (3.26)$$

with D_0 a linearized distensibility given by:

$$D_0 = \frac{1}{A_0} \left(\frac{\partial A}{\partial p} \right)_{p=p_0} \quad (3.27)$$

In the next section we will derive the wave number k for inviscid, viscosity dominated and general flow (i.e. large, small and intermediate values of the Womersley parameter α).

3.4.2. Wave speed and attenuation constant. The linearized one-dimensional mass and momentum equations for unsteady viscous flow through a distensible tube has been derived by integrating the continuity and momentum equations over a cross-section of the tube assuming the wave-length to be large compared to the diameter of the tube and the phase velocity of the wave to be large compared to the mean fluid velocity. Moreover it is assumed that the motion of the tube wall is restrained longitudinally. Due to the linearity assumed, the resulting Eqs. (3.18) and (3.22) can be solved in the frequency domain by substituting harmonic solutions

$$p(\omega, z, t) = \hat{p}(\omega, 0) e^{i(\omega t - kz)}, \quad (3.28)$$

$$q(\omega, z, t) = \hat{q}(\omega, 0) e^{i(\omega t - kz)}, \quad (3.29)$$

$$A(\omega, z, t) = \hat{A}(\omega, 0) e^{i(\omega t - kz)}, \quad (3.30)$$

where $\hat{p}(\omega, 0)$, $\hat{q}(\omega, 0)$ and $\hat{A}(\omega, 0)$ are the complex amplitudes representing both the amplitude and the phase of the waves measured at location $z = 0$, ω is the angular frequency and $k(\omega)$ is the wave number ; a complex number defined by:

$$k(\omega) = \frac{\omega}{c} - i \frac{\gamma(\omega)}{\lambda}. \quad (3.31)$$

Here c denotes the phase velocity of the waves and the wave length is given by $\lambda = 2\pi c/\omega$. The exponential decrease of the amplitude of the waves is described by the attenuation constant $\gamma(\omega) = -2\pi k_i/k_r$.

Viscoelastic wall behavior is described by an experimentally determined constitutive relationship between the cross-sectional area \hat{A} and the complex amplitude \hat{p} :

$$\hat{A} = C(\omega) \hat{p} \quad (3.32)$$

where $C(\omega)$ is the dynamic compliance. For thin walled visco-elastic tubes this relationship can also be derived from Eqs. (1.3) using a complex Young's modulus $E = E_r + iE_i$.

Large Womersley number flow

For large Womersley parameters the flow will be inviscid and the friction function f_0 can be neglected. Substitution of Eqs. (3.28–3.30) in Eq. (3.24) yields:

$$\begin{cases} i\omega C(\omega) \hat{p} - ik(\omega) \hat{q} = 0, \\ -ik(\omega) A_0 \hat{p} + i\omega \rho \hat{q} = 0, \end{cases} \quad (3.33)$$

with solution:

$$k_0(\omega) = \pm \sqrt{\frac{\omega^2 \rho C(\omega)}{A_0}} = \pm \frac{\omega}{c_0} \quad (3.34)$$

where the positive (negative) sign holds for waves traveling in the positive (negative) z -direction and c_0 denotes the Moens-Korteweg wave speed given by:

$$c_0(\omega) = \sqrt{\frac{A_0}{\rho C(\omega)}} = \sqrt{\frac{1}{\rho D_0(\omega)}}. \quad (3.35)$$

Note that the subscript 0 is used in k_0 and c_0 in order to obey conventions in literature despite the fact that k_∞ and c_∞ would be more meaningful

since $\alpha \rightarrow \infty$. For thin walled tubes the Moens-Korteweg wave speed can be derived from (1.3) and reads:

$$c_0 = \sqrt{\frac{1}{\rho} \frac{hE}{2a_0(1 - \mu^2)}} \quad (3.36)$$

Note that the wave number $k_0 = \omega/c_0$ is a real number expressing that the phase velocity c equals the Moens-Korteweg wave speed and that the attenuation constant γ equals zero:

$$\alpha \rightarrow \infty : \quad c(\omega) = c_0, \quad \gamma(\omega) = 0. \quad (3.37)$$

As there is no friction and the compliance is assumed to be real (no visco-elasticity), no attenuation ($\gamma(\omega) = 0$) of the wave will occur. The corresponding wave equation can be derived from Eq. (3.24): after elimination of the flow and keeping in mind that the friction function is neglected we obtain the differential equation:

$$\frac{\partial^2 p}{\partial t^2} - \frac{1}{\rho D_0} \frac{\partial^2 p}{\partial z^2} = 0 \quad (3.38)$$

This is a wave equation with wave speed $c_0 = \sqrt{1/\rho D_0}$. So for large α and real values for the distensibility D_0 the pressure wave travels without damping in z -direction.

Equation (3.33) can also be solved with respect to the ratio \hat{q}/\hat{p} between the flow and the pressure:

$$Y_0 = \frac{\hat{q}}{\hat{p}} = C(\omega) \frac{\omega}{k(\omega)} = \pm \frac{A_0}{\rho c_0}. \quad (3.39)$$

This ratio is referred to as the admittance Y_0 and is equal to the reciprocal value of the impedance:

$$Y \equiv \frac{1}{Z} \equiv \frac{\hat{q}}{\hat{p}}. \quad (3.40)$$

As $k(\omega)$ represents two waves (one wave traveling in positive z -direction ($k > 0$) and one wave traveling in negative z -direction ($k < 0$)) there are two flow and pressure waves: forward traveling waves $q_f = +Y p_f$ and backward traveling waves $q_b = -Y p_b$. The total pressure and flow is the sum of these waves $p(z, t) = p_f(z, t) + p_b(z, t)$ resp. $q(z, t) = q_f(z, t) + q_b(z, t)$.

Small Womersley number flow

For small Womersley parameters the flow will be dominated by viscous forces and the friction function f_0 can be approximated by its Poiseuille value $f_0 = 8\eta/a_0^2$ whereas the instationary inertia forces in the momentum equation can be neglected. Substitution of Eqs. (3.28–3.30) in Eq. (3.24) yields:

$$\begin{cases} i\omega C(\omega)\hat{p} - ik(\omega)\hat{q} = 0, \\ -ik(\omega)A_0\hat{p} + \frac{8\eta}{a_0^2}\hat{q} = 0, \end{cases} \quad (3.41)$$

and has a non-trivial solution if:

$$k(\omega) = \pm \sqrt{\frac{-8i\eta\omega C(\omega)}{A_0a_0^2}} = \pm \frac{\omega}{c_0} \sqrt{\frac{-8i}{\alpha^2}} = \pm \frac{2(1-i)}{\alpha} k_0 \quad (3.42)$$

where the positive (negative) sign now holds for waves traveling in the positive (negative) z -direction and c_0 denotes the Moens-Korteweg wave speed.

Now the wave number is a complex number and the phase velocity c and attenuation constant γ are given by:

$$\alpha \rightarrow 0 : \quad c(\omega) = \frac{1}{2}\alpha c_0, \quad \gamma(\omega) = 2\pi. \quad (3.43)$$

As the real and imaginary part of the wave number are equal, the wave is damped critically. This can also be seen from Eq. (3.24): after elimination of the flow and keeping in mind that the instationary inertia forces can be neglected we obtain the differential equation:

$$\frac{\partial p}{\partial t} = \frac{A_0a_0^2}{8\eta C_0} \frac{\partial^2 p}{\partial z^2} = \frac{a_0^2}{8\eta D_0} \frac{\partial^2 p}{\partial z^2}. \quad (3.44)$$

This is a diffusion equation with diffusion coefficient $D = a_0^2/8\eta D_0$. So for small α the wave equation reduces to a diffusion equation showing critical damping of the pressure in z -direction. This phenomena is responsible for the large pressure drop that is found in the micro-circulation where the Womersley parameter is low as a result of the small diameters of the vessels.

The admittance Y now is a complex number given by:

$$Y = \pm \frac{A_0}{\rho c_0} \frac{i+1}{4} \alpha = \frac{i+1}{4} \alpha Y_0. \quad (3.45)$$

Arbitrary Womersley number flow

Substitution of Eqs. (3.28–3.30), (3.32) and (3.23) in Eqs. (3.18) and (3.22) yields:

$$\begin{cases} i\omega C(\omega)\hat{p} - ik(\omega)\hat{q} = 0, \\ -ik(\omega)A_0\hat{p} + (i\omega\rho + f_0)\hat{q} = 0. \end{cases} \quad (3.46)$$

After putting the determinant of the resulting set to zero the following expression for the wave number k is found:

$$k(\omega) = \pm \frac{\omega}{c_0} \sqrt{\frac{1}{1 - F_{10}(\omega)}} = \pm k_0 \sqrt{\frac{1}{1 - F_{10}(\omega)}}. \quad (3.47)$$

Note that the wave number is again complex due to the friction function f_0 as defined in Eq. (3.23) or due to the visco-elasticity of the tube expressed in a complex value for the compliance $C(\omega)$. The phase velocity $c = \omega/k_r$ and attenuation constant $\gamma = -2\pi k_i/k_r = -\lambda k_i$ can be derived from Eq. (3.47) and are given in Fig. 22.

It has been mentioned that viscoelastic tubes will yield a complex compliance. From experiments it is shown that the viscous part of the modulus

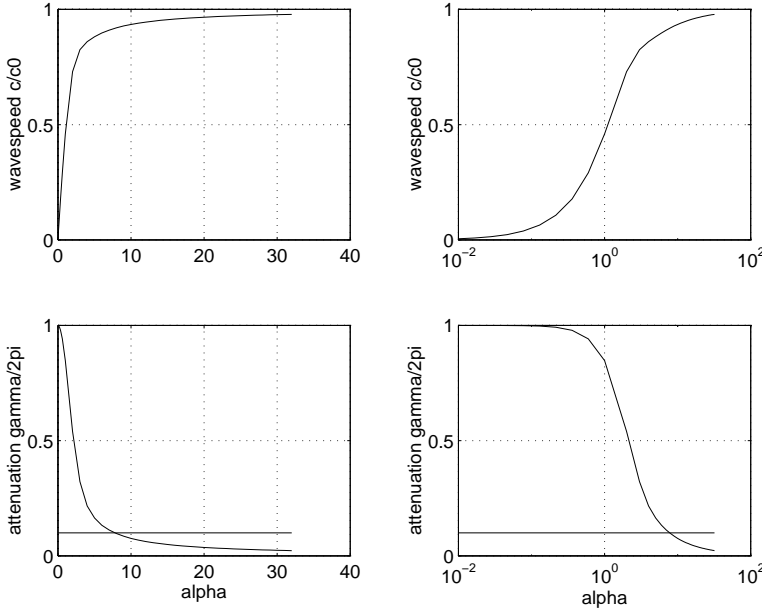


FIGURE 22. Phase velocity c/c_0 and attenuation constant $\gamma/2\pi$ as a function of α

is about 0.1 to 0.2 times the elastic part so $E = E_r(1 + if_v)$ with the fraction $f_v \approx 0.15$. For large alpha the visco-elasticity then will give a imaginary part in the wave number according to:

$$k = \frac{\omega}{c_0} \frac{1}{\sqrt{1 + if_v}} \approx k_0(1 - \frac{1}{2}if_v). \quad (3.48)$$

This line is indicated in Fig. 22 and shows that for larger α (high frequencies and large arteries) the visco-elastic properties of the wall are the main cause for the attenuation of the pressure waves.

Finally the admittance can be derived as:

$$Y = \frac{k_0}{k} Y_0 \quad (3.49)$$

and is given in Fig. 23.

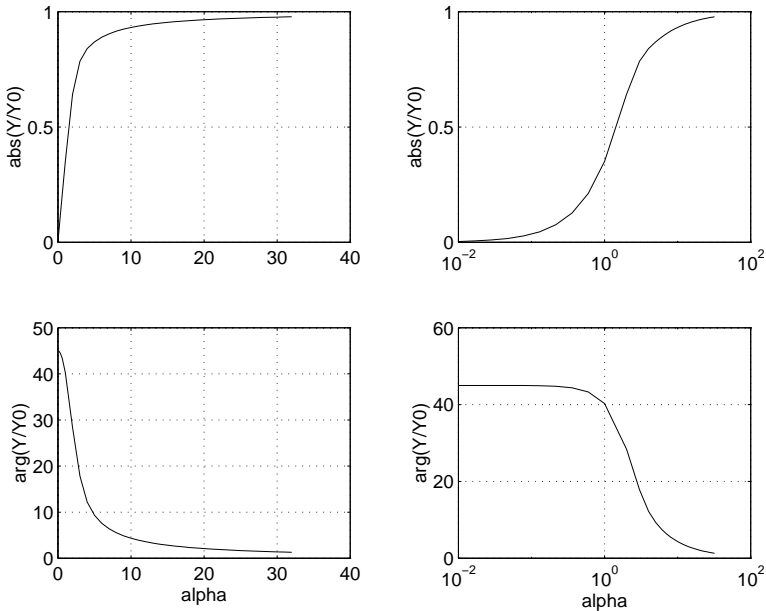


FIGURE 23. Absolute value and argument of Y/Y_0 as a function of α .

Propagation of a pressure pulse in homogeneous tubes

As an example in Fig. 24 the propagation of pressure waves in an elastic (left) and a visco-elastic (right) tube are computed. For this computation the following characteristic data for the carotid artery are used:

η	$3.5 \cdot 10^{-3}$	Pa·s	viscosity
a_0	$3 \cdot 10^{-3}$	m	radius
h	$a_0/10$	m	wall thickness
ρ	10^3	$\text{kg} \cdot \text{m}^{-3}$	density of fluid
E	$4.5 \cdot 10^5$	$\text{N} \cdot \text{m}^{-2}$	Young's modulus
μ	0.5	—	Poisson's ratio

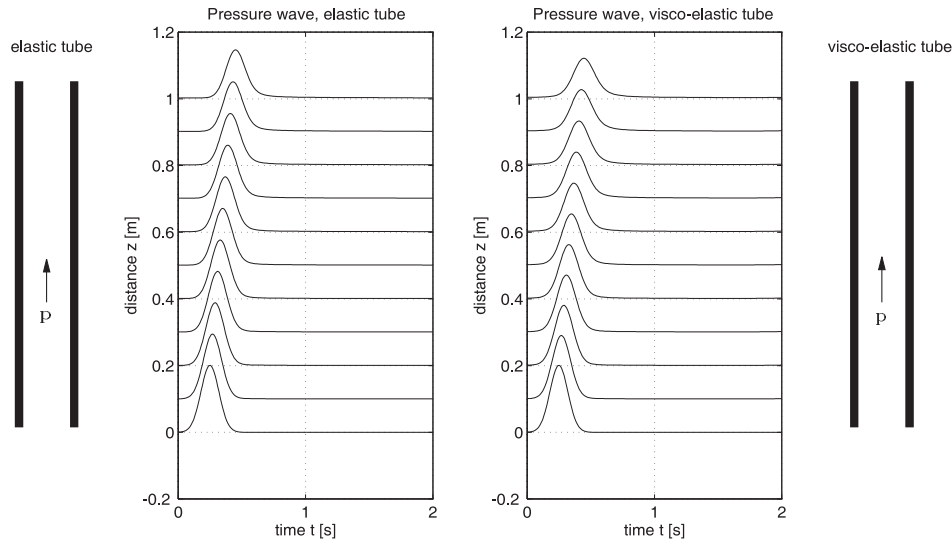


FIGURE 24. Propagation of pressure waves in an elastic tube (left) and a visco-elastic ($E = E(1 + i * 0.2)$) tube (right).

For the viscoelastic tube, the Young's modulus was taken to be $E(1+0.2i)$. Using Eq. (1.4) the distensibility and thus the compliance is determined. The wave number then was computed using Eqs. (3.47) and (3.35). The incident pressure pulse is given as:

$$p(0, t) = \exp\left(-\left(\frac{t - 0.25}{0.1}\right)^2\right). \quad (3.50)$$

Clearly the damping of the wave due to viscous forces (i.e. wall shear stress) and viscoelastic properties of the wall can be distinguished.

3.5. Wave Reflection

3.5.1. Wave reflection at discrete transitions. We will refer to transitions which are highly compact as discrete transitions. In these cases the length of the transition is so small compared to the wave length of the waves

so that there is no difference in pressure or rate of flow between both ends of the transition, and the reflection phenomena can be described based on the equations of continuity of pressure and rate of flow across the transition. Figure 25 shows a discrete transition as might be formed by an increase or decrease in wall thickness at $z = L$. If the incident pressure and flow wave are represented by p_i and q_i respectively, the reflected waves by p_r and q_r , and the transmitted waves by p_t and q_t , continuity of pressure and rate of flow at a transition at location $z = L$ can be expressed as:

$$p_i(\omega, L, t) + p_r(\omega, L, t) = p_t(\omega, L, t), \quad (3.51)$$

$$q_i(\omega, L, t) + q_r(\omega, L, t) = q_t(\omega, L, t). \quad (3.52)$$

The ratio between a single traveling pressure wave and its corresponding flow waves is dependent on the impedance Z or admittance Y of the tube. An expression for the impedance or admittance can be obtained by substituting Eqs. (3.28–3.30) and (3.32) in Eq. (3.18):

$$Y(\omega) = \frac{1}{Z(\omega)} = \frac{\hat{q}(\omega, z)}{\hat{p}(\omega, z)} = \frac{\omega C(\omega)}{k(\omega)}. \quad (3.53)$$

Note that normally the admittance is defined for waves traveling in positive z -direction i.e. $k > 0$. In that case the flow amplitude is given by $\hat{q} = +Y\hat{p}$. For $k < 0$ the wave is traveling in negative z -direction and for an admittance defined for positive k we have a flow amplitude $\hat{q} = -Y\hat{p}$.

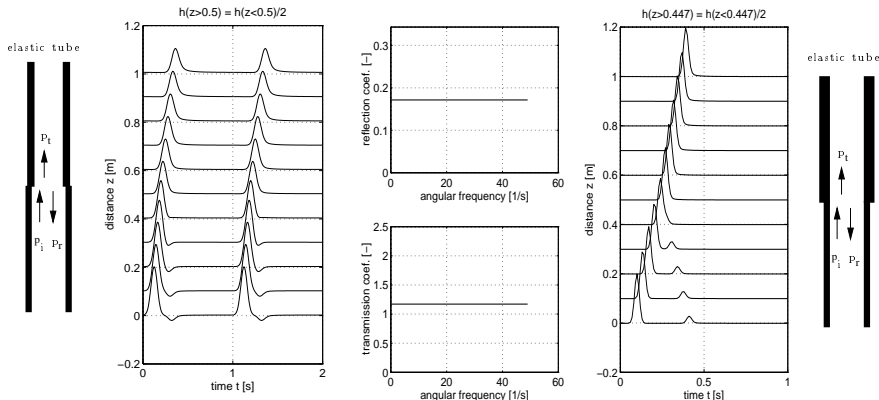


FIGURE 25. Wave reflection and propagation at discrete transitions formed by a sudden increase (left) and decrease (right) of the wall thickness.

Substitution of Eq. (3.53) in Eqs. (3.51) and (3.52) results in expressions for the reflection coefficient Γ_0 and the transmission coefficient T_{01} :

$$\Gamma_0(\omega) = \frac{\hat{p}_r(\omega, L)}{\hat{p}_i(\omega, L)} = \frac{Y_0(\omega) - Y_1(\omega)}{Y_0(\omega) + Y_1(\omega)}, \quad (3.54)$$

$$T_{01}(\omega) = \frac{\hat{p}_t(\omega, L)}{\hat{p}_i(\omega, L)} = \frac{2Y_0(\omega)}{Y_0(\omega) + Y_1(\omega)}, \quad (3.55)$$

where Y_0 is the admittance of the tube proximal to the transition, and Y_1 the admittance of the tube distal to the transition. The propagation of an incident wave $p_i = \hat{p}_i(\omega, 0) \exp(i(\omega t - k_0 z))$ in a tube with a discrete transition at $z = L$ can be expressed as:

$$\left\{ \begin{array}{l} z < L : \\ p(\omega, z, t) = p_i(\omega, z, t) + p_r(\omega, z, t) \\ \quad = \hat{p}_i(\omega, 0) e^{-ik_0(\omega)z} \left[1 + \Gamma_0(\omega) e^{-2ik_0(\omega)(L-z)} \right] e^{i\omega t}, \\ z > L : \\ p(\omega, z, t) = p_t(\omega, z, t) \\ \quad = \hat{p}_i(\omega, 0) e^{-ik_0(\omega)L} T_{01}(\omega) e^{-ik_1(\omega)(z-L)} e^{i\omega t}. \end{array} \right. \quad (3.56)$$

As an example we consider the wave reflection of a transition formed by a sudden increase and a sudden decrease of the wall thickness ($h(z < L) = a/10$ while $h(z > L) = a/5$ and $h(z > L) = a/20$ respectively. The resulting wave propagation for $L = 0.5$ is given in Fig. 25.

From these figures it can be seen that a sudden decrease in wall thickness and thus a sudden increase of the distensibility or stiffness (Eh) of the wall leads to a negative reflection of the incident wave and a transmitted wave with a decreased pressure amplitude and a decreased wave speed. For a sudden decrease of the stiffness the opposite phenomena occur.

In a similar way as in equation (3.56) expressions can be obtained for the reflection and transmission coefficient of a bifurcation of uniform tubes (see Fig. 26) at $z = L$, here referred to as a discrete bifurcation. In that case continuity of pressure and flow yields:

$$p_i(\omega, L, t) + p_r(\omega, L, t) = p_{t1}(\omega, L, t) = p_{t2}(\omega, L, t), \quad (3.57)$$

$$q_i(\omega, L, t) + q_r(\omega, L, t) = q_{t1}(\omega, L, t) + q_{t2}(\omega, L, t), \quad (3.58)$$

resulting in:

$$\Gamma_0(\omega) = \frac{\hat{p}_r(\omega, L)}{\hat{p}_i(\omega, L)} = \frac{Y_0(\omega) - (Y_1(\omega) + Y_2(\omega))}{Y_0(\omega) + (Y_1(\omega) + Y_2(\omega))} \quad (3.59)$$

$$T_{01}(\omega) = \frac{\hat{p}_{t_1}(\omega, L)}{\hat{p}_i(\omega, L)} = \frac{2Y_0(\omega)}{Y_0(\omega) + (Y_1(\omega) + Y_2(\omega))} \quad (3.60)$$

$$T_{02}(\omega) = \frac{\hat{p}_{t_2}(\omega, L)}{\hat{p}_i(\omega, L)} = T_{01}(\omega). \quad (3.61)$$

Here p_{t_1} and p_{t_2} are the waves transmitted into the daughter tubes, and Y_1 and Y_2 are the impedances of these daughter tubes. Expressions for the pressure waves are similar to the ones given for the discrete transition in Eqs. (3.56).

In Fig. 26 the wave reflection caused by a bifurcation of a tube with radius a_0 into two tubes with respectively radius a_1 and a_2 is given for $a_0 : a_1 : a_2 = 1 : 1 : 1$ (left) and $a_0 : a_1 : a_2 = 3 : 2.1 : 1.8$ (right). One can observe a negative and a positive reflection of the incident wave due to the fact that $a_0^2 < a_1^2 + a_2^2$ and $a_0^2 > a_1^2 + a_2^2$ respectively and a wave speed which is slightly higher in the branch with the smallest radius.

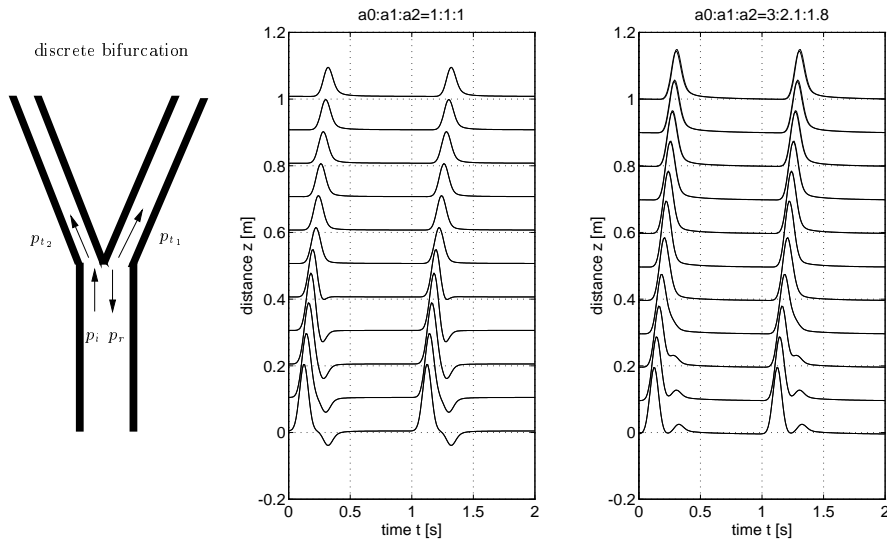


FIGURE 26. Wave reflection and propagation at a discrete bifurcation.

Note that the transmission and reflection coefficients given in Eqs. (3.54–3.55) and (3.59–3.61) are special cases of a general N -way junction with:

$$p_i(\omega, L, t) + p_r(\omega, L, t) = p_{t_j}(\omega, L, t), \quad j = 1, \dots, N, \quad (3.62)$$

$$q_i(\omega, L, t) + q_r(\omega, L, t) = \sum_{j=1}^N q_{t_j}(\omega, L, t), \quad (3.63)$$

resulting in:

$$\Gamma_0(\omega) = \frac{\hat{p}_r(\omega, L)}{\hat{p}_i(\omega, L)} = \frac{Y_0(\omega) - \sum_{j=1}^N Y_j(\omega)}{Y_0(\omega) + \sum_{j=1}^N Y_j(\omega)}, \quad (3.64)$$

$$T_{0j}(\omega) = \frac{\hat{p}_{t_j}(\omega, L)}{\hat{p}_i(\omega, L)} = \frac{2Y_0(\omega)}{Y_0(\omega) + \sum_{j=1}^N Y_j(\omega)}, \quad j = 1, \dots, N. \quad (3.65)$$

3.5.2. Multiple wave reflection: effective admittance. Consider two N -way junctions at a distance L_{mn} apart from each other as given in Fig. 27.

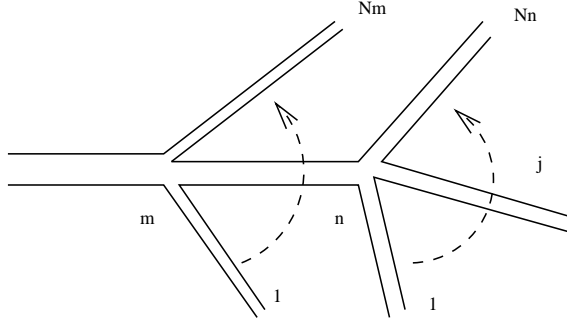


FIGURE 27. Multiple junctions.

At junction n we have:

$$\Gamma_n = \frac{Y_{mn} - \sum_{j=1}^{N_n} Y_{nj}^e}{Y_{mn} + \sum_{j=1}^{N_n} Y_{nj}^e}, \quad T_{nj} = \frac{2Y_{mn}}{Y_{mn} + \sum_{j=1}^{N_n} Y_{nj}^e}, \quad (3.66)$$

where Y_{nj}^e is the effective admittance of section nj at location n . If there are no reflected waves in section nj then $Y_{nj}^e = Y_{nj}$.

At junction m we have:

$$\Gamma_m = \frac{Y_m - \sum_{n=1}^{N_m} Y_{mn}^e}{Y_m + \sum_{n=1}^{N_m} Y_{mn}^e}, \quad T_{mn} = \frac{2Y_m}{Y_m + \sum_{j=1}^{N_m} Y_{mn}^e}, \quad (3.67)$$

with:

$$Y_{mn}^e = \frac{\hat{q}(\omega, L_1)}{\hat{p}(\omega, L_1)} = Y_{mn} \frac{\exp(ik_{mn}L_{mn}) - \Gamma_n \exp(-ik_{mn}L_{mn})}{\exp(ik_{mn}L_{mn}) + \Gamma_n \exp(-ik_{mn}L_{mn})}. \quad (3.68)$$

In this way it is possible to compute the pressure and flow in a complete transmission line network, starting from a distal impedance going back to the aorta. An example of such a computation is given in Fig. 28 where the input impedance at the aorta is given as a function of the frequency. A minimum of $|Z|$ is found corresponding with a phase angle of zero. In [4] this is attributed to a reflection from the aorta bifurcation.

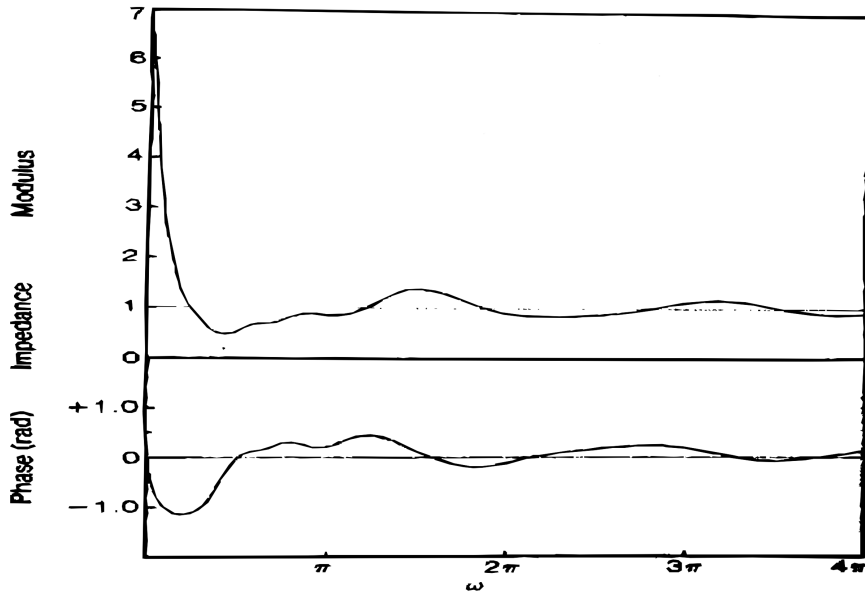


FIGURE 28. Input impedance at the aorta as a function of the frequency, after [4].

The reflection mentioned above can be explained from the expression we obtain after substitution of Eq. (3.66) in Eq. (3.68) yields:

$$Y_{mn}^e = Y_{mn} \frac{\sum_{j=1}^{N_n} Y_{nj}^e + i Y_{mn} \tan(k_{mn} L_{mn})}{Y_{mn} + i \sum_{j=1}^{N_n} Y_{nj}^e \tan(k_{mn} L_{mn})}. \quad (3.69)$$

For $k_{mn} L_{mn} = 0, \pm\pi, \pm 2\pi, \dots$ we find $Y_{mn}^e = \sum_{j=1}^{N_n} Y_{nj}^e$ and the section mn has no influence. These phenomena are illustrated in Fig. 29 showing the impedance Z_{mn}^e/Z_0 in a tube with characteristic impedance $Z_0 = Z_{mn}$ as a function of the frequency and distance from a termination with impedance $Z_T^e = 4Z_0$. Also the effect of attenuation is shown.

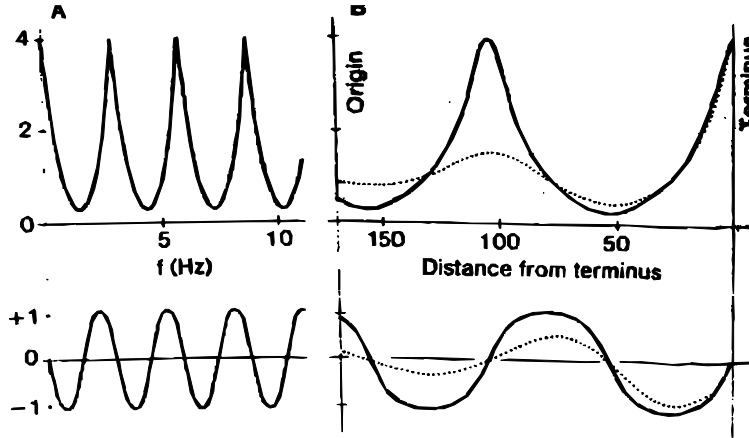


FIGURE 29. Effective impedance as a function of the frequency (left) and distance from terminus (right) with (...) and without (—) attenuation, [4].

From expression (3.68) (or 3.69) we can see that for $k_{mn} L_{mn} \ll 1$ we simply have $\exp(\pm ikL) = 1$ and after substitution of Eq. (3.66):

$$Y_{mn}^e = Y_{mn} \frac{1 - \Gamma_n}{1 + \Gamma_n} = \sum_{j=1}^{N_n} Y_{nj}^e \quad \text{if } k_{mn} L_{mn} \ll 1 \quad (3.70)$$

as if the section mn did not exist. If, however, $k_{mn} L_{mn}$ is small but still large enough that first order terms can not be neglected (i.e. $k_{mn}^2 L_{mn}^2 \ll 1$) we have:

$$Y_{mn}^e = Y_{mn} \frac{1 + ik_{mn} L_{mn} - \Gamma_n(1 - ik_{mn} L_{mn})}{1 + ik_{mn} L_{mn} + \Gamma_n(1 - ik_{mn} L_{mn})} \quad (3.71)$$

and after substitution of Eq. (3.66):

$$Y_{mn}^e = Y_{mn} \frac{ik_{mn}L_{mn}Y_{mn} + \sum_{j=1}^{N_n} Y_{nj}^e}{Y_{mn} + ik_{mn}L_{mn} \sum_{j=1}^{N_n} Y_{nj}^e} \quad \text{if } k_{mn}^2 L_{mn}^2 \ll 1. \quad (3.72)$$

If we neglect terms of $\mathcal{O}(k^2 L^2)$ we obtain:

$$Y_{mn}^e = \sum_{j=1}^{N_n} Y_{nj} + ik_{mn}L_{mn}Y_{mn} \left[1 - \left(\frac{\sum_{j=1}^{N_n} Y_{nj}^e}{Y_{mn}} \right)^2 \right]. \quad (3.73)$$

From this we can see that for intermediate long transitions only the phase of the admittance and not its absolute value is changed, [5].

So far, no attention was paid to reflections originating from peripheral vascular beds. However, these reflection phenomena might play an important role and can easily be taken into account. In the presence of reflected waves in the distal parts of a discrete transition, the reflection and transmission coefficient at an N-way junction read:

$$\Gamma_0(\omega) = \frac{Y_0 - \sum_{j=1}^N \frac{1-\Gamma_j^d}{1+\Gamma_j^d} Y_j}{Y_0 + \sum_{j=1}^N \frac{1-\Gamma_j^d}{1+\Gamma_j^d} Y_j}, \quad (3.74)$$

$$T_{0j}(\omega) = \frac{2Y_0}{Y_0 + \sum_{j=1}^N \frac{1-\Gamma_j^d}{1+\Gamma_j^d} Y_j}, \quad j = 1, \dots, N. \quad (3.75)$$

This result can directly be derived from the results for distal sections without reflection by replacing the admittance by its effective admittance using the reflection coefficients Γ_j^d of the distal sections at the junction (see 3.70). So the reflection from the distal vascular system is represented by the reflection coefficients Γ_j^d . These have to be determined from experimental data or can be estimated by modeling the distal part as a transition to an appropriate output impedance.

3.5.3. Vascular impedance and cardiac work. The importance of wave phenomena in the vascular system and the corresponding vascular impedance is clearly illustrated if we want to investigate the mechanical work done by the left ventricle. For each cardiac cycle this work is the integral over time of the pressure \times flow product:

$$W = \int_{t_0}^{t_0+T} pqdt. \quad (3.76)$$

This integral consists of two parts. The first part is the steady flow power W_s which is determined by the resistance R_0 of the vascular system (mainly the peripheral resistance) defined as the ratio between the mean pressure and the mean flow $R_0 = p_0/q_0$. The second part is the oscillatory flow power W_0 following from Eq. (3.76) and the vascular impedance for each harmonic n ($Z_n = |Z_n| \exp(i\theta_n)$). So:

$$W = \frac{1}{2} \sum_{n=1}^N q_n^2 |Z_n| \cos \theta_n + q_0^2 R_0. \quad (3.77)$$

In [4] the following values can be found:

	$q_0^2 R_0$	\sum_n
left ventricle	1400	200
right ventricle	155	73

For the systemic circulation the contribution of the higher harmonics to the total work is relatively low. This is due to the fact that $\cos \theta_n \ll 1$. As the value of Z_n directly influences the work that has to be done by the heart, knowledge of the influence of age, medicine and other factors on the value of Z_n is of great clinical importance.

4. Summary

In this lecture a short introduction to cardiovascular fluid mechanics is given. A simple (windkessel) model has been derived based on the knowledge that the cardiovascular systems is characterized by an elastic part (large arteries) and a flow resistance (micro circulation). In this model it is ignored that the fluid mechanics of the cardiovascular system is characterized by

complex geometries and complex constitutive behavior of the blood and the vessel wall. The vascular system, however, is strongly bifurcating and time dependent (pulsating) three-dimensional entrance flow will occur. In the large arteries the flow will be determined by both viscous and inertia forces and movement of the nonlinear viscoelastic anisotropic wall may be of significant importance. In the smaller arteries viscous forces will dominate and non-Newtonian viscoelastic properties of the blood may become essential in the description of the flow field.

Flow patterns in rigid straight, curved and branched tubes have been treated. The velocity profiles of fully developed Newtonian flow in a straight circular tube can easily be derived by integration of the Navier-Stokes equations in cylindrical coordinates using superposition of harmonics of the pressure pulse. Apart from a scale factor for the pressure, only one single parameter, the Womersley number $\alpha = a\sqrt{\omega/\nu}$, determines the character of the flow. For large values of this parameter the flow is dominated by inertia and flat velocity profiles are found oscillating 90° out of phase with the pressure gradient. For low values of α the flow is dominated by viscous forces and a quasi static Poiseuille flow is found that is 180° out of phase with the pressure gradient. For arbitrary values of α the velocity profiles are solutions of Bessel's function and can be interpreted as a composition of a viscosity dominated flow in the boundary layer and an inertia dominated flow in the core. The thickness of the boundary layer appears to depend on α according to $\delta/a = O(\alpha^{-1})$.

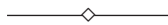
The flow in curved tubes with curvature ratio δ differs from that in straight tubes because also centrifugal forces are of importance. Due to these centrifugal forces, the pressure gradients in the bulk flow are not in equilibrium with the flow in the viscous boundary layers and a secondary flow is induced, resulting in a strongly disturbed axial flow. A new dimensionless parameter, the Dean number, defined as $Dn = (a/R_0)^{1/2}Re$, determines the importance of this secondary flow. The main features of the flow in branched tubes strongly resemble those of the flow in curved tubes.

Finally, linearized wave equations that govern the pressure and flow traveling through the arterial system are derived. For large values of the Womersley parameter these equations yield the Moens-Korteweg wave speed. For small values of the Womersley parameter a diffusion equation can be derived expressing perfusion flow in small arteries. For intermediate (arbitrary) values of the Womersley parameter wave speed and admittance can be ex-

pressed in terms of those derived for the Moens-Korteweg waves. Reflection of waves at discrete transitions are derived from continuity of pressure and rate of flow and allow determination of multiple wave reflection and the definition of effective admittance in order to determine vascular impedance and cardiac work.

References

1. M. ABRAMOWITZ and I. STEGUN, *Handbook of Mathematical functions* Dover Publications Dover 1964
2. W.M. COLLINS and S.C.R. DENNIS, *The steady motion of a viscous fluid in a curved tube*, Q.J.Mech. Appl. Math **28**:133–156, 1975
3. A.C. GUYTON, *Textbook of Medical Physiology*, Saunders 1967
4. W.R. MILNOR, *Hemodynamics*, Williams & Wilkins Baltimore, Hong Kong, London, Sidney 1989
5. T.J. PEDLEY, *The fluid mechanics of large blood vessels*, Cambridge University Press, Cambridge 1980
6. H. SCHLICHTING, *Boundary Layer Theory*, McGraw-Hill, New York 1960
7. A.J. WARD-SMITH, *Internal fluid flow*, Oxford 1980
8. J.R. WOMERSLEY, *The mathematical analysis of the arterial circulation in a state of oscillatory motion*, Technical report wadc-tr-56-614, Wright Air Development Center 1957



Full-Field Blood Velocity Measurement Techniques

P. VENNEMANN and J. WESTERWEEL

*Delft Technical University
Lab. for Aero- and Hydrodynamics
Leeghwaterstraat 21
2628 CA Delft
The Netherlands
p.vennemann@wbmt.tudelft.nl*

Perfusion monitoring, the investigation of instantaneous blood flow patterns, the derivation of endothelial shear stress distributions, and the measurement of blood volume flow rates require individual treatment in terms of spatial and temporal resolution and measured quantity. Further differentiation must be made for macro, meso and micro scale blood flow. With emphasis on micro particle image velocimetry, a range of different measurement techniques is concisely reviewed in the article. These are basically two full-field measurement techniques that do not rely on optical accessibility (nuclear magnetic resonance imaging and echo particle image velocimetry) and three techniques that are suitable for monitoring capillary flow (laser Doppler velocimetry—including time-varying speckle, laser speckle contrast imaging and particle image velocimetry—including particle tracking).

Key words: particle image velocimetry, laser Doppler velocimetry, laser speckle contrast imaging, nuclear magnetic resonance imaging, blood flow, shear stress

1. Introduction

The spatially resolved measurement of blood velocity distributions is a key-requisite in numerous fields of biomedical research. Examples are perfusion monitoring, identification of instantaneous flow patterns, derivation of shear stress distributions or the calculation of volume flow rates. All these topics require different treatment in terms of spatial and temporal resolution and measured quantity. For many perfusion monitoring problems, like the diagnosis of burn depth, it is sufficient to visualise the velocity distribution

as a scalar map. The spatial resolution of the map might even be coarser than the vessel diameter of the microcirculation. Temporal resolution is generally not needed, as most flows are stationary or periodic. Higher spatial resolution is required for the evaluation of volume flow rates. The determination of the volume flow rate from the measurement of the mean velocity or the centerline velocity in a blood vessel and the assumption of a parabolic velocity profile might be an estimate of sufficient accuracy in many cases. When the velocity profile is unknown (e.g. in bends, bifurcations, non-circular vessels, and at flow obstacles) it is necessary to measure the profile with high resolution over the diameter of the vessel. In a simple geometry, the measurement of the main velocity component is often sufficient. More complex geometries might require the measurement of two or even three velocity components. Pulsatile flows additionally require a temporal resolution that is half the period of the highest relevant harmonic. The derivation of wall shear stress from the velocity gradients near the flow boundary demands a very high spatial resolution that is significantly better than a blood cell-diameter.

A similar differentiation should be made for the fluid mechanical properties of the working fluid—blood. The treatment as a continuous or two-phase fluid and the consideration of non-Newtonian properties depend on the studied problem and the scale. At macro scale, when the ratio of blood cell size

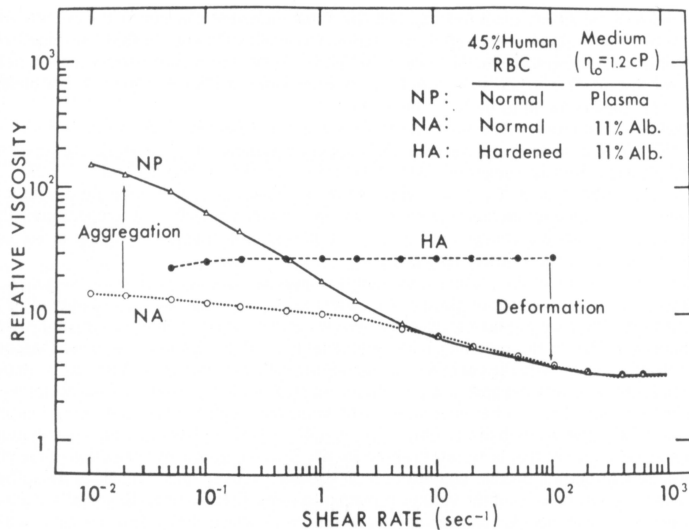


FIGURE 1. Relation between viscosity and shear rate for human blood (from [8])

and characteristic length of the flow domain is small, one might treat blood as a liquid of continuous phase. At low shear rates, however, non-Newtonian viscosity gains influence (Fig. 1) and blood can be considered as a Newtonian liquid with deformable objects. At intermediate scale, when blood cells and flow domain diameter are of the same magnitude, blood flow is generally treated as two-phase flow. Typical shear rates in arterioles, capillaries and venules range between 800 and 8000 1/s (Table 1). The blood viscosity can be assumed constant in this domain (Fig. 1). At even smaller scale (e.g. the plasma rich layer near a vessel wall that is generally cell depleted due to the Fåhraeus-Lindquist effect) we might treat blood cells and blood plasma separately.

TABLE 1. Reference values for velocity, diameter and shear rate in the human vascular network [7].

vessel	velocity [m/s]	diameter [mm]	shear rate [s ⁻¹]
aorta	0.4	25.0	155
arteries	0.45	4.0	900
arterioles	0.05	0.05	8000
capillaries	0.001	0.008	1000
venules	0.002	0.02	800
veines	0.1	5.0	160
vena cava	0.38	30.0	100

Several measurement principles and numerous modifications have been employed to meet the demands of the above mentioned situations. Some of the most widespread full-field velocity measurement techniques are briefly introduced in the subsequent section.

2. Measurement Techniques

The selection of full-field velocity measurement techniques is restricted to methods that measure velocities (scalar and vectorial) directly. This excludes perfusion measurement techniques that merely allow conclusions on mean and time averaged velocities. These would be, for example, radionuclide perfusion imaging such as single photon emission computed tomography (SPECT) and positron emission tomography (PET).

2.1. Laser Doppler Velocimetry

Laser Doppler velocimetry is a single point measurement technique with high temporal resolution. Systems that measure up to three velocity components are commercially available. Laser Doppler Velocimetry for spatial measurements is primarily implemented in three ways: scanning, simultaneous single point measurements with multiple probes, and differentiation of tracer particle position within the measurement volume. Full field laser Doppler systems generally provide only one velocity component.

The measurement principle of laser Doppler velocimetry is based on the optical Doppler effect: if a light source (or a light scattering tracer particle) is moved into the direction of a light-detector, the frequency of the reflected light is increased. If the light source moves away, the frequency is decreased. In practise this frequency shift is very small (10–100 kHz), if compared to the high frequencies of light (100 THz) and impossible to measure directly. The frequency shifted light is therefore interfered with a non-shifted reference beam. The resulting beat frequency equals the frequency shift and is directly related to the velocity of the light scatterer.

Interfering the scattered light and the reference beam is not easy and sensitive to errors. The different light paths might be affected by changing diffractive indices due to temperature variations, for example, so that most laser Doppler systems show a modification. Both laser beams are guided in a way that they intersect at an angle. The intersection volume defines the measurement location. A tracer particle passing this volume is illuminated from two different directions. The frequency shift of the reflected light is different for the two laser sources. The resulting beat is dependent on the angle of the two laser beams and the tracer velocity perpendicular to the axis, z , that bisects the angle, θ , between the beams.

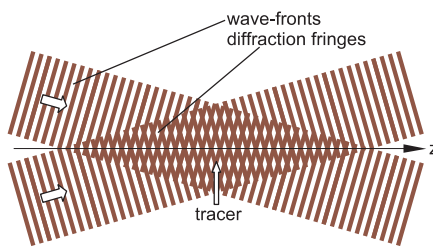


FIGURE 2. Interference pattern of two crossing laser beams.

A different way of looking at the concept of the two intersecting beams is to study the interference pattern within the measurement volume. The wave-fronts of the laser beams form interference fringes parallel to the optical axis of the focusing lens system (Fig. 2). When a tracer particle moves through the dark and bright spaces of the fringe system, it will reflect light at a frequency that is dependent from the fringe spacing and the velocity, v of the particle perpendicular to the fringes. Both perceptions lead to an identical relationship between particle velocity and measured frequency-shift, Δf :

$$v = \frac{\lambda}{2 \sin(\theta/2)} \Delta f. \quad (2.1)$$

Here, λ is the wavelength of the incident light. The penetration depth of the laser light is dependent on its wavelength. Infrared light penetrates several mm, red light up to 2 mm and green light hardly at all [6].

2.1.1. Full-field approach: scanning. Essex and Byrne [13] in 1991 described a scanning laser Doppler velocimetry system with continuously moving laser beams. The scanned measurement data is usually visualised as an image with colour-coded velocity information. The relative motion between laser and tissue, however, gave rise to significant artifacts. Wårdell et al. [40] circumvented this problem by using stepping motors for moving the scanning mirror. The scan time was 4 minutes for 4096 image points. Meanwhile, commercial scanning laser Doppler velocimetry systems (laser Doppler imagers) are available that, for example, map perfusion over areas of $50\text{ cm} \times 50\text{ cm}$ with 256×256 pixel resolution in about five minutes (Moor Instruments Ltd). The scanning devices lack a reference beam. Instead, Doppler shifted light from moving blood cells beat with reflected light from stationary tissue. Because of the low spatial resolution, there will be several blood cells in the measurement volume with different velocities. This results in a frequency distribution around a frequency representing the mean velocity rather than a single beat frequency.

Scanning laser Doppler velocimetry became a standard tool in diagnostics. Figure 3 shows a laser Doppler scan. The number of publications is enormous. Briers [6] identified a series of fields of applications in a review. One of the most important applications might be the diagnosis of burn depth. Pape et al. [25] published an audit of the use of laser Doppler imaging in the assessment of burns of intermediate depth. Superficial burns show an inflammatory response, which is indicated by high perfusion. This diagnosis can

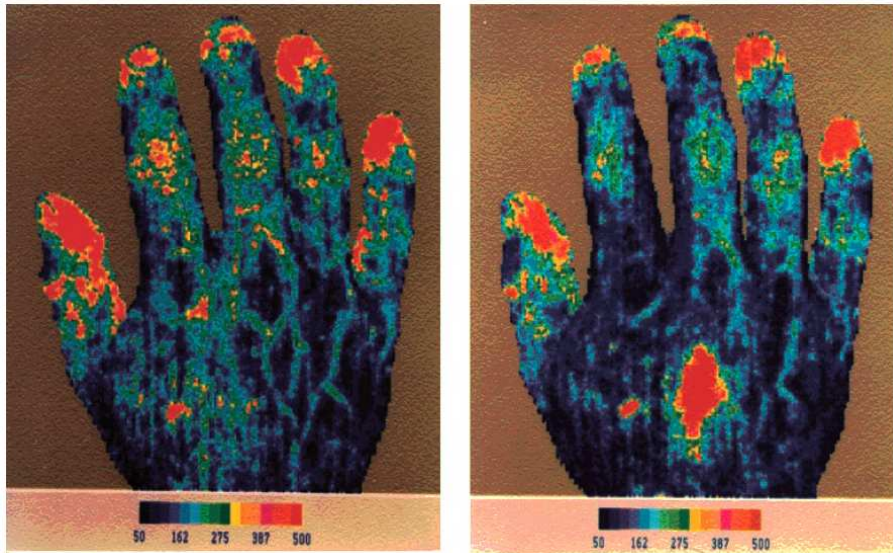


FIGURE 3. Laser Doppler scan before (left) and after (right) gently scratching the back of a hand [6].

be used to identify superficial burns from deeper burns that need surgical treatment.

2.1.2. Full-field approach: multi-probes. Serov et al. [28, 29] avoid scanning by replacing the widely used avalanche photo detector by a complimentary metal oxide semiconductor (CMOS) image sensor. In contrast to charge coupled device (CCD) sensors, some CMOS sensors allow the continuous conversion of photocurrent into output voltage. The Doppler shift ranges typically between 0 and 20 kHz for the microcirculation [29]. To attain a corresponding sampling rate, the area of interest had to be reduced to 64×8 pixel. A perfusion map of 256×256 pixel could be obtained by sampling 128 of those sub-windows one after the other. The repetition rate for measuring the full area is 90 s inclusive signal processing (mainly determined by the FFT) and screen display. The full-field illumination requires much more laser power than the scanning approach.

2.1.3. Profile approach: differentiation of tracer position. Czarske introduced a system that differentiates the position of the tracer particle within the measurement volume [9]. The set-up measures the velocity profile

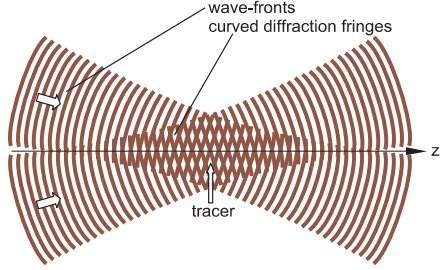


FIGURE 4. Interference pattern of two Gaussian laser beams-waists.

within an elongated measurement volume, along the optical axis of the focusing lens system. The wave fronts of the two crossing laser beams are curved close to the Gaussian beam waists. For this reason, the distance of the interference fringes within the measurement volume varies along the optical axis (Fig. 4). To determine the position of a tracer particle in the measurement volume, a second pair of laser beams with a different frequency (colour) is added to the set-up. Due to chromatic aberration of the focusing lens system, the beam waists of both beam pairs are shifted longitudinally with respect to each other. In this way, different fringe spacing gradients are obtained for both laser colours. The quotient of the two monochromatic burst frequencies, f_i , of a passing particle equals the quotient of the different interference fringe distances, d_i , at this position. Due to the different fringe spacing gradients, this quotient is unique for the position along the optical axis. The particle position, z , is then determined by means of a calibration function ϕ :

$$z = \phi \left(\frac{f_1(z)}{f_2(z)} \right) \quad (2.2)$$

Once the position of the particle is determined, one of the monochromatic burst signals is used to determine the velocity. The relative spatial resolution is reported to be 10% within a measuring length of 1.2 mm. The technique has not yet been applied to blood flow.

2.2. Laser Speckle Contrast Imaging

Laser speckle is a grainy, stationary interference pattern. It is produced when coherent light is scattered at a diffuse surface or a number of individual scatterers (like particles in a fluid) [23]. Interfering wavelets of different optical pathlengths fill the surrounding space with a random pattern. Individual

speckles are very small close to the diffuse surface and grow in size at larger distance. When scatterers move in a uniform manner, the speckle pattern moves at the same rate. Small displacements of scattering particles slightly change the speckle pattern. Large displacements alter the pattern entirely.

Laser Speckle Contrast Imaging is based on so called image speckle. That is, when a larger area is illuminated by a laser and projected on an image plane. A time-integrated image of stationary particles shows a speckle pattern of high contrast. Moving particles reduce the contrast due to the averaging of the instationary speckle pattern over time. An equation can be deduced that links flow velocity and reduction in contrast [14]. Speckle contrast is reduced by particle movement in any direction. This makes the technique sensitive for motion parallel as well as perpendicular to the measurement plane. The speckle pattern change due to motion along the line-of-sight is such that a relative movement of half a wavelength causes a full cycle of intensity change. The sensitivity to in-plane motion is significantly weaker, because it is only determined by the size of the speckle pattern [4]. The directional difference in sensitivity is the reason why the relationship between flow velocity and contrast reduction must be deduced for different types of velocity distributions. Therefore the type of velocity distribution must be known in advance.

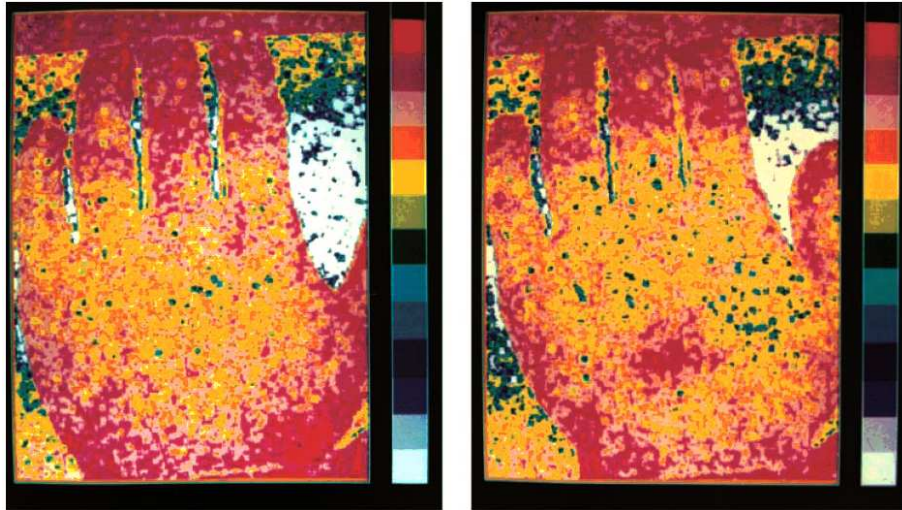


FIGURE 5. Laser speckle image before (left) and after (right) gently scratching the back of a hand [6].

Briers [5] advanced the development of laser speckle contrast imaging and concisely reviewed the technique. Figure 5 shows a laser speckle image. At present, laser speckle contrast imaging is developed into a standard perfusion measurement technique [42] that can be combined with other techniques to monitor blood flow, haemoglobin concentration and oxygenation simultaneously [12].

2.3. Time-varying Speckle

Time-varying speckle is based on the evaluation of temporal statistics of speckle fluctuations at a single point. In comparison to laser contrast imaging, that is based on image speckle, so called far-field speckle is utilised. A collimated laser beam illuminates a small point in the flow. Light from all points within this area interferes in the image plane and forms the speckle pattern. When the scatterers move, individual speckles at a fixed position fluctuate. The frequency spectrum of these fluctuations can be related to velocity information.

Briers [4] showed that the interference-based perception of far-field speckle can be interpreted in terms of the Doppler effect. To show the equivalence of the Doppler and the interferometry explanation, he considers a Michelson interferometer (Fig. 6). If the mirror in the measurement arm of the interferometer is moved, a small detector in the detection plane recognises a temporal intensity fluctuation. This fluctuation can be interpreted as the beat of the reference beam and the light that is reflected by the moving mirror. The frequency of the light that comes from the moving mirror is altered due to the Doppler effect. The detected intensity fluctuation can as well be explained by studying the optical path length, without considering the Doppler effect. The optical path—length of the beam that is reflected by the moving mirror is constantly altered due to motion. Depending on the actual mirror posi-

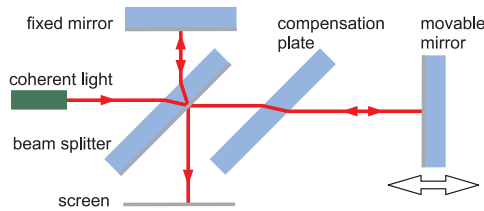


FIGURE 6. Michelson interferometer

tion constructive or destructive interference is recorded at the detector. The relation between intensity fluctuation frequency and mirror velocity can be shown to be identical in both cases.

The main difference between laser Doppler velocimetry and time-varying speckle is the absence of a separate reference beam. A Doppler spectrum is still present when light from particles with different velocities beat with each other. This spectrum, however, just provides information about the variation of velocities in the measurement volume rather than the mean velocity. When there are stationary tracers present in the measurement volume, the variation of velocities is a measure for the mean velocity. It now becomes obvious that this technique is basically identical to the laser Doppler imager (Sec. 2.1.1). Aizu and Asakura [2] also reviewed other statistical methods to extract the mean blood cell velocity from speckle fluctuations.

2.4. Particle Image Velocimetry

Particle image velocimetry relies on the visualisation of flow by means of small tracer particles. In general, the movement of the particles is recorded on two sequential, digital images. The displacement of the particles in the second image, relative to the position of the particles in the first image, is a measure for the velocity of the fluid. The displacement of the particles is calculated by means of a two-dimensional cross-correlation. Therefore, a small interrogation window of the first image is correlated with different sections of the second image until the maximum correlation magnitude between the image areas is found. This position is the most probable displacement of the particle pattern in the interrogation window. The local velocity is calculated by dividing the displacement of the particle pattern by the given time difference between the two images [1, 26].

For typical macro scale particle image velocimetry applications, a two-dimensional measurement plane is formed by illuminating a thin plane of the flow with a narrow laser light sheet, whereas for micro scale applications the strongly limited depth-of-focus of the microscope objective is used to sample a thin plane in which the particles are sharply imaged [27, 21, 24].

Closely related to particle image velocimetry are particle tracking techniques. Here the movement of individual particles is tracked manually or by appropriate computer programs. In contrast to particle image velocimetry, particle tracking velocimetry requires the distance between the tracer par-

ticles to be larger than the displacement [41]. Otherwise it is not possible to identify matching particle pairs. This restriction limits the resolution of particle tracking velocimetry.

Several research groups used particle image velocimetry or related particle tracking techniques to study blood flow. Tangelander et al. [35] labeled blood platelets with a fluorescent dye to measure flow velocities in arterioles of the rabbit mesentery (17 to 32 μm diameter). They determined the velocity profile by tracking the movement of platelets in dual flash video images. The velocity profiles were assembled by a number of individual measurements at different radial positions of the vessel. The illumination flashes were triggered by means of an ECG. Smith et al. [32] and Long et al. [19] adapted this technique by using artificial, fluorescent tracer particles of 470 nm diameter to enhance the spatial resolution. The velocity gradient in the near wall region of a mouse cremaster muscle venules could be estimated by manually tracking the movement of tracer particles at irregular distances from the flow boundary. The measurements neglected flow pulsation. Hitt et al. [15] applied a correlation technique to video images of the venous flow in the hamster cremaster muscle. Tsukada et al. [36] and Sugii et al. [33, 34] used particle image velocimetry to measure red blood cell velocity profiles in mesentery vessels of rats. Hove et al. [16] followed the course of small groups of erythrocytes through the heart of a zebrafish embryo. Vennemann et al. [38] used fluorescent liposomes of 400 nm diameter to resolve the velocity distribution in the beating heart of a chicken embryo. Figure 7 schemati-

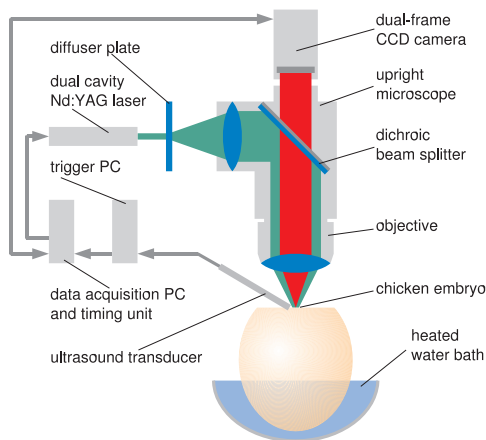


FIGURE 7. A μPIV set-up, using a fluorescence microscope.

cally shows the measurement set-up. A fluorescence microscope is used to separate velocity information and background light reflected from tissue and blood cells. An ultrasound Doppler velocimeter is used to synchronise the PIV measurement with the heart beat. In this way the advantages of ensemble correlation methods [22] can be used. Measurements were carried out at nine different cardiac phase angles. Figure 8 shows the measured velocity distribution in the developing ventricle at its maximum dilatation.

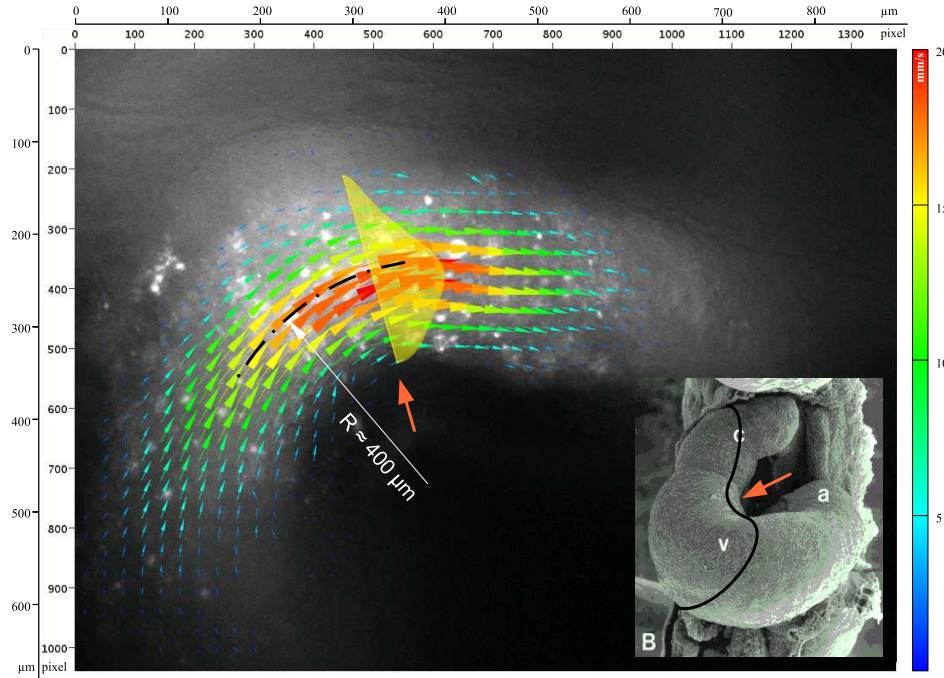


FIGURE 8. Blood velocity distribution in the developing ventricle of a chicken embryo after three days of incubation. Location and orientation of the measurement plane is indicated in the scanning electron micrograph from Männer [20].

The velocity has a maximum magnitude of 26 mm/s and peaks off-centre at the side of the inner curvature wall. The eccentricity of the flow profile can be explained by the curvature of the heart. The micrograph in Fig. 8 shows that the heart resembles a coiled tube. Dean [10] in 1927 introduced an analytical approximation for the fully developed, laminar velocity distribution in a coiled tube. The approximation is valid for low Dean numbers, D_n (Equation 2.3). The curvature of the coil, δ (the ratio of coil and vessel radii, R/a), is about 1/4 for the case shown in Fig. 8. The Reynolds number, $Re = 2au/\nu$,

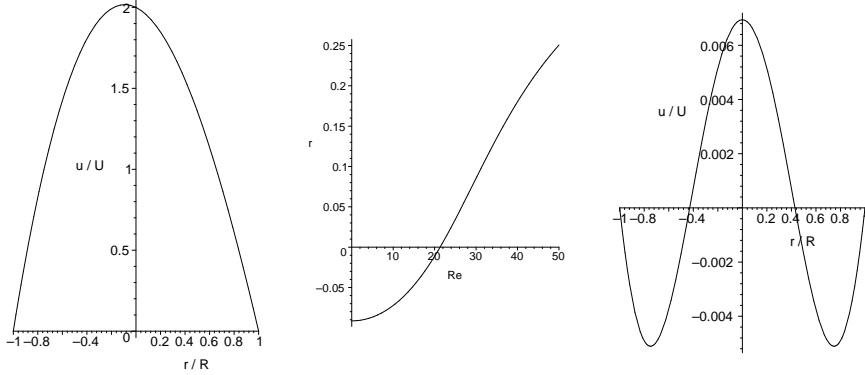


FIGURE 9. Left: axial velocity profile along the tube radius in the plane of coil curvature. Middle: Radial velocity peak position in the plane of coil curvature at varying Reynolds numbers (tube radius $a = 1$, coil radius $R = 4$). Right: secondary velocity profile in circumferential direction along the tube radius, perpendicular to the plane of coil curvature. The calculation closely follows Dean [10, 39].

with the mean velocity, u , and the kinematic viscosity, ν , is about unity. The left graph in Fig. 9 shows the axial velocity distribution along the vessel radius in the plane of coil curvature. The calculation [39] closely follows Deans analysis, higher order terms that were later added [11, 37] are omitted. The velocities are normalised by the mean velocity. Such as in the measurement the velocity peak is shifted to the inner curvature wall. The second graph of Fig. 9 shows the radial position of the velocity peak for different Reynolds numbers (curvature and vessel diameter remain at the current values). At higher Reynolds numbers ($Re > 20$) inertia forces gain influence and the velocity peak shifts into the direction of the outer curvature wall. The right graph in Fig. 9 illustrates the influence of secondary flow. It shows the circumferential velocity component along the tube radius, perpendicular to the plane of coil curvature. The maximum circumferential velocity is lower than 1% of the mean velocity and can be neglected. We therefore assume that the yellow velocity profile in Fig. 8 is oriented parallel to the optical plane of the camera. This qualifies the velocity profile for the determination of the local velocity gradient, du/dn , perpendicular to the wall. Under the assumption of an effective viscosity, η , the wall shear stress $\tau = \eta \cdot du/dn$ can finally be estimated.

$$Dn = \delta^{1/2} Re. \quad (2.3)$$

2.5. Echo Particle Image Velocimetry

Particle image velocimetry is not restricted to optically acquired images. Kim et al. [17, 18] used ultrasonic imaging to determine flow profiles in artificial models of arteries. In contrast to optical imaging, an ultrasound image is composed by scanning the field of interest. Scattering tracers, in general small gas bubbles, reflect echoes. The intensity of the echo is dependent on the reflective property of the tracers. The time of flight is used to determine the scanning depth. The time difference between two images in optical particle image velocimetry is replaced by the time difference between identical beam positions in two successive echo scans.

2.6. Nuclear Magnetic Resonance Imaging

Nucleons have an angular momentum which leads to a quantised magnetic moment. In case of a hydrogen atom the nucleus is composed of a single proton. The potential energy of the magnetic momentum in a homogeneous, external magnetic field is dependent on the direction of the momentum. The potential energy is minimised when momentum and field vectors point into the same direction and it is maximised when they point into opposite directions. In case of the hydrogen nucleus quantum mechanics permits just two possible orientations for the magnetic momentum: parallel and anti parallel with the outer magnetic field. The magnetic momentum of a hydrogen atom of low potential energy (parallel momentum vector and field vector) can be flipped into the high energy state (anti parallel vectors) by absorbing a photon of exactly the missing energy difference. Flipping a nuclear spin into this excited state is called nuclear magnetic resonance.

The nucleus flips back into its normal state by emitting a photon. The frequency of this photon is dependent on the energy difference of the normal and the excited state which is determined by the strength of the outer magnetic field.

Hydrogen atoms are usually bound into molecules. The atoms of the immediate vicinity interfere with the outer magnetic field and in this way they change the energy difference of normal and excited state. The frequency of a resonance photon can therefore identify different chemical environments.

In nuclear magnetic resonance tomography a second, inhomogeneous magnetic field is superimposed on the homogeneous magnetic field. The inhomogeneous field is shaped in a way that small resonance frequency bands can be assigned to a specific volume element of the measured tissue.

Blood flow influences the nuclear magnetic resonance signal in several ways. The signal from fast flowing blood, for example, vanishes. This is explained by the displacement of the protons between excitation and detection and is referred to as spin wash-out. This effect can be exploited for velocity measurements by measuring the signal amplitude at varying time periods between excitation and detection [30]. In this way a wash-out curve is produced that can be related to the flow velocity. Numerous other techniques for extracting flow velocity information from nuclear magnetic resonance imaging are reviewed by Smith [31]. Bauer et al. [3] demonstrated myocardial perfusion measurements in isolated rat hearts at a spatial resolution of $140 \times 140 \times 1500 \mu\text{m}$ and a temporal resolution of 40 seconds.

3. Conclusions

There are two full-field methods for blood flow measurements that do not rely on optical accessibility: nuclear magnetic resonance imaging and echo particle image velocimetry. Consequently, these are methods that allow the non-invasive investigation of blood flow in deeper tissue layers. The spatial resolution of both techniques restrict the measurements to macro- and intermediate-scale blood flow. Both techniques also suffer from low temporal resolution. This makes the handling of pulsatile flow or instantaneous flow patterns difficult. The clinical applicability of echo particle image velocity seems to be easier and cheaper than the relatively complex magnetic resonance imaging technique.

Basically three full-field velocity measurement principles remain, that are suitable for monitoring capillary flow: laser Doppler velocimetry (including time-varying speckle), laser speckle contrast imaging and particle image velocimetry (including particle tracking). Laser Doppler imaging and time-varying speckle imply low temporal resolution due to scanning. The multi-probes approach (Sec. 2.1.2) enhances the temporal resolution, but can not sample typical heart rates. The profile approach (Sec. 2.1.3) might be used for time resolved volume flow rate measurements in the microcirculation. Particle image velocimetry and particle tracking velocimetry allow the determination of vectorial velocities at a spatial resolution that is high enough for accurate wall shear stress measurements. Video rate or high speed imaging enables the resolution of typical heart rate frequencies.

References

1. R.J. ADRIAN, *Particle-imaging techniques for experimental fluid mechanics*, Annual Review of Fluid Mechanics **23**: 261–304, 1991
2. Y. AIZU and T. ASAKURA, *Coherent optical techniques for diagnostics of retinal blood flow*, Journal of Biomedical Optics **4**(1) : 61–75, 1999
3. W.R. BAUER, K.H. HILLER, P. GALUPPO, S. NEUBAUER, J. KÖPKE, A. HAASE, C. WALLER, and G. ERTL, *Fast high-resolution magnetic resonance imaging demonstrates fractality of myocardial perfusion in microscopic dimensions.*, Circ Res **88**(3) : 340–6, Feb 2001
4. J.D. BRIERS, *Laser Doppler and time-varying speckle: a reconciliation*, J. Opt. Soc. Am. A **13**(2) : 345–350, 1996
5. J.D. BRIERS, G. RICHARDS, and X.W. HE, *Capillary blood flow monitoring using laser speckle contrast analysis*, Journal of Biomedical Optics **4**(1) : 164–175, 1999
6. J.D. BRIERS, *Laser Doppler, speckle and related techniques for blood perfusion mapping and imaging.*, Physiol Meas **22**(4) : R35–66, Nov 2001
7. S.E. CHARM and G.S. KURLAND, *Blood Flow and Microcirculation*, Wiley 1974
8. S. CHIEN, *Shear Dependence of Effective Cell Volume as a Determinant of Blood Viscosity*, Science **168** : 977–979, 1970
9. J. CZARSKE, *Laser Doppler velocity profile sensor using a chromatic coding*, Meas. Sci. Technol. **12** : 52–57, 2001
10. W.R. DEAN, *Note on the motion of a fluid in a curved pipe*, Phil. Mag. Ser. 7 **4**(20) : 208–223, 1927
11. W.R. DEAN, *The stream-line motion of fluid in a curved pipe*, Phil. Mag. Ser. 7 **5**(30) : 673–695, 1928
12. A.K DUNN, A. DEVOR, H. BOLAY, M.L. ANDERMANN, M.A. MOSKOWITZ, A.M. DALE, and D.A. BOAS, *Simultaneous imaging of total cerebral hemoglobin concentration, oxygenation, and blood flow during functional activation*, Opt Lett **28**(1) : 28–30, Jan 2003
13. T.J. ESSEX and P.O. BYRNE, *A laser Doppler scanner for imaging blood flow in skin*, J Biomed Eng **13**(3) : 189–94, May 1991
14. A.F. FERCHER and J.D. BRIERS, *Flow visualization by means of single-exposure speckle photography*, Optics Communications **37**(5) : 326–330, 1981
15. D.L. HITT, M.L. LOWE, J.R. TINCER, and J.M. WATTERS, *A new method for blood velocimetry in the microcirculation*, Microcirculation **3**(3) : 259–62, Sep 1996
16. J.R. HOVE, R.W. KÖSTER, A.S. FOROUHAR, G. AVEDO-BOLTON, S.E. FRASER, and M. GHARIB, *Intracardiac fluid forces are an essential epigenetic factor for embryonic cardiogenesis*, Nature **421**(6919) : 172–177, Jan 2003

17. H.B. KIM, J.R. HERTZBERG, and R. SHANDAS, *Development and validation of echo PIV*, Experiments in Fluids **36**: 455–462, 2004
18. H.-B. KIM, J. HERTZBERG, C. LANNING, and R. SHANDAS, *Noninvasive measurement of steady and pulsating velocity profiles and shear rates in arteries using echo PIV: in vitro validation studies*, Ann Biomed Eng **32**(8): 1067–76, Aug 2004
19. D.S. LONG, M.L. SMITH, A.R. PRIES, K. LEY, and E.R. DAMIANO, *Microviscometry reveals reduced blood viscosity and altered shear rate and shear stress profiles in microvessels after hemodilution*, Proc. Natl. Acad. Sci. USA **101**(27): 10060–5, Jul 2004
20. J. MÄNNER, *Cardiac looping in the chick embryo: a morphological review with special reference to terminological and biomechanical aspects of the looping process*, The Anatomical Record **259**: 248–262, 2000
21. C.D. MEINHART, S.T. WERELEY, and J.G. SANTIAGO, *PIV measurements of a microchannel flow*, Experiments in Fluids **27**: 414–419, 1999
22. C.D. MEINHART, S.T. WERELEY, and J.G. SANTIAGO, *A PIV algorithm for estimating time-averaged velocity fields*, Journal of Fluids Engineering **122**: 285–289, 2000
23. W. MERZKIRCH, *Flow Visualization* Academic Press 1987
24. M.G. OLSEN and R.J. ADRIAN, *Out-of-focus effects on particle image visibility and correlation in microscopic particle image velocimetry*, Experiments in Fluids **29**(7): 166–174, 2000 Suppl.
25. S.A. PAPE, C.A. SKOURAS, and P.O. BYRNE, *An audit of the use of laser Doppler imaging (LDI) in the assessment of burns of intermediate depth*, Burns **27**(3): 233–239, May 2001
26. M. RAFFEL, C. WILLERT, and J. KOMPENHANS, *Particle image velocimetry: A practical guide* Springer 1998
27. J.G. SANTIAGO, S.T. WERELEY, C.D. MEINHART, D.J. BEEBE, and R.J. ADRIAN, *A particle image velocimetry system for microfluidics*, Experiments in Fluids **25**: 316–319, 1998
28. A. SEROV, W. STEENBERGEN, and F. DE MUL, *Laser Doppler perfusion imaging with a complimentary metal oxide semiconductor image sensor*, Optics Letters **27**(5): 300–302, 2002
29. A. SEROV, B. STEINACHER, and T. LASSE, *Full-field laser Doppler perfusion imaging and monitoring with an intelligent CMOS camera*, Optics Express **13**(10): 1681–1689, 2005
30. J.R. SINGER and L.E. CROOKS, *Nuclear magnetic resonance blood flow measurements in the human brain*, Science **221**(4611): 654–6, Aug 1983
31. M.A. SMITH, *The measurement and visualisation of vessel blood flow by magnetic resonance imaging*, Clin Phys Physiol Meas **11**(2): 101–23, May 1990

32. M.L. SMITH, D.S. LONG, E.R. DAMIANO, and K. LEY, *Near-wall micro-PIV reveals a hydrodynamically relevant endothelial surface layer in venules in vivo*, *Biophys J* **85**(1):637–45, Jul 2003
 33. Y. SUGII, S. NISHIO, and K. OKAMOTO, *In vivo PIV measurement of red blood cell velocity field in microvessels considering mesentery motion*, *Physiol Meas* **23**(2):403–16, May 2002
 34. Y. SUGII, S. NISHIO, and K. OKAMOTO, *Measurement of a velocity field in microvessels using a high resolution PIV technique*, *Ann N Y Acad Sci* **972**:331–6, Oct 2002
 35. G.J. TANGELDER, D.W. SLAAF, A.M. MULIJENS, T. ARTS, M.G. EGBRINK, and R.S. RENEMAN, *Velocity profiles of blood platelets and red blood cells flowing in arterioles of the rabbit mesentery*, *Circ Res* **59**(5):505–14, Nov 1986
 36. K. TSUKADA, H. MINAMITANI, E. SEKIZUKA, and C. OSHIO, *Image correlation method for measuring blood flow velocity in microcirculation: correlation 'window' simulation and in vivo image analysis*, *Physiol Meas* **21**(4):459–71, Nov 2000
 37. M. VAN DYKE, *Extended Stokes Series: laminar flow through a loosely coiled pipe*, *Journal of Fluid Mechanics* **86**:129–145, 1978
 38. P. VENNEMANN, K.T. KIGER, R. LINDKEN, B.C.W. GROENENDIJK, S. STEKELBURG DE VOS, T.L.M. TEN HAGEN, N.T.C. URSEM, R.E. POELMANN, J. WESTERWEEL, and B.P. HIERCKMATXM, *In vivo micro particle image velocimetry measurements of blood-plasma in the embryonic avian heart*, *J Biomech article in press* May 2005
 39. A.J. WARD-SMITH, *Internal fluid flow*, Clarendon Press 1980
 40. K. WÄRDELL, A. JAKOBSSON, and G.E. NILSSON, *Laser Doppler perfusion imaging by dynamic light scattering*, *IEEE Trans Biomed Eng* **40**(4):309–16, Apr 1993
 41. J. WESTERWEEL, *Fundamentals of digital particle image velocimetry*, *Meas. Sci. Technol.* **8**:1379–1392, 1997
 42. S. YUAN, A. DEVOR, D.A. BOAS, and A.K. DUNN, *Determination of optimal exposure time for imaging of blood flow changes with laser speckle contrast imaging*, *Appl Opt* **44**(10):1823–30, Apr 2005
-

Experimental Assessment of Wall Shear Flow

ULRICH KERTZSCHER, PERRINE DEBAENE,
LEONID GOUBERGRITS, and KLAUS AFFELD

*Biofluidmechanics Laboratory
Charité, Universitätsmedizin Berlin
Spandauer Damm 130
14050 Berlin
Germany
ulrich.kertzscher@charite.de*

The assessment of wall shear flow is of interest for different technical and scientific fields. One of the research fields is biofluidmechanics, where a close relationship is assumed between flow and biological phenomena. Special problems are encountered when assessing the wall shear flow in biofluidmechanics. The flow is often pulsatile, the walls are curved and even vaulted, sometimes the walls are flexible and the wall shear flow should also be assessed with a high spatial and temporal resolution.

An overview is given about existing methods to assess the wall shear flow. Some of these methods are point methods, others obtain a field. All of these methods have special advantages but also drawbacks. We therefore developed a new measurement method to investigate the flow close to a wall. This method is applicable at curved and vaulted walls, in unsteady flows, is non-intrusive, and obtains flow fields with spatial and temporal resolution.

The new method was validated in a steady and unsteady laminar flow in a rectangular duct and in a rectangular U-shaped duct with a backward facing step. The last validation step was in an U-shaped duct with a lenticular cross section and a backward facing step. The results correspond closely with either the analytical or the numerical solution.

1. Introduction

The assessment of wall shear flow is interesting for different technical and scientific fields. Examples are: removal of biofilms in medicine, cleaning of containers, cultivation of shear sensitive cells and development and research in the field of biofluidmechanics. The latter comprises of the development of blood pumps and artificial vessels as well as atherogenesis.

In 1856 Rudolf Virchow postulated the interaction between flow, blood and walls. This interaction is known as Virchow's Triad. It has often been proven qualitatively by researchers.

It is known that there is a close relationship between flow and biological phenomena, for instance thrombus formation [9] or atherosclerotic events [1]. In particular, the wall shear stress plays a role because it influences the structure and function of the endothelial cells [10] as well as the behaviour of platelets [6]. An example for a thrombus formation at an artificial heart valve and an example for the development of atherosclerosis, here at a carotid bifurcation, are shown in Fig. 1. However, quantification of the influence of flow parameters like wall shear stress on the wall is still lacking.

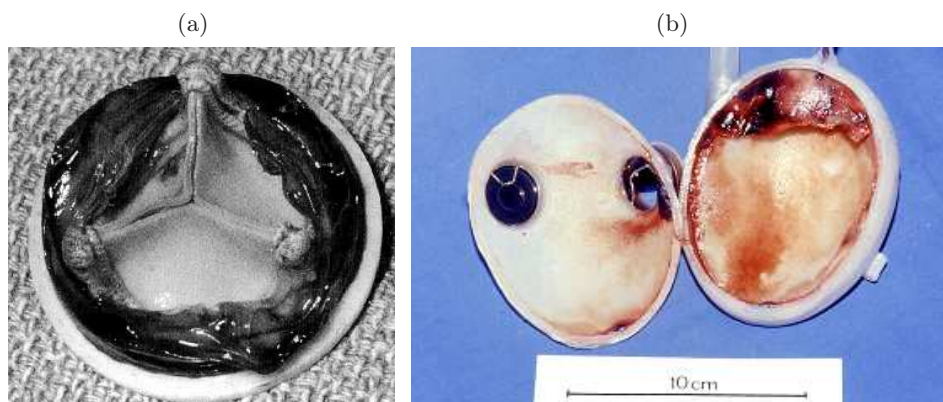


FIGURE 1. (a) Thrombus generation at an artificial heart valve [11], (b) Development of atherosclerotic lesions in a carotid bifurcation

The measurement of the flow close to the wall, especially of the wall shear stress, is a precondition to our understanding of atherosclerotic events and also our ability to avoid thrombus generation in artificial organs. Nevertheless this is a challenging experimental problem. Reasons for this are the pulsatile flow, the curved or vaulted as well as flexible walls, and, depending on the model, the small diameter. In addition one is interested in assessing the wall shear flow with high spatial and temporal resolution.

In Sec. 2 an overview is given about existing methods to assess the wall shear flow. In Sec. 3 a new method is presented to assess the wall shear flow including the wall shear stress.

2. Existing Methods to Assess the Wall Shear Flow

Many methods to assess the wall shear flow and wall shear stress exist. They can be divided into point or field methods.

2.1. Point Methods

Point methods yield the flow properties at the wall only at one point. Some of the point methods can be extended to field methods by using an array of probes. It is possible to extend the methods explained later with a hot wire and a surface fence, especially in the case of micro-electro-mechanical-systems. The disadvantages of the basic method are kept.

2.1.1. Preston tube. The Preston tube is a modified Pitot tube and measures the pressure profile p near the wall, Fig. 2. It is possible, from this profile, to calculate the velocity profile close to the wall and to calculate with Newton's equation the wall shear stress:

$$\tau_w = \eta \frac{\partial v}{\partial y} \Big|_w . \quad (2.1)$$

In this equation the wall shear stress τ_w is equal to the dynamic viscosity η multiplied with the velocity gradient at the wall. This method is quite invasive and not very accurate.

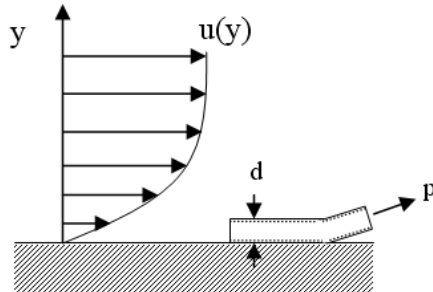


FIGURE 2. Preston tube

2.1.2. Surface hot films. A hot film element is introduced into the wall (Fig. 3). It should be flush with the wall and electrically heatable. The heat

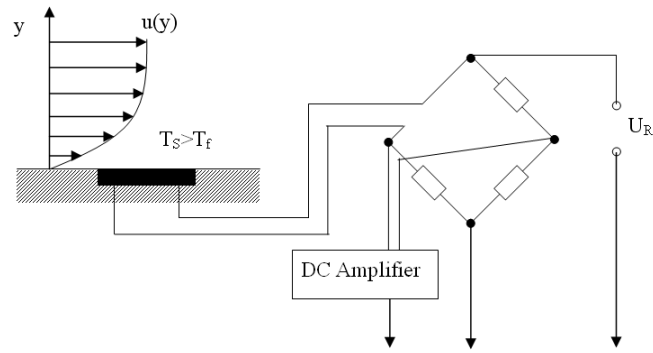


FIGURE 3. Surface hot film (T_s : Temperature of the hot film; T_f : Temperature of the fluid)

loss of the element is a measure for the velocity of the fluid close to the wall. From this velocity, the wall shear stress can be calculated. This method is almost non invasive and may be used to assess the mean wall shear stress. Problems arise if the temperature of the fluid is not constant. The heat loss in the wall has to be accounted for and a calibration procedure is always necessary.

2.1.3. Wall-fixed hot wire and pulsed hot wire. The principle of the wall-fixed hot wire is similar to the hot film measurements in the section before. Instead of a hot film, a hot wire with a small diameter is used and fixed close to the wall (Fig. 4). The heat loss of the hot wire is proportional to the velocity of the fluid. If the hot wire is close enough to the wall you

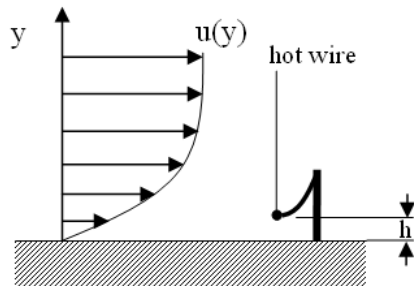


FIGURE 4. Wall-fixed hot wire

are able to calculate the wall shear stress from this velocity. In other words, the hot wire has to be in the viscous sublayer, where the velocity profile is linear. It is then possible to use Newton's equation (2.1). This method has to be calibrated before each measurement and just as for hot films you have to consider a temperature change in the fluid. This method is quite invasive. Quite similar to the hot wire method is the pulsed hot wire method: a hot wire is heated for a short period and the released heat is measured by a second hot wire further downstream. It is possible to assess the velocity from the distance and the time lag. Aside from the problems of the hot wire you have to account for the diffusion of heat. The heat cloud is not only transported by convection but also by diffusion.

2.1.4. Surface fence in the sublayer. The pressure loss is measured over a surface fence with the height h , Fig. 5. It is possible to calculate the velocity and the wall shear stress from the pressure difference before and after the fence. This method is very good in order to measure the time resolved shear stress if the fence is in the linear part of the velocity field, but is invasive and quite error-prone. Errors can be caused by a pressure gradient in the flow, imperfections of the fence or a blockage of the pressure ports.

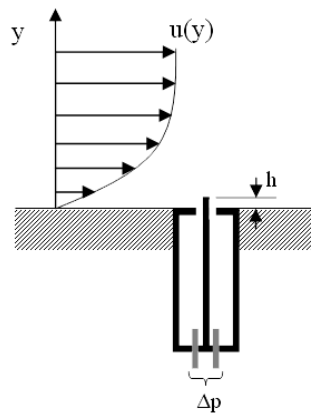


FIGURE 5. Surface fence

2.1.5. Laser Doppler velocimetry (LDV). This is a widely used non invasive method to measure the fluid velocity in one point. In the easiest case two laser beams with the same wave length are crossed, see Fig. 6. A mea-

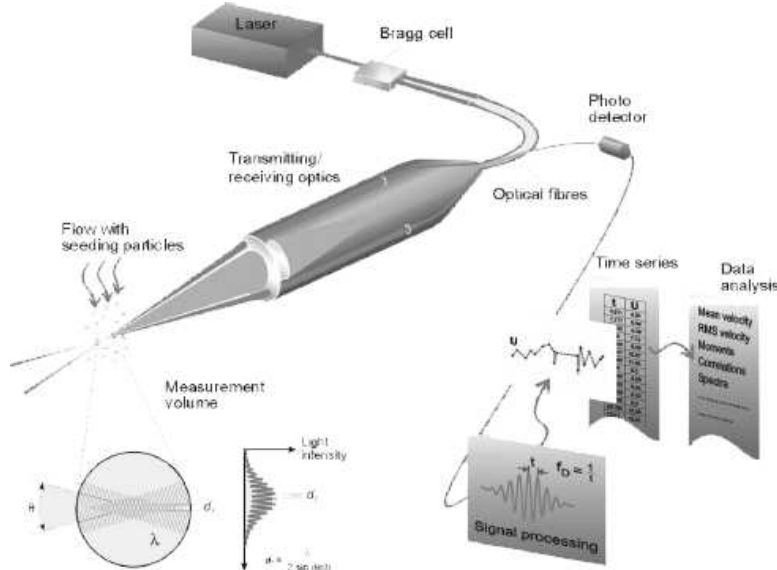


FIGURE 6. Laser Doppler velocimetry [4]

surement volume is defined by the two crossing laser beams. A fringe pattern which is caused by interference is visible in this volume. Tracer particles are added to the fluid. A tracer particle passing the measurement volume and therefore this fringe pattern, emits light with a frequency which depends upon the velocity of the particle. It is therefore possible to measure a velocity profile and to calculate the wall shear stress. This method has a high spatial and time resolution and it is not necessary to calibrate the system. This system can detect the flow direction when introducing a Bragg cell, which causes a defined frequency shift between the two laser beams. It is only a point method and the measurement of velocity fields is time consuming. Measurements in unsteady flows can be difficult.

2.2. Field Methods

Field methods yield the flow properties at the wall in an area.

2.2.1. Oil film interferometry. Small oil drops or a very thin oil film is distributed on the wall. After a certain amount of time in a steady flow, an oil wedge can be seen, Fig. 7. The distribution of the thickness of the oil can be measured by interferometry and is a measure of the wall shear stress.

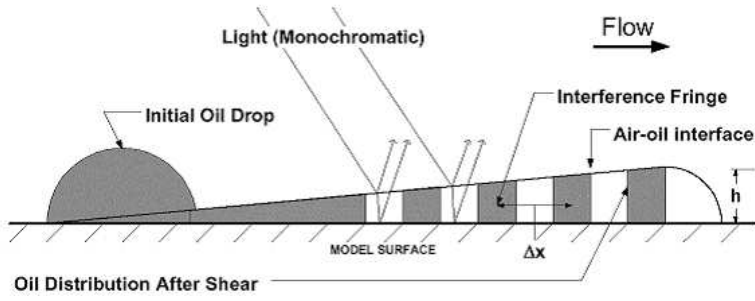


FIGURE 7. Oil film interferometry [16]

Some researchers tried to use this method in unsteady flows and to calculate the unsteady wall shear stress from the development of the oil wedge but to the knowledge of the authors their success was limited. The method is temperature dependent and it is usually necessary to calibrate the system.

2.2.2. Pressure sensitive paint. The pressure sensitive paint is distributed on the wall, see Fig. 8. The color change caused by pressure changes is recorded and it is possible to calculate the wall shear distribution after calibration. This is a method with a good resolution in time and space but it is not very sensitive and only applicable for higher pressures. Besides, the method is quite time and cost consuming.

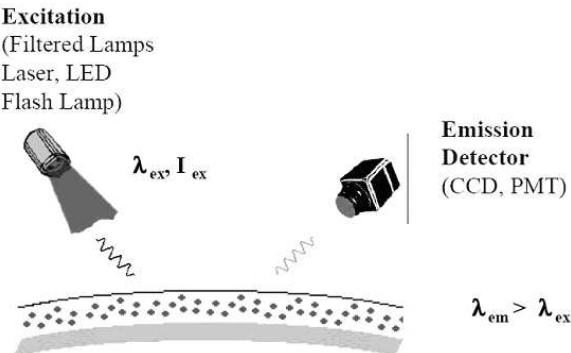


FIGURE 8. Pressure sensitive paint [2]

2.2.3. Paint erosion method. A water based colour-binder mixture is distributed on the wall. The erosion of the color is a qualitative measure of

the mean wall shear stress distribution. A quantitative analysis is theoretically possible and was investigated by our group. Figure 9 depicts the paint distribution after a certain amount of time in a stagnation point flow.

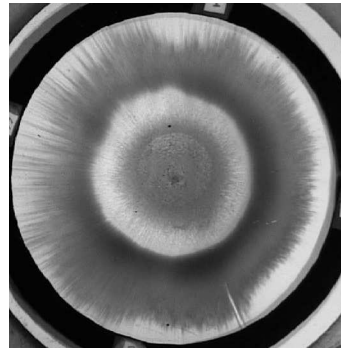


FIGURE 9. Paint distribution in a stagnation point flow

2.2.4. Laser photochromic velocimetry. A photochromic color is mixed into the fluid. This colour is completely transparent when illuminated with normal light, but visible if activated by ultraviolet light. Laser light is used to produce a regular coloured pattern in the fluid, for example, a grid pattern as can be seen in Fig. 10. This grid pattern is deformed under the influence of the flow. It is possible to calculate the velocity field in the volume from the recorded deformation of the pattern. In principle, it is possible to calculate the wall shear stress from the velocity field but the accuracy is limited. It is not easy to know the exact distance between the wall and a certain color point. Aside from this the method is more or less a procedure to assess the wall flow in a line.

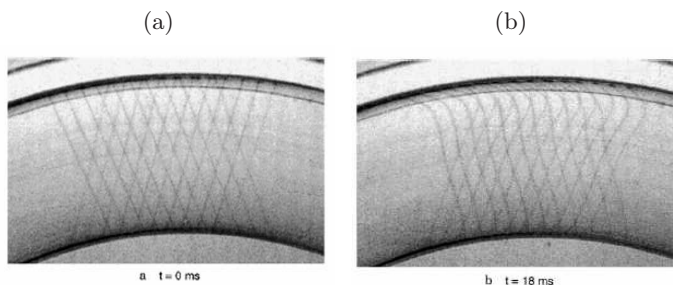


FIGURE 10. Deformation of a grid of photochromatic color under the influence of flow [12]

2.2.5. Particle image velocimetry (PIV). The basic idea of this powerful technique: tracer particles are mixed with the fluid and illuminated. By recording the position of the particles at two different points in time it is possible to assess the velocity of the particles through their displacement. In particle tracking velocimetry, every particle is considered. This method is limited to a certain seeding density. In PIV the flow is illuminated by a light sheet, see Fig. 11. The movement of the particles in the light sheet is recorded. The light sheet is divided into small interrogation areas and the movement of all particles within the interrogation area is evaluated by a correlation method. This method can be used to measure the velocity close to the wall. Unfortunately some problems arise there: distortion and deflection can occur at the wall because of the different refraction indices of the fluid and the wall. It is not easy to define the exact distance of the first measurement point to the wall.

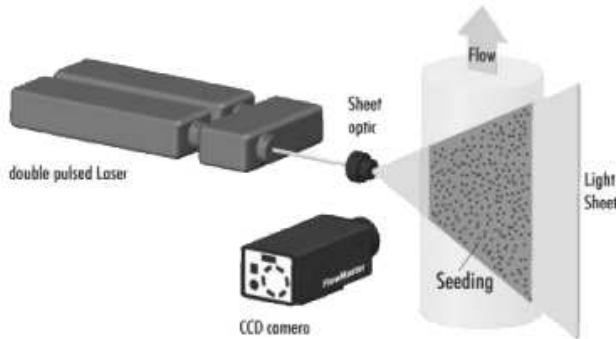


FIGURE 11. Particle image velocimetry [7]

2.2.6. 3D Scanning PIV. Multiple light sheets are produced with a rotating polygon mirror and a PIV analysis can be done in every individual light sheet (Fig. 12). If the light sheet is recorded from two directions, all three velocity components can be assessed in every light sheet. If the light sheets are quite close to each other this method can be considered three dimensional. This method is more or less limited to slower flows; the scanning velocity must be high enough. It is possible to produce the light sheets close to the wall and therefore calculate the wall shear stress field, but the resolution is limited by the thickness of the light sheet. This method is not applicable at vaulted walls.

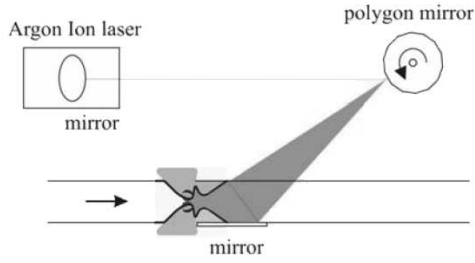


FIGURE 12. 3D Scanning PIV [15]

2.2.7. Holographic PIV. Another very interesting extension of the basic PIV idea is the holographic PIV, see Fig. 13. All particles in a volume are illuminated by diffusive laser light. These particles scatter the laser light which interferes with the light of a reference beam and is recorded by a holographic film. The volume information is divided into different layers and a PIV analysis is done for each layer. With this powerful technique it is, in principle, possible to measure the velocity close to the wall as a time resolved field. Until now, this method is very complex, time consuming and costly. For example, it is not easy to handle the enormous amount of data (about 100 Gigabyte per hologram).

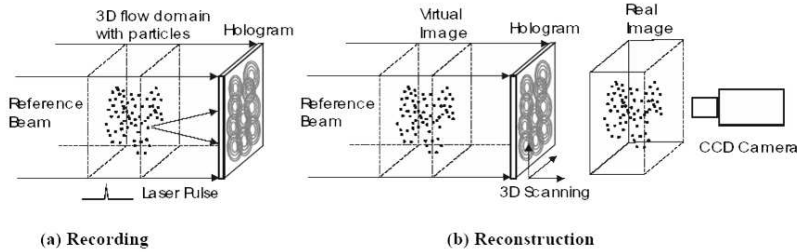


FIGURE 13. Holographic PIV [8]

2.2.8. Laser light sheet tomography. Similar to 3D Scanning PIV is the multicolour laser light sheet tomography. Many different colours are produced through mixing different laser colours. As a result, the particles in each layer are color coded. The layers may be as thin as $30\text{ }\mu\text{m}$ and it is possible to put the layers very close to each other. It is therefore possible to get a good spatial resolution close to the wall. Until now, the system is validated only

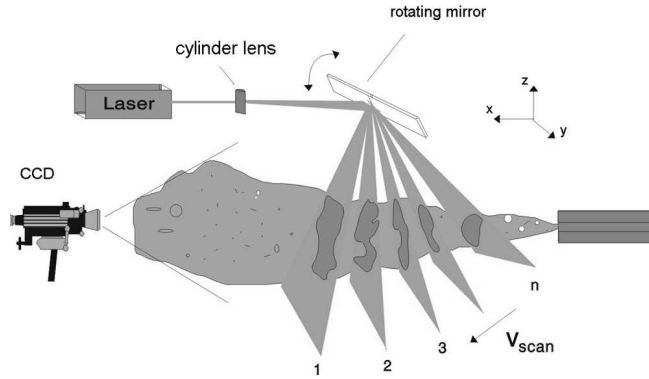


FIGURE 14. Laser light sheet tomography [13]

for gases, it is under development for fluids. Since the system works with light sheets it is possible to work with curved walls but not with vaulted.

2.3. Miscellaneous Methods

2.3.1. Ultrasonic Doppler method. Another possible use of the Doppler effect is ultrasound, see Fig. 15. The ultrasound wave is reflected by particles in the flow. The Doppler effect shifts the frequency of the incoming wave. This shift is a measure for the velocity in the direction of the ultrasound. With the use of a pulsed ultrasound it is possible to combine information about the frequency shift and the distance of the particle, which causes the shift. It is therefore possible to measure the velocity profile along a line. With this method only one component of the velocity is measured and only at two points close to the wall.

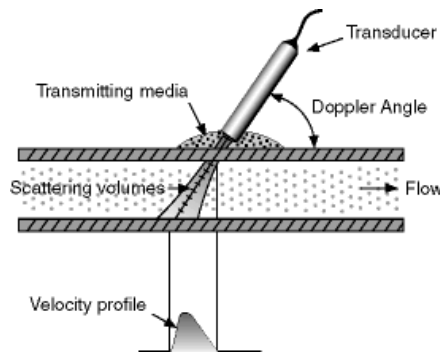


FIGURE 15. Ultrasonic Doppler method [14]

2.3.2. Laser Doppler profile sensor. With this highly sophisticated system it is possible to determine the position of a particle in the measuring volume of a LDV-system and to record the measuring signal from this particle. The distance of the particle to the wall is determined with the position. As a result, it is possible to measure a velocity profile in the wall vicinity with a very high precision. This method is very time consuming, costly and more or less a point measurement method.

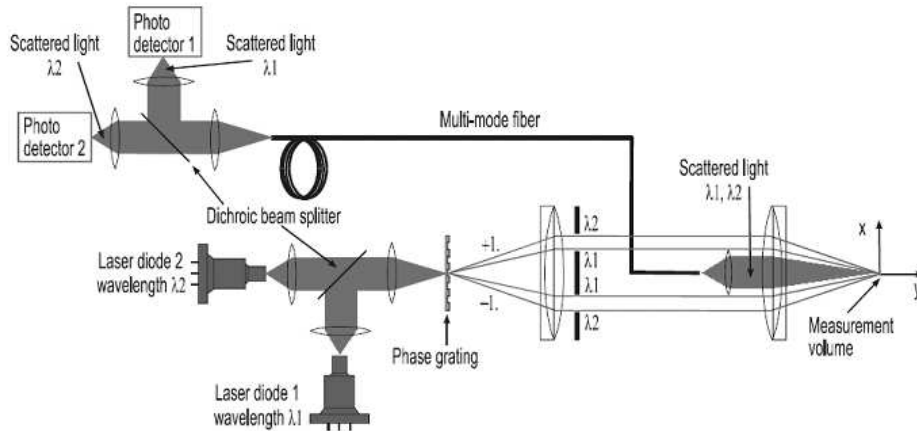


FIGURE 16. Laser Doppler profile sensor [3]

3. The New Method to Assess the Wall Shear Flow

All the methods in Sec. 2 have special advantages and disadvantages. Due to the problems in biofluidmechanics mentioned earlier, all the methods are of limited use. We therefore developed a new method with the following aims:

- noninvasive,
- determination of magnitude, direction and wall distance of the velocity field close to the wall,
- usable in unsteady flows,
- usable at curved and vaulted surfaces,
- easy to use, not too expensive.

3.1. Basic Idea and Realization of the New Method

As in conventional PIV, the new method is based on the observation and the digital recording of small, buoyant, light reflecting particles suspended in the fluid. Hence it is a particle image interrogation method. In the conventional 2D-PIV or PTV, a light sheet illuminates a plane in the flow. The particles in this plane light up and become visible. In the new method presented here, the whole flow near the wall is illuminated and all particles near the wall become visible. The transparent flow model is illuminated from the outside with monochromatic diffuse light. A dye is added to the fluid, which limits the penetration depth of the light into the flow model, see Fig. 17. According to optical laws, the penetration depth decreases if the concentration of the dye increases. Within the illuminated layer, the particles appear more or less bright, depending on their normal distance d_p to the wall. Particles near the wall appear brighter, i.e. have a higher gray value, than particles farther from the wall, see Fig. 18.

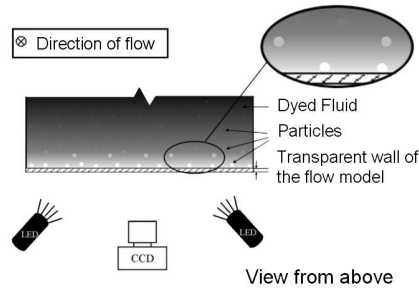


FIGURE 17. Basic principle of the new method

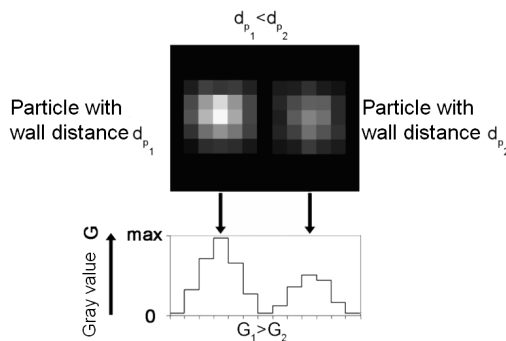


FIGURE 18. Gray value (G) of particles with different distances to the wall

An image processing leads to a separation of the near-wall flow into several layers. All the particles moving in one layer have the same gray value and, therefore, the same normal distance d_p to the wall. For each layer, the motion of the particles can be determined with a conventional PIV algorithm—either cross correlation or particle tracking, depending on the number of particles in the plane. This results in a vector field for each layer. If the concentration of the dye, the lighting and the size of the particles are properly chosen, the particles closest to the wall are within the laminar sub-layer. This permits the calculation of the wall shear stress τ_w according to Eq. (2.1). A vector field of the wall shear stress results.

As for conventional PIV, the particles for the new method have to be neutrally buoyant, they should not alter the flow and should not interact with each other. The tracer particles should have additional properties as well. They should be spherical and monodisperse, otherwise it is impossible to calculate the right wall distance. Moreover, the particles should reflect the light more efficiently than the usual PIV tracer particles because of the absorption of the emitted and of the reflected light in the dyed fluid.

Special particles were developed according to the above-mentioned requirements. Encapsulated alginate beads with glass hollow micro-spheres were manufactured by LUM GmbH (Germany). The beads were prepared with the vibrating nozzle technique, using an encapsulation device (Inotech Encapsulation, Switzerland) based on laminar jet break-up. The particles have a mean diameter of $350\text{ }\mu\text{m}$ with a standard deviation smaller than 3% [5] and a density of ca. 1 g cm^{-3} . The glass micro-spheres allow a density fitting of the beads and a good light scattering. These particles are large compared to particles used for conventional PIV, see section discussion.

Fluid, lighting and recording technique are interdependent, and have to be chosen so that the light absorption is sufficient, well defined and easily calculable. Furthermore, the lighting and recording techniques should be optimized, especially because the light amount reflected by the particles is quite small. We made use of a high-speed video camera having a resolution of 512×480 pixel at 250 fps (Fastcam Super 10 K, Roper Scientific MASD, USA). Sequences with max. 546 pictures can be recorded and saved instantaneously. The camera shows a maximum sensitivity at ca. 630–660 nm. To optimize the quality of the recording technique, these characteristics had been taken into account when choosing the light source. The bandwidth of the wavelength of the spectral distribution should not be larger than the

range of absorption of the dye. We used a diffuse light source composed of more than 60 red ultra bright Light Emitting Diodes (LED) (HLMP-ED31-SV000, Agilent Technologies Inc, USA). They have a dominant wavelength at 639 nm and a spectral halfwidth of 17 nm. Depending on the experiment and the velocity range we wanted to reach, we used water, or a mix of water and glycerin as an experimental fluid. A common blue food color named Patent Blue V (EEC Number: E131, Schuman und Sohn, Germany) was added to the fluid. This substance has a maximum absorption at 638 nm in water at pH= 5. The choice of this dye is based on two assumptions. First, the light absorption has to be optimized. This means that the absorption bands of the dye should be within the range of the dominant wavelengths of the LEDs. Furthermore, the absorption properties of the dye should be well defined and describable using common optical laws. Thus, it should be possible to calculate the maximal penetration depth of the light into the model according to the Beer Lambert law. The use of Patent Blue V fulfils both conditions.

3.2. Determination of the Particle-Wall Distance

The assessment of the relationship between the gray value of a particle and its distance from the wall is the foundation for the separation of the particles into different layers. To associate each gray value to a wall distance, a calibrating measurement was necessary. Particles in the fluid were moved in small steps from the wall. With our high speed camera the gray value was observed for every step. In Fig. 19 the result of such a calibration measurement is depicted. This calibration has to be done every time a fluid with a new colour concentration is used.

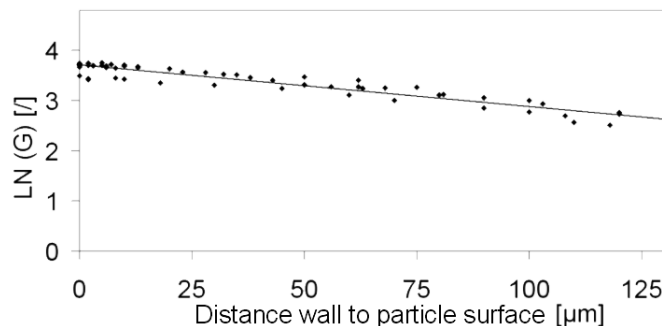


FIGURE 19. Observed gray value (G) depending on the particle distance to the wall

3.3. Validation of the New Method

The validation process was done in different steps. First, the validation was done using steady and pulsatile flows at planar walls. The next step was an investigation at planar walls with a complex steady flow. The last validation step used complex, steady flow at vaulted walls. The validation process is summarized in Fig. 20.

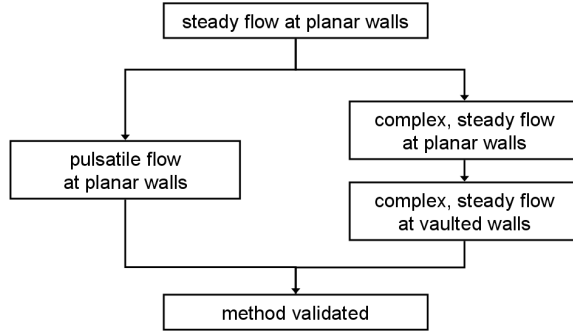


FIGURE 20. Validation of the new method

3.3.1. Validation in a steady flow at planar walls. As a steady flow at planar walls we have chosen a steady, laminar flow in a straight duct with a rectangular cross section. In Fig. 21 the dimensions of the duct and the well

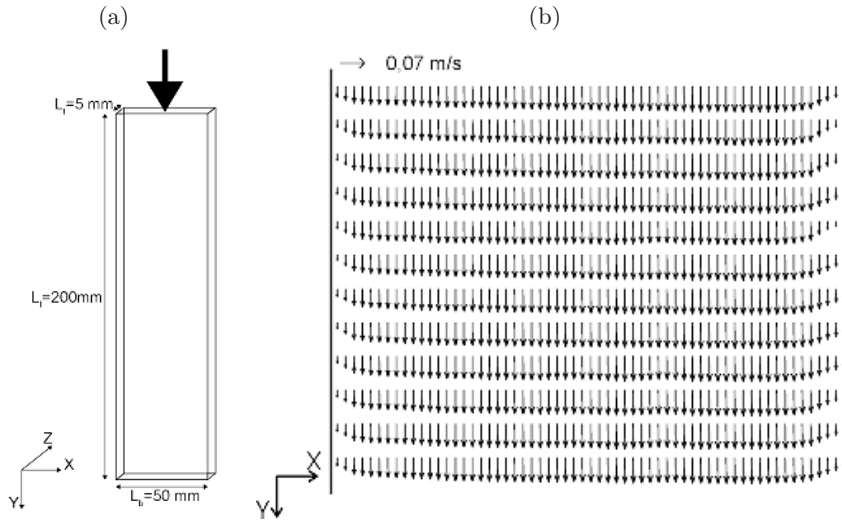


FIGURE 21. Rectangular duct and measured velocity field close to the wall

known velocity field close to the wall are depicted. The acquired experimental values of the velocity close to the wall were compared to the values of the analytical solution. The difference is about 10%.

3.3.2. Validation in a pulsatile flow at planar walls. For this validation step the same duct as before was investigated, but with a pulsatile flow. The flow curve is depicted in Fig. 22.

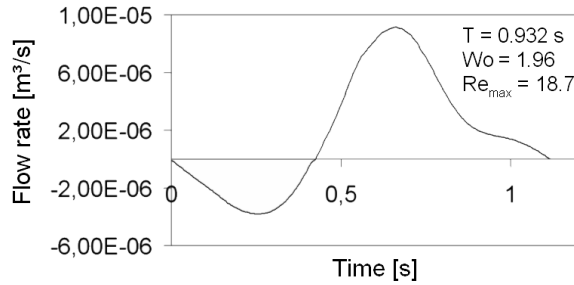


FIGURE 22. Flow curve of the investigated pulsatile flow (T : time period; Wo : Womersley number)

In this case it was not possible to compare the results of the new method with an analytical method. Therefore, the comparison was done with computational fluid dynamics (CFD) results. The CFD was performed with Fluent 6.2 (Fluent Inc., Lebanon, USA) and the preprocessor Gambit™ (Fluent Inc., Lebanon, USA). In Fig. 23 (left) CFD results for two wall distances and for one experiment are depicted. The experimental data was obtained from all

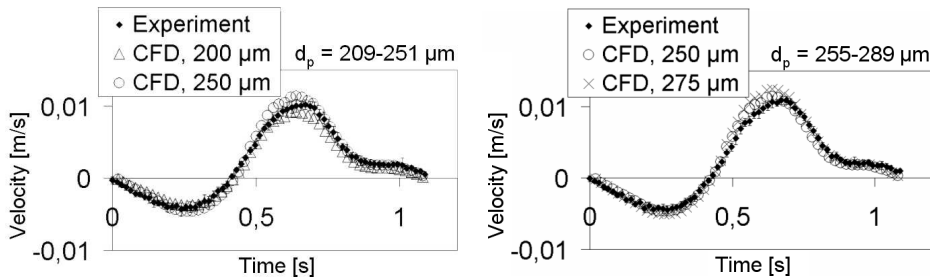


FIGURE 23. Comparison between experimental assessed velocity close to the wall and CFD-results. Left: Experimental velocity obtained from particles with a wall distance d_p between 209 µm and 251 µm. Right: Experimental velocity obtained from particles with a wall distance d_p between 255 µm and 289 µm.

particles with a wall distance between 209 μm and 251 μm . In Fig. 23 (right) the comparison is made for all particles with a wall distance between 255 μm and 289 μm and for CFD results for two wall distances. There is a very good agreement for both wall distance intervals. Note: CFD was validated in the central plane with conventional PIV.

3.3.3. Validation in a complex steady flow with planar walls. To prove the reliability of the new method in more complex flows than in the two sections before, we investigated the flow in an U-shaped duct with a so called backward facing step, see Fig. 24. The cross sections are rectangular. In such a flow model separation zones, reattachment zones, and secondary flow can be observed. To give an impression of the flow in this duct, the path lines for two cross sections are depicted in Fig. 25: a cross section in an x-z plane with the separation in the diagram above, and below in the x-y plane just in the middle of the duct. The impact of the secondary flow can be seen by the deformation of the path lines. The path lines are calculated with CFD.

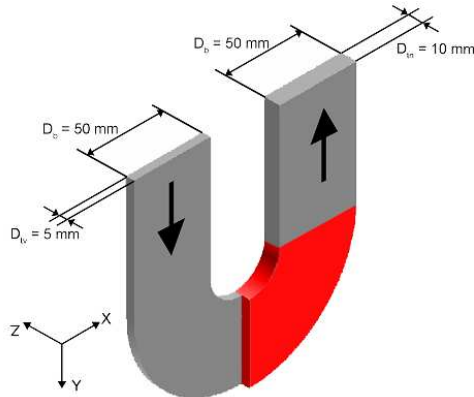


FIGURE 24. Dimensions of U-shaped duct with rectangular cross section, backward-facing step and red-colored investigation section

In Fig. 26 a comparison is depicted between experimentally and numerically obtained velocity vector fields at the wall for $Re = 30.1$ (Re is calculated with the mean velocity and depth before the step). On the left side, the experimental results for all particles with a wall distance between 223 μm and 250 μm is shown, on the right side the numerically obtained results (again with Fluent) for a wall distance of 240 μm . The reattachment line is clearly visible. The velocity fields show a good agreement. Path lines were calculated from these vector fields, see Fig. 27. The declination of the reattachment line

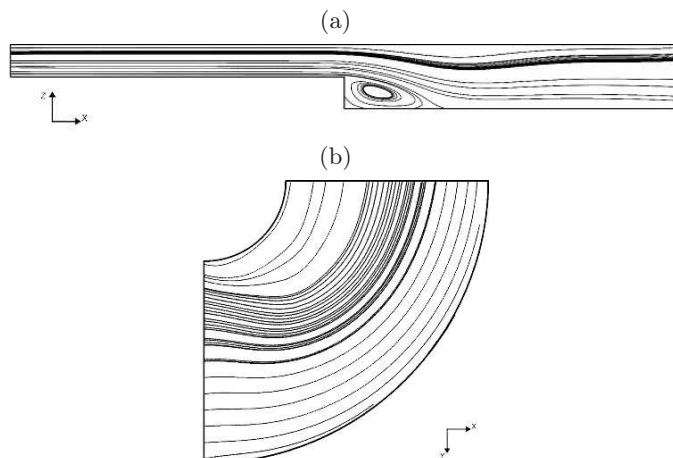


FIGURE 25. Path lines, acquired with CFD, in two cross sections ($Re = 50$)

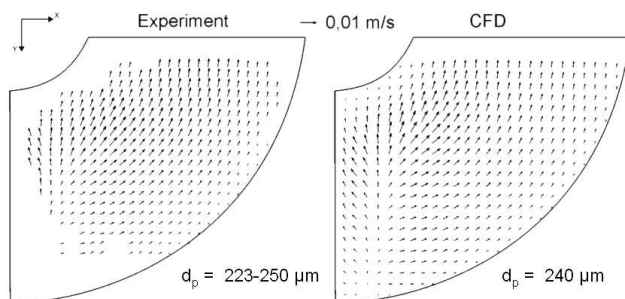


FIGURE 26. Comparison between experimentally and numerically obtained vector fields ($Re = 30.1$)

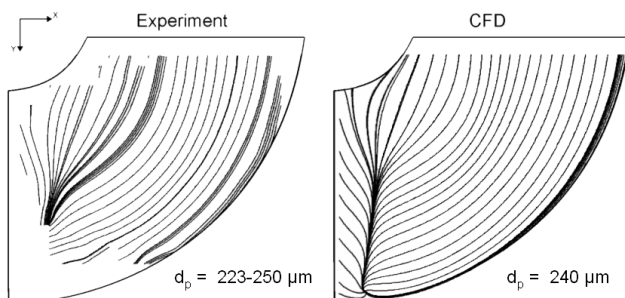


FIGURE 27. Path lines, calculated with the vector fields of Fig. 26 ($Re = 30.1$)

is visible. Please note, that these path lines are close to the wall, in Fig. 25 the path lines are in center cross sections.

For a quantitative comparison between the experiment and CFD, velocity profiles are considered at different y -positions, see Fig. 28. The comparison can be seen in Fig. 29 for the position y_4 . In Fig. 29(left) the experimental results for all particles with a wall distance between 184 μm and 220 μm is shown and compared to CFD calculations of two wall distances. The same is done in Fig. 29(right) for all particles with a wall distance between 223 μm and 250 μm . As expected, the experimental values lie between the CFD results.

In Fig. 30 a comparison of the experimentally and numerically obtained wall shear rate can be seen. The deviation is about 10 %.

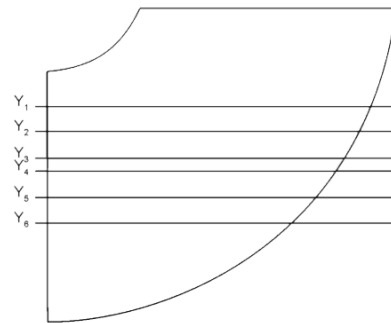


FIGURE 28. y -positions, where a quantitative comparison between experiment and CFD was done

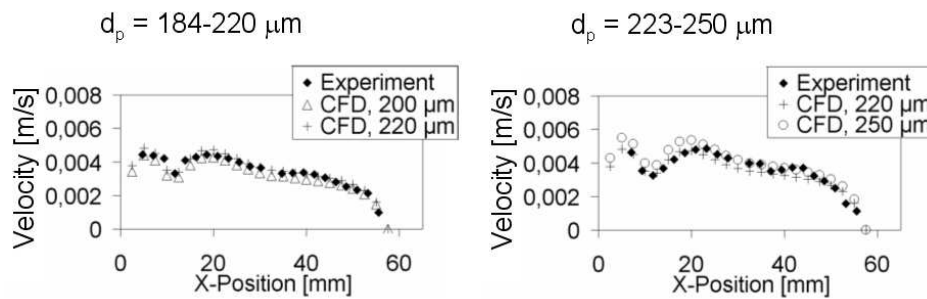


FIGURE 29. Comparison between experimental and numerical results for y_4 and $\text{Re} = 30.1$ for two different experimental wall distance ranges

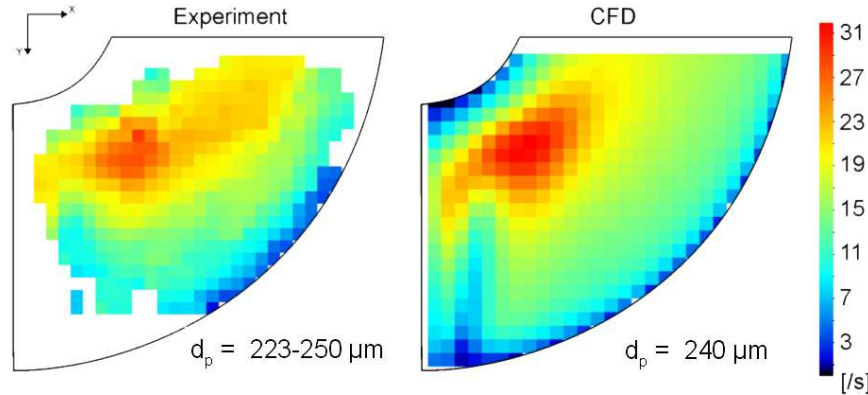


FIGURE 30. Wall shear rate. Experiment on the left side, numerical simulation on the right ($Re = 30.1$)

3.3.4. Validation in a complex steady flow with vaulted walls. The last validation step is an investigation of a complex flow with vaulted walls. The flow model is similar to before, but with a lenticular cross section, see Fig. 31. To give an impression of the flow in this special duct, depicted in Fig. 32 the path lines for the same two cross sections as in Fig. 25 are used: a cross section in x-z plane with the separation in the diagram above and below in the x-y plane just in the middle of the duct.

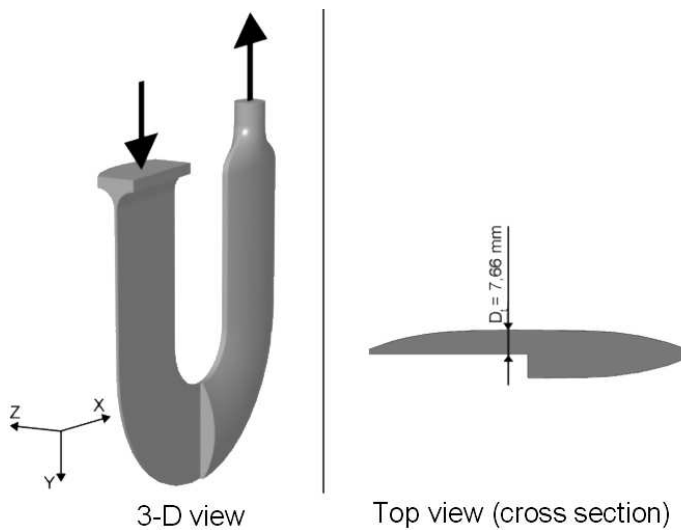


FIGURE 31. U-shaped duct with lenticular cross section and backward-facing step

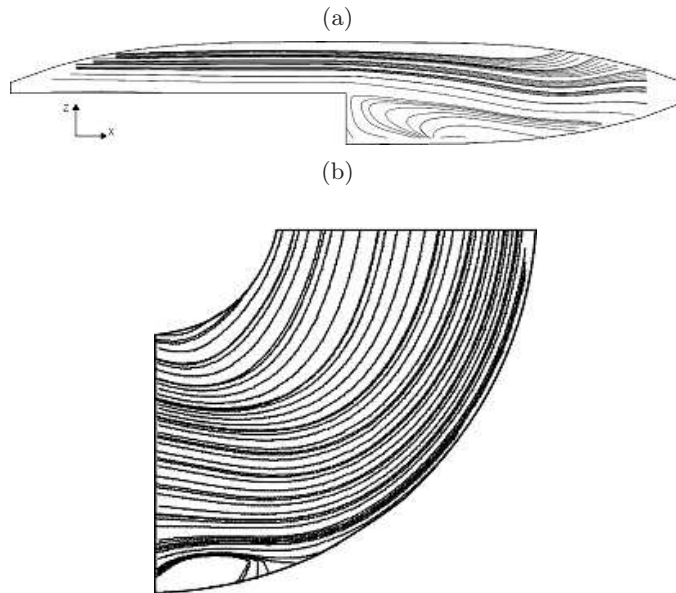


FIGURE 32. Path lines, acquired with CFD, in two cross sections ($Re = 50$)

As a validation step before a comparison between experimentally and numerically obtained velocity vector fields at the wall is done, see Fig. 33. On the left side, the experimental results for all particles with a wall distance between $230 \mu\text{m}$ and $270 \mu\text{m}$ is shown, on the right side the numerically obtained results for a wall distance of $250 \mu\text{m}$. The velocity fields show a good agreement. Path lines were calculated out of these vector fields, see Fig. 34. The flow is almost a stagnation point flow.

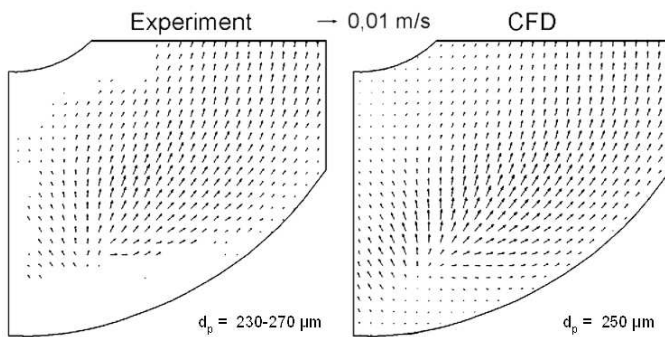


FIGURE 33. Comparison between experimental and numerically obtained vector fields ($Re = 36.6$)

For a quantitative comparison between the experiment and CFD, velocity profiles at position y_4 (see Fig. 28) are shown in Fig. 35. On the left the experimental results for all particles with a wall distance between 175 μm and 230 μm are shown and compared to CFD calculations of two wall distances. The same is shown in Fig. 35 (right) for all particles with a wall distance between 230 μm and 270 μm . Despite some deviations, the comparison is quite good.

Again, in Fig. 36 a comparison of the experimentally and numerically obtained wall shear rate can be seen. The deviation in this flow is about 15%.

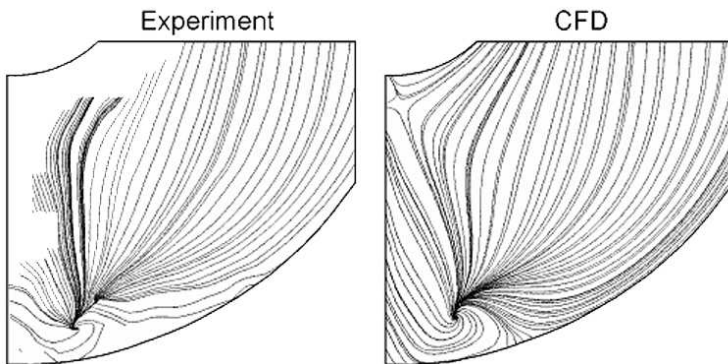


FIGURE 34. Path lines, calculated with the vector fields of Fig. 33 ($\text{Re} = 36.6$ and $d_p = 175 - 230 \mu\text{m}$)

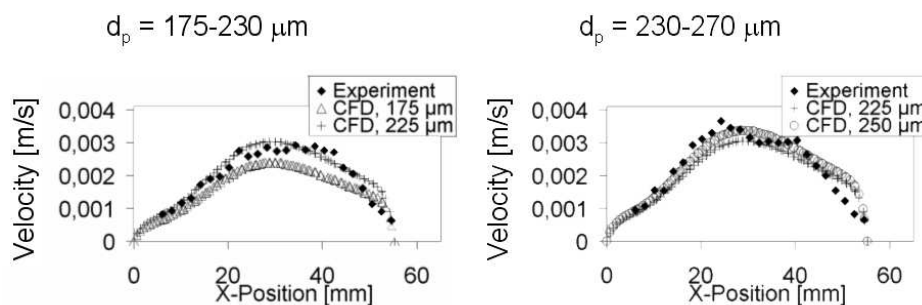


FIGURE 35. Comparison between experimental and numerical results for y_4 and $\text{Re} = 36.6$ (see Fig. 28) for two different experimental wall distance ranges

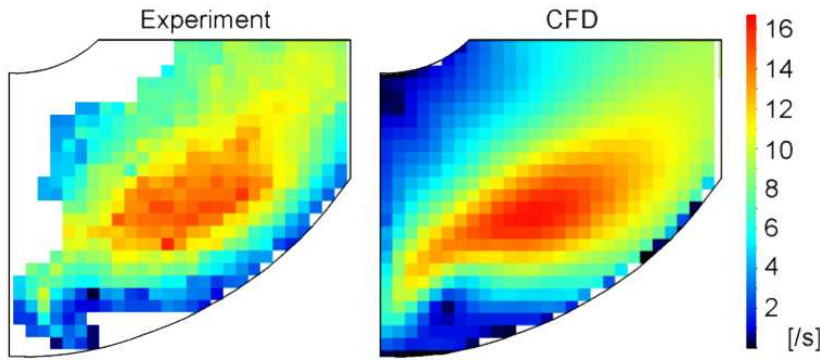


FIGURE 36. Wall shear rate. Experiment on the left side, numerical simulation on the right ($Re = 36.6$ and $d_p = 175 - 230 \mu\text{m}$)

4. Discussion and Future Work

After a review of different methods to assess the wall shear flow, a new method was presented. This new method is noninvasive, allows the assessment of the wall flow (magnitude, direction and wall distance) with an accuracy of about 10% and is usable in unsteady flows as well as at curved and vaulted surfaces. Reasons for deviations:

- too few particles close to the wall,
- instead of a certain wall distance, a wall distance range is considered,
- migration of particles perpendicular to the wall.

In addition, the size of particles should be minimized. However, despite their size, the results showed that it is possible to assess flow structures accurately. It was necessary to find a compromise between light scattering properties, neutral buoyancy, quality of monodispersity and financial restrictions. Nevertheless, we plan to manufacture smaller particles with a diameter of $100 \mu\text{m}$ without negatively affecting the monodispersity and keeping the same scattering properties as the bigger beads.

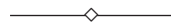
Future work will comprise of:

- flow assessment at rigid but arbitrarily vaulted walls (methods from cartography will be used),
- assessment of the third velocity component through using the method of optical flow,
- flow assessment at flexible walls.

References

1. T. ASAKURA and T. KARINO, *Flow patterns and spatial distribution of atherosclerotic lesions in human coronary arteries*, Circ. Res., **66**: 1045–1066, 1990.
2. T. BENCIC, *Pressure-sensitive paint research at GRC*, NASA Glenn Research Center, Optical Instrumentation Technology Branch, <http://www.grc.nasa.gov/WWW/OptInstr/resources/insights.pdf> (July 2005).
3. J. CZARSKE, L. BÜTTNER, T. RAZIK, H. MÜLLER, D. DOPHEIDE, S. BECKER and F. DURST, *Spatial-resolved velocity measurements of shear flows with a novel differential Doppler velocity profile sensor*, http://in3 дем.ist.utl.pt/lxlaser2002/papers/paper_21_1.pdf (July 2005).
4. DANTEC DYNAMICS, *Laser Doppler Velocimetry*, http://www.dantecdynamics.com/LDA/Principle/LDA_principle.jpg (July 2005).
5. C. HEINZEN, *Herstellung von mikrodispersen Mikrokugeln durch Hydroprilling*, Dissertation, Eidgenössische Technische Hochschule Zürich (1996).
6. M.H. KROLL, J.D. HELLUMS, L.V. MCINTIRE, A.I. SCHAFER and J.L. MOAKE, *Platelets and shear stress*, Blood, **88**: 1525–1541, 1996.
7. LAVISION, *System Components for Particle Image Velocimetry*, <http://www.piv.de/graphics/pivsetup.jpg> (July 2005).
8. H. MENG, *Tackling turbulence with holographic particle image velocimetry*, AIAA Fluid Dynamics Conference, 30 th, Norfolk, VA, 1999, <http://www.eng.buffalo.edu/Departments/mae/LFD/publications/1999/1999-2.pdf> (July 2005).
9. W. MORTON and R. CUMMING, *A technique for the elucidation of Virchow's Triad*, Ann NY Acad Sci, **283**, p.477, 1977.
10. R.M. NEREM, R.W. ALEXANDER, D.C. CHAPPELL, R.M. MEDFORD, S.E. VARNER and W.R. TAYLOR, *The study of the influence of flow on vascular endothelial biology*, Am. J. Med. Sci., **316**(3) : 169–175, 1989.
11. G.P. NOON, *Clinical use of cardiac assist devices*, [in:] T. Akutsu, K. Koyanagi [eds.], Heart Replacement—Artificial Heart **4**, pp.195–204, Springer Verlag, 1993.
12. H. PARK, J. A. MOORE, O. TRASS and M. OJHA, *Laser photochromic velocimetry estimation of the vorticity and pressure field \tilde{U} two-dimensional flow in a curved vessel*, Experiments in Fluids 26 (1999).
13. B. RUCK, *Statische-scannende Systeme*, GALA e. V., <http://www.gala-ev.de/images/Stat-Scan-Anordnung.jpg> (July 2005).
14. SIGNAL PROCESSING SA, *Ultrasonic Doppler velocimetry*, http://www.signal-processing.com/images/devices/working_principle.gif (July 2005).
15. M. TRIEP, CH. BRÜCKER and W. SCHRÖDER, *Visualization and high-speed PIV measurements of the flow downstream a dynamic mechanical model of the human vocal folds*, Aerodynamisches Institut der RWTH Aachen, http://in3 дем.ist.utl.pt/lxlaser2004/pdf/paper_23_1.pdf (July 2005).

16. E. ZANOUN, *Oil Film Interferometry for Wall Shear Stress Measurements*, LAS – BTU Cottbus, <http://www.tu-cottbus.de/LAS/images/D4-1.gif> (July 2005).



Flow in Artificial Valves and Blood Pumps

KLAUS AFFELD, DEIBRIS AGUILERA, PERRINE DEBAENE, LEONID
GOUBERGRITS, ULRICH KERTZSCHER, and TOBIAS TIMMEL

*Biofluidmechanics Laboratory
Charit , Universit tsmedizin Berlin,
Spandauer Damm 130,
14050 Berlin, Germany
klaus.affeld@charite.de*

A variety of impairments and diseases require the implantation of mechanical elements in the circulatory system. The ones most difficult to design are artificial valves and artificial blood-pumps. Blood can be considered as a Newtonian fluid under certain conditions. The greatest problem is caused by the tendency of the blood to form solid particles, called clots. Such clots are generated through the interaction of three qualities: of blood, of the wall, and finally of the flow. The latter is the one the fluiddynamicist can actively influence by avoiding flow separations. These are experimentally and numerically investigated and examples for unfavourable and for favourable designs are given.

Key words: *Blood flow, flow separation, artificial valves, thrombus generation*

1. Introduction

A variety of impairments and diseases require the implantation of mechanical elements in the circulatory system. The ones most difficult to design are artificial valves and artificial blood-pumps. The greatest difficulty arises, in that there is no material which can truly mimic the inner wall of the circulatory system. This wall is covered with specialized cells—the endothelium. Unimaginable for the engineer, each of the cells contains a flow sensor, which senses the shear stress of the flow. The cell orients itself to the flow, it gives a signal—nitric oxide—to the platelets to calm down and not to adhere [1]. This wonderful mechanism is absent when artificial materials are used, such as metals, polymers, ceramics, pyrolytic carbon or others. The engineer has

to try to create a good design which avoids just this stall and lowers shear stress. He will not come up with a valve that is as good as a healthy one, but one which is better than the diseased valve. The same is true, however to a much lesser degree, for the artificial blood pumps which have the objective to assist or even to replace the natural heart.

2. Blood as a Newtonian Fluid

Newton's famous formula (Fig. 1) combines the shear-stress of a fluid with the shear rate. Consequently, all fluids behaving according to this formula are called Newtonian fluids. But is blood such a fluid? More than 40 % of it consists of cells, which at times accumulate to form "rouleaux" (Fig. 2). These rolls cling together and at low shear rates the blood even resembles a solid. When sheared, blood becomes less viscous, and at high shear rates it behaves as a Newtonian fluid.

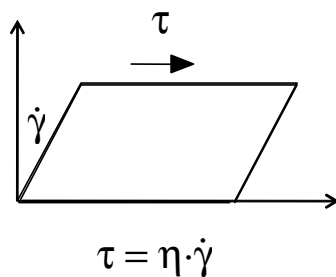


FIGURE 1. Newton's insight—his ingeniously simple formula enables us to compute most technical flows. Is it applicable to the special fluid, blood?

In the body, the blood is subjected to quite high shear-stress (Fig. 3). In the capillaries of various species, including humans, we encounter wall shear rates of up to ten thousand 1/s. In the vena cava, which is the central vessel with the slowest blood flow, we still encounter a wall shear rate of about 50 1/s. Above the point where this wall shear rate is reached, blood behaves as a Newtonian fluid [2]. At lower shear rates rouleaux formation can be observed. Typically, they take between ten to sixty seconds to form. From this follows that Newton's formula can be applied to all practical computations.

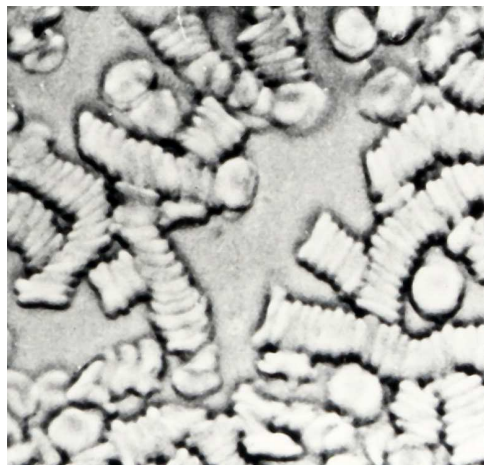


FIGURE 2. When not in motion, red blood cells attach to each other and form rouleaux. Blood becomes more viscous; almost a fragile solid.

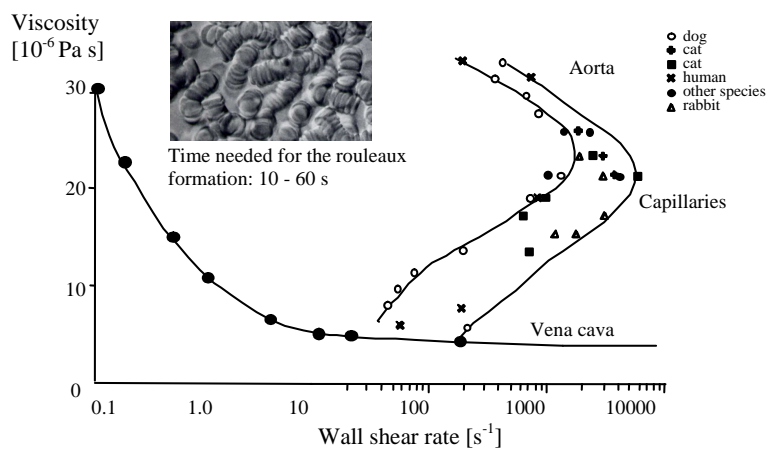


FIGURE 3. Blood becomes a non Newtonian fluid if it has 10 to 60 seconds to rest in a low shear rate zone. However, within the healthy body no such zone exists, as shown in the graph on the right side. The ordinate here denotes the position of the vessel in the body, [15].

3. The Role of Flow Separations

Only under pathological flow conditions is the time necessary for rouleaux formation given. An example of such flow conditions are flow separations. For instance, the flow over an air foil (Fig. 4) separates, as shown by Prandtl in his flow visualization experiments. In the case of an air foil, the flow separation

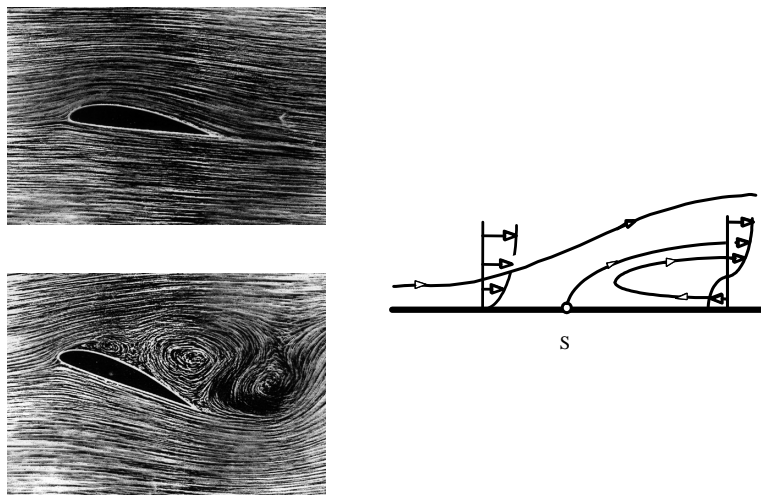


FIGURE 4. Attached flow around an air foil and flow separation at a higher angle of attack, as shown in Prandtl's famous flow visualization experiments. The right side shows a diagrammatic cross section through a flow separation.

results in the loss of lift and may induce the airplane to crash, causing many fatalities.

In the blood stream, flow separations also occur. They are not necessarily fatal, but if they endure, are dangerous to the patient. A schematic diagram of a flow separation can be seen in Fig. 4 (right side). At the stagnation point the flow detaches and a separation bubble may form. Within the separation bubble the blood circulates slowly, rouleaux formation may take place, and in addition, platelets are able to aggregate in the vicinity of the stagnation point. These adhered platelets emit thromboactive substances, which cause more platelets to be attracted until a thrombus is finally formed.

In this way, a connection between the flow of blood and thrombus generation may be observed. This was first observed by the eminent pathologist Rudolf Virchow, who published his findings as early as 1856 [3], see Fig. 5. During his many post-mortems, he observed thrombi and atherosclerotic alterations of the vessel wall at specific locations, especially at bifurcations. When a blood vessel bifurcates the blood velocity is decreased and in many cases flow separation occurs naturally. As new studies have shown, persistent low shear stress at the vessel wall modifies the endothelial cell layer, which transforms into smooth muscle cells and lipids [4]. In this way, fatty streaks develop which are the precursor of the atherosclerotic plugs which

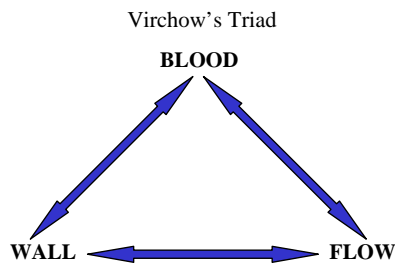


FIGURE 5. Virchow's triad shows a functional connection between the qualities of the blood, the vessel wall and the flow.

were observed by Virchow. Intuitively, he then formulated a triad of three entities:

- quality of the blood (activated platelets, lipids)
- quality of the flow (smooth flow along the wall, detached flow)
- quality of the wall (healthy endothelial cells, atherosclerotic plugs, artificial material)

Figure 6 shows some examples: atherosclerotic lesions on the inner side of the aorta and a thrombus at the metal ring of an artificial cardiac valve.

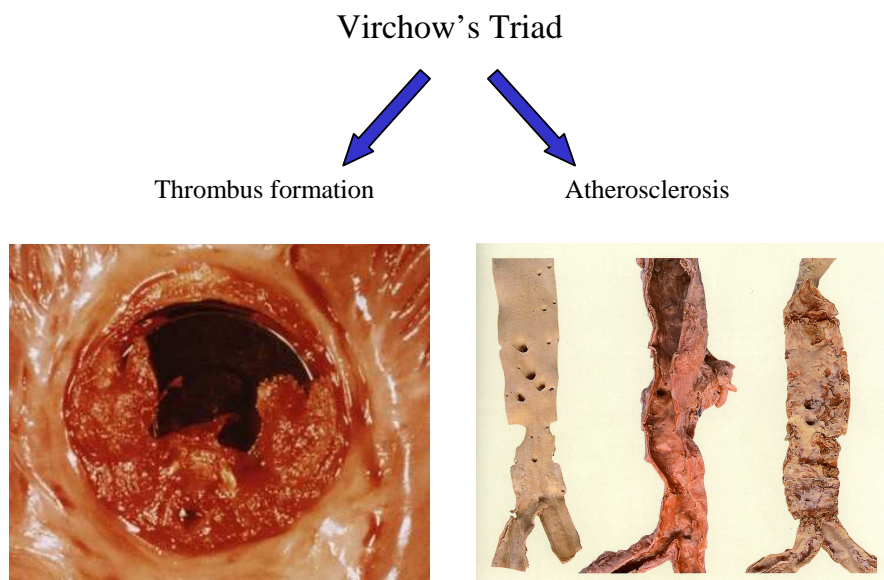


FIGURE 6. The result of a mismatch of blood, wall and flow: a thrombus at an artificial valve and a degeneration of the natural aortic wall.

The artificial materials which are at our disposal are all far inferior compared to the endothelial cells. All artificial materials may be considered thrombogenic. However there are materials which are a compromise between an artificial and the natural vessel wall. These materials are bioprosthetic materials, of which one example is the pericardium. This material is slightly cross-linked. It loses its immunological properties, but retains many mechanical properties. In that way, the tissue from a different species, for example the cow, may be harvested and sutured into a cardiac valve for a human. These valves do not require anticoagulants, and are therefore implanted in high numbers [5].

4. Flow Through Valves

Virchow's analysis indicates that there must be a delicate balance of the three above mentioned qualities. A thrombus can form if the quality of the flow is disturbed, as shown in Fig. 7. It shows a large thrombus at the edge of a bioprosthetic valve that had been used in a ventricular assist device [6]. A cross-section of a CFD (computational fluid dynamics) simulation shows an area of very slow blood flow in the sinuses of the valve duct.

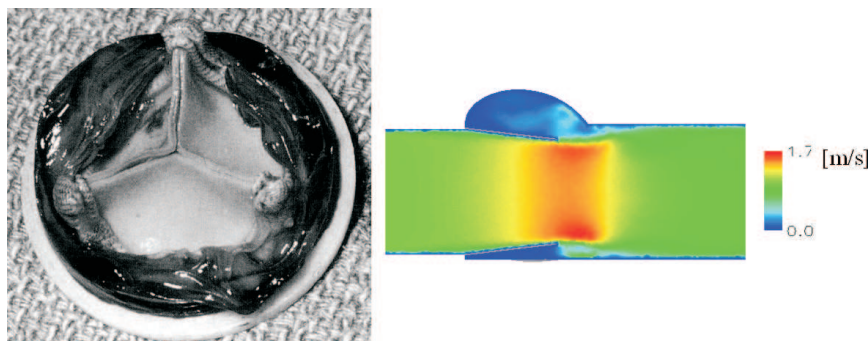


FIGURE 7. A thrombus at the sinus of a pericardial valve for a VAD (left). The cross-section of a CFD simulation (right) shows a low velocity in the sinus.

The frequent occurrence of thrombi in artificial heart valves was the reason to design and build a special flow channel. This flow channel uses, at a ten times enlarged scale, a Björk-Shiley valve, which had previously been transformed into a model with a 200 mm diameter, see Fig. 8. The advantage of this up scaling—keeping the Reynolds number similarity—is that the velocities are greatly reduced and the flow field is larger. Fine details of the

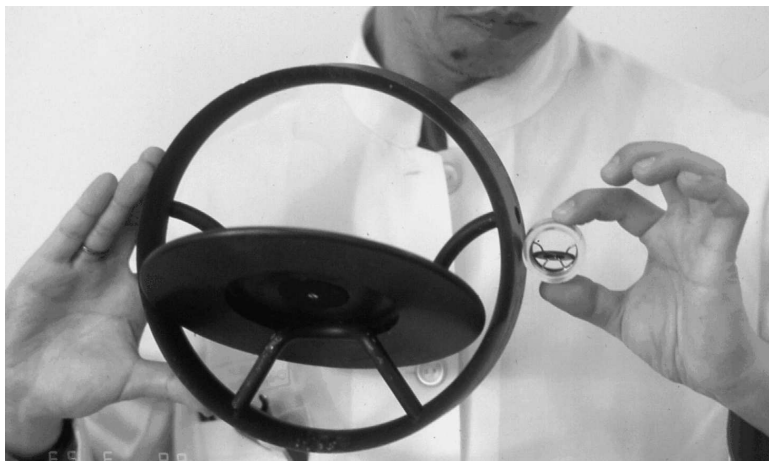


FIGURE 8. An enlarged model of the Björk-Shiley valve is shown and compared to the original.

flow are revealed. A schematic diagram is shown in Fig. 9. The fluid, water, is driven by a computer controlled axial flow pump which simulates the physiological aortic flow curve. The total volume is 600 liters. A whole cardiac cycle lasts several minutes and the fluid velocities are below ten centimeters per second, which is a precondition for effective flow visualization [7, 8].

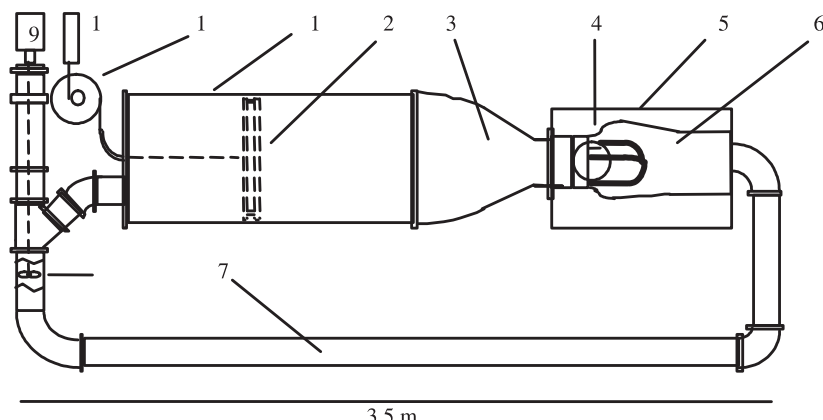


FIGURE 9. Water tunnel for 10:1 scaled up valve models. The flow is non-stationary, keeps the Reynolds-number similarity and as a result is very slow. The time expansion is about 200 fold. 1. tank, 2. piston, 3. contraction, 4. test valve, 5. observation tank, 6. aortic root, 7. return duct, 8. axial flow pump, 9. motor, 10. displacement transducer, 11. gear.

To visualize the flow through the heart valve, the water within the model of the aortic root is mixed with dye and illuminated with a light sheet. When the systolic flow is initiated, water enters the aortic valve and appears black. It more or less displaces the dyed water and makes the flow visible. Figure 10 shows a model of a tri-leaflet valve and Fig. 11—flow through such a valve. The entering flow forms a central jet, which barely mixes with the fluid in the aortic root. The fluid in the vicinity of the valve ring is not mixed at all. The flow simulates the blood flow through the valve shown in Fig. 7, and thus gives an explanation for the large thrombus. Figure 12 shows the flow through a Björk-Shiley valve. After opening, a flow separation is formed at the trailing edge of the occluder. One side of the valve ring is well rinsed—it appears completely black—while the flow is stagnant on the upper side. As a result a thrombus generation is likely at this site, and in fact the thrombus in Fig. 6 is exactly in this region. Figure 13 shows yet another valve—the St. Jude valve. It is a bi-leaflet valve with two occluders, which open like double-doors. The light sheet is parallel to the door axis and cuts through the middle of the flow channel. A turbulent jet is formed. However, a slow rinsing of the valve ring is also observed here.



FIGURE 10. 10:1 model of a polyurethane tri-leaflet valve

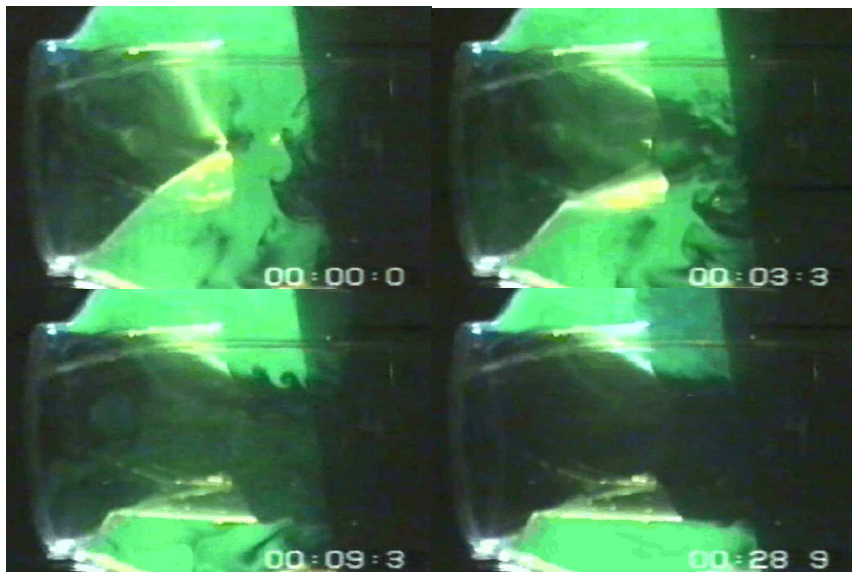


FIGURE 11. 10:1 model of a tri-leaflet valve during various phases of the systolic flow. The water in the aortic root is dyed and appears green. The water from the new systole is not dyed and appears black. This makes the washout visible.

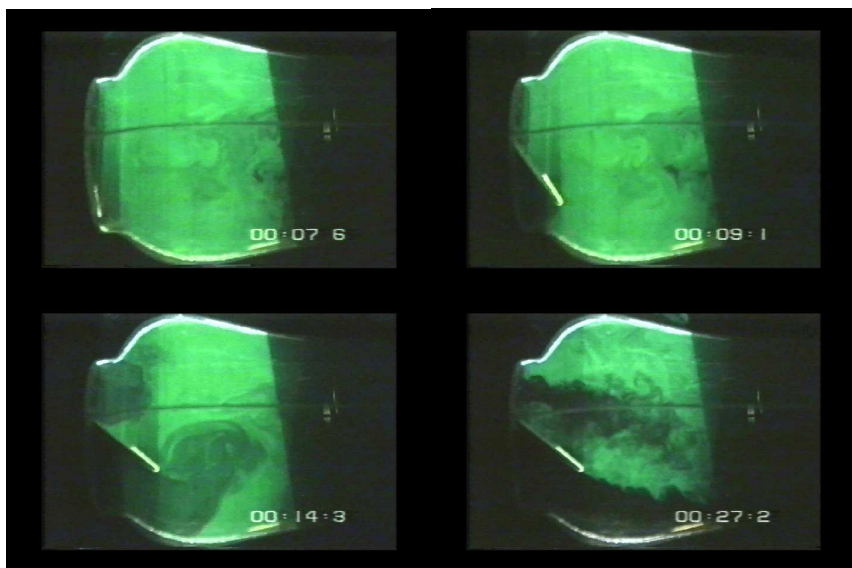


FIGURE 12. 10:1 model of the Björk-Shiley valve. A large flow separation appears at the trailing edge of the occluder. The fluid at the ring remains stationary.

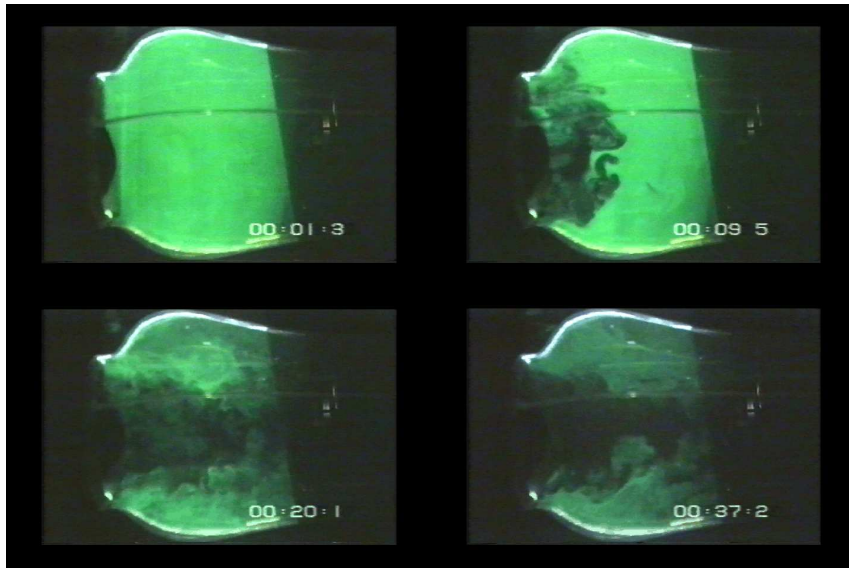


FIGURE 13. 10:1 model of the St. Jude valve. A turbulent jet forms in the middle. The fluid at the ring remains stationary.

5. New Valve Design

All of these experiments show that, in these models of artificial heart valves, flow separations are always present. Is it possible to design a valve without flow separations? The answer is probably not; at least it hasn't been achieved yet. The reason for this is that the aortic root is a vessel which acts as a diffuser. In other words, a jet enters a diverging vessel. This means that the flow is decelerated, and the pressure upstream is higher than the pressure downstream. In the boundary layer this has the effect that the flow is easily reversed and a flow separation takes place, as shown in Fig. 4.

The situation with the diverging channel, however, is not valid for an artificial valve in a ventricular assist device (VAD). In this case the engineer has full control over the design of the channel.

5.1. S-Valve

An example of a possible design, here a duct with an s-shaped center line, is shown in Fig. 14. The objective of this design is to avoid a flow separation, which may be seen in Fig. 12. The occluder (9) has a minimal angle of attack

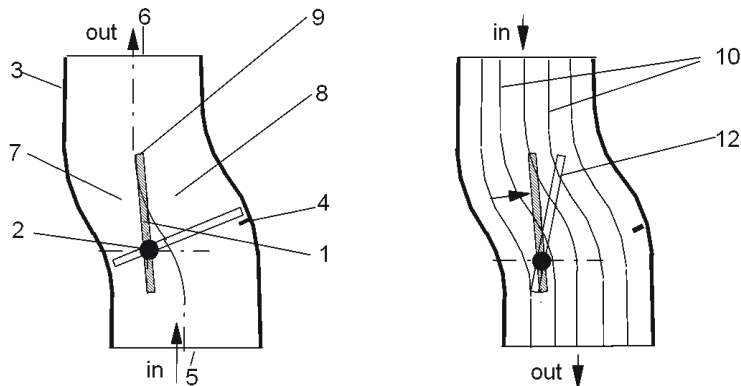


FIGURE 14. A schematic diagram of the S-Valve. Objective of this design is to avoid flow separation at the occluder.

to the incoming flow, which is labeled with the arrow (5) in the diagram. This is also true for the flow at the trailing edge. For the flow, this connotes an acceleration in area (8), and a deceleration in area (7). When the flow reverses (Fig. 14, right) in the first instance, friction does not play a role. The stream lines resemble that of a potential flow. In this way, they attack the occluder at an angle and also initiate the rotation around the axis. As a result, it moves from position (12) to full closure at (4). Had one placed the occluder in a straight duct, the stream lines at the initiation of the closure would be parallel to the occluder in the open position, and the valve would not close. With the s-shaped duct however, flow separation can be avoided, and closure times comparable to the normal Björk-Shiley valve can be achieved [9, 10].

The design of the duct with an otherwise unchanged Björk-Shiley valve is shown in Fig. 15. The CFD computation of the flow in an S-Valve, in comparison to the Björk-Shiley valve in a straight cylindrical duct, is depicted in Fig. 16.

Figure 17 shows a view of the wall shear stress of the same flow. The wall shear stress has very low values near the ring in the cylindrical duct, as well as in a large area downstream near the lower wall. In the S-Valve near the ring, the wall shear stress is much higher because the ring is integrated into the wall. Also, the area of wall shear stress is reduced downstream from the occluder. Figure 18 shows the washout process of the S-Valve in the large water channel. In accordance to the CFD studies only small flow separations appear.

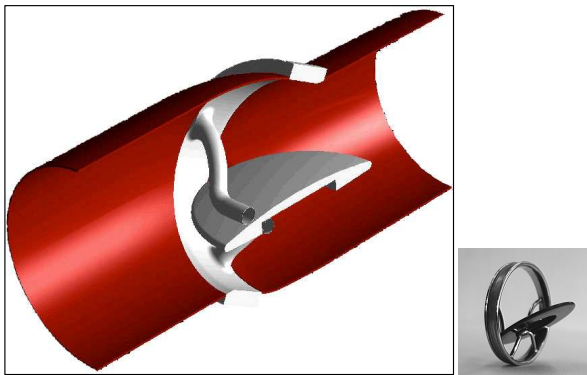


FIGURE 15. A view of a CAD model of an S-Valve. For practical purposes, it is a Björk-Shiley valve in a special duct.

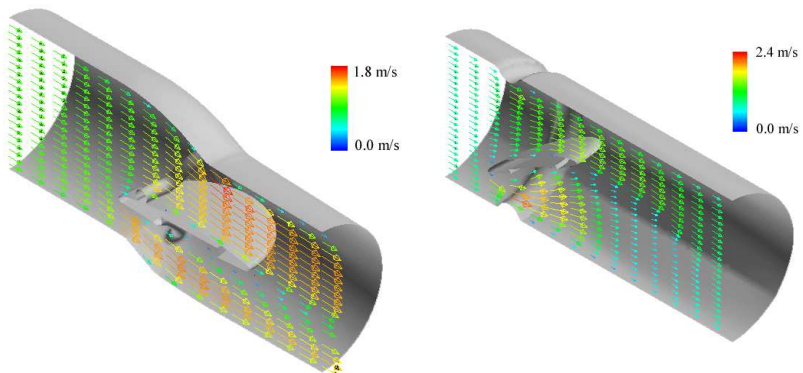


FIGURE 16. Comparison between the CFD flow field around an occluder in an S-shaped duct and in a straight duct.

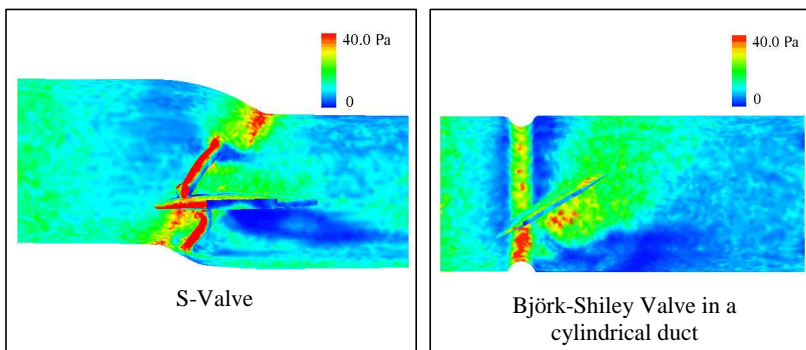


FIGURE 17. A comparison between the Wall shear stress of the two different arrangements.

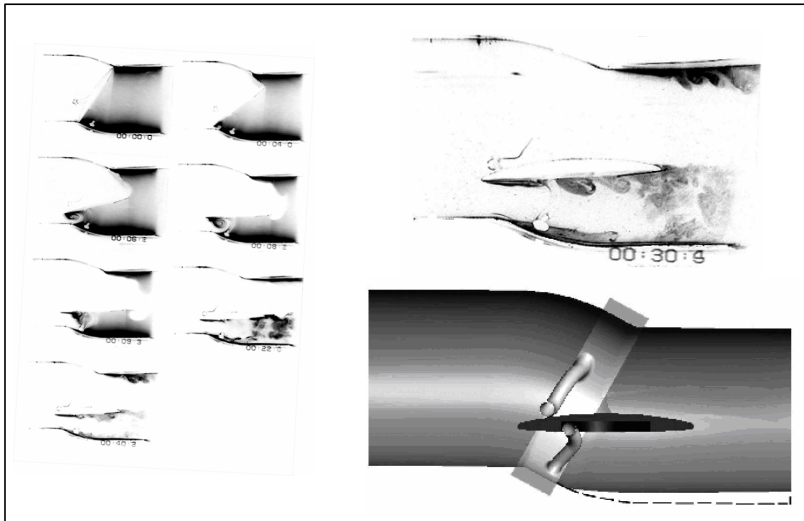


FIGURE 18. A washout experiment of the S-Valve in the large water tunnel.

These computations were tested in the above mentioned water channel in an enlarged 10:1 scale model. Large flow separations are absent; however, small areas of flow separation appear at the upper and lower walls of the duct and on the lower side of the occluder. This occurs during a time span of 30 seconds (enlarged model), which corresponds to a real-time of 6 milliseconds in the real model. Since 6 milliseconds comprises of only a small section of the systolic time of 300 milliseconds, a complete washout during this time span is achieved.

5.2. Purge Flow Valve

Yet another idea to increase the washout is pursued using the valve shown in Fig. 19. It is a mono-leaflet valve with a sinus [11]. When the valve opens, a part of the main flow impinges on a flow divider, which directs a part of the main flow into the sinus. In this way a purge flow is generated which greatly reduces the washout time. In a CFD study, shown in Fig. 20, a systematic variation of geometric parameters was performed. From 188 possible parametric combinations, 34 were selected and studied with the help of CFD [12]. The objective was to minimize the area of low wall shear stress. Figure 21 shows an example of the wall shear stress inside the sinus. From these results, 4 valves were selected, fabricated, and tested in a dye washout experiment.

IDEA:

Accept flow recirculation,
but wash out critical
regions periodically.

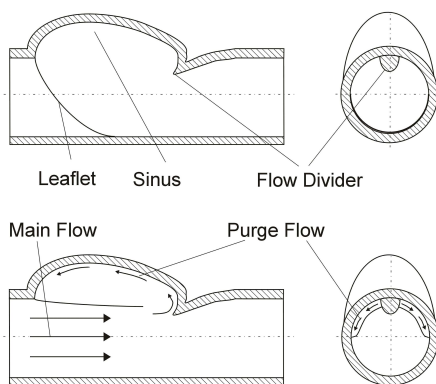


FIGURE 19. A schematic cross section of the purge flow valve.

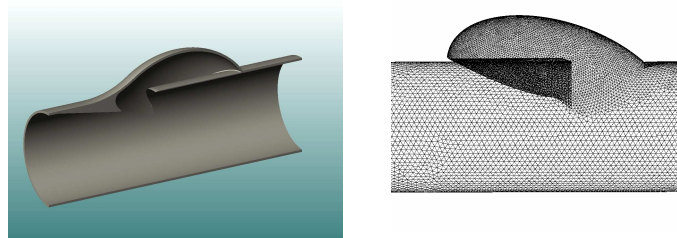


FIGURE 20. Variation of parameters which define a mono-leaflet purge flow valve.

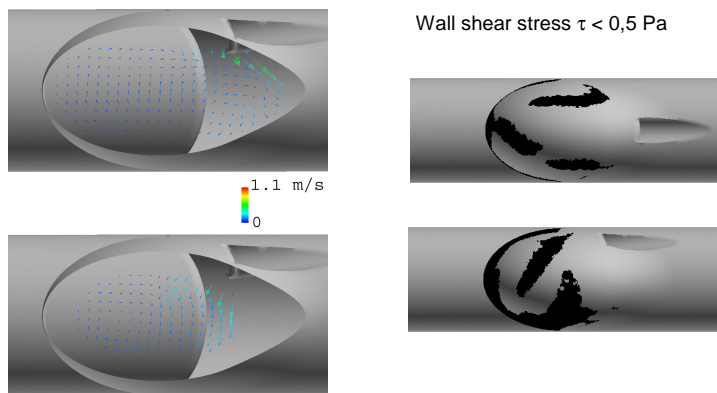


FIGURE 21. Wall shear stress as a function of different parameters.

The diagram (Fig. 22) shows that one valve has a faster washout and thus has superior qualities in comparison to the others. This technology can also be applied to a tri-leaflet valve, as is shown in Fig. 23.

Systematic variation of geometric parameters

- 188 possible parametric combinations
- Design of only 34 models (Taguchi method—Quality Management)

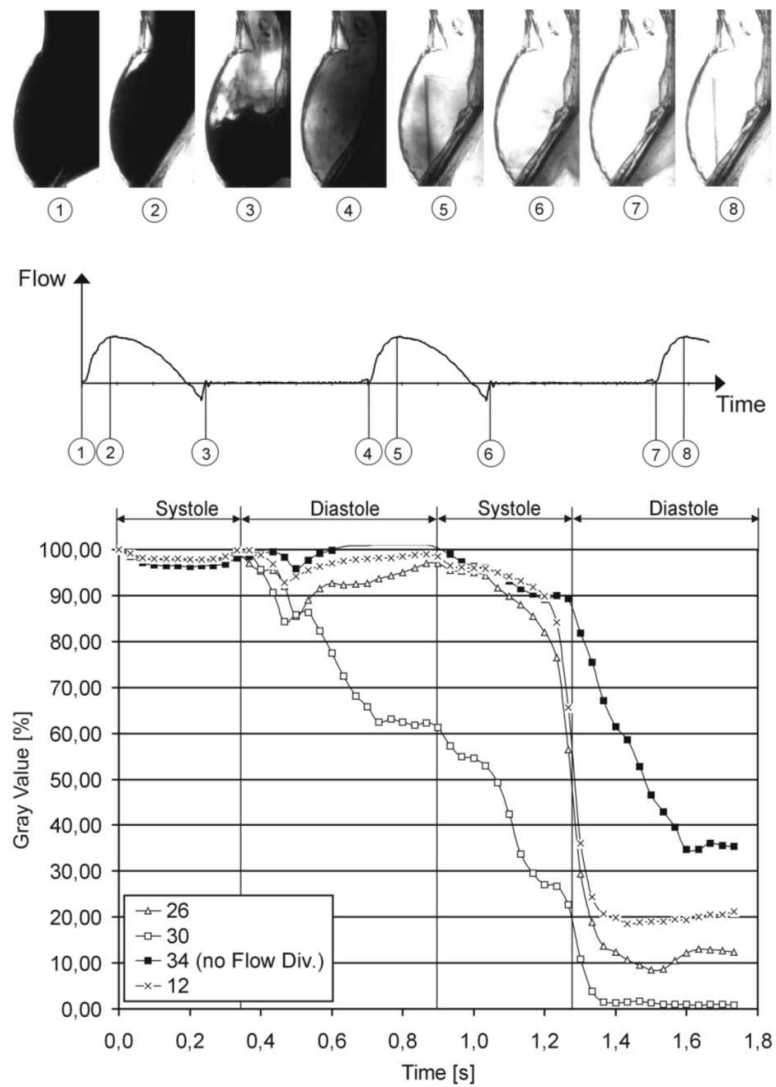


FIGURE 22. Results of wash out experiments of 4 different valves.

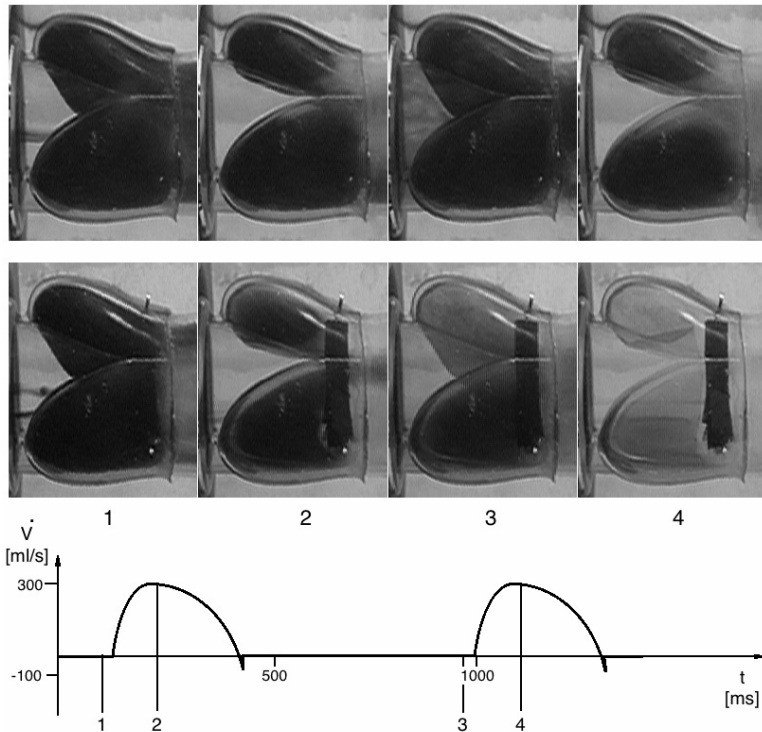


FIGURE 23. Washout experiment in a tri-leaflet valve without (above) and with purge flow (below).

5.3. Ball Valve

Another valve was also investigated, which applies a sphere as an occluder. Such valves were developed and implanted in great numbers during the early days of artificial heart valve implantations. Some, as for instance the Starr-Edwards valve, were quite successful, and worked in some patients for longer than 25 years. However, in many patients it did create a considerable pressure drop if the individual anatomy of this patient did not work well with the ball, which in the open position protrudes into the aortic root. Thus an individual match of the geometry of the valve and the patient's anatomy was a precondition for the success of the valve. As a result of this, different valve designs comprising of a flat disc instead of a ball were introduced. An example of such a valve is the Björk-Shiley valve, which was discussed above. The ball as a blunt body causes quite a resistance and large flow separations in its wake. This is true for a ball in an open space and also in a duct with

a geometry which is not matched to the ball, as was the case in most of the patients receiving Starr-Edwards valve.

6. Flow Through a Ventricular Assist Device (VAD)

However, this situation changes completely if one designs a ball valve for a VAD. Instead of the human anatomy, one has full control over the geometry of the duct. A ball moving through open space experiences large flow separations on the trailing side, because the fluid cannot follow the curvature of the ball. The flow beyond the greatest diameter is decelerated, thus creating the conditions for the flow separation. However, if a duct can be applied, its geometry can be designed so that the flow behind the largest diameter is accelerated. The outflow area of the duct is thus larger than the inflow area and the acceleration of the fluid leads to a pressure drop. This is the price which has to be paid for the absence of flow separation at the duct wall. However there remains one stagnation point downstream of the ball and this area creates a flow separation. Since the ball can move freely, it rotates a little bit with every pulse. As a result, the flow separation is always at a different location of the ball surface. This was investigated in a CFD model (Fig. 24) and by a variation of geometric parameters we managed to minimize areas of low shear stress.

In Fig. 25, the engineering solution of this valve, the guidance of the ball and the systolic stop are integrated into the housing, and a smooth inner surface without steps could be created. Figure 26 shows a sequence of a dye washout experiment in a large water channel. After a few milliseconds, a complete washout of the wall region has been attained.

Figure 27 shows yet another experiment: the flow inside a real-sized valve was assessed with Particle Image Velocimetry (PIV). The flow field agrees well with the other experimental methods. Also, Fig. 28 shows how such ball valves are integrated into a VAD, which in this case is a pneumatically driven blood pump. The inner surface is fabricated in halves including the valves and the flexible diaphragm.

Later, the balls are inserted and the two halves are joined to form one blood pump, which is shown in Fig. 29. The flow inside such a blood pump, which was assessed with PIV, is shown in Fig. 30. Shown is a circular flow with a jet from the inflow valve. The outflow takes place without flow separation. A more complicated flow is shown in Fig. 31. In this case the inflow

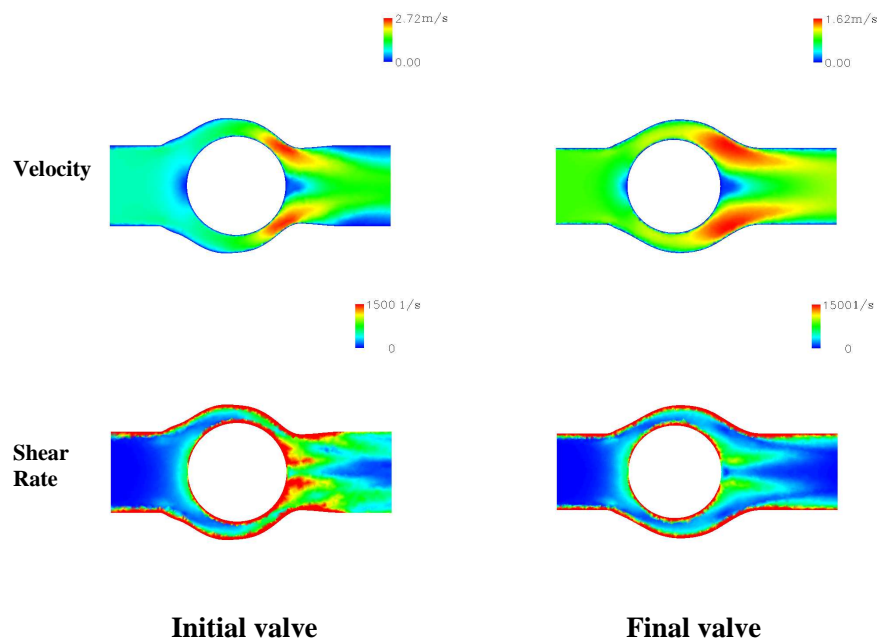


FIGURE 24. CFD results of flow through ball valves with different geometries.

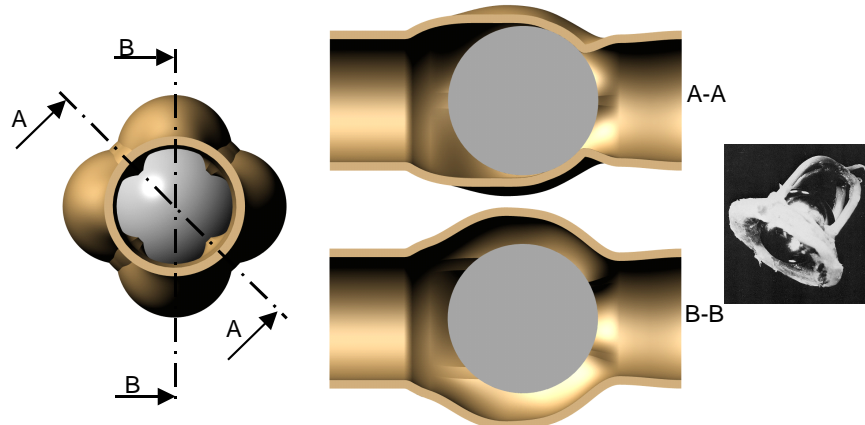


FIGURE 25. CAD view of a ball valve. Struts and stoppers are integrated into the housing.

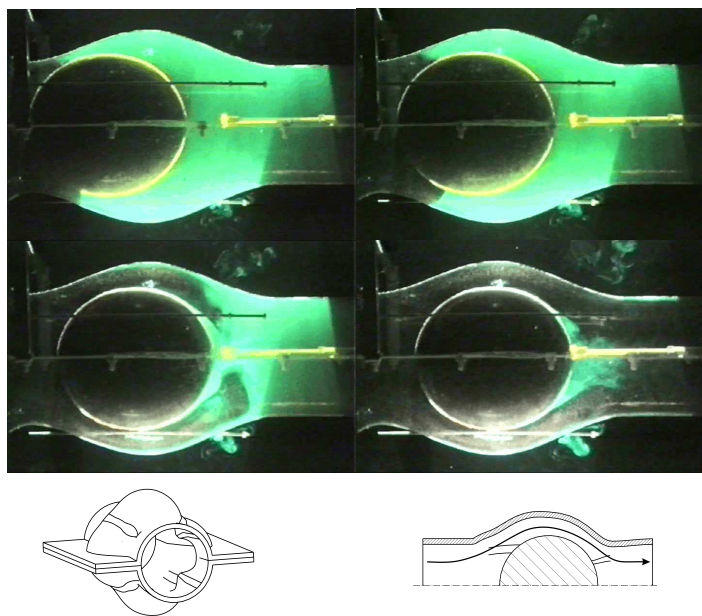


FIGURE 26. 10:1 model of a ball valve. Downstream of the ball a flow separation appears, but the walls are well washed out.

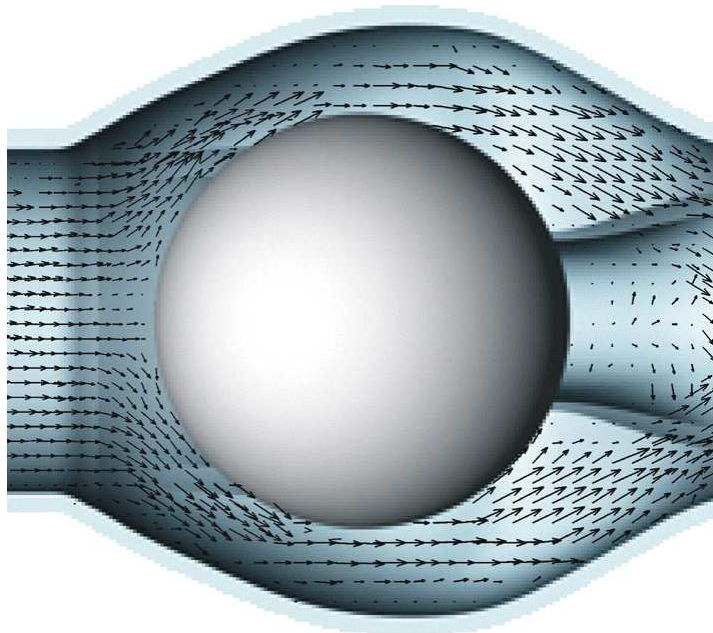


FIGURE 27. PIV results of the flow field within the ball valve.



FIGURE 28. Inlet and outlet valves which are integrated into a blood pump.



FIGURE 29. Pneumatic blood pump with integrated ball valves.

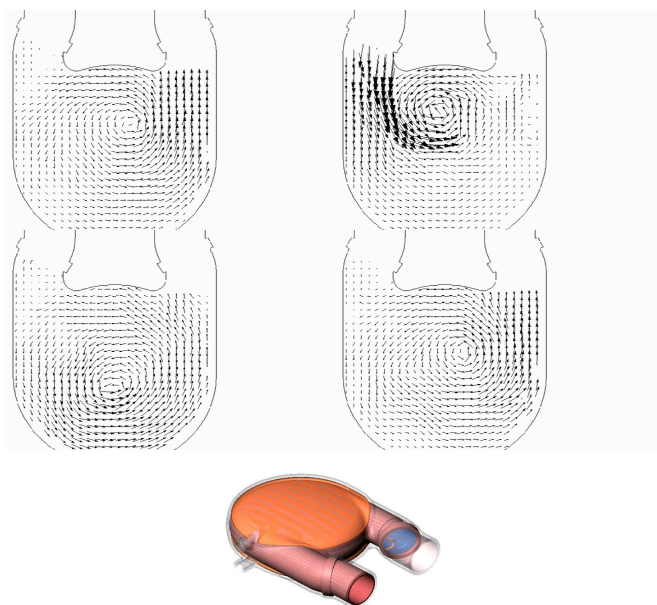


FIGURE 30. Flow field within a pneumatic blood pump on one symmetry plane, obtained with PIV.

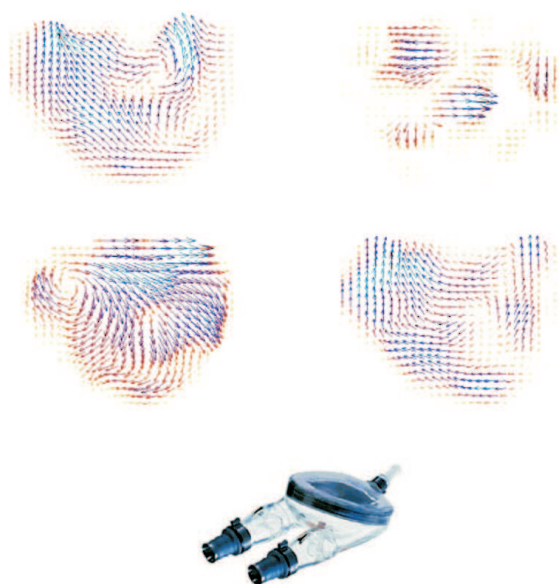


FIGURE 31. Flow field within a pneumatic blood pump with the diagram slanted in respect to the valves, obtained with PIV.

jet impinges at an angle into the flow chamber and the diaphragm acts on only one side of the blood pump. Both of these asymmetric design features create more complex flow fields, which can be observed in the vector field. The average wall shear stress has been shown as influential in the valve design, and it certainly has an influence in the design of the blood chamber. This was investigated in an experimental method, called the paint erosion method. The inner surface of a blood pump is painted with a water soluble paint, and then the blood pump is operated using water. In regions of high shear rate the paint is dissolved first, and regions of low shear rate remain covered with paint (Fig. 32). In this way the action of the wall shear rate inside the blood pump can be assessed.



FIGURE 32. The paint erosion method permits the visualization of the distribution of wall shear stress.

7. Models for Thrombus Generation

From the previous information, the conclusion can be drawn that the generation of a thrombus is the greatest danger for all of these implants. A thrombus is a mass composed of deposited platelets, red blood cells and

fibrin strands. Sometimes a thrombus is composed of platelets alone. This means in effect, that the platelets need to “know” that one has adhered and the next need to recognize this and adhere as well. How is this communication between platelets accomplished? This problem has been investigated with experimental and numerical models. In the experimental model, a fluid composed of plasma and subsequently activated platelets flows towards a glass plate and forms a stagnation flow [13]. The glass plate can be observed through a microscope.

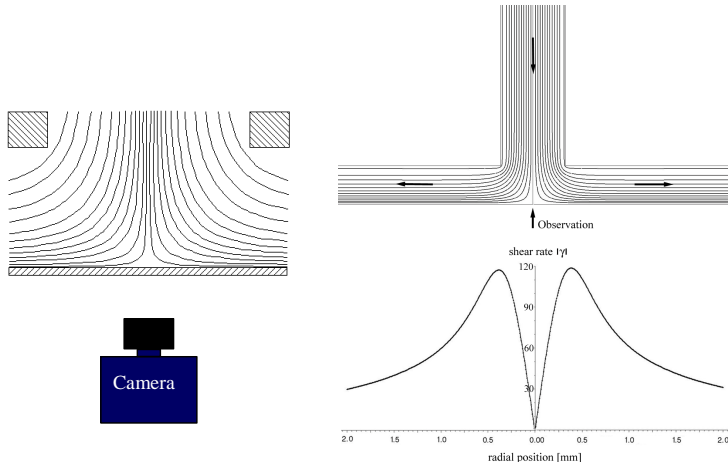


FIGURE 33. Schematic view of this stagnation flow experiment. The flow field and the resulting shear field at the wall has been computed.

Figure 33 shows the experimental arrangement. The stagnation flow has a central stagnation point where by definition the shear stress is zero. The shear stress increases radially, peaks and then decreases again. The activated platelets come close to the glass wall and some adhere, see Fig. 34.

They form specks of individual thrombi, each of them growing larger with time until they finally combine with each other and form a ring. From the final picture one can conclude that neither in the stagnation point nor at a very large radius does a thrombus form. Both areas coincide with a low or zero shear stress while at a specific shear stress the thrombi are formed massively. This was investigated in a numerical model: a deposited platelet is assumed to give off a messenger molecule like ADP, ATP, or thrombin. With the random walk method the diffusion of these molecules is simulated [14]. In this method one assumes random step which imitates the Brownian movement. A series of steps and a number of molecules form a three dimensional cloud. The

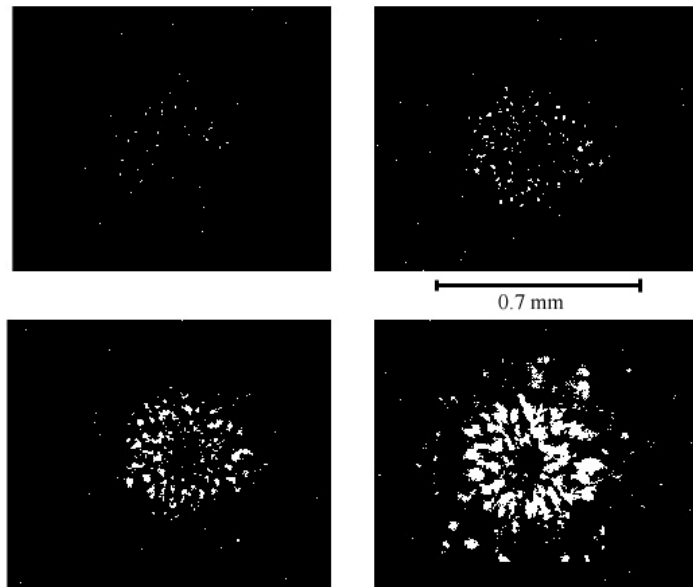


FIGURE 34. Thrombus formation caused by initial platelet adhesion. They grow in size and form larger specks in the form of a ring. The stagnation point in the center remains free of specks.

influence of the flow can be taken into account if at each random step the appropriate velocity is added. The flow field that was assumed has a zero velocity at the wall, and a velocity which increases linearly with the distance to the wall.

Figure 35 shows separate views of the cloud which is formed by diffusion alone, and also by the combination of diffusive and convective motion. The simulation shows that the convection helps to transport the messenger molecules. If one assumes an even stronger flow field than shown in the figure, one would achieve a very long and diluted cloud. From this one can intuitively deduce that diffusion alone does not achieve a transport of a messenger molecule to another platelet, and that a very strong flow does not achieve it either because the cloud becomes too diluted. There must be a combination of diffusive velocity and convective velocity which is favorable for thrombus generation. Since in our experiment the flow field has a radial symmetry, there is a ring of favorable shear rate at which specks of thrombi appear in the experiment. In order to understand this transfer of thrombin molecules to the platelet, a platelet was assumed which is carried by the flow in a certain distance from the wall. When the platelet passes the cloud of molecules

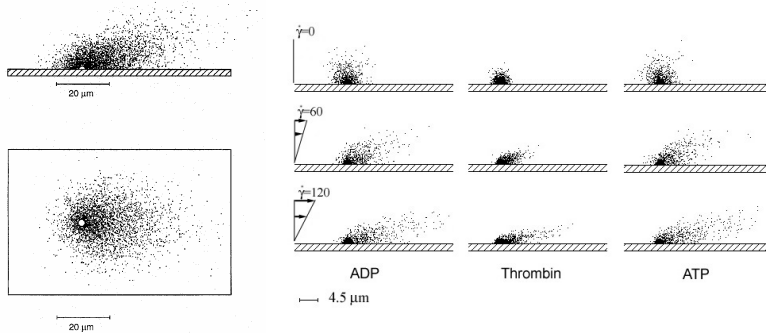


FIGURE 35. In this numerical simulation the random walk method is applied. Random Steps in x , z simulate the Brownian motion of a thromboactive substance. New molecules are emitted and plotted until a cloud is finally formed. If another platelet comes into contact with this cloud, it also becomes activated and emits thromboactive molecules.

which are emitted from the platelet on the wall it comes in contact with these molecules. It becomes activated as well.

In Fig. 36 the number of encountered molecules is plotted as a function of the shear rate and of the distance of the platelet from the wall. These curves show a definite peak, which confirms the observations of the experiment. In

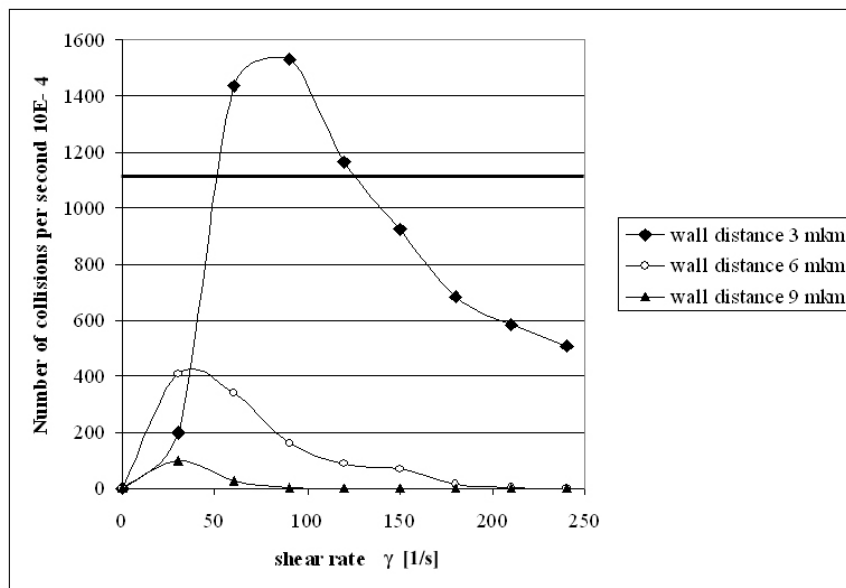


FIGURE 36. Platelets are hit by the molecules depending on the shear rate and the distance to the wall. There is a shear rate at which this occurrence peaks.

other words, there is a combination of the diffusive and convective velocities of the platelet which results in a maximum encounter between molecules and platelet. As a result of this combination the velocity of the platelet is such that thrombus generation is most likely. A cellular automat was designed using this result. As in the original experiment, it has a radial symmetry and at each radius a probability is assigned to each element. This probability is derived from the curve in Fig. 36 and the shear rate in Fig. 33. Another condition is implemented: when by chance a platelet adheres to the plate the probability in the adjacent sections downstream is increased, see Fig. 37. If one runs this cellular automat, the initial speck distribution quickly forms a ring which becomes more solid with time, see Fig. 38.

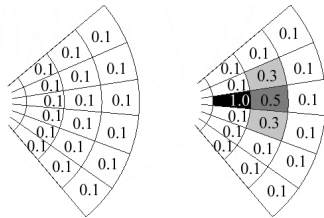


FIGURE 37. The distribution of the probability that a platelet will adhere within the circular grid of the cellular automat (left). If a platelet adheres, the probability in its wake is increased (right).

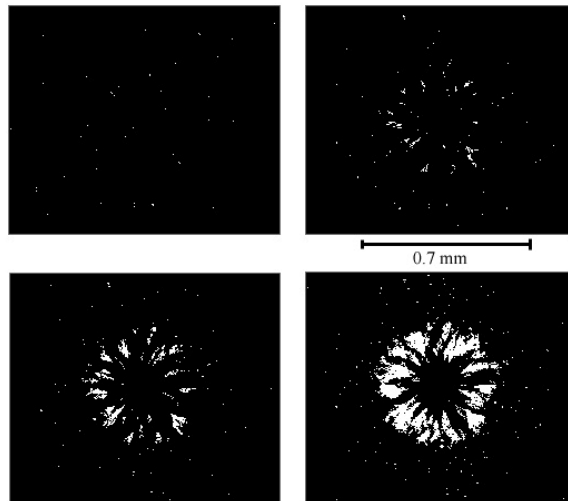


FIGURE 38. Numerical results of the simulation. It agrees well with the experimental results.

When this numerical result is compared to the experimental result, see Fig. 34, one perceives an agreement in regard to shape, distribution, and development. This indicates that the basic mechanism has been modeled correctly. Future work in this method has to include the thrombogenic qualities of the material in the wall and also the dynamic effects because during practical application, the stagnation point and the shear stress field are rarely stable, but instead move around. In addition the shear flow field within artificial elements is far more complex.

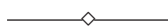
8. Conclusion

Modern experimental methods, such as the PIV-method, and numerical methods, such as CFD, have greatly contributed to our understanding of blood flow in the body. However, the unique feature of blood in connection with flow phenomena to coagulate and to become partly solid is not completely understood. We need to integrate the biology of the blood cells, especially the biology of the platelet, into our models. Thrombus generation is one of the most frequent complications found in patients with an artificial blood pump. This prevents these devices from becoming a destination therapy, which is badly needed. Further, little research has been performed on the influence of the flow on the white blood cell. Many of the patients with a VAD suffer from infections, which indicate that white blood cells are affected by the mechanical device. As a result, new experimental and numerical models are needed for a full control of blood in artificial devices.

References

1. P.H. STONE, A.U. COSKUN, S.KINLAY, M.E. CLARK, M.SONKA, A.WAHLE, O.J. ILEGBUSI, Y. YEGHIAZARIANS, J.J. POPMA, J. ORAV, R.E. KUNTZ, and C.L. FELDMAN, *Effect of endothelial shear stress on the progression of coronary artery disease, vascular remodeling, and in-stent restenosis in humans: in vivo 6-month follow-up study*, Circulation., **108**: 438–444, 2003.
2. C.R. HUANG and W. FABISIAK, *A rheological equation characterizing both the time-dependent and steady state viscosity of worifice human blood*, AIChE Symposium Series, pp.19–21, (1978).
3. R. VIRCHOW, *Phlogose und Thrombose im Gefäßsystem*, [in:] Gesammelte Abhandlungen zur wissenschaftlichen Medizin., Frankfurt am Main: Medinger Sohn und Company, pp.458–612, 1856.

4. P.H. STONE, A.U. COSKUN, Y. YEGHIAZARIANS, S. KINLAY, J.J. POPMA, R.E. KUNTZ, and C.L. FELDMAN, *Prediction of sites of coronary atherosclerosis progression: In vivo profiling of endothelial shear stress, lumen, and outer vessel wall characteristics to predict vascular behavior*, Curr. Opin. Cardiol., **18**:458–470, 2003.
5. A.P. YOGANATHAN, *Cardiac Valve Prostheses*, The Biomedical Engineering Handbook, J.D. Bronzino, [ed.], CRC Press, pp.1847–1870, 1995.
6. G.P. NOON, *Clinical use of cardiac assist devices*, [in:] Heart replacement. Artificial Heart **4**, T. Akutsu, H. Koyanagi, [eds.], Springer, pp.195–211, 1993.
7. K. AFFELD, P. WALKER, and K. SCHICHL, *A ten times enlarged model of artificial heart valve flow*, [in.] 2nd international symposium on biofluid mechanics and biorheology, Springer Verlag, 1990.
8. K. AFFELD, K. SCHICHL and A. ZIEMANN, *Flow Model Studies of Heart Valves*, [in:] New Frontiers in Cardiovascular Engineering, Malaga, Spain: Plenum Press, 1991.
9. K. AFFELD ET AL., *Technical obstacles on the road towards a permanent left ventricular assist device*, Heart and Vessels Suppl. **12**:28–30, 1997.
10. M. LAMBERTZ, K. AFFELD , and A. ZIEMANN, *Untersuchung einer neuen Herzklappe für Herzunterstützungssysteme*, Biomedizinische Technik, **43**(1):514–515, 1998.
11. K. AFFELD, L. GOUBERGRITS, and O. HOLBERNDT, *Novel cardiac assist valve with a purge flow in the valve sinus*, ASAIO J **44**, M642–647, 1998.
12. T. TIMMEL, L. GOUBERGRITS, and K. AFFELD, *Optimization and investigation of a novel cardiac assist valve with a purge flow*, Int J Artif Organs, **24**(11):777–783, 2001.
13. K. AFFELD ET AL., *Fluid mechanics of the stagnation point flow chamber and its platelet deposition*, Artif. Organs **1**:722–728, 1995.
14. K. AFFELD, L. GOUBERGRITS, U. KERTZSCHER, J. GADISCHKE, and A. REININGER, *Mathematical model of platelet deposition under flow conditions*, Int J Artif Organs, **27**(8):699–708, 2004.
15. R. COLMAN, J. HIRSH, V. MARDER, and E. SALZMAN, *Hemostasis and Thrombosis: Basic Principles and Clinical Practice*, (2nd ed.), J.B. Lippincott Company, Philadelphia 1987.



Heart Valves: Modelling Experiments

GIOVANNI PAOLO ROMANO

*Department of Mechanics and Aeronautics
Via Eudossiana 18, 00184 Roma, Italy
romano@dma.ing.uniroma1.it*

Experimental results on the flow fields close to prosthetic heart valves measured by means of Particle Image Velocimetry (PIV) are reported. The attention is also focused on the different mock-loops employed to simulate the whole systemic circulation. Four experiments are reported: a pulsed jet with focusing onto the forcing mechanism simulation; a left ventricle with mitral and aortic prosthetic valves; two different mock-loops for aortic valves testing. The obtained results indicate that PIV can give results useful for biomedical evaluations not only in terms of mean field but also for higher-order statistics, i.e. in respect to the evaluation of damages on blood cells.

Key words: *Heart valves, PIV, fluid-mechanics*

1. Introduction on Heart Valve Flows

In this paper, experiments on artificial heart valves and on the way in which these can be simulated by an artificial apparatus are considered. The relevance of these experiments is multiple: from the scientific point of view, there are several complex fluid-mechanics phenomena which take part close to heart valves and are still unclear; from the social point of view, a proper characterisation of implantable prosthetic heart valves is required to save patients from critical health conditions; from the technological point of view, biomedical devices involve advanced solution which must be investigated by comparable advanced measurement and data analysis techniques. To attain these aims, a strict coupling between different approaches must be considered; numerical and experimental methods, experimental investigations in physiological (“*in vivo*”) and in simulated (“*in vitro*”) conditions, agreement on testing conditions and procedures.

In this section, the physiological behaviour of the heart and the working conditions of heart valves are summarised. In Sec. 2, the requirements for proper “*in vitro*” testing of artificial heart valves are considered. In Sec. 3, the experimental technique and the relevant measurement problems are briefly presented, whereas in Sections 4 to 6 results on different mock-loops are reported. Remarks and future developments end the paper.

The operative conditions of the heart give origin to the cardiac cycle which is a complex sequence of events involving the heart itself and the whole organism. There are four heart valves involved in this cycle; in Fig. 1 the interior of the heart with the heart valves is shown. It is possible to notice the two atrial-ventricular (AV) valves (tricuspid and bicuspid or mitral) which separates right and left atrii from ventricles, and the two valves which allows blood to be pumped to lungs (pulmonary valve) and to the whole body through the aorta (aortic valve). As can be observed from the right part of the figure, there is a substantial difference among the tricuspid (and mitral) valves, having filamented leaflets (flap of tissue which constitute the valve), and the aortic (and pulmonary) valves which have a three leaflet configuration. The geometry of all valves is far from axial-symmetry; this is a very important point which must be considered in performing experiments on artificial valves.

The cardiac cycle is illustrated in Fig. 2, in which the non oxygenated blood (in blue) from the body enters into the right side of the heart (at the beginning the atrium and then the ventricle), while simultaneously the left part is filled with the oxygenated blood (in red) from the lungs. At this time, the AV valves are open while the other two are closed. After blood fills the

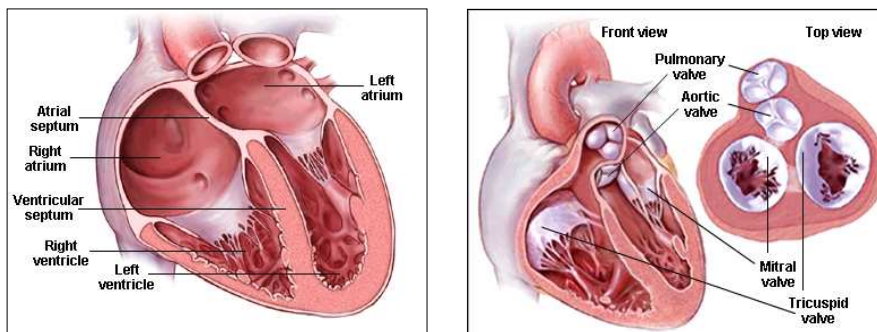


FIGURE 1. Internal division of the heart (on the left) and views of the four heart valves (on the right) (from GUIDANT, www.guidant.com).

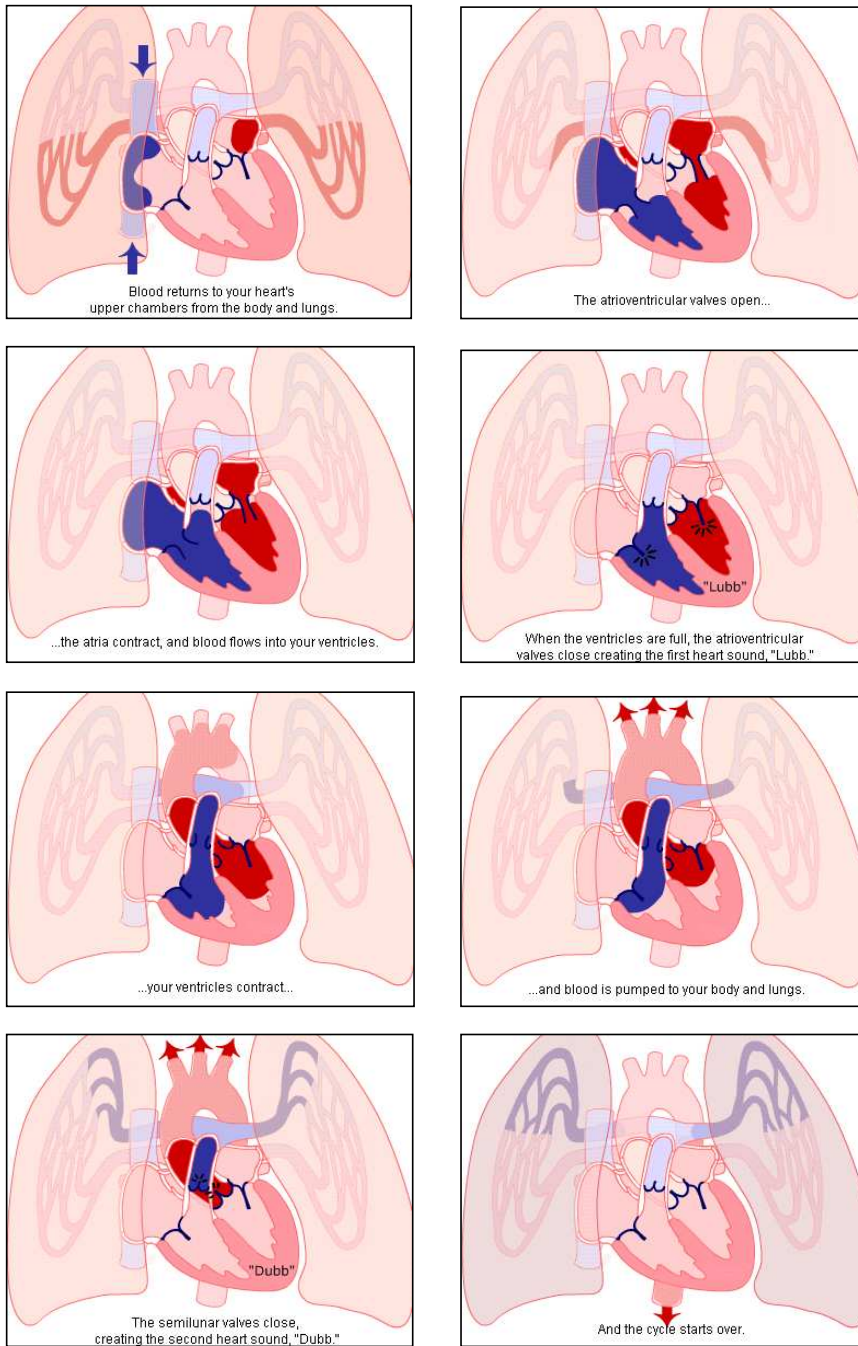


FIGURE 2. The cardiac cycle with oxygenated (red) and non oxygenated (blue) blood flowing into and from the heart (from GUIDANT, www.guidant.com).

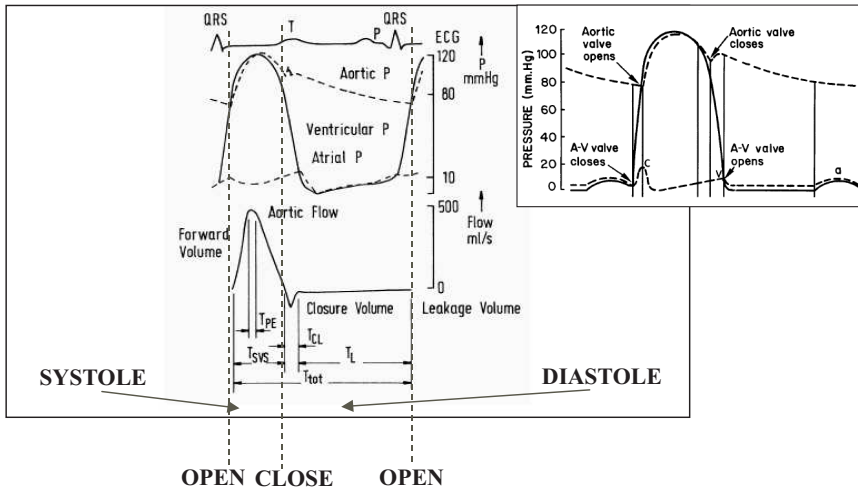


FIGURE 3. Behaviour of ECG signal, ventricular and aortic pressure (with expanded detail) and aortic flow rate during the cardiac cycle (from [1] www.engnetbase.com).

ventricles, the AV valves close and the other two open (due to the pressure difference between the ventricle and the regions downstream the valves themselves): oxygenated blood flows into the aorta, while non-oxygenated blood is directed towards the lungs. Then, the valves close and the cycle can start again.

As already written and as reported in Fig. 3, this cycle is controlled by the pressure difference among atrium and ventricle and the pressure difference among ventricle and aortic root; roughly speaking, the part of the cycle in which the atrial pressure overcomes the ventricular one is called diastole (AV valves are open), while the part in which the ventricular pressure is larger than the aortic pressure is called systole (the aortic valve opens). In the figure the echo cardio-graphic (ECG) trace and the corresponding aortic flow rate are also reported. The whole cycle gives rise to a strong unsteady, almost periodic (not sinusoidal) behaviour of the considered quantities (pressures, flow rates, ECG signals) which must be taken into account in simulating experimentally heart flow conditions.

The blood which is sent to the body is flowing into a complex system with smaller and smaller vessels (arteries and veins) which ended with arterioles and capillaries as schematically given in Fig. 4. This complex system (which has many similarities with complex hydraulics distributions systems or nets) has three main effects to be considered in experiments on heart valves:

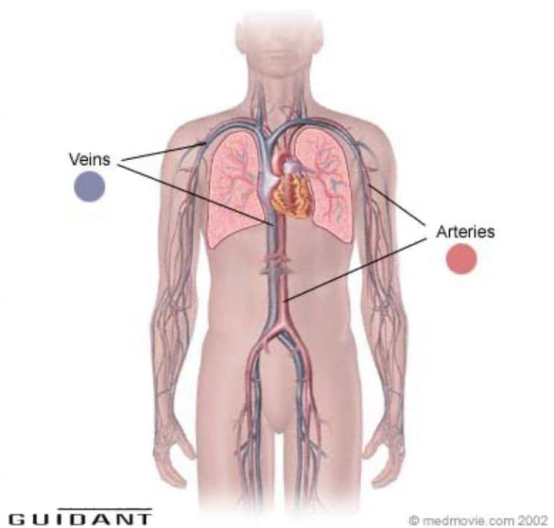


FIGURE 4. A simplified schematic of the blood circulation (from GUIDANT, www.guidant.com)

- the resistance to the flow due to the whole system (vascular resistance);
- the deformation of the wall of large arteries (arterial elasticity);
- the acceleration and deceleration of the blood into the vessels due to the cardiac cycle (arterial inertance).

These effects must be also taken in account for a proper experimental simulation of the heart working conditions.

Returning to the problem of the artificial heart valves, it must be considered that not only they have to resemble, as much as possible, the geometry of the problem, but also the flow induced phenomena. In particular, in Fig. 5 it is shown how some of the existent artificial aortic valves can alter the physiological behaviour of the flow; this will result in blood stagnation or recirculation which can generate thrombus and hemolysis, in energy losses through the valve in addition to bio-compatibility problems. Consider for example the cage-ball or the tilting disk flows in comparison to the natural normal case. This is why the recent advances in the field are towards bileaflet or even trileaflet valves which are more strictly related to the physiological case. The presence of the Valsalva sinuses (the cavities which incorporate the leaflets when opened in the natural case) also make the situation more complex in the artificial case (artificial leaflet do not open in the sinuses).

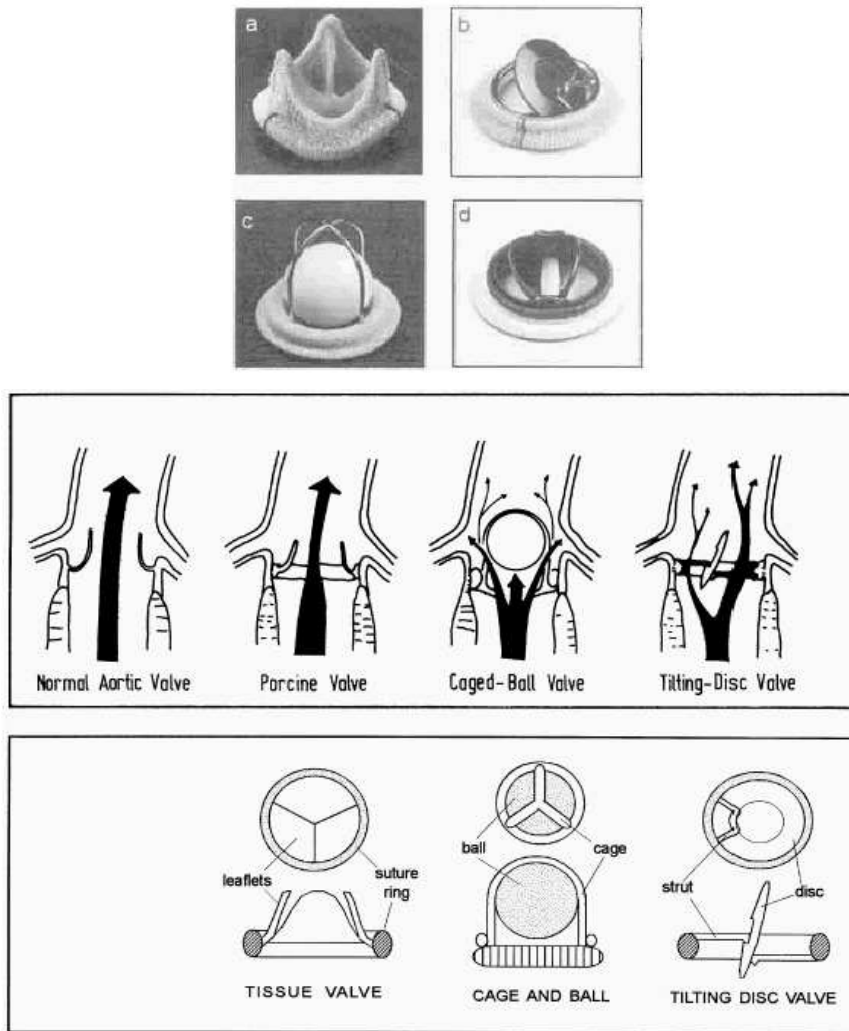


FIGURE 5. Different artificial aortic valves: photographs before implantation (at the top) and schematic of the flow behaviour after implantation (at the bottom) (from [1] www.engnetbase.com).

2. Artificial Simulation of the Systemic Circulation: Pulse Duplicators

Summarising the previous requirements, to mimic physiological flow conditions close to heart valves by means of a flow (hydraulic) circuit it is necessary to:

- simulate the unsteady cardiac cycle, in terms of beat frequency and stroke volumes, with proper forcing;
- simulate the blood pressures at several positions of the simulating circuit by proper set-up of the circuit itself;
- simulate the physical properties of the blood (*i.e.* density and viscosity) with a fluid which is effective to perform measurements with available techniques;
- simulate the vascular resistance with proper circuit elements (resistances);
- simulate the arterial elasticity with proper circuit elements (compliance and reservoirs);
- simulate the arterial inertance with proper circuit elements (inductance);
- simulate the complex geometry of the heart and of the initial part of the aorta with proper models;
- perform correct statistical analysis which takes into accounts the peculiarities of the considered signals and fields.

The previous requirements (need for resistance, compliance and inductance) frequently lead to the so called electrical analogy to account for the similarity among the two cases [5, 6].

These requirements hardly can be satisfied simultaneously. Historically, the first systems aiming to simulate the systemic circulation (also called pulse duplicators) do not consider the unsteady nature of the considered flow field. In Fig. 6, the pulse duplicator developed at Helmholtz Institute in Aachen by Reul *et al.* [2, 3] is shown. It consists of the aortic valve and root, fluid resistance and reservoir and forcing steady pump. The valve is mounted in a horizontal (non physiological) position. This apparatus was mainly used for visualisations and preliminary investigations.

Rather early the first unsteady pulse duplicators were developed; in Fig. 7, the one from the same Institute is shown consisting of atrial-ventricular models, aortic root model, compliances, resistances and inductances with unsteady adjustable forcing. The aortic and mitral valves are mounted in the vertical (physiologically correct) position. This system is very complete but also quite difficult to control. Some control parameters and velocity field results obtained with this mock-loop will be given in Sec. 6.2.

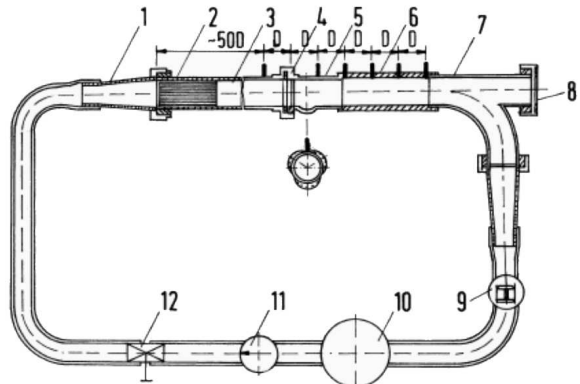


FIGURE 6. The Helmholtz Institute Aachen steady flow pulse duplicator (from [1] and [2]). (1) Flow inlet diffuser, (2) honeybomb, (3) inlet tube, (4) heart valve mounting ring, (5) model aortic root, (6) downstream measuring system, (7) bifurcation with optical observation window, (8) viewport allowing observation and recording of valve opening characteristics, (9) rotameter, (10) fluid reservoir, (11) centrifugal pump, (12) throttle valve.

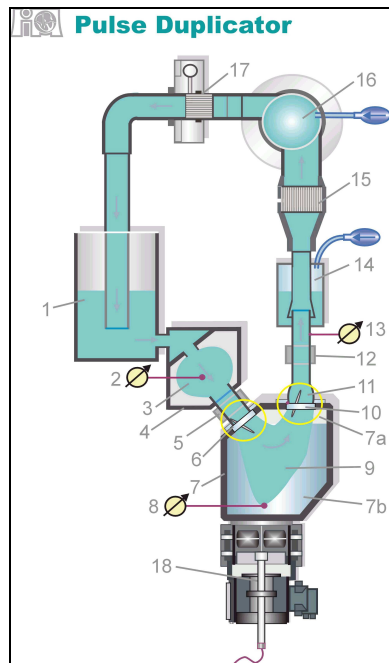


FIGURE 7. The recent Helmholtz Institute Aachen unsteady flow pulse duplicator (from [3]).

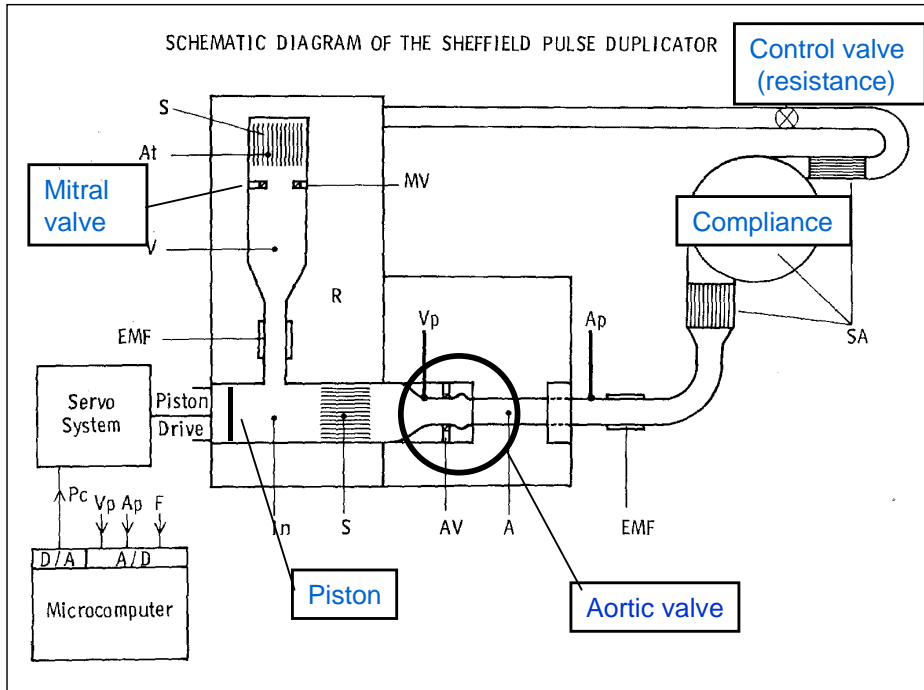


FIGURE 8. The Sheffield University unsteady flow pulse duplicator (from [4]).

In Fig. 8, the mock-loop developed at the University of Sheffield is shown; it is quite similar to the previous one except for the horizontal placement of the valve, the absence of ventricle with geometric similarity and the use of a rotating rather than linear motor. Some control parameters and velocity field results obtained with this mock-loop (namely the one at Istituto Superiore di Sanita' (ISS) in Italy) will be given in Sec. 6.1.

Commercial mock-loop started to be developed; an example is in Fig. 9, in which the Vivitro system with simulated left atrium and ventricle, compliances and resistances and forced by a waveform generator is shown. The aortic and mitral valves are placed in the vertical physiological position.

The standard measurement conditions to test heart valve flows are the following: cardiac output from 3 to 81/min, beat frequency equal to about 70 Hz, systolic duration equal to about 300 ms, mean aortic pressure equal to 100 mmHg and mean atrial pressure equal to about 10 mmHg. The working fluid is usually a water-glycerine mixture which ensure (at ambient temperature) matching with viscosity and density of blood and simultaneous transparency for measurement with optical methods.

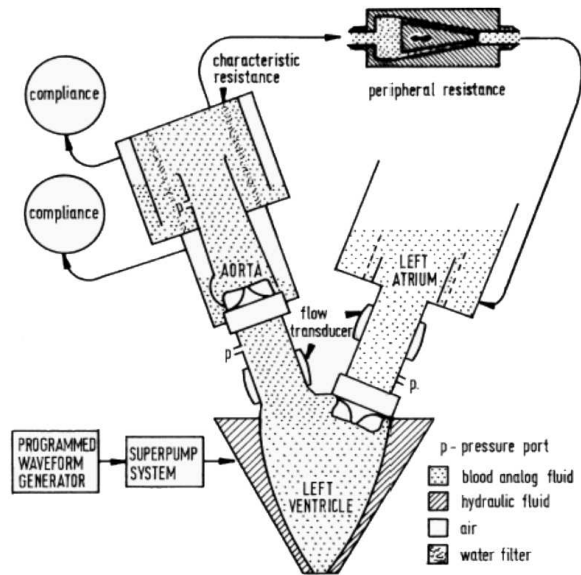


FIGURE 9. The commercial Vivitro unsteady flow left heart simulator (from [1] www.engnetbase.com).

3. The Experimental Technique: Particle Image Velocimetry (PIV)

It is not within the scope of this paper to describe the experimental techniques used in this investigation which are under the name of Particle Image Velocimetry (PIV). The reader is referred to [14, 15] and references therein for details. Here, only the main principles and specific problems for the considered investigation are reported.

In Fig. 10, a schematic of PIV is given: the flow is seeded with proper tracer particles (seeding) which have to follow the flow as much as possible. Providing that the test section is transparent, particles are illuminated by a strong light source (usually but not necessarily a laser). Images of the flow are taken by a videocamera which can be synchronised with the laser if light pulses are used or with a high rate framing in the case of continuous illumination (High-Speed PIV). Images contain positions of framed particles at two or several instants; by determining the distance between positions in consecutive frames it is possible to obtain the velocity of the particles themselves (the time interval between laser pulses or camera frames is known). To perform the displacement determination, dedicated software have been developed by many universities and producers; cross-correlation functions allow

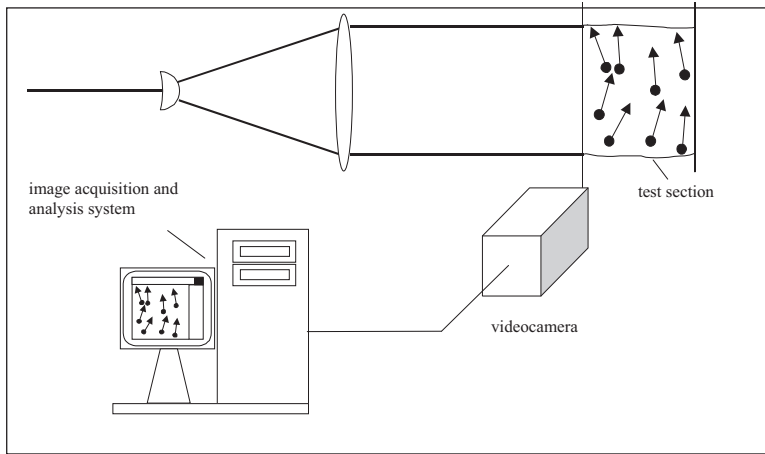


FIGURE 10. Schematic of a PIV system.

to derive the displacement of a group of particle statistically (proper PIV), while single particle displacements can be derived by tracking the particle along their trajectories (Particle Tracking Velocimetry, PTV).

The PIV technique is optical, non intrusive (except for the tracer particles), is linear without need for calibration and give two- or three-dimensional (Stereo-PIV) velocity fields. In the context of measurements in small vessels for biomedical applications, the following points must be considered with care:

- image distortions due to the curved geometry of the vessels;
- light reflections from the background and from the walls of the vessels.

In Fig. 11, an example of the former distortion at the aortic root is given; it is clear how the curved geometry makes distorted the grid placed inside the vessel (made by glass blown). To avoid this, in the second part of the figure, the inner and outer part of the glass blown aorta have been filled with a water-glycerine mixture which ensures a much better index matching.

In Fig. 12, the second problem is considered; in the first figure the aortic root field (valve at the top) shows many reflections from the walls and also internal to the test section (due to the curvature of the section). In the second part of the figure, the subtraction of the minimum intensity in each pixel, evaluated over a sample of 50 images of the flowing particles, allows to eliminate almost all reflections. This helps a lot in determining the particle displacements both with PIV and PTV. In the third part of the figure, an

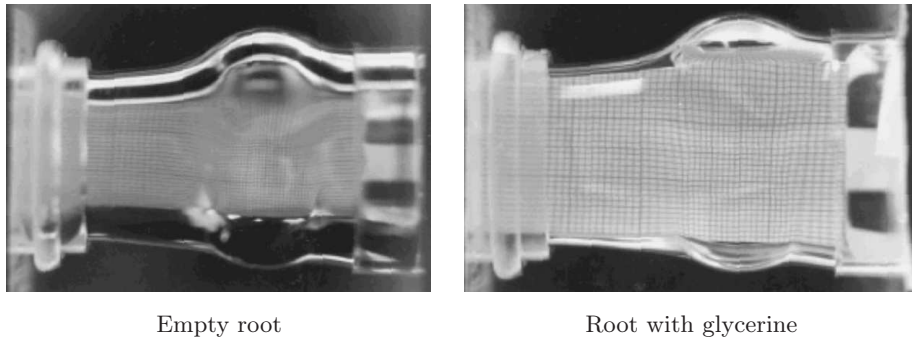


FIGURE 11. Image distortion due to glass blown aortic root geometry (left) and index-matching correction with water-glycerine mixture (right) (from [1] www.engnetbase.com).

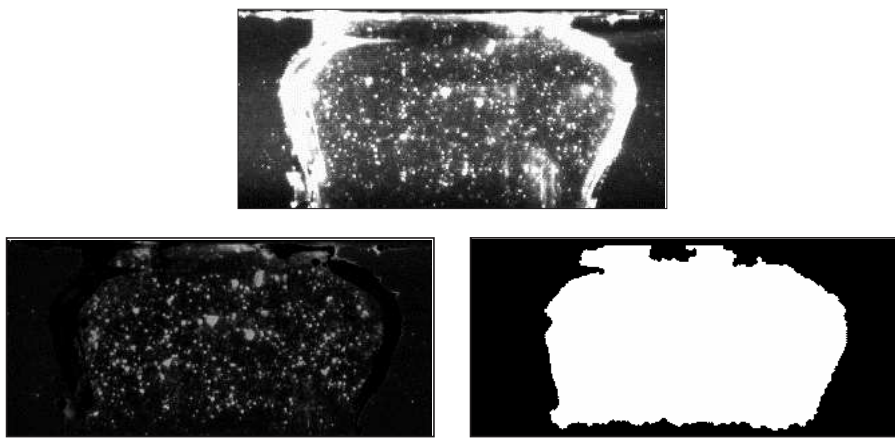


FIGURE 12. An instantaneous image of tracer particles in the aortic root of the Sheffield type pulse duplicator at ISS (at the top), image after background (minimum intensity) subtraction (at the bottom left) and automatic mask image (at the bottom right).

automatic mask has been derived for the considered field; this procedure allows to compute the flow field only where the mask is white (test section) and to avoid the computation outside the interest field (black region).

Image pre-processing (as well as image post-processing) as that depicted previously, can give large improvement in the determination of velocity fields with PIV related techniques.

4. Investigation on a Pulsed Jet

The first experimental results concern with a quite simple flow condition, a pulsed jet from an orifice; this set-up has been considered to investigate the effect of the forcing signal shape and amplitude on the resulting flow field.

In Fig. 13, the experimental set-up used for this experiment is shown; it consists of a piston driven by a synchronous linear programmable motor (arbitrary shape, amplitude and frequency) which forces the flow into an orifice; the hydraulic circuit is completed by valves to reduce regurgitation as much as possible. The peak Reynolds number is equal to 2.5×10^4 ; conventional cross-correlation PIV has been used. Details are given in [9, 12, 13].

In Fig. 14 the used forcing signal displacements and velocities are given; they are sinusoidal, exponential, ramp1 (faster) and ramp2 (slower). Each imposed signal consists of 1000 data points with feedback control (digital optical encoder) ensuring 0.1% deviation from the imposed signal. These signals have been selected to reproduce flow rate data which can occur in simulating heart valve flows.

An overview of the flow field downstream the orifice is given in Fig. 15; each of the plots is obtained as phase averaging (averaging at the same position of the piston) of 50 instantaneous fields. The vector and vorticity fields show a vortex ring (on the plane only two counter rotating vortices) travels from right to left. It is followed by a trailing jet, i.e. two shear layers of distributed vorticity.

Concerning averages and statistics evaluation, it is important to point

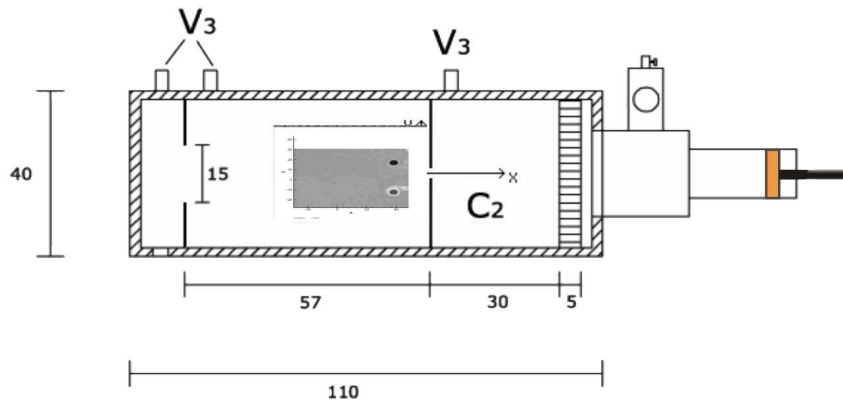


FIGURE 13. The experimental set-up for the pulsed jet configuration.

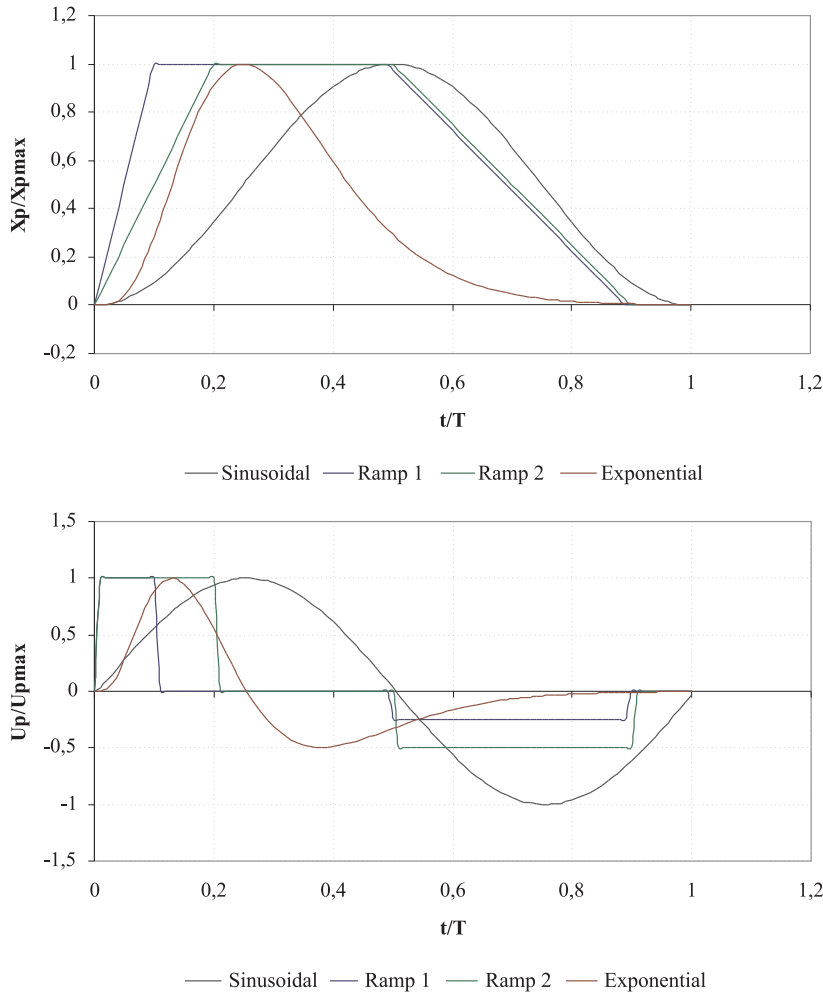


FIGURE 14. The forcing signals for the motor: displacement (at the top) and velocity (at the bottom).

out two aspects: first of all, phase averaging is strictly required to capture the correct velocity fields in pulsating flow conditions. Usual time averaging would give non useful results. This means that the motion of the driving system must be coupled with the image acquisition system. Secondly, the number of images required for statistics could be crucial.

To this end, in Fig. 16, the vertical (transverse) mean velocity is given for a number of phase averaged images from 10 to 1000; the overall field is independent on the number of employed samples for statistics.

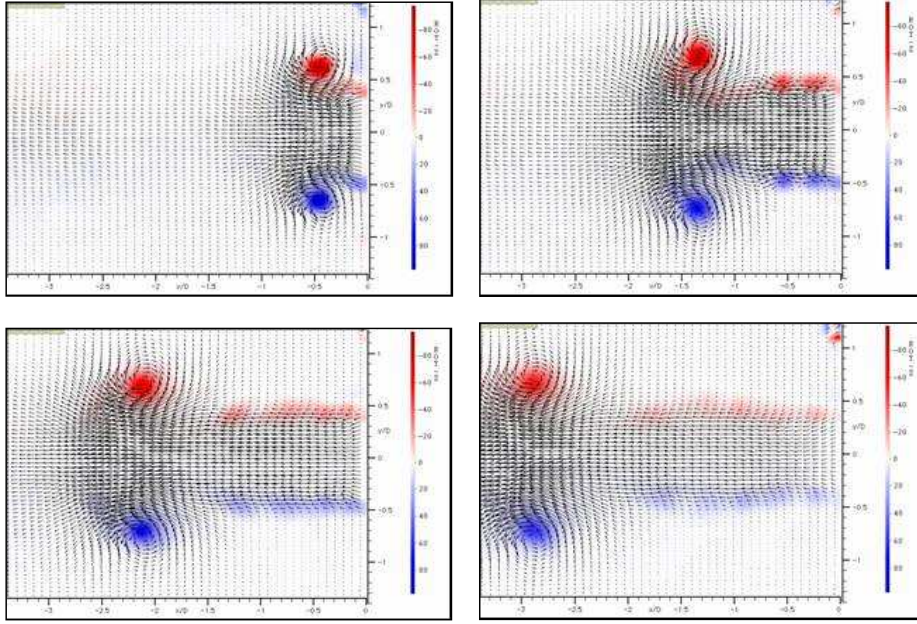


FIGURE 15. Overview of the phase averaged velocity vector and vorticity fields at four different phases for the sinusoidal forcing (flow rate equal to 70 ml). Mean flow from the right.

This is also confirmed by Fig. 17, where the profiles of mean axial velocity and vorticity along the dotted line of Fig. 16 are given for different sample number. They are practically coincident. This result concerns with first-order statistics (mean values). When second-order is considered, the situation changes; in Fig. 18, the RMS horizontal velocity is given for the same sample numbers as before; in this case, while in the low fluctuation regions (in blue) a rather low number of samples is sufficient (50–100), in the high fluctuation regions (in green and red) the required number of samples for statistical convergence is higher (500 or 1000). This statement is confirmed in Fig. 19, in which profiles of the RMS horizontal velocity and of Reynolds stresses are presented; especially the last quantity requires a high number of samples to converge statistically.

After establishing the required number of samples for statistical convergence, the analysis was focused onto the effect of the flow rate for the same forcing signal. In Fig. 20, three different flow rates are considered for the sinusoidal signal (50 ml, 70 ml, and 90 ml). The horizontal phase averaged

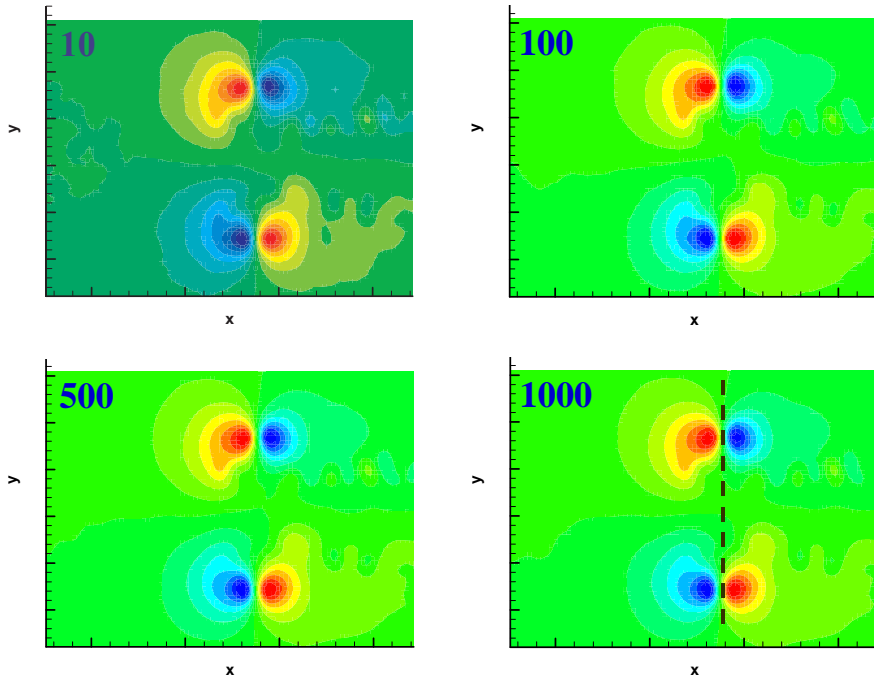


FIGURE 16. Statistical analysis on the phase averaged vertical velocity as a function of the number of samples used; sinusoidal forcing with flow rate equal to 70 ml.

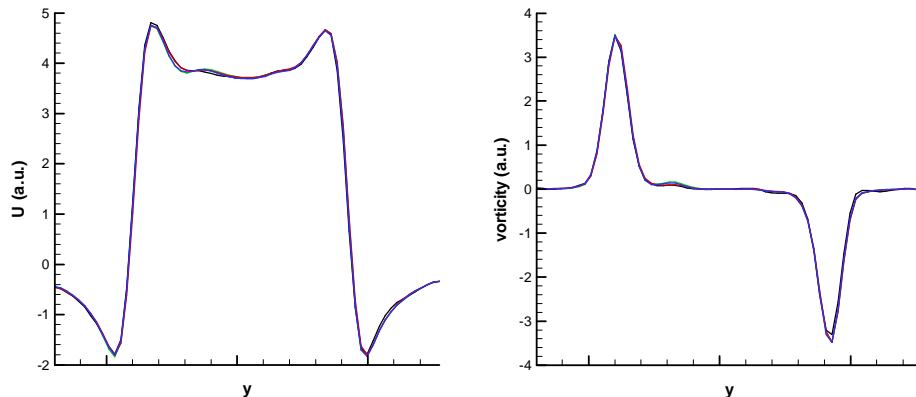


FIGURE 17. Statistical analysis on the phase averaged horizontal velocity (on the left) and vorticity (on the right) profiles as a function of the number of samples; sinusoidal forcing with flow rate 70 ml. Number of samples equal to 10 (black lines), 100 (red lines), 500 (green lines) and 1000 (blue lines).

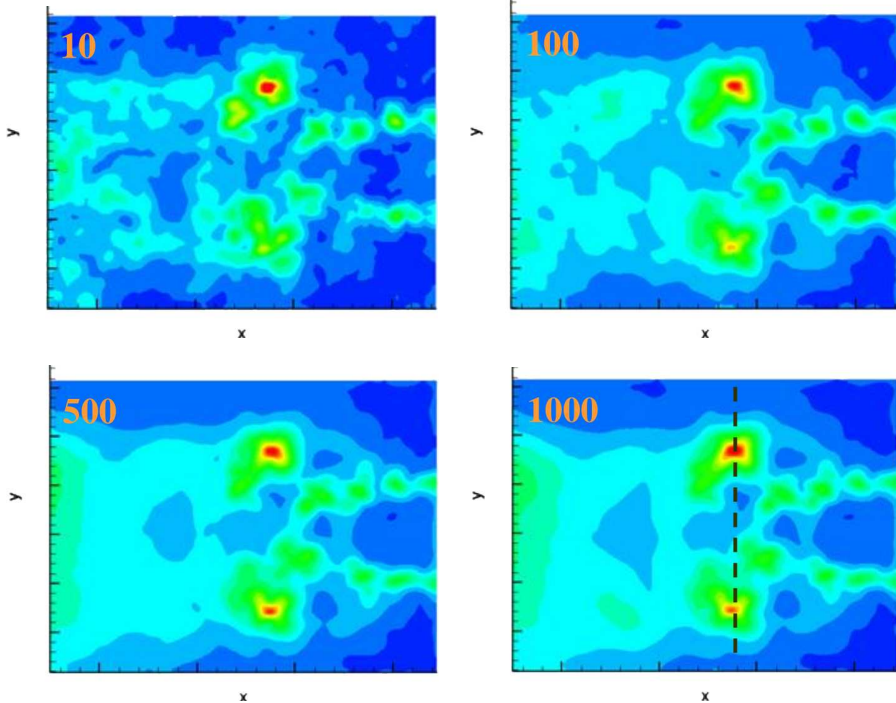


FIGURE 18. Statistical analysis on the phase averaged RMS horizontal velocity as a function of the number of samples used; sinusoidal forcing with flow rate equal to 70 ml.

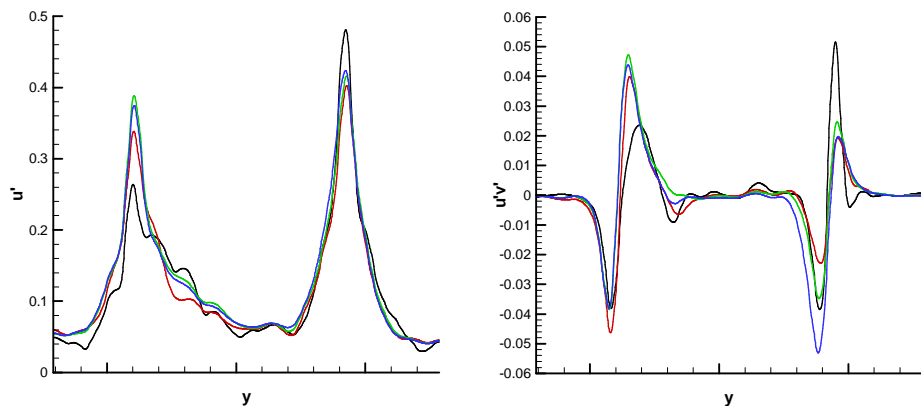


FIGURE 19. Statistical analysis on the phase averaged RMS horizontal velocity (on the left) and Reynolds stress (on the right) profiles as a function of the number of samples; sinusoidal forcing with flow rate 70 ml. Number of samples equal to 10 (black lines), 100 (red lines), 500 (green lines) and 1000 (blue lines).

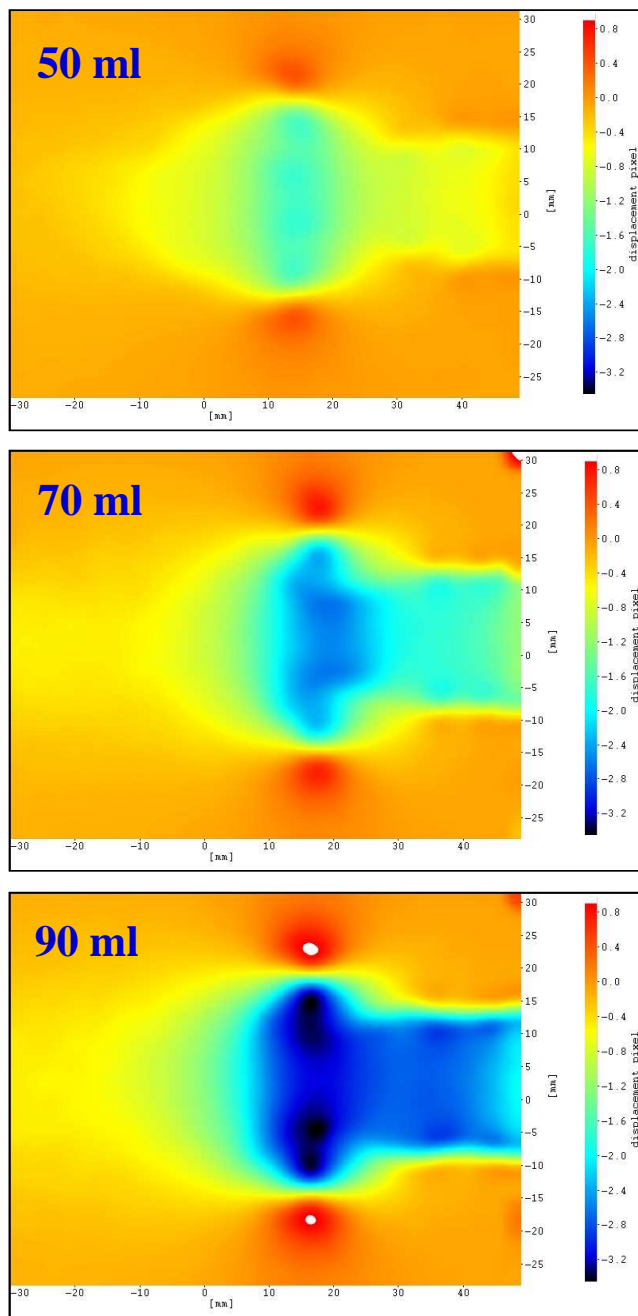


FIGURE 20. Phase averaged horizontal velocity component at different flow rates (same colorbar) at almost the same positions; sinusoidal forcing.

velocity shows two main effects: the intensity of the vortex ring of course increases as the flow rate (the same colorbar is used). Secondly, while for the 50 ml case the vortex ring is almost isolated, for the higher flow rates there is a connection with the trailing jet which follows the main ring.

The interaction between the two (vortex ring and trailing jet) is even better pointed out by the analysis of the second-order statistics; in Fig. 21, the RMS of the vertical velocity is given for the same data of Fig. 20. The two isolated counter rotating vortices are clearly identified for the 50 ml case, while the strong connection and interaction with the trailing jet is emphasised in the 70 ml and 90 ml conditions. This happens under the form of a continuous layer (70 ml) or of discrete vortical elements (90 ml). Similar results have been obtained for the other tested signals at the different flow rates. Thus, increasing the flow rate downstream of an orifice not only increases the intensity of the vortical structures but also change the way in which they interact with the neighbour fluid [16].

The other effect which is investigated is the one related to the shape of the driving signal (as reported in Fig. 14). The horizontal phase averaged velocity of the four tested signals is given in Fig. 22 at the same flow rate (70 ml); even in this case differences appear not only in the form of different intensities of the vortex ring (same colorbar used), but also in the form of different topology. In particular, the interaction with the trailing jet is through an almost continuous layer for the sinusoidal and slow ramp (ramp2) conditions, whereas distinct vortical structures are observed for the exponential and fast ramp (ramp1). This is because the latter have a more impulsive forcing (i.e. over a shorter time interval) to drive the piston in comparison to the former.

As shown in Fig. 23, the analysis of second-order statistics confirm these findings; the discrete vortical structures are clearly visible in the results of the exponential and the ramp1 (on a lower extent for the ramp2 also).

The results from the ramp1 also indicate a strong interaction among the primary vortex ring and that which can be called the secondary vortex ring; in the other phases the two exploit a precession one around the other. Thus, the effect of the signal shape, as for the flow rate, is also visible both on the intensity and on the shape and interaction of the created vortical structures.

Velocity profiles have been computed from the previous phase averaged velocity field; at the inlet, these profiles can be compared to investigate the birth of the vortex ring (all the relevance of this work in connection to heart valve application is strictly limited to the near orifice flow). In Fig. 24, the

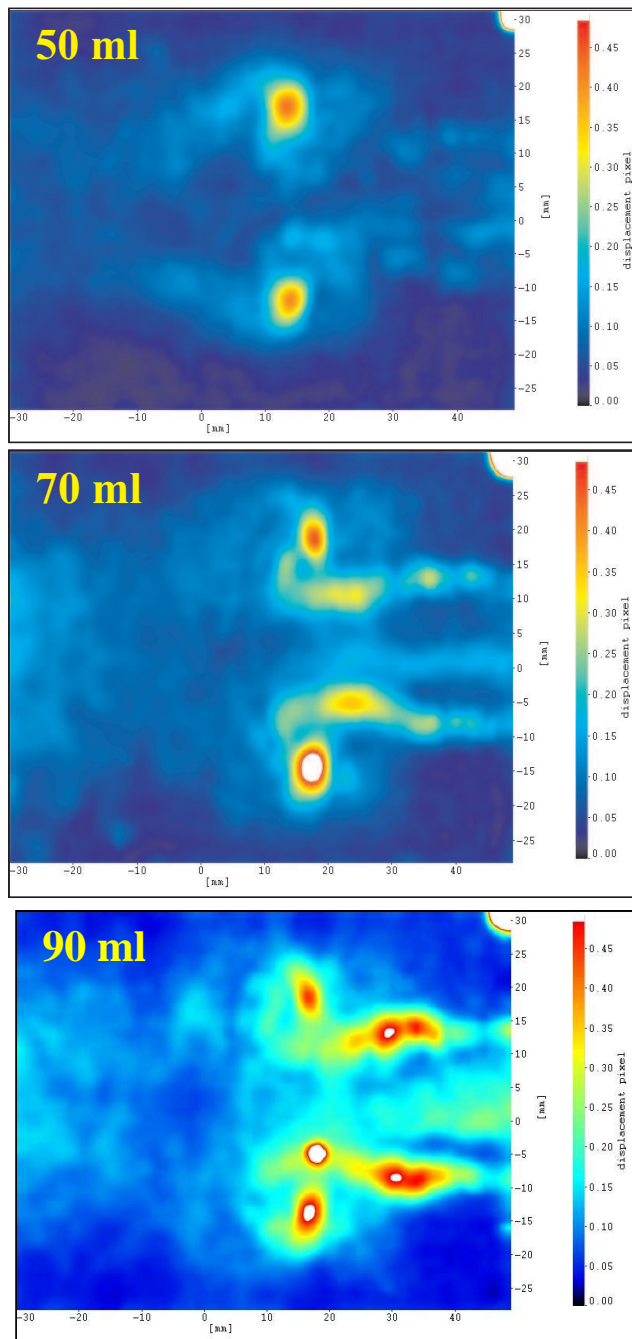


FIGURE 21. Phase averaged RMS vertical velocity component at different flow rates (same colorbar) at almost the same positions; sinusoidal forcing.

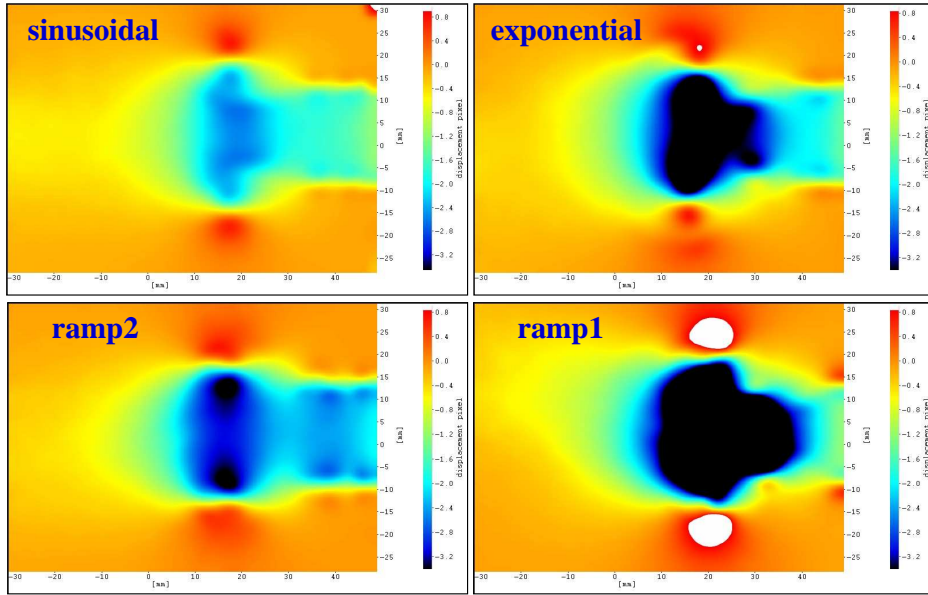


FIGURE 22. Phase averaged horizontal velocity component for different forcing signals (same colorbar) at almost the same positions; flow rate equal to 70 ml.

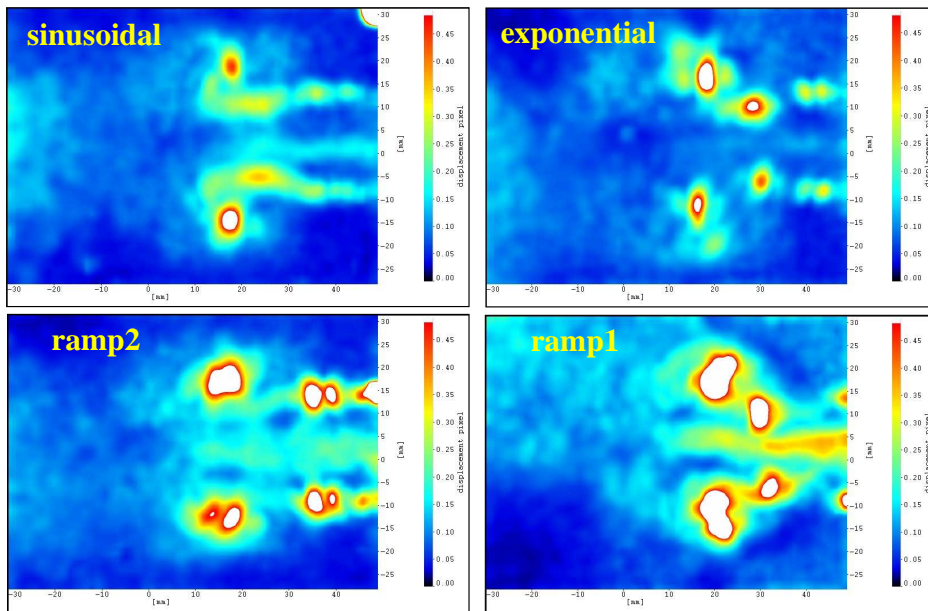


FIGURE 23. Phase averaged RMS vertical velocity component for different forcing signals (same colorbar) at almost the same positions; flow rate equal to 70 ml.

profiles for the four different tested signals are given. In the first part of the figure, the data are normalized by the maximum discharge velocity (*i.e.* the maximum horizontal velocity at the inlet) for the phase of maximum velocity (positive velocities) and normalized by the maximum regurgitation velocity (*i.e.* the maximum horizontal negative velocity at the inlet) for the phase of regurgitation (negative velocity). Even if there is a slight collapse for the curves during the discharge, there are strong differences for the results during regurgitation. In the second part of the figure, all data are non-dimensional

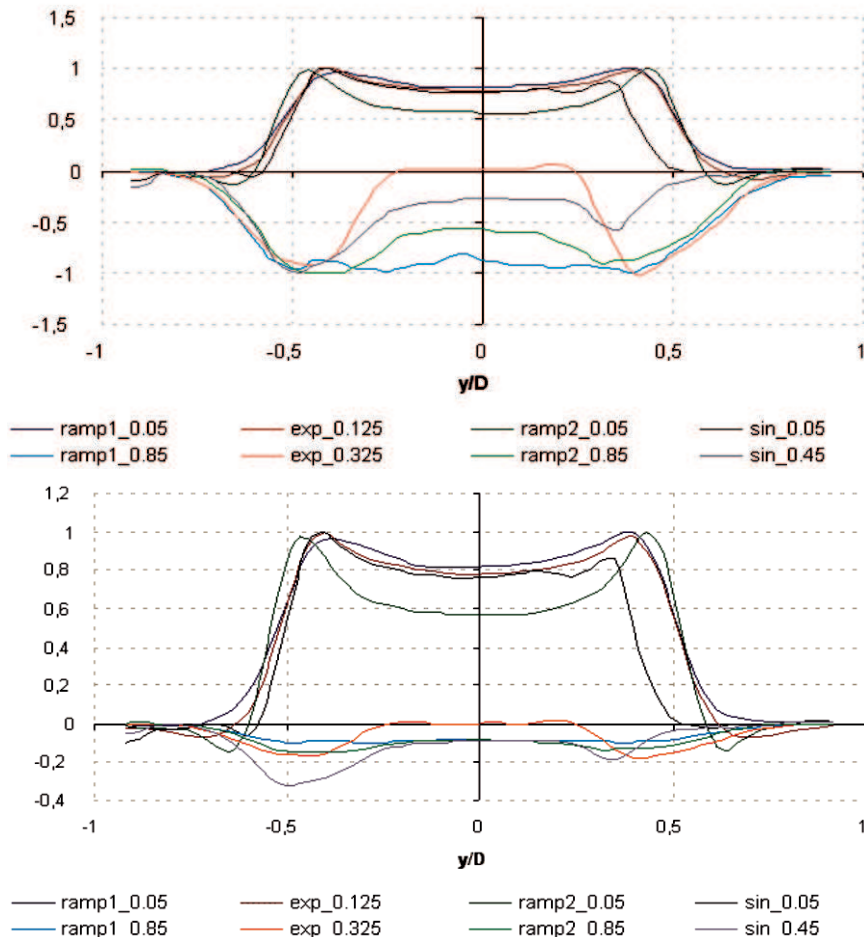


FIGURE 24. Phase averaged horizontal velocity component inlet profiles for different forcing signals; normalized by the maximum discharge and regurgitation velocities (at the top) and by the maximum discharge velocity (at the bottom); flow rate equal to 70 ml.

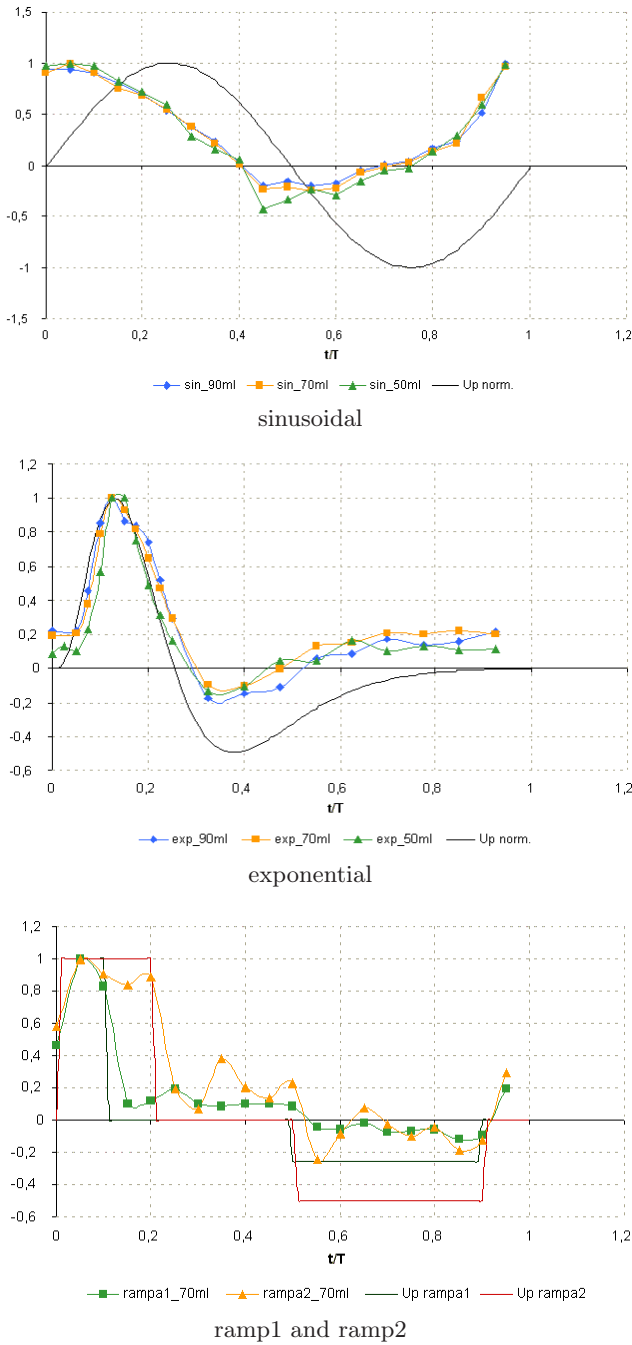


FIGURE 25. Average inlet velocity measured by inlet velocity profiles of Fig. 24 (in different colours for different flow rates); comparison with given motor velocities in continuous black lines (from Fig. 14) for the different forcing signals.

by the maximum discharge velocity. Also in this case the collapse of the results is poor during discharge and regurgitation especially for the fast ramp case. Thus, this result confirms that there is not a simple scaling when considering different forcing signals for such a kind of flows; results obtained with a given forcing signal at a given flow rate hardly can be generalised to other conditions. For heart valve testing, this means that exact signals for flow rate and pressure must be used (*i.e.* the pulse duplicator must be tuned with particular care).

From the above inlet profiles, flow rate can be computed easily by integration; the results are given in Fig. 25 for the four signals tested at the different flow rate; in the figure the velocity imposed to the piston by the motor for each forcing signal is also given (as reported in Fig. 14).

For the exponential and the ramps the results are in good agreement with the imposed signals showing that the hydraulic circuit responds almost in phase with the piston movement; for the sinusoidal forcing, there is a phase shift indicating that the circuit replies with some delay to a more regular movement in comparison to the others. The shape of the signals show that the discharge phase is activated properly and that the discharge is attenuated although not completely avoided (in some sense this is an important result for applications of the circuit to heart valves due to the fact that some regurgitation is always present in prosthetic valves. There are not noticeable differences among the results obtained at different flow rates.

5. Simulation of Left Ventricle with Mitral and Aortic Valves

The second reported experiment concerns with a simulation of the left ventricle with mitral and aortic valves; in this experiment, the tilting disks valves have been used, while the ventricle is made by transparent, deformable silicone rubber. The experimental set-up is shown in Fig. 26; in the first part of the figure, the alignment of the laser and videocamera in respect to the left ventricle model (forced by a linear motor controlled by PC similar to the one described in Sec. 4) are presented. In the second part of the figure, the silicone rubber ventricle model is detailed; the open mitral valve at the top can be clearly noticed. When the piston moves, the ventricle has to adjust its volume accordingly. In the third part of the figure, the flow rate variation in time is given (the signal is based on physiological laws as those presented in Sec. 1); note that the diastole corresponds to the filling of the ventricle. Water is used as working fluid.

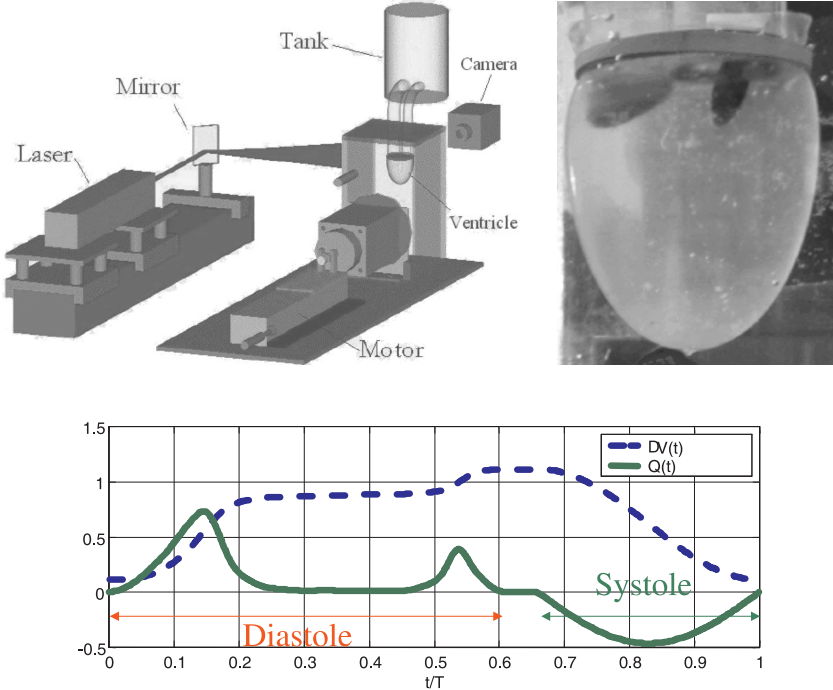


FIGURE 26. The experimental set-up for the left ventricle configuration (at the top) with details on the silicone rubber ventricle (at the centre) and on the flow rate in the cycle (at the bottom).

Images have been recorded by a high speed camera (up to 500 Hz at full resolution) and Particle Tracking Velocimetry was used to determine particle trajectories and velocities [17]. Further details on the experimental set-up and procedures are given in [8, 10, 11].

An overview of the flow behaviour is given in Fig. 27 where particle trajectories are depicted; at the opening of the mitral valve (first figure), the flow enters into the ventricle and due to the tilting valve it takes the form of two adjacent jets forming vortex rings as in the previous experiments (Sec. 4).

During the diastole, these jets hit the wall of the ventricle at different positions (the left jet on the left part and the right jet on the right part) (second part of the figure); this interaction causes a flow along the ventricle wall which turns back towards the inlet forming several smaller vortical structures (third figure). When the mitral valve closes, the flow in the ventricle is almost at rest everywhere (fourth figure).

Phase averaged velocity are obtained from the particle trajectories; they are projected into a regular grid and shown in Fig. 28 together with the vor-

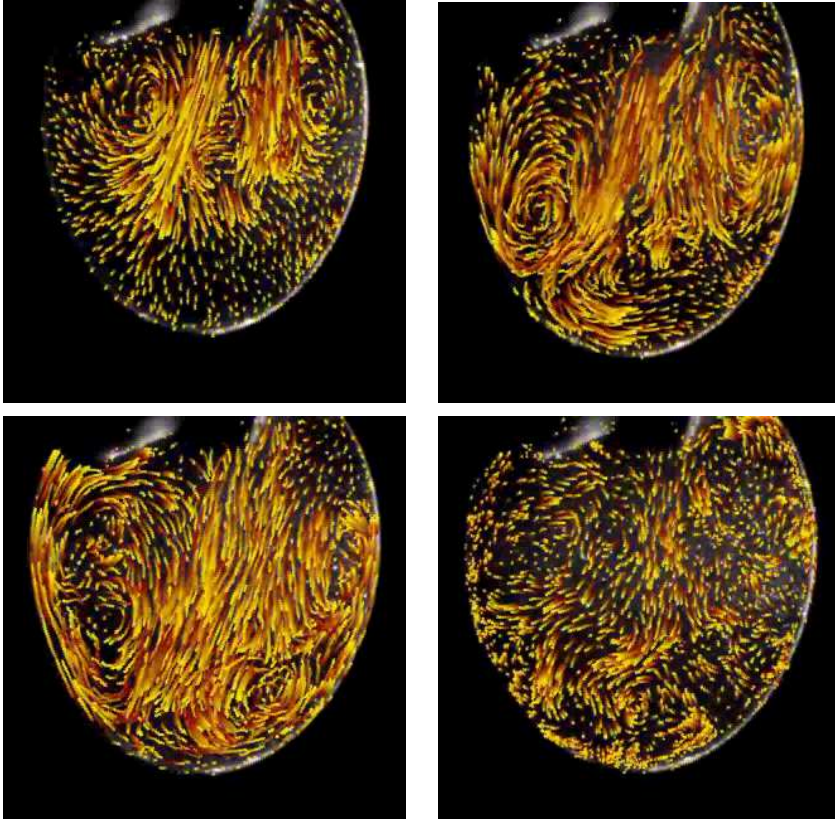


FIGURE 27. Particle trajectories at four phases of the cycle; mean flow from the top.

ticity; the phases are almost the same as those presented in Fig. 27 (indicated by red dots over the flow rate curve in each figure). Two opposite signs vorticity layer are obtained at the opening of the valve (first figure); this result is different from that of an isolated vortex ring and seems to be better described by two vortex rings connected to trailing jets (see Sec. 4).

In the second part of the figure, the two vortices are going to hit the ventricle walls but are still well defined; a layer of opposite sign vorticity is detached from the wall due to the induced velocity field by the stronger vortex ring (on the left). After the impact on the wall, layers of distributed vorticity return towards the inlet along the wall (third part of the figure); this is a clear effect due to confinement into the ventricle. The final figure does not correspond to the fourth of Fig. 27; it is obtained immediately after the second peak in the flow rate (so called A wave, while the first maximum is called

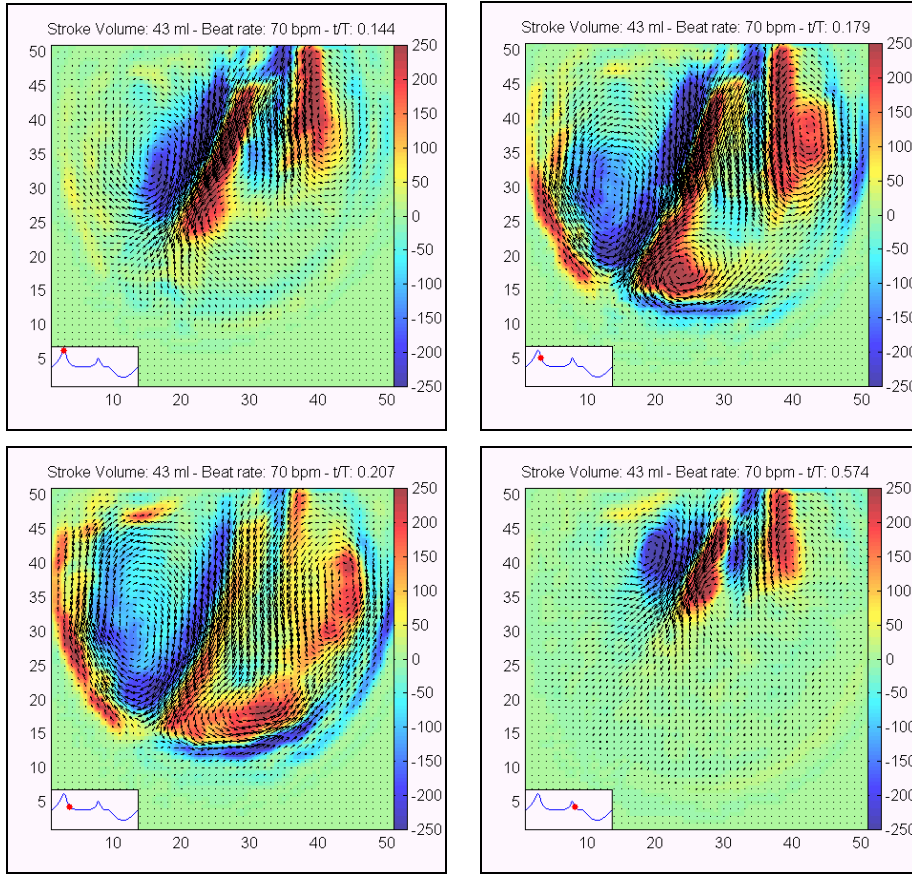


FIGURE 28. Phase averaged velocity vectors and vorticity contours at four phases of the cycle (indicated by the red dots).

E wave), when the mitral valve re-opens for a short interval. A new couple of jet is observed but the intensity is fairly smaller than before; they will dissipate before colliding on the ventricle wall. This presented measurements have been performed with an equivalent beat rate equal to 70 Hz and a flow rate equal to 31/min.

It is important to point out that frequencies have been rescaled to account for differences between the used fluid (water) and blood; Reynolds (equal to about 700) and Womersley (equal to about 19) numbers similarity is achieved.

Higher-order statistics is computed on these data; in Fig. 29, the turbulent kinetic energy (*i.e.* the sum of mean square fluctuating velocities on the measurement plane) non-dimensional by the average outlet velocity is given

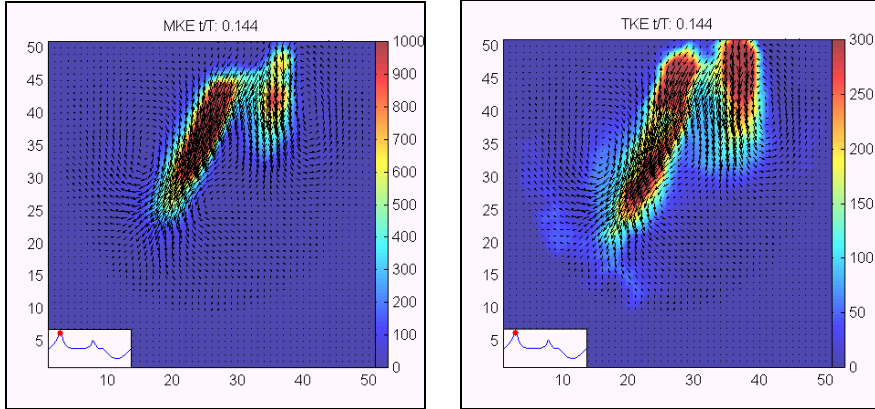


FIGURE 29. Phase averaged mean (on the left) and turbulent (on the right) kinetic energy at one phase of the cycle (indicated by the red dots).

(on the right part). It is compared with the sum of the phase averaged mean velocity components on the plane (i.e. the average kinetic energy) made non-dimensional as before. They are evaluated at the first peak of the flow rate, E wave). It is clear that the turbulent fluctuating part gives a substantial contribution in comparison to the average term (in the order of 30%), so that it cannot be neglected even at this quite small Reynolds number.

A comparison similar to the previous one has been performed on the viscous and turbulent shear stresses; they are obtained from the eigenvalues of the viscous and Reynolds stress tensors on the measurement plane (i.e. four components). The results obtained for the two, at the same phase as Fig. 29, are given in Fig. 30; in this case, the relevance of the turbulent contribution is much larger than before. There is almost a factor 100 between the viscous and turbulent contributions; this situation is quite common in blood flow investigations so that turbulent contributions to stress on blood cells are usually the largest.

The presented results concern with statistics obtained in time (or better in phase) at each point (Eulerian statistics); however, the PTV technique allows to derive also statistics along particle trajectories (Lagrangian statistics). Examples of results obtained with Lagrangian statistics are given in the next section; the reader is referred to [8, 10, 11] for other results on Lagrangian statistics obtained in the silicone ventricle model.

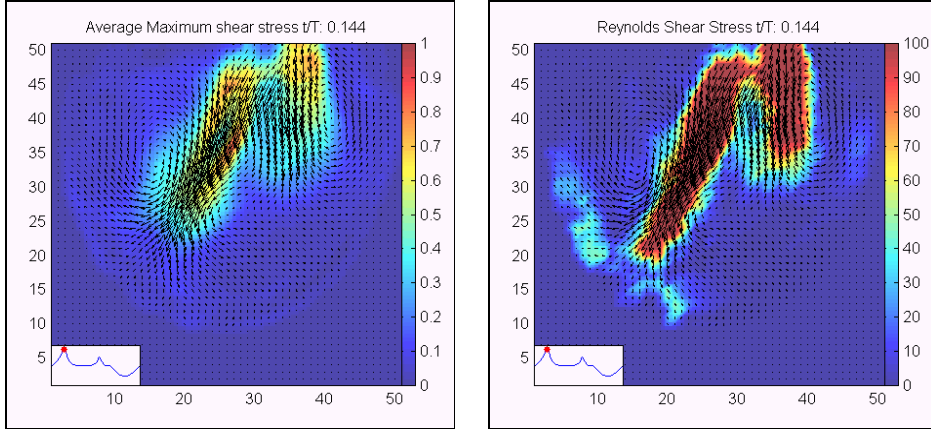


FIGURE 30. Phase averaged maximum viscous (on the left) and turbulent (on the right) shear stresses at one phase of the cycle (indicated by the red dots).

6. Simulation of Aortic Valves

Two main examples will be given of aortic flows downstream aortic valves; the first concerns with the Sheffield type mock-loop developed at ISS [7, 11] and the second with the Aachen unsteady pulse duplicator.

6.1. Sheffield Mock-Loop (ISS)

The experimental set-up of this experiment is given in Fig. 31 (refer to Sec. 2 for the figure and description of the mock-loop); in the first part of the figure a detailed view of the measurement region (aortic root) with position of the valve (bileaflet) and of the Valsalva sinuses is given (it is a pyrex replica of the real geometry). In the second part of the figure, the bileaflet valve is shown, while in the third part of the figure the control curve obtained for the flow rate is presented (beat rate equal to 70 Hz, flow rate equal to 11/min). In comparison to results on the ventricle presented in the previous section, the opening phase for the aortic valve is the systole while closing phase takes place in diastole. The working fluid is a water-glycerine (33%) mixture in Reynolds number (equal to 3200) and Womersley number (equal to about 10) similarities.

The measurements have been performed by means of a high-speed camera (the same used in Sec. 5) computing particle displacements by means of PTV [17].

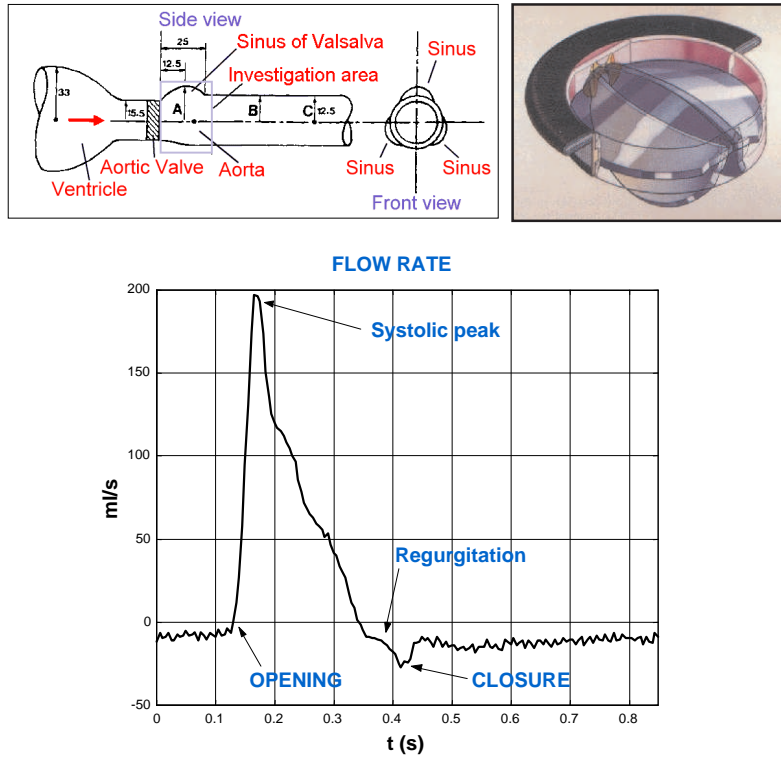


FIGURE 31. The experimental set-up for the aortic valve with Sheffield mock-loop (ISS) configuration; detail of the aortic root (top left), of the aortic bileaflet valve (top right) and of the flow rate during the cycle (bottom).

Some of the results obtained for the phase averaged fields are presented in Fig. 32 at the different phases; at the opening of the aortic valve (the phase is indicated by a red dot on the side of each figure), two jets start to develop directed towards the walls of the aortic root (the wake of the leaflet at the centerline partially obstructs the flow). As the valve opens the two leaflets generates three jets which fill all the flow field (second figure taken at the systolic peak). Immediately after the systolic peak (third figure), a recirculation starts into the Valsalva sinus on the right part of the investigated field; the main flow moves towards the left part of the field. After the closure of the valve (fourth figure) there is a clear backflow indicating some regurgitation; at this phase, the vortex in the Valsalva sinus changes sign.

As already stated, the interest in using PTV rather than PIV is in the possibility of deriving Lagrangian statistics, i.e. statistics of particles along

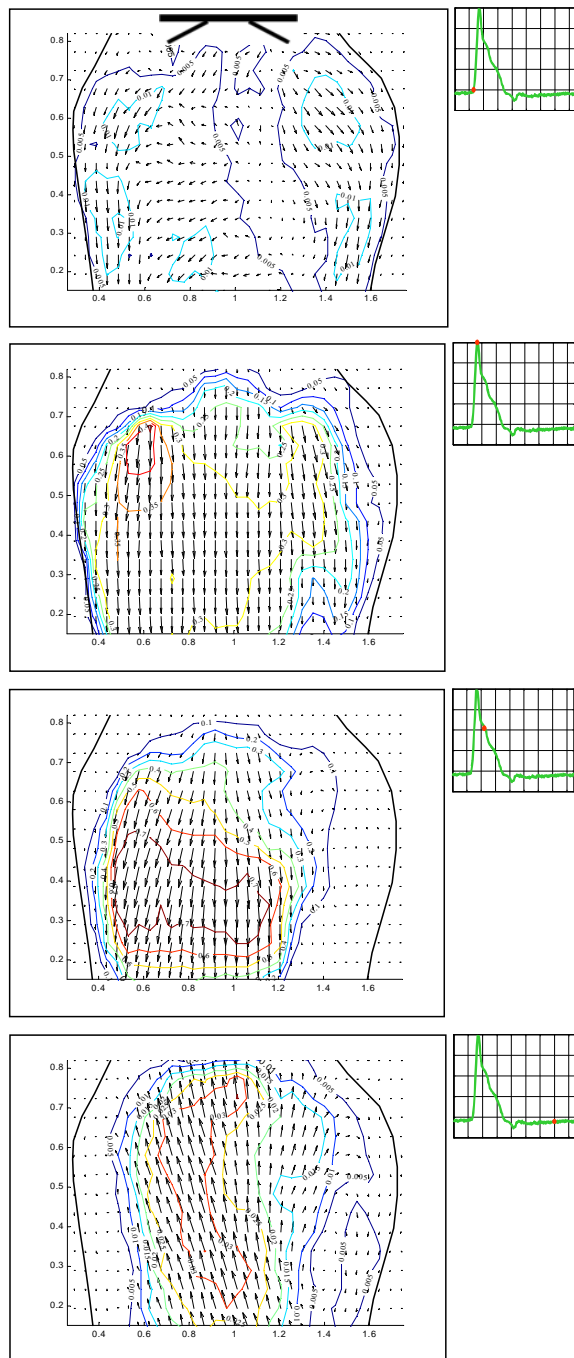


FIGURE 32. The phase averaged vector and axial velocity contour fields at four phases of the cycle (indicated by the red dots); the flow is from the top.

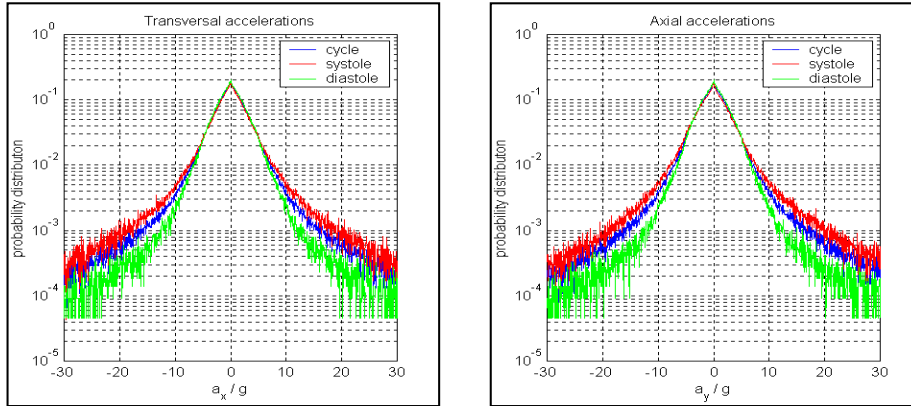


FIGURE 33. PDFs of transverse (on the left) and axial (on the right) accelerations from Lagrangian statistics during systole, diastole and the whole cardiac cycle.

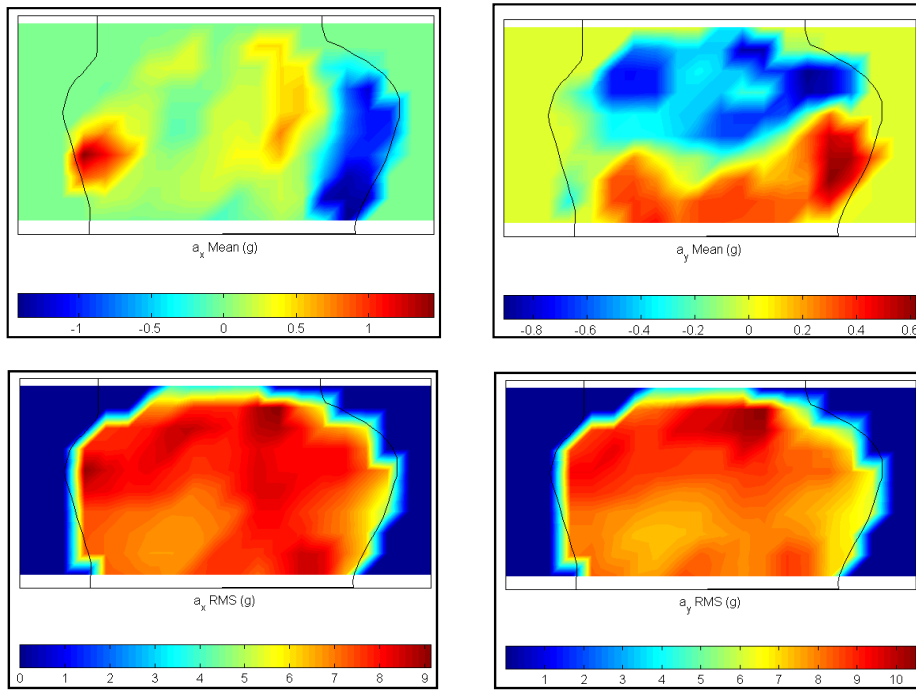


FIGURE 34. Transverse (on the left) and axial (on the right) accelerations from Lagrangian statistics during systole; average accelerations (at the top) and RMS of accelerations (at the bottom).

their trajectory. This is the most significant part which could allow to evaluate the accelerations, forces and stresses on each single blood cell. With this goal in mind, particle accelerations have been computed from the measured particle velocities along trajectories; in Fig. 33, the probability density functions (PDF) of transverse (indicated by a_x) and axial (indicated by a_y) accelerations all over the aortic root are evaluated. They are computed for the whole cycle (in blue) and separately for the systole (red) and diastole (green). It is observed that accelerations during systole are usually larger than those during diastole (both transverse and axial); moreover, axial and transverse accelerations are of the same order of magnitude (the average RMS value is about $3g$, where g is the gravity acceleration). Lastly, there are a few, but finite number, of particles experiencing accelerations larger than $20g$ (in absolute value).

The spatial distribution of the determined acceleration is given in Figs. 34 (systole) and 35 (diastole); in these figures, the average and RMS values of

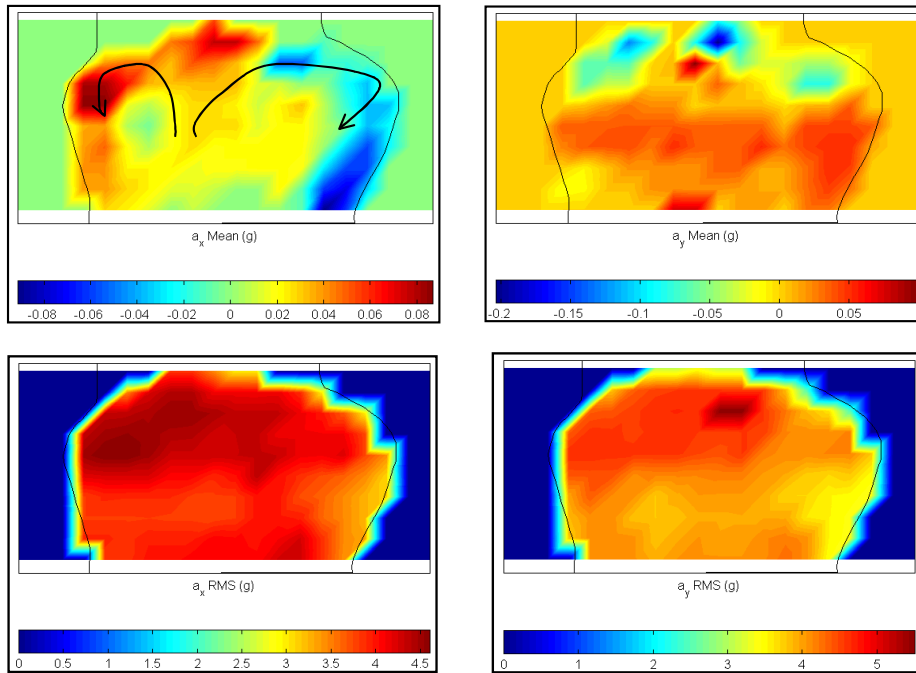


FIGURE 35. Transverse (on the left) and axial (on the right) accelerations from Lagrangian statistics during diastole; average accelerations (at the top) and RMS of accelerations (at the bottom).

the accelerations have been reported. During systole, the mean value of the transverse acceleration (first plot in Fig. 34) shows that the highest values are limited to the edge of recirculation regions and close to the jet reattachment points on the wall. The mean axial accelerations (second plot in Fig. 34), are negative (deceleration) at the expanding part of the root and positive in the contracting part. The RMS values for both transverse and axial accelerations (third and fourth plots in Fig. 34), are distributed much more uniformly than the mean.

The values are larger than the mean; the highest are obtained immediately downstream of the valve, indicating that inertial forces on blood cells are significant in this region.

During diastole, the mean value of the transverse acceleration (first plot in Fig. 35) shows that the highest values are observed close to the aortic

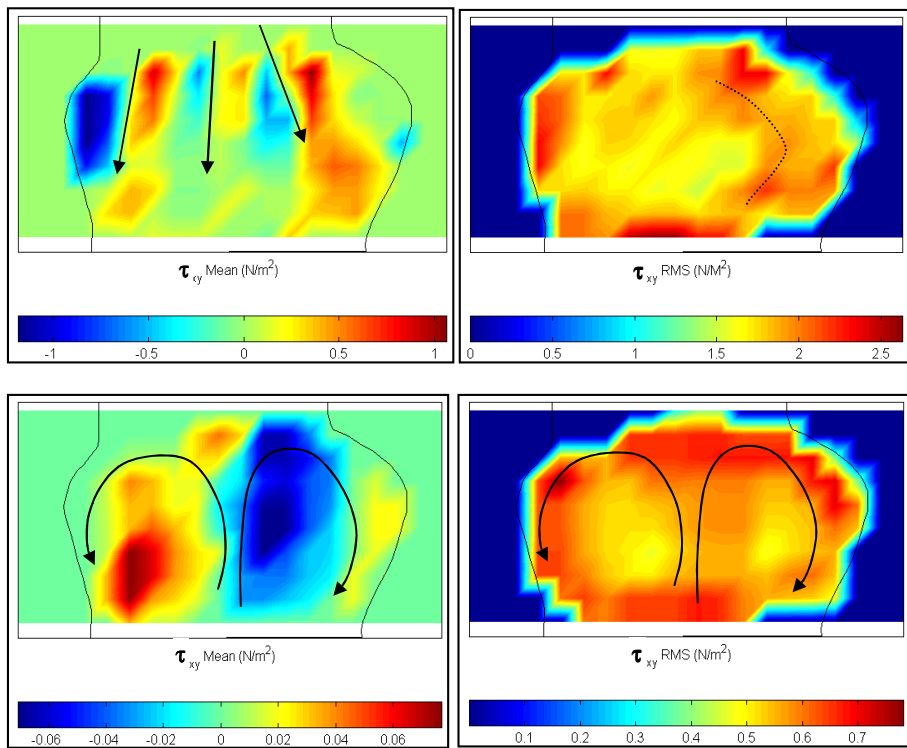


FIGURE 36. Viscous shear stress, average (on the left) and RMS (on the right) values from Lagrangian statistics during systole (at the top) and diastole (at the bottom).

root walls and at the top of the recirculation regions due to regurgitation (indicated by arrows). The mean axial accelerations (second plot in Fig. 35), due to the inverse flow in comparison to systole, are positive at the expanding part of the root and negative in the contracting part. All the mean values are lower than those during systole. Also during diastole the RMS values for both transverse and axial accelerations (third and fourth plots in Fig. 35), are distributed much more uniformly and with larger values in comparison to the mean. Even in this case the maxima are located close to the valve section. The RMS values are of the same order of magnitude than those during systole, thus indicating the relevance of measurements in the aortic root during the diastolic phase also.

Viscous stresses have been calculated from the data; in Fig. 36, the results for the mean and RMS values during systole and diastole are given. During systole (first two plots) the mean value indicates a three jet configuration, while RMS is maximum at the boundaries and in the recirculation region. During diastole (two plots at the bottom), the structure of a single regurgitant jet is depicted (lower mean values in comparison to systole); RMS values are of the same order of magnitude than during systole.

6.2. Aachen Mock-Loop

The experimental set-up is shown in Fig. 37 (refer to Sec. 2 for the figure and description of the mock-loop); in the first part of the figure a plot of obtained aortic, ventricular and atrial pressure curves is presented. As already stated in Sec. 2, it is quite complicated to set-up properly the circuit to obtain such curves, but the result is very similar to physiological ones. In the second part of the figure, the aortic pressure (which is the most critical one to control) is presented for three different measurements; as can be observed, once the circuit is properly set-up the variations from cycle to cycle are quite small. In the third part of the figure the flow rate downstream the aortic root is given (beat rate equal to 70 Hz, flow rate equal to 5 l/min). The working fluid is a water-glycerine (35%) mixture in Reynolds number (equal to 8000) and Womersley number (equal to about 10) similarities.

The measurements have been performed by means of a commercial cross-correlation PIV system (manufactured by LaVision GmbH). A huge amount of data has been recorded and elaborated; only examples will be given in the following.

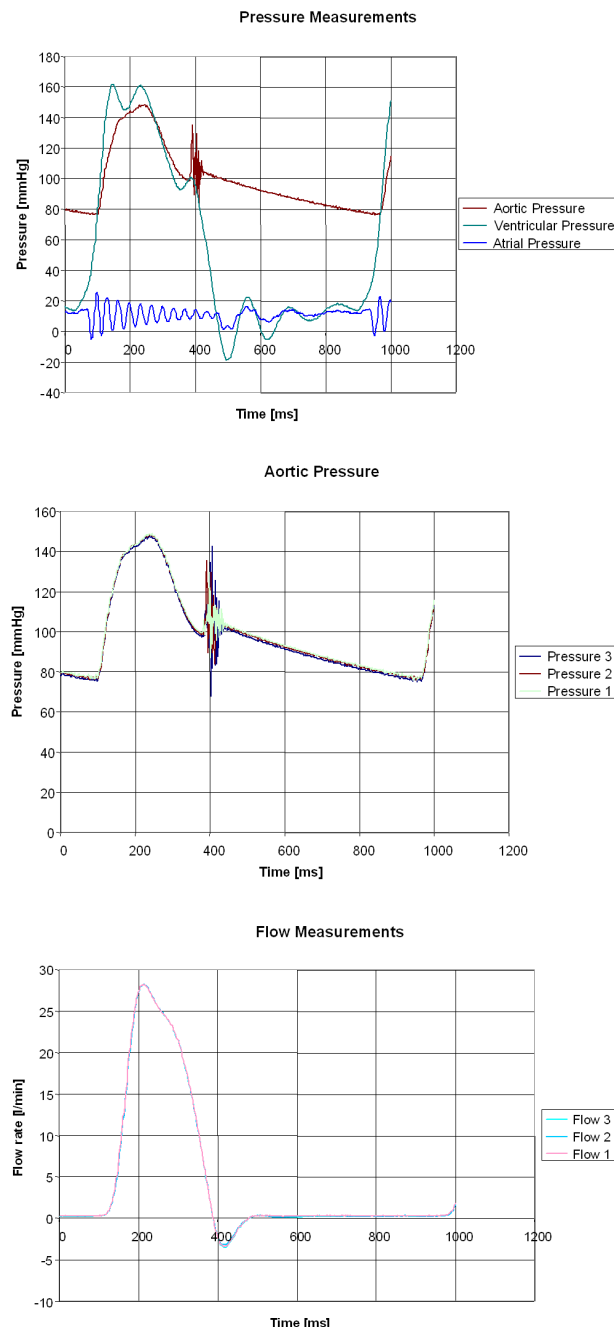


FIGURE 37. The experimental pressures (at the top), aortic pressure variations over three cycles (at the centre) and flow rate (at the bottom) for the aortic valve with Aachen mock-loop configuration.

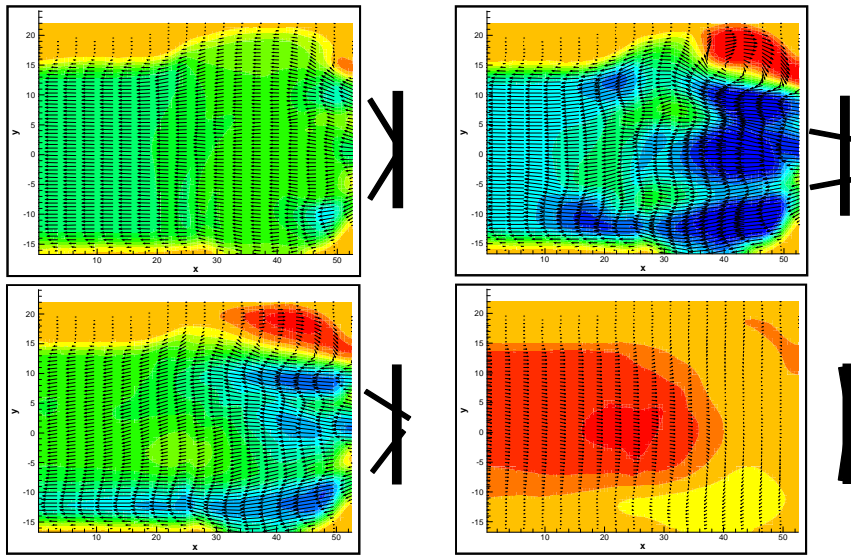


FIGURE 38. Phase averaged vector and axial velocity contour fields at four phases of the cycle (valve leaflet positions are indicated on the right of each plot); the flow is from the right.

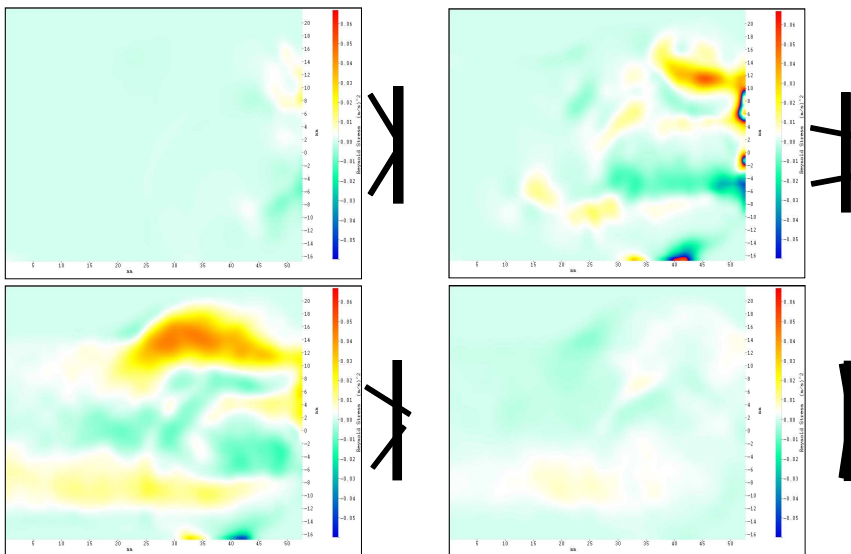


FIGURE 39. Phase averaged Reynolds turbulent stress fields at four phases of the cycle (valve leaflet positions are indicated on the right of each plot); the flow is from the right.

In Fig. 38, vector and horizontal velocity plots are given at four different phases. The valve bileaflet positions are also indicated on the left of the figures. The flow starts to move immediately after valve opening (first figure); then a three jets condition develops (second figure) as also reported in previous measurements. In the Valsalva sinus (at the top right corner), a recirculation region is observed which enlarges up to the phase in which valve leaflets start to close (third figure); at this phase, the three jets are still observed although attenuated. After valve closure (fourth figure), the backflow (regurgitation) takes place all over the field (except in the portion of the Valsalva sinus at the bottom right corner).

Higher-order statistics can be evaluated; as an example, the Reynolds turbulent stresses are presented in Fig. 39. The highest values are found at the upper Valsalva sinus (which is the only one completely investigated on the measurement plane) in a region which enlarges during the cycle. High values are also found at the jet boundaries especially at the bottom part.

7. Remarks and Future Developments

Remarks and conclusions will be given for each experiments. For the pulsed jet configuration (Sec. 4):

- optimal design and control of mock-loops is a crucial point in artificial valve testing;
- strong differences in the flow field are observed when changing forcing signal shape and flow rate, i.e. scaling is not allowed (velocity profiles);
- depending on flow rate and signal shape, concentrated or trailing jet structures in the wake of the main vortex ring are observed;
- these is evidence of an interaction between vortex ring and vorticity from previous vortex rings (at previous cardiac cycle);
- a preliminary statistical analysis for determining number of samples and type of statistics is required.

For the left ventricle silicone model (Sec. 5):

- average and turbulent kinetic energy have to be measured for proper heart valve evaluation;
- turbulent and viscous maximum shear-stresses are needed to point out the phenomena that more likely cause damage to blood-cells;
- the turbulent contributions cannot be neglected and seldom are the most relevant even at quite small Reynolds numbers;

- inertial forces on blood cells have to be measured from accelerations (i.e. from Lagrangian measurements).

For the Sheffield type mock-loop for aortic valve testing (Sec. 6.1):

- the fluid-mechanics phenomena in the aortic root as at least as complicated as those in the ventricle;
- three jet configuration during systole and regurgitation during diastole are derived;
- accelerations of fluid particle are significant and on average larger than those in the ventricle;
- it is important to evaluate average and RMS accelerations especially in recirculation regions and close to the valve;
- the comparison between mean shear stress and RMS values points out that the former permit the comprehension of the structure of the mean flow but underestimates the amplitude of the viscous forces on blood cells.

For the Aachen type mock-loop for aortic valve testing (Sec. 6.2):

- the set-up of a complex mock-loop for systemic circulation and prosthetic heart valve testing is not simple; once obtained it is stable;
- for the two-leaflets valve, the three jets configuration is visible independently on the employed mock-loop;
- regurgitation is also present on this mock-loop;
- large recirculation in the Valsalva sinus are observed leading to high RMS and Reynolds stress (due to vortex oscillations);
- there is a factor larger than 10 between velocities and second-order statistics determined at systolic peak and those in diastole.

The following points can be established as relevant for future investigations in the field of heart valve experimental testing:

- establish as much as possible procedures and apparatus (circuit, geometry, forcing, fluid, sampling) needed for proper valve testing;
- perform effective 3D experiments and numerics;
- evaluate accelerations and forces in a frame moving with the fluid particles;
- attain much higher spatial and temporal resolutions in experiments;

- perform simultaneous measurements of velocity, pressure and temperature fields.

Acknowledgements

Many of the results presented in this paper have been obtained within the framework of European Project IST 2002 37548 SMART-PIV (Development of an interactive integrated PIV system based on miniaturized optical sensor technology for implantable biomedical device design); all partners are acknowledged. The author wish to thank Dr. M. Falchi and Prof. G. Querzoli for the help in setting up the experiments and performing the measurements. Many thanks also to Prof. Z. Del Prete for setting up the driving motor for the pulsed jet apparatus, to Prof. A. Cenedese for providing the results on the left ventricle and to Dr. M. Grigioni for the helpful discussions and comments on the ISS data.

References

1. C.T. LEONDES, *Biomechanical Systems: Techniques & Applications*, Vol. II, Cardiovascular Techniques, <http://www.engnetbase.com/ejournals/books/>, 2004.
2. H. REUL, N. TALUKDER, and W. MULLER, *Fluid mechanics of the natural mitral valve*, Journal of Biomechanics, **14**:361–372, 1981.
3. H. REUL, J. VAN SON, U. STEINSEIFER, B. SCHMITZ, A. SCHMIDT, C. SCHMITZ, and G. RAU, *In vitro comparison of bileaflet aortic heart valve prothesis*, Journal of Cardiovascular Surgery, **106**:412–420, 1993.
4. M. GRIGIONI, C. DANIELE, G. D'AVENIO, and V. BARBARO, *A discussion on the threshold limit for hemolysis related to Reynolds shear stress*, Journal of Biomechanics, **32**:1107–1112, 1999.
5. Y.C. FUNG, *Biodynamics: circulation*, Springer-Verlag, 1997.
6. T.J. PEDLEY, *The fluid mechanics of large blood vessels*, Cambridge University Press, 1980.
7. A. BALDUCCI, M. GRIGIONI, G. QUERZOLI, G.P. ROMANO, C. DANIELE, and G. D'AVENIO, *PIV and PTV measurements downstream an artificial heart valve*, Experiments in Fluids, **36**(1): 204–213, 2004.
8. A. CENEDESE, Z. DEL PRETE, M. MIOZZI, and G. QUERZOLI, *A laboratory investigation of the flow in the left ventricle of a human heart with prosthetic, tilting disk valves*, Experiments in Fluids, Online First, 2005.

-
9. M. FALCHI, Z. DEL PRETE, B. WIENEKE, G. QUERZOLI, and G.P.ROMANO, *The flow field at the outlet of a pulsed jet under different periodic signals*, Euromech Colloquium 456, Experimental and computational Biofluid Mechanics, Aachen, Germany, 2004.
 10. A. CENEDESE, Z. DEL PRETE, M. MIOZZI, and G. QUERZOLI, *Investigations of the blood flow inside the left ventricle of the heart*, Euromech Colloquium 456, Experimental and computational Biofluid Mechanics, Aachen, Germany, 2004.
 11. A. BALDUCCI, M. GRIGIONI, G. QUERZOLI, and G.P.ROMANO, *Measurements of forces on blood cells downstream an artificial aortic valve*, PIVNet2 Workshop on PIV in Biomedical Flows, Aachen, 2003.
 12. M. FALCHI and G.P. ROMANO, *Experimental study on vortex rings dynamics in a pulsed jet using Particle Image Velocimetry*, Proceedings of 4th International Symposium on Turbulence and Shear Flow Phenomena, Williamsburg, USA, 2005.
 13. M. FALCHI, G.QUERZOLI, and G.P. ROMANO, *Investigation of a pulsed jet by means of Robust Image Velocimetry*, Proceedings of 6th International Symposium on Particle Image Velocimetry, Pasadena, USA, 2005.
 14. R.J.ADRIAN, *Particle Image Velocimetry for experimental fluid mechanics*, Annual Review of Fluid Mechanics, **23**: 261–304, 1991.
 15. M. STANISLAS, J. KOMPENHANS, and J. WESTERWEEL, *Particle Image Velocimetry: Progress Towards Industrial Application*, Springer-Verlag, 2000.
 16. M. GHARIB, E. RAMBOD, and K. SHARIFF, *A universal time scale for vortex ring formation*, Journal of Fluid Mechanics, **360**: 121–140, 1998.
 17. A. CENEDESE and G. QUERZOLI, *Particle tracking velocimetry: measuring in the Lagrangian reference frame*, Von Karman Lecture Series 2000-2001, Von Karman Institute, Bruxelles, Belgium, 2000.
-

Heat Transfer in Humans—Local and Whole-Body

G.M.J. VAN LEEUWEN and A.A. VAN STEENHOVEN

Technische Universiteit Eindhoven
Postbus 513, 5600 MB, Eindhoven, the Netherlands
g.m.j.v.leeuwen@tue.nl

Temperature plays an important role in the functioning of biological (sub)systems. Here, efforts that have been made to calculate temperature distributions in humans will be reviewed. First, attention will be on the small scale. Different ways of modelling the crucial influence of blood flow will be described. The collective effect is reasonably successfully described by a heatsink. Predicting detailed inhomogeneous temperature distributions requires accounting for effects of individual vessels. Second, aspects involved in calculating an overall temperature distribution in different environmental conditions will be explained. Main mechanisms with which the body maintains its core temperature are vasoaction, sweating and shivering.

Key words: *Tissue heat transfer, bio heat equation, discrete vessel thermal model, thermoregulation.*

1. Introduction

Temperature influences the functioning of biological (sub)systems. Mammals are homeothermic: normally core temperature varies only within narrow bounds. For humans, normal core temperature is about 37°C. Even small differences in this temperature may have significant consequences for the behaviour of individual cells and the body as a whole. These temperature dependencies of biological processes can be used to clinical effect. There are several situations in which clinicians want to change the temperature of the whole body or part of the body. One example is the induction of higher temperatures (43°C) in a tumour as an adjuvant therapy against cancer (hyperthermia therapy); another example is the cooling of patients during surgery to protect sensitive tissues. Taking action might also be necessary to

maintain/restore normal temperature, e.g. when environmental conditions are harsh, to prevent morbidity or performance degradation. Examples are hypothermic low birth-weight babies, and athletes competing in high temperatures. It also works the other way: the functioning of biological systems influences their temperature. Hence, measurement of temperature can be used in clinical diagnosis (e.g. Fig. 1). Core temperature is routinely measured to monitor progress of disease and recovery; local temperature elevations can indicate infections or tumours.



FIGURE 1. A common clinical diagnostic device: the simple oral or rectal thermometer.

In order to control the temperature or just to monitor it, an understanding is necessary of the heat transfer processes within the human body and between the human body and the environment. This understanding is necessary to predict the outcome of thermal interventions (e.g. predict power density of heating system necessary for a desired rise in tumour temperature in local hyperthermia), and/or to provide information on temperature where it would otherwise be limited due to limitations on (invasive) thermometry.

This text will look at the processes taking place and at different types of models that have been developed to describe these. It will both look at the physics of heat transfer (the passive system), and at the thermoregulatory processes that take place to maintain a steady core temperature. It will become clear that the convective heat transfer by the blood plays a very important role in the development of temperatures both on the scale of the whole-body and on a local scale.

2. Heat Transfer within the Tissue; Continuum Models

2.1. Tissue Equations; Heat Sink and Effective Conductivity

Heat transfer within the body takes place by means of conduction and convection. Conduction is the transfer of heat from hot to cold via transfer of kinetic energy of constituting particles, without net displacement of the particles themselves. In an isotropic medium the conductive heat flow density ϕ_k

$[\text{Wm}^{-2}]$ is governed by Fourier's law: $\phi_{\mathbf{k}} = -k\nabla T$ with k $[\text{Wm}^{-1}\text{K}^{-1}]$ the thermal conductivity of the medium. Generation of heat in a tissue volume element must lead to net outflow of heat from the element, or to heating of the tissue:

$$M = -\nabla \cdot k_{\text{tis}} \nabla T + \rho_{\text{tis}} c_{\text{tis}} \frac{\partial T}{\partial t}$$

with M the volumetric rate of heat generation (metabolic rate and possibly absorbed power) $[\text{Wm}^{-3}]$, ρ_{tis} the tissue density $[\text{kg m}^{-3}]$, and c_{tis} the tissue specific heat $[\text{Jkg}^{-1}\text{K}^{-1}]$. Should the conductivity be uniform, and the problem stationary, this equation reduces to the Laplace equation, which for some simple cases can be analytically solved. Within the human body, pure conduction problems are very rare because most of the body is perfused by blood.

Heat may also be transferred due to flow of a medium: convection. Convective heat transfer is governed by a set of equations describing conservation of mass, momentum, and energy. Here, simultaneously solving them for the detailed blood vessel network will not be attempted. The importance of the convective heat transfer by the blood for body temperatures may be deduced from the fact that the human heart typically pumps 5 liter blood per minute through the body. If this is multiplied by the density and by the specific heat it is seen that the cardiac output is equivalent to about 300 WK^{-1} . This means that if the blood changes on average just 0.25 K in temperature on its journey through the body it redistributes almost the same amount of heat as is produced by an average human in rest.

There are roughly 100 thousand kilometer of blood vessels within the body along which the blood-tissue heat transfer takes place. So, in an average $(10 \text{ cm})^3$ cube of tissue there is more than a thousand kilometers of blood vessels present. That is a lot of surface area for the blood to exchange heat with the tissue. It should be obvious that it will be difficult to compute a detailed temperature distribution in even a very small part of the body accounting for all the blood vessels individually. Fortunately, the thermal effect of the blood vessels can be described collectively with some success.

In 1948 Harry H. Pennes [1] devised what has become known as the bio heat equation, or alternatively the heatsink equation, in which the effect of all vessels is lumped together.

$$\rho_{\text{tis}} c_{\text{tis}} \frac{\partial T}{\partial t} = \nabla \cdot k_{\text{tis}} \nabla T - c_b W_b (T - T_{\text{art}}) + M. \quad (2.1)$$

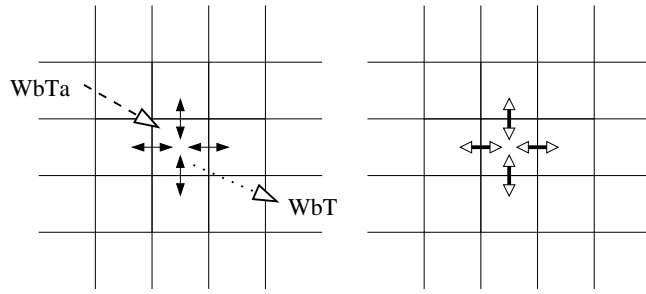


FIGURE 2. Two dimensional representation of the heat transferred into and out of a tissue element for the Pennes heatsink model and the limited k_{eff} model.

This continuum equation has one extra term with respect to the conduction equation. In this term, c_b is the specific heat of blood, W_b the blood perfusion in the tissue [$\text{kg m}^{-3} \text{s}^{-1}$], and T_{art} the temperature of the arterial blood entering the volume. The bio heat equation describes blood to tissue heat transfer as if it all takes place in the capillaries: blood reaches the capillaries with the temperature still that of the major supply artery. In the capillaries thermal equilibration to the tissue temperature takes place, leading to the ‘heatsink’ term in Eq. (2.1). Subsequently, in the venous return system again all heat transfer with the tissue is assumed negligible. The bio heat equation has established itself as the most used continuum description of tissue heat transfer. The results can be quite accurate, especially in tissues that are highly perfused such as the brain. The cause for the better accuracy at higher perfusion is that in highly perfused tissue a relatively large proportion of the heat transfer does take place in the smallest vessels. To put it slightly differently, increasing blood flow in the branching vessel network will lead to later thermal equilibration of blood with tissue, further into the network, closer to the capillaries.

As an example of the use of the Pennes equation, the temperature difference between the blood going to the brain and the returning blood will be estimated. In the central brain, convective heat transfer by the blood is so dominant that conduction can be neglected. From Eq. (2.1), this means that in the stationary situation the metabolic heat production rate must equal $c_b W_b (T - T_{\text{art}})$. Using $c_b = 3.6 \text{ kJ K}^{-1} \text{kg}^{-1}$, $W_b = 9 \text{ kg m}^{-3} \text{s}^{-1}$ and a metabolic heat production in the brain of 10 kW m^{-3} this means that the temperature of the brain (and of the returning blood) is roughly 0.3°C higher than the temperature of the incoming blood.

As implied before, heat transfer between tissue and blood *does* take place before and after the capillaries. In fact, for the arterial blood it was demonstrated that by the time blood flows into vessels $60\ \mu\text{m}$ in diameter and smaller the equilibration process is complete. On the one hand, this means that the effect of blood is not only dependent on the volumetric perfusion distribution $W_b(\mathbf{r})$, but also on the positions of the large vessels of the vasculature. On the other hand, this leads to two possible additional terms in the continuum heat transfer equation. One is associated with the net mass flow of blood and was first proposed by Wulff [2] as a replacement for the heatsink term.

$$\rho_{\text{tis}} c_{\text{tis}} \frac{\partial T}{\partial t} = \nabla \cdot k_{\text{tis}} \nabla T - c_b \rho_b \mathbf{U} \cdot \nabla T + M$$

In this equation the convection term, in which \mathbf{U} is the local mean apparent blood velocity [m s^{-1}], accounts completely for the effect of blood flow. In reality, significant unidirectional flow on meaningful length scales is rare in the body. The other possible additional term to the heat transfer equation is an increased tissue thermal conductivity. It was first introduced by Chen and Holmes in 1980, [3]. They proposed to model heat transfer from large vessels individually, to use the last individually calculated blood temperature T_{art}^* for the remaining heat sink term and to add two convective terms to the heatsink formulation:

$$\rho_{\text{tis}} c_{\text{tis}} \frac{\partial T}{\partial t} = \nabla \cdot k_{\text{tis}} \nabla T - c_b W_b(T - T_{\text{art}}^*) - \rho_b c_b \mathbf{U} \cdot \nabla T + \nabla \cdot k_p \nabla T + M$$

The new perfusion based term, containing k_p , states that part of the effect of blood flow is qualitatively the same as an increase in thermal conductivity. The term arises from the net thermal effect of flow in vessels where the macroscopic net flow is zero because the flow in one vessel is matched by the same flow in the opposite direction in (an)other vessel(s). After it was observed that blood vessels often occur in countercurrent pairs, it was even suggested that just an increased effectivity, without heatsink, could describe the effect of blood flow in some tissues. Incomplete countercurrent heat exchange does indeed qualitatively behave as an extra conduction term. After anatomical and theoretical studies of peripheral muscle tissue Weinbaum and Jiji, [4], formulated a bio heat equation in which the thermal effect of blood was described solely by an effective conductivity tensor k_{eff} . The dependence of k_{eff} on the vasculature was derived for homogeneous tissue containing vessels

with radius r_{ves} as

$$k_p + k_{\text{tis}} = (k_{ij})_{\text{eff}} = k_{\text{tis}} \left(\delta_{ij} + \frac{\pi^2}{4\sigma k_{\text{tis}}^2} n r_{\text{ves}}^2 k_b \text{Pe}^2 l_i l_j \right).$$

Here δ_{ij} is the Kronecker delta function, i and j are the directions of the heat flux and temperature gradient, σ is a shape factor (describing vessel-tissue heat transfer), n is the vessel pair density [m^{-2}], and l_i , l_j are direction cosines. Pe is the Peclet number equal $2\rho_b c_b r_{\text{ves}} u_b / k_b$, in which u_b is the blood velocity [ms^{-1}]. This relation for k_{eff} does not quite show the complexities involved, and an alternative equation will be derived below.

2.2. Vessel Pairs and Effective Conductivity

It is worth taking a look at how a pair of countercurrent vessels contributes to the net heat flow. Consider a cross section of a tissue block with a vessel pair with equal but opposite flows, and a temperature gradient in the direction of the axis of the tissue cylinder. The contribution of the countercurrent vessel pair to heat transfer in the vessels' direction will both be proportional to the volume flow in the vessels, and to the temperature difference between the blood in the vessels. The difficulty lies with the second factor. The blood temperature difference depends on what has gone on before, not just on the local tissue temperature gradient. If the length scale of the gradient is sufficiently large, the temperature difference between the two vessels will be proportional to the gradient. Heat transfer proportional to gradient

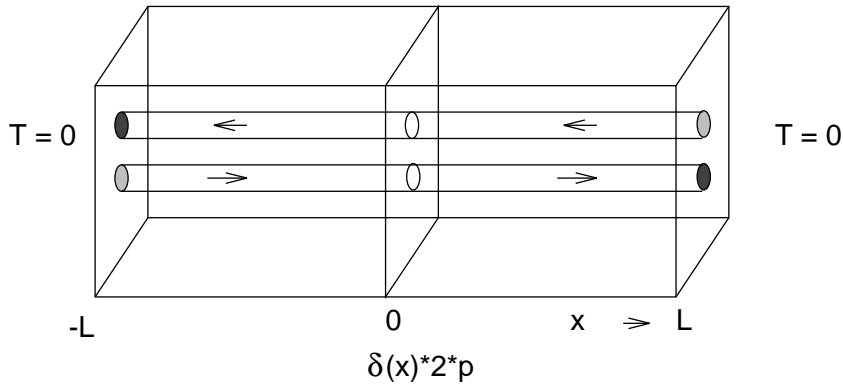


FIGURE 3. Two countercurrent vessels with same inflow temperature in a block with heating in central plane, with the four walls coplanar to the vessels thermally insulated, and the two faces at constant temperature.

means that in this case indeed the vessels contribute a term equivalent to Fourier's law for conduction. For the smallest vessels, that equilibrate quickly with the tissue, a short length scale of the gradient will suffice. This means that an effective conductivity description is often accurate for small vessels. However, because of the small flow and the small temperature difference between the vessels (because of same rapid equilibration) the contribution of the smallest vessels to the conductivity is small. For larger vessels a larger effective conductivity is possible, but the required large length scale for the gradient might not always be present, making the behaviour of the vessels qualitatively different, and possibly much more heatsink like.

A simple theoretical analysis of a countercurrent pair in tissue gives a quantitative but not completely rigorous description of this behaviour. A three-equation formulation reduces the complex 3-D temperature distribution to three axial profiles, [5]. One axial profile, $T(z)$, describes the tissue temperature as averaged over the tissue cross section. The other two profiles, $T_{\text{art}}(z)$ and $T_{\text{vein}}(z)$, describe the vessel mixing-cup temperatures (e.g. [6]) of the countercurrent vessels

$$T_{\text{mix-cup}} \equiv \frac{\int_0^{r_{\text{ves}}} T_b(r) u_b(r) 2\pi r dr}{\int_0^{r_{\text{ves}}} u_b(r) 2\pi r dr}.$$

The three governing differential equations can be written as

$$k_{\text{tis}} \frac{\partial^2 T}{\partial z^2} - nk_{\text{tis}} \sigma_{\Sigma} \left[T - \frac{T_{\text{art}} + T_{\text{vein}}}{2} \right] + M = \rho_{\text{tis}} c_{\text{tis}} \frac{\partial T}{\partial t}$$

$$\begin{aligned} \pi r_{\text{ves}}^2 \rho_b c_b u_b \frac{dT_{\text{art}}}{dz} &= -k_{\text{tis}} \sigma_{\Delta} (T_{\text{art}} - T_{\text{vein}}) \\ &\quad + \frac{k_{\text{tis}} \sigma_{\Sigma}}{2} \left[T - \frac{T_{\text{art}} + T_{\text{vein}}}{2} \right] + \pi r_{\text{ves}}^2 P \end{aligned}$$

$$\begin{aligned} \pi r_{\text{ves}}^2 \rho_b c_b u_b \frac{dT_{\text{vein}}}{dz} &= -k_{\text{tis}} \sigma_{\Delta} (T_{\text{art}} - T_{\text{vein}}) \\ &\quad - \frac{k_{\text{tis}} \sigma_{\Sigma}}{2} \left[T - \frac{T_{\text{art}} + T_{\text{vein}}}{2} \right] - \pi r_{\text{ves}}^2 P \end{aligned}$$

The mutual heat exchanges are calculated using the conduction coupling constants, or shape coefficients, σ_{Δ} and σ_{Σ} . The constant σ_{Δ} determines

the heat transfer between the vessels, σ_Σ determines the net heat transfer between vessel pair and tissue. The values of these coupling constants can be calculated on the basis of 2-D stationary temperature distributions. They only depend on the geometry (vessel size and spacing, tissue cross section), not on the flow in the vessels. $M(z)$ is the sum of metabolic heat and volumetric power absorption (e.g. from microwaves), $P(z)$ is absorbed power only as the metabolic rate in the blood is zero.

When a sinusoidal profile with arbitrary period $4L$ for the average tissue temperature is considered, it is easy to show that the solution for the sum of $T_{\text{art}} + T_{\text{vein}}$ is also a sinusoidal and in phase with $T(z)$. The difference $T_{\text{art}} - T_{\text{vein}}$ is also sinusoidal but is out of phase by $\pi/2$, so in phase with the tissue temperature gradient. From these solutions a relation for the effective conductivity can be worked out:

$$k_{\text{eff}} = k_{\text{tis}} \left(1 + \sqrt{\frac{\sigma_\Sigma}{\sigma_\Delta}} \frac{\text{Pe}^* L_{\text{cc}}^*}{1 + \pi^2 L_{\text{cc}}^{*2}/4} \right), \quad (2.2)$$

$$\text{Pe}^* \equiv \frac{\rho_b c_b L u_b r_{\text{ves}}^2}{k_{\text{tis}} r_{\text{tis}}^2}, \quad L_{\text{cc}}^* = \frac{\pi \rho_b c_b u_b r_{\text{ves}}^2}{\sqrt{\sigma_\Sigma \sigma_\Delta} k_{\text{tis}} L}.$$

Here Pe^* is a modified Peclet number, and L_{cc}^* is a dimensionless parameter describing the length of countercurrent thermal equilibration with respect to the length of the sine period. It can be seen that k_{eff} goes asymptotically to a maximum when L increases. When L goes to zero, the contribution of the vessels to the conductivity goes to zero. This is because for very small L the amplitude of the sinusoidal vessel temperatures will go to zero, resulting in a more heatsink-like effect of the vessels. One further thing to note about the relation 2.2 is that for small L_{cc}^* the extra conductivity is quadratic in the blood volume flow. In summary, large vessels can potentially contribute a lot to the effective conductivity, but this requires a gradient with a long length scale to build up the temperature difference. This is also illustrated in Fig. 4 where it is shown how two countercurrent vessels increase their share of the heat transport where the distance from the discontinuity increases. Tissue temperature gradients with small length scales, for instance in the case of interstitial heating with needles, will necessarily experience a relatively low effective conductivity.

The above analysis suggests that continuum models have non-trivial inherent limitations. Even homogeneously vascularised tissue may have spatially varying optimum continuum parameters, based on different distances

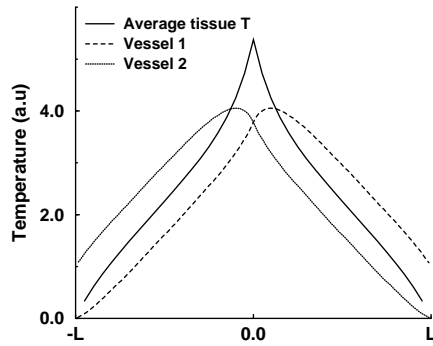


FIGURE 4. Profiles for two counter-current vessel temperatures and average tissue temperature in tissue block with heating in central plane, see Fig. 3. The varying contribution of the vessels to the heat transport can be appraised from the variation in tissue temperature gradient.

with respect to the boundary conditions. May be as a result of this complex behaviour, there has been considerable debate in the past over the applicability of the different paradigms (heatsink, effective conductivity). These differences were difficult to resolve, because of inherent difficulties in experimental measurements, [7, 8], but also because different experimental set-ups may lead to different dominant behaviour. Now, however, there seems to be a somewhat better understanding of the limitations of each of the paradigms. This is partly thanks to the development and experiences with numerical models that describe the influence of individual blood vessels.

Even now increasingly powerful computers, sophisticated models, and imaging techniques, have made it possible to account for the thermal effects of individual vessels, there is still an important role for continuum models. Creating a detailed vasculature for an individual patient requires an enormous effort. For some applications the continuum models will be good enough not to make this effort. Even when discrete vessel modelling is applied, this will often not be possible for all of the thermally significant vessels, in which case the discrete vessel model is used in combination with a continuum description.

3. Discrete Vessel Thermal Model

It is obvious that one of the inherent disadvantages of all continuum models is that they don't account for temperature inhomogeneities surrounding

the large vessels, simply because these are not modelled. One field where one is very much interested in these inhomogeneities is that of treatment of tumours with local hyperthermia, [9]. Hyperthermia is the heating of tumours to about 43°C, not so much to directly kill tumour cells, but as an adjuvant therapy to make radiotherapy more effective. In local (rather than regional or whole-body) hyperthermia in particular, very heterogeneous temperature distributions may be brought about by arteries with normal blood temperature entering the heated volume. These temperature inhomogeneities may have serious consequences for the efficacy of the treatment. Therefore, especially in this field, the effects of individual vessels on the temperature distribution have been studied and increasingly sophisticated numerical models have been developed.

3.1. Analytic Solution for a Vessel in a Tissue Cylinder

It is instructive to first look at the analytical solution for the very simple geometry of one vessel embedded in a tissue cylinder, see Fig. 5. It introduces the important concept of thermal equilibration length, and results will be used later on in the discrete vessel thermal model. Consider a straight blood vessel in a concentric tissue cylinder with constant temperature on the outside cylindrical surface, constant conductivity k_{tis} , and no heat generation in the tissue. The governing differential equation in the tissue surrounding the vessel

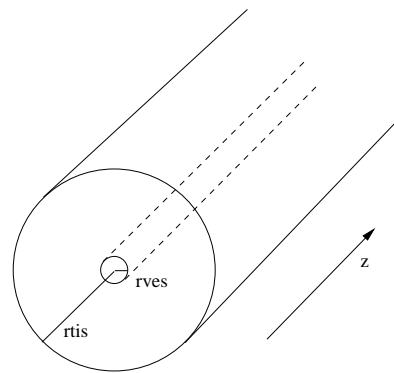


FIGURE 5. Geometry: a straight vessel in a tissue cylinder with constant boundary temperature

is written in cylindrical coordinates as

$$k_{\text{tis}} \left(\frac{\partial^2 T}{\partial r^2} + \frac{1}{r} \frac{\partial T}{\partial r} + \frac{1}{r^2} \frac{\partial^2 T}{\partial \theta^2} + \frac{\partial^2 T}{\partial z^2} \right) = \rho_{\text{tis}} c_{\text{tis}} \frac{\partial T}{\partial t}.$$

The solution to this problem is considerably simplified if it is assumed that conduction in the axial direction can be neglected. Furthermore, the stationary solution must be cylindrically symmetric because of the fixed temperature on the tissue boundary. So, what is left is a one-dimensional differential equation for the radial tissue temperature profile. The solution is given by

$$T(r) = T(r_{\text{ves}}) + (T(r_{\text{tis}}) - T(r_{\text{ves}})) \frac{\ln(r/r_{\text{ves}})}{\ln(r_{\text{tis}}/r_{\text{ves}})}.$$

The tissue temperature at the vessel wall is unknown, but can be found since the radial heat flux ϕ must be continuous over the vessel wall. The heat flux in the tissue at the vessel wall boundary can be calculated by

$$\phi_{w+} = -k_{\text{tis}} \left. \frac{dT}{dr} \right|_{r_{\text{ves}}} = -k_{\text{tis}} \frac{T(r_{\text{tis}}) - T(r_{\text{ves}})}{\ln(r_{\text{tis}}/r_{\text{ves}}) r_{\text{ves}}}.$$

Inside the vessel, the heat flux at the wall can be written as

$$\phi_{w-} = -\frac{1}{2r_{\text{ves}}} \text{Nu} k_{\text{b}} (T(r_{\text{ves}}) - T_{\text{art}}). \quad (3.1)$$

The Nusselt number Nu is a dimensionless heat transfer coefficient, providing a measure for the heat transfer at a boundary of a flowing fluid. Here $\text{Nu} = hD/k_{\text{b}}$, where h is the convective heat transfer coefficient [$\text{Wm}^{-2}\text{K}^{-1}$] defined by $h = \phi_{w-}/(T_{\text{mix-cup}} - T_{\text{wall}})$ and D is the vessel diameter. For a number of cases, expressions for the Nusselt number have been derived. In a cylinder, for a Newtonian fluid with Poiseuille flow and thermally developed flow, $\text{Nu} = 3.66$ if the wall temperature is constant along the vessel, whereas $\text{Nu} = 4.36$ if instead the heat flux through the wall is constant, [6]. In this case, the presence of the tissue between vessel and the outer boundary with constant temperature causes the Nusselt number to fall between these two values. However, for thermally undeveloped flow Nu may be higher than both.

From the continuity requirement for the radial heat flux through the wall, the wall temperature is found to be

$$T(r_{\text{ves}}) = T_{\text{art}} + \frac{T(r_{\text{tis}}) - T_{\text{art}}}{1 + \frac{1}{2} \text{Nu} \frac{k_{\text{b}}}{k_{\text{tis}}} \ln \frac{r_{\text{tis}}}{r_{\text{ves}}}}.$$

Substitution in Eq. (3.1) gives an expression for the heat flux into the vessel. This heat flux causes the blood temperature to change along the vessel direction, and the axial profile for the vessel temperature can now be determined from the differential equation:

$$\pi r_{\text{ves}}^2 u_b \rho_b c_b \frac{dT_{\text{art}}}{dz} = 2\pi r_{\text{ves}} \phi_w = \pi \text{Nu} k_b \frac{T(r_{\text{tis}}) - T_{\text{art}}}{1 + \frac{1}{2} \text{Nu} \frac{k_b}{k_{\text{tis}}} \ln \frac{r_{\text{tis}}}{r_{\text{ves}}}}. \quad (3.2)$$

The solution is:

$$T_{\text{art}}(z) = T(r_{\text{tis}}) + (T_{\text{art}}(0) - T(r_{\text{tis}})) e^{-z/L_{\text{eq}}}, \\ L_{\text{eq}} = \rho_b c_b u_b r_{\text{ves}}^2 \left(\frac{1}{k_b \text{Nu}} + \frac{1}{2k_{\text{tis}}} \ln \frac{r_{\text{tis}}}{r_{\text{ves}}} \right). \quad (3.3)$$

The thermal equilibration length L_{eq} describes the rate of thermal equilibration of the blood to the surrounding tissue. Clearly, the thermal equilibration length varies very strongly with varying radius. There is an explicit quadratic dependence of L_{eq} on vessel radius in Eq. (3.3), but in addition the flow velocity u_b will usually also be larger in a larger vessel. For several sizes of vessels approximate equilibration lengths have been tabulated in Table 1. From this table it can be deduced that most of the thermal equilibration must take place in the arteries with diameters in the range 0.2–2.0 mm. Note that because of branching the total surface area increases for every generation of smaller vessels.

TABLE 1. Equilibration length calculated for blood vessels of different sizes. Calculated assuming the vessel influences a tissue cylinder ten times larger than the vessel, [10].

vessel type	diameter mm	length cm	u_b cm/s	L_{eq} cm
aorta	25	40	100	1.5×10^5
large arteries	3	20	13	290
main branches	1	10	8	20
secondary branches	0.6	4	8	7.2
tertiary branches	0.14	1.4	3.4	0.17
terminal branches	0.05	0.1	2	0.013
arterioles	0.02	0.2	0.3	0.0003
capillaries	0.008	0.1	0.07	0.00001

3.2. Numerical Modelling of Detailed Vessel Networks

The impact of blood vessels on the temperature distribution can be calculated analytically only for very basic configurations. The modelling of the thermal impact of a complex, detailed discrete vasculature has to be done numerically.

In this text the computer program DIVA, [11] (for Discrete VAsculature) developed at the Utrecht University Medical Centre will be discussed in some detail. This program is unique in some important aspects, but shares essential properties with other models. Key of most models is that to be able to handle detailed vasculature the blood radial temperature profile is just described by the blood mixing-cup temperature. An analytical solution is used to describe vessel-tissue heat transfer. Unique for DIVA is that the vessels are described independently from the solid tissue: tissue and vessel do share the same coordinate system but are described by separate structures, in separate files. Whereas the tissue anatomy is described on a regular rectangular grid, the blood vessels are described as geometrical, curved tracks in 3-D with associated diameter and blood flow. So, for example, it is possible to change the resolution of one independent of the other.

When DIVA is employed to calculate a tissue temperature distribution including effects of discrete vessels, DIVA starts with an initialization routine. In this, possibly lengthy, initialization the relative positions of all the vessels with respect to the tissue are evaluated. For each elementary vessel part, two sets of voxels (volume elements) in the tissue are determined, see Fig. 6. One set consists of the tissue voxels that are located immediately surrounding

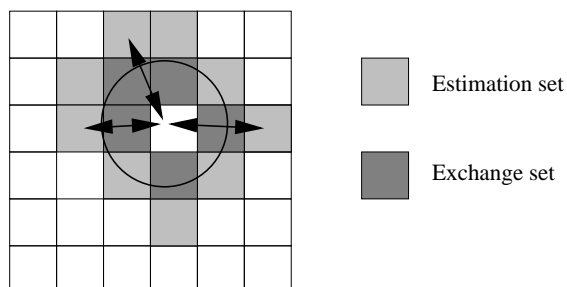


FIGURE 6. A piece of tissue layer with a vessel passing through in perpendicular direction. Dynamically determined estimation set voxels (light grey) and exchange set voxels (dark grey) have been drawn. Arrows show distances from vessel centre to estimation voxels as used in the calculation of the heat flow rates.

the vessel. These voxels are the so-called estimation set voxels, they are used in determining the heat flux between vessel element and tissue. The second set of voxels, named exchange set voxels, are tissue voxels that are within the vessel element and that border estimation set voxels. In these voxels the computed heat exchange between vessel and tissue is accounted for in the tissue. The vessel shown in Fig. 6 happens to be larger than voxel-size. A vessel can alternatively be small compared to the voxels. In that case, to guarantee a non-empty exchange set, the voxels along the vessel centre-line will be included in the exchange set, irrespective of whether the voxel centre is located within the vessel or not. For each such exchange set voxel, the four surrounding voxels will be included in the estimation set.

For the calculation of the time evolution of the temperature in the tissue DIVA uses a finite-difference scheme. The heat exchange between vessels and tissue is calculated using the estimation set. For each of the estimation set voxels, the heat flux at the vessel wall is determined using the analytical solution developed in Sec. 3.1. Each heat flux estimate is based on the tissue node temperature and the exact distance from vessel centre-line to specific tissue voxel centre. The local heat fluxes are calculated using the right part of Eq. (3.2), assuming the local heat flux is the same as if the temperature distribution immediately around the vessel were cylinder symmetric. Every estimation set voxel thus yields an estimate for the flux, and if the temperature distribution is indeed close to cylinder symmetrical the heat flux estimates will be quite close. The heat fluxes are subsequently averaged and multiplied by the vessel element wall area to result in the rate of heat exchange. When multiplied by the time-step the heat exchanged in one iteration is found. In the tissue this exchanged heat is equally distributed over the exchange set voxels associated with the vessel element. As such, the exchange set voxels will not have a temperature that corresponds to an actual temperature. Rather, these voxels that underlie vessel elements have a temperature that makes the heat exchange correct. Detailed testing has shown that the method gives accurate results, even if the temperature distribution around the vessels is quite different from cylindrically symmetric, [12].

The heat exchange must also be accounted for in the vessel. First, DIVA calculates the temperature rise from the heat exchange and the heat capacity of the volume of blood within the vessel element:

$$\Delta T_{\text{bl}} = \frac{\langle \phi_w \rangle 2\pi r_{\text{ves}} \Delta s \Delta t}{\pi r_{\text{ves}}^2 \Delta s \rho_b c_b}$$

Here $\langle \phi_w \rangle$ is the averaged heat flux, and Δs is the length along the vessel element. After adding the respective temperature changes to the temperatures of all the vessel elements that make up the vessel, the next step is to account for the flow of the blood. This is done by shifting the axial temperature profile the appropriate amount for the time-step, and then interpolating the profile to get the new temperatures at the locations of the vessel element centres. For short equilibration lengths, heat fluxes will change rapidly along the length of the vessels. To minimize discretisation errors, in actual fact DIVA interpolates radial heat fluxes between consecutive vessel elements based on the path length traveled.

The vasculature in a real tissue block forms a branching network. DIVA models this as collections of connected vessel segments that form either arterial or venous vessel ‘trees’, see Fig. 7. In an arterial tree the flow is in the direction of the branching; in a venous tree the flow is in the opposite direction. The volume flows in the vessel segments can be individually set in

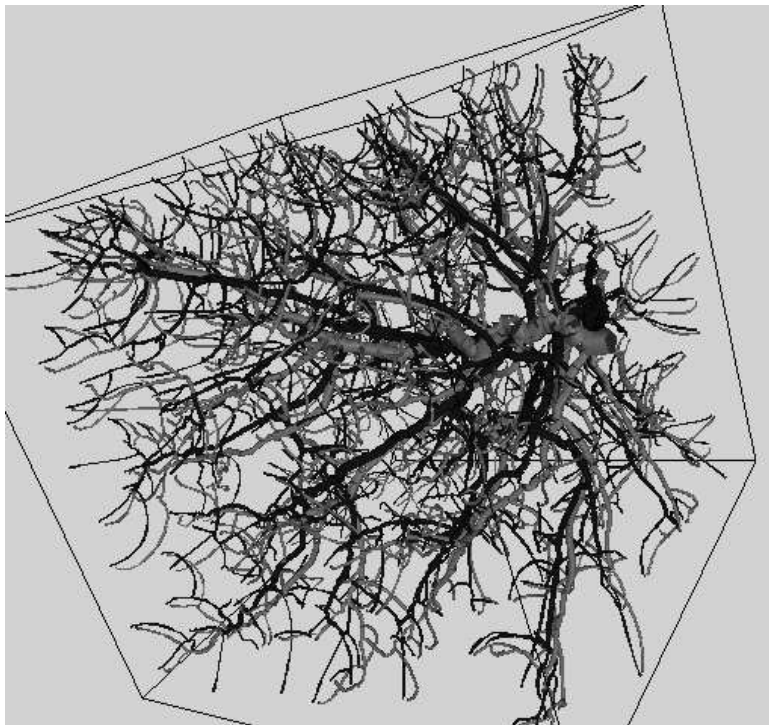


FIGURE 7. Detailed computer-generated arterial and venous vessel trees employed in numerical studies using the DIVA thermal model, [13].

the vessel tree description file. DIVA allows that the sum of the flows in the daughter branches is not equal to the flow in the parent branch. It is indeed desirable that conservation of flow is not guaranteed, as flow lost to vessels that are too small to be modelled discretely can be accounted for this way.

At some point, arterial blood in the model will flow out off the discrete vessel structure. Either at the end of a terminal vessel, or as bleed-off at a branch-point. In clinical practice it is difficult to obtain a detailed description of a patient's vasculature, so this point may be sooner rather than later. In reality the blood will flow in smaller vessels that may still have a (very) significant thermal effect. It may be the case that the blood as it reaches the end of the terminal branches is still far from thermally equilibrated with the surrounding tissue. In that case, the most obvious way forward is to use the Pennes heatsink Eq. (2.1). Naturally, the individual outflow temperatures of the terminal branches are substituted for T_{art} in the heatsink term. It is less obvious *where* the heatsink with this temperature should be applied. There could be very many different terminal branches, with quite different outflow temperatures. Or, for a rather rudimentary vessel network, there could be just a few branches with outflow points that have a very poor correspondence to the actual perfusion distribution. DIVA has several ways of dealing with the outflow. If the discrete vessel network is very detailed, the density of terminal branches may be a reasonable match of the perfusion distribution in the tissue. For that case, the DIVA model offers the possibility of assigning volumes to every branch. These volumes, which might be spheres but can also be different, are assumed to be the tissue volumes that are supplied by blood from the vessel branch in question. From the mass flow in the terminal vessel and the volume of the tissue where the local heatsink is applied, the local perfusion in the affected voxels realised by the branch can be calculated. The heatsink term can now be applied in the tissue. It must be noted that some voxels may receive blood from more than one source, whereas other voxels may not receive any blood at all. Serious artefacts can occur because of this, especially for discrete vasculatures consisting just of a few main branches. In that case it is more appropriate to calculate the average temperature of the blood over all terminating arteries and use this one temperature for the whole tissue volume, together with the local perfusion, to calculate the local heat sink term.

So far, there has been not much mention of the dynamics of the important parameters that govern the heat transfer. Tissue physical properties such as

thermal conductivity are dependent on temperature. Often these variations are neglected, but care should be taken when temperature changes a lot. It should be obvious that change in tissue parameters will be highly significant if heat is used for tissue ablation. Blood flow will also vary under varying circumstances. Blood flow, however, is not just determined by local temperature, but is dependent on temperatures at other body sites too. This will be discussed in greater detail in Sec. 5.2.

Varying the tissue and blood flow parameters does not conceptually make a difference to the thermal model. It aims to follow the time evolution of the temperature distribution, so if the temperature dependencies are known, the information is available to change properties as appropriate each timestep. In practice, it can make the modelling quite a bit more cumbersome.

4. Application: the Temperature Rise Caused by a Mobile Phone

To demonstrate the many aspects that play a role in predicting tissue temperatures including the effects of discrete vessels, as an example the calculation of the rise in temperature caused by a mobile phone will be described. The motivation for this study, [14] were safety concerns over the effect on the brain of the electromagnetic radiation transmitted by a mobile phone's antenna. Safety regulations for the GSM900 frequency band, 880–915 MHz, were based on the thermal effects, but the relation between absorbed power and temperature had not been precisely studied before. Experimental studies have severe limitations; this numerical study set out to compute both power and temperature for a typical adult head.

First, a detailed description of the anatomy had to be obtained. For both the electromagnetic computations and temperature computations a detailed 3-D distribution of physical properties was necessary. For the temperature computations in addition a detailed description of the vasculature was needed, of which the relative positions with respect to the tissue should be known. To obtain the vasculature, phase-contrast Magnetic Resonance Angiography (MRA) scans were made of the head of a volunteer. A characteristic of this MRA technique is that it, as part of the procedure, acquires T_1 -weighted MR images which give information about the solid tissue. These 3-D MR intensity images were used to create a 3-D tissue type distribution using computer-aided segmentation. Because the different tissue types

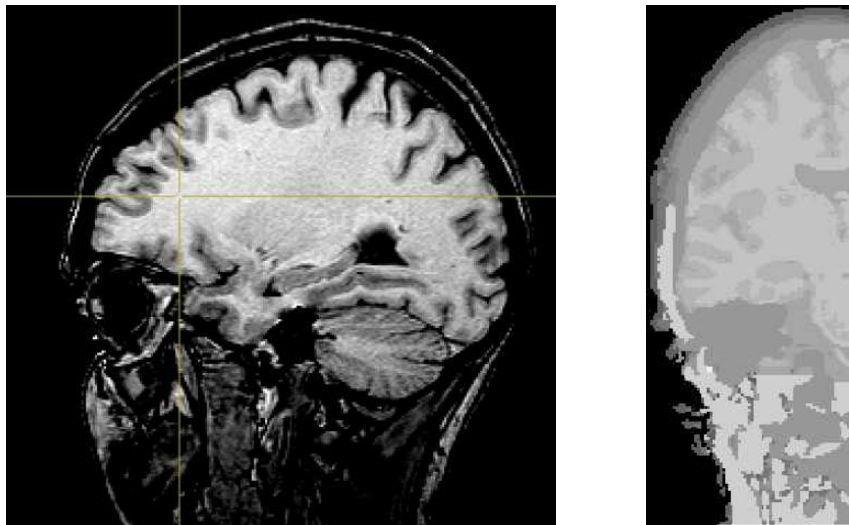


FIGURE 8. Left: a sagittal slice (through an eye) of the original MR data; right: a coronal slice through the segmented 3-D head.

did not have exclusive ranges of MR image values, the segmentation had to be done partially by hand, especially in the thin superficial layers. Distinguished tissue types were, a.o., skin, fat, bone, brain grey matter, white matter, CSF, and muscle. The required distribution of physical properties was now available through a look-up table relating local tissue type with required property. The discrete vasculature was interactively built, tracing the visible vessels in the 3-D MRA images. The result of the tracking was six wireframe skeletons representing vascular trees. These were still rather crude, with smallest diameters approximately 0.7 mm. The appropriate flow directions were determined from an anatomical atlas. Next, corresponding to the different perfusions of the tissue types in the head, smaller vessels were added to these tracked vessels quasi at random. The rationale was that this would best mimic the behaviour of the vascularized tissue; even if the exact locations of the smallest vessels are not correct. For the aim of this study, the statistics of the temperature distribution were far more interesting than the exact locations of the temperature. But also in developing a hyperthermia treatment plan for a specific patient, this 'additional generic vasculature' approach is interesting as it offers the best possible temperature predictions—at the cost of extra computation time.

The electromagnetic power density distribution in the head caused by

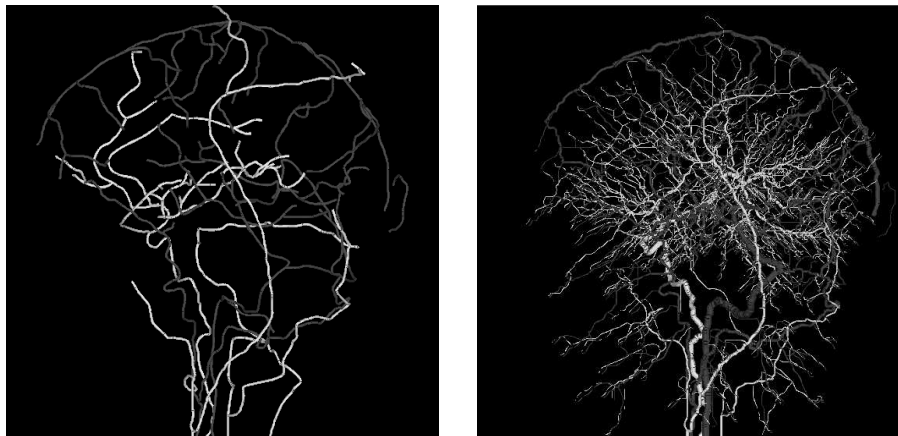


FIGURE 9. Left: a view of the manually tracked vessels. Right: the vasculature including computer generated smaller vessels.

the transmitting dipole antenna was calculated using the finite-difference time domain (FDTD) method. Thermal simulations with the DIVA model determined the stationary temperature distributions in the head with and without operating antenna. Air in the DIVA model (ambient and in the nasal passage) can not flow. The convective and radiative heat transfer from the skin was modelled by fixing the temperature of the air voxels and adjusting the thermal conductivity to the voxel size such that in effect a heat transfer coefficient between skin surface and air of $8 \text{ W K}^{-1} \text{ m}^{-2}$ was modelled.

The typical maximum average output of a mobile phone is 0.25 W. For this power, the highest SAR (Specific Absorption Rate) in a 10 g cube of tissue was 0.91 W kg^{-1} . Because of the different electromagnetic properties of the tissues the EM power absorption does not monotonically decrease with depth, but is higher in the brain than in skull. The temperature distributions with and without power were first calculated for a whole head using the Pennes heatsink equation. Then high resolution ($(1 \text{ mm})^3$ voxels) temperature simulations for the region of interest were done with DIVA and the discrete vasculature, with boundary conditions determined by the heatsink simulations. Because of thermal conduction the temperature rise distribution is much smoother than the EM absorption distribution. The maximum rise caused by the EM absorption is highest in the skin at 0.16°C , and the maximum rise in the brain is 0.11°C .

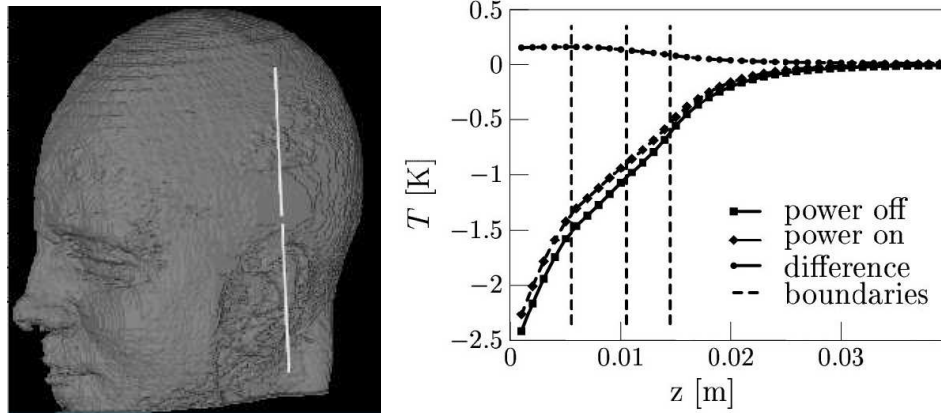


FIGURE 10. Left: the model antenna at its modelled position with respect to the head. Right: the temperature rise caused by the absorbed power, and temperature profiles with, and without power ($T_{\text{art}} \equiv 0$).

5. Whole-body Models, Human Thermoregulation

5.1. Introduction

The human body, when healthy, maintains a core temperature of about 37°C with only small deviations. The core consists of the brain and the internal organs in the trunk, see Fig. 11. Temperatures in the remaining parts of the body—‘the periphery’: surface tissue and the limbs—are much less constant. The core temperature is maintained even though the environmental conditions can vary a lot. This is done partly by behaviour (e.g. clothing, drinking cold or hot liquids), and partly by the body’s thermoregulatory system. Sweating and shivering are easily perceptible thermoregulatory reactions in warm and cold environments respectively. Less perceptible but just as important are changes in blood flow. By increasing or reducing blood flow to the skin, the body can increase or lower the skin temperature and hence its heat transfer to the environment.

There are many parameters that have an influence on the temperature distribution. Heat transfer to the environment through radiation, convection, conduction and evaporation, depend on wall temperatures, ambient temperature distribution, air speed relative to body parts, vapour pressure in air, the sweat response, evaporative and conductive heat resistance of clothing, heat capacities, conductivities, and temperatures of objects in contact, the

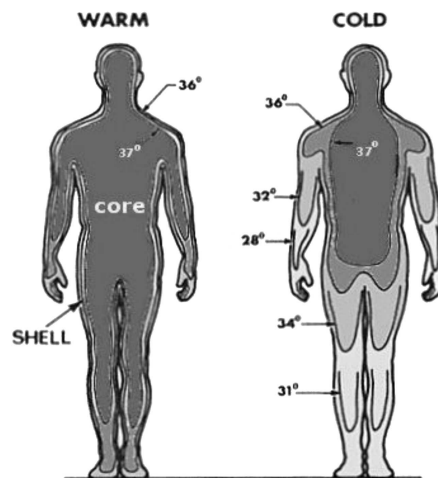


FIGURE 11. The human body can be thought of as consisting of an isothermal core and a periphery with variable temperature.

strength of the sun, etc. Heat production depends on activity level, body weight and composition, local tissue temperatures, shiver response, food intake, drugs, individual differences, illness, sleep deprivation, etc. Heat transfer within the body depends on sizes and locations of blood vessels in all of the body, blood volume flows, the tissue thermal properties, etc.

The applicability of a mathematical model for the calculation of whole-body temperature distributions depends on the precision with which all of the above are described.

First a few words on the biology of thermoregulation. The temperature of the human body is controlled in the hypothalamus. The hypothalamus receives temperature information from temperature receptors in the skin and mucous membranes, and from internal structures, which include the hypothalamus itself. The hypothalamic thermostat works together with other hypothalamic, autonomic and higher nervous thermoregulatory centers to keep the core temperature constant. Some of these thermoregulatory responses are involuntary, passed on by the autonomic nervous system, some are neurohormonal and others are semi-voluntary or voluntary behavioral responses. How exactly the cold and warm thresholds for action are determined is unknown. There is a daily variation, and also influences such as menstrual cycle, food intake, infection, and drugs can vary the thresholds. The difference between the warm and cold thresholds is called the interthreshold range, and this range is typically 0.4°C . The thermoregulatory responses kick in outside

the interthreshold range. Responses can influence either the amount of heat produced by the body, or the rate of heat transfer to the environment.

Low-cost thermoregulatory responses are applied before more costly (in terms of energy, water, minerals) responses. It is relatively inexpensive to decrease or increase blood flow to the skin in order to reduce or enlarge heat transfer from the body to the environment. Hence, vasoaction is used earlier than shivering and sweating. By vasoconstriction or vasodilatation the blood flow to the superficial capillaries can be varied between just over 0% to close to 30% of cardiac output. In a hot environment, sweating is extremely important. Even if the ambient temperature is higher than the body temperature, the body might still transfer heat to the surroundings by sweating if the humidity is not too high. For an adult, the maximum rate of sweating may lie between 10 and 15 liters in 6 hours. Alternatively, in a cold environment the amount of heat produced by the body may be increased by shivering. This uncontrolled muscle action can double or even more than quadruple the total metabolic rate. Non-shivering thermogenesis does also exist in humans, but loses its significance when growing up.

5.2. Mathematical Modelling

Several models have been developed to describe whole-body heat transfer, from just two nodes describing the core and the periphery (e.g. [15]) to multi-segment, multi-layered models. Many of the aspects and their complexities that play a role in accurate modelling of body temperature will be examined here by means of a discussion of the model developed by Dusan Fiala, [16, 17].

5.2.1. Anatomy of the Passive System Two node models may be useful in a somewhat narrow range of simple boundary conditions, and where only core temperature and skin temperature are needed. Typical application of these models is the evaluation of thermal comfort, [18]. To model a wider range of conditions a more detailed description of the anatomy must be used. The anatomy in the model published by Fiala in 1999 was built from ten elements, refining the earlier six segment model by Stolwijk, [19]. The elements describe head, face, neck, thorax, abdomen, shoulders, arms, hands, legs, feet, see Fig. 12. The back of the head is modelled as part of a sphere, all the other elements are cylindrical. Each of the elements consists of concentric layers of different tissue. The different tissue types in the anatomy are brain,

lung, bone, muscle, fat, skin and viscera. Each layer may be divided in several nodes in the radial direction, with a higher density of nodes in the outer layers. Most elements are also divided in several sectors, typically posterior, anterior and inferior, to be able to model inhomogeneous boundary conditions (e.g. smaller radiation view factors for inferior legs). There are no subdivisions in the axial direction. Each element is described by its physical dimensions, the layer thicknesses, and for each layer the tissue properties k_{tis} , ρ_{tis} and c_{tis} , the basal perfusion W_b , and the basal metabolic rate q_m .

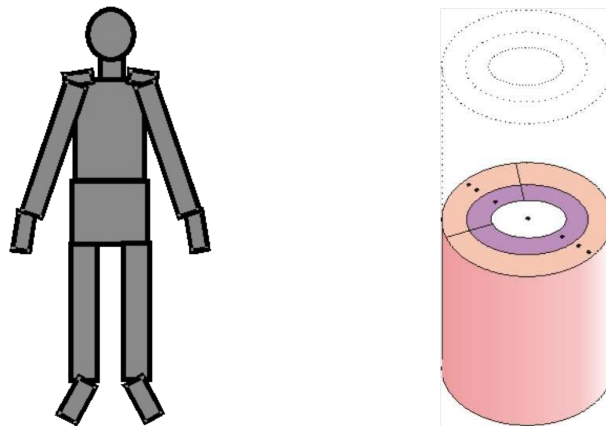


FIGURE 12. Schematic representation of the model anatomy. The model is built from cylinders and a sphere for the head (left); the elements are divided in concentric layers, apart from the core, are divided in sectors (right).

The model anatomy has the length, weight and body composition of an average man. By scaling the dimensions and varying the fat layer also different body types may be modelled. In many ways the anatomy is crude. A cross section through any of the real body parts would look quite a bit different. This goes especially for the two hands which are modelled as one cylinder with length 62 cm and radius 2.26 cm. However, the crude anatomy need not be a problem for the aims of this model. If the different volumes of tissue in the elements, and the surface areas for the elements are correct, both heat production and heat loss may be accurately predicted. The exact locations of the bones in the element won't matter a great deal. On the other hand, an accurate representation of the superficial layers is very important. In the model, the skin has two layers. The inner skin models the cutaneous plexus, where perfusion takes place and metabolic heat is generated. The perfusion in

the inner skin can change a lot under the influence of the thermoregulation. In the outer skin no perfusion or metabolic rate is modelled.

Within the tissue, heat transfer is modelled using the Pennes bioheat equation discussed before, in the appropriate coordinate systems:

$$\rho_{\text{tis}} c_{\text{tis}} \frac{\partial T}{\partial t} = k_{\text{tis}} \left(\frac{\partial^2 T}{\partial r^2} + \frac{\omega}{r} \frac{\partial T}{\partial r} \right) - c_b W_b (T - T_{\text{art}}) + M$$

with $\omega = 1$ for cylindrical coordinates and $\omega = 2$ for spherical coordinates. There is no axial conduction component as all the elements have only one node in the axial direction, and conduction between neighbouring elements is not modelled. In reality, under normal conditions, temperature gradients in the axial direction will be small, so this simplification has not much impact. The arterial temperature T_{art} is the temperature of the blood after countercurrent heat exchange. The method to solve the temperatures is by using a finite-difference scheme to discretize the bioheat equation.

Heat exchange between the blood in afferent arteries and in efferent veins on the way from heart to tissue and vice versa is modelled using countercurrent heat exchange coefficients (Fig. 13):

$$\Phi_{\text{ccx}} = h_x (T_{\text{art}} - T_{\text{vein}}). \quad (5.1)$$

Here, Φ_{ccx} is the total heat exchange between the vessels [W], h_x is the countercurrent heat exchange coefficient [WK^{-1}], T_{art} is the arterial blood tempera-

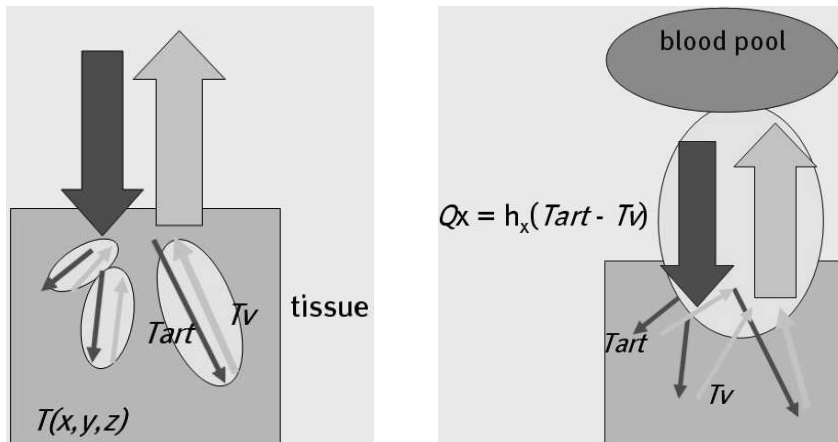


FIGURE 13. Conceptual difference between the local effective conductivity, Eq. (2.2)(cf. highlighted ellipsoids in left figure), and the countercurrent heat exchange coefficient for an element, Eq. (5.1) (highlighted ellipsoid right).

ture after countercurrent heat exchange and T_{vein} is the venous temperature before countercurrent heat exchange. It must be noted that all of the elements have their own countercurrent heat exchange coefficient, large for the hands and feet and zero for head, thorax and abdomen. Values for the coefficients were estimated by a trial-and-error procedure in which simulated local skin temperatures were made to match experimental values. The heat exchange causes a temperature change according to

$$T_{\text{bp}} - T_{\text{art}} = \frac{\Phi_{\text{ccx}}}{\dot{m}_b c_b} = \frac{h_x(T_{\text{art}} - T_{\text{vein}})}{\dot{m}_b c_b} \quad (5.2)$$

with T_{bp} the temperature of the blood pool, i.e. the temperature of the blood as it is in the heart. Directly from Eq. (5.2), for the temperature of the blood in the arteries reaching the tissue we have

$$T_{\text{art}} = \left(\frac{C}{C + h_x} \right) T_{\text{bp}} + \left(\frac{h_x}{C + h_x} \right) T_{\text{vein}}$$

with C the 'capacity rate' of the blood, defined as:

$$C = \dot{m}_b c_b = \rho_b c_b \int W_b \, dV.$$

The venous temperature T_{vein} before countercurrent heat exchange is equal to the perfusion averaged temperature of the tissue in the element. This befits the Pennes bioheat equation, as it implies there is no heat exchange between veins and tissue

$$T_{\text{vein}} = \frac{\int W_b T \, dV}{\int W_b \, dV}.$$

The central bloodpool temperature T_{bp} is every time step calculated as the mixing-cup average temperature over all the elements of the venous blood flows after countercurrent heat exchange. This means there is no heat storage in the blood pool. The venous return temperatures are given by

$$T_{\text{vein,ccx}} = \left(\frac{C}{C + h_x} \right) T_{\text{vein}} + \left(\frac{h_x}{C + h_x} \right) T_{\text{bp}}.$$

Solving for the blood pool temperature:

$$\begin{aligned}
 T_{bp} &= \frac{\sum_i T_{vein,ccx,i} C_i}{\sum_i C_i} \\
 \Rightarrow T_{bp} &= \frac{\sum_i \left[\left(\frac{C_i}{C_i + h_{x,i}} \right) T_{vein} + \left(\frac{h_{x,i}}{C_i + h_{x,i}} \right) T_{bp} \right] C_i}{\sum_i C_i} \\
 \Rightarrow T_{bp} &= \frac{\sum_i \left(\frac{C_i}{C_i + h_{x,i}} \right) \int_{V_i} W_b T \, dV}{\sum_i \left(\frac{C_i}{C_i + h_{x,i}} \right) \int_{V_i} W_b \, dV} \quad (5.3)
 \end{aligned}$$

with C_i the capacity rates for the respective elements. From Eq. (5.3) the blood pool temperature can be calculated from the tissue temperatures.

The metabolic heat production in the tissue is the sum of the basal value q_m and additional terms that may be caused by the local thermoregulation, shivering (part of the global thermoregulation), and exercise. The basal metabolism of the total standard anatomy turns out to be 87 W, which is commensurate with measurements. The metabolism will change if the body is no longer in the thermal neutral situation. For all tissues in the model, the basal metabolic rate varies according to the Q_{10} effect describing the dependence of biological reactions on local tissue temperature

$$q_{m,bas} = q_{m,bas,0} \times 2^{(T-T_0)/10^\circ\text{C}}.$$

If work is being done by the modelled subject, extra heat is generated. In the model, activity level in met (1 met $\equiv 58.2 \text{ W m}^{-2}$) is supplied as input to calculate the actual metabolic heat production. Activity level is a measure of the total power generated by the subject. For a reclining resting person the activity is 0.8 met. Confusingly, next to the unit ‘met’, used mainly by engineers, there is also the unit ‘METS’, used by physiologists, with 1 METS = 3.5 ml oxygen consumption per kg body mass per minute. There is no fixed conversion constant between the two units; for an average man 1 met is roughly 1.25 METS. When work is done on the outside world, this is done with an efficiency that varies but is never much more than 25%. The remainder of the power used goes into heating the muscles. In the Fiala model, the efficiency with which work is done is calculated from the activity level based on

regression analysis. The resulting heat production is divided over the muscle tissue according to the appropriate distribution coefficients for the type of work. Fiala gives two sets of work distribution factors: for standing and for seated work. Of course dedicated distribution factors for specific activities might be used if these are known.

5.2.2. Heat Exchange with the Environment Heat exchange with the environment takes place at the skin, and in the lungs/respiratory tract. The heat exchange by convection between skin surface at T_{sf} and ambient air T_{air} is described by a combined convection coefficient that considers both natural and forced convection

$$\phi_c = h_{c,mix} \times (T_{sf} - T_{air}) . \quad (5.4)$$

The $h_{c,mix}$ are dependent on body location, and on the temperature difference between the surface and air, and the effective airspeed $v_{air,eff}$.

$$h_{c,mix} = \sqrt{a_{nat}\sqrt{T_{sf} - T_{air}} + a_{frc}v_{air,eff} + a_{mix}} .$$

The coefficients a_{nat} , a_{frc} and a_{mix} are different for each element and were obtained from regression analysis of experiments in which local convective heat losses were measured for a heated full-scale manikin. Note that the convective heat transfer does not linearly depend on the temperatures, but that using the linearization in Eq. (5.4) will make it possible to solve for the temperatures using linear algebra. For the standard body, the mean convection coefficient is just over $3 \text{ Wm}^{-2}\text{K}^{-1}$ for a temperature difference of 7°C between surface and air for all body elements. With a body surface area of 1.86 m^2 this rather small difference corresponds to a convective heat loss of about 40 W for the nude body. For a temperature difference of 10°C the convection coefficient increases to about $4.2 \text{ Wm}^{-2}\text{K}^{-1}$, leading to a convective loss of nearly 80 W , almost the total metabolic heat production in rest.

Heat exchange through radiation in the infra-red part of the electromagnetic spectrum, ϕ_{rad} , see Fig. 14, depends on the temperature difference between skin surface and surrounding walls. This is because air is almost completely transparent for infrared radiation. The equation describing radiative heat transfer between two infinite parallel surfaces, one at T_{sf} and the other at T_{wall} is

$$\phi_r = \sigma \frac{T_{sf}^4 - T_{wall}^4}{\frac{1}{\epsilon_{sf}} + \frac{1}{\epsilon_{wall}} - 1}$$



FIGURE 14. Emitted infra-red radiation can be captured and used to visualize surface temperature.

where $\sigma = 5.6710^{-8} \text{ W m}^{-2} \text{ K}^{-2}$ is the Boltzmann constant, and ϵ_{sf} and ϵ_{wall} are the emission coefficient of the object and the opposing wall. The temperatures are the absolute temperatures in Kelvin. Calculation of the radiative heat transfer for different skin sectors of the body requires accounting for the geometry. In the Fiala model this is done by different view factors and introduction of $T_{\text{sr,m}}$ the mean temperature of the surrounding surfaces. The value of $T_{\text{sr,m}}$ is defined as the temperature of a fictitious uniform envelope “seen” by the body sector, which causes the same radiative heat exchange as the actual surroundings. This was linearised as:

$$\begin{aligned}\phi_r &= h_r \times (T_{\text{sf}} - T_{\text{sr,m}}), \\ h_r &= \sigma \epsilon_{\text{sf}} \epsilon_{\text{sr,m}} \psi_{\text{sf-sr,m}} (T_{\text{sf}}^2 + T_{\text{sr,m}}^2) (T_{\text{sf}} + T_{\text{sr,m}}).\end{aligned}$$

with $\psi_{\text{sf-sr,m}}$ the view factor for the sector. The view factors vary from 0.1 to unity. They were determined on the basis of how much individual skin sectors are concealed from the surrounding walls by other body parts. Sets of view factors have been calculated for different body postures. The ratio of the effective radiant area to the real area is 0.80 for standing and 0.74 for the seated standard body. The emissivity of the skin is 0.99, that of the surroundings typically 0.93 indoors.

It is possible that there is significant heat transfer from irradiation by the sun or other high temperature sources. This can be modelled in the skin sectors by terms

$$\phi_{\text{sR}} = \alpha_{\text{sf}} \psi_{\text{sf-sr}} s$$

with α_{sf} the surface absorption coefficient, s [Wm^{-2}] the radiant intensity, and ψ_{sf-sr} the view factor between the skin sector and the surrounding envelope.

Even without thermoregulatory sweat response, there can be heat loss from the skin due to evaporation, caused by the vapour pressure in the skin being higher than in the ambient air. The heat loss caused by this spontaneous evaporation is determined by the skin moisture permeability and the evaporative coefficient at the skin surface. The former, alternatively written as a resistance $1/R_{e,sk}$, has been measured as $0.003 \text{ Wm}^{-2}\text{Pa}^{-1}$. The evaporative coefficient at the skin surface $U_{e,cl}^*$ can be related to the convective heat transfer from the surface by the Lewis number, which gives the ratio of characteristic lengths of diffusion of mass and heat $Le_{\text{air}} = 0.0165 \text{ KPa}^{-1}$:

$$U_{e,cl}^* = Le_{\text{air}} h_{c,\text{mix}}.$$

The spontaneous evaporative heat flux from the nude skin is equal to the driving vapour pressure difference divided by the sum of the resistances

$$\phi_e = \frac{P_{osk,\text{sat}} - P_{v,\text{air}}}{R_{e,sk} + \frac{1}{U_{e,cl}^*}}. \quad (5.5)$$

Here, $P_{osk,\text{sat}}$ is the vapour pressure within the outer skin layer. Because there is always moisture present in the superficial skin layer, this is equal to the saturation vapour pressure for water at the superficial skin temperature. $P_{v,\text{air}}$ is the ambient vapour pressure, it is calculated on the basis of the input ambient temperature and relative humidity.

Clothes play a key role in maintaining thermal comfort. Clothes provide a resistance against convective and radiative heat losses, as well as against evaporation. Clothing insulation, I_{cl} , is measured in Clo units, with $1 \text{ clo} = 0.155 \text{ m}^2\text{KW}^{-1}$. A typical summer clothing ensemble has a clo value of 0.6, whereas winter clothing is about 1 clo. A full polar outfit may get up to 4 clo. The trouble when using a multi-segment thermal model is that these thermal insulation values give information on the overall effect, but don't say anything about insulation values for specific parts of the body. So, instead of using the *overall* thermal insulation values in modelling, these values are first converted into the relevant local values. Fiala did this by utilizing the numerical whole-body model itself to mimick the experiments, determining the overall parameters for a list of garments. The local effect of clothing is described with the use of three local insulation values I_{cl}^* , f_{cl}^* , and i_{cl}^* . The

effect of the air between the skin and the clothes is included in these values. The local effective heat transfer coefficient U_{cl}^* [$\text{Wm}^{-2}\text{K}^{-1}$] of multiple layers of clothing worn on a skin sector is computed as

$$U_{\text{cl}}^* = \frac{1}{\sum_j (I_{\text{cl}}^*)_j + \frac{1}{f_{\text{cl}}^*(h_{\text{c,mix}} + h_r)}}.$$

The parameter $(I_{\text{cl}}^*)_j$ describes the extra thermal insulation of layer j , and f_{cl}^* is the ratio of the outer surface of the clothes, from which convective and radiative transfer to the ambient will occur, to the surface of the skin. It can be seen that in principle heat transfer can also be increased due to the extra layer: this can happen if the extra layer provides little insulation but increases the surface area significantly, cf. cooling fins for electrical components.

Similarly, the evaporative coefficient $U_{\text{e,cl}}^*$ including clothing now becomes

$$U_{\text{e,cl}}^* = \frac{\text{Le}_{\text{air}}}{\sum_j \left(\frac{I_{\text{cl}}^*}{i_{\text{cl}}^*} \right)_j + \frac{1}{f_{\text{cl}}^* h_{\text{c,mix}}}}$$

where i_{cl}^* is the local moisture permeability index of the clothing layer. The heat loss by evaporation can subsequently again be calculated according to Eq. (5.5).

Heat loss also occurs through breathing. There is both a dry heat loss because air will be warmed by the body, and there is heat loss because of evaporation in the lungs and airways. Typically respiratory heat loss accounts for more than 10% and up to 30% of the total heat loss. Since the respiratory heat losses are this significant and vary with environmental conditions and metabolic rate, it is important to model them correctly. The latent heat exchange due to evaporation of water from the lungs depends on the whole body metabolism and the difference between humidity of air breathed in and breathed out, which again depends on the ambient air temperature and the vapour pressure of the ambient air. It is modelled as, [20]

$$E_{\text{rsp}} = 4.373 \times \int q_m \, dV (0.028 - 6.5 \times 10^{-5} T_{\text{air}} - 4.91 \times 10^{-6} P_{v,\text{air}}).$$

The air temperature T_{air} in this relation must be given as the numerical value of the temperature in degrees centigrade, the vapour pressure in Pascal. The relation is valid for a wide range of ambient conditions. The dry heat loss due to the temperature difference between inspired air and expired air can

be calculated from the air flow and the temperature and vapour pressure of the ambient air:

$$C_{\text{rsp}} = 1.948 \times 10^{-3} \times \int q_m \, dV (32.6 - 0.066 \times T_{\text{air}} - 1.96 \times 10^{-4} P_{v,\text{air}}).$$

To account for the respiratory heat loss $E_{\text{rsp}} + C_{\text{rsp}}$ in the body, this loss is distributed over the body elements that model the lungs and the pulmonary tract. Most of the loss is in the nasal cavity, so most of the heat loss in the model is accounted for in the muscle layers of the face element. Only 30% of the respiratory heat loss is debited to the lungs.

5.2.3. Thermoregulation Now that most features of the model's passive system have been described, attention can be directed to the active system, which controls the passive system. The four thermoregulatory responses that need to be modelled are vasoconstriction, vasodilatation, sweating, and shivering.

The thermoregulatory responses in the model are generated by differences between actual and thermoneutral temperatures for the sensors in the body. The relevant temperatures are that of the hypothalamus, i.e. the temperature of the core node of the head, and the mean skin temperature. The thermoneutral temperatures are those temperatures that are obtained for the body if the passive model with basal values for blood flow, and metabolic rates is modelled in a thermoneutral environment. The thermoneutral state is calculated for a nude, reclining subject in an ambient temperature of 30°C, relative humidity 40%, and relative air velocity 0.05 m/s. In this situation the passive system predicts a hypothalamus temperature of 37.0°C, and a mean skin temperature of 34.4°C. Respective contributions for the heat losses in this thermoneutral state are 21.8 W for convection, 36.9 W for radiation, 19.3 W for evaporation through the skin, and 8.9 W for respiratory losses (adding up to 87 W). Basal skin flow is 0.4 l min⁻¹.

The thermoregulatory relations were found by using regression analysis on measured data from a large number of experiments. It must be noted that the thermoregulatory relations described below were devised with the use of a particular passive model. The control relations work quite well, and will give a good impression of the qualitative behaviour of the thermoregulatory responses. However, these specific relations are only accurate in conjunction with the passive system with which they were developed. Significant changes in the passive system, whereas they are refinements in implementation or

different data for parameters such as skin blood flow, will require repetition of the process of developing the thermoregulatory relations that constitute the active system.

To find a control relation for shivering as a function of deviations from the thermoneutral state, about ten sets of experiments from the literature were evaluated. The heat produced by shivering was obtained by measuring the total heat output and subtracting the other contributions (basal metabolic rate and work-related). In a specific set of experiments subjects were exposed to a sudden change in environmental temperature from 24°C to 5°C. When the measured shivering was related to the temperature error signal from the skin $\Delta T_{sk,m} \equiv T_{sk,m} - T_{sk,m,0}$, it was found that also the dynamics of the skin temperature played a role. Regression analysis on the full set of experiments involving cold exposure also showed a dependence of shivering on the core temperature.

The resulting control equation for the shiver parameter, Sh [W], in the Fiala model has the form

$$\begin{aligned} Sh = 10 & [\tanh(0.48\Delta T_{sk,m} + 3.62) - 1] \Delta T_{sk,m} - 27.9\Delta T_{hy} \\ & + 1.7\Delta T_{sk,m} \frac{dT_{sk,m}}{dt} - 28.6 \end{aligned}$$

In this relation, temperature differences must be entered as the numerical value of the difference in degrees centigrade. It has been found that there is a maximum to the heat that can be generated by shivering, roughly 300 to 380 W for an adult. Accordingly, shivering in the model is capped at 350 W. The place in the body where the heat is generated is in the muscle tissue of several elements. So-called shivering distribution coefficients apportion the total heat production over the elements of the body. By far the biggest portions of the shivering power are generated in the thorax (distribution coefficient 63.5%) and abdomen (24%). After the heat production for an element has been determined, this is shared out over the muscle nodes according to volume. The extra metabolic activity is accompanied by a corresponding rise in blood flow to the muscle.

Vasoaction is modelled by two control parameters that manipulate skin blood flow of an element i , SBF $_i$ [$m^3 s^{-1}$], in the following way

$$\beta_i = \frac{\beta_{0,i} + a_{dl,i}Dl}{1 + a_{cs,i}Cs \times e^{-\eta Dl}} \times 2^{\frac{T_{sk,i} - T_{sk,i,0}}{10^\circ C}}. \quad (5.6)$$

Here, $\beta_i = \rho_b c_b SBF_i [\text{WK}^{-1}]$, whereas $\beta_{0,i}$ is the corresponding basal value. $Cs[-]$, is the vasoconstriction control parameter, and Dl is the vasodilatation control parameter $[\text{WK}^{-1}]$. $a_{dl,i}$ and $a_{cs,i}$ are distribution coefficients. The Cs and Dl control parameters are whole-body parameters, so the same for all elements. Local temperatures only influence the skin blood flow through the last factor that doubles the flow for every 10°C temperature rise. This is similar but different from the other tissues where increase in blood flow is explicitly driven by the extra metabolism due to the Q_{10} effect.

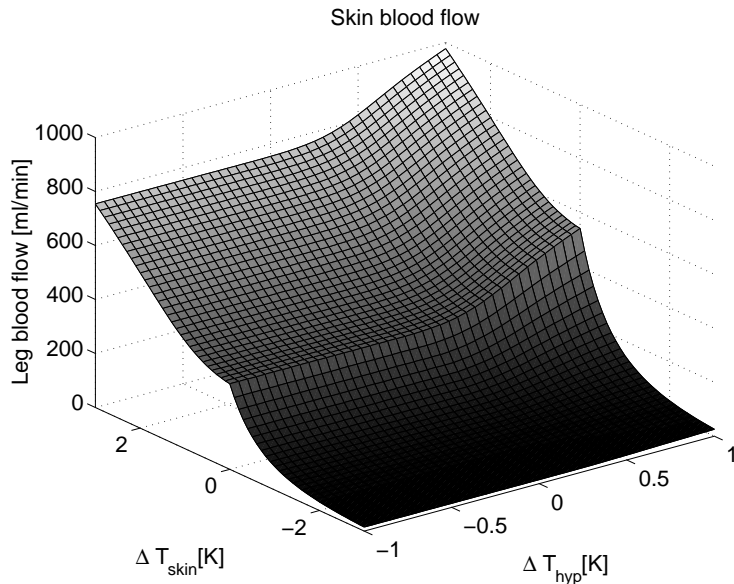


FIGURE 15. Skin blood flow in the leg as a function of difference between neutral temperatures and actual mean skin and hypothalamic temperatures. Total skin blood flow over all elements is bound by a maximum, not considered here.

The vasoconstriction parameter was a.o. derived from internal temperatures of subjects in the cold. From the regression analysis, the following control equation for the vasoconstriction parameter Cs was found

$$Cs = 35 [\tanh(0.34\Delta T_{sk,m} + 1.07) - 1] \Delta T_{sk,m} + 3.9 \Delta T_{sk,m} \frac{dT_{sk,m}}{dt} \quad (5.7)$$

Thus, also the vasoconstriction is dependent on dynamic skin temperature behaviour, but it is not directly dependent on the hypothalamus temperature. The relation is only valid for low temperatures: if the vasoconstriction parameter falls below zero, the value zero is used in Eq. (5.6). Likewise, the

dynamic term in Eq. (5.7) is only pertinent for dropping skin temperatures and is omitted for rising temperatures.

The regression analysis for the vasodilatation parameter Dl involved experiments in hot environment and/or exercise. The analysis resulted in

$$\begin{aligned} Dl = & 21 [\tanh(0.79\Delta T_{sk,m} - 0.70) + 1] \Delta T_{sk,m} \\ & + 32 [\tanh(3.29\Delta T_{hy} - 1.46) + 1] \Delta T_{hy}. \end{aligned}$$

Again, only if the relation results in a positive value for Dl is the outcome used in Eq. (5.6), otherwise zero is used. Also, there is a maximum to the total skin blood flow. This maximum is dependent on how much of the cardiac output is required by the muscles.

The heat loss from sweating was obtained from experiments by taking the overall measured latent loss and subtracting respiratory losses and the predicted amount of spontaneous moisture diffusion through the skin $E_{sw} = E_{exp} - (E_{rsp} + E_{diff})$ [W]. In the regression analysis, the sweat control variable Sw [g min^{-1}] was derived from the heat loss through

$$Sw = \frac{E_{sw} \times 6 \times 10^4}{\lambda_{H_2O} \sum_i a_{sw,i} \times 2^{\frac{T_{sk,i} - T_{sk,i,0}}{10^\circ C}}}.$$

The number in the numerator is for the unit conversion from kg/s to the more convenient g/min. The $\lambda_{H_2O} = 2256 \text{ kJ kg}^{-1}$ is the heat of vaporization of water. The last factor in the denominator takes into account how eventually the local sweat rates are calculated from the sweat parameter. That is, local sweat rates are dependent on the local skin temperature

$$Sw_i = a_{sw,i} \times Sw \times 2^{\frac{T_{sk,i} - T_{sk,i,0}}{10^\circ C}}.$$

In a hot environment a rise in skin temperature will trigger sweating, whereas an increase in core temperature is the main driving influence during exercise in cool conditions. The regression analysis resulted in

$$\begin{aligned} Sw = & [0.8 \tanh(0.59\Delta T_{sk,m} - 0.19) + 1.2] \Delta T_{sk,m} \\ & + [5.7 \tanh(1.98\Delta T_{hy} - 1.03) + 6.3] \Delta T_{hy}. \end{aligned}$$

This relation takes into account that a lower than normal hypothalamic temperature counteracts the effect on sweating of higher than normal skin temperatures, and vice versa. The maximum rate of sweating for an adult is

approximately 30 g min^{-1} , and this is the value at which sweating is capped in the model. The resulting evaporation heat loss including sweating can be found by adding the extra vapour flow to the spontaneous diffusion in the skin:

$$\phi_{e,i} = U_{e,cl}^* (P_{sk,i} - P_{v,air}) = \frac{\lambda_{H_2O}}{A_{sk,i}} S_{Wi} + \frac{P_{osk,i,sat} - P_{sk,i}}{R_{e,sk}} \quad (5.8)$$

Because the vapour pressure at the skin surface $P_{sk,i}$ can be evaluated by re-arranging Eq. (5.8), the evaporative heat loss can be calculated. A further complication is that sweat is accumulated if the skin surface vapour pressure is higher than the saturation vapour pressure. The model does account for storage of sweat in that case.

6. Discussion of the Whole-body Thermal Models

For the many graphs of the regression analysis and examples of the behaviour of the resulting model under different conditions the reader is referred to the original papers, [16, 17]. By and large the model does well in predicting the average thermal behaviour of groups subjected to a variety of thermal conditions. This is to be expected as over the test group, both the anatomy and also the less tangible stable and transient individual characteristics will tend to the average. It is of course a prerequisite that the base underlying model system gives a reasonable description of the real system, and the thermoregulatory relations are based on a large amount of data. However, even the average experimental results for groups are sometimes significantly different from model predictions. This can in part be attributed to the usually small group size for this type of experiments, but also to systematic differences between what may seem similar experiments. Typically, to reduce confounding factors, an experiment on a group will be standardized with respect to initial conditions, but this can lead to some systematic differences between experiments. Cultural, climatic, and population differences between studies may also play a role.

Not every single feature of the numerical model by Fiala has been included in the above description. Nonetheless, the account should have given the interested reader a feeling for the complexities involved. It should not come as a surprise that the model will not as a simple matter predict highly accurate absolute temperature distributions for an arbitrary individual under every succession of conditions. To get good individual predictions from the model,

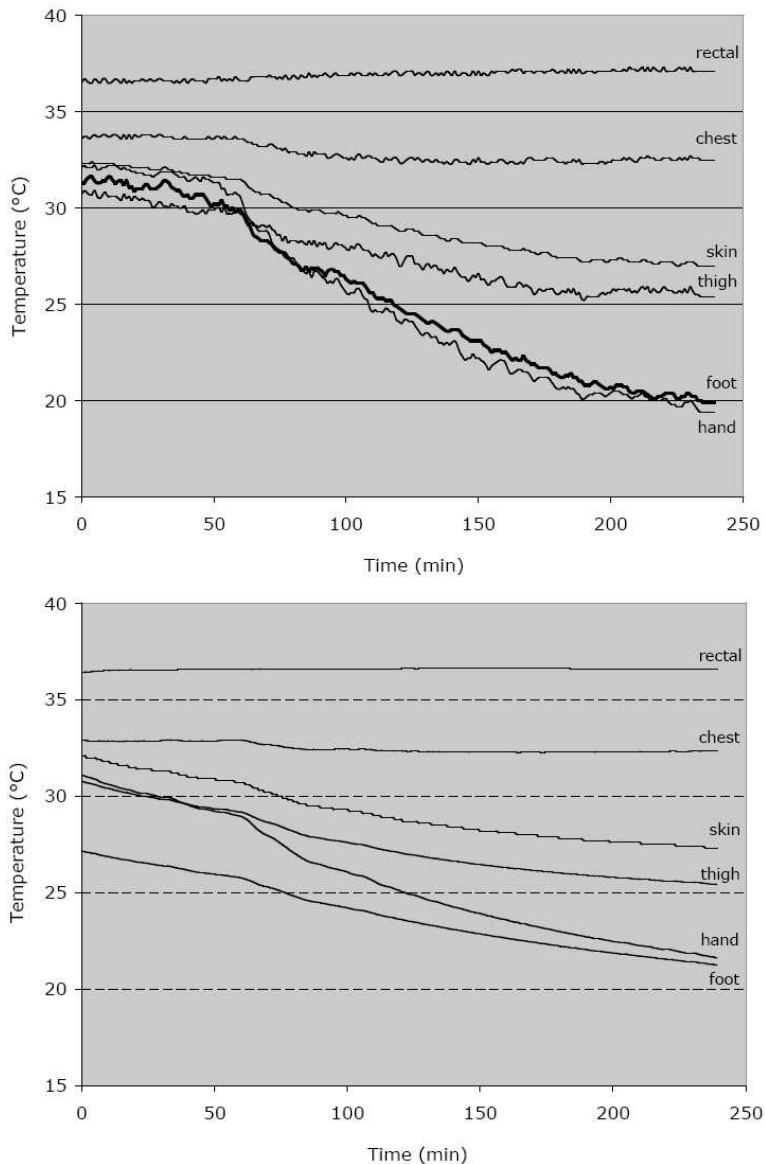


FIGURE 16. Measured (top) and modelled (bottom) temperatures for cold exposure, Fiala model adapted for the individual subject, [21].

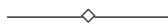
the model should be tailored to the individual, Fig. 16. Adapting the model anatomy of the standard human to reflect the true height, weight and fat percentage of the individual may be easily done. Other individual properties, such as the basal metabolic rate, may be less readily measured, as well as they

might be less constant in time. It will be difficult to very precisely predict the temperature distribution for an individual in irregular conditions. If there is a clinical interest in predicting these temperatures, data should be collected for these specific conditions and the model correspondingly updated. This may eventually lead to an even more dynamic model. For the individual patient, the accuracy of predictions can be further increased by updating characteristics of the model real-time on the basis of measurements during the procedure.

References

1. H.H. PENNES, *Analysis of tissue and arterial blood temperature in the resting human forearm*, Journal of Applied Physiology, **1**:93–122, 1948
2. W. WULFF, *The energy conservation equation for living tissue*, IEEE Transactions on Biomedical Engineering, **21**:494–495, 1974
3. M.M. CHEN and K.R. HOLMES, *Microvascular contributions in tissue heat transfer*, Annals of the New York Academy of Sciences, **335**:137–151, 1980
4. S. WEINBAUM and L.M. JIJI, *A new simplified bioheat equation for the effect of local average tissue temperature*, ASME Journal of Biomechanical Engineering, **107**:131–139, 1985
5. J.W. BAISH, P.S. AYYASWAMY, and K.R. FOSTER, *Heat transport mechanisms in vascular tissues: A model comparison*, ASME Journal of Biomechanical Engineering, **108**:324–331, 1986
6. W.M. KAYS and M.E. CRAWFORD, *Convective heat and mass transfer*, McGraw-Hill Book Company, New York 1980
7. J. CREZEE, J. MOOIBROEK, C.K. Bos, and J.J.W. LAGENDIJK, *Interstitial heating: experiments in artificially perfused tongues*, Physics in Medicine and Biology, **36**:823–833, 1991
8. R.J. RAWNSLEY, R.B. ROEMER, and A.W. DUTTON, *The simulation of discrete vessel effects in experimental hyperthermia*, Journal of Biomechanical Engineering, **116**:256–262, 1994
9. J.F. VAN DER KOIJK, J. CREZEE, G.M.J. VAN LEEUWEN, J.J. BATTERMANN, and J.J.W. LAGENDIJK, *Dose uniformity in MECS interstitial hyperthermia: the impact of longitudinal control in model anatomies*, Physics in Medicine and Biology, **41**:429–444, 1996
10. J. CREZEE and J.J.W. LAGENDIJK, *Temperature uniformity during hyperthermia: the impact of large vessels*, Physics in Medicine and Biology, **37**:1321–1337, 1992
11. A.N.T.J. KOTTE, G.M.J. VAN LEEUWEN, J. DE BREE, J.K. VAN DER KOIJK, and J.J.W. LAGENDIJK, *A description of discrete vessel segments in thermal modelling of tissues*, Physics in Medicine and Biology, **41**:865–884, 1996

12. G.M.J. VAN LEEUWEN, A.N.T.J. KOTTE, J. CREZEE, and J.J.W. LAGENDIJK, *Tests of the geometrical description of blood vessels in a thermal model using counter-current geometries*, Physics in Medicine and Biology, **42**:1515–1532, 1997
13. G.M.J. VAN LEEUWEN, *Numerical modelling of heat transfer in hyperthermia*, PhD Thesis, Universiteit Utrecht, 1998
14. G.M.J. VAN LEEUWEN, J.J.W. LAGENDIJK, B.J.A.M. VAN LEERSUM, A.P.M. ZWAMBORN, S.N. HORNSLETH, and A.N.T.J. KOTTE, *Calculation of change in brain temperatures due to exposure to a mobile phone*, Physics in Medicine and Biology, **44**:2367–2379, 1999
15. A.P. GAGGE, J.A.J. STOLWIJK, and Y. NISHI, *An effective temperature scale based on a simple model of human physiological regulatory response*, ASHRAE Trans, **77**:247–257, 1971
16. D. FIALA, K.J. LOMAS, and M. STOHRER, *A computer model of human thermoregulation for a wide range of environmental conditions: The passive system*, Journal of Applied Physiology, **87**:1957–1972, 1999
17. D. FIALA, K.J. LOMAS, and M STOHRER, *Computer prediction of human thermoregulatory and temperature responses to a wide range of environmental conditions*, International Journal of Biometeorology, **45**:143–159, 2001
18. P. HÖPPE, *The physiological equivalent temperature—a universal index for the biometeorological assessment of the thermal environment*, International Journal of Biometeorology, **43**:71–75, 1999
19. J.A.J. STOLWIJK, *A mathematical model of physiological temperature regulation in man*, NASA contractor report CR-1855, Washington DC, 1971
20. P.O. FANGER, Thermal Comfort—Analysis and Applications in Environmental Engineering, McGraw-Hill Book Company, New York 1973
21. W.D. VAN MARKEN LICHTENBELT, A.J.H. FRIJNS, A.M.J. VAN OOIJEN, D. FIALA, A. KESTER, and A.A. VAN STEENHOVEN, *Validation of an individualized model of human thermoregulation for predicting responses to cold*, submitted



Do Doppler Systems Color Arteries Red?

ARNOLD P.G. HOEKS¹ and ROBERT S. RENEMAN²

Cardiovascular Research Institute Maastricht (CARIM)

¹*Dept. Biophysics, CARIM*

²*Dept. Physiology, CARIM*

University Maastricht

PO BOX 616, 6200 MD Maastricht, the Netherlands

¹*A.Hoeks@bf.unimaas.nl*

²*R.Reneman@fys.unimaas.nl*

Ultrasound techniques provide in real-time detailed information about the structure and hemodynamic functioning of the cardiovascular system. The Doppler technique, either continuous wave (CW) or pulsed, facilitates direct measurement of the time-dependent blood velocity at a specific site. The gradual development of Doppler techniques from the “simple” CW systems to advanced color Doppler systems has expanded the possibilities to relate deviant blood flow velocity behaviour to changes in structure and functioning of the vessel wall. This chapter will discuss in detail the signal analytic aspects of Doppler instrumentation, and address the trade-offs and the interrelationships between resolution in the time, spatial and frequency domain.

Key words: *Doppler systems, instrumentation, velocity estimation, signal processing*

1. Introduction

Since the introduction of ultrasound Doppler systems for human applications in 1960 by Satomura [1] and coincidentally by Franklin [2], the Doppler technique to estimate the blood velocity pattern gradually gained an established place in the assessment and evaluation of the dynamic characteristics of the arterial and venous circulation and in the diagnosis of vascular disorders. To appreciate its value in clinical practice, as will be demonstrated in the accompanying chapters, we will first address the concept and evolution of Doppler systems and demonstrate their applicability by providing a few examples.

If sound waves with a frequency f_e are reflected by a moving acoustical interface, then the interface will induce a shift f_d in the sound frequency proportional to the velocity v of the interface. This is known as the Doppler principle [3], originally described for light. It was the Dutchman Buys Ballot who described the phenomenon for sound waves, [4] after an attempt to falsify the concept for sound using musicians with absolute hearing and a moving train. To demonstrate the principle, consider a single wave impinging perpendicularly on an interface with velocity v in the same direction as the incident sound. The wave will have a velocity relative to the interface of $c + v$, while after reflection the relative velocity is changed to $c - v$ with c being the speed of sound in the medium. The time required for total reflection of one wavelength λ equals $\lambda/(c + v)$. In the meantime the front of the wave has covered a distance λ' with $\lambda'(f_e + f_d) = c$ and $\lambda f_e = c$. Solving the above relations for f_d results in $f_d = 2f_e v/(c - v)$. Since c in tissue is far much greater (about 1500 m/s) than blood velocities (v will generally not exceed 1 m/s) the expression may be simplified to $f_d = 2f_e v/c$ for applications in flowing blood. If the paths of the interface (Fig. 1) and of the sound waves are inclined with respect to each other, with an enclosed angle α , the interface velocity with respect to the sound waves will be reduced to $v \cos \alpha$ and the expression becomes

$$f_d = \frac{2f_e v \cos \alpha}{c}. \quad (1.1)$$

For blood flow examinations transducers are employed to convert electric signals to sound and the reflected and backscattered signal to electric signals. Only the velocity component relative to the sound transducer (emitter and receiver) contributes to the Doppler effect (Fig. 1). If the enclosed angle is 90° (perpendicular observation), the Doppler shift frequency will be zero, while for angles between 90° and 270° the shift frequency will be negative.

Assuming a relative velocity of blood of $v = 1$ m/s and an emission frequency of 5 MHz the Doppler shift frequency will be $f_d = 6.1$ kHz ($c = 1500$ m/s). Generally, blood flow velocities are below 1 m/s, only in and im-

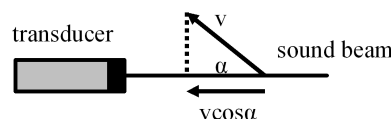


FIGURE 1. Only the velocity component relative to the transducer contributes to the Doppler effect.

mediately distal to a stenosis velocities up to 5 m/s may be reached. Hence, the Doppler shift frequencies are in the audio range and can be evaluated aurally.

Angles unequal to zero will only lead to a received signal, if the dimension of the reflector is small with respect to the wavelength of the ultrasound used, causing scattering of the sound in all directions. This requirement is met by the red blood cells with an ellipsoid dimension of 5–8 μm . If they travel with different velocities, then also a spectrum of Doppler frequencies rather than a single frequency component will be received [5]. From a physical and statistical point of view this is too simplistic because, due to the tight packing (6 million cells per mm^3), for any blood cell another can be found in the direct neighborhood that will cancel the backscattered wave. However, for blood flows the Doppler effect originates from variations in packaging density rather than from individual cells.

Although the concept of Doppler systems seems to be rather simple, they heavily rely on basic signal analysis concepts. The most fundamental one is the relation between the effective signal bandwidth B and the effective duration T of the corresponding impulse response [6]: $BT \geq 0.5$. The effective bandwidth is defined as the square root of the mean squared deviation of the central frequency; the same definition applies to the effective duration of the impulse response. The minimum value of 0.5 for the time-bandwidth product is attained for a Gaussian shaped spectral distribution (the corresponding impulse response is then also Gaussian shaped). In daily practice the above rule is simplified to $BT = 1$ with B and T the width of the spectral distribution and the impulse response at half the maximum value, respectively (Fig. 2). For a bandpass filter with a width of 2 MHz the duration will be 0.5 μs and increasing the bandwidth will reduce the duration. For a low-

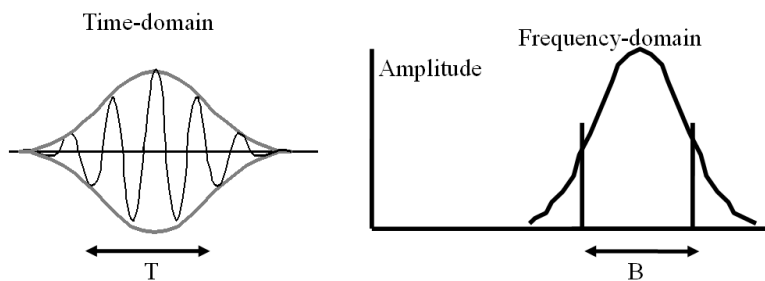


FIGURE 2. The product of the duration T and bandwidth B is approximately 1.

pass filter both positive and negative frequencies should be considered, which results in a bandwidth of twice the cut-off frequency.

As indicated above, an observation interval T allows a frequency resolution of Δf Hz. Recalling the Doppler equation (Eq. (1.1)), a spectral resolution of Δf_d relates to a velocity resolution Δv as:

$$\Delta f_d = \frac{2f_e \Delta v \cos \alpha}{c} \quad \text{or} \quad \Delta v = \frac{c}{2T f_e \cos \alpha}. \quad (1.2)$$

Hence, for the same observation interval T the velocity resolution will improve with a higher emission frequency (or an observation angle close to zero). On the other hand, in tissue the sound energy relative to emitted energy decreases proportional with the sound frequency and the path, setting an upper bound on the incident frequency.

In vascular studies and in vascular medicine the blood velocity is measured by placing a probe, containing the transducers for emission and reception of ultrasound, on the skin. The direction of the probe is interactively varied to locate an artery until a balance is found between the amplitude and the pitch of the Doppler ultrasound. As we will show, an important class of Doppler systems needs only one transducer, acting alternatively as emitter and receiver.

2. Continuous Wave (CW) Systems

2.1. Hardware Configuration

The simplest configuration to extract the Doppler shift information from the blood velocity distribution is a Continuous Wave (CW) system. It employs separate transducers (Fig. 3) for emission and reception of ultrasound (although theoretically also a single transducer would suffice). The sensitivity range of the probe is confined within the intersection of the emitted beam

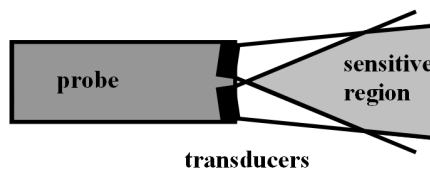


FIGURE 3. A CW probe has separate transducers for continuous emission and reception of ultrasound waves. The sensitive region of the probe is where both beams overlap.

and the sensitivity range of the receiver crystal (Fig. 3). Hence, the sample volume of a CW Doppler system is quite large and does not convey information about the depth the Doppler signals are originating from. On the other hand the system exhibits a high sensitivity, making it easy to locate a vessel of interest by listening to the Doppler sound. Nowadays the Doppler unit to emit and process the received signal is the size of an average sized calculator and is therefore popular by medical doctors to check rapidly whether an artery is still patent.

Before we go into the details of signal processing in Doppler systems, we will first discuss the concept of complex signals, which can be considered as an extension of real signals as we observe in common life. Any cosine (or sine) wave is described by its amplitude A and frequency ω , e.g. the signal $s(t) = A \cos(\omega t)$, where t denotes time. The argument of the cosine is also called the (instantaneous) phase of the signal. Since $s(t)$ has 2 degrees of freedom it is impossible to extract unambiguously the current phase or amplitude from a sample (or a few samples) of an unknown signal. This problem is solved by considering the sample as a projection of a complex signal on the (real) x-axis (Fig. 4). The sequence of x-axis samples is called the in-phase signal as opposed to the sequence of the corresponding projections on the y-axis (imaginary axis) denoted as in-quadrature signal. The amplitude of the signal is the radius (the square root of the sum of squares of the real and imaginary signals), while the instantaneous phase follows from the arctangent of the imaginary and real component. The combination of a real and imaginary signal is called a complex signal. The in-quadrature signal is derived from

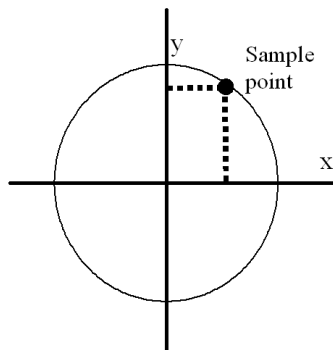


FIGURE 4. A complex signal is composed of a real (in-phase) and an imaginary (in-quadrature) component.

the in-phase signal by shifting the phase over 90 degrees independent of the frequency, i.e. the cosine-component is converted into a sine-component. This can be accomplished in the time-domain as well as in the frequency domain. A complex signal is commonly denoted as $s(t) = A(t) \exp(j\omega t) = A(t)(\cos(\omega t) + j \sin(\omega t))$, with $A(t)$ the amplitude of the envelope of the signal, $\omega = 2\pi f$ the angular frequency and j the symbol for the complex component.

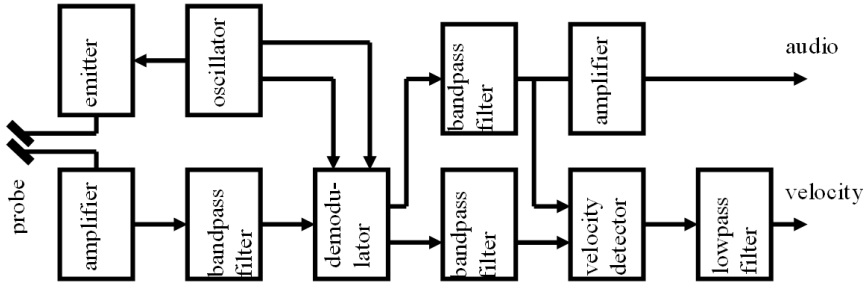


FIGURE 5. Block diagram of CW Doppler system

The basic configuration of a CW Doppler system is depicted in Fig. 5. An internal oscillator provides the emitter amplifier with a sine wave with a constant amplitude and frequency, the emission frequency. The receiver amplifier has a large dynamic range to accommodate the large echoes from structures, e.g. vessel walls, as well as the low amplitude signals backscattered by the red blood cells. The bandpass filter suppresses all noise in the received signal outside the bandwidth of interest (30 kHz) to improve the signal to noise ratio (SNR). The demodulator is a crucial element in Doppler systems, because it shifts the frequency spectrum centered at the emission frequency to zero frequency by multiplying its input signal $r(t) = A(t) \cos((\omega_e + \omega_d)t)$ by the quadrature oscillator signal:

$$\begin{aligned}
 d(t) &= r(t)\{\cos(\omega_e t) + j \sin(\omega_e t)\} = A(t) \cos((\omega_e + \omega_d)t)\{\cos(\omega_e t) + j \sin(\omega_e t)\} \\
 &= 0.5A(t)[\cos(\omega_d t) + \cos((2\omega_e + \omega_d)t) + j\{\sin(\omega_d t) + \sin((2\omega_e + \omega_d)t)\}].
 \end{aligned} \tag{2.1}$$

The imaginary (labeled with j) and real components are processed by separate channels. The signal components at a double emission frequency are effectively suppressed by a lowpass audio filter with a cut-off frequency of about 15 kHz, depending on the emission frequency employed and the

anticipated maximum velocity. The demodulation process as indicated in Eq. (2.1) applies for all frequency components the received signal is composed of, so also for a signal with zero or a very low Doppler frequency, presumably originating from stationary or slowly moving structures, e.g. vessel walls. Reflections of the latter may have amplitudes exceeding the amplitude of blood induced signals by at least a factor of 100 (40–60 dB). To suppress these low frequencies the audio filter is converted to a bandpass filter, where the lower cut-off frequency (in the range of 300 to 600 Hz) sets also a lower bound for the (blood) velocities that can be detected. If this cut-off frequency is set too low the echoes from strongly reflecting structures will interfere with and may even temporarily dominate the audio signal to determine [7]. Generally the wall filter can be set at a lower value for the same emission frequency, if venous flows are investigated.

2.2. Audio Evaluation

The demodulated bandpass filtered quadrature signals contain Doppler shift frequencies in the audio range. Both quadrature channels sound exactly the same. Aural evaluation may be impaired if the Doppler information of both a vein and an artery is conveyed. However, generally the vein and artery will have an opposite flow direction with respect to the probe. Under this condition the arterial and venous signals can be separated by a proper combination of the quadrature signals (Fig. 6). The cosine function is even, i.e. $\cos(-\omega_d) = \cos(\omega_d)$, while the sine function is odd, i.e. $\sin(-\omega_d) = -\sin(\omega_d)$. Phase shifting the cosine over 90 degrees independent of frequency (Hilbert filter) yields a sine component with the same sign as the quadrature compo-

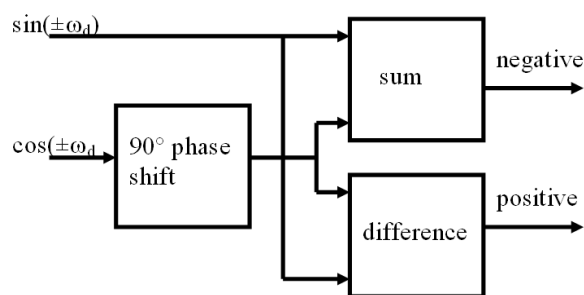


FIGURE 6. With a 90° phase shifter separate audio-outputs for positive and negative Doppler frequencies can be derived from the quadrature Doppler signal.

ment for positive frequencies, but an opposite sign for negative frequencies. Hence, the sum will give only an output for positive frequencies, while the difference becomes non-zero for negative frequencies. In this way velocity direction information is recovered.

2.3. Velocity Estimation

An important characteristic of a Doppler system is its capability to estimate the instantaneous frequency averaged over a short interval (e.g. 20 ms) within the observed region [8]. The Doppler equation relates the average frequency to an average (blood) velocity. Usually in CW Doppler systems the principle of a zero crossing counter is used to estimate the average frequency. For this purpose only the sign of the quadrature signals is retained, so at any instant it is only known in which quadrant the phase vector is located, but its precise direction (phase) remains unknown (Fig. 7). If the phase vector changes from the third to the fourth quadrant only the in-phase component will change sign from negative to positive. Under that condition a short (0.1 ms) positive pulse is generated. Alternatively, if the in-phase component changes sign in the reverse direction, while the in-quadrature component remains negative, i.e. the phase vector moves from the fourth to the third quadrant, a negative pulse is generated. Subsequently the positive and negative pulses are low pass filtered with a cut-off frequency of about 20 to 30 Hz (response time 50 to 30 ms), yielding a velocity output (after proper calibration) as a continuous function of time. The filter process may be applied to the sum of positive and negative pulses or for both outputs separately. One should realize that the sum of the velocity outputs is not equal to the velocity of the summed outputs, because in the first case the amplitude information

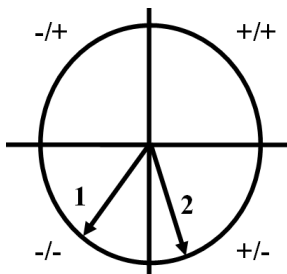


FIGURE 7. A quadrature sign processor (zero crossing detector) allows detection of velocity direction.

is not properly taken into account. The output of a zero crossing detector is only accurate for signals with a narrow bandwidth with respect to the center frequency, but the error will be substantial (10%) for wide band signals [9, 10]. Moreover, under poor signal-to-noise conditions large errors may occur, especially for zero crossings detectors acting on only a one-way phase shift direction. We will later discuss a more advanced option to estimate the average velocity.

2.4. Spectral Analysis

Any signal in the time domain can be decomposed into its constituent components in the frequency domain (Fourier analysis). To allow proper interpretation the signal should be stationary within a given time window, i.e. its statistical characteristics should be constant. Due to the pulsatile nature of blood flow, Doppler signals only comply with this requirement for a short period of time. Therefore the quadrature Doppler signal is broken down into short segments of 10 ms that are subjected to Fourier analysis. For that purpose the quadrature signals are sampled and converted to digital numbers at a sample frequency, which should be at least twice the maximally anticipated frequency to avoid aliasing. In the latter case the phase vector would rotate over more than 180° (Fig. 7), which would be interpreted as a phase shift of less than 180° in the opposite direction. The observed Doppler frequency then deviates in magnitude and in sign from the original one. The spectral amplitude distribution of the subsequent time segments constitutes the spectrogram with on the horizontal axis time and on the vertical axis the (Doppler) frequency. The amplitude of each spectral component is displayed as shades of grey [5, 11]. The selected length of the time window dictates the width of each spectral bin (spectral resolution); for 10 ms segments this will be 100 Hz. Increasing the length of the time segments will improve resolution at the expense of blurring the time-dependent features of the signal, e.g. acceleration time. To avoid this problem the time segments are normally half-overlapping, resulting in twice as many spectra for the same total length of the signal. Spectral analysis is rather insensitive to the signal-to-noise ratio. Even if the SNR = 1, the spectral distribution of the Doppler signal will remain clearly visible in the spectrogram. This is due to the fact that the noise will evenly be distributed over the entire spectral range, while the Doppler signal will be concentrated within a relatively small frequency band.

As blood flow accelerates from end-diastole to peak-systole the number of observed blood cells will remain more or less the same and one would expect that the Doppler signal amplitude will hardly change. However, the increased friction on blood cells due to shear stresses causes spatially a more inhomogeneous density distribution and a concomitant increase in amplitude [12–14]. On the other hand, in the frequency domain in peak-systole the signal power is distributed over a larger range, causing a substantial modulation of the spectral amplitude over the cardiac cycle. This modulation is attenuated by displaying the logarithm of the spectral amplitude with the additional advantage that the appearance of the spectrogram is rather insensitive for the gain settings.

A common parameter to extract from the spectrogram is the frequency envelope because it is rather insensitive to the observed velocity distribution and noise [15, 16]. However, there never is a sharp cut-off for the maximum frequency. The sensitive region of a Doppler system depends on the local shape of the ultrasound beam and, for pulsed Doppler systems, the axial length of the sample volume (see next section). The transit time depends on the path of the scatterers through the sensitive region and the velocity. Because of the time bandwidth product the transit time will cause blurring of the frequency spectrum (geometric broadening) which will vary throughout the cardiac cycle. For pulsed Doppler systems operating with an emission burst of 6 periods the blurring may amount to 16% of the peak frequency corresponding to the maximum velocity. In the past, several maximum frequency estimators have been proposed [17–21] and each of them use some arbitrary criterion for the maximum frequency with respect to the spectral Doppler amplitude and the noise background.

3. Pulsed Doppler Systems

CW Doppler systems have the advantage that they have an unlimited velocity range and that they are easy to use. On the other hand they have a poor range selectivity which makes them less suited for regions with different flow patterns, e.g. cardiac cavities or extremities where the arterial blood flow may reverse in end-diastole. Pulsed Doppler systems, like echo systems, allow the interrogation of the blood flow at a selected depth. Moreover, they can easily be combined with echo systems to provide visual feedback about the site of measurement.

The concept of pulsed Doppler systems is based on the notion that signals are fully determined by samples provided that, according to the Nyquist theorem, the sample frequency exceeds twice the maximally anticipated signal frequency (see previous section). This observation implies that the received signal intermittently rather than continuously can be applied to the input of the demodulator (Fig. 8), or that the ultrasound can be emitted in bursts, with a corresponding increase in bandwidth of the receiver filter. Because the signal from the selected depth range is only intermittently present at the output of the demodulator, it has to be captured with a sample-and-hold to retain the value until it is updated in the next reception cycle (Fig. 8).

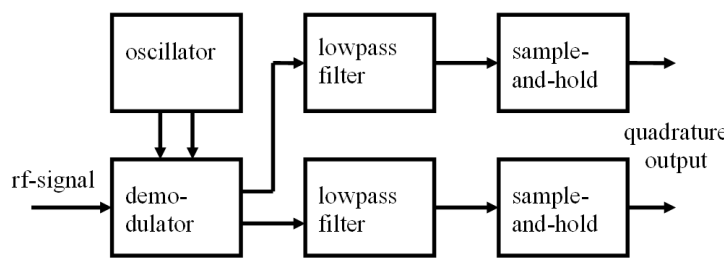


FIGURE 8. Demodulator of a pulsed Doppler system

The function of the lowpass filters following the demodulator is the same as those for a CW system (to remove the double emission frequency), but the design is completely different. Because it has to accommodate short bursts, the bandwidth should be enlarged considerably. Let us assume a burst of 6 periods, then the fractional bandwidth (bandwidth divided by center frequency) of the received radio-frequency (rf) signal equals 1/6. A fourth order characteristic provides a roll-off of 24 dB/octave, so the filter will reach an attenuation of about 70 dB at the center frequency. This is sufficient regarding the dynamic range of the received signal, which will be of the same order. Shorter bursts would even require a sharper roll-off. However, in practice longer bursts up to 10 periods will be used in pulsed Doppler mode to avoid the effect of depth-and-frequency depending attenuation on the center frequency. The sample-and-hold is activated at a preset delay with respect to the time of emission, corresponding to the desired depth of interest, and acts as a gate for the demodulated and filtered signal. As stated, the active length of the gate is given by the bandwidth of the lowpass filter, which was set according to the burst length used. This also sets the axial length of the sample

volume while its lateral dimensions are determined by the local shape of the ultrasound beam [22]. It should be stressed that the demodulator of a pulsed Doppler system cannot detect the Doppler shift, because of the short observation time. Instead it provides the phase of the rf-signal with respect to the oscillator reference signals. The phase gradually changes with depth rather than due to motion. Only the output of the sample-hold reveals the Doppler signal. It has a staircase appearance and is directly suited for conversion to digital format to perform wall filtering. In a digital filter the cut-off frequency is directly related to its update frequency, i.e. the pulse repetition frequency (PRF) of the pulsed Doppler system.

A pulsed Doppler system samples the Doppler signal from a specific depth at a rate equal to the PRF of the system. This is sufficient to accommodate without aliasing Doppler signals from physiological flows (peak velocities up to 1.5 m/s) but inappropriate for pathophysiological velocities as in arterial stenoses or stenosed cardiac valves. Aliasing will show up on the spectrogram as a roll-over: frequencies exceeding the upper limit of PRF/2 will appear at the bottom near $-PRF/2$ and vice versa. This can easily be solved by shifting the baseline upward or downward, depending on the direction requiring the largest range. Baseline shifting will extend the frequency range to maximally PRF, but then the flow should remain unidirectional. Some systems provide a further extension by the high PRF (Hi-PRF) option. Let us assume that the system is suited (depth attenuation) and set for flow velocity assessment at a depth of 10 cm. Doubling the PRF and halving the depth delay to 5 cm will force the system to sample the signals from a depth of 5 cm with respect to the current emission and from a depth of 10 cm with respect to the previous emission. If the region at 5 cm does not contain flow, then the Doppler signal is appropriately obtained from a depth of 10 cm at a double rate, thereby extending the velocity range. The drawback is that the depth-depending gain only operates over a short range, putting a high demand on the dynamic range of the system, especially if the PRF is tripled or quadrupled.

If the Doppler signals are retained in their sampled (digital) form, then a zero crossing counter is unsuited to estimate the average Doppler frequency, because transitions over 2 quadrants may occur. In 1985 Kasai proposed an alternative based on the argument of the autocorrelation $C(1)$ at lag 1 of the

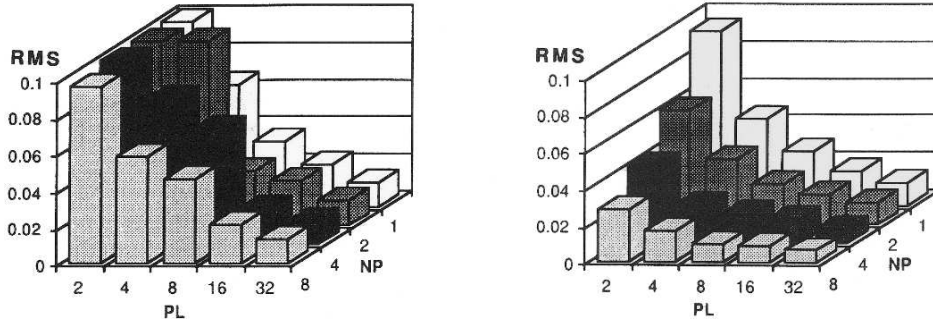


FIGURE 9. The RMS error (λ PRF) of the standard pulsed Doppler velocity estimate (left picture) does not vary with the number of periods (NP) but improves with increasing package length (PL) while the velocity estimate based on cross-correlation (Sec. 5) of the radio-frequent (rf) signal improves with both PL and NP for a signal with a fractional bandwidth of 0.25, SNR = 10 dB, mean velocity is 0, and width velocity distribution 0.1 λ PRF.

sampled quadrature Doppler signals $d(t)$, [23]:

$$C(1) = \frac{1}{PL - 1} \sum_{j=1}^{PL-1} d^*(j)d(j+1). \quad (3.1)$$

In Eq. (3.1) PL is the package length (the number of Doppler signals considered) and $d^*(j)$ is the conjugate of $d(j)$, i.e. the sign of the imaginary part is reversed. As expected the precision of the velocity estimate decreases with the square root of the package length (Fig. 9). Only for a SNR < 10 dB, a short package length ($PL \leq 10$), a mean velocity close to PRF/2 and a moderate width of the velocity distribution (0.2PRF) the precision may be poorer than 10% of the PRF, but for most conditions the precision will be better than 5% of the PRF [24–26]. Unlike the zero-crossing meter, the approach of the complex autocorrelator still functions properly if the instantaneous frequency exceeds PRF/2, provided that the velocity averaged over the time window is not subject to aliasing. To maintain the dynamic characteristics of the velocity waveform, the observation window should be about 10 ms, which converts to a package length of 100 for a PRF of 10 kHz (maximum depth 7.5 cm). This quite large number ensures precise detection of the average velocity, even if sophisticated wall suppression filters, like singular value decomposition, are applied [27, 28].

4. Multigate Pulsed Doppler Systems

The digital and computer techniques, emerging in the 1980's, facilitated reliable data processing of the sampled Doppler signals, e.g. vessel wall suppression, mean velocity detection and spectral analysis. The associated high processing power allowed to integrate parallel processing channels for each sample volume into single circuitry with serial processing, accommodating many sample volumes. Given this technology it was a small step to extend the number of consecutive sample volumes drastically to 64 and even 128 samples along a line of insonation [29–31]. A prerequisite is a large dynamic range for the analog-to-digital conversion of the outputs of the demodulator (Fig. 8) because at that stage the weak Doppler signals from blood particles are still mixed with the large amplitude echo signals from stationary and slowly moving structures like vessel walls. A total dynamic range of 72 dB (12 bits) allows for echo signals that are a factor 100 (40 dB) to 1000 (60 dB) stronger than blood Doppler signals without saturating the analog-to-digital converter. With multigate Doppler systems one can measure the time-dependent velocity distribution over the cross-section of an artery lumen as a function of time [32, 33].

The detail of the eventually obtained instantaneous velocity distribution largely depends on the spatial resolution that can be attained. As stated before a short duration of the emitted acoustic pulse requires a large bandwidth, which enlarges the effects of depth- and frequency dependent attenuation. Hence, the central frequency of the received signals will be shifted down; consequently the velocity will be overestimated (Eq. (1.1)). To solve this problem, the local central frequency of received radio frequent (rf) signals is estimated simultaneously [25, 34], using autocorrelation of the demodulated rf signals with depth lag 1 (Eq. (3.1)) over short depth segments. However, the required roll-off of the phase detection filters following the demodulators sets a lower bound for the pulse duration. This is why preference is given to direct processing of the rf signals. One should realize that not only the pulse duration but also the local beamwidth in combination with the angle of observation affect the radial resolution of the velocity estimate. For an angle of 60°–70° between flow direction and the incident beam it does not have sense to make the pulse much smaller than 1/4 of the local beamwidth (Fig. 10); further shortening will hardly affect the observed range in the radial direction of the blood vessel.

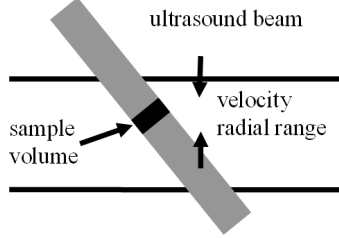


FIGURE 10. The spatial resolution in the radial range is affected by both the axial (length sample volume) and lateral (local beamwidth) resolution of the ultrasound system.

5. RF Processing

Estimation of the average velocity (Doppler frequency) after demodulation in a system with a high spatial resolution requires correction for the effects of depth and frequency dependent attenuation and will also make the velocity estimate more noise sensitive, because of the decreased SNR. Because of these problems a switch is made to direct processing of the received radio frequency (rf) signals, captured digitally with a relatively high conversion frequency. The average displacement of reflectors within a depth window over repeated observations then follows from the location of the peak of the cross-correlation [35] of the two-dimensional rf matrix $r(l, d)$:

$$\hat{C}(\delta) = \sum_l \sum_d r(l, d)r(l + 1, d + \delta). \quad (5.1)$$

As opposed to conventional Doppler processing, averaging is performed over the cross-correlation of subsequent rf signals over a depth window rather than correlation between rf signal and reference (oscillator) signal. The quality of the estimate improves with the length of the windows, in both depth (axial length sample volume) and time (PRF). The problem is to find the location of the peak. The rate of oversampling of the rf signal is reflected in the number of sample points within the main lobe of the cross-correlation function: a high oversampling is required to get a detailed cross-correlation [36]. This will put a high demand on processing power, also because for each sample point in depth the reflections of stationary and slowly moving reflectors should be removed prior to cross-correlation. A simple way to perform the latter operation is the removal of the baseline off-set, as observed over the time-window, but also higher order approaches have been suggested [37–

39]. To estimate precisely the displacement from a coarsely sampled cross-correlation function, various interpolation algorithms have been considered [40], but they all incorporate to some extent the anticipated shape of the auto-correlation of a received echo which may vary with the fractional bandwidth of the rf signal. The result of the above rf processing is a direct estimate of the average displacement, expressed in terms of the sampling distance in depth direction. In this approach the reference is the previously observed rf signal rather than an oscillator signal, eliminating the need for center frequency estimation and scaling. Most importantly the displacement estimate tends to work properly, even under poor SNR conditions (0 dB with the signal and noise levels based on the same spectral range). The phase detector in traditional pulse Doppler systems smoothes phase transitions prior to velocity estimation, while the rf processing technique retains in the displacement detection algorithm the information on phase transitions originating from the randomly distributed scatterers [24] by reversing the sequence of operations and selective averaging in the depth direction (Eq. (5.1)).

The cross-correlation function of a periodic (rf) signal exhibits the same periodicity, causing side lobes. For narrow band signals (ultrasound bursts containing several periods) these side lobes may incidentally attain higher values than the main lobe, resulting in displacement aliasing. However, employing short pulses will cause rapid decorrelation and attenuates the side lobes. That is why this approach is especially suited for displacement (velocity) estimation in systems with a high spatial resolution.

A weak point of the displacement estimation as outlined above is the required range of correlation lags, spanning a displacement range of one to two wavelengths. However, the number of required lags can be reduced to 3 if the rf signals are converted to a complex signal and the shape of the rf spectrum is known [41]. Because of the frequency characteristics of ultrasound transducers the spectral power density distribution $G(f)$ can be approximated by a Gaussian shape modeled as:

$$G(f) = \frac{2(N + S)}{B\sqrt{2\pi}} \exp\left(\frac{-2(f - f_c)^2}{B^2}\right). \quad (5.2)$$

It is thereby assumed that due to dedicated filtering the signal power S and noise power N cover the same root-mean square (RMS) frequency range B around a center frequency f_c . The two-dimensional cross-correlation function $C(\tau, \delta)$, as function of the time lag τ and depth lag δ (both in seconds), will be the inverse Fourier transform of the power spectral distribution

(Wiener-Khinchin relation), taking into account the time shift δ' due to the displacement $\Delta x = v\tau = c\delta'/2$ of the scatterers with velocity v towards the transducer in between observations:

$$C(\tau, \delta) = \int_0^\infty G(f) \exp\{2\pi f j(\delta + 2v\tau/c)\} df. \quad (5.3)$$

The basic transformation for a Gaussian pulse is:

$$F^{-1} [\exp(-af^2)] = \exp(-at^2). \quad (5.4)$$

Then the autocorrelation function ($\tau = 0$) is given by:

$$C(0, \delta) = \frac{2(N+S)}{B\sqrt{2\pi}} \exp\left(\frac{-2\delta^2}{B^2}\right) \exp\{2\pi j f_c \delta\} \quad (5.5)$$

and the cross-correlation function for $\tau \neq 0$ by:

$$C(\tau, \delta) = \frac{2S}{B\sqrt{2\pi}} \exp\left(\frac{-2(\delta + 2v\tau/c)^2}{B^2}\right) \exp\{2\pi j f_c (\delta + 2v\tau/c)\}. \quad (5.6)$$

At this point the conversion can be made to discrete correlation coefficients by considering sampling in depth and in time. The rf signal is sampled with a frequency f_s which should be a factor 4 higher than the central frequency f_c to accommodate high frequency signals, because of the bandwidth B , [41]. This sets the unit of the depth lag to $\delta = 1/f_s$. The temporal sampling interval equals 1/PRF. Eq. (5.6) contains 5 unknown variables (v, f_c, B, S, N) which can be solved by considering the estimates for $C(0,0)$, $C(1,0)$ and $C(0,1)$

$$C(0,0) = \frac{2(S+N)}{B\sqrt{2\pi}}, \quad (5.7)$$

$$C(0,1) = \frac{2(S+N)}{B\sqrt{2\pi}} \exp\left(\frac{-2}{f_s^2 B^2}\right) \exp\{2\pi j f_c / f_s\}, \quad (5.8)$$

$$C(1,0) = \frac{2S}{B\sqrt{2\pi}} \exp\left(\frac{-8v^2}{B^2 c^2 \text{PRF}^2}\right) \exp\{4\pi j f_c v / c \text{PRF}\}. \quad (5.9)$$

The argument of the estimate for the autocorrelation coefficient provides the estimate for the center frequency of the received signal, while the argument of the estimate for the cross-correlation coefficient, normalized for the

estimated center frequency, gives the velocity:

$$\hat{f}_c = f_s \arg\{\hat{C}(0, 1)\}/2\pi, \\ \hat{v} = \frac{c\text{PRF}}{2f_s} \frac{\arg\{\hat{C}(1, 0)\}}{\arg\{\hat{C}(0, 1)\}}, \quad (5.10)$$

$$\hat{B} = \frac{\sqrt{2}}{f_s \sqrt{\ln \hat{C}(0, 0) - \ln |\hat{C}(0, 1)|}}, \quad (5.11)$$

$$\frac{S}{N} = \frac{|\hat{C}(1, 0)|}{\hat{C}(0, 0) \exp\left(\frac{-8v^2}{B^2 c^2 \text{PRF}^2}\right) - |\hat{C}(1, 0)|}.$$

The estimates for the center frequency, the bandwidth and the SNR can be used to validate the velocity estimate, e.g. if the SNR exceeds a given threshold the estimate is accepted, otherwise it will be zero. The cross-correlation coefficients of the complex rf signals, obtained via a Hilbert filter, within a data matrix with dimensions NS in depth and PL in time are estimated as:

$$\hat{C}(\tau, \delta) = \frac{\sum_{d=1}^{NS-\delta} \sum_{t=1}^{NP-\tau} r(t, d)r^x(t + \tau, d + \delta)}{(NS - \delta - 1)(PL - \tau - 1)}. \quad (5.12)$$

To get the best performance, the length of the depth window is set to the axial resolution of the system as follows from the estimates for center frequency and bandwidth. Simulations have shown (Fig. 9b) that the above estimator based on complex correlation function has a precision of less than 1% of the PRF for an rf signal with a fractional bandwidth of 0.5 for a wide range of signal conditions [41]. To improve robustness and detail in the velocity distribution, data windows are chosen half-overlapping in depth and in time, rendering a large number of velocity estimates per second for a depth range of 1–2 cm.

The common wall filter is a highpass filter and, hence, suppresses Doppler frequencies within a range around zero frequency. Considering a slowly moving structure like a vessel wall (or its reverberations within the lumen), the cut-off frequency and roll-off should be set high to avoid that in the early systolic phase the filter will leak signals from the structure. Clearly a zero order filter (removing the mean level) will not do. An alternative is to use above velocity estimator (Eq. (5.10)) estimator prior to wall filtering [42].

Then the signals of structures will dominate and the estimator provides the Doppler shift frequency as function of time, providing simultaneously information about the displacement of wall structures over time [42]. The wall Doppler shift is subsequently used to shift the complex rf signals in frequency, maintaining the spectral peak of the Doppler signals at zero frequency and allowing the highpass filter to function optimally. Since the spectral dispersion of the structures is limited, the selection of the cut-off frequency is only limited by the length of the time-window [27, 28, 43, 44]. After blood velocity detection the estimated velocities have to be corrected for the imposed shift in signal frequency.

Processing of rf data puts some demands on the echo-systems. First of all the rf signal should be accessible, while the phase relationship between emission and data capture is maintained. Moreover, the echo system should be capable to operate in echo M-mode with a high PRF (10 kHz for a 7.5 MHz system) to avoid frequency aliasing. Finally, capturing rf signals at a sample rate of 4 times the expected carrier frequency (25 MHz) at a PRF of 10 kHz over a range of 20 mm, covering an artery) produces a huge amount of data over an observation time of a few seconds.

6. Shear Stress

The shear stress is the drag per unit area exerted by the endothelium on the flowing blood. This will slow down the velocity of the blood close to the wall and for a straight vessel without bifurcations eventually result in a velocity distribution across the lumen with the highest velocity in the center of the lumen. A steep velocity gradient at the wall-lumen interface, indicated as shear rate (SR), corresponds to a high shear stress (SS):

$$SS = \eta \left. \frac{\partial v(r)}{\partial r} \right|_{r=R} = \eta SR \quad [\text{Pa}]. \quad (6.1)$$

The blood viscosity η varies with the shear rate: a low mean wall shear rate ($r = R$) causes a high blood viscosity. Especially at low shear rates (below 200 s^{-1}) the viscosity will increase sharply, rendering viscosity measurements by means of a blood sample impractical. However, for physiological shear rates the non-Newtonian character of blood can be accounted for using plasma viscosity (η_0 [Pas]), haemotocrit (Ht [%]) and wall shear rate, [45]:

$$\log(\eta) = \log(\eta_0) + (0.03 - 0.0076 \log(SR))Ht. \quad (6.2)$$

If we assume that the emitted ultrasound burst has effectively a length of 2 periods (a relative bandwidth of 0.5) and the received rf signal has a center frequency of 6.1 MHz, the length of the sample volume will be on the order of 0.25 mm which matches the anticipated beamwidth of 1 mm within the focal zone of a transducer. Processing the rf data in half-overlapping segments in depth and in time results in an interspacing of 0.125 mm, thereby retaining the spatial and temporal details in the velocity distribution (Fig. 11). As stated in the previous section, a wall filter adapting dynamically to the velocities of the artery walls allows detection of low velocities which may occur close to the vessel wall. These velocities may behave erratically, because velocity estimates have been set to zero based on the observed SNR while other velocity estimates have been accepted although they have an unreliable value. Smoothing with a 3×3 median filter preserves the edges of the velocity distribution. The next step is to compute the radial derivative of the observed velocity distribution for each time instant and at each site, starting from the middle of the lumen, resulting in the time-dependent shear rate distribution. Near the wall the shear rate will attain the highest value and the maximum within a range of 2 mm is accepted as the wall shear rate, [42]. As a consequence the position at which the wall shear rate is obtained dynamically varies over the cardiac cycle with the motion of the walls (Fig. 11). To reduce minor curvature effects and associated secondary flow effects, the wall shear rates at the near and far wall (from the viewpoint of the ultrasound transducer) are averaged.

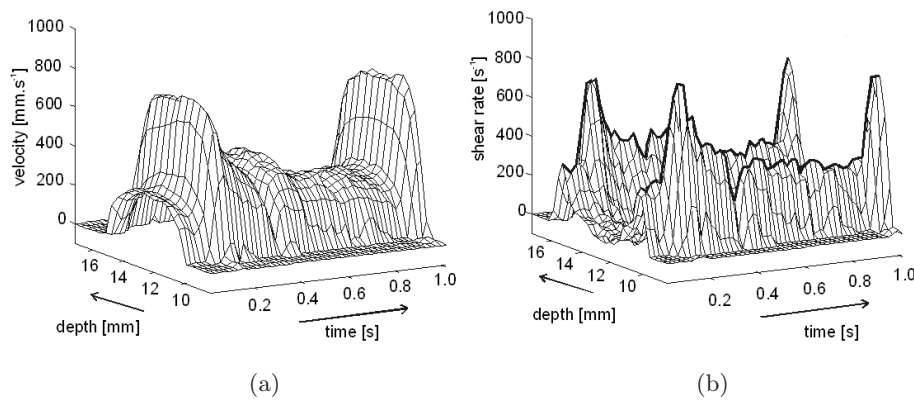


FIGURE 11. Time-dependent velocity (left) and shear rate (right) distribution in the common carotid artery of a young volunteer

Although the adaptive wall filter permits the detection of relatively low velocities, it remains impossible to detect the velocity gradient exactly at the wall lumen interface, also because computation of the velocity gradient involves 2 neighboring sample volumes with a non-zero velocity estimate. For a 7.5 MHz system the actual velocity gradient is computed at a distance of 0.3 mm from the wall [46]. For an artery with a diameter of 6 mm, this will cause an underestimation of the true velocity gradient on the order of 10%. On the other hand it may be assumed that at that radial position the effects of shear thinning are negligible and that the estimated whole blood viscosity (Eq. (6.2)) can be used.

One may consider using color Doppler systems in color M-mode (Sec. 7) to assess the time-dependent wall shear rate. These systems, however, have a poor spatial resolution, because they employ long ultrasound bursts (Sec. 1) in Doppler mode. Moreover, the wall filters are not balanced to effectively separate Doppler signals from the wall and from the blood with about the same velocity relative to the ultrasound transducer. Generally the wall filter is the key problem to assess the velocity gradient close to the wall. Let us assume that the cut-off frequency of the filter corresponds to a velocity of 3 cm/s, then the minimal velocity gradient for consecutive sample volumes spaced at 0.3 mm equals 100 s^{-1} . Only if the velocity gradient is higher than this estimated value it can be attributed to the velocity distribution.

Since it remains problematic to measure directly the time-dependent wall shear rate researchers evaded to indirect methods, [47–50]. For a steady flow the velocity distribution in a straight vessel will eventually develop a parabolic shape, provided that the entrance length is sufficiently long. Then the wall shear rate is directly related to the center stream velocity v which can easily be measured with available Doppler systems [51]:

$$\text{SR} = 2nv/D. \quad (6.3)$$

In this expression D stands for the lumen diameter and n indicates the exponent of the modeled velocity distribution (which is 2 for a parabolic velocity profile). For dynamic pulsatile conditions the shape of the velocity distribution will vary over the cardiac cycle, but it is assumed that the mean shape is still parabolic. However, direct comparison between direct and indirect measurements shows that the indirect method underestimates the mean and peak-systolic shear rate, and, hence, peak and mean wall shear stress, especially for compliant vessels, [52]. For elastic arteries the exponent is higher than 3, indicating a blunted velocity profile.

It is generally accepted that the lumen diameter is adjusted to the prevailing shear stress, [53–56]. At high shear stresses the endothelium will produce vasodilating agents, like NO and prostacyclines [57], increasing arterial diameter and, hence, keeping the shear stress within limits. At a low shear stress, however, less of these vasodilating autocoids and endotheline (a vasoconstricting agent) will be released, causing vasoconstriction. It is assumed that regulation of the shear stress eventually results in a mean shear stress of 1.5 Pa (15 dyne/cm²). In the common carotid artery we indeed observed shear stresses of about 1.3 Pa, but in the brachial [52] and the femoral [58] artery substantially lower mean stresses were found, ranging between 0.5 and 0.3 Pa. The latter arteries supply vascular beds with a high variation in blood demand (factor 20–30), depending on the level of exercise, and an associated variation in peripheral resistance. For this condition it is virtually impossible to adjust dynamically the artery diameter to retain a shear stress of 1.5 Pa. A high shear stress may after all damage the endothelium, [59]. That is why arteries in the extremities have a substantially lower mean shear stress at rest, [50, 60] to accommodate without endothelial damage the high blood flow in exercise.

7. Color Doppler Imaging

Blood cells exhibit a low echogenicity compared to structures like vessel walls. Consequently blood appears black on an echo-image, but by using the brightness information it is rather easy to locate normal arteries using. The situation changes for arteries with calcified walls and a suspected low or absent blood flow. Moreover, thrombotic formations as a result of vulnerable plaques have a higher echo level than blood and the difference with vessel walls is not so obvious anymore. That is why some decades ago it was proposed to extend the potentials of multigate Doppler systems to 2-dimensional flow maps where the velocity information is superimposed in color (color Doppler) on the echo-image in B-mode, [23]. The direct visualization of the anatomical relationship between structures and flow makes it directly clear where anomalies are to be expected.

To obtain flow maps a large number of sample volumes distributed along the ultrasound beam have to be repetitively interrogated in pulsed Doppler mode. An observation time of 1 ms (4 to 8 subsequent emission and processing cycles) will do to obtain a crude estimate for the velocity distribution

[15, 26, 28, 61–69], whereafter the beam is switched to another direction and the process is repeated. In this way 16 velocity maps composed of 64 lines can be produced per second. Although pulsed Doppler processing is subject to aliasing, it does not seem to be a problem for color mode systems because aliasing artifacts will show up as a mosaic pattern: the random distribution of high velocities with opposite directions are easily identified as jets with a high velocity as may occur in and distal to stenotic heart valves and artery stenoses.

Large flow maps composed of many lines or a low PRF because of the required depth of investigation will reduce the flow map rate to below 10 frames per second, which becomes prohibitive to fully appreciate the dynamic behavior of arterial flow and cardiac action. That is why for the flow map, preference is given to a subsector of the echo-image, which is also intermittently updated. Because of the short observation time, the estimated velocities are rather noisy prohibiting numeric quantification. Moreover the short observation time sets a lower limit to the cut-off frequency of the vessel wall filter, leaving a void between the color map and the wall. For a more accurate assessment of flow anomalies the system is switched to single M-line color mode or to single gate Doppler permitting frequency analysis of a sample volume positioned, using the echo and flow map information.

It may depend on the application, but in most situations one is interested in the presence of blood flow rather than its magnitude. For those situations it is not necessary to calculate the velocity map: it is sufficient to detect the amplitude of the Doppler signals [70–74] and to display its 2-dimensional distribution in color mode (power Doppler, angio Doppler). A drawback is that the information about flow direction is lost. On the other hand one may average over a longer time, reducing estimation artifacts in the image.

8. Conclusions

Color Doppler systems differentiate the flow direction with a color (red or blue) while the flow velocity is indicated by the brightness of the color. The question remains whether the color is indeed linked to the sign of the observed Doppler shift or to the type of vessel (artery or vein). In Sec. 1 it was argued that particles moving towards the transducer would induce a positive Doppler shift, but at many stages within a Doppler system the assigned phase relationship is rather arbitrary. This applies to the reference signals for

the demodulator (Sec. 2.1), for the inputs of the velocity estimator (Sec. 2.3) and for the audio signal separator (Sec. 2.2). If the inputs are swapped the system still functions properly, although the sign of the velocity output will be reversed. The situation becomes even more complicated for rf processing (Sec. 5). There the direction of the displacement is linked to the time elapsed after emission: a positive displacement is then associated with a shift to a greater depth. For Eq. (5.3) this was corrected for by assigning to the time-shift, due to a negative displacement (motion towards the transducer), with a positive sign, while strictly speaking the sign should be negative.

Also in their application Doppler systems are not consistent. Spectra are most easily interpreted if they are displayed in a positive fashion. Whether arteries are interrogated with the probe direction aligned with the suspected flow direction or rather in the opposite direction depends on the local anatomy. It is easier to observe the carotid arteries with the probe directed towards the head, while in the brachial arteries the probe direction is opposed to the main flow direction. But arteries may also exhibit a reversed flow direction. A well-known example is the flow direction in the ophthalmic artery, which changes sign if the blood pressure in the cerebral circulation is relatively low due to an obstruction in the internal carotid artery. Also the flow direction in the right common carotid artery may be reversed if the brachiocephalicus (connecting the aorta to the right carotid artery and the subclavian artery) is occluded. Then the right arm is indirectly supplied by flow from the head.

Because of the reported ambiguities in hardware, application and disease it is nice that Doppler systems are equipped with a switch to change the polarity of the observed velocities. Color Doppler systems do not color arteries red, however, it is the user who determines the displayed polarity, i.e. the assignment of the red and blue color.

References

1. T. YOSHIDA, M. MORI, Y. NIMURA, G. HIKITA, S. TAKA GISHI, K. NAKANISHI and S. SATOMURA, *Analysis of heart motion with ultrasonic Doppler method and its clinical application*, Am Heart J, **61**: 61–75, 1961.
2. D.L. FRANKLIN, W. SCHLEGEL and R.F. RUSHMER, *Blood flow measured by Doppler frequency shift of back-scattered ultrasound*, Science, **134**: 564–565, 1961.
3. C. DOPPLER, *Ueber das farbige Licht der Doppelsterne und einige anderer Gestirne des Himmels*, presented at Gesellschaft der Wissenschaften, Prag, 25 Mai, 1842.

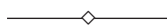
4. C.H.D. BUIJS BALLOT, *Akustische Versuche auf der Niederländische Eisenbahn, nebst gelegentlichen bemerkungen zur Theorie des Hrn Prof. Doppler*, Annalen Physik Chemie, **66**:321–351, 1845.
5. R.S. RENEMAN and M.P. SPENCER, *Local Doppler audio spectra in normal and stenosed carotid arteries in man*, Ultrasound Med Biol, **5**(1):1–11, 1979.
6. D. GABOR, *Theory of communications*, Journal IEE, **93**:429–457, 1946.
7. R.S. RENEMAN, H.F. CLARKE, N. SIMMONS, and M.P. SPENCER, *In vivo comparison of electromagnetic and Doppler flowmeters: with special attention to the processing of the analogue Doppler flow signal*, Cardiovasc Res, **7**:557–566, 1973.
8. P.J. FISH, P.R. HOSKINS, C. MORAN and W.N. McDICKEN, *Developments in cardiovascular ultrasound. Part I: signal processing and instrumentation*, Med Biol Eng Comput, **35**:561–569, 1997.
9. P.A. PERONNEAU, J.P. BOURNAT, A. BUGNON, A. BARBET and M. XHAARD, *Theoretical and practical aspects of pulsed Doppler flowmetry: real-time applications to the measure of instantaneous velocity profiles*, [in:] *Cardiovascular applications of ultrasound*, R.S. Reneman, [Ed.], pp.66–84, Amsterdam-London: North-Holland Publ. Co., 1974.
10. R.W. GILL, *Performance of the mean frequency Doppler modulator*, Ultrasound Med Biol, **5**:237–247, 1979.
11. A.P.G. HOEKS, M. HENNERICI and R.S. RENEMAN, *Spectral composition of Doppler signals*, Ultrasound Med Biol, **17**:751–760, 1991.
12. D.G. PAENG, R.Y. CHIAO and K.K. SHUNG, *Echogenicity variations from porcine blood I: the “bright collapsing ring” under pulsatile flow*, Ultrasound Med Biol, **30**:45–55, 2004.
13. D.G. PAENG and K.K. SHUNG, *Cyclic and radial variation of the Doppler power from porcine whole blood*, IEEE Trans Ultrason Ferroelectr Freq Control, **50**:614–622, 2003.
14. D. PAENG, P. CAO and K.K. SHUNG, *Doppler power variation from porcine blood under steady and pulsatile flow*, Ultrasound Med Biol, **27**:1245–1254, 2001.
15. P.R. HOSKINS, *A review of the measurement of blood velocity and related quantities using Doppler ultrasound*, Proc Inst Mech Eng, **213**:391–400, 1999.
16. P.R. HOSKINS, P.J. FISH, W.N. McDICKEN and C. MORAN, *Developments in cardiovascular ultrasound. Part 2: arterial applications*, Med Biol Eng Comput, **36**:259–269, 1998.
17. R. MORAES, N. AYDIN and D.H. EVANS, *The performance of three maximum frequency envelope detection algorithms for Doppler signals*, J. Vasc. Invest., **1**:126–134, 1995.
18. K. MARASEK and A. NOWICKI, *Comparison of the performance of three maximum Doppler frequency estimators coupled with different spectral estimation methods*, Ultrasound Med Biol, **20**:629–638, 1994.

19. L.Y.L. MO, L.C.M. YUN and R.S.C. COBBOLD, *Comparison of four digital maximum frequency estimators*, Ultrasound Med Biol, **14**:355–363, 1988.
20. A. NOWICKI, P. KARLOWICZ, M. PIECHOCKI and W. SECOMSKI, *Method for the measurement of the maximum Doppler frequency*, Ultrasound Med Biol, **11**:479–486, 1985.
21. T. D'ALESSIO, *Objective algorithm for maximum frequency estimation in Doppler spectral analysers*, Med Biol Eng Comput, **23**:63–68, 1985.
22. A.P.G. HOEKS, C.J. RUISEN, P. HICK and R.S. RENEMAN, *Methods to evaluate the sample volume of pulsed Doppler systems*, Ultrasound Med Biol, **10**:427–434, 1984.
23. C. KASAI, K. NAMEKAWA, A. KOYANO and R. OMOTO, *Real-time two-dimensional blood flow imaging using an autocorrelation technique*, IEEE Trans Son Ultrason, **SU-32**:458–464, 1985.
24. A.P.G. HOEKS, T.G.J. ARTS, P.J. BRANDS and R. S. RENEMAN, *Comparison of the performance of the cross correlation and Doppler autocorrelation technique to estimate the mean velocity of simulated ultrasound signals*, Ultrasound Med Biol, **19**:727–740, 1993.
25. T. LOUPAS, J.T. POWERS and R.W. GILL, *An axial velocity estimator for ultrasound blood flow imaging, based on a full evaluation of the Doppler equation by means of a two-dimensional autocorrelation approach*, IEEE Trans Ultrason Ferroelectrics Freq Control, **42**:672–688, 1995.
26. H. TORP, K. KRISTOFFERSEN and B.A.J. ANGELSEN, *Autocorrelation techniques in color flow imaging: signal model and statistical properties of the autocorrelation estimates*, IEEE Trans Ultrason Ferroelectrics Freq Control, **41**:604–612, 1994.
27. L.A.F. LEDOUX, P.J. BRANDS and A.P.G. HOEKS, *Reduction of the clutter component in Doppler ultrasound signals based on singular value decomposition: a simulation study*, Ultrason Imaging, **19**:1–18, 1997.
28. H. TORP, *Clutter rejection filters in color flow imaging: a theoretical approach*, IEEE Trans Ultrason Ferroelectrics Freq Control, **44**:417–424, 1997.
29. M. BRANDESTINI, *Topoflow—a digital full range Doppler velocity meter*, IEEE Trans. Sonics and Ultrasonics, **SU-25**:287–293, 1978.
30. A.P.G. HOEKS, R.S. RENEMAN and P.A. PERONNEAU, *A multi-gate pulsed Doppler system with serial data processing*, IEEE Trans. Sonics Ultrason, **SU-28**:242–247, 1981.
31. P. TORTOLI, F. GUIDI, G. GUIDI and C. ATZENI, *Spectral velocity profiles for detailed ultrasound flow analysis*, IEEE Trans Ultrason Ferroelectrics Freq Control, **43**:654–658, 1996.
32. R.S. RENEMAN, T. VAN MERODE, P. HICK and A.P.G. HOEKS, *Flow velocity patterns in and distensibility of the carotid artery bulb in subjects of various ages*, Circulation, **71**:500–509, 1985.

33. R.S. RENEMAN, T. VAN MERODE, P. HICK and A.P.G. HOEKS, *Cardiovascular applications of multi-gate pulsed Doppler systems*, Ultrasound Med Biol, **12**: 357–370, 1986.
34. S.I. RABBEN, S. BAERUM, V. SORHUS and H. TORP, *Ultrasound-based vessel wall tracking: an auto-correlation technique with RF center frequency estimation*, Ultrasound Med Biol, **28**: 507–517, 2002.
35. O. BONNEFOUS and P. PESQUE, *Time domain formulation of pulse-Doppler ultrasound and blood velocity estimation by cross correlation*, Ultrason Imaging, **8**: 73–85, 1986.
36. J.A. JENSEN, *Range/velocity limitations for time-domain velocity estimation*, Ultrasound Med Biol, **19**: 741–749, 1993.
37. A.P.G. HOEKS, J.J.W. VAN DE VORST, A. DABEKAUSEN, P. J. BRANDS and R.S. RENEMAN, *An efficient algorithm to remove low frequency Doppler signals in digital Doppler systems*, Ultrason Imaging, **13**: 135–144, 1991.
38. J.A. JENSEN, *Stationary echo canceling in velocity estimation by time-domain cross-correlation*, IEEE Trans Ultrason Ferroelectrics Freq Control, **12**: 471–477, 1993.
39. M. SCHLAIKJER, S. TORP-PEDERSEN and J.A. JENSEN, *Simulation of RF data with tissue motion for optimizing stationary echo canceling filters*, Ultrasonics, **41**: 415–419, 2003.
40. X. LAI and H. TORP, *Interpolation methods for time-delay estimation using cross-correlation method for blood velocity measurement*, IEEE Trans Ultrason Ferroelectrics Freq Control, **46**: 277–290, 1999.
41. P.J. BRANDS, A.P.G. HOEKS, L.A.F. LEDOUX and R. S. RENEMAN, *A radio frequency domain complex cross-correlation model to estimate blood flow velocity and tissue motion by means of ultrasound*, Ultrasound Med Biol, **23**: 911–920, 1997.
42. P.J. BRANDS, A.P.G. HOEKS, J. WILLIGERS, C. WILLEKES and R.S. RENEMAN, *An integrated system for the non-invasive assessment of vessel wall and hemodynamic properties of large arteries by means of ultrasound*, Eur. J. Ultrasound, **9**: 257–266, 1999.
43. S. BJAERUM, H. TORP and K. KRISTOFFERSEN, *Clutter filters adapted to tissue motion in ultrasound color flow imaging*, IEEE Trans Ultrason Ferroelectrics Freq Control, **49**: 693–704, 2002.
44. Y.M. YOO, R. MANAGULI and Y. KIM, *Adaptive clutter filtering for ultrasound color flow imaging*, Ultrasound Med Biol, **29**: 1311–1320, 2003.
45. J.P.A. WEAVER, A. EVANS and D.N. WALDER, *The effect of increased fibrinogen content on the viscosity of blood*, Clin Sci, **36**: 1–10, 1969.
46. F.J.H. GIJSSEN, P.J. BRANDS, F.N. VAN DE VOSSE and J. D. JANSSEN, *Assessment of wall shear rate measurements with ultrasound*, J. Vasc. Invest., **4**: 187–196, 1998.

47. A. GNASSO, C. IRACE, C. CARALLO, M.S. DE FRANCESCHI, C. MOTTI, P.L. MATTIOLI and A. PUJIA, *In vivo association between low wall shear stress and plaque in subjects with asymmetrical carotid atherosclerosis*, *Stroke*, **28**: 993–998, 1997.
48. A. GNASSO, C. CARALLO, C. IRACE, V. SPAGNUOLO, G. DE NOVARA, P.L. MATTIOLI and A. PUJIA, *Association between intima-media thickness and wall shear stress in common carotid artery in healthy male subjects*, *Circulation*, **94**: 3257–3262, 1996.
49. A. GNASSO, C. CARALLO, C. IRACE, M.S. DE FRANCESCHI, P. L. MATTIOLI, C. MOTTI and C. CORTESE, *Association between wall shear stress and flow-mediated vasodilation in healthy men*, *Atherosclerosis*, **156**: 171–176, 2001.
50. A. SCHMIDT-TRUCKSASS, A. SCHMID, C. BRUNNER, N. SCHERER, G. ZACH, J. KEUL and M. HUONKER, *Arterial properties of the carotid and femoral artery in endurance-trained and paraplegic subjects*, *J Appl Physiol*, **89**: 1956–1963, 2000.
51. A.P.G. HOEKS and R.S. RENEMAN, *Flow patterns and arterial wall dynamics*, [in:] *Cerebrovascular ultrasound*, M.G. Hennerici and S.P. Meairs, [eds.], pp.77–87, Cambridge: University Press, 2001.
52. R. DAMMERS, F. STIFFT, J.H. TORDOIR, J.M. HAMELEERS, A.P. HOEKS and P.J. KITSLAAR, *Shear stress depends on vascular territory: comparison between common carotid and brachial artery*, *J. Appl. Physiol.*, **94**: 485–489, 2003.
53. C.D. MURRAY, *The physiological principle of minimum work. I: The vascular system and the cost of blood volume*, *Proc. Nat. Acad. Sci. USA*, **12**: 207–214, 1926.
54. A. KAMIYA, R. BUKHARI and T. TOGAWA, *Adaptive regulation of wall shear stress optimizing vascular tree function*, *Bulletin Math Biol*, **46**: 127–137, 1984.
55. M. ZAMIR, P. SINCLAIR and T.M. WONNACOTT, *Relation between diameter and flow in major branches of the aorta*, *J. Biomech.*, **25**: 1303–1310, 1992.
56. C.K. ZARINS, M.A. ZATINA, D.P. GIDDENS, D.N. KU and S. GLAGOV, *Shear stress regulation of artery lumen diameter in experimental atherogenesis*, *J. Vasc. Surg.*, **5**: 413–420, 1987.
57. R. BUSSE and I. FLEMING, *Pulsatile stretch and shear stress; physical stimuli determining the production of endothelium-derived relaxing factors*, *J. Vasc. Res.*, **35**: 73–84, 1998.
58. L. KORNET, A.P. HOEKS, J. LAMBREGTS and R.S. RENEMAN, *Mean wall shear stress in the femoral arterial bifurcation is low and independent of age at rest*, *J. Vasc. Res.*, **37**: 112–122, 2000.
59. M.R. ROACH and N.B. SMITH, *Does high shear stress induced by blood flow lead to atherosclerosis*, *Persp Biol Medicine*, **26**: 287–303, 1983.
60. P.C. DE GROOT, F. POELKENS, M. KOOIJMAN and M.T. HOPMAN, *Preserved flow-mediated dilation in the inactive legs of spinal cord-injured individuals*, *Am. J. Physiol. Heart Circ. Physiol.*, **287**: H374–380, 2004.
61. D.F. SWITZER and N.C. NANDA, *Doppler color flow mapping*, *Ultrasound Med Biol*, **11**: 403–416, 1985.

-
62. A. KURJAK, Z. ALFIREVIC and M. MILJAN, *Conventional and color Doppler in the assessment of fetal and maternal circulation*, Ultrasound Med. Biol., **14**:337–354, 1988.
 63. J. HOLEN, M. NANA, J. LOCKHART and R. WAAG, *Doppler color flow in echocardiography: analytical and in-vitro investigations of the quantitative relationship between orifice flow and color jet dimension*, Ultrasound Med. Biol., **16**:543–551, 1990.
 64. A. KITABATAKE, J. TANOUCHI, Y. YOSHIDA, T. MASUYAMA, M. UEMATSU and T. KAMADA, *Quantitative color flow imaging to measure the two-dimensional distribution of blood flow velocity and the flow rate*, Jap. Circulation J., **54**:304–308, 1990.
 65. W. STEINKE, H. KLOETZSCH and M. HENNERICI, *Carotid artery disease assessed by color Doppler flow imaging. Correlation with standard Doppler sonography and angiography*, AJNR, **11**:259–266, 1990.
 66. C. RANKE, U. HENDRICKX ROTH, F. BRASSEL, A. CREUTZIG and K. ALEXANDER, *Color and conventional image-directed Doppler ultrasonography: accuracy and sources of error in quantitative blood flow measurements*, J. Clin. Ultrasound, **20**:187–193, 1992.
 67. P.N.T. WELLS, *Today's state of the art: does colour velocity imaging overtake colour Doppler?*, J. Vasc. Investigation, **1**:38–43, 1995.
 68. A. HERMENT, G. DEMOMENT and P. DUMÉE, *Improved estimation of low velocities in color Doppler imaging by adapting the mean frequency estimator to the clutter rejection filter*, IEEE Trans Biomed Eng, **43**:919–927, 1996.
 69. K. FERRARA and G. DEANGELIS, *Color flow mapping*, Ultrasound Med Biol, **23**:321–345, 1997.
 70. M.A. MOEHRING and M.P. SPENCER, *Power M-mode Doppler (PMD) for observing cerebral blood flow and tracking emboli*, Ultrasound Med Biol, **28**:49–57, 2002.
 71. M. BRUCE, M. AVERKIOU, K. TIEMANN, S. LOHMAIER, J. POWERS and K. BEACH, *Vascular flow and perfusion imaging with ultrasound contrast agents*, Ultrasound Med Biol, **30**:735–743, 2004.
 72. M. SAQQUR, N. DEAN, M. SCHEBEL, M.D. HILL, A. SALAM, A. SHUAIB and A.M. DEMCHUK, *Improved detection of microbubble signals using power M-mode Doppler*, Stroke, **35**:e14–17, 2004.
 73. S. HUBER, R. STEINBACH, O. SOMMER, I. ZUNA, H. CZEMBIREK and S. DELORME, *Contrast-enhanced power Doppler harmonic imaging-influence on visualization of renal vasculature*, Ultrasound Med. Biol., **26**:1109–1115, 2000.
 74. L. ALLARD and G. CLOUTIER, *Power Doppler ultrasound scan imaging of the level of red blood cell aggregation: an in vitro study*, J. Vasc. Surg, **30**:157–168, 1999.



Concepts for High Resolution Blood Flow Imaging with High Frequency Ultrasound

MICHAEL VOGT

*Institute of High Frequency Engineering
Ruhr-University Bochum, IC 6/133,
44780 Bochum, Germany
Michael.Vogt@rub.de*

In this paper the design of a high frequency ultrasound (HFUS) pulsed wave Doppler (PWD) system for blood flow imaging in small vessels is presented. High frequency and broadband ultrasound in the 50 MHz range is utilized in order to obtain a good spatial resolution. Echo signals are analyzed making use of combined time/frequency domain approaches for axial blood flow velocity estimation. Furthermore, an approach for the estimation of the radial blood flow velocity component with rotational symmetric sound beams is presented. With the help of these approaches, the magnitude and sign of the axial flow velocity in sound propagation direction and the magnitude of the velocity component perpendicularly are accessible. The implemented PWD system and the proposed flow estimation approaches have been tested with the help of simulations and flow phantom measurements. Results of the system's validation and results of in vivo images on small blood vessels are presented.

Key words: *High frequency ultrasound, blood flow, pulsed wave Doppler*

1. Introduction

Ultrasound Doppler systems enable the assessment of blood flow in organs and vessels by measuring blood flow velocities and perfusion [1]. In dermatology and other applications, small vessels with low blood flow velocities are of special interest [2–6]. High resolution and robust flow estimation concepts have to be applied under these conditions.

A PWD system with a high frequency spherically focused single element transducer (50 MHz center frequency, 80% relative bandwidth) has been designed and implemented. A waveform generator is utilized for transmit signal

generation, and radio frequency (RF) echo signals are directly digitized with a transient recorder. Periodic sequences of pulsed signals are transmitted with an adjustable and predefined pulse repetition frequency (PRF) at discrete lateral transducer positions for flow and perfusion imaging across blood vessel's cross sections [6–13]. Flow in vessels can be separated in axial and radial flow velocities components in sound propagation direction and transversely, respectively, in the context of the utilized spherically focused single element transducer [8, 10–11].

Consecutive sequences of echo signals are acquired over time of flight (“micro time axis”) and over repeated pulse transmissions (“macro time axis”). Digitized data is represented in the two dimensional micro/macro time axis space, which enables an easy interpretation and motivation of different concepts for blood flow velocities estimation. Conventional frequency domain and time domain approaches as well as time/frequency domain approaches for the estimation of axial blood flow velocities are discussed. Trade-offs between a good spatial resolution and a good velocity resolution are analyzed. It is shown that combined time/frequency domain approaches can advantageously be applied in the context of broadband systems [7, 9, 12]. Furthermore, an approach for the estimation of the magnitude of radial flow velocities is proposed. The statistics of echo signals from blood, which transversely cross the sound beam, is analyzed in this approach [8, 10–11, 14–15].

Implementations of wall-filters, which are utilized to suppress the stationary echoes from the non moving tissue, that are significantly larger than the echoes from blood, are discussed. Power-mode images and color flow images are calculated off-line.

Simulations and flow phantom measurements have been performed in order to test and validate the implemented PWD system and the proposed flow estimation strategies. Furthermore, *in vivo* measurements on small blood vessels at the back of a human hand have been performed. It will be shown that the implemented system is capable of detecting and measuring blood flows in small vessels with diameters down to $100\text{ }\mu\text{m}$ with flow velocities in the range of some few mm/s.

2. High Frequency Ultrasound for High Resolution Blood Flow Imaging

A sufficiently good spatial resolution has to be achieved and sensitive flow estimation approaches have to be applied for blood flow imaging in small vessels with very small diameters and very small blood flow velocities. High frequency and broadband ultrasound in the 50 MHz range is utilized to fulfill these requirements.

2.1. Measurement Configuration

Because HFUS arrays operating at frequencies above 30 MHz are not yet available, a spherically focused single element transducer is utilized for the measurements. The measurement configuration is shown in Fig. 1.

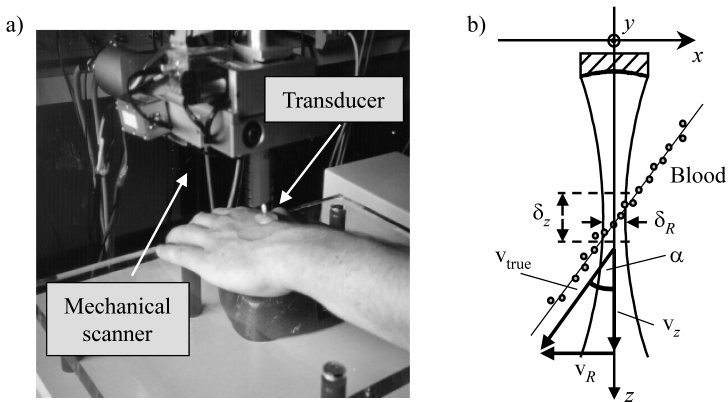


FIGURE 1. a) measurement setup, b) flow geometry: true flow velocity v_{true} , axial and radial flow velocities v_z and v_R .

Movement artifacts, which might occur during in vivo measurements, have to be avoided. A mechanically stable measurement platform that fixes the transducer relative to the blood vessels under investigation, see Fig. 1 a), has been designed. The transducer is positioned above the blood vessel, whereby an angle α between the direction of sound propagation (axial direction) z and the flow direction is given, see Fig. 1 b). Ultrasound gel is used as sound propagation medium between the transducer and the tissue. For morphological skin imaging with HFUS, usually water is used as coupling medium. This is achieved by mechanically scanning the transducer inside a water bath inside a small tank with a slot at the bottom side, which is

placed on the skin surface [6, 16–18]. But this is not appropriate for blood flow measurements because blood flow inside the small vessels would collapse under the mechanical load. For this reason, ultrasound gel is used as sound propagation medium. Air bubbles, which might be present in the gel, significantly disturb the propagation of HFUS. Hence, air bubbles have to be avoided as much as possible.

The ultrasound waves, which are emitted by the transducer, are backscattered at the moving blood particles, mainly the erythrocytes, inside the blood plasma. Because a rotational symmetric ultrasound transducer with a narrow sound beam is utilized for imaging, the true velocity v_{true} of moving blood particles can be separated into the axial flow velocity v_z in axial direction z and in a flow velocity v_R in the radial direction R perpendicularly to the direction of sound propagation, see Fig. 1 b).

$$v_z = v_{\text{true}} \cos \alpha, \quad v_R = v_{\text{true}} \sin \alpha, \quad v_{\text{true}} = \sqrt{v_z^2 + v_R^2}. \quad (2.1)$$

The magnitude and the sign of the axial flow velocity v_z can be estimated, i.e. blood flow towards the transducer and that away from it can be distinguished from each other and quantified with the signal processing concepts introduced below. It will be shown that the radial traverse of blood particles through the sound beam causes a modulation of the echo signal. This modulation can be analyzed in order to estimate the radial flow velocity v_R . Given the rotational symmetry of the transducer, it is evident, even at this point, that the *direction* of the radial flow cannot be measured.

The transducer is mechanically scanned along the lateral direction x and measurements are repeated with the transducer being stopped at discrete lateral positions x_n to obtain spatially resolved flow measurements.

2.2. Pulse Echo Measurements Utilizing High Frequency Ultrasound

A spherically focused ultrasound transducer is utilized for all measurements in order to achieve a high measurement sensitivity and a good radial resolution. Pulse echo measurements are performed emitting pulsed ultrasound waves, which propagate along the pencil-like sound beam. Ultrasound waves, which are backscattered at acoustical inhomogeneities inside the tissue and at the moving blood particles, are received by the same transducer. The resulting radio frequency (RF) echo signal is directly sampled over time

of flight (TOF). Under these conditions, the spatial resolution δ_R of the system in radial direction R depends on the sound field characteristics, i.e. on the focusing, the transducer's center frequency f_0 and the aperture diameter D . The system's capability to separate scatterers along the sound beam analyzing echo signals over TOF, i.e. the axial resolution δ_z in the direction of sound propagation z , depends on the transducer's bandwidth B [6, 16–17]:

$$\begin{aligned}\delta_R &= \frac{c}{f_0} F \approx 1600 \mu\text{m} \frac{1}{(f_0/\text{MHz})} F, \\ \delta_z &= \frac{2c \ln 2}{\pi B} \approx 706 \mu\text{m} \frac{1}{(B/\text{MHz})}.\end{aligned}\quad (2.2)$$

In Eq. (2.2) $c \approx 1540 \text{ m/s}$ is the speed of sound and $F = z_0/D$ denotes the ‘f-number’ with the focus length z_0 and the aperture diameter D . The dispersive nature of the tissue attenuation happens to be remarkably prominent in the case of high frequency broadband ultrasound, making it strongly frequency dependent. Because the attenuation increases with increasing frequency, echo signals are shifted down regarding center frequency and bandwidth with increasing depth. Consequently, radial and axial resolutions are degraded over depth [6, 16–17].

2.3. Echo Signal Acquisition for Blood Flow Measurements

Pulsed signals are emitted for spatially resolved measurements along the axial direction. Echo signals, which are backscattered at moving blood particles inside the transducer's sound beam, show a Doppler shift relative to the transmit signal.

A single moving scatterer with a constant axial flow velocity v_z is considered for an analytical description, first. With the speed of sound c and the system's impulse response $h(t)$, the scatterer's axial position $z(t)$ over time and the relationship between the transmit signal $s_T(t)$ and the echo signal $s_E(t)$ are:

$$\begin{aligned}z(t) &= z_0 + v_z t, & s_E(t) &= h(t) * s_T(a(t - t_0)), \\ a &= 1 - \frac{2v_z}{c}, & t_0 &= \frac{2z_0}{c}.\end{aligned}\quad (2.3)$$

Because blood flow velocities are much smaller than the speed of sound, the scaling factor in Eq. (2.3) is very close to one, i.e. $a \approx 1$. Consequently,

long-term observations have to be performed to be able to estimate the axial flow velocity v_z .

In order to analyze the Doppler shift due to the axial scatterer movement the concept of *continuous wave Doppler (CWD) systems* is considered first [1]. In this approach, a sinusoidal continuous wave (CW) transmit signal $s_T(t)$, i.e. a narrowband signal at angular frequency ω_0 , is emitted from a transducer. The echo signal $s_E(t)$, which is caused by backscattering at moving blood particles, is received with another transducer, that is located closely beside the first one, and shows an angular Doppler frequency shift ω_D . The analytical transmit signal $s_{T+}(t)$ and analytical echo signal $s_{E+}(t)$ are given by the following relationships, see Eq. (2.3):

$$s_{T+}(t) = A_0 e^{j\omega_0 t}, \quad s_{E+}(t) = A'_0 e^{j(\omega_0 - \omega_D)t}, \quad \omega_D = \omega_0 \frac{2v_z}{c}. \quad (2.4)$$

The Doppler frequency ω_D is proportional to the axial flow velocity v_z , and is very small compared to the angular frequency ω_0 , which is chosen to be the transducer's center frequency. Usually, the echo signal is quadrature demodulated, i.e. mixed with the CW transmit signal downwards to the base band. As a result, the quadrature demodulated signal (I/Q-signal: in-phase/quadrature phase signal) $s_D(t)$ is obtained:

$$s_D(t) = s_{E+}(t) e^{-j\omega_0 t} = A''_0 e^{-j\omega_D t}. \quad (2.5)$$

Assuming $s_D(t)$ to be analyzed over a long time interval, a spectral analysis delivers directly information about the distribution of axial flow velocities inside the intersection of the two transducer's sound beams [1].

In *PWD systems*, on the other hand, broadband pulsed signals with a *short pulse duration* are emitted in order to obtain a good axial resolution, as motivated above. If only a *single* pulsed signal is emitted, the scaling of the echo signal in Eq. (2.3) is too small to be analyzed with respect to the axial flow velocity v_z . For this reason, *trains of consecutive broadband pulses* with an adjustable and predefined PRF $f_{PRF} = 1/T$ are emitted in PWD systems [1, 2–3, 7].

While the TOF of the ultrasound waves from the transducer to the backscattering structures and back is on the order of several μs , the PRF is some orders of magnitude higher, i.e. on the order of several ms. The analysis of the consecutive echo signals, which are caused by the consecutively

emitted transmit pulses, enables a long-term observation of moving scatterers. It is already evident from this description that a sampling procedure is involved in this approach. In Fig. 2, a simulated sequence of RF echo signals for one single point-like moving point scatterer inside the transducer's sound beam is shown.

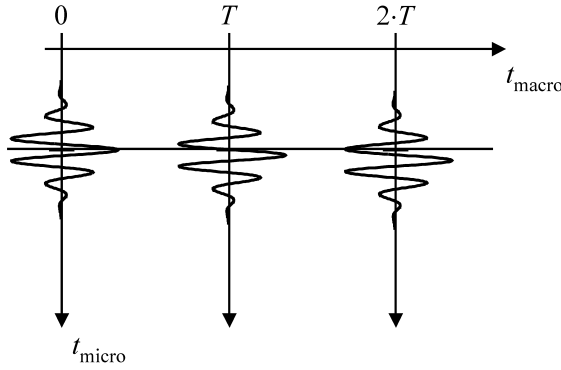


FIGURE 2. Simulated sequence of RF echo signals for one single point-like moving scatterer

In the simulation, a fractional bandwidth $B/f_0 = 80\%$, i.e. a very broadband system, was presumed. The above described PWD concept is analogous to a stroboscopic measurement setup with a periodically triggered flashlight, which illuminates a moving object. With each flash, a “snapshot” is obtained, i.e. the object’s movement is sampled over time. Consequently, the PRF is a crucial parameter, which determines the maximum unambiguously measurable axial flow velocity $v_{z,\max}$ in PWD systems [1]:

$$v_{z,\max} = \frac{c}{4} \frac{f_{RPF}}{f_0}. \quad (2.6)$$

In Fig. 2 the consecutive echo signals, which result from each pulsed transmit signal, are shown side by side. In this representation, the “micro time axis” is equivalent to the TOF, which is, scaled by the speed of sound c , proportional to the axial coordinate z . Consecutive transmissions with the given PRF define the “macro time axis” with a sampling from pulse to pulse. It can be seen that the axial scatterer movement results in an echo signal movement along the micro time axis for consecutive pulses along the macro time axis. Below, this circumstance is utilized to estimate the scatterer’s axial flow velocity. Whereas only a single point-like scatterer was considered so far, the echo signal from blood is caused by the superposition of the ultrasound waves

that are backscattered at many individual blood particles. Consequently, the “speckle” texture, which is very typical for ultrasound images, is also found in the echo signal sequences that are caused from backscattering at blood.

3. High Frequency Ultrasound Pulsed Wave Doppler System Implementation

The block diagram of the implemented PWD system is shown in Fig. 3.

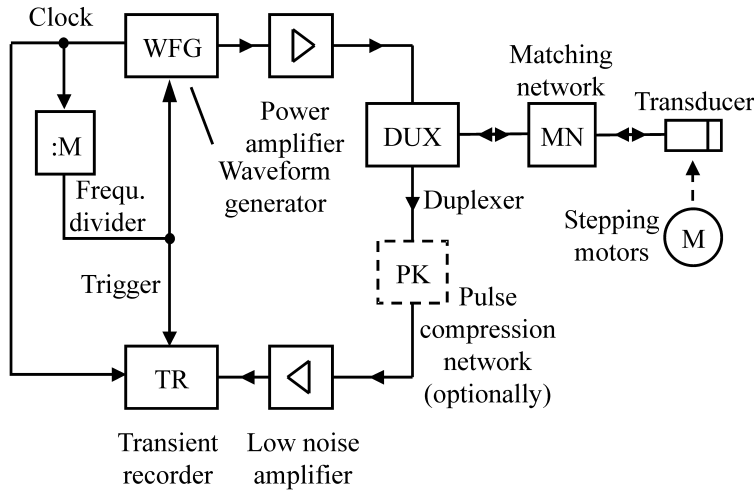


FIGURE 3. Block diagram of the implemented PWD system

The single element transducer is excited with a transmit signal, which is generated by a waveform generator (WFG; Model 2045 polynomial waveform synthesizer, Analogic Inc., USA: 500 MHz maximum sampling frequency, 8 bit amplitude resolution) with a subsequent power amplifier (Model 250L, Amplifier Research Inc., Souderton, PA, USA). Arbitrary signals within a limited bandwidth can easily be generated feeding digitized data of a desired signal into the WFG. In the receive path, the RF echo signal is amplified with a low noise amplifier (AU-1301, Miteq Inc., Hauppauge, NY, USA: 30 dB gain). Thereafter, the RF signal is directly sampled and digitized with a transient recorder (TR; RTD 720, Tektronix Inc., Beaverton, OR, USA: 500 MHz sampling frequency, 8 bit amplitude resolution). Pulse echo measurements are performed, i.e. the same transducer is utilized for transmission and reception of ultrasound waves. A duplexer (DUX) is utilized to actively switch

the transducer between the transmitter during signal transmission and the receiver during echo signal reception.

It is essential to synchronize the transmitter and the receiver in the PWD system in order to acquire the echo signal sequences in an appropriate way. Furthermore, a well defined and adjustable PRF is required. For these reasons, the clock signal of the WFG is connected with the external clock input of the TR. Furthermore, both devices, the WFG and the TR, are triggered with the same signal, which is derived from the clock signal with an adjustable frequency divider. The PRF is thus an integral divider of the 500 MHz clock signal, see Fig. 3. With each trigger event, a pulsed transmit signal is emitted and the resulting RF echo signal is acquired after a constant time delay, which is adjustable in the WFG.

The electrical matching between the transducer and the driving electronics can be improved with an optional matching network between the DUX and the transducer. A reactance matching network was specially designed for this purpose. However, the design of a *broadband* matching network is a difficult and challenging task. Consequently, the system's bandwidth is lower with the network than without it [16]. The transducer can be mechanically scanned in the two orthogonal directions in the horizontal plane using two stepping motors (Iselautomation KG, Eichenzell, Germany). A controlled DC-motor (Physik Instrumente GmbH, Karlsruhe, Germany) is utilized to mechanically move the transducer in axial direction. This allows the positioning of the transducer's focus in a desired depth, which is usually the center of the region of interest (ROI). In Fig. 4, a photograph of the implemented PWD system is shown.

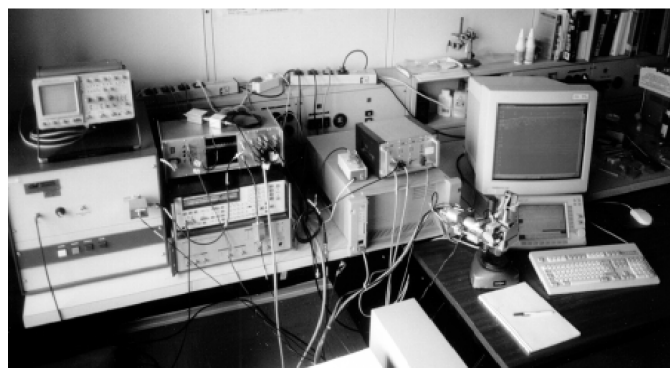


FIGURE 4. Photograph of the implemented PWD system

4. High Resolution Blood Flow and Perfusion Imaging

The acquired echo signal sequences are analyzed with the aim to quantify blood flow velocities and perfusion with a high resolution. Appropriate estimation approaches are required in the context of very broadband signals, which are applied in the implemented PWD system. Spatial and velocity resolution, i.e. the system's ability to spatially resolve flow conditions and to differentiate flow velocities, are crucial parameters in this context.

4.1. Parameters for the Quantification of Blood Flow and Perfusion

In contrast to the *morphological* nature of B-mode (B: “brightness”) imaging of biological tissues Doppler techniques allow for *functional imaging*, i.e. they enable to quantify blood flow. Though several parameters like flow velocities profiles, mean flow velocities, volume flow, quantified turbulences, etc. are of interest from the physiological point of view, not all of them are directly accessible with ultrasound. Furthermore, a suitable visualization of measured data is an important issue in the medical application. The following flow visualization modalities are typically applied in medical sonography [1]:

- **Duplex mode:** The axial flow velocity *distribution* of blood particles inside one single point of interest is estimated and visualized over time. This allows to analyze flow velocity changes over time in great detail.
- **Color flow mapping (CFM):** *Mean* axial flow velocities of blood particles are estimated point-wise in a user-defined ROI. Estimated mean axial velocities are visualized in a color-coding scheme and superimposed to a grayscale B-mode image. This facilitates a detailed analysis of the *spatial* distribution of mean flow velocities over time.
- **Power mode:** The *energy* of signals, which are backscattered at moving blood particles, is point-wise estimated in a user-defined ROI, and results are visualized in a color-coding scheme. The perfusion of organs can be analyzed in this mode. Blood flow is only qualitatively visualized and no information about flow velocities is included.

The schematic in Fig. 5 shows the relationship between the different parameters and the actually given distribution of axial flow velocities. It is assumed, that the likelihood $L(v_z)$ for a given axial flow velocity v_z is estimated at each point of interest along the z axis. In the figure, $L(v_z)$ is normalized to its maximum.

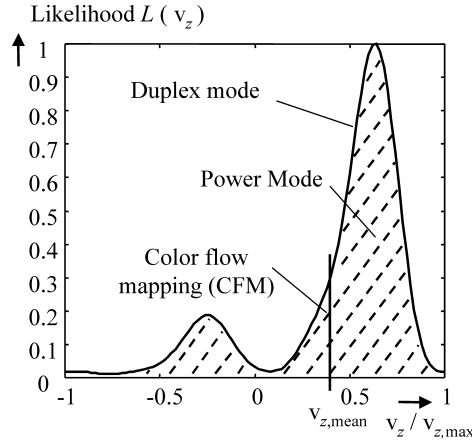


FIGURE 5. Parameters and imaging modalities for flow and perfusion quantification

For color flow mapping the mean flow velocity, $v_{z,\text{mean}}$ is calculated as the centroid, i.e. the first moment over the zero order moment, of the velocity distribution $L(v_z)$:

$$v_{z,\text{mean}} = \frac{\int v_z L(v_z) dv_z}{\int L(v_z) dv_z}. \quad (4.1)$$

Several approaches for the estimation of the axial flow velocity distribution as well as an approach for the estimation of the mean radial flow velocity component with rotational symmetric sound beam transducers are discussed below.

4.2. Axial Flow Velocity Estimation

It was already discussed above that the flow of scatterers along the axial coordinates results in a movement of consecutive echo signals along the micro time axis from pulse to pulse, see Fig. 2. Conventionally, sequences of *narrowband* burst signals, i.e. trains of low-frequency pulsed signals, that modulate the amplitude of a carrier signal at the system's center frequency f_0 , are transmitted in PWD systems. Under these conditions, the axial flow velocity distribution can be estimated sampling the sequence of quadrature demodulated echo signals at *constant* lags on the micro time axis for consecutive pulses along the macro time axis. Employing the fast Fourier transform (FFT) of sampled data, estimates for the axial flow velocity distribution in

each depth along the sound beam are obtained (FFT-approach) [1, 7]. Because spectral information is analyzed, this procedure can be classified as a *frequency domain* approach. Kasai et al. proposed a very efficient technique for estimating the mean axial flow velocity analyzing the autocorrelation function of sampled data [19].

However, these approaches are not appropriate in the context of *broad-band* transmit signals, which are utilized in the implemented PWD system in order to obtain a good spatial resolution in the axial direction of sound propagation. The reason for this is that the envelope of the short duration pulsed signals significantly passes through the range gates from pulse to pulse, i.e. through the points at constant depths along the micro time axis. This can be seen in Fig. 6, which shows another simulated echo signals sequence for six discrete moving point-like scatterers with different axial flow velocities. For the simulation, again, a very broadband system with a fractional bandwidth $B/f_0 = 80\%$ was presumed:

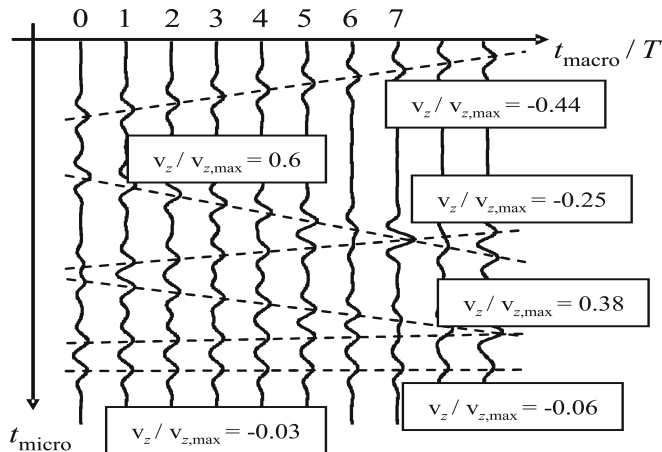


FIGURE 6. Simulated sequence of RF echo signals for 6 discrete single point-like moving scatterer [7]

The axial scatterer movement can be observed over a very small number of pulses only by sampling the echo signals sequence at constant lags on the micro time axis. As a result of this, a *spectral broadening* occurs applying the FFT approach, what is the more distinct the higher the axial flow velocity is. For this reason, the axial flow velocity resolution, which quantifies the system's ability to resolve different axial flow velocities, is the worse the higher the axial flow velocity is [7].

More recently, new approaches for the analysis of the RF echo signals in the *time domain* have been introduced. The *mean* axial flow velocity of moving blood particles is analyzed by calculating the cross correlation function of consecutive RF echo signals, i.e. of signals recorded along the micro time axis, for consecutive pulses along the macro time axis (RF-CC approach: Radio frequency cross correlation). Because the axial scatterer movement is directly estimated by analyzing the time domain characteristics of the echo signals, this technique is classified to be a *time domain* approach. This approach, however, suffers the drawback of estimating merely the means axial flow velocity instead of the more desirable velocity distribution.

The pulsed echo signals sequence for single point-like scatterer, which move with a constant axial flow velocity along the sound beam, shows a constant time shift from pulse to pulse along the micro time hence the scatterer moves along *lines of constant inclination* in the two-dimensional micro and macro time axes space, see Fig. 6. Consequently, the axial scatterer movement can be tracked by sampling the sequence of echo signals along trajectories, which correspond to different axial flow velocities. For each trajectory, the likelihood for given scatterer with a corresponding axial flow velocity is estimated. This is done by analyzing the sampled RF echo signal or the sampled quadrature demodulated signal (WMLE approach: wideband maximum likelihood estimator/Butterfly Search Algorithm [6–7, 20–23]). Because spectral and time domain information is combined in these approaches, they are classified as *combined time/frequency domain* approaches, here [12].

Figure 7 shows the estimated axial velocity distributions for the echo signals sequence that are shown in Fig. 6. Results obtained with the FFT approach and with the Butterfly Search Technique are shown [7].

It can be seen that the axial resolution and the axial velocity resolution, which quantifies the system's capability to distinguish the axial positions and axial flow velocities of moving scatterers, are better with the Butterfly Search Technique than with the FFT approach. Furthermore, utilizing the FFT, spatial and velocity resolutions depend on the axial flow velocities [6–7]. This is due to enlarged spectral broadening brought about by shorter times of observation, in which the scatterer movement can be analyzed.

In conclusion, the tracking of the axial scatterer movement in the context of the Butterfly Search approach enables a long-time analysis of the echo signals sequence along the macro time axis independent of the transmit signal pulse width. Consequently, axial flow velocity distribution estimates have

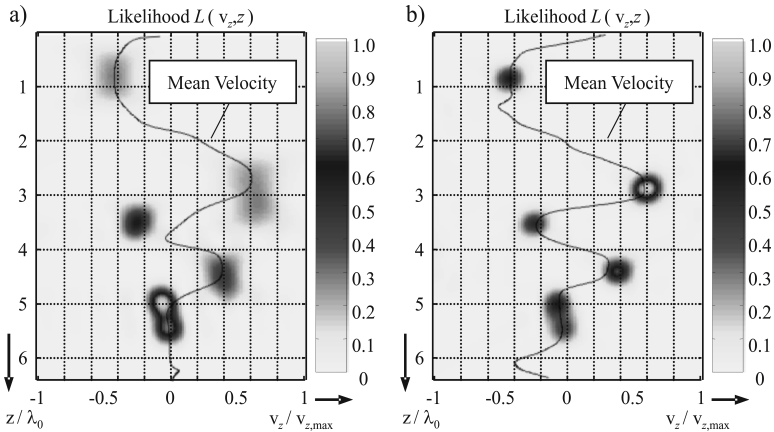


FIGURE 7. Estimated axial velocity distribution: a) FFT approach, b) Butterfly Search Technique [7]

a lower variance with the Butterfly Search approach than with the FFT approach albeit at the expense of much higher computational cost.

4.3. Radial Flow Velocity Estimation

So far only axial scatterer movements in the direction of sound propagation were considered and it was assumed that the scatterers movement in transverse direction is of no further consequence. Actually, the traverse of blood particles through the sound beam causes a modulation of consecutive echo signals from pulse to pulse.

With the given rotational symmetry of the sound beam of the spherically focused transducer's sound beam, it is assumed that the point spread function (PSF) $h(t, z', R')$, which is the system's response for a single point-like scatterer at an axial and lateral position $z = z'$ and $R = R'$, is separable into an axial component $h_z(t, z')$ and a radial component $h_R(R', z')$:

$$h(t, z', R') = h_z(t, z') h_R(R', z'). \quad (4.2)$$

The system's response regarding axial scatterer movements was already discussed above. If the scatterers pass the sound beam in transverse direction, see Fig. 1 b), and if the observation time is sufficiently large, a significant modulation of the echo signals sequence along the macro time axis is caused. This modulation depends on the transducers' sound field characteristics. The magnitude of the radial flow velocity v_R can be estimated with measurements

of the PSF as a reference. However, the *direction* of the radial flow cannot be measured with the rotational symmetry of the sound beam. Because of the speckle texture, which is inherent in the echo signals backscattered at moving blood particles, the speckle statistics has to be analyzed. In the proposed estimation approach, this is performed analyzing the auto-covariance function (ACVF) of the echo signals envelope [8, 10–11].

Again, simulated echo signals sequences have been utilized to establish and to evaluate the estimation approach. The simulations were based on the geometry in Fig. 8.

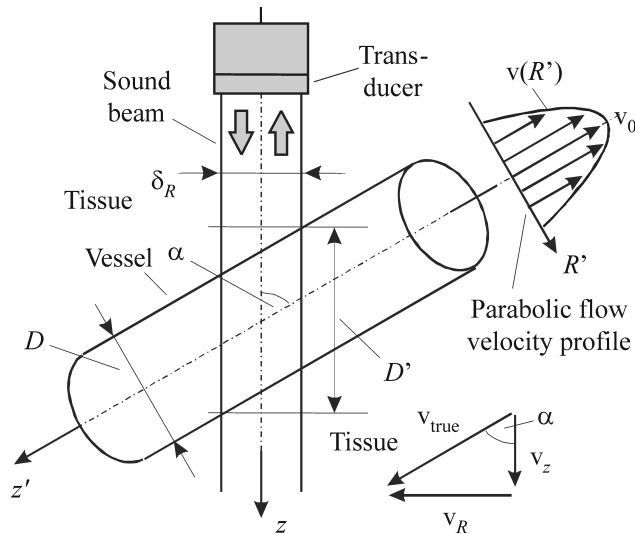


FIGURE 8. Flow simulations: Vessel diameter D , insonation angle α

Laminar flow with a parabolic true velocity profile inside a vessel with a given diameter D was assumed. Furthermore, uniformly distributed point-like scatterers were assumed to be located inside the vessel. As an example Fig. 9 shows a simulated echo signals envelope sequence for a single transducer position.

An incident angle $\alpha = 90^\circ$, i.e. a transverse flow relative to the direction z of sound propagation, was chosen. The system's axial and radial resolution in the simulation were $17 \mu\text{m}$ and $54 \mu\text{m}$ respectively like in the implemented PWD system. A vessel diameter $D = 450 \mu\text{m}$, a peak flow velocity of $v_{\text{true},\text{max}} = 22 \text{ mm/s}$ and a PRF $f_{\text{PRF}} = 3200 \text{ Hz}$ was assumed. A number $M = 50$ of echo pulses was simulated, i.e. the observation time was about 16 ms.

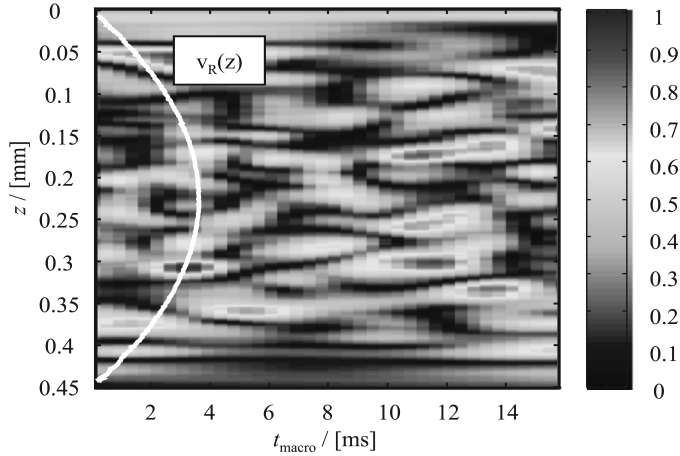


FIGURE 9. Simulated echo signals envelope sequence

It can be seen in Fig. 9 that the given speckle pattern decorrelates fastest in the center of the vessel, where the radial flow velocity is the largest. On the other hand, the echo signals are almost stationary at the vessel walls because the flow velocity reaches zero, i.e. no scatterer movement is given. Consequently, the rate of the decorrelation of echo signals along the macro time axis is a measure for the magnitude of the radial flow velocity. However, the actual sound beam characteristics, i.e. the radial component $h_R(R', z')$ of the PSF, see Eq. (4.2), has to be known.

Calibration measurements have been performed to measure the system's PSF. A tungsten wire with a $7\text{ }\mu\text{m}$ diameter, which is significantly smaller than the transducer's axial and radial resolution and the wavelength at the system's $f_0 = 50\text{ MHz}$ center frequency, was utilized as a point-like imaging object. Because of the focused sound beam characteristics, which significantly changes over depth z , see Fig. 1 b), the wire was imaged in several depths [8, 10-11, 16].

The mean radial flow velocity is estimated in each depth z analyzing the envelope of the echo signals sequence along the trajectory in the micro and macro time axis space that corresponds to the estimated mean axial flow velocity at the same depth. The decorrelation of speckle is analyzed by calculating the ACVF of the sampled data, see Fig. 10.

The ACVF of the B-mode data of the measured PSF is utilized as reference. The ACVF of measured data is a replica of the ACVF of the radial

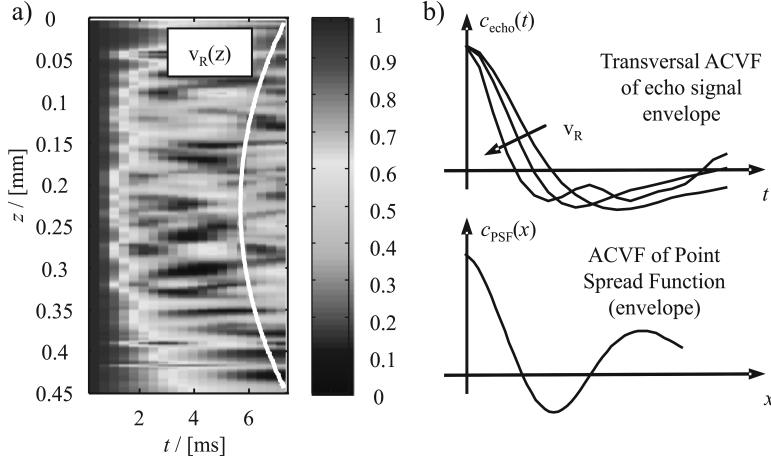


FIGURE 10. a) ACVF of echo signal envelope over depth z , b) connection between ACVF of echo signal envelope and ACVF of measured PSF

component $h_R(R', z')$ of the PSF, which is scaled by the unknown mean radial flow velocity v_R [8, 10-11]:

$$c_{\text{PSF}}(x) = c_{\text{echo}}(v_R t). \quad (4.3)$$

The estimated mean radial flow velocities over depth are shown in Fig. 11. The radial flow velocity profile is reconstructed under the simulated conditions, but the variance of flow velocity estimates is relatively high.

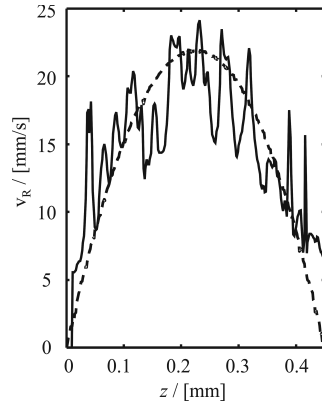


FIGURE 11. Estimated radial flow velocity over depth

4.4. Stationary Echo Cancellation and Perfusion Estimation

Echo signals, which result from backscattering in the tissue, are stationary signals, i.e. they do not change from pulse to pulse as long as movement artifacts can be neglected. In contrast, echoes from the backscattering at moving blood particles change from pulse to pulse along the macro time axis. Because echoes from blood are significantly smaller than the echoes from the tissue, it is desirable to suppress the stationary echoes prior the estimation of flow velocities. Furthermore, if echoes from backscatter at blood are separated from backscatter from the tissue, the signal energy is a parameter for perfusion imaging, which is utilized for power mode imaging.

Making use of the fact that stationary echoes are constant components of the sampled data along the macro time axis for constant lags on the micro time axis, i.e. at constant depths z , this suppression can be performed by digital filtering. The “*wall-filter*” has to be a digital high-pass filter. If a finite impulse response (FIR) filter of an *odd* order N is applied, the relationship between the digital input signal x_n and the digital output signal y_n can be described as follows:

$$y_n = \sum_{i=0}^N h_i x_{n-i}, \quad \text{with: } h_i = -h_{N-i}. \quad (4.4)$$

The impulse response in Eq. (4.3) ensures that a constant input signal x_n results in an output signal $y_n = 0$, what is desired in order to suppress the stationary echo signals. In Fig. 12 the magnitude of the filter’s transfer function is shown for different filter orders N and for the approximation of a rectangular transfer characteristics with a cut-off-frequency corresponding to an axial cut-off flow velocity $v_{z,\text{cut}} = 0.1 \cdot v_{z,\text{max}}$.

Another possible wall-filter implementation, which is a very straight forward approach, is to estimate the mean value of the input signal sequence x_n , $n = 1, 2, \dots, M$, which is utilized for velocities estimation. At the wall-filter’s output, the following signal sequence y_n is assigned:

$$\bar{x} = \frac{1}{M} \sum_{i=1}^M x_i, \quad y_n = x_n - \bar{x}, \quad n = 1, 2, \dots, M. \quad (4.5)$$

The relationship between the wall-filter input and output in Eq. (4.5) is a non-causal relationship.

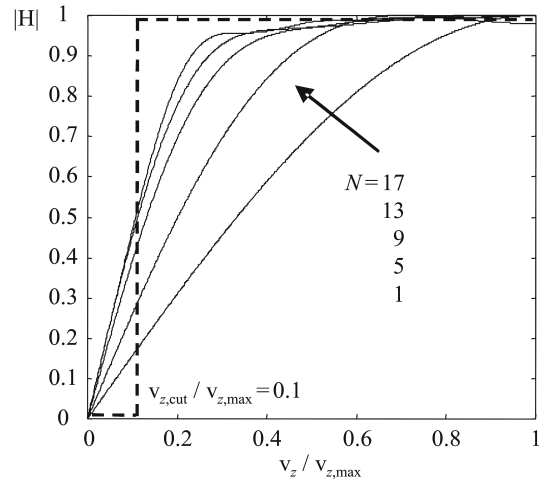


FIGURE 12. Wall-filter transfer function (magnitude) for different filter orders N

5. Flow Phantom Measurements

Flow phantom measurements have been performed in order to evaluate the proposed PWD system and the proposed approaches for flow velocities estimation. Equivalent to the simulations discussed in the context with Fig. 8, it was intended to perform the measurements under well defined conditions. Flow phantoms were specially designed for this purpose, see Fig. 13.

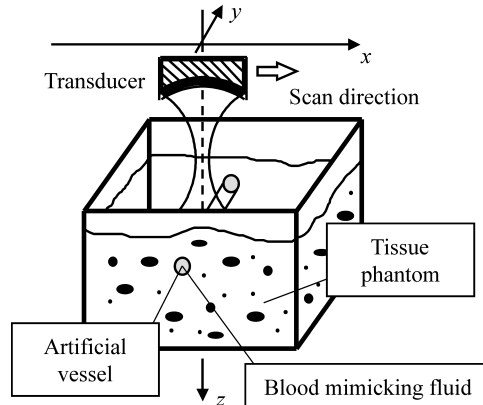


FIGURE 13. Flow phantom: artificial vessel embedded in agar with silica gel particles

Artificial vessels with a well defined diameter were produced by embedding metal wires in blocks of agar that was used as tissue mimicking material. Silica gel particles were added into the agar to obtain an acoustic backscattering. The artificial vessels, which were obtained after removal of the wires, were perfused with a well defined volume flow using a motor driven syringe pump. A blood mimicking fluid, which consists of particles of yeast in a solution of glycerol and water, was used for the measurements.

In Fig. 14 the envelope of echo signals sequences, which have been acquired at a flow phantom with $D = 450 \mu\text{m}$ diameter, $\alpha \approx 65^\circ$ insonation angle and $0.177 \text{ mm}^3/\text{s}$ volume flow, is shown.

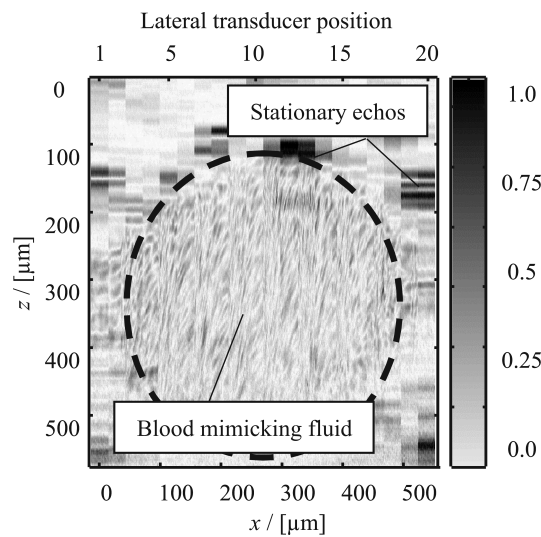


FIGURE 14. Flow phantom measurement: envelope of acquired echo signals sequences at discrete lateral transducer positions

The echo signals sequences at the discrete lateral transducer positions are shown side by side. In each sequence the echoes from $M = 50$ transmit pulses were acquired with a PRF $f_{\text{PRF}} = 800 \text{ Hz}$. Stationary echo signals from the tissue phantom are horizontal lines in the echo signal sequences. The echoes from the moving scatterers inside the blood mimicking fluid are visible as slanted lines, compare Fig. 6. A parabolic flow profile with a maximum flow velocity $v_{\text{true,max}} = 2.22 \text{ mm/s}$ is expected under the given flow conditions. The expected maximum axial and radial flow velocities are $v_{z,\text{max}} = 0.94 \text{ mm/s}$ and $v_{R,\text{max}} = 2.0 \text{ mm/s}$, respectively, with the given insonation angle.

The estimated axial and radial flow velocity profiles are shown in Fig. 15. The axial flow velocity profile estimate shows a maximum at the artificial vessel's center and smaller flow velocities towards the vessel wall. The maximum estimated axial flow velocity $\hat{v}_{z,\max} = 0.66 \text{ mm/s}$ is smaller than expected. This can be explained by the given uncertainty about the actual insonation angle α in the measurement. Equivalent to the above discussed flow simulation, the variance of the estimated radial flow velocities profile is relatively high. The mean estimated radial flow velocity $\hat{v}_{R,\max} = 2.2 \text{ mm/s}$ at the artificial vessel's center is in the expected range [10]:

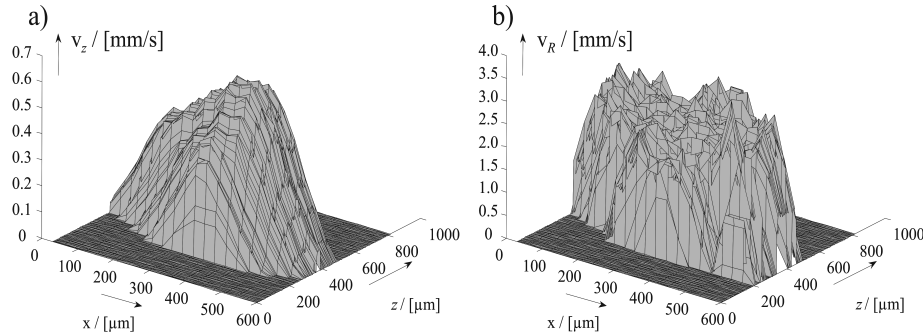


FIGURE 15. a) estimated axial flow velocity profile, b) estimated radial flow velocity profile [10]

6. In Vivo Measurements

The implemented PWD system was developed for blood flow imaging in small vessels with small flow velocities. In vivo measurements have been performed at small veins at the back of a human hand, see Fig. 1. Echo signals frames were acquired with a PRF $f_{PRF} = 1 \text{ kHz}$ and an insonation angle $\alpha \approx 65^\circ$.

In Fig. 16 a cutout of RF echo signals sequences at consecutive lateral transducer positions are shown before and after wall-filtering.

The wall-filter, which is described in Eq. (4.5), was utilized. Again, the echoes from the tissue and the vessel wall are visible as horizontal line. They are suppressed significantly after wall-filtering. The echo signal energy after the wall-filter is utilized as a measure to decide at each point in the color flow image and power mode image whether flow is visualized or not. If the energy is below a user-defined threshold, the morphological B-mode image

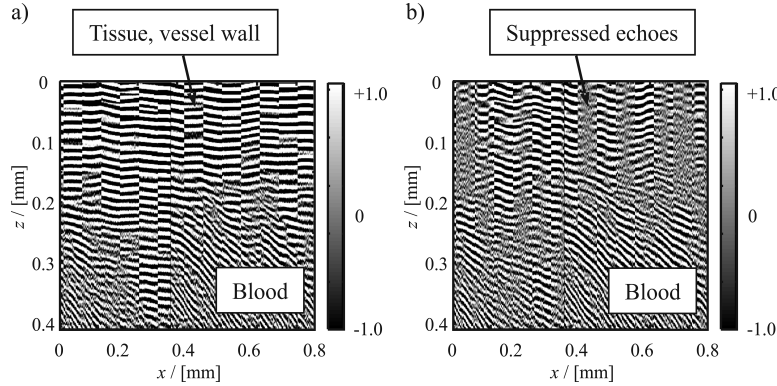


FIGURE 16. In vivo imaging: echo signals sequences: a) before wall-filtering, b) after wall-filtering

information is visualized. If the energy is larger than the threshold, the flow information is imaged.

The color flow image in Fig. 17 a) shows the mean axial flow velocity distribution over the vessel's cross section.

The maximum estimated axial flow velocity is $\hat{v}_{z,\max} \approx 5 \text{ mm/s}$. In the power mode image in Fig. 17 b) the perfused cross-section is qualitatively visible. The echo signal power is the highest at the vessel's center. This is

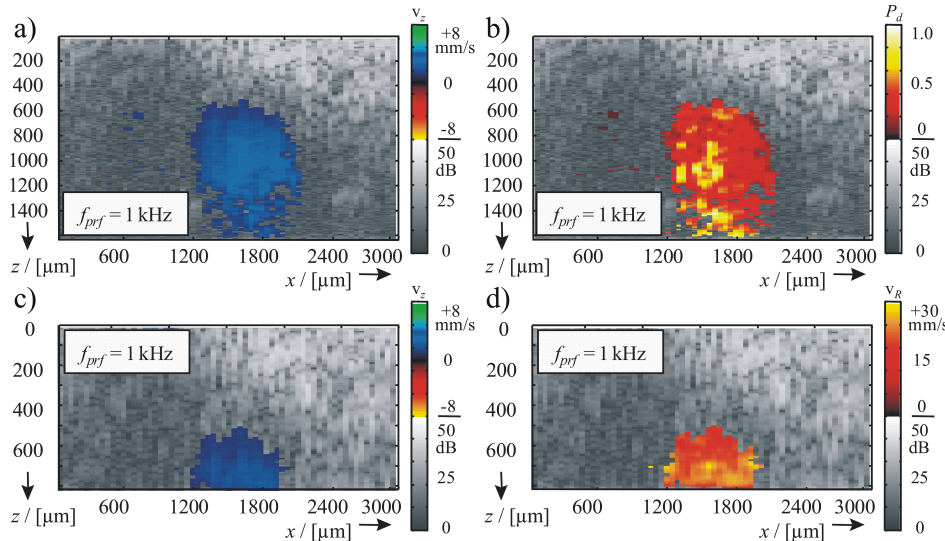


FIGURE 17. Vein at back of human hand: a) mean axial flow velocities, b) power mode, c) mean axial flow velocities, d) mean radial flow velocities.

because the signal energy after the wall filter is the higher the more backscattering blood particles are given and the higher the flow velocities are. Estimated mean axial flow velocities and mean estimated radial flow velocities are shown in Fig. 17c) and d). Because the signal to noise ration (SNR) of acquired signals is too low at higher depths, the color flow images are shown over a more limited depth range:

The estimated mean radial flow velocities distribution shows a maximum at the vessel's center and a decrease towards the vessel wall, as well. The transducer is mechanically scanned along the lateral coordinate x in order to acquire echo signal sequences at consecutive lateral transducer positions. Because of the cyclic heart beat and the relatively long time between consecutive acquisitions, the PWD system is synchronized to the heart beat cycle. This is achieved by triggering the data acquisition at each transducer position with the output of a photo-plethysmography system, which optically measures the heart beat cycle. Under these conditions, the color flow map represents the mean flow velocities at a constant phase of the cyclic heart beat.

7. Summary and Conclusions

A concept for the utilization of high frequency and broadband ultrasound for high resolution blood flow imaging in small vessels was presented. A PWD system with a spherically focused single element transducer with 50 MHz center frequency and 80% fractional bandwidth has been designed and implemented. High frequency and broadband ultrasound is utilized in order to achieve a good spatial resolution. Transmit signals are generated with a waveform generator, and echo signals are directly sampled with a transient recorder. Transmitter and receiver are synchronized with each other to acquire data with a well defined timing reference.

Referring to the cylindrical symmetric sound beam characteristics, the true flow velocity was separated into the axial flow velocity component in the direction of sound propagation and the radial component in transverse direction. Acquired echo signals sequences were analyzed in a two dimensional space with the micro and macro time axes.

It was shown that *combined time/frequency domain* approaches for axial flow velocities estimation can advantageously be applied in the context of broadband transmit signals. Furthermore, an approach for the estimation

of the magnitude of radial flow velocities was presented. The proposed estimation techniques were evaluated by flow simulations and flow phantom measurements.

The designed PWD system was successfully implemented. Results of flow phantom measurements show that flow velocities in the range of some few mm/s in artificial vessels as small as 100 μm in diameter are reliably estimated with the proposed approaches. In vivo measurements have been performed at small veins at the back of a human hand. It was shown that axial and radial flow velocities profiles in vessels with diameters as small as about 500 μm can be assessed.

Acknowledgement

This work has been conducted at the Institute of High Frequency Engineering of the Ruhr-University Bochum, Germany. The support of Prof. Dr.-Ing. Helmut Ermert is greatly appreciated.

References

1. J.A. JENSEN, *Estimation of Blood Velocities Using Ultrasound*, Cambridge University Press, 1996.
2. D.A. CHRISTOPHER, B. G. STARKOSKI, P.N. BURNS, and F.S. FOSTER, *A high frequency pulsed-wave Doppler ultrasound system for detecting and imaging blood flow in the microcirculation*, IEEE Ultrasonics Symposium, San Antonio, Texas, 1996.
3. D.A. CHRISTOPHER, P.N. BURNS, B.G. STARKOSKI, and F.S. FOSTER, *A high frequency pulsed-wave Doppler ultrasound system for the detection of blood flow in the microcirculation*, Ultras. in Med. and Biol., **23**:997–1015, 1997.
4. D.E. GOERTZ, D.A. CHRISTOPHER, J.L. YU, R.S. KERBEL, P.N. BURNS, and F.S. FOSTER, *High frequency color flow imaging of the microcirculation*, IEEE Ultrasonics Symposium Proceedings Sendai, pp.1525–1528, 1998.
5. D.E. GOERTZ, J.L. YU, R.S. KERBEL, P.N. BURNS, and F.S. FOSTER, *High frequency 3D flow imaging of the microcirculation*, IEEE Ultrasonics Symposium Proceedings Lake Tahoe, pp.1481–1484, 1999.
6. H. ERMERT, M. VOGT, C. PASSMANN, S. EL GAMMAL, K. KASPAR, K. HOFFMANN, and P. ALTMAYER, *High frequency ultrasound (50-150 MHz) in dermatology*, [in:] Skin Cancer and UV Radiation, P. Altmeyer, K. Hoffmann, and M. Stücker, [eds.], pp.1023–1051, Springer, Berlin, Heidelberg, New York, 1997.

7. M. VOGT and H. ERMERT, *Application of high frequency broadband ultrasound for high resolution blood flow measurement*, [in:] Proceedings of the IEEE 1997 Ultrasonics Symposium, pp.1243–1246, 1997.
8. M. VOGT and H. ERMERT, *High resolution true velocity mapping with a 50 MHz pulsed wave Doppler system for dermatology*, [in:] Proceedings of the IEEE 1998 Ultrasonics Symposium, pp.1529–1532, 1998.
9. M. VOGT and H. ERMERT, *Comparison of blood flow imaging concepts with coherent and incoherent RF carriers in the 50 MHz ultrasound region for application in dermatology*, [in:] Proceedings of the IEEE 1999 Ultrasonics Symposium, pp.1499–1502, 1999.
10. M. VOGT, C. CURIO, H. ERMERT, S. EL GAMMAL, K. KASPAR, K. HOFFMANN, M. STÜCKER, and P. ALTMAYER, *Kombinierte Erfassung von axialem und transversalem Blutfluß mit einem 50 MHz-Ultraschall-B-Bild-System für die Dermatologie*, Zeitschrift für Medizinische Physik, **1**:30–36, 1999.
11. M. VOGT, H. ERMERT, S. EL GAMMAL, K. KASPAR, K. HOFFMANN, M. STÜCKER, and P. ALTMAYER, *High resolution estimation of axial and transversal bloodflow with a 50 MHz pulsed wave Doppler system for dermatology*. [in:] Acoustical Imaging, **24**, Kluwer Academic/Plenum Publishers, New York, 2000.
12. M. VOGT, A. PLUTA, and H. ERMERT, *Comparison of time and frequency domain approaches for blood velocity estimation in small vessels using high frequency ultrasound*, [in:] Proceedings of the IEEE 2000 Ultrasonics Symposium, pp.1521–1524, 2000.
13. M. VOGT, *Direct sampling and baseband conversion in Doppler systems for high-frequency ultrasound blood flow measurements*, Electronics Letters, **41**(14):789–790, 2005.
14. R.F. WAGNER, S.W. SMITH, J.M. SANDRIK, and H. LOPEZ, *Statistics of speckle in ultrasound B-scans*, IEEE Trans. Sonics and Ultras., **30**(3):156–163, 1983.
15. W. LI, A.F.W. VAN DER STEEN, C.T. LANCEE, I. CESPEDES, and N. BOM, *Blood flow imaging and volume flow quantitation with intravascular ultrasound*, Ultras. in Med. and Biol., **24**(2):203–214, 1998.
16. M. VOGT, K. KASPAR, P. ALTMAYER, K. HOFFMANN, and S. EL GAMMAL, *High frequency ultrasound for high resolution skin imaging*, Frequenz, **55**(1–2):12–20, 2001.
17. M. VOGT and H. ERMERT, *High frequency ultrasound for high resolution imaging: Technical concepts and applications in dermatology*, [in:] Proceedings of the Workshop on Ultrasound in Biomeasurements, Diagnostics and Therapy, A. Nowicki and J. Litniewski, [eds.], pp.115–121, Abimed Lecture Notes vol.2, IPPT PAN, CoE Abimed, Warsaw 2005.
18. M. VOGT and H. ERMERT, *Biomicroscopy of the skin utilizing high frequency ultrasound in a multi modal approach*, [in:] Proceedings of the Workshop on Ultrasound in Biomeasurements, Diagnostics and Therapy, A. Nowicki and J. Litniewski, [eds.],

- pp.69–73, Inst. of Fundamental Technological Research, Polish Academy of Sciences (IPPT PAN, ABIOMED), Warsaw, Poland.
19. C. KASAI, K. NAMEKAWA, A. KOYANO, and R. OMOTO, *Real-time two-dimensional blood flow imaging using an autocorrelation technique*, IEEE Trans. Ultrason. Ferroelec. Freq. Contr., SU-**32**: 458–464, 1985.
 20. K.W. FERRARA, *Blood flow measurement using ultrasound*, [in.] Biomedical Engineering Handbook, J.D. Bronzino, [ed.], CRC Press, IEEE Press, pp.1099–1118, 1995.
 21. K.W. FERRARA and V.R. ALGAZI, *A new wideband spread target maximum likelihood estimator for blood velocity estimation-part I: theory*, IEEE Trans. Ultrason. Ferroelec. Freq. Contr., **38**: 1–16, 1991.
 22. K.W. FERRARA and V.R. ALGAZI, *A new wideband spread target maximum likelihood estimator for blood velocity estimation-part II: evaluation of estimators with experimental Data*, IEEE Trans. Ultrason. Ferroelec. Freq. Contr., **38**: 17–26, 1991.
 23. S.K. ALAM and K.J. PARKER, *The butterfly search technique for estimation of blood velocity*, Ultrasound in Med. and Biol., **21**: 657–670, 1995.
-

Experimental Blood Flow Investigations in Large Human Arteries

PAOLO FIDANZATI, TIZIANO MORGANTI, LUCA BASSI
and PIERO TORTOLI

*Electronics and Telecommunications Department
University of Florence
Via S. Marta, 3 – 50139 Florence, Italy
piero.tortoli@unifi.it*

Extension of classic spectral analysis to all Doppler signals backscattered along an ultrasound (US) M-line has been proved useful to provide detailed information on blood flow behaviour in major human arteries. Application of a 2D auto correlation processing method to the echo signals reflected from the arterial walls has allowed their elastic properties to be investigated, too.

This paper reviews some of the main activities developed at the Microelectronics Systems Design (MSD) Laboratory of the University of Florence with the aim of extracting valuable hemodynamic and mechanic information from the US M-line echo signals.

Key words: *Doppler ultrasound, velocity profiles, arterial mechanics*

1. Introduction

Ultrasound (US) non invasive investigations are capable of providing useful information on either the hemodynamics and the mechanics of large human arteries [1, 2]. To achieve simultaneously both pieces of information we have developed a real-time digital processing board, to be connected to an external US transmitter-receiver (TX-RX) unit.

Next sections report on the main features of such board and the complete experimental setup in which it has been used. Results of different applications are then reported, for hemodynamic investigations in the CCA and aorta, and for non invasive HCT measurement. Estimation of the board processing capability to simultaneous distension measurement is then described, and some examples of in vitro and in vivo experiments are reported.

2. Materials and Methods

The typical experimental setup used in our blood vessel investigations consists of either a custom made US transmitter-receiver (TX-RX) unit, or a commercial ecographic US machine (Megas, Esaote S.p.A., Florence, Italy), paired with a proprietary multigate acquisition processing board [3] (Fig. 1).

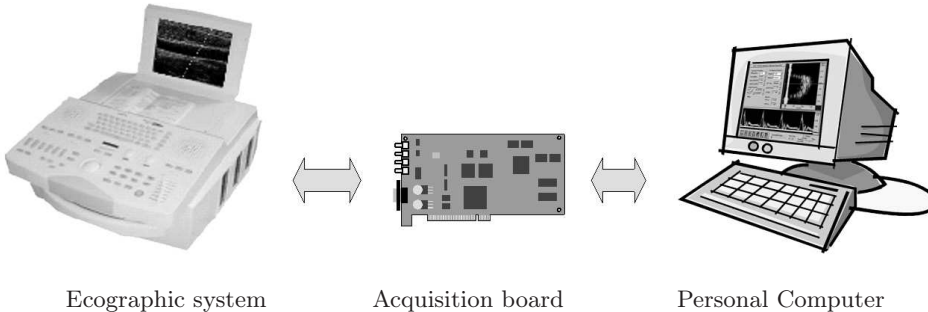


FIGURE 1. Experimental setup

When the ecographic apparatus is used, brightness mode (B-mode) imaging capability is exploited to explore the region of interest (ROI) and choose a single line of investigation (M-line) across the image. When the orientation of such line has been fixed, the pulsed wave (PW) mode is switched on. US bursts, focused along the selected line, are transmitted and received every pulse repetition interval (PRI).

The received echo signals are amplified and coherently demodulated to provide base band in phase/quadrature (I/Q) channels.

The multigate processing system is a PCI-bus plug in card, hosted in a PC. Such board first performs the required analogue conditioning of the base band signals coming from the US system. Such signals are then digitized with two 10 MSPS 14-bit ADCs, generating 128 digital complex samples for each pulse transmitted at the pulse repetition frequency (PRF=1/PRI) rate. This resolution is necessary to preserve the high input dynamic range due to the possible simultaneous presence of both strong and weak US echoes.

The dedicated real time signal processing is performed by a TMS320C6202 DSP (Texas Instruments Inc., TX) [3]. Elaborated data are sent to the host PC through the PCI bus for real time display. Raw data can also be stored on the PC hard disk.

The system is provided with a dedicated software on the PC that lets the user viewing in real time all the results of the signal processing, and reviewing raw data stored on the disk, to perform post processing operations and measurements.

I/Q signals coming from a selected gate are also processed in real time on the PC with a Hilbert transform based method [4, 5] that allows the separation of the Forward and Reverse (Fw/Rv) signal components (related to positive and negative velocities, respectively). Fw/Rv samples, produced at PRF rate are resampled [6] to match the digital audio standard formats (44.1 or 48 kHz) and played with a low latency (< 60 ms) on stereo speakers through the sound card of the host PC [7]. Audio data can also be saved on the hard disk in uncompressed (.wav) or compressed (.mp3) format [8]. All the audio signal processing is made in real time on the PC with a dedicated software, with no extra load for the DSP unit on the acquisition/processing board.

3. Hemodynamics Investigations

The multigate Doppler system is capable of giving precise information about the blood velocity distribution inside the vessel (velocity profile). The DSP elaborates the samples coming from different depths, with an optimized 128-point FFT algorithm, that generates, for each depth, the corresponding power spectral density. The result of this elaboration is the so called spectral profile, a matrix of 128×128 data, computed every 20 ms [9]. These spectral data are sent to the host PC and displayed in real time.

3.1. In vivo Test

Experimental investigations in human common carotid arteries (CCAs) have proved that the velocity profiles generally assume a parabolic shape during diastole and early systole, and become flat during the systolic peak. However there are some particular conditions in which the shape of the profile changes more appreciably: for example, during the deceleration phase when the velocity near the walls results higher than in the vessel center, and the profile assumes an "M" shape.

As an example Fig. 2 shows a typical spectrogram detected in the center of the CCA of a healthy volunteer. The velocity profiles corresponding to the time instants highlighted in vertical lines in the reference spectrogram

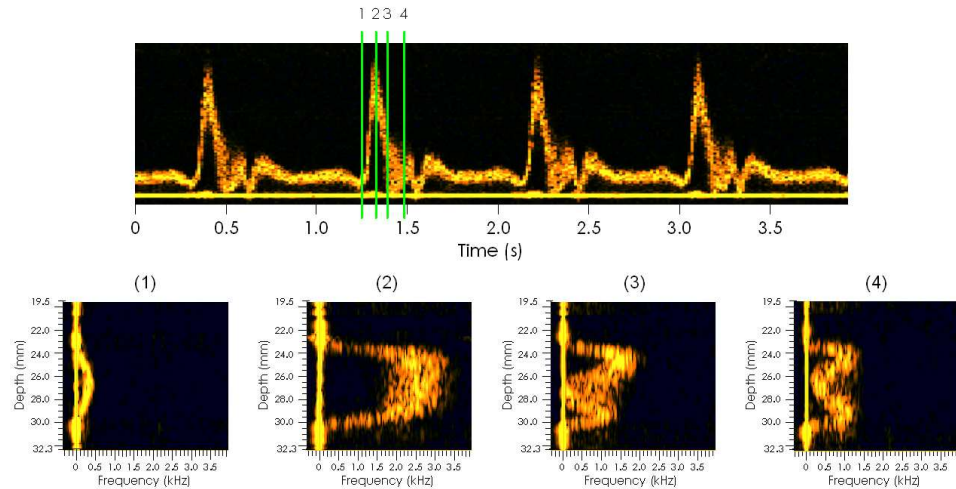


FIGURE 2. Shapes of the spectral profiles in different phases of the cardiac cycle. It can be noticed an asymmetric shape for profile #3 and an “M” shape for profile #4.

are also shown [9]. Frequency (i.e. speed) is here plotted on the X axis, and depth on the Y axis, while the intensity of the spectra are colour coded for each point.

The same acquisition system has also been used with a dedicate esophageal probe (Arrow International, PA, USA) to investigate the aortic blood flow. In vivo tests have been made in patients under general anaesthesia or in the intensive care area at the E. André hospital of Lyon, under the direction of

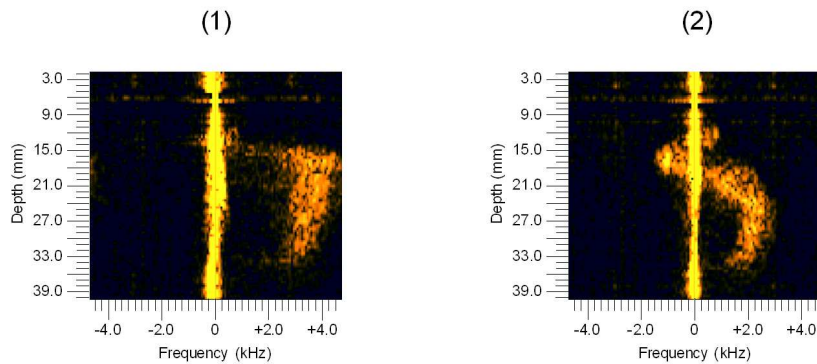


FIGURE 3. Instantaneous spectral profiles detected in the aortic artery. (1) during the systolic peak of the cardiac cycle; (2) during the systolic deceleration, in a location between the arch and the descending aorta.

Dr. R. Muchada. Such tests confirm that blood flow behaviour in the aorta is more complex than in CCA, especially at the level of the aortic arch or in not physiologic circumstances. Velocity profiles are flat during the systolic acceleration but not during the full cardiac cycle, showing in most cases an asymmetrical shape, including both positive and negative components (Fig. 3) [9, 10, 11].

4. Hematocrit Measurements

Doppler echoes can be conveniently used to measure the US attenuation in blood. Previous studies have shown a linear relationship between US attenuation and the hematocrit (HCT) [12, 13]. The attenuation coefficient can thus be used to determine the HCT, once the transmitting frequency is fixed and after a suitable calibration of the system is made.

Previous work used the echoes coming from two different gates inside the vessel [14], measuring the attenuation as the difference in the received power at such gates. However this method results too sensitive to the selected gates and suffers for a lack of stability and repeatability.

A new technique has been recently introduced, which evaluates the attenuation coefficient with a robust averaging method using echo-signals from all depths inside the vessel.

In vitro measurements have been done at the US Department of the IPPT-PAN, Warsaw, with samples of whole porcine blood and separated plasma with HCT ranging from 1% to 65% using a 20 MHz unfocused transducer. Steady and pulsatile flow conditions, similar to those existing in the brachial artery, have been simulated with a suitable pump.

The attenuation coefficient, determined by the reduction of Doppler amplitude with increasing depth, confirms the linear relation to hematocrit with a good correlation coefficient ($R = 0.992$ for pulsatile flow).

Preliminary application of the new estimation technique in a first group of 12 patients has produced encouraging results. The mean error has been of only 3% HCT, with a maximum error of 5% HCT.

5. Arterial Mechanics Investigations

In arterial mechanics investigations, the interest is not limited to blood flow, but extended to the movements of the vessel walls. The analysis of

such movements, in fact, can provide information on the arterial distensibility/stiffness, as related to atherosclerosis and vascular aging [15].

One of the goals in this analysis is the accurate estimation of the vessel diameter and its changes during the cardiac cycle. Approaches are currently based on the integration of estimated wall velocity. The latter is obtained using the autocorrelation method with central frequency estimation, which has been shown to be an unbiased velocity estimator [16, 17, 18].

The DSP-based system is capable of estimating the arterial distension simultaneously with the spectral profiles as described in the previous section.

5.1. Vessel Walls Identification

The estimation of instantaneous arterial walls positions during the cardiac cycle first needs a rough selection of the gates that actually include the wall echoes. Such selection is obtained in real time by combining the classic tracking method [19] with the power gradient extreme search (GES).

The US system has to be set up so that echoes from the two vessel walls are each in one half of the spectral profile display. The A-mode signal and its gradient are then computed: the gradient extremes are searched spanning back and forth from the central depth of the spectral profile (gate 64). The first gate corresponding to a local power gradient minimum (maximum) with a value lower (higher) than a suitable given threshold is selected as the starting anterior (posterior) wall position [19].

5.2. Tissue Motion Estimation

Tissue velocity is determined by processing the clutter signal, which is originated by the strong echoes coming from nearly stationary targets (walls). Samples taken around the wall gates over subsequent PRIs are self correlated. The self correlation along the slow time axis provides the phase shift relative to the wall motion [20, 21], while that one done along the depth axis provides an estimate of the received pulse average frequency. The latter estimate is useful to compensate the frequency dependent US attenuation [16, 18].

The described algorithm has been validated in vitro using a machine based on a precision linear actuator (T-LA-28S, Zaber Technologies Inc, Canada). This machine is capable of generating cyclic and repeatable displacements (peak to peak amplitude 610 μm) of a plexiglas plate carrying a sample of tissue mimicking material. We measured an average displacement of 607 μm ,

with a global repeatability of less than $2\text{ }\mu\text{m}$ (including mechanical inaccuracies, measurement system errors and drifts).

Tissue motion estimation has been implemented to investigate the changes in the vessel diameter from the difference between systolic and diastolic diameter (distension) of the CCA.

A preliminary test has been performed on 33 healthy volunteers aging in the range of 16–70 years. For the measurements the optimal placement of the transducer has been achieved taking into account the symmetry of the spectral profile [22] and the quality of the displacement waveforms, displayed in real time on the host PC.

The average vessel diameter measured over 50 explored arterial segments was 6.9 mm ($\text{SD}=0.66\text{ mm}$), while the average distension was $499\text{ }\mu\text{m}$ ($\text{SD}=188\text{ }\mu\text{m}$). The intra-measure repeatability, expressed as the SD of the amplitude measured for the same volunteer in neighbouring cardiac cycles, was only $28\text{ }\mu\text{m}$. As an example, Fig. 4, reports the displacement of both vessel walls (near and far) and the relative distension for subsequent cardiac cycles, in the CCA of one of the volunteers.

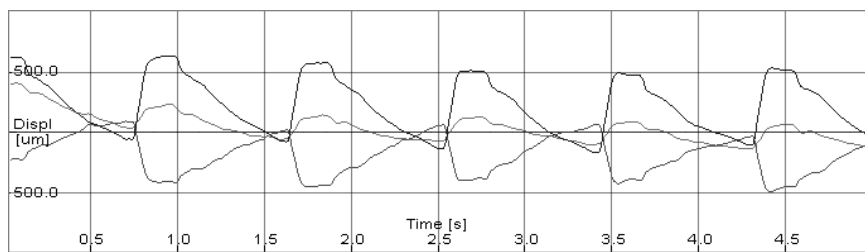


FIGURE 4. Displacement and distension in a CCA over several subsequent cardiac cycles. Upper line: distension; Middle line: near wall displacement; Lower line: far wall displacement.

6. Conclusion

This paper has reviewed the main applications of a real time US signal processing system implemented at the MSD Lab of the University of Florence.

Such system has been shown capable of providing significant information on hemodynamics of large vessels like the CCA and the aortic arch. More recently, the capability of investigating the mechanics of major human arteries has been added. The average diameter and distension measured in the CCAs of 33 healthy volunteers have been 6.9 mm and $499\text{ }\mu\text{m}$, respectively.

The average standard deviation between distension measurements over consecutive cardiac cycles was only $28\mu\text{m}$, thus showing the high resolution of the proposed method. Preliminary non invasive measurements of hematocrit have also been obtained. Although more measurements are necessary, the mean error measured in a first group of 12 volunteers was only 3% HCT, with a maximum error of 5% HCT.

The high programmability of the system makes it suitable for further applications currently under consideration.

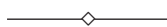
Acknowledgements

Scientific advice by A. Nowicki and W. Secomski (IPPT PAN, Warsaw, Poland) for hematocrit measurements, and by R. Muchada (Hopital E. André, Lyon, France) for aortic blood flow experiments, are gratefully acknowledged.

References

1. D.H. EVANS, AND W. N. MC DICKEN, *Doppler Ultrasound—Physics, Instrumentation and Signal Processing* (2nd edition), Wiley, Chichester (UK), 2000.
2. J.A. JENSEN, *Estimation of Blood Velocities Using Ultrasound: a Signal Processing Approach*, Cambridge University press, UK, 1996.
3. G. Bambi, T. Morganti, S. Ricci, E. Boni, F. Guidi, C. Palombo, and P. Tortoli, *A novel ultrasound instrument for investigation of arterial mechanics*, *Ultrasoundics*, **42**: 731–737, 2004.
4. N. AYDIN, L. FAN, and D.H. EVANS, *Quadrature-to-directional format conversion of Doppler signals using digital methods*, *Physiol. Meas.*, **15**: 181–199, 1993.
5. B.A. COGHLAN, and M. G. TAYLOR, *Directional Doppler techniques for detection of blood velocities*, *Ultrasound Med. Biol.*, **2**: 181–188, 1976.
6. J.O. SMITH and P. GROSSET, *A flexible sampling-rate conversion method*, Proc. ICASSP 1984, San Diego, **2**: 19.4.1–19.4.2, 1984.
7. G. Bambi, P. Fidanzati, T. Morganti, S. Ricci, and P. Tortoli, *Real-Time digital processing of Doppler ultrasound signals*, Invited Paper, Proc. of ICASSP 2005, Philadelphia, **5**: 977–980, 2005.
8. T.L. POEPPING, J. GILL, A. FENSTER, AND D. HOLDSWORTH, *MP3 compression of Doppler ultrasound signals*, *Ultrasound Med. Biol.*, **29**(1): 65–76, 2003.
9. P. TORTOLI, F. GUIDI, G. GUIDI, C. ATZENI, *Spectral velocity profiles for detailed ultrasound flow analysis*, *IEEE Trans. Ultras. Ferro. Freq. Contr.*, **43**: 654–659, 1996.

10. P. TORTOLI, G. Bambi, F. GUIDI, and R. MUCHADA, *Towards a better quantitative measurement of aortic flow*, Ultrasound Med. Biol., **28**(2) : 249–257, 2002.
11. P. TORTOLI, V. MICHELASSI, G. Bambi, F. GUIDI, and D. RIGHI, *Interaction between secondary velocities, flow pulsation and vessel morphology in the common carotid artery*, Ultrasound Med. Biol., **29**(3) : 407–415, 2003.
12. S. MARUVADA, K.K. SHUNG, S.H. WANG, *High-frequency backscatter and attenuation measurements of porcine erythrocyte suspensions between 30–90 MHz*, Ultrasound Med. Biol., **28**(8) : 1081–1088, 2002.
13. S.H. WANG and K.K. SHUNG, *An approach for measuring ultrasonic backscattering from biological tissues with focused transducers*, IEEE Trans. Biomedical Eng., **44**(7) : 549–554, 1997.
14. W. SECOMSKI, A. NOWICKI, F. GUIDI, P. TORTOLI, and P.A. LEWIN, *Noninvasive in vivo measurements of hematocrit*, J. Ultrasound Med., **22** : 375–384, 2003.
15. G.M. LONDON, and J.N. COHN, *Prognostic application of arterial stiffness: task forces*, Am. J Hyperten., **15**(8) : 754–758, 2002.
16. T. LOUPAS, J.T. POWERS, and W. GILL, *An axial velocity estimator for ultrasound blood flow imaging, based on a full evaluation of the Doppler equation by means of a two-dimensional autocorrelation approach*, IEEE Trans. Ultrason., Ferroel., Freq. Cont., **42**(4) : 672–688, 1995.
17. P.J. BRANDS, A.P.G. HOEKS, L.A.F. LEDOUX, and R.S. RENEMAN, *A radio frequency domain complex cross-correlation model to estimate blood flow velocity and tissue motion by means of ultrasound*, Ultrasound Med. Biol., **23**(6) : 911–920, 1997.
18. S.I. RABBEN, S. BJÆRUM, V. SØRHUS, and H. TORP, *Ultrasound-based vessel wall tracking: an auto-correlation technique with RF center frequency estimation*, Ultrasound Med. Biol., **28**(4) : 507–517, 2002.
19. A.P.G. HOEKS, X. DI, P.J. BRANDS, and R.S. RENEMAN, *An effective algorithm for measuring diastolic artery diameters*, Archives of Acoustics, **20** : 65–76, 1995.
20. A.P.G. HOEKS, P.J. BRANDS, and R.S. RENEMAN, *Assessment of the arterial distension waveform using Doppler signal processing*, J. Hypertens. Suppl., **0**(6) : S19–22, 1992.
21. C. KASAI, K. NAMEKAWA, A. KOYANO, R. OMOTO, *Real-time two-dimensional blood flow imaging using an autocorrelation technique*, IEEE Trans. Sonics Ultrason., **32** : 458–464, 1985.
22. P. TORTOLI, G. GUIDI, and P. PIGNOLI, *Transverse Doppler spectral analysis for a correct interpretation of flow sonograms*, Ultrasound Med. Biol., **19**(2) : 115–121, 1993.



Geometrical Multiscale Models for the Cardiovascular System

LUCA FORMAGGIA and ALESSANDRO VENEZIANI

MOX—Modeling and Scientific Computing

Department of Mathematics “F. Brioschi”

Politecnico di Milano Piazza L. da Vinci 32, 20133 Milan, Italy

alessandro.veneziani@mate.polimi.it

These notes address the set up of mathematical and numerical models for the cardiovascular system and the numerical coupling of models having a different level of detail (from 3D down to lumped parameters models), in what has been called the “geometrical multiscale approach”. We present at first the basic features of reduced (1D and lumped parameter) models for the cardiovascular network. Then we address both mathematical and numerical issues arising when coupling models with a different level of detail. Finally, we present some numerical results.

Key words: *Blood flow problems, heterogeneous modeling, multiscale techniques*

1. Introduction

One of the major difficulties encountered when modeling in an accurate way the human cardiovascular system is that it is in fact formed by a closed network with a high level of inter-dependency. The flow dynamics of the blood in a specific vascular district (*local haemodynamics*) is strictly related to the global, systemic dynamics. For instance, the distribution of blood flow inside the various vascular districts, which is a systemic feature, influences for the blood dynamics in each district (local feature). Besides, the study of local flow feature is important since pathologies like the formation of local intimal thickening or plaques is strongly influenced by the local hemodynamics (see e.g. [68]). On the other hand, *local* alteration in vascular lumen induces a *global redistribution of the blood flow*, giving rise to compensatory mechanisms that, at some extents, can ensure a sufficient blood flow in the districts downstream the stenosis. Neglecting such effect provides only a partial infor-

mation (see e.g. [3, 5]). This reciprocal influence between local and systemic hemodynamics has led to the concept of *geometrical “multiscale”* modelling of the circulation. Actually, the term “multiscale” is often used with different meanings in different fields of mathematical and numerical modelling. (e.g. wavelets, turbulence modelling etc.). Therefore, in order to avoid ambiguities, we indicate by the term *geometrical* our present multiscale perspective. In fact, this feature is common to all many problems involving modeling subregions of a larger and complex system, such as hydraulic or electric networks. Examples are the simulation of exhaust systems of Diesel engines (see [13]), and the design of electric circuits (see [4]).

A multiscale perspective is relevant even when one is interested just on the description of the local flow. Indeed, the formulation of a mathematical well posed problem requires the specification of boundary data (see [61]). The vascular walls are physical boundaries and the correct conditions are suggested by physical assumptions such as the continuity of the velocity field. However, *artificial boundaries* have to be introduced to bound the vascular district at hand. They are the interface between the district under consideration and the remainder of the circulatory system. Boundary conditions on such boundaries are, in fact, influenced by the “multiscale” nature of the circulation. Whenever such data are not available from specific (and accurate!) measurements, a proper boundary condition would require a mathematical description of the action of the circulatory system on the vascular district at hand. Clearly, since it is not affordable to describe the whole circulatory system at the same level of detail, this mathematical description must rely on simpler models.

While the local model will be typically based on the solution of the incompressible Navier-Stokes possibly coupled with the dynamics of the vessel walls (see e.g. [1, 46]), the systemic model will be given by *1D models* or by *lumped parameters* models based on the solution of a system of ordinary differential equation (in time) for the average mass flow and pressure in the different compartments forming the cardiovascular system.

Besides their intrinsic relevance, these “simple-minded” models are of great interest in our multiscale perspective. Indeed, they provide a systemic description of the main phenomena related to the circulation (such as the compensatory mechanisms mentioned above) at a low computational cost. They may thus be coupled with an accurate (but local) description of a vascular district of interest. The mathematical and numerical issues related to

this coupling are nontrivial. The different level of detail of the different models is reflected by different mathematical features. Navier-Stokes equations are a system of non-linear partial differential equations which are essentially parabolic for the velocity, while the 1D models are (mainly) based on hyperbolic partial differential equations, and the lumped parameter models do not feature a spatial dependency and are described by means of ordinary differential equations in the time variable (for this reason, they are also called “0D models”). A particular care has therefore to be taken in managing the interfaces between these models in order to have mathematically well posed problems and to guarantee accurate numerical results.

In these notes, we will start with a short introduction of simple-minded models for the circulation. We will consider 1D models at first (Section 2), their derivation and their numerical treatment. We will also briefly address some specific issue such as the 1D modeling of curved pipes. Then, we will introduce lumped parameter models (Section 3), their basic features and the set up of systemic models. The specific mathematical and numerical problems arising in the coupling of these models are addressed in Sections 4 and 5. Numerical results are finally presented in Sec. 6, illustrating the effectiveness of the multiscale approach not only for academic test cases but also in simulations of real medical interest.

2. The Basic 1D Model

We introduce the simplest non-linear 1D model for blood flow in compliant vessels. For more details, see [1] or [3].

The basic equations are derived for a tract of artery free of bifurcations, which is idealised as a cylindrical compliant tube (see Fig. 1). We will denote by $I = (t_0, t_1)$ the time interval of interest and for the sake of convenience we will take $t_0 = 0$. By Ω_t we indicate the spatial domain which is supposed to be a circular cylinder filled with blood, which is changing with time under the action of the pulsatile fluid.

We will mainly use Cartesian coordinates, yet when dealing with cylindrical geometries it is handy to introduce a cylindrical coordinate system. Therefore, in the following we indicate with \mathbf{e}_r , \mathbf{e}_θ and \mathbf{e}_z the radial, circumferential and axial unit vectors, respectively, (r, θ, z) being the corresponding coordinates. We assume that the vessel extends from $z = 0$ to $z = l$ and the vessel length l is constant with time.

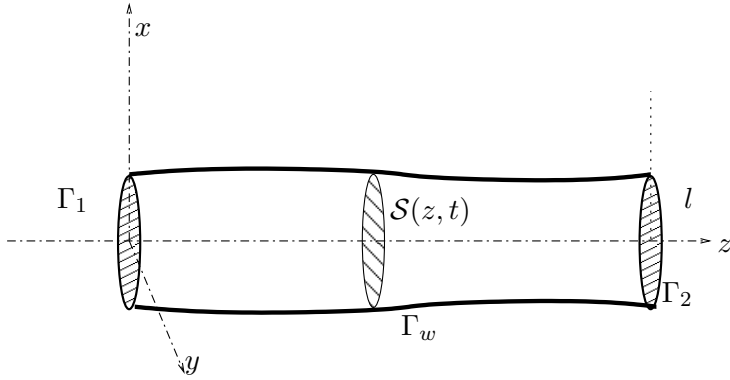


FIGURE 1. Simplified geometry. The vessel is assumed to be a straight cylinder with circular cross section.

The basic model is deduced by making the following simplifying assumptions.

- A.1. *Axial symmetry.* All quantities are independent from the angular coordinate θ . As a consequence, every axial section $z = \text{const}$ remains circular during the wall motion. The tube radius R is a function of z and t .
- A.2. *Radial displacements.* The wall displaces along the radial direction solely, thus at each point on the tube surface we may write $\boldsymbol{\eta} = \eta \mathbf{e}_r$, where $\eta = R - R_0$ is the displacement with respect to the reference radius R_0 .
- A.3. *Fixed rectilinear cylindrical vessels.* This simply means that the vessel will expand and contract around its axis, which is fixed in time.
- A.4. *Constant pressure on each axial section.* We assume that the pressure P is constant on each section, so that it depends only on z and t .
- A.5. *No body forces.*
- A.6. *Dominance of axial velocity.* The velocity components orthogonal to the z axis are negligible compared to the component along z . The latter is indicated by u_z and its expression in cylindrical coordinates is supposed to be of the form

$$u_z(t, r, z) = \bar{u}(t, z)\varphi(rR^{-1}(z)) \quad (2.1)$$

where \bar{u} is the *mean velocity* on each axial section and $\varphi : \mathbb{R} \rightarrow \mathbb{R}$ is a *velocity profile*. The fact that the velocity profile does not vary in time and space is in contrast with experimental observations and numerical results carried out with full scale models. However, it is a necessary assumption for the derivation of the reduced model. One may then think φ as being a profile representative of an average flow configuration.

A generic axial section will be indicated by $\mathcal{S} = \mathcal{S}(t, z)$. Its measure A is given by

$$A(t, z) = \int_{\mathcal{S}(t, z)} d\sigma = \pi R^2(t, z) = \pi(R_0(z) + \eta(t, z))^2. \quad (2.2)$$

The mean velocity \bar{u} is then given by $\bar{u} = A^{-1} \int_{\mathcal{S}} u_z d\sigma$, and from (2.1) it follows easily that φ must be such that

$$\int_0^1 \varphi(y) y dy = \frac{1}{2}$$

We will indicate with α the *momentum-flux correction coefficient*, (sometimes also called *Coriolis coefficient*) defined as

$$\alpha = \frac{\int_{\mathcal{S}} u_z^2 d\sigma}{A \bar{u}^2} = \frac{\int_{\mathcal{S}} \varphi^2 d\sigma}{A}, \quad (2.3)$$

where the dependence of the various quantities on the spatial and time coordinates is understood. It is possible to verify that $\alpha \geq 1$. In general this coefficient will vary in time and space, yet in our model it is taken constant as a consequence of (2.1).

A possible choice for the profile law is the parabolic profile $\varphi(y) = 2(1 - y^2)$ that corresponds to the well known Poiseuille solution characteristic of steady flows in circular tubes. In this case we have $\alpha = 4/3$. However, for blood flow in arteries it has been found that the velocity profile is, on average, rather flat. Indeed, a profile law often used for blood flow in arteries (see for instance [56]) is a power law of the type $\varphi(y) = \gamma^{-1}(\gamma + 2)(1 - y^\gamma)$ with typically $\gamma = 9$. Correspondingly, we have $\alpha = (\gamma + 2)/(\gamma + 1) = 1.1$. The choice $\alpha = 1$, which indicates a completely flat velocity profile, simplifies the analysis, so it is quite often adopted.

The mean flux Q , defined as $Q = \int_{\mathcal{S}} u_z d\sigma = A \bar{u}$, is one of the main variables of our problem, together with A and the pressure P .

There are (at least) three ways of deriving a 1D model for an incompressible fluid filling a compliant pipe. The first one moves from the incompressible Navier-Stokes equations and performs an asymptotic analysis by assuming that the ratio R_0/L is small, thus discarding the higher order terms with respect to R_0/L , [7]. The second approach derives the model directly from the basic conservation laws written in integral form. The third approach consists of integrating the Navier-Stokes equations on a generic section \mathcal{S} .

Following the last approach and exploiting the assumptions stated above, it is possible to obtain the following system of equations (see [1, 3]): for $z \in (0, L)$ and $t \in I$

$$\begin{cases} \frac{\partial A}{\partial t} + \frac{\partial Q}{\partial z} = 0, \\ \frac{\partial Q}{\partial t} + \alpha \frac{\partial}{\partial z} \left(\frac{Q^2}{A} \right) + \frac{A}{\rho} \frac{\partial P}{\partial z} + K_r \left(\frac{Q}{A} \right) = 0, \end{cases} \quad (2.4)$$

where the unknowns are A , Q and P and α is here taken constant, and K_r is a coefficient proportional to the blood viscosity.

In order to close system (2.4), where three unknowns, P , A and Q are related by two equations, we have to provide a relation for the pressure. A complete mechanical model for the structure of the vessel wall would provide a differential equation which links the displacement and its spatial and temporal derivatives to the force applied by the fluid. Here we will adopt instead an hypothesis quite commonly used in practice, namely, that the inertial terms are negligible and that the elastic stresses in the circumferential direction are dominant. Under these assumptions, the wall mechanics reduces to an algebraic relation linking pressure to the wall deformation and consequently to the vessel section A . Actually, we may assume that the pressure satisfies a relation like

$$P(t, z) - P_{ext} = \psi(A(t, z); A_0(z), \beta(z)), \quad (2.5)$$

where we have outlined that the pressure will in general depend also on $A_0 = \pi R_0^2$ and on a set of coefficients $\beta = (\beta_0, \beta_1, \dots, \beta_p)$, related to physical and mechanical properties, that are, in general, *given* functions of z (see [1]). Here P_{ext} indicates the external pressure exerted by the organs outside the vessel (often taken equal to 0). For instance, by exploiting the well known linear elastic law for a cylindrical vessel and using the fact that

$$\eta = (\sqrt{A} - \sqrt{A_0})/\sqrt{\pi} \quad (2.6)$$

we can obtain the following expression for ψ

$$\psi(A; A_0, \beta_0) = \beta_0 \frac{\sqrt{A} - \sqrt{A_0}}{A_0}. \quad (2.7)$$

We have identified β with the single parameter β_0 that from the modelling assumptions is $= (\sqrt{\pi}h_0E)/(1 - \xi^2)$ (see however the next remark for the numerical estimate of β_0). The algebraic relation (2.5) assumes that the wall is instantaneously in equilibrium with the pressure forces acting on it (see for instance [1] or [46]). More sophisticated models may be introduced by employing a differential law for the vessel structure, including the inertia and the viscoelasticity of the wall: the interested reader is referred to [1].

By exploiting relation (2.5) we may eliminate the pressure P from the momentum equation. To that purpose we will indicate by $c_1 = c_1(A; A_0, \beta)$ the following quantity

$$c_1 = \sqrt{\frac{A}{\rho} \frac{\partial \psi}{\partial A}}, \quad (2.8)$$

which has the dimension of a velocity and, as we will see later on, is related to the speed of propagation of simple waves along the tube.

By simple manipulations (2.4) may be written in *quasi-linear* form as follows

$$\frac{\partial}{\partial t} \mathbf{U} + \mathbf{H}(\mathbf{U}) \frac{\partial \mathbf{U}}{\partial z} + \mathbf{B}(\mathbf{U}) = \mathbf{0}, \quad (2.9)$$

where,

$$\mathbf{U} = \begin{bmatrix} A \\ Q \end{bmatrix},$$

$$\mathbf{H}(\mathbf{U}) = \begin{bmatrix} 0 & 1 \\ \frac{A}{\rho} \frac{\partial \psi}{\partial A} - \alpha \bar{u}^2 & 2\alpha \bar{u} \end{bmatrix} = \begin{bmatrix} 0 & 1 \\ c_1^2 - \alpha \left(\frac{Q}{A} \right)^2 & 2\alpha \frac{Q}{A} \end{bmatrix}, \quad (2.10)$$

and

$$\mathbf{B}(\mathbf{U}) = \begin{bmatrix} 0 \\ K_R \left(\frac{Q}{A} \right) + \frac{A}{\rho} \frac{\partial \psi}{\partial A_0} \frac{dA_0}{dz} + \frac{A}{\rho} \frac{\partial \psi}{\partial \beta} \frac{d\beta}{dz} \end{bmatrix}.$$

A *conservation form* for (2.9) may be found as well and reads

$$\frac{\partial \mathbf{U}}{\partial t} + \frac{\partial}{\partial z} [\mathbf{F}(\mathbf{U})] + \mathbf{B}(\mathbf{U}) = \mathbf{0}, \quad (2.11)$$

where

$$F(\mathbf{U}) = \begin{bmatrix} Q \\ \alpha \frac{Q^2}{A} + C_1 \end{bmatrix}, \quad \mathbf{B}(\mathbf{U}) = \mathbf{B}(\mathbf{U}) - \begin{bmatrix} 0 \\ \frac{\partial C_1}{\partial A_0} \frac{dA_0}{dz} + \frac{\partial C_1}{\partial \beta} \frac{d\beta}{dz} \end{bmatrix},$$

and C_1 is a primitive of c_1^2 with respect to A , given by

$$C_1(A; A_0, \beta) = \int_{A_0}^A c_1^2(\tau; A_0, \beta) d\tau.$$

System (2.11) allows to identify the vector \mathbf{U} as the the *conservation variables* of the problem.

In the case we use relation (2.7) we have

$$c_1 = \sqrt{\frac{\beta_0}{2\rho A_0}} A^{\frac{1}{4}}, \quad C_1 = \frac{\beta_0}{3\rho A_0} A^{\frac{3}{2}}. \quad (2.12)$$

It is possible to prove that if $A \geq 0$, the matrix \mathbf{H} possesses two real eigenvalues. Furthermore, if $A > 0$ the two eigenvalues are distinct, that means that (2.9) is a *strictly hyperbolic* system of partial differential equations (for the proof, see e.g. [1]).

Remark 1. An energy analysis of system (2.11) is carried out in [15].

Remark 2. The coefficients of the 1D model obtained depend on physical parameters related to the physical properties of the blood and the vascular wall, namely α , β_0 , K_r and A_0 . The accurate estimation of these parameters is a non trivial task. In [33] a nonlinear least square approach is proposed for the parameters estimate based on experimental data. In particular, in this work the parameter β_0 is estimated starting from “synthetic” data given by 3D fluid-structure interaction simulations. Numerical results reported show that the parameter estimation can be significantly different from the values computed by analytical formulas such as $\beta_0 = (\sqrt{\pi} h_0 E)/(1 - \xi^2)$ based on the simplifying assumptions, yielding however numerical results closer to the 3D data.

Characteristics analysis

The hyperbolic nature of the problem at hand allows its reformulation in terms of ordinary differential equations. This reformulation is based on the

so-called *characteristic analysis* and can be useful in the numerical solution of the problem. We briefly address this topic here. For a more detailed analysis see [1].

Let $(\mathbf{l}_1, \mathbf{l}_2)$ and $(\mathbf{r}_1, \mathbf{r}_2)$ be two couples of left and right eigenvectors of the matrix \mathbf{H} in (2.10), respectively. The matrices \mathbf{L} , \mathbf{R} and $\mathbf{\Lambda}$ are defined as

$$\mathbf{L} = \begin{bmatrix} \mathbf{l}_1^T \\ \mathbf{l}_2^T \end{bmatrix}, \quad \mathbf{R} = \begin{bmatrix} \mathbf{r}_1 & \mathbf{r}_2 \end{bmatrix}, \quad \mathbf{\Lambda} = \text{diag}(\lambda_1, \lambda_2) = \begin{bmatrix} \lambda_1 & 0 \\ 0 & \lambda_2 \end{bmatrix}. \quad (2.13)$$

Since right and left eigenvectors are mutually orthogonal, without loss of generality we choose them so that $\mathbf{LR} = \mathbf{I}$. Matrix \mathbf{H} may then be decomposed as

$$\mathbf{H} = \mathbf{R}\mathbf{\Lambda}\mathbf{L}, \quad (2.14)$$

and system (2.9) written in the equivalent form

$$\mathbf{L} \frac{\partial \mathbf{U}}{\partial t} + \mathbf{\Lambda L} \frac{\partial \mathbf{U}}{\partial z} + \mathbf{LB}(\mathbf{U}) = \mathbf{0}, \quad z \in (0, L), \quad t \in I. \quad (2.15)$$

If there exist two quantities W_1 and W_2 which satisfy

$$\frac{\partial W_1}{\partial U} = \mathbf{l}_1, \quad \frac{\partial W_2}{\partial U} = \mathbf{l}_2, \quad (2.16)$$

we will call them *characteristic variables* of the hyperbolic system. We point out that in the case where the coefficients A_0 and β are not constant, \mathbf{W}_1 and \mathbf{W}_2 are not autonomous functions of \mathbf{U} .

By setting $\mathbf{W} = [W_1, W_2]^T$ system (2.15) may be elaborated into

$$\frac{\partial \mathbf{W}}{\partial t} + \mathbf{\Lambda} \frac{\partial \mathbf{W}}{\partial z} + \mathbf{G} = \mathbf{0}, \quad (2.17)$$

where

$$\mathbf{G} = \mathbf{LB} - \frac{\partial W}{\partial A_0} \frac{dA_0}{dz} - \frac{\partial W}{\partial \beta} \frac{d\beta}{dz}. \quad (2.18)$$

If we consider the *characteristic line* $y_i(t)$ which satisfies the differential equation

$$\frac{d}{dt} y_i(t) = \lambda_i(t, y_i(t)), \quad i = 1, 2 \quad (2.19)$$

then (2.17) may be rewritten as

$$\frac{d}{dt} W_i(t, y_i(t)) + G_i(W_1, W_2) = 0, \quad i = 1, 2 \quad (2.20)$$

where we have made evident the dependence of G_i on the characteristic variables.

Equations (2.19) and (2.20) represent a possible reformulation of the problem at hand in terms of ordinary differential equations for the characteristic variables W_i . The role of these variables is relevant both at the mathematical and numerical level (see [32, 24]), in particular in the prescription of the boundary conditions.

Boundary conditions

System (2.4) must be supplemented by proper boundary conditions. The number of conditions to apply at each end equals the number of characteristics entering the domain through that boundary. Since we are only considering sub-critical flows *we have to impose exactly one boundary condition at both $z = 0$ and $z = L$* . An important class of boundary conditions are the so-called *non-reflecting or 'absorbing'* ones. They allow the simple wave associated to the outgoing characteristic variable to exit the computational domain with no reflections. Following [60, 25] non-reflecting boundary conditions for one dimensional systems of non-linear hyperbolic equations in conservation form like (2.11) may be written as

$$\mathbf{l}_1 \cdot \left(\frac{\partial \mathbf{U}}{\partial t} + \mathbf{B}(\mathbf{U}) \right) = 0 \text{ at } z = 0, \quad \mathbf{l}_2 \cdot \left(\frac{\partial \mathbf{U}}{\partial t} + \mathbf{B}(\mathbf{U}) \right) = 0 \text{ at } z = l,$$

for all $t \in I$, which in fact, by defining $R_i = \mathbf{l}_i \mathbf{B}$, may be written in the form

$$\frac{\partial W_1}{\partial t} + R_1(W_1, W_2) = 0 \text{ at } z = 0, \quad \frac{\partial W_2}{\partial t} + R_2(W_1, W_2) = 0 \text{ at } z = l, \quad (2.21)$$

where we have put into evidence the possible dependence of R_1 and R_2 on W_1 and W_2 through the dependence of \mathbf{B} on \mathbf{U} . Boundary conditions of this type are quite convenient at the outlet (distal) section, particularly whenever we have no better data to impose on that location.

At the inlet (proximal) section instead one usually desires to impose values of pressure or mass flux derived from measurements or other means. Let us suppose, without loss of generality, that $z = 0$ is an inlet section. Whenever an explicit formulation of the characteristic variables is available, the boundary condition may be expressed directly in terms of the entering characteristic variable W_1 , i.e., for all $t \in I$

$$W_1(t) = g_1(t) \text{ at } z = 0, \quad (2.22)$$

g_1 being a given function. However, seldom one has directly the boundary datum in terms of the characteristic variable, since is normally given in terms of physical variables. In these cases, some specific techniques can be devised for recovering the characteristic variable from the physical data. For instance, if $A(t)$ is available at $z = 0$, one could formulate:

$$W_1(t) = W_1(A(t), W_2(t))$$

where W_2 is the outgoing characteristic variable that can be obtained by *extrapolation*, moving backward in time along the characteristic line $y_2(t)$. More details about this approach can be found e.g. in [1].

2.1. Numerical Approximation

We will here consider the equations in conservation form (2.11) and the simple algebraic relationship (2.7).

There are many different schemes for the numerical simulation of this kind of problem: the interested reader is referred e.g. to [14, 32, 48]. Here, we adopt a second order Taylor-Galerkin scheme which might be seen as the finite element counterpart of the well known Lax-Wendroff scheme. It has been chosen for its excellent dispersion error characteristics and its simplicity of implementation.

The basic idea of the scheme is to exploit the Taylor expansion of the solution in time up to the second time derivative and then to use the equations of the problem (2.11) for replacing the time derivatives with space derivatives and terms of order zero. This yields a semi-discrete problem (continuous in space, discrete in time). The space discretization is then obtained with a Galerkin Finite Element approach. A complete description of the method applied to the problem at hand can be found in [1].

Using the abridged notations

$$\mathbf{F}_{LW}(\mathbf{U}) = \mathbf{F}(\mathbf{U}) - \frac{\Delta t}{2} \mathbf{H}(\mathbf{U}) \mathbf{B}(\mathbf{U})$$

and

$$\mathbf{B}_{LW}(\mathbf{U}) = \mathbf{B}(\mathbf{U}) + \frac{\Delta t}{2} \mathbf{B}_U(\mathbf{U}) \mathbf{B}(\mathbf{U}),$$

the discretization of the problem reads: given \mathbf{U}_h^0 obtained by interpolation from the initial data, for $n \geq 0$, find $\mathbf{U}_h^{n+1} \in \mathbf{V}_h$ which $\forall \psi_h \in \mathbf{V}_h^0$ satisfies

the following equations for the interior nodes

$$\begin{aligned} (\mathbf{U}_h^{n+1}, \boldsymbol{\psi}_h) &= (\mathbf{U}_h^n, \boldsymbol{\psi}_h) + \Delta t \left(\mathbf{F}_{LW}(\mathbf{U}_h^n), \frac{d\boldsymbol{\psi}_h}{dz} \right) \\ &\quad - \frac{\Delta t^2}{2} \left(\mathbf{B}_U(\mathbf{U}_h^n) \frac{\partial \mathbf{F}(\mathbf{U}_h^n)}{\partial z}, \boldsymbol{\psi}_h \right) - \frac{\Delta t^2}{2} \left(\mathbf{H}(\mathbf{U}_h^n) \frac{\partial \mathbf{F}}{\partial z}(\mathbf{U}_h^n), \frac{d\boldsymbol{\psi}_h}{dz} \right) \\ &\quad - \Delta t (\mathbf{B}_{LW}(\mathbf{U}_h^n), \boldsymbol{\psi}_h), \quad (2.23) \end{aligned}$$

together with the relation for boundary nodes obtained from the boundary and compatibility conditions, as discussed in the sequel. Here (\cdot, \cdot) stands for the usual L^2 scalar product. By taking $\boldsymbol{\psi}_h = [\psi_i, 0]^T$ and $\boldsymbol{\psi}_h = [0, \psi_i]^T$, for $i = 1, \dots, N$ we obtain N discrete equations for continuity and momentum, respectively, for a total of $2(N+2)$ unknowns (A_i and Q_i for $i = 0, \dots, N+1$).

The second order Taylor-Galerkin scheme (2.23) entails a CFL stability bound on the time step:

$$\Delta t \leq \frac{\sqrt{3}}{3} \min_{0 \leq i \leq N} \left[\frac{h_i}{\max_{k=i}^{i+1} (c_{\alpha,k} + |\bar{u}_k|)} \right], \quad (2.24)$$

where $c_{\alpha,i}$ and \bar{u}_i here indicate the values of c_α and \bar{u} at mesh node z_i , respectively.

2.1.1. Boundary and compatibility conditions. Formulation (2.23) provides the values only at internal nodes, since we have chosen the test functions $\boldsymbol{\psi}_h$ to be zero at the boundary. The values of the unknowns at the boundary nodes must be provided by the application of the *boundary* and *compatibility* conditions.

The boundary conditions previously discussed are not sufficient to close the problem *at numerical level* since they provide just two conditions, yet we need to find four additional relations. We want to stress that this problem is linked to the numerical scheme, not to the differential equations, which indeed only require one condition at each end (at least for the flow regime we are considering here). Without loss of generality, let us consider the boundary $z = 0$ (analogous consideration may be made at $z = L$). As we have seen, the boundary conditions will provide at each time step a relation of the type

$$\phi(A_0^{n+1}, Q_0^{n+1}) = q_0(t^{n+1}),$$

being q_0 the given boundary data. For instance, imposing the pressure would mean choosing $\phi(A, Q) = P = \psi(A; A_0(0), \beta(0))$, while imposing the mass flux would just mean $\phi(A, Q) = Q$. Finally, a non reflecting condition is obtained by $\phi(A, Q) = W_1(A, Q)$ and in this case q_0 is normally taken constant and equal to the value of W_1 at a reference state (typically $(A, Q) = (A_0, 0)$). Thus, in general ϕ is a non linear function.

This relation should be supplemented by a *compatibility condition*. In general, the compatibility conditions are obtained by projecting the equation along the eigenvectors corresponding to the characteristics that are exiting the domain. Therefore, we have to discretise the following set of equations at the two vessel ends [48]:

$$\mathbf{l}_2 \cdot \left(\frac{\partial}{\partial t} \mathbf{U} + H \frac{\partial \mathbf{U}}{\partial z} + \mathbf{B}(\mathbf{U}) \right) = 0, \quad z = 0, t \in I, \quad (2.25a)$$

$$\mathbf{l}_1 \cdot \left(\frac{\partial}{\partial t} \mathbf{U} + H \frac{\partial \mathbf{U}}{\partial z} + \mathbf{B}(\mathbf{U}) \right) = 0, \quad z = L, t \in I. \quad (2.25b)$$

There are different techniques for considering these conditions in the numerical scheme: the interested reader is referred to [1].

2.2. Network of 1D Models

The vascular system is in fact a network of vessels that branches repeatedly and a model of just an artery is of little use. A simple and effective idea is to describe the network by 'gluing' together one dimensional models. Yet, we need to find proper interface conditions (i.e. mathematically sound and easy to treat numerically). The technique may be adopted also in the case of abrupt changes of vessel characteristics (see [20]).

The flow in a bifurcation is intrinsically three dimensional; yet it may still be represented by means of a 1D model, following a domain decomposition approach, if one is not interested in the flow details inside the branch (see e.g. [42]). Figure 2 (left) shows a model for a bifurcation. We have simplified the real geometric structure by imposing that the bifurcation is located exactly on one point and neglecting the effect of the bifurcation angles. An alternative technique is reported in [57], where a separate tract containing the branch is introduced.

In order to solve the three problems in Ω_1 (main branch), Ω_2 and Ω_3 we need to find appropriate interface conditions. The hyperbolic nature of the problem tells us that we need three conditions.

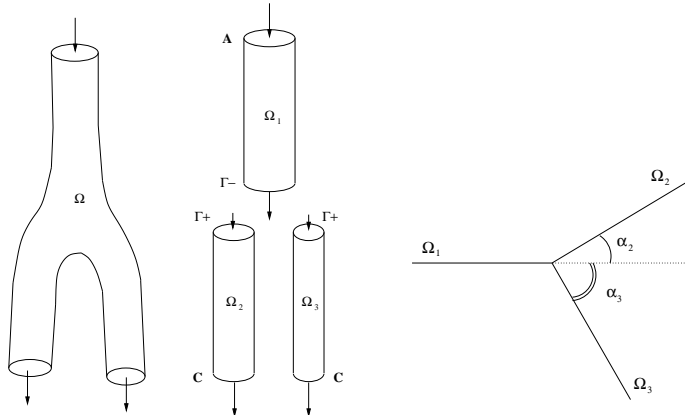


FIGURE 2. Left: One dimensional model of bifurcation by domain decomposition technique. Right: A sketch of a branching.

We first state the conservation of mass across the bifurcation, i.e.

$$Q_1 = Q_2 + Q_3, \quad \text{at } z = \Gamma, t \in I. \quad (2.26)$$

We note that the orientation of the axis in the three branches is such that a positive value of Q_1 indicates that blood is flowing from the main branch Ω_1 into the other two. An energy analysis allows us to conclude that a proper interface condition would entail the condition $P_{t,1}Q_1 - P_{t,2}Q_2 - P_{t,3}Q_3 \geq 0$, where $P_t := P + 1/2\rho|\mathbf{u}|^2$ is the *total pressure*. It is expected that the complex flow in the bifurcation will cause an energy dissipation and consequently a decrease in the total pressure in the direction of the flow field across the bifurcation, and this loss should be related to the fluid velocity (or flow rate) and to the bifurcation angles. A possibility to account for this is to impose, at $z = \Gamma$, that

$$\begin{aligned} P_{t,1} - \text{sign}(\bar{u}_1)f_1(\bar{u}_1) &= P_{t,2} + \text{sign}(\bar{u}_2)f_2(\bar{u}_2, \alpha_2), \\ P_{t,1} - \text{sign}(\bar{u}_1)f_1(\bar{u}_1) &= P_{t,3} + \text{sign}(\bar{u}_3)f_3(\bar{u}_3, \alpha_3), \end{aligned} \quad (2.27)$$

where α_2 and α_3 are the angles of the branches Ω_2 and Ω_3 with respect to the main one (see Fig. 2 right); f_1 , f_2 and f_3 are suitable positive functions and equal to zero when the first argument is zero.

In the numerical scheme, (2.26) and (2.27) will be complemented by three compatibility relations (see Sect. 2.1.1). We have thus a non linear system for the six unknowns A_i^{n+1} , Q_i^{n+1} , $i = 1, 2, 3$, at the interface location Γ , which can be solved by a Newton method.

2.3. Modeling of Curved Pipes

One of the most relevant assumptions in devising the basic 1D model is that the axis of the (cylindrical) vessel is rectilinear. Actually, if we remove this hypothesis, it is still possible to define a main flow direction in the domain, namely the curvilinear abscissa along the axis, and however the blood dynamics in the other directions is no longer negligible (secondary motion zones): for a detailed description of the fluid dynamics in this case, see [43]. Nevertheless, there are some vessels which are clearly curved (aorta, femoral arteries, etc.). For these vessels, the basic 1D model (2.4) can be considered only as a rough description, possibly introducing a subdivision into subsegments sufficiently short to be considered straight and connected one to the other with a suitable angle $\neq 0$ (see Fig. 3 left). Alternatively, here we would like to briefly address the definition of 1D models which are able to account for the effects of the transversal dynamics on the axial one, having the computational cost of the “simple-minded” model (2.4). The task is not easy, since we want to devise a sort of 1D models for the cheap description of a genuinely 3D dynamics, so we call these models “psychologically 1D”.

Simplified models for curved pipes can be obtained for small curvatures of the vessels with a perturbation analysis of the rectilinear model (see [11]).

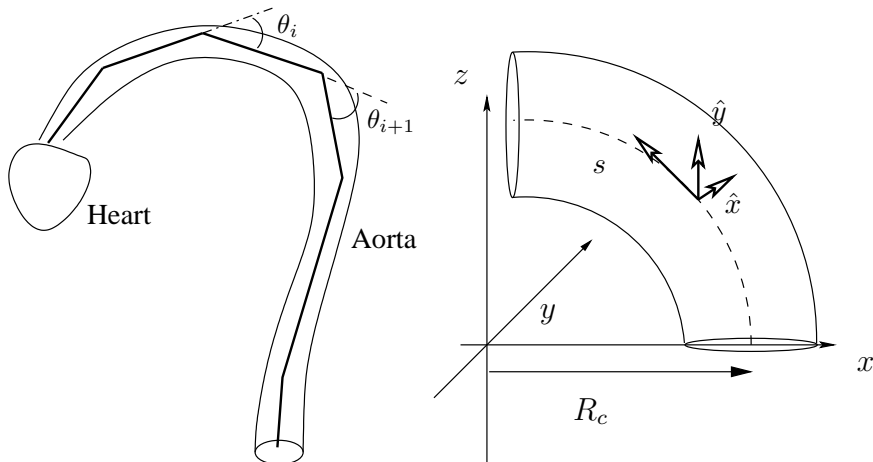


FIGURE 3. Left: Representation of a curved pipe as a set of straight cylinders.
Right: Frame of reference for a planar curved pipe.

Let us consider the nondimensional parameter:

$$D = 2\sqrt{2} \sqrt{\frac{R_w}{R_c}} \text{Re} \quad (2.28)$$

where R_w is the vessel radius, R_c is the curvature radius of the vessel axis ($R_c \rightarrow \infty$ in the straight case) and Re is the Reynolds number of the rectilinear case. D is called *Dean number*. Simplified models can be obtained for small values of the Dean number, which are for instance able to correctly compute the stagnation points of the secondary motion zones. For large values of D these models need to be suitably corrected, and the analysis becomes by far more difficult: a complete description of this approach can be found in [43], Chap. 4. A different approach that can be considered in the definition of psychologically 1D models for curved pipes relies on the *theory of Cosserat curves* considered by Green and Naghdi in [21, 22] (see also [17]). If we consider the reference frame (\hat{x}, \hat{y}, s) of Fig. 3 right, the basic idea of the Green and Naghdi approach is to represent the velocity field $\mathbf{u}(\hat{x}, \hat{y}, s, t)$ with respect a set of *shape functions* depending only on the coordinates in the normal section \hat{x}, \hat{y} :

$$\mathbf{u}(\hat{x}, \hat{y}, s, t) = \sum_{n=0}^N \omega_n(s, t) \boldsymbol{\varphi}(\hat{x}, \hat{y}), \quad (2.29)$$

where ω_n are the coefficients of the velocity profile. This can be considered as a generalization of the straight vessel case, where we set for the axial velocity, $u_z(x, y, z, t) = \varphi(x, y)\bar{u}(z, t)$ being $\bar{u}(z, t)$ the average velocity and $\varphi(\hat{x}, \hat{y})$ a given velocity profile. In general, when a basis functions set is selected, the unknowns are the coefficients ω_n , that can be computed by solving a suitable set of equations derived by mass and momentum conservation principles.

In principle, the accuracy of these models can be tuned by choosing a suitably large N , i.e. having a basis functions set rich enough. However, even for small values of N , mathematical difficulties of the obtained model imply high numerical costs (see [17]).

2.3.1. A curved pipe model. If we integrate any function $f(x, y, s, t)$ over the volume of pipe $V(\varepsilon)$, bounded by two normal sections at a distance ε one to the other and let $\varepsilon \rightarrow 0$, we get (see [17]):

$$\lim_{\varepsilon \rightarrow 0} \frac{1}{\varepsilon} \int_{\bar{s}-\varepsilon/2}^{\bar{s}+\varepsilon/2} \iint_{\mathcal{S}} \sqrt{g} f(x, y, \bar{s}, t) dx dy ds = \iint_{\mathcal{S}} \sqrt{g} f(x, y, \bar{s}, t) dx dy$$

where $\mathcal{S} = \mathcal{S}(\bar{s}, t)$ is the section normal to the vessel axis and \sqrt{g} is the metric tensor invariant, accounting for the integration over a curved axis. In particular, for a rectilinear pipe $g = 1$, while for a curved vessel in the plane (y, s) with a constant curvature radius R_C , $\sqrt{g} = (\hat{y} + R_C)/\hat{y}$. Associated to this integral over the section \mathcal{S} , we introduce the following operators:

$$P_{11}(\cdot) \equiv \iint_{\mathcal{S}} \sqrt{g} \cdot d\hat{x}d\hat{y}, P_{21}(\cdot) \equiv \iint_{\mathcal{S}} \sqrt{g} \cdot \hat{x}d\hat{x}d\hat{y}, P_{22}(\cdot) \equiv \iint_{\mathcal{S}} \sqrt{g} \cdot \hat{y}d\hat{x}d\hat{y}. \quad (2.30)$$

Consider now the 3D Navier-Stokes equations written with respect to the reference frame (\hat{x}, \hat{y}, s) with the velocity field represented by (2.29). In particular, we assume for the axial velocity

$$u_s = \left(1 - \frac{\hat{x}^2 + \hat{y}^2}{R^2}\right) (a(s, t) + b(s, t)\hat{x} + c(s, t)\hat{y}),$$

which is a generalization of the classical parabolic profile (first term), while for the transversal velocity components, we simply postulate a linear dependence: $u_{\hat{x}} = \dot{\eta}\hat{x}/R$, $u_{\hat{y}} = \dot{\eta}\hat{y}/R$, where $\dot{\eta}$ is the wall velocity. The unknowns of the problem are therefore the coefficients $a(s, t)$, $b(s, t)$ and $c(s, t)$ and the vessel radius $R(s, t)$. A more convenient set of unknowns is:

$$A \equiv \pi R^2, \quad Q \equiv \frac{\pi}{2} R^2 a, \quad H \equiv \frac{\pi}{12} R^4 b, \quad G \equiv \frac{\pi}{12} R^4 c.$$

For the determination of these unknowns we need four equations that can be obtained by applying the average operator P_{11} to the continuity equation and the operators P_{11} , P_{21} and P_{22} to the axial momentum equations. The resulting psychologically 1D model reads:

$$\left\{ \begin{array}{l} \frac{\partial A}{\partial t} + \frac{\partial Q}{\partial s} = 0 \\ \frac{\partial Q}{\partial t} + \frac{1}{R_C} \frac{\partial G}{\partial t} + \frac{4}{3} \frac{\partial}{\partial s} \frac{Q^2}{A} + 6\pi \frac{\partial s}{\partial} \frac{H^2}{A^2} + \frac{\beta\sqrt{A}}{2\rho A_0} \frac{\partial A}{\partial s} + 8\pi\nu \frac{Q}{A} + \frac{24\pi\nu}{R_C} \frac{G}{A} = 0 \\ \frac{\partial H}{\partial t} + 2 \frac{\partial}{\partial s} \frac{HQ}{A} + \frac{1}{2} \frac{H}{A} \frac{\partial Q}{\partial s} + 24\pi\nu \frac{H}{A} = 0 \\ \frac{\partial G}{\partial t} + \frac{1}{6\pi R_C} \frac{\partial QA}{\partial t} + 2 \frac{\partial}{\partial s} \frac{GQ}{A} + \frac{G}{2A} \frac{\partial Q}{\partial s} + \frac{\hat{\beta}}{A^{3/2}} \frac{\partial A}{\partial s} + 24\pi\nu \frac{G}{A} + \hat{\nu}Q = 0 \end{array} \right. \quad (2.31)$$

where $\hat{\beta} := \beta/(8\pi\rho A_0 R_C)$, $\hat{\nu} := 3\nu/R_C$.

More complex model can be devised for instance by assuming a different profile for the transversal velocity components (see [17]).

In Fig. 4 we illustrate the solution of (2.31) at different time steps for a curved planar pipe with $R_C = 5$ cm. G is non null because of the curvature of the pipe (taken from [17]), while H is null since the pipe is planar.

In Fig. 5 the solution for a pipe with $R_C = 1$ cm is shown in order to outline the asymmetry on the axial velocity profile induced by the curvature (taken from [17]).

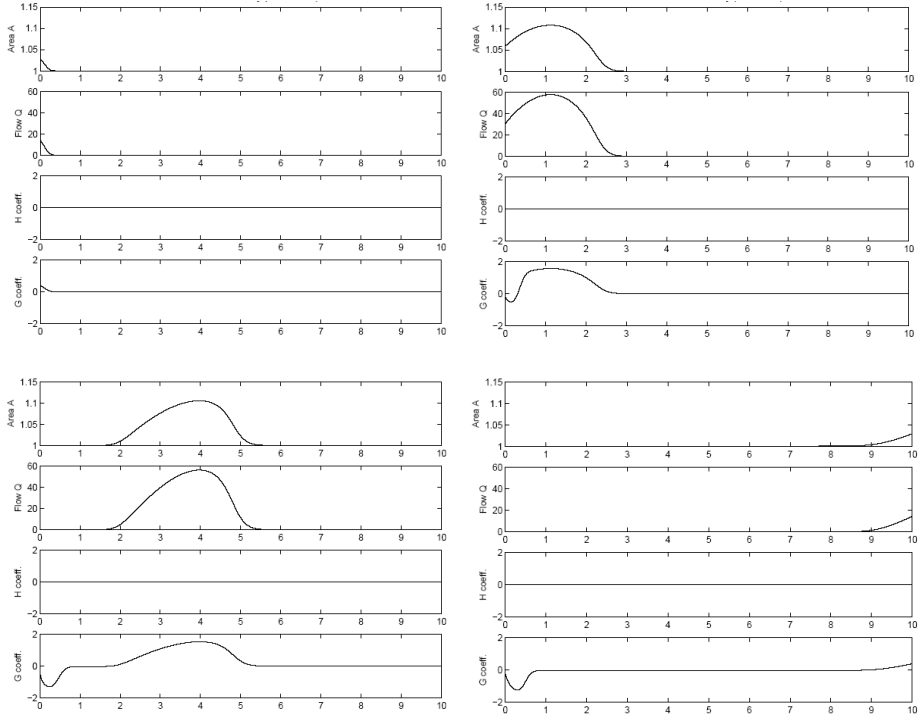


FIGURE 4. Solution (A , Q , H , G respectively) at $t = 0.0005$ s (top, left), $t = 0.005$ s (top, right), $t = 0.010$ s (bottom, left), $t = 0.025$ s (bottom, right) for the model (2.31), with $R_C = 5$ cm (the pipe length is 5 cm). A wave comes into the pipe at the inlet. H is null due to the symmetry of the problem (curved pipe in the (x, s) plane). G is $\neq 0$ for the presence of the curvature. Pictures taken from [17].

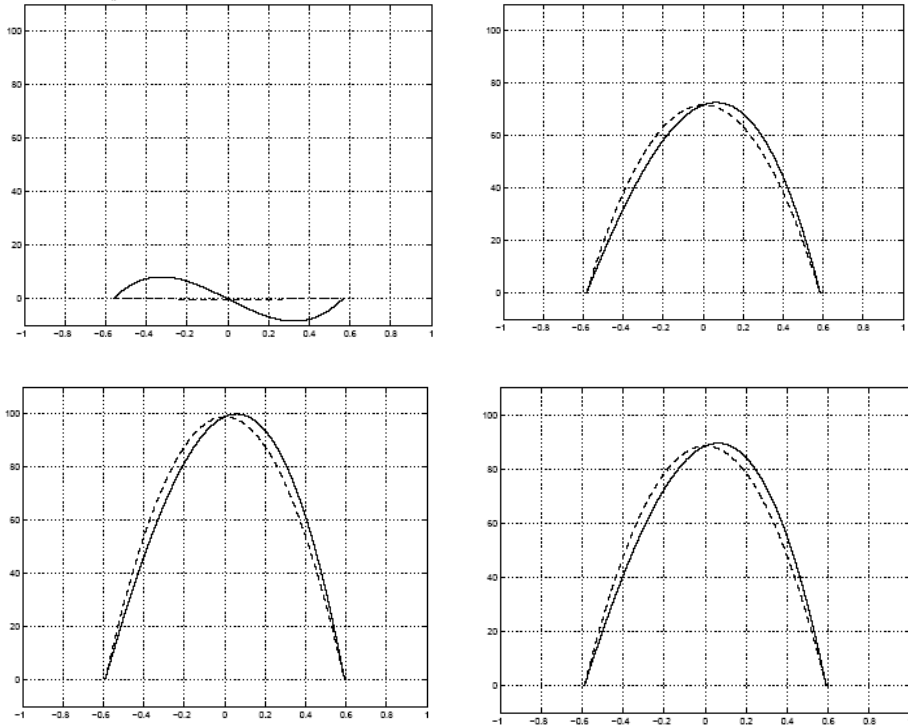


FIGURE 5. Solution in a curved pipe with $R_C = 1$ cm at $t = 0.005$ s for different values of the curvilinear abscissa s . Representation of the axial velocity profiles along \hat{x} (continuous line) and \hat{y} (dotted line). The asymmetry of the profile induced by the curvature is evident. Pictures taken from [17].

2.4. Simple-minded Models of Blood Solutes Dynamics

In haemodynamics simulations it is sometimes of interest not only the blood dynamics, but also the dynamics of solutes (oxygen, lipids, etc.) which are convected by the blood to the tissues and peripheral organs (see e.g. [51, 52, 69]). In the perspective of setting up a multiscale model for the circulation, we therefore need some simplified models also for the blood solutes. Suppose that the solute concentration $\gamma(\mathbf{x}, t)$ fulfills a (linear) advection-diffusion equation in the form

$$\frac{\partial \gamma}{\partial t} - \mu \Delta \gamma + \mathbf{u} \cdot \nabla \gamma = 0$$

in the domain Ω_t (\mathbf{u} is the blood velocity), together with a suitable initial condition $\gamma(\mathbf{x}, 0) = \gamma_0(\mathbf{x})$. A Dirichlet condition $\gamma = \gamma_{\text{ext}}$ can be given on

the vascular wall [12] or more realistically a Robin condition $\mu \nabla \gamma \cdot \mathbf{n} = \alpha(\gamma_{\text{ext}} - \gamma)$ (\mathbf{n} unit outward normal vector, [67]). By proceeding in a way similar to the one adopted for the Navier-Stokes equations, it is possible to deduce a “simple-minded” model for the blood solute dynamics (see [12, 67]). More precisely, let $\Gamma = A\gamma$ be the *linear concentration*. It is possible to deduce for Γ in a cylindrical straight vessel with $z \in (0, l)$ the 1D equation:

$$\frac{\partial \Gamma}{\partial t} + \frac{\partial}{\partial z} \left(\omega \frac{\Gamma Q}{A} \right) + K_c \frac{\Gamma}{A} = f(\gamma_{\text{ext}}) \quad (2.32)$$

to be completed with suitable boundary condition. Here, K_c is a coefficient depending on the viscosity μ and the concentration profile over the transversal section and ω depends on the axial blood velocity. Equation (2.32) can be therefore coupled to (2.11) for a model of the blood and solutes dynamics. For instance, in Fig. 6 (taken from [67]) the concentration at a given instant of the simulation is shown in a bifurcation in the neighborhood of the bifurcation tip.

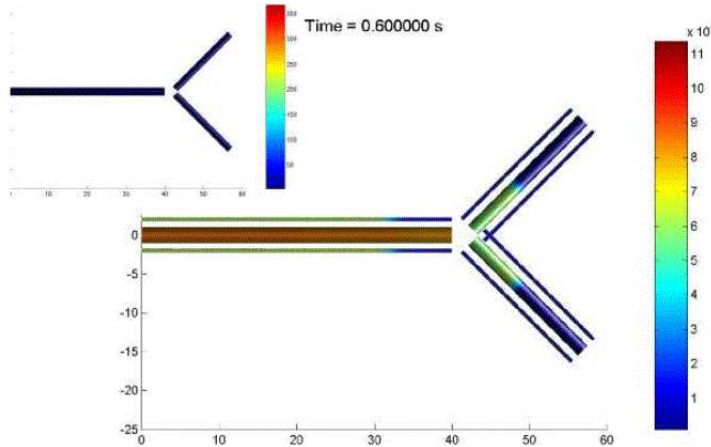


FIGURE 6. Concentration of a blood solute computed with the 1D model (2.32) coupled with 1D blood flow model (2.11) (small picture on the left) in a bifurcation geometry. Picture taken from [67]

3. Lumped Parameters Models for the Circulation

Many biological systems feature complex mechanisms given by the interaction of elementary components. A possible and effective description of such systems is based on the identification of these elementary components, often called *compartments* (see e.g. [9]) and their mutual interaction. In the case of cardiovascular modeling, we could say that *a compartment is a part of the system which is reasonable to consider as a whole, according to the needed accuracy in the description of circulation. The behavior of the blood in a compartment is described in terms of quantities (typically the flow rate and pressure) “averaged” (in space) over the whole compartment.* The mathematical description of this system can be therefore provided by:

1. the description of each compartment;
2. the description of the interactions among the compartments.

The number of the compartments involved depends on the level of accuracy requested to the model. For instance, if one wants to investigate heart failures with the purpose of increasing the cardiac function without a significant (and dangerous) increment of the systolic pressure, a two-compartments description of the cardiovascular system can be enough, featuring the left ventricle and the systemic circulation respectively (see [38], Chap. 13). The *Windkessel* and *Westkessel* models are instances of two-compartments model (the heart and the vascular system), the latter featuring a more precise description of the vascular compartment. More complex examples can be found in [27], Chap. 5, and [29], Chap. 14, where an accurate sensitivity analysis of the parameters of a four-compartments description of the cardiovascular system is carried out. Other references are [30] and [66]. A recent derivation of lumped parameter models based on the Laplace transformation can be found in [41].

Lumped parameters models that we are going to introduce in view of multiscale modeling are, in fact, compartments models which can be described by following the two steps mentioned above. In particular we will firstly introduce lumped parameters models (Sec. 3.1 and 3.2) for a simple compliant cylindrical vessel and for the heart. Then in Sect. 3.3, we will consider the assembly of models for the whole circulation.

3.1. Lumped Parameter Models for a Cylindrical Compliant Vessel

Let us consider again the simple cylindrical artery Ω illustrated in Fig. 1. Starting from equations (2.11), we observe that

$$\frac{\partial A}{\partial t} = 2\pi R \frac{d\eta}{dt} \approx 2\pi R_0 \frac{\partial\eta}{\partial t},$$

and we will assume

$$\frac{\partial A}{\partial t} = \frac{3\pi R_0^3}{2Eh} \frac{\partial P}{\partial t}.$$

In the sequel, we will set

$$k_1 := \frac{3\pi R_0^3}{2Eh}.$$

In order to provide a lumped description of the behavior of the blood in the whole district Ω we need to perform a further averaging of (2.11) over the axial coordinate. To this aim, it is useful to introduce the following notation. We define as *the (volumetric) mean flow rate over the whole district* the quantity

$$\hat{Q} = \frac{1}{l} \int_{\mathcal{V}} u_z dv = \frac{1}{l} \int_0^l \int_{\mathcal{A}(z)} u_z d\sigma dz = \frac{1}{l} \int_0^l Q dz. \quad (3.1)$$

Similarly, we define the *mean pressure over the whole compartment* as

$$\hat{p} = \frac{1}{l} \int_0^l P dz. \quad (3.2)$$

Integrating over the axial coordinate, and assuming that (see [3]):

1. the contribution of the convective terms may be neglected,
2. the variation of A with respect to z is small compared to that of P and Q ,

we obtain the equations:

$$k_1 l \frac{d\hat{p}}{dt} + Q_2 - Q_1 = 0 \quad (3.3)$$

and

$$\frac{\rho l}{A_0} \frac{d\hat{Q}}{dt} + \frac{\rho K_R l}{A_0^2} \hat{Q} + P_2 - P_1 = 0 \quad (3.4)$$

where

$$\begin{aligned} Q_1(t) &:= Q(t, 0), & P_1(t) &:= P(t, 0), \\ Q_2(t) &:= Q(t, l), & P_2(t) &:= P(t, l). \end{aligned} \quad (3.5)$$

These equations represent a lumped parameters description of the blood flow in the compliant cylindrical vessel Ω , and involve the mean values of the flow rate and the pressure over the domain, as well as the upstream and downstream flow rate and pressure values. The coefficients in equations (3.3), (3.4) have been obtained from the integration process. They are in fact the lumped parameters which summarize the basic geometrical and physical features of the dynamic system formed by the blood flow and the vessel wall. Let us try to summarize their meaning.

R In (3.4) we set $R := (\rho K_R l)/(A_0^2)$. If we assume a parabolic velocity we have

$$R = \frac{8\pi\rho\nu l}{\pi^2 R_0^4} = \frac{8\mu l}{\pi R_0^4},$$

where R represents the *resistance* induced to the flow by the blood viscosity. Different expressions for R can be obviously obtained for different velocity profiles or if a non Newtonian rheology is introduced into the model (see e.g. [3, 53, 64]).

L In (3.4) we set $L := (\rho l)/(A_0) = (\rho l)/(\pi R_0^2)$. L represents the inertial term in the momentum conservation law and will be called the *inductance* of the flow.

C In (3.3) we set $C := k_1 l = (3\pi R_0^3 l)/(2Eh)$. C represents the coefficient of the mass storage term in the mass conservation law, due to the *compliance* of the vessel.

With this notation, equations (3.3), (3.4) becomes

$$\begin{cases} C \frac{d\hat{p}}{dt} + Q_2 - Q_1 = 0 \\ L \frac{d\hat{Q}}{dt} + R\hat{Q} + P_2 - P_1 = 0. \end{cases} \quad (3.6)$$

Now, assume that some upstream and downstream data are available. For instance, suppose that Q_1 and P_2 are given. Then, (3.6) represents a system of two equations for four unknowns, \hat{Q} , \hat{p} , P_1 and Q_2 . In order to close mathematically the problem we need some further assumptions. In particular, the dynamics of the system is represented by \hat{p} and \hat{Q} , i.e. by the unknowns that are under time derivative (the *state variables*), so it is reasonable to

approximate the unknowns on the upstream and downstream sections with the state variables, that is

$$\hat{p} \approx P_1, \quad \hat{Q} \approx Q_2.$$

With these additional assumptions, which are reasonable for a short cylindrical pipe, the lumped parameters model becomes:

$$\begin{cases} C \frac{dP_1}{dt} + Q_2 = Q_1 \\ L \frac{dQ_2}{dt} + RQ_2 - P_1 = P_2. \end{cases} \quad (3.7)$$

where the upstream and downstream prescribed data have been plugged into the right hand side. This system can be illustrated by the electric \mathcal{L} -network shown in Fig. 7 (left). The compliance has been gathered on section Γ_1 , where the flow rate is prescribed, and the inertial effects have been allocated on Γ_2 , where the mean pressure is provided.

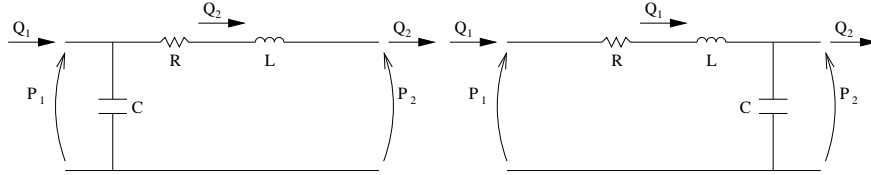


FIGURE 7. Lumped \mathcal{L} -network (left) and \mathcal{L} -inverted network (right) equivalent to a short pipe

In the electric network analogy, the blood flow rate is assimilated to the current, while the blood pressure corresponds to the voltage (see Tab. 1).

In a similar way, if the pressure P_1 and the flow rate Q_2 are prescribed, we still approximate the unknown quantities on the upstream and downstream

TABLE 1. Correspondence table of the analogy between electric and hydraulic networks.

HYDRAULIC	ELECTRIC
Pressure	Voltage
Flow rate	Current
Blood viscosity Blood inertia Wall compliance	Resistance R Inductance L Capacitance C

sections with the state variables, i.e. $\hat{p} \approx P_2$, $\hat{Q} \approx Q_1$, yielding the system whose electric analog, called \mathcal{L} -inverted network, is given in Fig. 7, right.

The case when the mean pressures P_1 and P_2 are prescribed, can be modelled by a cascade connection of \mathcal{L} and \mathcal{L} -inverted lumped representations, yielding a \mathcal{T} -network (Fig. 8). Similarly, if both the flow rates Q_1 and Q_2 are prescribed, the vessel Ω is described by the electric π -network, obtained as a cascade connection of a \mathcal{L} -network and a \mathcal{L} -inverted network (Fig. 9).

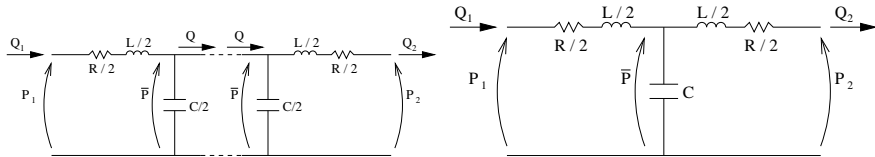


FIGURE 8. Cascade connection of a \mathcal{L} -inverted and a \mathcal{L} -network (left), lumped \mathcal{T} -network (right).

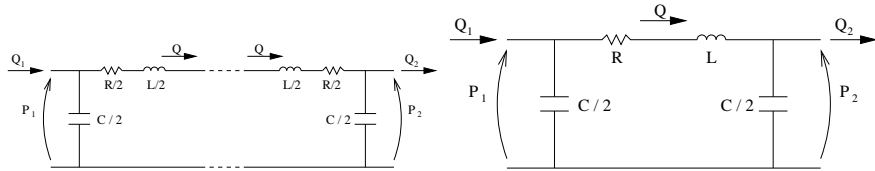


FIGURE 9. Cascade connection of a \mathcal{L} -network and a \mathcal{L} -inverted one (left), lumped π -network (right).

Let us observe that the four different circuits arise from four different possible assumptions about the kind of data prescribed on the upstream and downstream sections. With a little abuse of notation we could call them ‘‘boundary data’’¹⁾. The four different lumped models can be considered therefore as the lumped parameters simplification of four different ‘‘boundary’’ values problems.

Finally observe that some of the simplifying assumptions introduced can be removed (or reduced) by modifying the network: for more details, see [3].

¹⁾Actually, in the simplification leading to lumped parameters models the dependence on the space variables has been lost in the averages, so there is no ‘‘boundary’’ of the domain.

3.2. Lumped Parameters Models for the Heart

The heart is a special “compartment” of the vascular system that need a specific representation in the lumped parameters framework. The structure of the heart and its relationship with its functionality are not completely understood and recent investigations show that the ventricular myocardium can be unwrapped by blunt dissection into *a single continuous muscle band* (see [59]). This could modify the accurate mathematical modeling as well as medical investigations and surgical interventions on the heart. For the purpose of these notes, however, we simply refer to a classical description of the heart, which is subdivided into two parts, called to the right and the left heart, respectively, separated by the *septum*. The right heart supplies the pulmonary circulation, while the left pumps the blood into the systemic tree. Each side consists of two chambers, the atrium and the ventricle, separated by the atrioventricular valves (the *tricuspid* valve in the right side, the *mitral* valve in the left one). Their role is to receive fluid at low pressure and transfer it to a higher pressure region. In other words, each side acts as a *pump* (see [27]). Each ventricle can be described *as a vessel where the most significant feature is the compliance and the compliance changes with time* (see [10, 27, 29, 55]).

The starting point for a possible mathematical model is the relation that links pressure and radius of an elastic spherical ball filled with fluid. Here and in the following we take $P_{\text{ext}} = 0$. We have

$$\pi R^2 P = 2\pi E h_0 R \frac{R - R_0}{R_0},$$

where R_0 is the reference sphere radius, which is the one reached when $P = 0$, h_0 a reference thickness of the ball surface and E the Young modulus. The contraction of the cardiac muscle may be taken into account by an increase of E (stiffening) and by a shortening of the muscle length (that is a reduction of R_0). It is more convenient to express this relation as a function of the volume V , instead of the radius. By recalling that $V = 4\pi R^3/3$, a linearisation procedure leads to

$$P = \frac{E(t)h_0}{2\pi R_0^3(t)} (V - V_0(t)),$$

where we have indicated the coefficients that change in time because of the action of the muscle. This simplified model does indeed describe the major

characteristic of the ventricle. If we indicate

$$C(t) = \frac{2\pi R_0^3(t)}{E(t)h_0},$$

we may re-write the relation in the more compact form

$$V(t) = C(t)P(t) + V_0(t).$$

By deriving with respect to time we obtain

$$\frac{dV}{dt} = Q = \frac{dC}{dt}P + C\frac{dP}{dt} + M_Q(t) \quad (3.8)$$

where Q represents the (incoming) flow rate and $M_Q = dV_0/dt$ is the action exerted by the contraction of the cardiac muscle.

A lumped representation (electric analog) of each ventricle²⁾ is given in Fig. 10, where R accounts for an additional viscous resistance inside the ventricle, whose relevance has been recently pointed out by [58] and M_Q is represented by a generator of current.

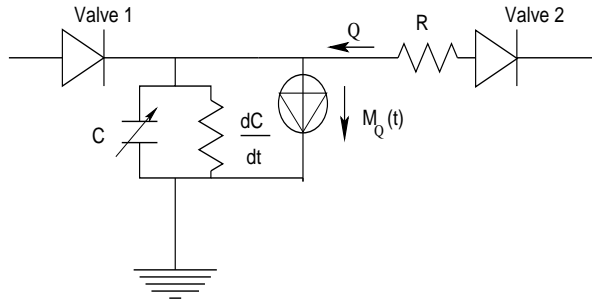


FIGURE 10. Network for the lumped parameters modeling of a ventricle.

In Fig. 10 the presence of heart valves has been taken into account by diodes which allow the current flow in one direction only³⁾. Observe that the presence of the valves *introduces a nonlinear relation* in the lumped parameters model.

²⁾A mechanical representation of the heart working based on the classical Hill's model for the muscle can be found in [30] and [66]. See also [2]

³⁾The same representation can be used also for the valves in the venous system, whenever needed.

3.3. Lumped Parameters Models for the Circulatory System

The compartments previously described are the elementary bricks for building models for the whole system. As previously pointed out, the number of compartments depends on the accuracy requested to the model and, definitely, on the number of vessels that it is worthwhile to represent separately as single units.

The connection among the compartments is driven by *flux and momentum conservation* at the interfaces. As a direct consequence of the electric analogy the quantities that are matched are Q and the pressure P . There is a difference in this respect to the coupling of 1D models (see Sect. 2.2), where the total pressure is considered. This choice is indeed consistent with the hypothesis of negligible convective terms.

In the electric analog, these relations correspond to the application of the classical *Kirchhoff laws* for the nodes (conservation of current) and the nets (conservation of the voltage). An sketch of the possible connection of different compartments is given in Fig. 11.

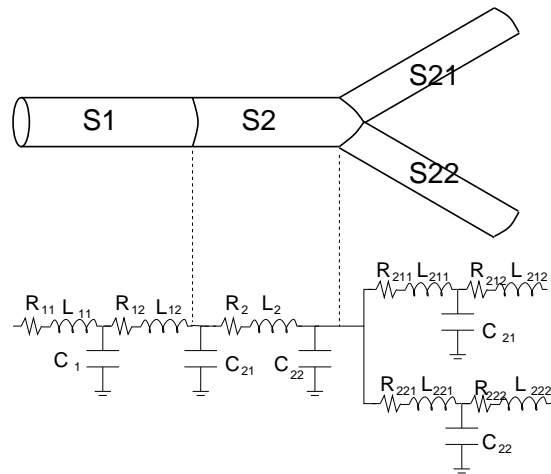


FIGURE 11. Lumped parameters model for a branched vessel as a cascade of T and π networks.

A detailed electric analog for the circulation is provided in [64] and in [40], where hundreds of elementary compartments are accounted for.

From the mathematical viewpoint, a general representation of lumped parameters models is a Differential-Algebraic-Equations (DAE) system in

the form

$$\begin{cases} \frac{d\mathbf{y}}{dt} = B(\mathbf{y}, \mathbf{z}, t) & t \in (0, T] \\ G(\mathbf{y}, \mathbf{z}) = 0 \end{cases} \quad (3.9)$$

together with the *initial condition vector* $\mathbf{y}|_{t=t_0} = \mathbf{y}_0$. Here, \mathbf{y} is the vector of the state variables (associated to capacitors and inductors), \mathbf{z} are other variables of the network and G the algebraic equations that derive from the Kirchhoff laws. If we suppose that the Jacobian matrix $J := \partial G / \partial \mathbf{z}$ is non singular⁴⁾, by the implicit function theorem we can express \mathbf{z} as function of \mathbf{y} and resort to the reduced Cauchy problem

$$\begin{aligned} \frac{d\mathbf{y}}{dt} &= \Phi(\mathbf{y}, t) = A(\mathbf{y}, t)\mathbf{y} + \mathbf{r}(t) & t \in (0, T], \\ \mathbf{y} &= \mathbf{y}_0, \quad \text{at } t = t_0. \end{aligned} \quad (3.10)$$

The time dependence of matrix A is due to the heart action and is related to the variable ventricles compliances, while the dependence of A on \mathbf{y} is due to the presence of diodes (non linear term). The forcing term \mathbf{r} depends on t through the function $M_Q(t)$.

From classical results of calculus, it is possible to prove that (a) if $\Phi(\mathbf{y}, t)$ is continuously differentiable there exists a time interval $[0, T^*]$ in which the solution of the problem exists and is unique; (b) if, moreover, the derivatives $\partial\Phi_i/\partial y_j$ are bounded in all the time interval $[0, T]$, then the solution of the Cauchy problem exists and is unique in $[0, T]$.

In the sequel, we will suppose that the previous hypotheses are verified.

From the numerical point of view, the nonlinear ordinary differential system (3.10) can be solved by means of classical methods. For this reason we do not dwell here with the numerical solving of lumped parameter models and refer the interested reader to e.g. [47].

4. Basic Numerical Issues for Multiscale Modeling

Our goal is now to investigate specific problems arising from the mathematical and numerical coupling of different models for blood flow, ranging from the Navier-Stokes equations down to lumped parameters models. In particular, we will have to manage the interfaces between models featuring a different level of detail. It is to be expected that the more accurate (pointwise) model would need on the interfaces more data than the mean models

⁴⁾In this case, the DAE system is said to be *of index 1*.

could give, being by far less accurate. The data referred to the simple-minded submodel are indeed a spatial average of the pointwise quantities which are, on the other side, considered by the accurate local submodel and that would be needed on the interfaces in order to make it well posed the Navier-Stokes boundary problem. We have, therefore, the problem of giving a well posed formulation of the local subproblem, filling up the defective data set provided by the reduced submodels. The main concern of multiscale modeling is to carry out this completion minimizing, as far as possible, the perturbations on the numerical solution. For example, if the flow rate (*mean value*) is known on the upstream section of a vascular district, there are many velocity profiles (*pointwise values*) on that section that can be associated to such mean data and, therefore, can be prescribed to the Navier-Stokes problem. However, the choice of a specific profile will strongly influence (or perturb) the numerical solution in a non-controlled way. The present Section illustrates some techniques for avoiding the prescription of a velocity profile and, in general, for reducing perturbations on the numerical solution when solving 3D problems with average (defective) boundary data.

4.1. Defective Boundary Data Problems

For the sake of clarity, let us provide a general statement of defective boundary data problems. Let Ω be a bounded domain of \mathbb{R}^d , $d = 2$ or 3, whose boundary $\partial\Omega$ is decomposed into the union of Γ_{wall} and several disjoint sections $\Gamma_0, \Gamma_1, \dots, \Gamma_n$, $n \geq 1$ (see Fig. 12).

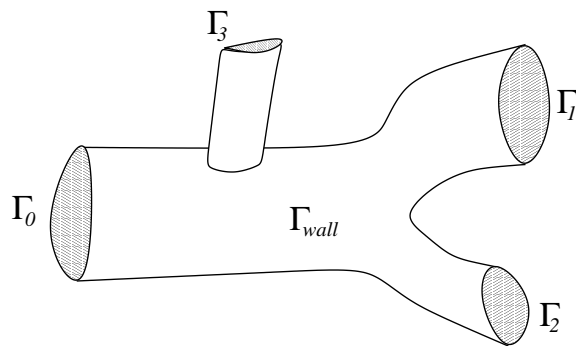


FIGURE 12. The partition of the boundary of the domain Ω .

For the sake of simplicity, we suppose that the domain is rigid, so that we are interested in solving the Navier-Stokes equations in Ω :

$$\left\{ \begin{array}{l} \frac{\partial}{\partial t}\mathbf{u} + \mathbf{u} \cdot \nabla \mathbf{u} + \nabla p - \nu \Delta \mathbf{u} = \mathbf{f}, \quad t > 0 \\ \operatorname{div}(\mathbf{u}) = 0, \quad t > 0 \\ \mathbf{u} = \mathbf{u}_0, \quad t = 0, \\ \mathbf{u} = 0 \quad \mathbf{x} \in \Gamma_{\text{wall}}. \end{array} \right. \quad (4.1)$$

Two different kinds of boundary conditions are of some interest in the multiscale coupling and will be considered on the sections Γ_i , $i = 0, \dots, n$.

The first condition refers to the *mean pressure problem*, which requires that

$$\frac{1}{\operatorname{meas}(\Gamma_i)} \int_{\Gamma_i} p \, ds = P_i(t), \quad i = 0, \dots, n. \quad (4.2)$$

The second condition we address is the *flow rate problem*

$$\int_{\Gamma_i} \mathbf{u} \cdot \mathbf{n} \, ds = Q_i(t), \quad \text{for } i = 0, \dots, n. \quad (4.3)$$

Observe that, due to the fluid incompressibility and the rigidity of the wall, a compatibility relation must exist among the fluxes Q_i , namely:

$$Q_0 + Q_1 + \dots + Q_n = 0. \quad (4.4)$$

The initial-boundary value problem (4.1) with either (4.2) or (4.3) is not well-posed from a mathematical point of view due to the average (non-pointwise) nature of the boundary data on the artificial boundaries (see [61]). A possible way for completing the lackness of data is the one proposed in [26]. Following this approach, a particular *weak or variational formulation of the boundary problem* is devised which allows to fulfill conditions (4.2) (resp. (4.3)) at some extent, giving rise to a well-posed problem. In fact, this formulation forces in an implicit way some natural (Neumann-like) boundary conditions which selects one particular solution among all the possible ones of the original differential problem. The completion of the defective boundary data set is essentially an implicit by-product of the choice of the suitable variational formulation, which is based on a natural set of boundary conditions, less perturbative than essential (Dirichlet) ones.

This approach is really effective for the numerical solution of the mean pressure drop problem (see [61]). In solving the flow rate problem, it is not

straightforward for what concerns the selection of an appropriate finite dimensional space for the space discretization. Here, we will address therefore a reformulation of the flow rate problem proposed in [16], more suitable for the numerical purposes.

4.1.1. A Lagrange multiplier approach for flow rate boundary conditions. Consider the initial-boundary values problem given by (4.1) and the net flux conditions (4.3). We assume that the compatibility condition (4.4) is fulfilled.

Rather than (defective) boundary conditions, (4.3) can be regarded as a set of *constraints* for the solution of the problem at hand. Starting from this viewpoint, a possible way for forcing such constraints resorts to the Lagrange multiplier approach. According to this strategy, the equations to be solved are *penalized* by the presence of the constraint, weighted by suitable (unknown) coefficients, the Lagrange multipliers⁵⁾. The original problem is therefore reformulated in an *augmented* fashion, due to the presence of the multipliers (see e.g. [23]).

In the present case, this approach leads to the following variational problem: look for $\mathbf{u} \in V$, $p \in M$ and $\lambda_1, \dots, \lambda_n \in \mathbb{R}$ such that, for all $\mathbf{v} \in V$ and $q \in M$,

$$\begin{cases} \left(\frac{\partial}{\partial t} \mathbf{u} + \mathbf{u} \cdot \nabla \mathbf{u}, \mathbf{v} \right) + \nu(\nabla \mathbf{u}, \nabla \mathbf{v}) + \sum_{i=1}^n \lambda_i \int_{\Gamma_i} \mathbf{v} \cdot \mathbf{n} - (p, \operatorname{div}(\mathbf{v})) = \langle \mathbf{f}, \mathbf{v} \rangle, \\ (q, \operatorname{div}(\mathbf{u})) = 0, \\ \langle \phi_i, \mathbf{u} \rangle = Q_i, \quad i = 0, \dots, n, \end{cases} \quad (4.5)$$

for all $t > 0$, with $\mathbf{u} = \mathbf{u}_0$ for $t = 0$.

The mathematical analysis of this probem (its equivalence to the mean flux problem stated above and its well-posedness) can be found in [16] and [62].

In order to discretize equation (4.5), we introduce a Galerkin approximation based on the finite dimensional spaces $V_h \subset V$ and $M_h \subset M$, which we assume to satisfy the well-known LBB condition (see e.g [48], Chap. 9.):

$$\forall q_h \in M_h \quad \exists \mathbf{v}_h \in V_h, \mathbf{v}_h \neq 0 : \quad (q_h, \operatorname{div}(\mathbf{v})_h) \geq \beta_h |q_h|_{L^2} |\mathbf{v}_h|_{H^1}. \quad (4.6)$$

⁵⁾We remind that in the same perspective, the pressure of the incompressible Navier-Stokes equations can be regarded as the Lagrange multiplier of the incompressibility constraint—see e.g. [48].

Let $(\mathbf{u}_h, p_h, \lambda_{1h}, \dots, \lambda_{nh})$ be the solution of the discrete problem. We denote by $(u_i)_{i=1\dots dN}$ (resp. $(p_i)_{i=1\dots M}$) the components of \mathbf{u}_h (resp. p_h) with respect to a basis $\{\mathbf{v}_i\}$ of V_h (resp. $\{q_i\}$ of M_h). Finally, we introduce the vectors $U = (u_1, \dots, u_{dN}) \in \mathbb{R}^{dN}$, $P = (p_1, \dots, p_M) \in \mathbb{R}^M$ and $\Lambda = (\lambda_{1h}, \dots, \lambda_{nh}) \in \mathbb{R}^n$. Then the discrete counterpart of (4.5) gives rise to the following algebraic system of equations

$$\begin{cases} AU + D^T P + \Phi^T \Lambda &= F, \\ DU &= 0, \\ \Phi U &= Q, \end{cases} \quad (4.7)$$

where $A \in \mathbb{R}^{dN \times dN}$ is the stiffness matrix, $D \in \mathbb{R}^{M \times dN}$ is the matrix associated to the divergence operator and Φ is the $n \times dN$ matrix whose lines are given by the vectors $\phi_i = (\int_{\Gamma_i} \mathbf{v}_1 \cdot \mathbf{n} ds, \dots, \int_{\Gamma_i} \mathbf{v}_{dN} \cdot \mathbf{n} ds)$, $i = 1, \dots, n$.

It is possible to prove that this system is non singular, [16]. However, this system is not a classical Navier-Stokes problem, so its numerical solution should require the set up of an “ad hoc” solver. On the other hand, there is no numerical convenience in setting up a solver computing simultaneously U , P and Λ , since the matrix associated to system (4.7) is supposed to be very ill conditioned in real applications. Therefore, as for the standard Navier-Stokes problem (see [48]), it is worthwhile to resort to splitting methods which reduce the problem to a series of smaller and easier to solve steps. This can be done in different ways (see [62]). Here we illustrate a strategy that has the advantage of separating the fluid (velocity and pressure) from the multipliers computation. In this way, if a Navier-Stokes solver is available (for instance a commercial package), it can be actually adopted for solving the augmented problem.

We rewrite (4.7) in the form

$$\begin{bmatrix} S & \tilde{\Phi}^T \\ \tilde{\Phi} & 0 \end{bmatrix} \begin{bmatrix} X \\ \Lambda \end{bmatrix} = \begin{bmatrix} G \\ Q \end{bmatrix} \quad (4.8)$$

where $\tilde{\Phi} = [\Phi, 0] \in \mathbb{R}^{n \times (dN+M)}$, $X = [U, P]^T$, $G = [F, 0]^T$. The matrix S corresponds to the discretization of the Navier-Stokes problem with Neumann conditions on the boundaries where the net fluxes are prescribed. If the two discrete spaces V_h and M_h satisfy the LBB condition (4.6), S is non singular (see, e.g. [8, 48]). We can then eliminate the unknown X from (4.8), obtaining a system for the Lagrange multiplier:

$$\tilde{\Phi} S^{-1} \tilde{\Phi}^T \Lambda = \tilde{\Phi} S^{-1} G - Q. \quad (4.9)$$

This system can be solved by an appropriate iterative method. For instance, if we denote $R := \tilde{\Phi}S^{-1}\tilde{\Phi}^T$ and $\mathbf{b} := \tilde{\Phi}S^{-1}G - Q$, we could resort to the classical preconditioned GMRes scheme⁶⁾ (see e.g. [54]). In particular, this requires to solve a Navier-Stokes problem at each iteration and this can be carried out by means of a standard solver. This could seem quite expensive. However, the matrix R is usually small, being its dimension equal to the number of artificial boundaries, so the number of iterations required will be accordingly small. Moreover, the computational efficiency can be improved by finding good preconditioners of R . Other approaches rely on finding suitable approximations for system (4.7) cheaper to solve (see e.g. [63]).

4.1.2. Numerical results. In order to assess the proposed methodologies, we consider a case where the analytical solution of the Navier-Stokes equations is known. More precisely, we consider the *Womersley* solution, which describes the transient flow in a cylindrical pipe associated to a time-periodic pressure gradient (see e.g. [38]). As such, it is a transient counterpart of the well known Poiseuille solution.

We have considered a straight cylinder, imposing homogeneous Neumann boundary conditions at the inflow, while at the outflow we prescribe the flow rate associated to the Womersley solution. The results are shown in Fig. 13. Here, the computed velocity field at two different times is illustrated, together with the corresponding exact axial velocity profile. The solution obtained agrees very well with the analytical one. A single condition on the flow rate at the outflow, imposed through a Lagrange multiplier, is sufficient to recover the Womersley flow. It is worthwhile outlining that *the Womersley profile is an outcome of the computation, it has not been forced anyway*. Other analytical tests can be found in [62].

In Fig. 14 we report the solution of the net flux problem obtained by solving a steady flow rate problem with the Lagrange multiplier approach in a real geometry of the total cavopulmonary connection. The solution has been obtained with a commercial solver (Fluent). Again, we point out that the velocity profiles are not prescribed but they are an outcome of the numerical simulation.

⁶⁾In the case of a Stokes problem, R is symmetric and positive definite, so the Conjugate Gradient method can be adopted.

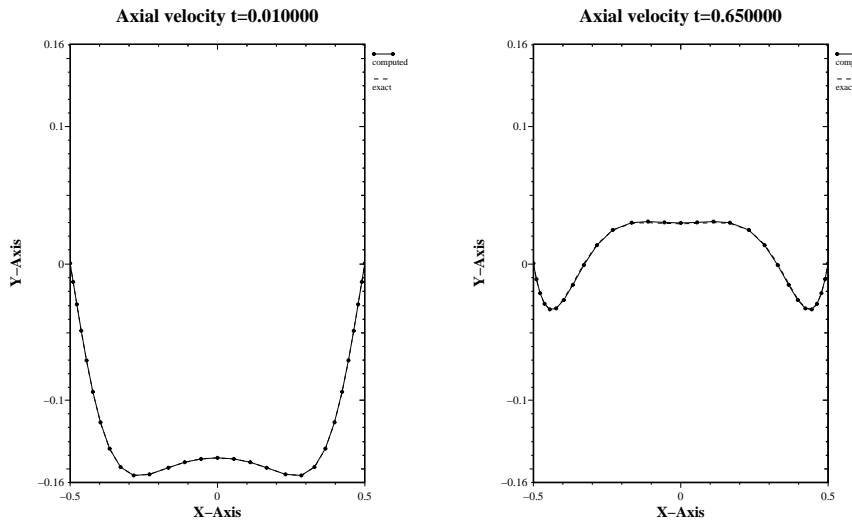


FIGURE 13. 3D numerical solutions obtained at two different instants imposing a periodic flux. The continuous line is the numerical solution, the dotted line is the analytical one.

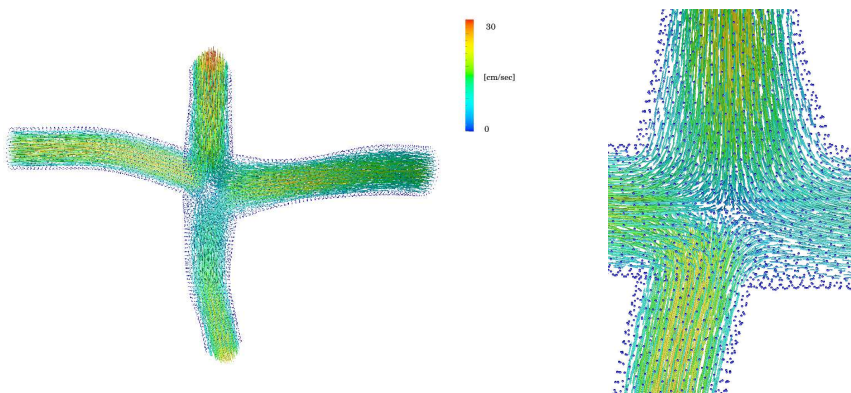


FIGURE 14. Cavo-pulmonary connection: velocity field computed with the Lagrangian multiplier approach. Simulations carried out with a commercial solver (Fluent).

5. Multiscale Models

Having developed techniques for managing local 3D problems with mean boundary data in a numerically sound way, we are now in position of describing complete geometrical multiscale models, both from a mathematical and numerical viewpoints. We will start considering a 3D and a 0D model, discussing its well posedness and numerical methods for the coupling. Then, we will address numerical methods for 3D-1D coupling (Sect. 5.2). We will finally consider the coupling of 1D and 0D models.

Numerical results of medical interest are presented in Sect. 6.

5.1. Coupling 3D and 0D Models

We wish to represent the whole circulatory system by an electric circuit except on a specific region Ω , where blood flow is modelled by the Navier-Stokes equations, as illustrated in Fig. 15. Here, the compliance of the local vascular district is neglected for the sake of simplicity, hence Ω is constant in time. Let us assume that the network faces the district Ω by capacitors C_i ($i = 1, \dots, \bar{n}$) as shown in the picture. In particular, we put in evidence the representation in terms of a network of the vascular regions in the immediate neighborhood of the 3D model. In [50] we have extensively investigated this problem. In particular these parts of the lumped network have been called the *bridging regions*. In this picture, we have three bridging regions corresponding to the three inflow/outflow of Ω . We are essentially coupling a lumped representation of the circulation with the mean pressure problem for the Navier-Stokes equations. The boundary mean pressures are not given, but are state variables of the lumped model to be computed. The heterogeneous multiscale problem is therefore given by coupling subproblems that can be proved to be separately well posed. It is reasonable to expect that the global multiscale model is well posed. This well posedness has been proved in [50] starting from classical fixed point techniques.

The role of the interface conditions in the splitting procedure is naturally driven by the specific topology of the network at the interfaces. In the case of Fig. 15, the interface flow rates are not state variables of the lumped system, and, therefore, they are well suited to play the role of a forcing term for the ordinary differential system. However, depending on the choice of the bridging regions, the matching between the network and the Navier Stokes system could be pursued, for instance, by interchanging the role of flux and pressure at the interfaces.

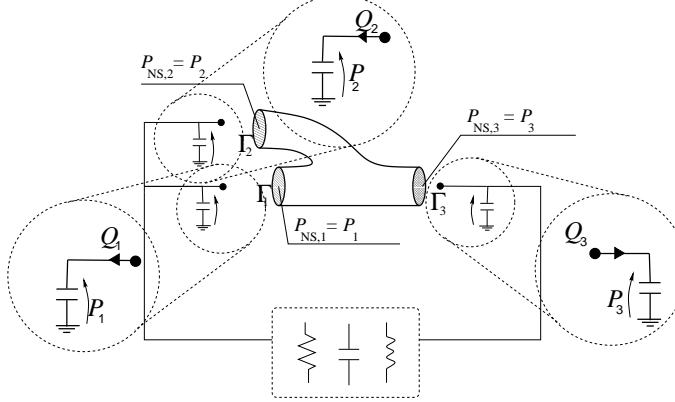


FIGURE 15. Scheme of coupling between the whole system and a local district. The lumped representation of the three bridging regions at the interfaces with the Navier-Stokes model is highlighted in the dashed circles.

In this case we should suppose that the flow rates are provided to the Navier-Stokes system by the network, which in turn receives pressure data. For instance, in the network configuration of Fig. 16, the interface pressure is not a state variable of the lumped system, so it is a good candidate for being a forcing term of the ordinary differential system, provided by the Navier-Stokes solution. On the other hand, the interface flow rates, which in the electric analogy correspond to the current at the interfaces and are state variables for the system, become boundary data for the Navier-Stokes problem. In this case, we formulate a net flux problem for the Navier-Stokes model, to be faced according to the Lagrange multiplier approach.

For the numerical treatment of these coupled models, it is natural to resort to an iterative approach based on the splitting of the whole problem into its basic components, the ODE system from one hand and the Navier-Stokes equations from the other one.

For the sake of clarity, suppose to deal with the coupled problem represented in Fig. 16. A compact representation of a possible numerical scheme is given in Fig. 17 (left). In this scheme, an explicit time advancing method is used for the lumped parameters model, computing the new state at t^{n+1} of the circulatory network starting from the previous one (at t^n) and the pressure data given by the Navier-Stokes solver. In this way we compute the flow rates at the current time step $n + 1$ that become boundary data for solving a flow rate Navier-Stokes problem (with the Lagrangian multiplier

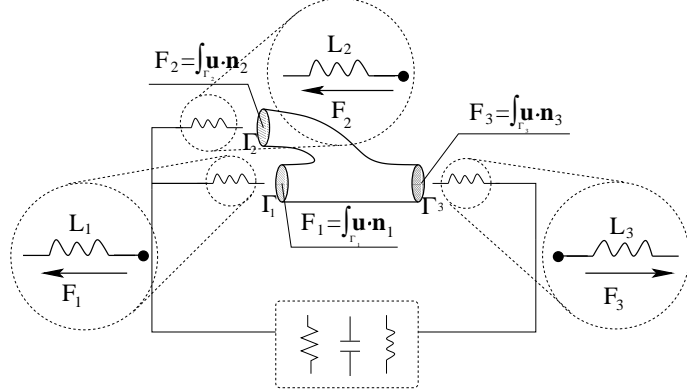


FIGURE 16. Scheme of coupling between the whole system and a local district where the bridging regions are given by inductors.

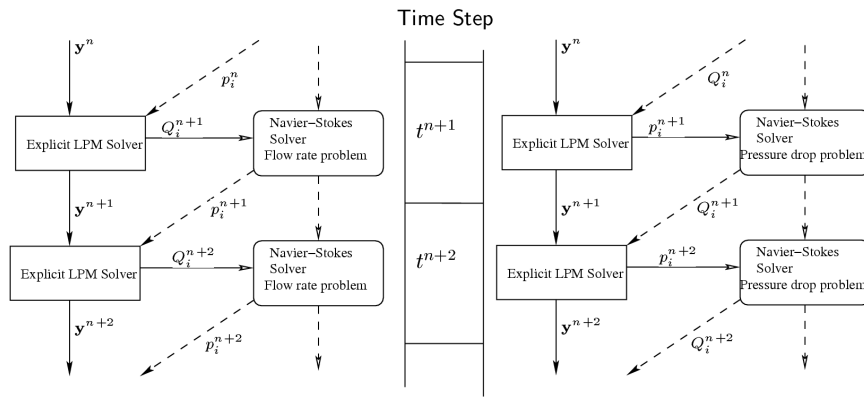


FIGURE 17. Possible numerical scheme for the coupling of a Lumped Parameter Model (LPM) and the Navier-Stokes problem: on the left the case corresponding to Fig. 16, on the right the one corresponding to Fig. 15.

approach). For solving the coupled problem of Fig. 15, the corresponding numerical scheme is in Fig. 17 right.

Numerical results and discussion about these methods can be found in [45], [50] and in [37]. In the latter work, in particular, the 3D compliant case is addressed, that requires specific interface conditions for the compliant vascular wall. We mention also an example of multiscale 3D-0D models proposed in [6], illustrating the relevance of the multiscale approach in the numerical simulation of the blood flow in a carotid bifurcation. CT scans of a stenosed carotid artery have been used for reconstructing a 3D geometry

both of a occluded and of a healthy (by modification of the original images) carotids. Numerical results have been obtained both for a stand-alone and a multiscale model (see Fig. 18) in the two geometries. The results outline the relevance of the description of the whole circulatory cerebral system in prescribing correct boundary conditions and definitely obtaining significant numerical results.

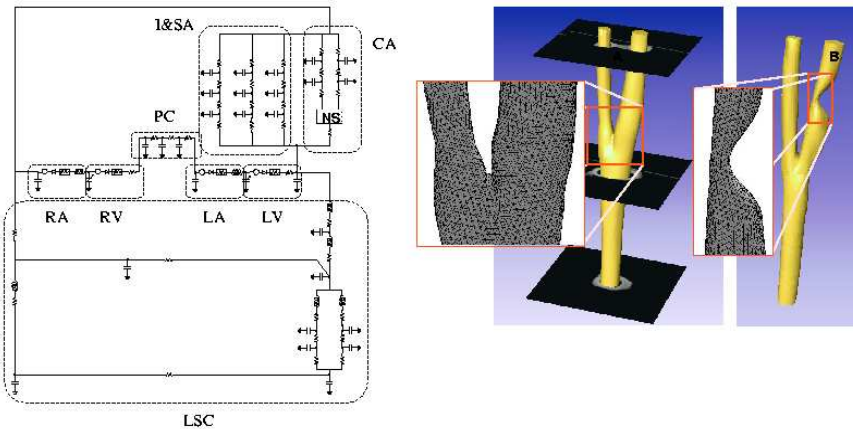


FIGURE 18. Left: Lumped parameter model for the multiscale carotid simulation.
Right: Healthy and stenosed carotid model. Taken from [6].

Remark 3. In the last years, numerical methods for solving complex real problems in scientific computing by means of *domain decomposition methods* (DDM) have received great attention: as a recent reference, we quote [49]. The numerical approach to problems of increasing complexity quite naturally compell the identification of simpler “subproblems” that can be solved separately from the others, in order to setting up more effective numerical algorithms. Among the others possible examples, we quote fluid-structure interaction problems in hemodynamics, both at the mechanical and biochemical level (see [39, 51, 52, 69]).

In our framework, it is reasonable to assimilate the flux data to (mean) *Dirichlet* data, since they refer to the velocity field, while (mean) pressure data can be assimilate to *Neumann* condition, since they refer to the pressure, i.e. to the normal stress tensor which is a natural condition for the classical variational formulation of the Navier-Stokes equations. In this respect, the iterative algorithms presented above (and the ones that will be introduced for the 3D-1D coupling) can be considered an extension of the *Dirichlet-*

Neumann substructuring iterative method, widely adopted in the context of DDM. This link can provide suggestions for setting up some improvements in the algorithms, exploiting the theoretical framework of DDM.

5.2. Coupling 1D and 3D Models

Let us consider now the coupling of 3D and 1D models. Since we are still dealing with a reduced model, involving mean quantities and the point-wise Navier-Stokes model, we will have to handle “defective” data problems, according to the strategies illustrated in Sect. 4. In particular, as we have pointed out in the previous section, if we consider a compliant 3D domain, specific interface conditions will be needed by the differential problem associated to the vessel wall description in the 3D model. Moreover, the mathematical hyperbolic nature of 1D models will require a careful treatment of the interface conditions, based on a characteristics analysis (see Sect. 2). Since the 1D models are more accurate than the 0D ones, we have more possibilities in devising interface conditions. *A priori*, it is reasonable to look for the continuity of different quantities at the interface Γ_a , namely the flux, the mean pressure (or the total mean pressure), or the normal stresses or also the characteristic variables incoming to the 1D domains and, in the case of a compliant 3D domain, the interface area. The continuity of some of these quantities will be enough to force all the others: a complete discussion of the different possible interface conditions set is carried out in [15] and [16]. To these references the reader is referred (see also [1]) for some numerical results and examples.

Here we limit ourselves to point out that at the numerical level, the explicit coupling of 3D and 1D solver similar to the one illustrated for the 3D and 0D models can be affected by numerical instabilities, depending e.g. on the physical properties of the vascular walls. In these cases, we need to resort to an *implicit* coupling, achieved by iterating the computation of the 3D and the 1D problems at each time step, as it is illustrated in Fig. 19. In this scheme, we are supposing that the 1D model computes the pressure at the interface and the incoming characteristic variable W_1 is imposed at its inlet from the flow rate and the area computed by the 3D model. Relaxation parameters ε_1 and ε_2 can be tuned for improving the convergence of the scheme. A suitable stopping criterion will be adopted for ending the inner loop at each time step.

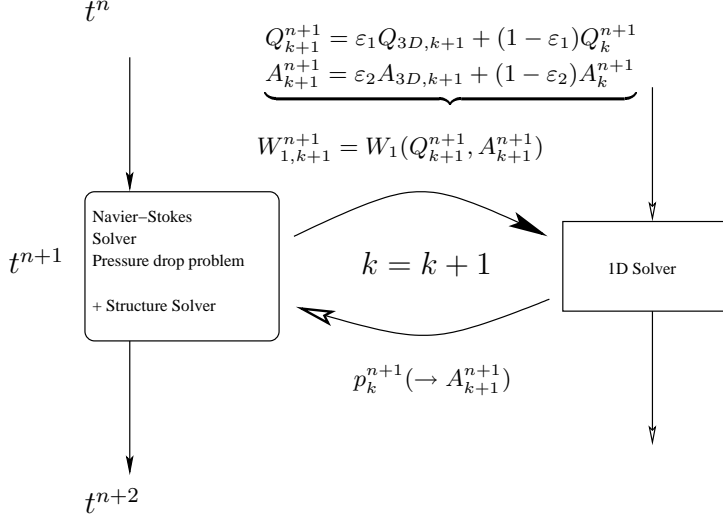
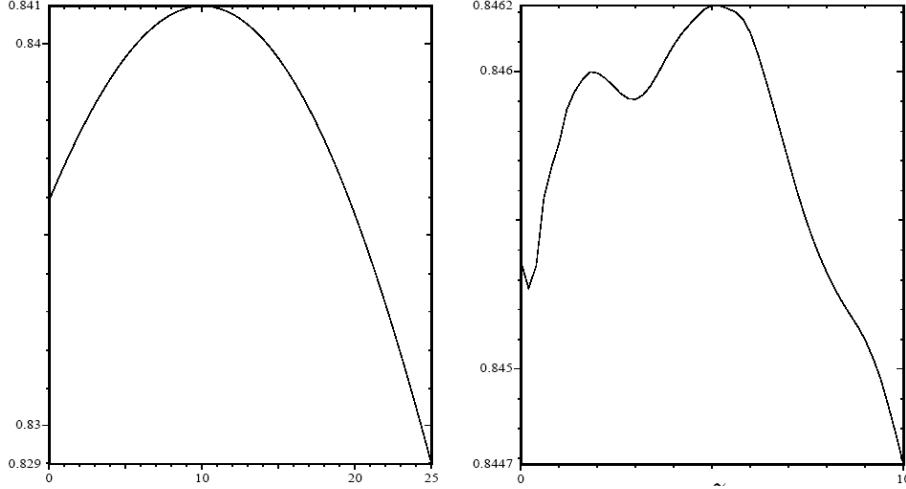


FIGURE 19. Implicit coupling of 3D and 1D solvers.

FIGURE 20. Left: Area in the upstream 1D model in the physiological case ($t = 0.016$ s); Right: Area in the upstream 1D model in the stented artery: observe the overload induced by the reflections due to the presence of the stent. Taken from [44].

In Fig. 20 (taken from [44]) we illustrate an example of the results obtained with this scheme in the numerical solution of a coupled 1D-3D-1D

model. The 3D model is supposed to be rigid. This can be regarded as the model of an artery with a stent, which is really stiffer than the physiological vascular tissue. In particular, it is possible to appreciate the overload in the proximal (=upstream with respect to the stent) 1D domain in the pressure, induced by the (physiological) reflections at the interface with the 3D stented model.

5.3. Coupling 0D and 1D Models

We finally consider the coupling of 1D and 0D models. Since we are actually coupling reduced models, both dealing with average (in space) quantities, we will not have defective boundary problems to solve. The crucial issues, in this case, are the boundary treatment of the 1D models, and the branching numerical treatment, addressed in Sect. 2.2.

The mathematical analysis of this class of heterogeneous problems can be carried out by means of fixed point techniques (see [18]) in a way similar to the one followed for the coupling of 3D and 0D models. See also [34]. The numerical solution can be in some cases obtained by coupling the discretized equations (in space and time for the 1D model, in time for the 0D one) in a monolithic solver. In general, it is however possible to resort to an iterative approach similar to the ones presented in the previous sections, in which a 1D and a 0D solvers are iteratively called in the multiscale numerical device.

The practical interest for this kind of models relies in the set up of systemic models for the description of the pressure wave propagation in the arterial tree (1D model) induced by the heart action (0D model), see [58], [19]. In particular, in [19] a 1D network including the largest 55 arteries (see Fig. 21 left) is coupled with the heart lumped parameter model given in Sect. 3.2 and a three elements Windkessel model for the peripheral circulation. The numerical coupling of the heart model and the 1D network has been obtained by following the scheme illustrated in Fig. 22. As a matter of fact, the two models are coupled only during the systolic phase, while in the diastolic one a null flux condition is imposed at the entrance of the aorta. The opening and closing of the aortic valve is driven by the comparison between the ventricular and the aortic pressure.

In Fig. 23 the relevance of the multiscale approach is clearly put in evidence: if the action of the heart is simply modelled by a prescribed boundary

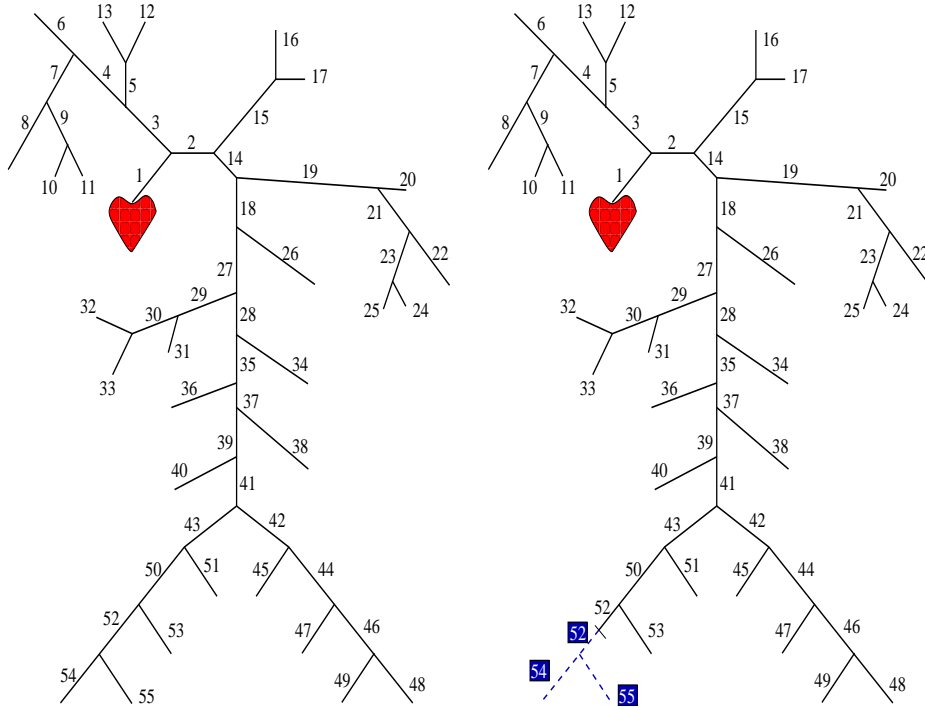


FIGURE 21. Arterial tree composed of a set of 55 straight vessels, described by 1D models (see [65]). On the right a pathological case, in which some of the vessel are supposed to be completely occluded.

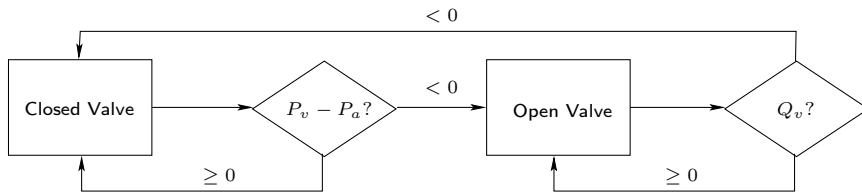


FIGURE 22. Flow chart representation of the aortic valve modeling.

condition at the inlet of the aorta (as it is usually done—left column), the results can be significantly different, with an underestimation of the heart overload due for instance to a pathological occlusion (dotted lines).

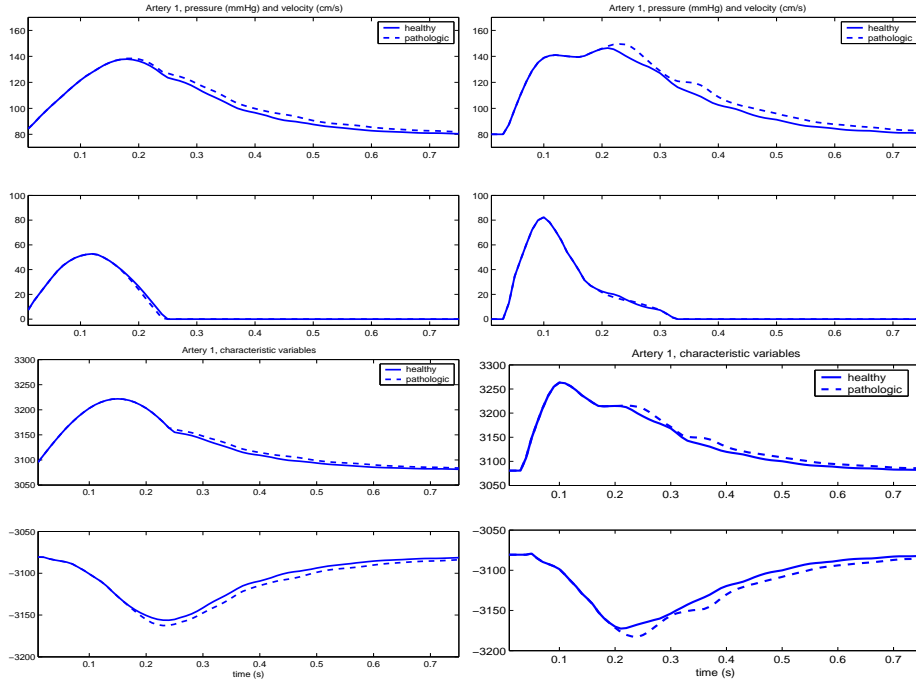


FIGURE 23. Comparison between the results obtained with standard proximal conditions (left) and the multiscale coupling with the ventricular model (right). Values of velocity and pressure in the mid-point of the aorta are presented in the first two rows. The last two rows illustrate a comparison between the Riemann invariants W_1 and W_2 , respectively. Adult circulation in a physiologic (solid) and pathologic (dotted) test case are simulated.

6. Numerical Results in a Case of Clinical Interest

Numerical results obtained in more realistic contexts, still based on the approach of the present work, can be found in [31, 35, 36]. In these references the adoption of geometrical multiscale models has given good results for analysing, by means of numerical simulations, the dynamics of flow patterns in morphologically complex vascular districts in the context of paediatric surgery. The proposed methodology was in particular applied to a reconstructive procedure, used in cardiovascular paediatric surgery to treat a group of complex congenital malformations. There are different solutions for carrying out this kind of interventions (see [35, 36] and Fig. 24) and it is not easy, in general, to state which should be considered the best for the patient at hand. In the multiscale models adopted in this analysis, a 3D realistic morphology

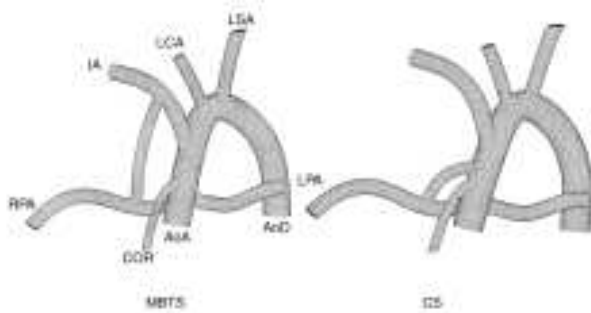


FIGURE 24. Two possible realizations of the Norwood operation: Modified Blalock-Taussig shunt (left) and Central Shunt (right), from [35].

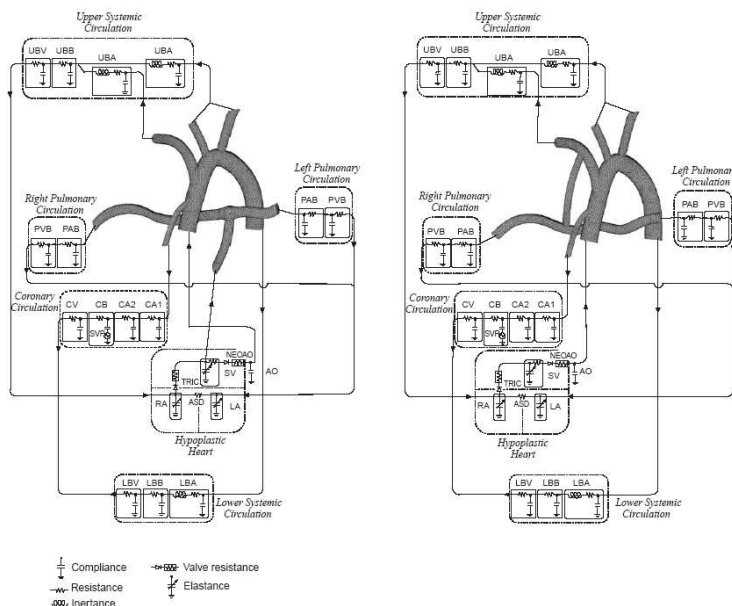


FIGURE 25. Multiscale model of the Modified Blalock Taussig Shunt (left) and of the right ventricle—pulmonary artery shunt or *Sano operation* (right, from [36]).

including the innominate artery, the pulmonary, carotid and subclavian arteries and the shunt are coupled to a lumped model composed by different blocks describing the rest of the pulmonary circulation, the upper and lower body, the aorta, the coronary system and the heart (see Fig. 25). Due to the complexity of the vascular 3D, the adoption of stand-alone classical fluid dynamics model failed to give accurate description of the velocity and pressure

fields (see [31]). With the adopted multiscale approach, i.e. using boundary conditions that account for the circulatory system, this was avoided and the inlet velocity profile reversal was correctly reproduced (In Fig. 25 and Fig. 26 we report some snapshots of the computed local solution). The prediction of both the local and the global haemodynamics after a surgical correction, leads to the quantification of pressure drops across the repaired region as well as to that of flow distribution into the major cardiovascular districts, which is an extremal important issue. Geometrical multiscale numerical modeling can help therefore the surgeon in the optimal choice of shunt size and placement.

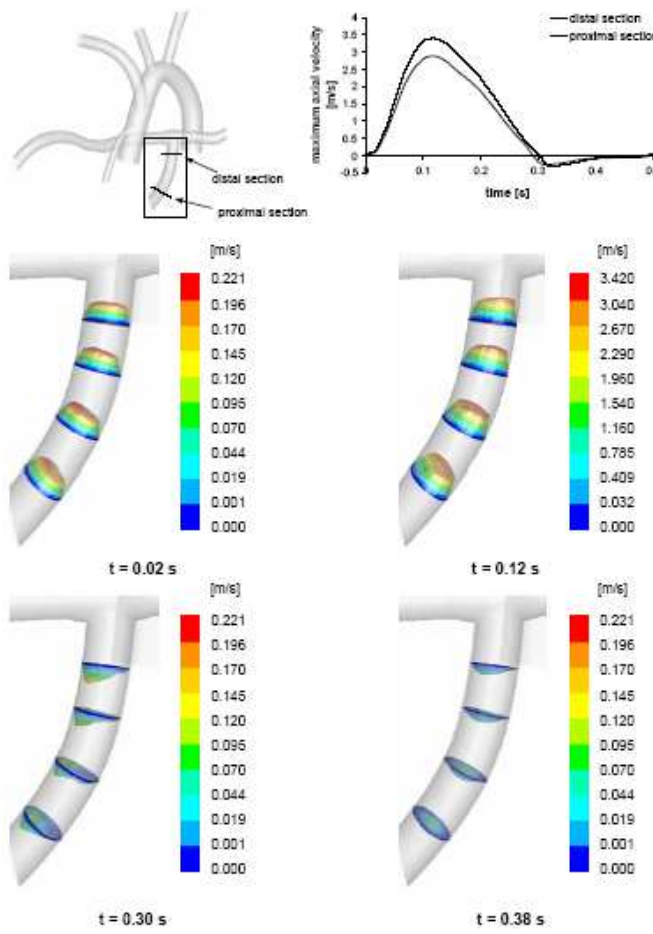


FIGURE 26. Velocity fields at different instants of the heart beat in the Sano operation (from [36]).

Acknowledgements

The authors wish to acknowledge all the people that, at various and different level, have collaborated to the results described in the report. In alphabetical order, Jean-Frederic Gerbeau, Daniele Lamponi, Vuk Milisic, Fabio Nobile, Tiziano Passerini, Alfio Quarteroni, Stefania Ragni, Simon Tweddle, Christian Vergara. They also acknowledge the collaboration with Gabriele Dubini and Francesco Migliavacca of the Laboratory of Biological Structures, Structural Engineering Department, Politecnico di Milano, and S. Sherwin and J. Peiro, Imperial College, London. This research would not have been possible without the support of various sponsoring agencies. In particular, the European Union, (through to the RTN Project “HaeMOdel”), the Italian “Ministero Università e Ricerca Scientifica e Tecnologica” and the “Fondazione Politecnico” and Siemens support of the Project ANEURISK (2005).

References

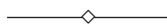
1. A. QUARTERONI and L. FORMAGGIA, *Mathematical Modelling and Numerical Simulation of the Cardiovascular System*, [in:] N. Ayache [ed.] Computational Models for the Human Body, Elsevier, Amsterdam 2004.
2. M.E. BELIK, T.P. USYK, and A.D. McCULLOCH, *Computational Methods for Cardiac Electrophysiology*, [in:] N. Ayache [ed.] Computational Models for the Human Body, Elsevier, Amsterdam 2004.
3. L. FORMAGGIA and A. VENEZIANI, *Reduced and Multiscale Models for the Human Cardiovascular System*, MOX Rep. n.21, June 2003 (Von Karman Lecture Notes, 7th Lecture Series on Biological Fluid Dynamics)
4. G. ALÌ , A. BARTEL, and M. GUNTHER, *Electrical RLC networks and diodes*, Technical Report RT237/01, Istituto per le Applicazioni del Calcolo “M. Picone”, Italian National Research Council, <http://www.na.iac.cnr.it>, 2001.
5. J.P. ARCHIE and R.P. FELDTMAN, *Critical stenosis of the internal carotid artery*, *Surgery*, **89**: 67–70, 1981.
6. R. BALOSSINO, F. MIGLIAVACCA, G. DUBINI, G. PENNATI, L. FORMAGGIA, M. TUVERI, and A. VENEZIANI, *Influence of boundary conditions on fluid dynamics in models of the cardiovascular system: a multiscale approach applied to the carotid bifurcation*, submitted to ASME J. Biomech. Eng., 2005.
7. A. BARNARD, W. HUNT, W. TIMLAKE, and E. VARLEY, *A theory of fluid flow in compliant tubes*, *Biophys. J.*, **6**: 717–724, 1966.

8. F. BREZZI and M. FORTIN, *Mixed and Hybrid Finite Elements*, SSCM n.5, Springer-Verlag 1991.
9. J. BRONZINO, [ed.] *The Biomedical Engineering Handbook*, chapter 157: Compartmental Models of Physiologic Systems, by C. Cobelli and M.P. Saccomani, pp.2375–2385, CRC Press, 1999.
10. J. BRONZINO, [ed.] *The Biomedical Engineering Handbook*, chapter 158: Cardiovascular Models and Control, by W.D. Timmons, pp.2386–2403, CRC Press, 1999.
11. W.R. DEAN, *The stream-line motion of fluid in a curved pipe*, Philos. mg. ser. 7, n.5, pp.673–695, 1928.
12. C. D'ANGELO, and V. MILISIC, *Reduced model for a coupling of axisymmetric Navier-Stokes equations with a reaction diffusion model for concentration*, submitted, available at the web site iacs.epfl.ch
13. G. D'ERRICO, A. ONORATI, and G. FERRARI, *An integrated 1d-2d fluid dynamic model for the predictions of unsteady flows in i.c. engine duct system*, [in:] IMECH In. Conf. “Computational and Experimental Methods in Reciprocating Engines”, 2000.
14. J. DONEA, S. GIULIANI, H. LAVAL, and L. QUARTAPELLE, *Time-accurate solutions of advection-diffusion problems by finite elements*, Comp. Meth. Appl. Mech. Engng., **45**: 123–145, 1984.
15. L. FORMAGGIA, J.F. GERBEAU, F. NOBILE, and A. QUATERONI *On the coupling of 3d and 1d navier-stokes equations for flow problems in compliant vessels*, Comp. Math. Appl. Mech. Eng., **191**: 561–582, 2001.
16. L. FORMAGGIA, J.F. GERBEAU, F. NOBILE, and A. QUATERONI *Numerical treatment of defective boundary conditions for the Navier-Stokes equation*, SIAM J. Num. Anal., **40**(1): 376–401, 2002.
17. D. LAMPONI, *One dimensional and multiscale for blood flow circulation*, PhD thesis, Thesis 3006, EPFL, Lausanne, 2004.
18. M.A. FERNANDEZ, V. MILISIC, and A. QUATERONI, *Analysis of a geometrical multiscale blood flow model based on the coupling of ODE and Hyperbolic PDE's*, SIAM MMS, **4**: 215–236, 2005.
19. L. FORMAGGIA, D. LAMPONI, M. TUVERI, and A. VENEZIANI, *Numerical modeling of a 1D arterial network coupled with a lumped parameter representation of the heart*, submitted, (available at the web site mox.polimi.it), 2005.
20. L. FORMAGGIA, D. LAMPONI, and A. QUATERONI, *One dimensional models for blood flow in arteries*, J. Eng. Math. n.47, pp.251–276, 2003.
21. A.E. GREEN and P.M. NAGHDI, *A direct theory of viscous fluid in pipes. I. Basic general developments*, Phil. Trans. Royal Soc. London, 1993.
22. A.E. GREEN, P.M. NAGHDI, and M.J. STALLARD, *A direct theory of viscous fluid in pipes. I. Flow of incompressible viscous fluid in curved pipes*, Phil. Trans. Royal Soc. London, 1993.

23. R. GLOWINSKI and P.L. TALLEC, *Augmented Lagrangian and Operator Splitting Methods in Nonlinear Mechanics*, Studies in Applied Mathematics, SIAM, Philadelphia, 1989.
24. E. GODLEWSKI and P.-A. RAVIART, *Numerical Approximation of Hyperbolic Systems of Conservation Laws, Applied Mathematical Sciences*, **118**, Springer, New York 1998.
25. G. HEDSTROM, *Nonreflecting boundary conditions for nonlinear hyperbolic systems*, J. Comp. Physics, **30**: 222–237, 1979.
26. J. HEYWOOD, R. RANNACHER, and S. TUREK, *Artificial Boundaries and Flux and Pressure Conditions for the Incompressible Navier–Stokes Equations*, Int. J. Num. Meth. Fluids, **22**: 325–352, 1996.
27. F. HOPPENSTEADT and C. PESKIN, *Mathematics in Life Sciences and Medicine*, Springer-Verlag, New York 1992.
28. G. JAGER, N. WESTERHOF, and A. NOORDERGRAF, *Oscillatory flow impedance in electrical analog of the arterial system*, Circ. Res., **16**: 121–133, 1965.
29. J. KEENER and J. SNEYD, *Mathematical Physiology* Springer-Verlag, New York 1998.
30. E. KRAUSE, *Modeling of the circulatory system*, Lecture Notes of the VKI Course on Fluid Dynamics and Biological Flow, Course 04-1998, 1998.
31. K. LAGANÀ, G. DUBINI, F. MIGLIAVACCA, R. PIETRABISSA, G. PENNATI, A. VENEZIANI, and A. QUARTERONI, *Multiscale modelling as a tool to prescribe realistic boundary conditions for the study of surgical procedures*, Biorheology, **39**: 259–364, 2002.
32. R. LEVEQUE, *Numerical Methods for Conservation Laws*. Birkhauser, Basel 1990.
33. V. MARTIN, F. CLÉMENT, A. DECOENE, and J.F. GERBEAU *Parameter identification for a one-dimensional blood flow model*, to appear, ESAIM Proceedings, 2005.
34. V. MILISIC and A. QUARTERONI, *Analysis of lumped parameter models for blood flow simulations and their relation with 1D models*, M2AN, **28**: 613–632, 2004.
35. K. LAGANA, R. BALOSSINO, F. MIGLIAVACCA, G. PENNATI, E.L. BOVE, M.R. DE LEVAL, and G. DUBINI, *Multiscale modeling of the cardiovascular system: application to the study of pulmonary and coronary perfusions in the univentricular circulation*, J. Biomech., **38**: 1129–1141, 2005.
36. F. MIGLIAVACCA, R. BALOSSINO, G. PENNATI, G. DUBINI, T.Y. HSIAB, M.R. DE LEVAL, and E.L. BOVE, *Multiscale modelling in bio fluid dynamics: Application to reconstructive paediatric cardiac surgery*, J. Biomech, to appear, 2005.
37. A. MOURA and C. VERGARA, *Flow rate boundary conditions in compliant domains and applications to the multiscale modelling of the cardiovascular system*, in preparation, 2005.
38. W. NICHOLS and M. O'ROURKE, *Mc Donald's Blood Flow in Arteries*, Edward Arnold Ltd., Third edition, London 1990.

39. F. NOBILE, *Numerical approximation of fluid-structure interaction problems with applications to hemodynamics*, PhD th., École Polytechnique Fédérale Lausanne, 2001.
40. A. NOORDERGRAAF, H. BOOM, and P. VERDOUW, *A human systemic analog computer*, 1st Congr. Soc. Ballistocardiographic Res., p.23, A. Noordergraaf [ed.], 1960.
41. M.S. OLUFSEN and A. NADIM, *On deriving lumped models for blood flow and pressure in the systemic arteries*, Math. Biosc. and Eng., **1**(1):61–80, 2004.
42. M. OLUFSEN and J. OTTESEN, *A fluid dynamical model of the aorta with bifurcations*, Tekst 297, Rotskilde Univ., 1995.
43. T. PEDLEY, *The Fluid Mechanics of Large Blood Vessels*, Cambridge Univ. Press, Cambridge, 1980.
44. T. PASSERINI, *Multiscale Models for the Vascular System: Numerical Coupling of 3D and 1D models*, Degree Thesis in Biomedical Eng., Politecnico di Milano [in italian; available at the web site mox.polimi.it], 2005.
45. A. QUARTERONI, S. RAGNI, and A. VENEZIANI, *Coupling between lumped and distributed models for blood flow problems*, Comp. Vis. Science, **4**:111–124, 2001.
46. A. QUARTERONI, M. TUVERI, and A. VENEZIANI, *Computational vascular fluid dynamics: problems, models and methods*, Comp. Vis. Science, **2**(4):163–197, 2000.
47. A. QUARTERONI, R. SACCO, and F. SALERI, *Numerical Mathematics*, Springer-Verlag, New York 2002.
48. A. QUARTERONI and A. VALLI, *Numerical Approximation of Partial Differential Equations*, Springer Verlag Series in Computational Mathematics n.23, 1994.
49. A. QUARTERONI and A. VALLI, *Domain Decomposition Methods for Partial Differential Equations*, Oxford University Press, Oxford, 1999.
50. A. QUARTERONI and A. VENEZIANI, *Analysis of a geometrical multiscale model based on the coupling of ODE's and PDE's for blood flow simulations*, Mult. Mod. Simul., **1**(2):173–195, 2003.
51. A. QUARTERONI, A. VENEZIANI, and P. ZUNINO, *A domain decomposition method for advection-diffusion processes with application to blood solutes*, SIAM J. Sci. Comp., **23**(6):1959–1980, 2002.
52. A. QUARTERONI, A. VENEZIANI, and P. ZUNINO, *Mathematical and numerical modeling of solutes dynamics in blood flow and arterial wall*, SIAM J. Num. Anal., **39**(5):1488–1511, 2002.
53. V. RIDEOUT and D. DICK, *Difference-differential equations for fluid flow in distensible tubes*, IEEE Trans. Biomed. Eng., **BME-14**(3):171–177, 1967.
54. Y. SAAD, *Iterative Methods for Sparse Linear Systems*, PWS Publishing Company, Boston 1996.
55. K. SAGAWA, H. SUGA, and K. NAKAYAMA, *Instantaneous pressure-volume ratio of the left ventricle versus instantaneous force-length relation of papillary muscle*, [in:]

- J. Baan, A. Noordergraaf, and J. Raines, [eds.], *Cardiovascular System Dynamics*, pp.99–105, 1978.
56. N. SMITH, A. PULLAN, and P. HUNTER, *An anatomically based model of coronary blood flow and myocardial mechanics*, SIAM J. Appl. Math., **62**(3) : 990–1018, 2003.
 57. J. STETTLER, P. NIEDERER, and M. ANLIKER, *Theoretical analysis of arterial hemodynamics including the influence of bifurcations, part I: Mathematical model and prediction of normal pulse patterns*, Annals of Biomedical Engineering, **9** : 145–164, 1981.
 58. F. MERENDA, N. STERGIOPULOS, *LV-arterial tree interaction and aortic waveforms: a varying elastance based study*, in preparation, 2005.
 59. F. TORRENT-GUASP, *The Cardiac Muscle*, Juan March Foundation, Madrid, 1973.
 60. K. THOMPSON, *Time dependent boundary conditions for hyperbolic systems*, J. Comp. Physics, **68** : 1–24, 1978.
 61. A. VENEZIANI, *Boundary conditions for blood flow problems*, [in:] *Proc. ENUMATH97, Heidelberg*, R. Rannacher [ed.], pp.596–607
 62. A. VENEZIANI and C. VERGARA, *Flow rate defective boundary conditions in haemodynamics simulations*, Int. J. Num. Meth. Fl., 2004.
 63. A. VENEZIANI and C. VERGARA, *An approximate method for solving incompressible Navier-Stokes problem with flow rate conditions*, in preparation, 2005.
 64. N. WESTERHOF, F. BOSMAN, C. VRIES, and A. NOORDERGRAAF, *Analog studies of the human systemic arterial tree*, J. Biomech., **2** : 121–143, 1969.
 65. J.J. WANG, and K. PARKER, *Wave propagation in a model for arterial circulation.*, J. Biomech., **37** : 457–470, 2004.
 66. M. ZACEK and E. KRAUSE, *Numerical simulation of the blood flow in the human cardiovascular system*, J. Biomech., **29**(1) : 13–20, 1996.
 67. S. VELE and U. VILLA, *1D Models for blood dynamics and solutes*, [in italian], Degree Thesis, Politecnico di Milano, available at the web site mox.polimi.it
 68. C. ZARINS, *Hemodynamics in atherosclerosis*, [in:] W. Moore, [ed.], *Vascular Surgery. A Comprehensive Review*, pp.86–96. W.B. Saunders, Philadelphia, PA, 1991.
 69. P. ZUNINO, *Mathematical and numerical modeling of mass transfer in the Vascular System*, PhD thesis, École Polytechnique Fédérale Lausanne, 2002.



Mathematical and Numerical Modelling of Cardiovascular Flows

JACEK SZUMBARSKI¹⁾ and JEREMI K. MIZERSKI²⁾

¹⁾*Department of Aerodynamics, Warsaw University of Technology*
jasz@meil.pw.edu.pl

²⁾*2nd Department of Cardiosurgery, Institute of Cardiology*
ul. Alpejska 42, 04-628 Warsaw, Poland
jeremi@data.pl

The rudiments of the numerical simulations of flows in domains relevant to haemodynamic applications are provided. In the first part of these notes, the problem of adequate modeling of the boundary conditions is addressed. It is argued that “classical” repertoire of such conditions is not sufficient and more general approach of the “deficient” formulations of the inlet/outlet conditions should be resorted. In the second part of the notes, a detailed description of the spectral element implementation of the Navier-Stokes solver using the formulation with “deficient” inlet/outlet conditions is given. Results of the computations presented in the notes include some test cases as well as the pulsatile flows in the model of the Blalock-Taussig shunt. The latter case is also considered in the third part of the notes, where the results of the numerical simulations obtained with the commercial package Fluent 6.2 are presented.

Key words: *Navier-Stokes equation, spectral elements, deficient inlet/outlet conditions, Blalock-Taussig shunt, cardiovascular flows*

Introduction

These notes have been written on the basis of the authors’ lecture during BF2005 meeting and they consist of three parts. In the first part, we summarize the basic governing equations and discuss the problem of the boundary conditions, which can be consistently set for a flow problem, when different forms of the weak velocity/pressure formulation are used. The problem of adequate modeling of the inlet and outlet conditions is discussed in this framework. We provide arguments that standard repertoire of the boundary conditions is not sufficient to perform realistic simulations of pulsatile flows

in cardiovascular systems. Next, an alternative approach to inlet/outlet conditions, introduced by Heywood et al. [12] and improved by Formaggia et al. [24], is explained in some details. The advantages of this new method in the contexts of haemodynamic simulations are shortly discussed.

The second part of the lecture is devoted to a detailed presentation of the numerical method design and implemented by the authors. The solution method is based on the weak formulation of the initial-boundary problem for the governing equation, where new generalized approach to inlet/outlet conditions is incorporated. The problem of discretization in time and space (using spectral elements) is discussed in some details. Some particular efficiency-improving algorithms are described. Finally, the results of numerical tests are presented and encountered difficulties are demonstrated.

In the third part, we present results of numerical simulations of the Blalock-Taussig shunt obtained by Jeremi Mizerski in his doctoral thesis with the commercial CFD package Fluent 6.2, [25]. It has been found rather difficult to find program and parameter setting, which ensure efficient and accurate results. We show Fluent screenshots demonstrating the applied settings, which resulted in successful calculations. The quasi-compressibility effect of the used solver is demonstrated by evaluation of the balance of volumetric flow rates at all inlets and outlets to the computational domain. Nevertheless, it is argued that obtained results, especially flow patterns, are medically relevant and useful.

1. General Mathematical Issues

1.1. Mathematical Model of a Viscous Incompressible Flow

The governing equations for an incompressible fluid flow stem from two basic principles of classical mechanics of continuum: the mass conservation and the second Newton's law. They are formulated for a fluid region, i.e. for the moving fluid portion consisting of the fixed set of fluid elements (or particles). Originally, the governing equations have the form of integral balances. For sufficiently regular fields we can apply the Reynolds transport theorem and obtain the flow description in terms of partial differential equations. This standard procedure can be found in any handbook on the fluid mechanics. In particular, we recommend excellent handbooks [1,2], also the report [21].

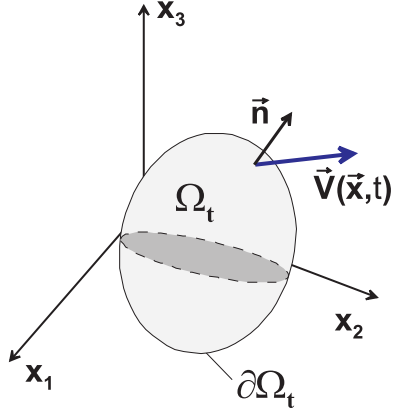


FIGURE 1. The volume of fluid and notation used in text

- Mass conservation \Rightarrow the continuity equation:

$$\frac{d}{dt} \int_{\Omega_t} \rho d\mathbf{x} = 0 \quad \Rightarrow \quad \partial_t \rho + \nabla \cdot (\rho \mathbf{u}) = 0 \quad \Rightarrow \quad \nabla \cdot \mathbf{u} = 0. \quad (1.1)$$

- 2nd Newton's law \Rightarrow the momentum equation (the equation of motion):

$$\begin{aligned} \frac{d}{dt} \int_{\Omega_t} \rho \mathbf{u} d\mathbf{x} &= \int_{\Omega_t} \rho \mathbf{g} d\mathbf{x} + \int_{\partial\Omega_t} \mathbf{T} \mathbf{n} ds \\ &\Downarrow \\ \rho [\partial_t \mathbf{u} + (\mathbf{u} \cdot \nabla) \mathbf{u}] &= \text{Div } \mathbf{T} + \rho \mathbf{g}. \end{aligned} \quad (1.2)$$

Here \mathbf{u} is the velocity field, p is the static pressure field and ρ denotes the (fixed) fluid density. The symbol \mathbf{T} denotes the stress tensor, while \mathbf{g} is the external field of the body force. If the \mathbf{g} field is potential (like a gravitational field, for instance) then the body force term can be included into the pressure term.

An equivalent form of the momentum equation for an incompressible fluid can be written as

$$\rho \partial_t \mathbf{u} + \text{Div}(\rho \mathbf{u} \otimes \mathbf{u} - \mathbf{T}) = \rho \mathbf{g}. \quad (1.3)$$

The component wise form of the momentum equation in the Cartesian coordinate system is

$$\rho \partial_t u_j + \rho \sum_{k=1}^3 u_k \partial_{x_k} u_j - \sum_{k=1}^3 \partial_{x_k} T_{jk} = \rho g_j. \quad (1.4)$$

In order to obtain a mathematically complete description of the fluid motion, a constitutive relation has to be defined. This is a relation between stresses and kinematics. It is generally accepted that cardiovascular flows in large and medium-sized arteries can be adequately simulated using basic Newtonian or generalized Newtonian models of fluid rheology. The basic ingredient in these models is the deformation rate tensor

$$D = \frac{1}{2} (\nabla \mathbf{u} + \nabla \mathbf{u}^T), \quad D_{jk} = \frac{1}{2} (\partial_{x_k} u_j + \partial_{x_j} u_k). \quad (1.5)$$

The stress tensor is now defined as follows

$$\mathbf{T} = -p\mathbf{I} + 2\mu\mathbf{D}, \quad T_{jk} = -p\delta_{jk} + \mu(\partial_{x_k} u_j + \partial_{x_j} u_k) \quad (1.6)$$

where μ [kg/(m s)] is the dynamic viscosity of the fluid. In the basic Newtonian model, the viscosity is assumed constant, meaning it does not depend on the flow kinematics. In such case, the momentum equation can be written in several equivalent forms, namely

$$\begin{aligned} \rho [\partial_t \mathbf{u} + (\mathbf{u} \cdot \nabla) \mathbf{u}] &= -\nabla p + 2\mu \nabla \cdot \mathbf{D} + \rho \mathbf{g}, \\ \rho [\partial_t \mathbf{u} + (\mathbf{u} \cdot \nabla) \mathbf{u}] &= -\nabla p + \mu \Delta \mathbf{u} + \rho \mathbf{g}, \\ \rho [\partial_t \mathbf{u} + (\mathbf{u} \cdot \nabla) \mathbf{u}] &= -\nabla p - \mu \nabla \times (\nabla \times \mathbf{u}) + \rho \mathbf{g}. \end{aligned} \quad (1.7)$$

Assuming a fixed viscosity of blood is not feasible if excessive areas of very low shear rate appear persistently within the flow domain. In such case, one can switch to one of the generalized Newtonian models, which accounts for a shear-thinning property of blood. In more complicated situations, the application of even more sophisticated viscoelastic models may occur necessary. Detailed exposition of these topics can be found in the lecture notes [20] (the lectures by Adelia Sequeira and Robert Owens) and references cited therein.

The generalized Newtonian models are based on the relation (1.6) between stress and deformation, but the viscosity is now considered to be shear-dependent. Thus, the constitutive relation can be expressed in the form of

$$\mathbf{T} = -p\mathbf{I} + 2\mu(\dot{\gamma})\mathbf{D} \quad (1.8)$$

where the strain rate $\dot{\gamma}$ is the frame-invariant quantity defined as follows

$$\dot{\gamma} = \sqrt{2\text{tr}(\mathbf{D}^2)} = \sqrt{2\mathbf{D} : \mathbf{D}} = \sqrt{2 \sum_{i,j=1}^3 D_{ij}^2} = \sqrt{2} \|D\|_F \quad (1.9)$$

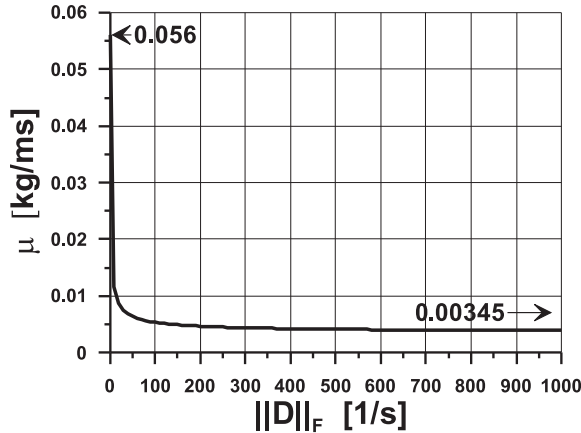


FIGURE 2. Carreau-Yasuda model as used by A. Sequeira and S. Deparis, [20]

In the above, the symbol $\|\mathbf{D}\|_F$ denotes the Frobenius norm of the deformation rate tensor.

As an example consider the Carreau-Yasuda model of a shear-thinning fluid. The formula for the viscosity is given as

$$\mu(\dot{\gamma}) = \mu_\infty + (\mu_0 - \mu_\infty)(1 + \lambda\dot{\gamma}^2)^\alpha \quad (1.10)$$

where μ_0 and μ_∞ denote the values of the dynamic viscosity in the limit of vanishing and infinite shear rate, respectively. In Fig. 2, the variation of the viscosity for the parameter values ($\mu_0 = 0.056 \text{ kg m}^{-1}\text{s}^{-1}$), $\mu_\infty = 0.00345 \text{ kg m}^{-1}\text{s}^{-1}$, $\alpha = -0.3216$, $\lambda = 3.313 \text{ s}$) chosen by Sequeira and Deparis [20] is shown.

1.2. Boundary Conditions for Incompressible Viscous Fluid Flows

In this paragraph we will discuss the problem of the boundary condition, which can be consistently enforced in the incompressible flow of a viscous fluid. Our exposition closely follows the problem description provided by Max Gunzburger in his excellent book [5] on finite element methods. The general idea is to consider various possible forms of the weak (variational) formulations of the governing equations and see what sort of the boundary information can be a priori assumed.

Consider an abstract computational domain Ω . Let the boundary $\partial\Omega$ be divided into parts as shown in the Fig. 3.

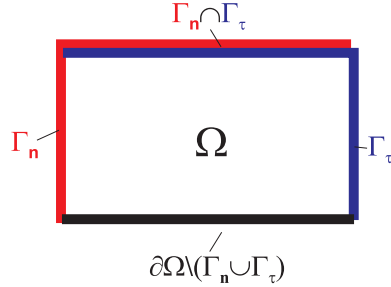


FIGURE 3. The boundary of computational domain—general settings

The following (essential) boundary conditions are postulated:

$$\begin{aligned} \Gamma_n : \mathbf{u} \cdot \mathbf{n} &= \xi(s), \\ \Gamma_\tau : \mathbf{u} \times \mathbf{n} &= \boldsymbol{\eta}(s). \end{aligned} \quad (1.11)$$

In other words, the normal component of the velocity field has a prescribed distribution at the part of the boundary Γ_n , while the tangent component (being actually equal to $\mathbf{n} \times \boldsymbol{\eta}(s)$) is given at Γ_τ . In general, there exists a nonempty product $\Gamma_n \cap \Gamma_\tau$, where full velocity vector is defined.

Since we are going to work with primitive variables (i.e. velocity and pressure), the following functional spaces are introduced:

- the velocity space

$$\mathbf{u} \in V = \left\{ \mathbf{v} \in [H^1(\Omega)]^3 : \mathbf{v} \times \mathbf{n} = 0 \text{ at } \Gamma_\tau, \quad \mathbf{v} \cdot \mathbf{n} = 0 \text{ at } \Gamma_n \right\},$$

where H^1 denotes the first Sobolev space of functions which are square-integrable in Ω together with their partial derivatives of the first order

- the pressure space $p \in Q = L_0^2(\Omega)$ or $p \in Q = L^2(\Omega)$. Here, $L^2(\Omega)$ is the space of square-integrable functions in Ω , while $L_0^2(\Omega)$ is a linear subspace of $L^2(\Omega)$ containing functions which integral over the whole domain amounts to zero. Such normalization is necessary to avoid ambiguity of the pressure, which occurs if the boundary conditions are expressed in terms of purely kinematical quantities (velocity or vorticity).

The general variational form of the governing equation can be written as

$$\begin{aligned} (\partial_t \mathbf{u}, \mathbf{v}) + a(\mathbf{u}, \mathbf{v}) + b(\mathbf{v}, p) + c(\mathbf{u}, \mathbf{u}, \mathbf{v}) &= (\mathbf{f}, \mathbf{v}) + d(\mathbf{v}), \\ b(\mathbf{u}, q) &= 0, \quad \mathbf{v} \in V, \quad q \in Q. \end{aligned} \quad (1.12)$$

In the above, the following notation has been used:

$$b(\mathbf{v}, p) = - \int_{\Omega} p \nabla \cdot \mathbf{v} d\mathbf{x} \text{ — pressure term,} \quad (1.13)$$

$$c(\mathbf{u}, \mathbf{u}, \mathbf{v}) = \int_{\Omega} \mathbf{v} \cdot \nabla \mathbf{u} \cdot \mathbf{u} d\mathbf{x} \text{ — convective term (nonlinear),} \quad (1.14)$$

$$(\mathbf{f}, \mathbf{v}) = \int_{\Omega} \mathbf{f} \cdot \mathbf{v} d\mathbf{x} \text{ — volume force term.} \quad (1.15)$$

The viscous term $a(\mathbf{u}, \mathbf{v})$ and the boundary term $d(\mathbf{v})$ depend on the form of the Navier-Stokes equation. Each of these forms generates a different form of the variational formulation and corresponding (natural) boundary conditions.

Consider first the “standard” form, where the viscous term in Navier-Stokes equation is expressed using the Laplacian of the velocity field

$$\rho (\partial_t \mathbf{u} + \nabla \mathbf{u} \cdot \mathbf{u}) = -\nabla p + \mu \Delta \mathbf{u} + \rho \mathbf{f}, \quad \nabla \cdot \mathbf{u} = 0. \quad (1.16)$$

We will refer to this form as the Form A. There is an instructive exercise to show that the viscous and boundary terms can be expressed as

$$a(\mathbf{u}, \mathbf{v}) = \mu \int_{\Omega} \nabla \mathbf{u} : \nabla \mathbf{v} d\mathbf{x}, \quad (1.17)$$

$$d(\mathbf{v}) = \int_{\partial\Omega \setminus \Gamma_n} [-p + \mu (\mathbf{n} \cdot \nabla \mathbf{u} \cdot \mathbf{n})] (\mathbf{v} \cdot \mathbf{n}) ds + \int_{\partial\Omega \setminus \Gamma_\tau} \mu [(\nabla \mathbf{u} \cdot \mathbf{n}) \times \mathbf{n}] \cdot (\mathbf{v} \times \mathbf{n}) ds. \quad (1.18)$$

In order to obtain a solvable problem we have to prescribe the integrands in square brackets in the formula (1.18). In other words, we have to impose natural boundary conditions, namely

$$\begin{cases} -p + \mu (\mathbf{n} \cdot \nabla \mathbf{u} \cdot \mathbf{n}) = \xi(t, s) & \text{at } \partial\Omega \setminus \Gamma_n, \\ \mu [(\nabla \mathbf{u} \cdot \mathbf{n}) \times \mathbf{n}] = \eta(t, s) & \text{at } \partial\Omega \setminus \Gamma_\tau. \end{cases} \quad (1.19)$$

Note that the quantities we define of the indicated portions of the boundary do not have any particular physical interpretation. One can think that for

that reason such approach is useless. However, we will show later that it is not a case. On the contrary—this formulation is a basis for some very useful generalization to be described later.

Final variational form of the Navier-Stokes equations can now be written as

$$\begin{aligned} \rho \int_{\Omega} (\partial_t \mathbf{u} + \nabla \mathbf{u} \cdot \mathbf{u}) \cdot \mathbf{v} d\mathbf{x} + \mu \int_{\Omega} \nabla \mathbf{u} : \nabla \mathbf{v} d\mathbf{x} - \int_{\Omega} p \nabla \cdot \mathbf{v} d\mathbf{x} &= \rho \int_{\Omega} \mathbf{f} \cdot \mathbf{v} d\mathbf{x} \\ &+ \int_{\Gamma \setminus \Gamma_n} \xi (\mathbf{v} \cdot \mathbf{n}) ds + \int_{\Gamma \setminus \Gamma_\tau} \boldsymbol{\eta} \cdot (\mathbf{v} \times \mathbf{n}) ds \quad (1.20) \end{aligned}$$

For sufficiently regular solutions, this formulation implies that the boundary conditions (1.19) will be satisfied.

Consider now the form (to be referred to as the Form B) where the deformation rate tensor \mathbf{D} appears directly in the viscous term of the momentum equation. This form of the governing equations, which is valid also for generalized Newtonian fluid, can be written as follows:

$$\rho (\partial_t \mathbf{u} + \nabla \mathbf{u} \cdot \mathbf{u}) = -\nabla p + 2\nabla \cdot (\mu \mathbf{D}_{\mathbf{u}}) + \rho \mathbf{f}, \quad \nabla \cdot \mathbf{u} = 0 \quad (1.21)$$

where $\mathbf{D}_{\mathbf{u}} = \frac{1}{2} (\nabla \mathbf{u} + \nabla^T \mathbf{u})$ is the deformation rate tensor. Again, it left to the Reader as an exercise to show that the corresponding viscous and boundary terms are

$$a(\mathbf{u}, \mathbf{v}) = 2 \int_{\Omega} \mu \mathbf{D}_{\mathbf{u}} : \mathbf{D}_{\mathbf{v}} d\mathbf{x} \quad (1.22)$$

$$d(\mathbf{v}) = \int_{\partial \Omega \setminus \Gamma_n} [-p + 2\mu (\mathbf{n} \cdot \mathbf{D}_{\mathbf{u}} \cdot \mathbf{n})] (\mathbf{v} \cdot \mathbf{n}) ds + \int_{\partial \Omega \setminus \Gamma_\tau} 2\mu [(\mathbf{D}_{\mathbf{u}} \cdot \mathbf{n}) \times \mathbf{n}] \cdot (\mathbf{v} \times \mathbf{n}) ds. \quad (1.23)$$

Consequently, the natural boundary conditions to be imposed are

$$\begin{cases} \sigma_n \equiv -p + 2\mu (\mathbf{n} \cdot \mathbf{D}_{\mathbf{u}} \cdot \mathbf{n}) = \xi(t, s) & \text{at } \partial \Omega \setminus \Gamma_n, \\ \boldsymbol{\sigma}_\tau \equiv 2\mu [(\mathbf{D}_{\mathbf{u}} \cdot \mathbf{n}) \times \mathbf{n}] = \boldsymbol{\eta}(t, s) & \text{at } \partial \Omega \setminus \Gamma_\tau. \end{cases} \quad (1.24)$$

In contrast to the Form A (Eq. (1.16)), the above conditions have a straightforward interpretation: they simply define the boundary distributions of the

normal and/or the tangent component of the surface stress. They are often called the traction conditions.

The final variational form of the Navier-Stokes equation for this case reads

$$\begin{aligned} \rho \int_{\Omega} (\partial_t \mathbf{u} + \nabla \mathbf{u} \cdot \mathbf{u}) \cdot \mathbf{v} d\mathbf{x} + 2 \int_{\Omega} \mu \mathbf{D}_{\mathbf{u}} : \mathbf{D}_{\mathbf{v}} d\mathbf{x} - \int_{\Omega} p \nabla \cdot \mathbf{v} d\mathbf{x} = \rho \int_{\Omega} \mathbf{f} \cdot \mathbf{v} d\mathbf{x} \\ + \int_{\partial\Omega \setminus \Gamma_n} \xi (\mathbf{v} \cdot \mathbf{n}) ds + \int_{\partial\Omega \setminus \Gamma_\tau} \boldsymbol{\eta} \cdot (\mathbf{v} \times \mathbf{n}) ds \quad (1.25) \end{aligned}$$

Let us finally consider the third option—the Form C. This time the viscous term in the momentum equation is written using the curl operator and the vorticity field. We have

$$\rho (\partial_t \mathbf{u} + \nabla \mathbf{u} \cdot \mathbf{u}) = -\nabla p - \mu \nabla \times \boldsymbol{\omega} + \rho \mathbf{f}, \quad \nabla \cdot \mathbf{u} = 0 \quad (1.26)$$

where the vorticity field $\boldsymbol{\omega} = \nabla \times \mathbf{u}$ is used. The viscous and boundary terms for this case are expressed by the following formulae

$$a(\mathbf{u}, \mathbf{v}) = \mu \int_{\Omega} \boldsymbol{\omega} \cdot (\nabla \times \mathbf{v}) d\mathbf{x}, \quad (1.27)$$

$$d(\mathbf{v}) = - \int_{\partial\Omega \setminus \Gamma_n} p (\mathbf{v} \cdot \mathbf{n}) ds - \int_{\partial\Omega \setminus \Gamma_\tau} \mu [\mathbf{n} \times (\boldsymbol{\omega} \times \mathbf{n})] \cdot (\mathbf{v} \times \mathbf{n}) ds \quad (1.28)$$

and thus the corresponding natural boundary conditions are

$$\begin{cases} p = \xi(t, s) & \text{at } \partial\Omega \setminus \Gamma_n, \\ \mathbf{n} \times (\boldsymbol{\omega} \times \mathbf{n}) = \boldsymbol{\eta}(t, s) & \text{at } \partial\Omega \setminus \Gamma_\tau. \end{cases} \quad (1.29)$$

The physical interpretation is again direct: we need to define the boundary distribution of the static pressure and/or the tangent component of the vorticity field at the indicated parts of the boundary. Final variational form of the Navier-Stokes equation for this case is

$$\begin{aligned} \rho \int_{\Omega} (\partial_t \mathbf{u} + \nabla \mathbf{u} \cdot \mathbf{u}) \cdot \mathbf{v} d\mathbf{x} + \mu \int_{\Omega} (\nabla \times \mathbf{u}) \cdot (\nabla \times \mathbf{v}) d\mathbf{x} - \int_{\Omega} p \nabla \cdot \mathbf{v} d\mathbf{x} \\ = \rho \int_{\Omega} \mathbf{f} \cdot \mathbf{v} d\mathbf{x} + \int_{\partial\Omega \setminus \Gamma_n} \xi (\mathbf{v} \cdot \mathbf{n}) ds + \int_{\partial\Omega \setminus \Gamma_\tau} \mu \boldsymbol{\eta} \cdot (\mathbf{v} \times \mathbf{n}) ds \quad (1.30) \end{aligned}$$

1.3. Modeling Inlet/Outlet Condition in Cardiovascular Simulation

In this part of the notes we will briefly discuss the problem of adequate selection of the inlet and outlet conditions in the cardiovascular simulations. We will assume that the flow domain has been “extracted” from the larger vessel system and therefore its boundary consists of the material part (walls of the vessels) and the inlet/outlet part. The latter is merely the effect of the “extraction” process—in principle, ideal inlet/outlet conditions should not impose any additional restrictions of the flow field.

Consider the repertoire of the boundary conditions described in the previous section from such point of view. Ideally, we would like to have full information about all components of the velocity vector at all inlets and outlets. If such information were available, all boundary conditions would be of the essential kind. Such situation, very desirable from the CFD viewpoint, is not realistic since detailed inlet/outlet velocity profiles (and their history in time!) cannot be measured at reasonable costs. Thus, we have to work with much less information about the flow field at inlet/outlet sections. Mathematically speaking: we have to resort some of the natural boundary conditions.

Some possible choices are:

- Setting one essential condition (typically, setting the tangent velocity to zero) and one natural condition, e.g. the static pressure or the normal stress. If I/O sections are sufficiently far away from bifurcations in the vessel system, the static pressure can be assumed uniform within each section and the section-averaged value obtained from simplified models (1D or lumped-parameter) can be used in full 3D simulations. Also, the normal stress is nearly uniform and does not differ much from the static pressure, because the viscosity-driven term is usually very small. Moreover—for flat I/O sections the surface-integral average of this term is zero.
- Setting two natural conditions. The advantage of such choice is that explicit setting of the tangent velocity (to zero) is avoided. Assumption of vanishing tangent velocity can be criticized for being not quite physical. Indeed, if a vortex structures appears in the flow domain, it will be convected towards some outlet section and it will inevitably generate nonzero tangent velocity while leaving the computational region. For

further purpose we will refer to this issue as a vortex-passage problem. We can also try to set both components of the surface stress, however, it is difficult to predict a reasonable distribution of the tangent stress. In particular, the tangent stress cannot be assumed to be zero since such choice is incompatible even with unidirectional flow fields of the Hagen-Poiseuille or Womersley flows.

The final conclusion is that none of the combinations of the boundary conditions are really satisfactory. The inlet/outlet conditions offered above are either too demanding (i.e. they require to excessive knowledge about the flow field) or too restrictive (i.e. the kinematical constrains implied by the conditions are likely to eliminate important physical effects from the simulation).

1.4. Deficient Boundary Conditions

In this section we discuss new approach to inlet/outlet conditions, which removes (at least partly) limitations of the classical repertoire of the boundary conditions described above, [12, 22, 24].

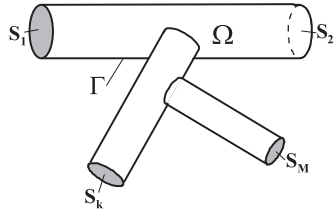


FIGURE 4. A system of branched vessels—geometry and notation

Consider again the computational domain modeling a selected part of the vessel system (see Fig. 4),

$$\begin{aligned}\Gamma_{\text{wall}} = \Gamma_n = \Gamma_\tau, \quad \Gamma_{\text{i/o}} &= \bigcup_k S_k \\ \partial\Omega &= \Gamma_{\text{wall}} \cup \Gamma_{\text{i/o}}\end{aligned}$$

and the Form A (Eq.(1.16)) of the governing equations. We have already

shown that the corresponding boundary term is given as

$$\begin{aligned} d(\mathbf{v}) = \sum_k \int_{S_k} [-p + \mu (\mathbf{n} \cdot \nabla \mathbf{u} \cdot \mathbf{n})] (\mathbf{v} \cdot \mathbf{n}) ds \\ + \sum_k \int_{S_k} \mu [(\nabla \mathbf{u} \cdot \mathbf{n}) \times \mathbf{n}] \cdot (\mathbf{v} \times \mathbf{n}) ds. \end{aligned}$$

Assume at the inlet/outlet sections S_k the following conditions:

$$\begin{aligned} p - \mu (\mathbf{n} \cdot \nabla \mathbf{u} \cdot \mathbf{n}) &= \Pi_k(t), \\ (\nabla \mathbf{u} \cdot \mathbf{n}) \times \mathbf{n} &= 0, \end{aligned} \quad (1.31)$$

where $k = 1, 2, \dots, M$. Then, the boundary term reduces to the simple form

$$d(\mathbf{v}) = \sum_k \Pi_k(t) \Phi_k(\mathbf{v}), \quad (1.32)$$

where the functionals of the volumetric flow rate $\Phi_k(\mathbf{v}) = \int_{S_k} \mathbf{v} \cdot \mathbf{n} ds$ are introduced. The final variational form of the Navier-Stokes equations is

$$\rho (\partial_t \mathbf{v} + \nabla \mathbf{v} \cdot \mathbf{v}, \mathbf{v}) + \mu (\nabla \mathbf{v}, \nabla \mathbf{v}) - (p, \nabla \cdot \mathbf{v}) = \rho (\mathbf{f}, \mathbf{v}) - \sum_{k=1}^M \Pi_k(t) \Phi_k(\mathbf{v}) \quad (1.33)$$

A natural question arises about the physical interpretation of the functions $\Pi_k(t)$. We will show that, under certain geometric conditions, the functions $\Pi_k(t)$ describe the temporal variations of the section-averaged static pressure. Indeed, let us integrate the formula (1.31a) over the inlet/outlet section S_k

$$\int_{S_k} [p - \mu (\mathbf{n} \cdot \nabla \mathbf{u} \cdot \mathbf{n})] ds = \Pi_k(t) |S_k|.$$

Assume next that S_k is a flat surface, i.e. the normal vector \mathbf{n} is the same at all points of S_k . Then the following equality holds

$$\int_{S_k} (\mathbf{n} \cdot \nabla \mathbf{u} \cdot \mathbf{n}) d\sigma = 0. \quad (1.34)$$

Proof:

$\mathbf{n} = [1, 0, 0]$, $\zeta = [0, \zeta_2, \zeta_3]$ — normal vector at the flat contour ∂S_k ,

$$\begin{aligned} \int_{S_k} \mathbf{n} \cdot \nabla \mathbf{u} \cdot \mathbf{n} &= \int_{S_k} \partial_{x_1} u_1 dx_2 dx_3 = - \int_{S_k} (\partial_{x_2} u_2 + \partial_{x_3} u_3) dx_2 dx_3 \\ &= - \oint_{\partial S_k} (u_2 \zeta_2 + u_3 \zeta_3) dx_2 dx_3 = 0. \end{aligned}$$

Thus, we conclude

$$\Pi_k(t) = \frac{1}{|S_k|} \int_{S_k} p ds$$

is a section-averaged pressure at S_k .

What is the meaning of the second boundary condition (1.31b)? Choosing the same geometric setting as in the aforementioned proof, it is immediate to show that this condition is equivalent to

$$\partial_{x_1} u_2 = \partial_{x_1} u_3 = 0. \quad (1.35)$$

Thus, the second condition is equivalent to the homogeneous Neumann condition formulated for the tangent velocity components. This condition seems to be better suited for the inlet/outlet modeling since no explicit restriction on the velocity itself is imposed. However, to the authors' best knowledge, the impact of this condition on the vortex-passage phenomenon has not yet been systematically studied.

The advantages of using deficient boundary conditions for inlets and outlets can be summarized as follows:

- Inlet/outlet section-average pressure is prescribed, but no particular surface distribution of the pressure field is explicitly assumed;
- There are no explicit restriction imposed on the normal or tangent velocity distributions;
- Additional kinematic constrains can be incorporated in the formulation of the flow problem. For instance, we can specify the time variation of the volumetric flow rate through a given inlet/outlet. In such case, the section-averaged pressure $\Pi_k(t)$ corresponding to this inlet/outlet works as the Lagrange multiplier, which is a priori unknown and has to be determined in the solution process.

2. Numerical Simulation of Nonstationary Laminar Flows in a Pipe System Using Spectral Elements

In this part of the lecture we present a particular simulation method based on the usage of deficient boundary conditions, spectral element approximations in space and the OIFS¹⁾ time integration scheme. We describe main ingredients of the method as well as selected algorithms, which are essential for numerical efficiency. More detailed exposition can be found in the paper [17].

2.1. Introduction

The objectives are to develop a complete computational method and its efficient implementation to perform computer simulations of nonstationary flows in complex vessel systems. The test example for the solver is the simplified model of the modified Blalock-Taussig shunt, which will be described in more details in the Part 3 of these notes.

The numerical method described in this chapter can be considered the first stage of development of the future numerical package for cardiovascular simulations. Therefore, the following assumption have been made

- Time-independent geometry of the computational domain;
- Newtonian liquid model of blood rheology;
- Inlet/outlet conditions should be formulated in terms of “easily” measurable or estimable (integral) quantities: section-averaged static pressure or volumetric flow rates. Various combinations of such conditions should be possible.
- Application of the high-order spatial approximation with hexahedral spectral elements;
- Application of higher-order time-integration schemes.

2.2. Formulation of the Flow Problem

The computational domain and be presented schematically as in Fig. 5
 Γ — solid boundary of the flow domain Ω ,
 S_k — inlet/outlet sections ($k=1,..,N$).

¹⁾OIFS—Operator-Integration-Factor Splitting

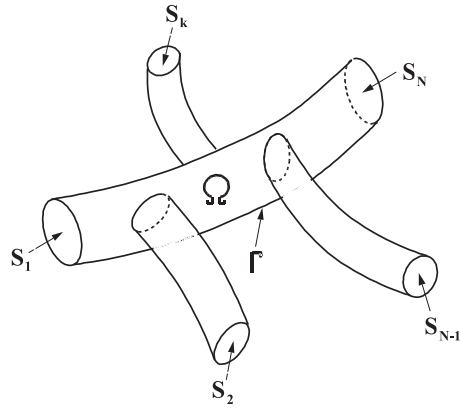


FIGURE 5. Computational domain

Governing equations are

$$\begin{cases} \rho(\partial_t \mathbf{v} + \nabla \mathbf{v} \cdot \mathbf{v}) = -\nabla p + \mu \nabla^2 \mathbf{v}, \\ \nabla \cdot \mathbf{v} = 0 \end{cases} \quad (2.1)$$

and the boundary conditions are defined as follows:

- Material boundary:

$$\Gamma : \mathbf{v}|_{\Gamma} = \mathbf{0}, \quad (2.2)$$

- Inlet/outlet conditions:

- VF-type

$$\Phi_i(\mathbf{v}) \equiv \int_{S_i} \mathbf{v} \cdot \mathbf{n} ds = F_i(t), \quad i = 1, \dots, N_{\text{VF}}, \quad (2.3)$$

- AP-type

$$\frac{1}{|S_{N_{\text{VF}}+i}|} \int_{S_{N_{\text{VF}}+i}} p ds = P_i(t), \quad i = 1, \dots, N_{\text{AP}}. \quad (2.4)$$

The variational formulation is stated as follows:

Find:

$$\begin{aligned}\mathbf{v} \in V &= \{\mathbf{v} \in [H^1(\Omega)]^3 : \mathbf{v}|_{\Gamma} = 0\}, \\ p \in Q &= L^2(\Omega), \\ \lambda_i(t) &\in R, \quad i = 1, \dots, N_{\text{VF}} \text{ (Lagrange multipliers)},\end{aligned}$$

such that

$$\begin{aligned}\rho(\partial_t \mathbf{v} + \nabla \mathbf{v} \cdot \mathbf{v}, \mathbf{v}) + \mu(\nabla \mathbf{v}, \nabla \mathbf{v}) + \sum_{i=1}^{N_{\text{VF}}} \lambda_i \Phi_i(\mathbf{v}) + \sum_{i=1}^{N_{\text{AP}}} P_i(t) \Phi_{N_{\text{VF}}+i}(\mathbf{v}) \\ - (p, \nabla \cdot \mathbf{v}) = 0,\end{aligned}$$

$$(q, \nabla \cdot \mathbf{v}) = 0 \quad \forall \mathbf{v} \in V, \quad \forall q \in Q,$$

and

$$\begin{aligned}\Phi_i(\mathbf{v}) &= F_i(t), \quad i = 1, \dots, N_{\text{VF}}. \\ \mathbf{v}|_{t=t_0} &= \mathbf{v}_0 \quad \text{— initial condition}\end{aligned}$$

It follows from the Sec. 1.4 that the classical boundary conditions corresponding to the above formulation are

$$\begin{cases} p - \mu(\mathbf{n} \cdot \nabla \mathbf{u} \cdot \mathbf{n}) = P_k \text{ at } S_k, & k = 1, \dots, N_{\text{AP}}, \\ p - \mu(\mathbf{n} \cdot \nabla \mathbf{u} \cdot \mathbf{n}) = \lambda_k \text{ at } S_k, & k = N_{\text{AP}} + 1, \dots, N_{\text{AP}} + N_{\text{VF}}, \\ (\nabla \mathbf{u} \cdot \mathbf{n}) \times \mathbf{n} = 0 \text{ at } S_k, & k = 1, \dots, N_{\text{AP}} + N_{\text{VF}}. \end{cases} \quad (2.5)$$

It has been also shown already that the physical interpretation of $P_k(t)$ (given functions) and $\lambda_k(t)$ (to be evaluated) is the section-averaged static pressure.

2.3. Time Integration Schemes

In order to develop accurate yet computationally efficient numerical method one has to care about the choice of appropriate time integration scheme. Here we discuss shortly some possibilities. To make our discussion simpler, we will consider a model initial-value problem

$$\begin{cases} u'(t) = \underbrace{Lu}_{\text{linear term}} + \underbrace{N(u)u}_{\text{nonlinear term}} + \underbrace{f}_{\text{forcing term}}, \\ u(0) = u_0. \end{cases} \quad (2.6)$$

In the context of the incompressible flow simulation, the reasonable choice is to apply the stiff-stable backward-differentiation formulae (BDF). In general, the K-order BDF method can be written in the form of

$$\beta_0 u^{(n+1)} - \sum_{k=1}^K \beta_k u^{(n+1-k)} = \Delta t \left[L u^{(n+1)} + N(u^{(n+1)}) u^{(n+1)} + f^{(n+1)} \right] \quad (2.7)$$

The coefficients of the BDF methods of different order have been summarized in the Table 1.

TABLE 1.

K	β_0	β_1	β_2	β_3	β_4
1	1	1	—	—	—
2	3/2	2	-1/2	—	—
3	11/6	3	-3/2	1/3	—
4	25/12	4	-3	4/3	-1/4

The BDF methods are implicit and thus unconditionally stable. On the other hand, the nonlinear boundary-value problem has to be solved at each time step, which is computationally very demanding, especially in the context of the CFD. It is desirable to avoid solving a huge nonlinear problem at each time step, even though the unconditional stability will be lost. A number of different approaches can be proposed, like:

- (A) Extrapolation of the nonlinear term (of the same order as BDF), see [7, 13, 19]. The nonlinear term is extrapolated from its values at previous time steps as follows

$$N^{(n+1)} \approx \sum_{k=1}^K \alpha_k N^{(n+1-k)}, \quad (2.8)$$

$$N^{(n+1-k)} \equiv N(u^{(n+1-k)}) u^{(n+1-k)}, \quad k = 0, 1, \dots, K.$$

TABLE 2.

K	α_1	α_2	α_3	α_4
1	1	—	—	—
2	2	-1	—	—
3	3	-3	1	—
4	4	-6	4	-1

Table 2 contains the coefficients of the extrapolation methods of different order. In the CFD application, the Stokes problem has to be solved at each time step of the flow simulation.

- (B) Linearization of the nonlinear term based on the velocity extrapolation [7, 23].

More sophisticated approach consists of extrapolating the velocity that appears in the algebraic way, while these parts of the nonlinear term where the velocity id differentiated remain in the original implicit form.

$$N(u^{(n+1)})u^{(n+1)} \rightarrow N(u_*)u^{(n+1)}, \quad u_* = \sum_{k=1}^K \alpha_k u^{(n+1-k)}. \quad (2.9)$$

This way we obtain linear approximation of the nonlinear term, which in the CFD applications leads to the Oseen problem to be solved at each time step. The latter problem is more difficult to solve than the Stokes problem, but the method will posses better stability properties.

- (C) Operator-Integration-Factor-Splitting Methods [7, 10, 14, 17, 19].

This method is based on the idea of the operator splitting. At each time step the following linear problem has to be solved

$$\beta_0 u^{(n+1)} - \sum_{k=1}^K \beta_k \hat{u}_k^{(n+1)} = \Delta t L u^{(n+1)}, \quad (2.10)$$

$$\hat{u}_k^{(n+1)} \equiv \hat{u}_k(t_{n+1}),$$

where \hat{u}_k are defined as the solutions to the following initial value problems

$$\begin{cases} \frac{d}{dt} \hat{u}_k = N(\hat{u}_k) \hat{u}_k, \\ \hat{u}_k(t_{n+1-k}) = u^{(n+1-k)}. \end{cases} \quad (2.11)$$

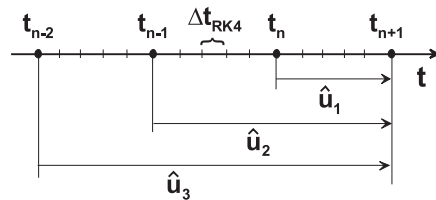


FIGURE 6. The OIFS method—more details in text

The initial-value problems are solved numerically with any higher order explicit method, which behaves well for purely convective problems (4-order Runge-Kutta, Taylor-Galerkin methods). The integration step is chosen as $\Delta t_{\text{RK4}} = \Delta t/M$, where typically $M \leq 5$. The overall order of accuracy is equal to the minimum of the number K and the order of the method used for the systems (2.11).

2.4. Finite Dimensional Approximation

Whichever time discretization method is used, a boundary value problem for partial differential equations is obtained at each simulation step. In order to obtain approximate solution, the following basic fields in the velocity space V are introduced

$$\begin{aligned} \mathbf{v}_1 &= [w_1, 0, 0], \quad \mathbf{v}_2 = [w_2, 0, 0], \dots, \quad \mathbf{v}_{N_V} = [w_{N_V}, 0, 0], \\ \mathbf{v}_{N_V+1} &= [0, w_1, 0], \quad \mathbf{v}_{N_V+2} = [0, w_2, 0], \dots, \quad \mathbf{v}_{2N_V} = [0, w_{N_V}, 0], \\ \mathbf{v}_{2N_V+1} &= [0, 0, w_1], \quad \mathbf{v}_{2N_V+2} = [0, 0, w_2], \dots, \quad \mathbf{v}_{3N_V} = [0, 0, w_{N_V}]. \end{aligned} \quad (2.12)$$

The velocity field at a given time instant is approximated by the linear combination of the basic fields

$$\mathbf{v}^{(m+1)} = \sum_{j=1}^{N_V} \left(\mathbf{u}_1^{(m+1)} \right)_j \mathbf{v}_j + \sum_{j=1}^{N_V} \left(\mathbf{u}_2^{(m+1)} \right)_j \mathbf{v}_{N_V+j} + \sum_{j=1}^{N_V} \left(\mathbf{u}_3^{(m+1)} \right)_j \mathbf{v}_{2N_V+j} \quad (2.13)$$

Analogously, the basic function $\{q_j\}$ in the Q are introduced and the pressure approximation is defined as

$$p^{(m+1)} = \sum_{j=1}^{N_Q} \left(\boldsymbol{\pi}^{(m+1)} \right)_j q_j. \quad (2.14)$$

Hence, at each time instant $3N_V + N_Q$ coefficients, which represent the instantaneous velocity and pressure fields, have to be computed.

It can be shown that in the effect the discretization procedure the following algebraic structures are obtained

$$\begin{aligned}
(\mathbf{M}_V)_{ij} &= (w_i, w_j) \equiv \int_{\Omega} w_i w_j d\mathbf{x} \quad \text{— mass matrix,} \\
(\mathbf{K}_V)_{ij} &= (\nabla w_i, \nabla w_j) \equiv \int_{\Omega} \nabla w_i \cdot \nabla w_j d\mathbf{x} \quad \text{— Laplace (“stiffness”) matrix,} \\
\mathbf{A} &= \frac{\beta_0}{\Delta t} \mathbf{M}_V + \nu \mathbf{K}_V \quad \text{— Helmholtz matrix,} \\
(\mathbf{D}_{\alpha})_{ij} &= -(q_i, \partial_{X_{\alpha}} w_j), \quad \alpha = 1, 2, 3, \quad \text{— divergence/gradient matrices,} \\
(\mathbf{\Lambda}_{\alpha}^{\mathbf{F}})_{ij} &= \Phi_i(\mathbf{v}_j), \quad i = 1, \dots, N_{\text{VF}}, \quad \text{— I/O volumetric flux matrices} \\
(\mathbf{\Lambda}_{\alpha}^{\mathbf{P}})_{ij} &= \Phi_{N_F+i}(\mathbf{v}_j), \quad i = 1, \dots, N_{\text{AP}}, \\
j &= (\alpha - 1)N_{\text{V}} + 1, \dots, \alpha N_{\text{V}}, \quad \alpha = 1, 2, 3. \\
\left(\mathbf{r}_{\alpha}^{(m+1)} \right)_i &= -\frac{1}{\Delta t} \sum_{k=1}^K \beta_k \left((\hat{\mathbf{v}}_k^{(m+1)})_{\alpha}, w_i \right), \quad \text{— r-h-s vector} \\
i &= 1, \dots, N_{\text{V}}, \quad \alpha = 1, 2, 3. \tag{2.15}
\end{aligned}$$

2.5. Spectral Element Method

In this section we describe briefly the main features of the spectral element discretization using hexahedral elements and the nodal (or collocation) approach. The computational domain is meshed with hexahedral cells. Each cell can be mapped into the standard cube $[-1, 1]^3$ where all differentiation and integration operations are carried out.

The mapping from a physical element to the standard cube can be defined in different forms dependently on the geometrical information included. In

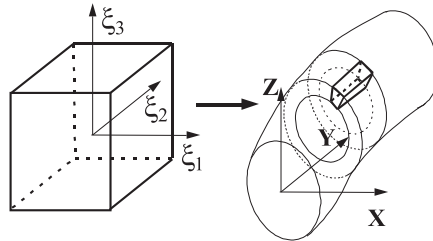


FIGURE 7. The standard cube and physical element

the simplest variant, the vertex-based transformation of the standard cube to a physical element can be written as follows

$$\begin{aligned} \mathbf{x}(\xi_1, \xi_2, \xi_3) = & \frac{1}{8} (1 - \xi_1) (1 - \xi_2) (1 - \xi_3) \mathbf{x}_1 + \frac{1}{8} (1 + \xi_1) (1 - \xi_2) (1 - \xi_3) \mathbf{x}_2 \\ & + \frac{1}{8} (1 + \xi_1) (1 + \xi_2) (1 - \xi_3) \mathbf{x}_3 + \frac{1}{8} (1 - \xi_1) (1 + \xi_2) (1 - \xi_3) \mathbf{x}_4 \\ & + \frac{1}{8} (1 - \xi_1) (1 - \xi_2) (1 + \xi_3) \mathbf{x}_5 + \frac{1}{8} (1 + \xi_1) (1 - \xi_2) (1 + \xi_3) \mathbf{x}_6 \\ & + \frac{1}{8} (1 + \xi_1) (1 + \xi_2) (1 + \xi_3) \mathbf{x}_7 + \frac{1}{8} (1 - \xi_1) (1 + \xi_2) (1 + \xi_3) \mathbf{x}_8 \end{aligned} \quad (2.16)$$

More sophisticated curvilinear transformations are also possible—the practical implementations are usually based on the Gordon-Hall blending procedure (see for instance [7], pp.183-184).

Each cell of the grid is equipped with the pair of internal collocation meshes, which are the transformation images of the two standard collocation grid in the cube $[-1, 1]^3$: one for the velocity and another one for the pressure. The standard velocity collocation mesh is constructed as follows

$$\begin{aligned} \xi_V^{(0)} = -1, \quad \xi_V^{(M_V-1)} = 1, \\ \left\{ \xi_V^{(j)}, \quad j = 1, \dots, M_V - 2 \right\} \quad \text{— roots of the Jacobi pol. } P_{M_V-2}^{1,1} \end{aligned} \quad (2.17)$$

and the corresponding local basic functions in $[-1, 1]^3$ are defined as

$$b_{ijk}^V(\xi_1, \xi_2, \xi_3) = L_i^V(\xi_1) L_j^V(\xi_2) L_k^V(\xi_3), \quad i, j, k = 0, \dots, M_V - 1 \quad (2.18)$$

where $L_i^V(\xi_V^{(j)}) = \delta_i^j$, ($j = 0, \dots, M_V - 1$) are the Lagrange interpolating polynomials corresponding to the nodes (2.17).

The pressure collocation nodes are constructed in the similar manner:

$$\left\{ \xi_P^{(j)}, \quad j = 0, \dots, M_P - 1 \right\} \quad \text{— roots of the Legendre pol. } P_{M_P-1}. \quad (2.19)$$

The local basic pressure functions are then defined in the following form

$$b_{ijk}^P(\xi_1, \xi_2, \xi_3) = L_i^P(\xi_1) L_j^P(\xi_2) L_k^P(\xi_3), \quad i, j, k = 0, \dots, M_P - 1 \quad (2.20)$$

where $L_i^P(\xi_P^{(j)}) = \delta_i^j$, ($j = 0, \dots, M_P - 1$) are the Lagrange's interpolating polynomials corresponding to the nodes (2.19).

Since detailed expositions of the spectral element approach can be found in several recent handbooks and monographs [3, 4, 6, 7], we will merely summarize some basic features of this approach:

- Straightforward interpretation of the coefficients of the velocity and pressure expansions with respect to the local basic functions—the coefficients are simply the values of velocity or pressure at the corresponding collocation nodes.
- Differentiation: local velocity representations are differentiated inside the standard element and the derivatives are re-interpolated on the collocation mesh (the pseudo-spectral approach). Next, the derivatives with respect to physical coordinates are computed with the use of the (inverse) Jacobi matrices.
- Volume and surface integrals are calculated with the use of Gauss-Jacobi-Lobatto and Gauss-Legendre formulae based on the velocity and pressure collocation meshes, respectively.
- The local basic functions are L^2 -orthogonal with respect to the Gauss integration. Consequently, the mass matrix \mathbf{M}_V (also the pressure mass matrix \mathbf{M}_P used in a preconditioner of the conjugate gradient iterations) is purely diagonal.
- Div-stability condition (necessary for the Stokes matrix be invertible) is fulfilled when $N_V \geq N_P + 2$.

2.6. Summary of the Computational Method

In this section we give a brief description of the OIFS-based spectral element method using hexahedral grids. The numerical problem involves computation of the velocity and pressure fields as well as the Lagrange multipliers (section-averaged pressures at VF-type inlets/outlets). Superposition of special Stokes solutions is used to construct the full solution at each time instant.

A. Preparatory stage (time-independent space discretization and fixed Δt)

The following Stokes problems are solved

$$\begin{bmatrix} \mathbf{A} & \mathbf{0} & \mathbf{0} & (\mathbf{D}_1)^T \\ \mathbf{0} & \mathbf{A} & \mathbf{0} & (\mathbf{D}_2)^T \\ \mathbf{0} & \mathbf{0} & \mathbf{A} & (\mathbf{D}_3)^T \\ \mathbf{D}_1 & \mathbf{D}_2 & \mathbf{D}_3 & \mathbf{0} \end{bmatrix} \begin{bmatrix} \mathbf{u}_1^{\{k\}} \\ \mathbf{u}_2^{\{k\}} \\ \mathbf{u}_3^{\{k\}} \\ \pi^{\{k\}} \end{bmatrix} = \begin{bmatrix} -(\Lambda_1^F)^T \mathbf{e}^{\{k\}} \\ -(\Lambda_2^F)^T \mathbf{e}^{\{k\}} \\ -(\Lambda_3^F)^T \mathbf{e}^{\{k\}} \\ \mathbf{0} \end{bmatrix}, \quad (2.21)$$

where

$$e_j^{\{k\}} = \begin{cases} 0 & \text{if } j \neq k, \\ 1 & \text{if } j = k. \end{cases}$$

Then, the following array is created

$$\mathbf{T}_F = \begin{bmatrix} f_1^{\{1\}} & \dots & f_1^{\{N_{VF}\}} \\ \vdots & \vdots & \vdots \\ f_{N_{VF}}^{\{1\}} & \dots & f_{N_{VF}}^{\{N_{VF}\}} \end{bmatrix}, \quad (2.22)$$

where

$$f_j^{\{k\}} = \left(\sum_{\alpha=1}^3 \mathbf{A}_{\alpha}^F \mathbf{u}_{\alpha}^{\{k\}} \right)_j, \quad j = 1, \dots, N_{VF}. \quad (2.23)$$

If the flow domain and grid geometry as well as the time integration steps are fixed, the above solutions are computed once and forever.

B. Main simulation stage

The computational procedure to update the solution at $t = t_n$ to $t = t_{n+1}$ consists of the following steps:

1. Integration of convective terms (K -steps OIFS)

$$\frac{d}{dt} (\hat{\mathbf{u}}_{\alpha})_k = -C_{\alpha} [(\hat{\mathbf{u}}_1)_k, (\hat{\mathbf{u}}_2)_k, (\hat{\mathbf{u}}_3)_k] (\hat{\mathbf{u}}_{\alpha})_k, \quad \alpha = 1, 2, 3. \quad (2.24)$$

$$(\hat{\mathbf{u}}_{\alpha})_k (t = t^{(m-k+1)}) = \mathbf{u}_{\alpha}^{(m-k+1)}, \quad k = 1, \dots, K.$$

Numerical integration: 4th order Runge-Kutta method with the sub-step $\Delta t/M_S$ up to the time instant $t^{(m+1)} = t^{(m)} + \Delta t$. As a result we get

$$(\hat{\mathbf{u}}_{\alpha})_k^{(m+1)} = (\hat{\mathbf{u}}_{\alpha})_k (t = t^{(m+1)}), \quad \alpha = 1, 2, 3, \quad k = 1, \dots, K. \quad (2.25)$$

2. Solution of the reduced Stokes problem

$$\begin{bmatrix} \mathbf{A} & \mathbf{0} & \mathbf{0} & (\mathbf{D}_1)^T \\ \mathbf{0} & \mathbf{A} & \mathbf{0} & (\mathbf{D}_2)^T \\ \mathbf{0} & \mathbf{0} & \mathbf{A} & (\mathbf{D}_3)^T \\ \mathbf{D}_1 & \mathbf{D}_2 & \mathbf{D}_3 & \mathbf{0} \end{bmatrix} \begin{bmatrix} \mathbf{u}_1^{\{0\}} \\ \mathbf{u}_2^{\{0\}} \\ \mathbf{u}_3^{\{0\}} \\ \boldsymbol{\pi}^{\{0\}} \end{bmatrix}^{(m+1)} = \begin{bmatrix} \mathbf{r}_1 \\ \mathbf{r}_2 \\ \mathbf{r}_3 \\ \mathbf{0} \end{bmatrix}^{(m+1)}, \quad (2.26)$$

where

$$\mathbf{r}_\alpha^{(m+1)} = -\frac{1}{\Delta t} \sum_{k=1}^K \beta_k \mathbf{M}_V(\hat{\mathbf{u}}_\alpha)_k^{(m+1)} - (\boldsymbol{\Lambda}_\alpha^P)^T \mathbf{P}^{(m+1)}, \quad \alpha = 1, 2, 3. \quad (2.27)$$

Solution procedure consists in the following 3 steps

$$(i) \quad \mathbf{A} \tilde{\mathbf{u}}_\alpha = \mathbf{r}_\alpha^{(m+1)} - \mathbf{D}_\alpha^T \boldsymbol{\pi}^{\{0\}(m)}, \quad \alpha = 1, 2, 3. \quad (2.28)$$

$$(ii) \quad \mathbf{S} \boldsymbol{\pi}' = \sum_{\alpha=1}^3 \mathbf{D}_\alpha \tilde{\mathbf{u}}_\alpha, \quad \mathbf{S} = \sum_{\alpha=1}^3 \mathbf{D}_\alpha \mathbf{A}^{-1} \mathbf{D}_\alpha^T, \quad (2.29)$$

$$\boldsymbol{\pi}^{\{0\}(m+1)} = \boldsymbol{\pi}^{\{0\}(m)} + \boldsymbol{\pi}',$$

$$(iii) \quad \mathbf{A} \mathbf{u}'_\alpha = -\mathbf{D}_\alpha^T \boldsymbol{\pi}', \quad \mathbf{u}_\alpha^{\{0\}(m+1)} = \mathbf{u}_\alpha^{\{0\}(m)} + \mathbf{u}'_\alpha, \quad \alpha = 1, 2, 3. \quad (2.30)$$

3. Determination of the Lagrange multipliers

The following linear system containing N_{VF} equations is solved

$$\mathbf{T}_F \boldsymbol{\lambda}^{(m+1)} = \mathbf{F}^{(m+1)} - \sum_{\alpha=1}^3 \boldsymbol{\Lambda}_\alpha^F \mathbf{u}_\alpha^{\{0\}(m+1)}. \quad (2.31)$$

The physical interpretation of the computed multipliers: the section-averaged static pressure at VF-type inlets/outlets, at the time $t = t_{n+1}$.

4. Computing the final form of the solution at the time $t = t_{n+1}$

The final solution is constructed as the linear combination of the Stokes solutions

$$\begin{Bmatrix} \mathbf{u}_1^{(m+1)} \\ \mathbf{u}_2^{(m+1)} \\ \mathbf{u}_3^{(m+1)} \\ \boldsymbol{\pi}^{(m+1)} \end{Bmatrix} = \begin{Bmatrix} \mathbf{u}_1^{\{0\}(m+1)} \\ \mathbf{u}_2^{\{0\}(m+1)} \\ \mathbf{u}_3^{\{0\}(m+1)} \\ \boldsymbol{\pi}^{\{0\}(m+1)} \end{Bmatrix} + \sum_{k=1}^{N_{VF}} \lambda_k^{(m+1)} \begin{Bmatrix} \mathbf{u}_1^{\{k\}} \\ \mathbf{u}_2^{\{k\}} \\ \mathbf{u}_3^{\{k\}} \\ \boldsymbol{\pi}^{\{k\}} \end{Bmatrix} \quad (2.32)$$

2.7. Selected Numerical Algorithms

2.7.1. Preconditioned conjugate gradients (PCG). The PCG method [8] is used to solve linear systems with the Helmholtz and Uzawa matrices (both are SPD-symmetric and positive definite). Here is the summary of this algorithms for the SPD system $\mathbf{S}\mathbf{x} = \mathbf{b}$.

Start: $\mathbf{x}^{(0)}; \mathbf{r}^{(0)} = \mathbf{b} - \mathbf{S}\mathbf{x}^{(0)}$; solve $\mathbf{P}\tilde{\mathbf{r}}^{(0)} = \mathbf{r}^{(0)}$; $\mathbf{p}^{(0)} = \tilde{\mathbf{r}}^{(0)}$.

For $k = 1, 2, \dots$:

$$(i) \quad \alpha_k = -(\tilde{\mathbf{r}}^{(k)}, \mathbf{r}^{(k)}) / (\mathbf{p}^{(k)}, \mathbf{S}\mathbf{p}^{(k)}),$$

$$(ii) \quad \mathbf{x}^{(k+1)} = \mathbf{x}^{(k)} - \alpha_k \mathbf{p}^{(k)}$$

$$(iii) \quad \mathbf{r}^{(k+1)} = \mathbf{r}^{(k)} + \alpha_k \mathbf{S}\mathbf{p}^{(k)} \quad \rightarrow \text{convergence test } \|\mathbf{r}^{(k+1)}\| / \|\mathbf{b}\| < \varepsilon,$$

$$(iv) \quad \text{solve } \mathbf{P}\tilde{\mathbf{r}}^{(k+1)} = \mathbf{r}^{(k+1)},$$

$$(v) \quad \beta_k = (\tilde{\mathbf{r}}^{(k+1)}, \mathbf{r}^{(k+1)}) / (\tilde{\mathbf{r}}^{(k)}, \mathbf{r}^{(k)}),$$

$$(vi) \quad \mathbf{p}^{(k+1)} = \tilde{\mathbf{r}}^{(k+1)} + \beta_k \mathbf{p}^{(k)}.$$

The Helmholtz system can be efficiently preconditioned by the diagonal matrix

$$\mathbf{P} = \text{diag}\left\{\frac{\beta_0}{\Delta t} \mathbf{M}_V + \mu \mathbf{K}\right\}.$$

Fast computation of the pressure correction is much more tricky!

2.7.2. Preconditioning in the pressure solver. The overall performance of the Navier-Stokes solver depends mostly on the efficiency of the pressure determination. The corresponding algebraic problem is defined as follows

$$\mathbf{S}\pi' = \sum_{\alpha=1}^3 \mathbf{D}_{\alpha} \tilde{\mathbf{u}}_{\alpha}, \quad \mathbf{S} = \sum_{\alpha=1}^3 \mathbf{D}_{\alpha} \mathbf{A}^{-1} \mathbf{D}_{\alpha}^T, \quad (2.33)$$

where

$$\mathbf{A} = \frac{\beta_0}{\Delta t} \mathbf{M}_V + \mu \mathbf{K}_V.$$

It has been demonstrated [9, 15] that appropriate preconditioning matrix for this problem (suitable for both low and higher Reynolds numbers) can be constructed in the following form

$$\mathbf{P}^{-1} = \nu \mathbf{M}_{\mathbf{P}}^{-1} + \frac{\beta_0}{\Delta t} \mathbf{E}^{-1}, \quad (2.34)$$

where

$$\mathbf{E} = \sum_{k=1}^3 \mathbf{D}_k \mathbf{M}_{\mathbf{V}}^{-1} \mathbf{D}_k^T$$

and \mathbf{M}_P denotes the pressure mass matrix (diagonal). We still need an efficient method for solving internally (i.e., at each iteration of the PCG method) the system with the matrix \mathbf{E} , which itself is poorly conditioned.

2.7.3. Solution of $\mathbf{Eq} = \mathbf{r}$. This section is based upon the references [10, 16, 17, 19]; we shall use the following notation:

N_P — number of the pressure collocation nodes in each spectral element

K — number of the spectral elements in the flow domain

$N = \dim E = N_P \cdot K$ — global number of the pressure nodes

Consider the rectangular matrix \mathbf{J} , where $\dim(\mathbf{J}) = (N, K)$, such that:

- each column of \mathbf{J} has a structure of K blocks with N_P entries,
- in k -th column all blocks are zero except the k -th block, which is filled with 1's.

Thus, the columns of the matrix \mathbf{J} are the orthonormal vectors in R^N and $\mathbf{J}^T \mathbf{J} = \mathbf{I}$. Next, the K -dimensional subspace

$$\Pi = \{\boldsymbol{\pi} \in R^N : \boldsymbol{\pi} = \mathbf{Ju}, \mathbf{u} \in R^K\} \text{ in } R^N$$

is introduced. Conceptually, the space Π contains representations of piecewise constant fields in the computational domain, i.e. such fields which are uniformly distributed within each individual spectral element.

The solution is sought in the form of the sum of the piecewise constant “background” and the “correction” belonging to the orthogonal space Π^\perp

$$\mathbf{q} = \mathbf{J}\mathbf{q}_0 + \mathbf{q}_1, \quad \mathbf{q}_0 \in \mathbf{R}^K. \quad (2.35)$$

Projection operator on Π^\perp along $E(\Pi)$ is introduced as

$$\mathbf{P}_{\Pi^\perp} = \mathbf{I} - \mathbf{E}\mathbf{J}\mathbf{E}_0^{-1}\mathbf{J}^T, \quad (2.36)$$

where $\mathbf{E}_0 = \mathbf{J}^T \mathbf{E} \mathbf{J}$. Then, the vector \mathbf{q}_1 is determined as the (unique) element from Π^\perp satisfying the following linear system

$$\mathbf{H}\mathbf{q}_1 = \mathbf{P}_{\Pi^\perp}\mathbf{r}, \quad \mathbf{H} = \mathbf{P}_{\Pi^\perp}\mathbf{E}. \quad (2.37)$$

The linear system (2.34) is solved using PCG iterations with the block $\{E\}$ preconditioner [10, 19]. The efficient way to deal with the local systems for each individual element is to use the method of fast diagonalization. The vector \mathbf{q}_0 is determined from the following SPD system containing K equations, solved by the noniterative method (e.g., the Compressed-Sparse-Row-based Choleski solver)

$$\mathbf{E}_0 \mathbf{q}_0 = \mathbf{J}^T (\mathbf{r} - \mathbf{E} \mathbf{q}_1) \quad (2.38)$$

The computational performance of the pressure solver preconditioning (Pentium IV 2.6 GHz, 512 KB cache, 512 MB RAM), where $K = 1536$, $N = 5$, $\varepsilon = 10^{-10}$ has been summarized in the Table 3.

TABLE 3. Performance of pressure solver

M_{INT}	0	5	10	12	15	18	20
M	420	39	22	18	15	13	13
Time [s]	1398.8	198.5	150.9	136.3	129.1	125.8	134.9
Acceler.	1	7	9.3	10.3	10.8	11.1	10.4

M_{INT} denotes the number of internal PCG iterations for the linear system with the matrix \mathbf{H} and M is the number of PCG iterations of the pressure solver.

2.7.4. Efficient solution of long sequences of large linear systems with the same SPD matrix. The overall computational performance can be improved much not only by using a sophisticated preconditioner. The smart choice of the initial approximations turns out to be equally important. In the nonstationary simulation, using the flow state from the previous time step seems to be a good idea. Surprisingly enough, this approach is rather disappointing. In this section we give a brief account of much better method proposed by Paul Fisher

In the general setting, consider the sequence of the large linear systems. These systems have the same SPD matrix \mathbf{A} , but different right-hand side vectors. The Fisher's projection method [11] can be described as follows:

Initiation:

$$\mathbf{Ax}^{(1)} = \mathbf{b}^{(1)} \rightarrow \mathbf{e}_1 = \mathbf{x}^{(1)} / \left\| \mathbf{x}^{(1)} \right\|_A, \quad \left\| \mathbf{x}^{(1)} \right\|_A = \sqrt{\langle \mathbf{x}, \mathbf{x} \rangle_A} \equiv \sqrt{\langle \mathbf{x}, \mathbf{Ax} \rangle}$$

for $k = 2, 3, \dots$:

- (a) Having the \mathbf{A} -orthonormalized system of $k - 1$ vectors $\mathbf{e}_1, \mathbf{e}_2, \dots, \mathbf{e}_{k-1}$, we define the vector

$$\tilde{\mathbf{x}} = \sum_{j=1}^{k-1} \alpha_j \mathbf{e}_j$$

such that

$$\langle \mathbf{e}_j, \mathbf{b}^{(k)} - \mathbf{A}\tilde{\mathbf{x}} \rangle_{\mathbf{A}} = 0.$$

It is easy to show that

$$\alpha_j = \langle e_j, b^{(k)} \rangle.$$

- (b) We seek the solution of the k -th system as $\mathbf{x}^{(k)} = \tilde{\mathbf{x}} + \mathbf{x}'$, where $\mathbf{Ax}' = \mathbf{b}^{(k)} - \mathbf{A}\tilde{\mathbf{x}} \equiv \mathbf{b}'$ is solved iteratively by the PCGM with the stopping criterion $\|\mathbf{r}'\|_2 / \|\mathbf{b}^{(k)}\|_2 < \varepsilon$. One can easily show that $\mathbf{r}' \equiv \mathbf{r}$.
- (c) To continue the procedure, the next basic vector \mathbf{e}_k has to be determined. To this end, we calculate the part of the solution orthogonal to the subspace spanned by the basic vectors generated so far

$$\mathbf{x}'_{\perp} = \mathbf{x}' - \sum_{j=1}^{k-1} \beta_j \mathbf{e}_j$$

where $\beta_j = \langle \mathbf{e}_j, \mathbf{x}' \rangle_A = -\langle \mathbf{e}_j, \mathbf{r}' \rangle$.

The following equivalent form, which avoids multiplication by the matrix \mathbf{A} , can be derived

$$\|\mathbf{x}'_{\perp}\|_A \equiv \sqrt{\langle \mathbf{x}', \mathbf{Ax}' \rangle} = \sqrt{\langle \mathbf{x}^{(k)}, \mathbf{b} - \mathbf{r}' \rangle - \sum_{j=1}^{k-1} (\alpha_j + \beta_j)^2},$$

and finally we get $\mathbf{e}_k = \mathbf{x}'_{\perp} / \|\mathbf{x}'_{\perp}\|_A$. If k becomes too large (say $k = K_{\max}$) the procedure is re-started: $\mathbf{e}_1 = \mathbf{x}^{K_{\max}} / \|\mathbf{x}^{K_{\max}}\|_A$.

Figure 8 shows the computational time per single simulation step, when the Fisher's method is implemented. In the presented case, the sequence is re-started every 100 time steps. After the restart, the computational time is quite large but it drops drastically after several steps. The average computational time per one integrations step is about 17 s (Pentium IV, 2.6 GHz, 1536 elements, $N_V = 6$, $N_P = 4$).

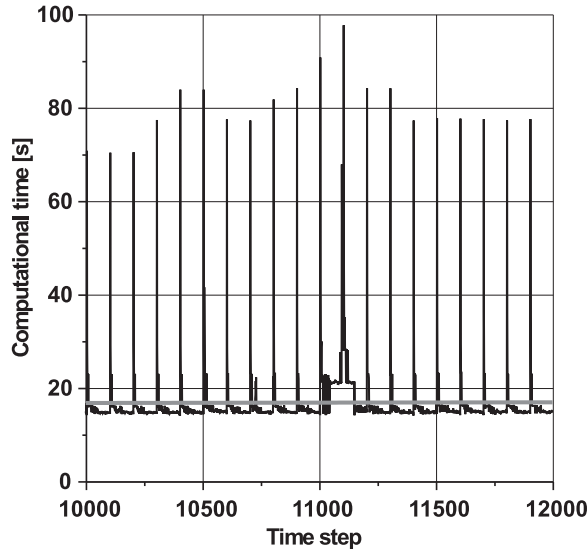


FIGURE 8. Performance of the Fisher's projection method—more details in the text

2.8. Sample Results, Encountered Difficulties and Further Development

2.8.1. Simulation of an unsteady flow in the T-shaped junction

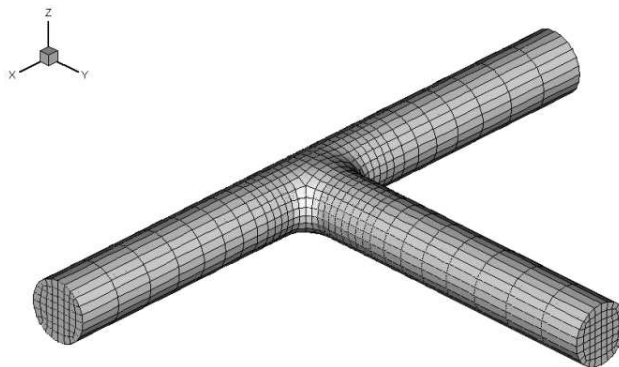


FIGURE 9. Hexahedral meshes for the T-shape pipe junction containing 1536 or 3048 spectral elements. The computations have been performed with $(N_V, N_P)=(5,3)$ or $(N_V, N_P)=(6,4)$.

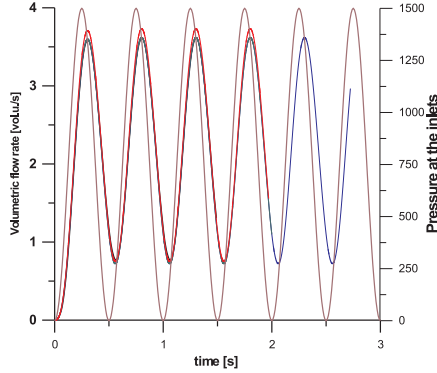


FIGURE 10. The volume flux of the test flow plotted as a function of time, calculated for different grids and collocation meshes: grid A with (5,3) mesh (blue line), grid A with (6,4) mesh (green line) and grid B with (5,3) mesh (red line). The black line corresponds to reference result obtained with FIDAP. The brown line depicts the time dependence of the prescribed inlet pressure.

2.8.2. Laminar flow in the T-junction accelerated from rest to a steady state

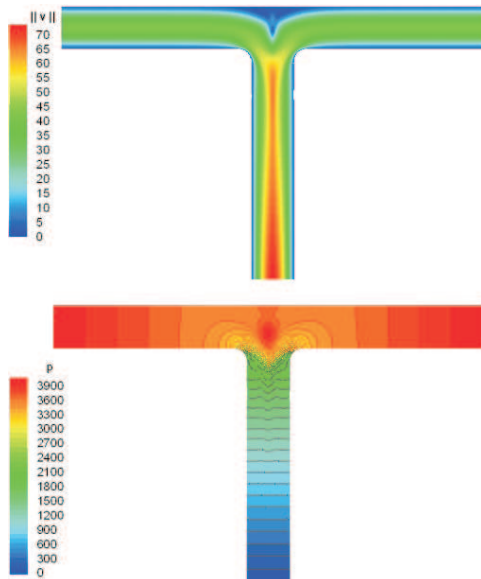


FIGURE 11. Contour maps of the steady-state velocity magnitude and the static pressure computed at the symmetry plane. The velocity units are cm/s; the pressure/density is shown in the bottom color map (the values are in cm^2/s^2).

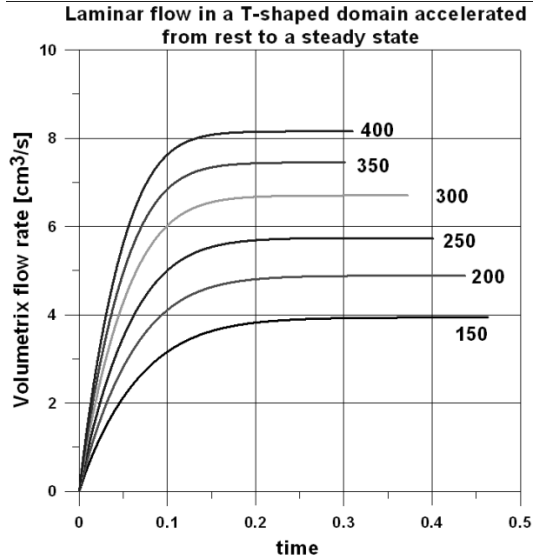


FIGURE 12. The volumetric flow rate as a function of time, for different driving pressure difference between the inlets and the outlet (the pressure units are Pa, the density is 10^3 kg/m^3).

2.8.3. Laminar pulsatile flow in the simple model of the Blalock-Taussig shunt

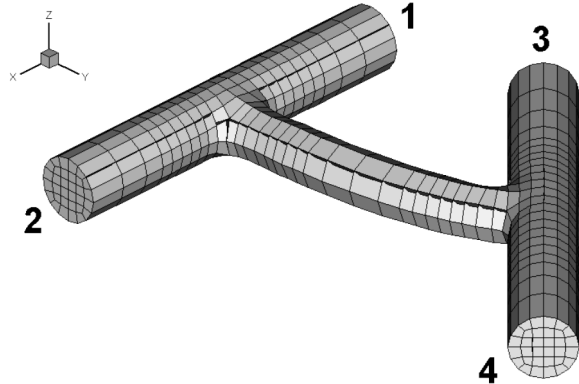


FIGURE 13. Geometric model of the BT shunt. In the figure, the smaller test grid of 1672 spectral elements is shown. The presented results have been computed for similar geometry but using the grid of 3760 spectral elements. The density of the internal collocation mesh has been set to $(N_V, N_P) = (6, 4)$.

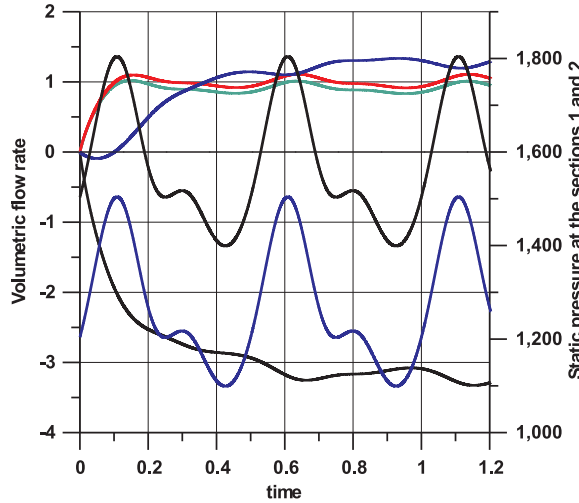


FIGURE 14. Temporal variation of the volume fluxes calculated for the BT shunt using AP-type conditions at all inlet/outlet sections. The black lines show the volume flux and static pressure at the inlet section 3. The blue lines represent the same data for the outlet section 4. The green and red lines show the temporal variations of the volume fluxes at the outlet sections 1 and 2, respectively. The pressure applied at these outlets was fixed in time and equal to zero.

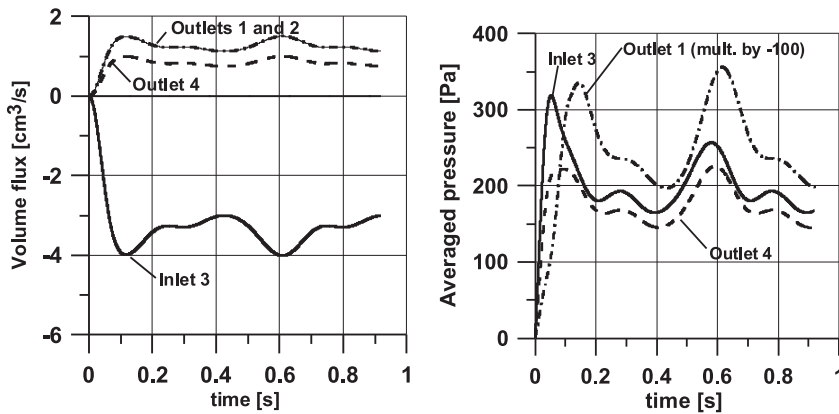


FIGURE 15. Pulsatile laminar flow in the BT shunt using VF-type inlet/outlet conditions. The left picture shows assumed volumetric flow rates at all I/O sections. The volume-flux distribution ratios are fixed in time and equal 37,5%, 37,5% and 25% for the outlets 1, 2 and 4, respectively. The right picture shows the computed temporal histories of the section-averaged static pressure at the I/O sections. Note the initial peak of the inlet pressure, which prevents the flow reversal at the outlet 4.

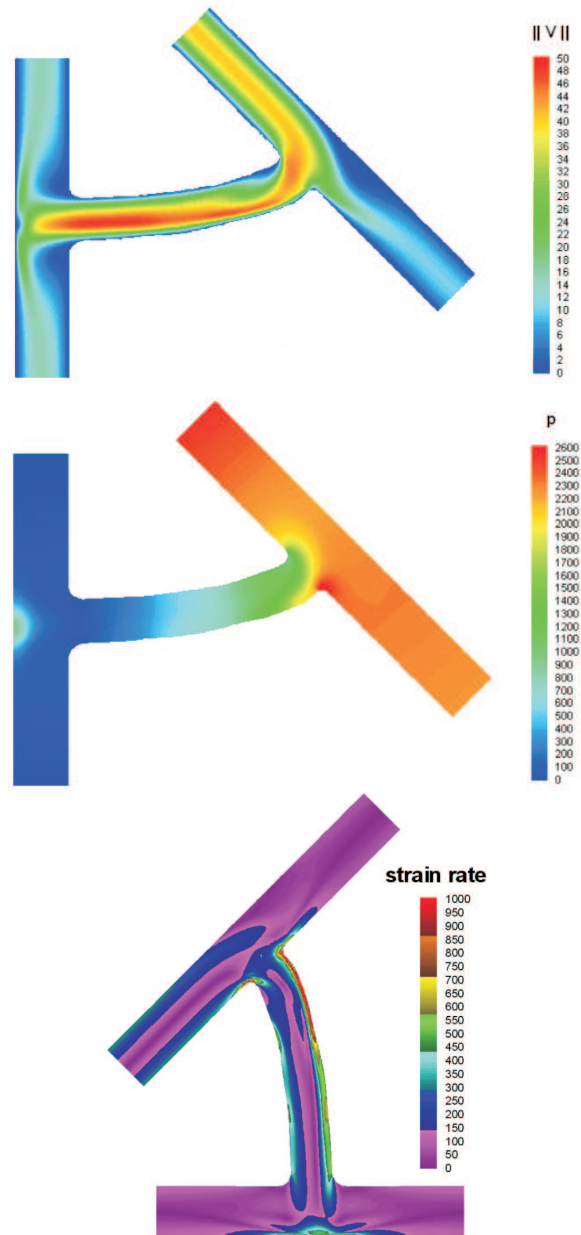


FIGURE 16. Top and center pictures: the contour plots of the velocity magnitude and the field of the static pressure to density ratio in the symmetry plane, computed for the time of the maximal flow rate. Bottom picture: the contour plot of the corresponding strain rate.

2.8.4. Encountered difficulties. Numerical instability of yet not understood origin appears at the inlet section. The scenario of the instability development can be characterized as follows.

First, rapid increase of a cross-flow (tangent) velocity is observed, which gives rise intensive generation of the “spikes” of the streamwise velocity. Eventually, the flow field quickly “blows up”. The characteristic structure in the inlet velocity field is shown in Fig. 17.

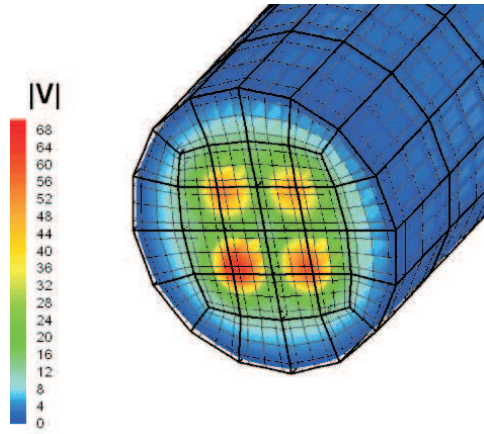


FIGURE 17.

2.8.5. Further development. The work of the improved versions of the spectral solver is in progress. In particular:

1. Experimental 2D codes with different inlet/outlet conditions (including zero tangent velocity, anyway!) are being developed (some undergraduate student’s projects are carried out in the Faculty of Aeronautical and Power Engineering, Warsaw University of Technology). The main purpose is to investigate numerically stability properties of the spectral solvers with “deficient” inlet/outlet conditions.
2. Work on efficient parallelization of the solver(s) (with collaboration of the Interdisciplinary Center of Mathematical Modeling, University of Warsaw) will be continued.
3. Development of the spectral-element 3D nonstationary convection-diffusion solver based on preconditioned BiCGStab [8] iterations is in progress.

4. Implementation and computational tests of new high-order Yosida methods [18, 23] are planned.

3. Numerical Modeling of Blalock-Taussig Shunt Using Commercial CFD Package FLUENT

The last part of the lecture covered the clinical application of findings and assumptions given by the computational flow analysis in the group of patients undergoing the systemic to pulmonary shunting operation.

3.1. Clinical Background and General Considerations

Systemic to pulmonary shunt operation was first performed on November 20th 1944 by Alfred Blalock. The patient undergoing that procedure was young girl suffering from congenital heart malformation of the type of tetralogy of Fallot (ToF). The most typical clinical finding in that subjects is cyanosis resulting from low oxygen saturation of arterial blood. Natural response to that condition is overproduction of the red blood cells (RBC) and augmentation of the hematocrit (HCT-RBC to plasma ratio) which leads to the strokes and haemorrhagic complications. The aim of the operation was to augment the oxygen saturation of the arterial blood by redirecting part of the blood flowing through the systemic circulation back to the pulmonary circulation. The concept was developed by Hellen Brook Taussig, cardiologist, who noticed deterioration of clinical status in the subjects suffering from ToF at the time of natural occlusion of the ductus arteriosus.

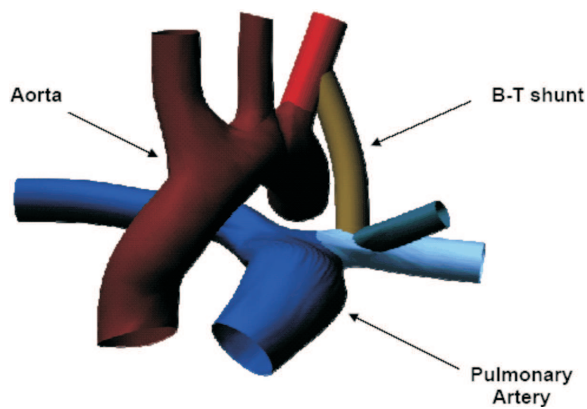


FIGURE 18. The general overview of the localization of B-T shunt

Contemporarily the modified Blalock-Taussig anastomosis is very important first stage of palliation in many forms of congenital heart malformations, especially requiring Fontan-like circulation as a final solution. The patency of first stage palliation (mBT) delimits the time step length and the time interval for the further surgical interventions.

3.2. Definition of the Model Geometry

Due to the complication of the geometry of the aortic arch and the pulmonary artery branching the volume of the model submitted for further investigation was greatly reduced and simplified.

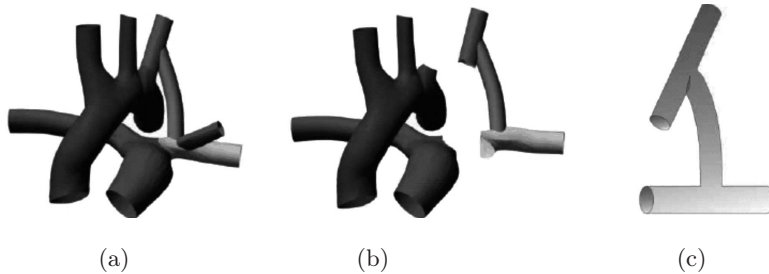


FIGURE 19. (a) Complete volume of the great vessels and prosthetic shunt, (b) abstracted region of the systemic to pulmonary shunt, (c) geometry of the numerical model

Final geometry was meshed with standard domain meshing commercial software GambitTM, [25]. The obtained tetrahedral mesh consisted of 90 829 cells, 187 793 faces and 18 367 nodes. Total volume of the model was: $1.85929 \times 10^{-6} \text{ m}^3$ (1.86 ml).

3.3. Definition of Boundary Conditions

Boundary conditions were also greatly simplified. The walls of the model were defined as rigid with no slip condition applied. Fluid flowing through the domain was defined as Newtonian viscous with the following parameters: $\rho = 1060 \text{ kg/m}^3$ and $\nu = 0.004 \text{ kg/ms}$.

SA inflow (red arrow in Fig. 20) is defined as time dependant mass flow inlet. The user defined function is equipped with basic driving curve of mass flux changes and the linear interpolation between the given time instants is used. The flow direction is set to be normal with respect to the inlet surface and the distribution of the mass flux (ρv_n) is assumed uniform.

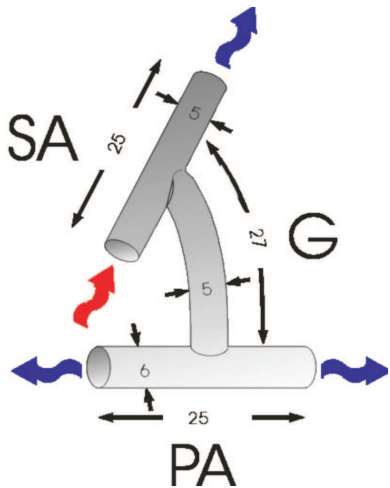


FIGURE 20. Dimensions in mm and flow directions in the B-T shunt computational model

- SA outlet (blue arrow in Fig. 20) was defined as: outflow with flow rate weighting = 0.5,
- PA outlets (blue arrows) were defined as: outflow with flow rate weighting = 1.

Such definition results in flowing flow distribution:

- 20% of volumetric flow continues towards the SA outlet,

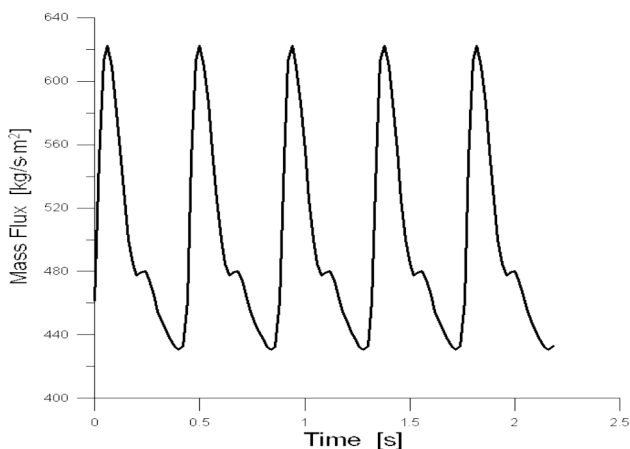


FIGURE 21. Mass flux driving curve at the SA inlet

- 80% of the volumetric flow is redirected towards both PA outlets,
- PA outlets flow was equally split between both of them.

The outflow distribution was chosen according to the clinical findings based upon postoperative echocardiography.

With the outflow conditions, all flow parameters (except pressure) were extrapolated to the outflow section from within the domain in such a manner that the diffusion fluxes are zero (homogeneous Neumann b.c.). Such approach is justified providing that the outflow is reasonably close to a fully-developed state.

3.4. Solver Settings

The most of the default values were applied for solving the flow equations inside the defined geometry.

- Viscous model: laminar,
- Pressure-velocity coupling: simple,
- Fixed time step: $\Delta t = 2 \times 10^{-4}$ s,
- Convergence criterion: $\varepsilon = 10^{-7}$.

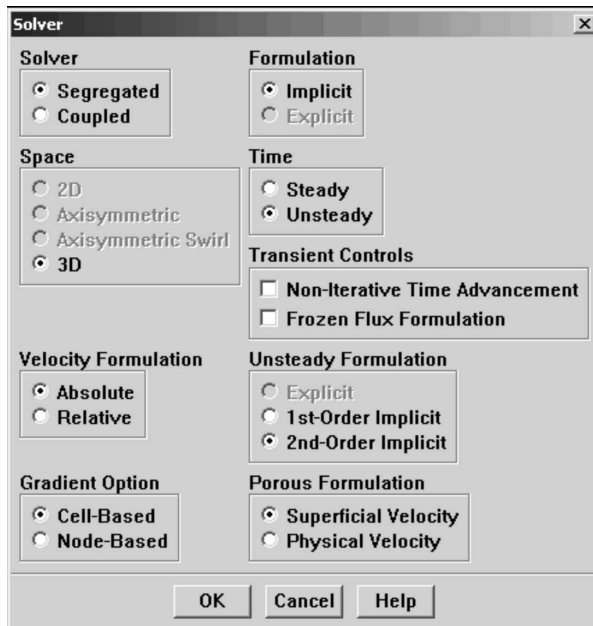


FIGURE 22. Solver settings—FLUENT 6.2.18

3.5. Results and Conclusions

Computer models included left subclavian artery, graft, and left pulmonary artery, and represented the average geometry of the graft in two groups of patients. The size of the blood vessels was the same in both models, but the graft was longer and narrower in model B (clotted grafts) than in model A (patent grafts). Shear stress fields were calculated, and the volume within the model with high shear rate (over 2500 1/s) was determined, in different phases of the cardiac cycle.

About 80% of inflowing blood was directed to the pulmonary circulation. In both models we observed a large recirculation region at the inlet to the graft accompanied by a high shear stress region at the opposite wall of the graft. The region of high stress was less than 0.5% of total volume of the system in model A (patent grafts), and over 4% of total volume in model B (clotted grafts).

Narrow and long grafts create flow patterns with high shear stress that promote platelet activation leading to augmented risk of clot formation. Therefore the graft geometry may be one of crucial factors in mBT anastomosis failure.

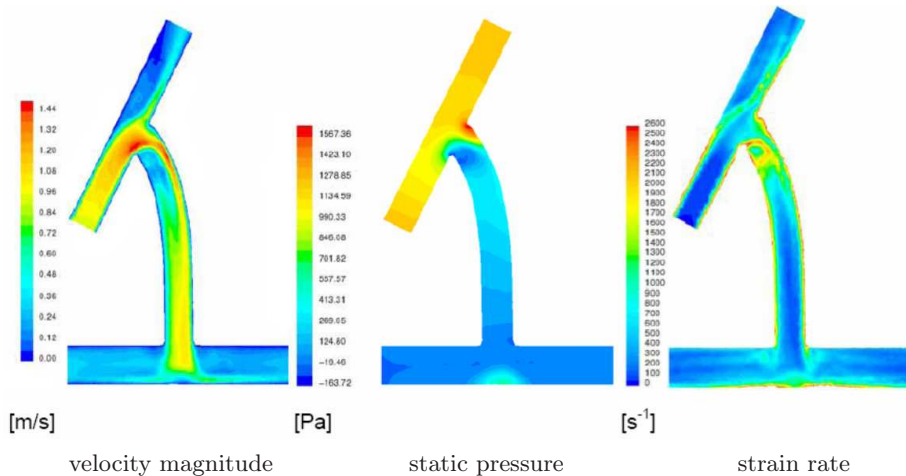


FIGURE 23. Results obtained during systolic phase of the simulation

The most important findings from the medical point of view were the results being in best agreement with the findings common in invasive and non invasive clinical examinations.

The best example of that was perfect explanation of the pressure loss at the inlet of the graft commonly found in hemodynamic postoperative study of the patients undergoing the mBT shunting.

The second important finding was the visualization of the high shear stress regions at the inlet of the prosthetic vessel. Shear stress is considered the most important mechanical factor directly influencing biochemical reactions like thrombosis and intimal hyperplasia in vascular system.

Numeric models gave the unique opportunity to study in "patient safe" environment such conditions like:

- Hydraulic pressure loss in the B-T shunt,
- regions of high shear rate can be localized,
- vulnerability of the flow to the geometry of the proximal anastomosis.

During the evaluation period of the results we found some quasi-compressibility occurring in solving method although the setting of the solver explicitly was set to non-compressible.

TABLE 4. "Quasi-compressibility" effect of the solver results in relatively large error in instantaneous volumetric flux balance

Inlet/outlet	Mass flow rate [g/s]	Vol. flow rate [cm ³ /s]	Avg. density [g/cm ³]
1 (Out)	4.69714	4.297437	1.09301
2 (Out)	4.69714	4.291925	1.09441
3 (In)	-11.74285	-10.04857	1.16861
4 (Out)	2.34857	2.142215	1.09633
Σ	0.0	-0.683007	—

From the computational point of view some safeguards and pitfalls had to be mentioned for the "non engineer" user of the commercial packages. All of the results obtained from the CFD methods has to be carefully evaluated and the sole judge of their applicability for the medical doctor has to be common sense and critical analysis.

Acknowledgement

This project was funded by Polish Committee of Scientific Research, grant 7 T11F 018 20.

References

1. R. ARIS, *Vectors, Tensors and the Basic Equations of Fluid Mechanics*, Dover, New York 1962.
2. G.K. BATCHELOR, *An Introduction to Fluid Dynamics*, Cambridge University Press, Cambridge 1967.
3. J.P. BOYD, *Chebyshev and Fourier Spectral Methods*, 2nd Ed., Dover, Mineola, New York 2001.
4. C. CANUTO, M.Y. HUSSAINI, A. QUARTERONI, and T.A. ZANG, *Spectral Methods in Fluid Dynamics*, Springer Verlag, Berlin/New York 1988.
5. M. GUNZBURGER, *Finite Element Methods for Viscous Incompressible Flows: A Practical guide to Theory, Practice and Algorithms*, Academic Press, Boston, 1989.
6. G. KARNIADAKIS and S.J. SHERWIN, *Spectral/hp Element Methods for CFD*, Oxford University Press, 1999.
7. M.O. DEVILLE, P.F. FISHER, and E.H. MUND, *High-Order Methods for Incompressible Fluid Flow*, Cambridge University Press, 2002.
8. Y. SAAD, *Iterative Methods for Sparse Linear Systems*, 2nd Ed., SIAM, 2003.
9. J. CAHOUET and J.P. CHABARD, *Some Fast 3D Finite Element Solvers for the Generalized Stokes Problems*, Int. J. Numer. Meth. Fluids, **8**: 869–895, 1986.
10. W. COUZY and M.O. DEVILLE, *Spectral-Element preconditioners for the Uzawa pressure operator applied to incompressible flows*, J. Scientific Computing, **9**(2) : 107–122, 1994.
11. P.F. FISHER, *Projection techniques for iterative solution of $\mathbf{A}\mathbf{x} = \mathbf{b}$ with successive right-hand sides*, Comput. Methods. Appl. Mech. Eng., **163** : 193–204, 1998.
12. J.G. HEYWOOD, R. RANACHER, and S. TUREK, *Artificial boundaries and flux and pressure conditions for the incompressible Navier-Stokes equations*, Int. J. Numerical Methods in Fluids, **22** : 325–352, 1996.
13. G. KARNIADAKIS, M. ISRAELI, S.A. ORSZAG, *High-Order Splitting methods for the Incompressible Navier-Stokes Equations*, J. Comp. Phys., **97** : 414–443, 1991.
14. Y. MADAY, A.T. PATERA, and E.M. RONQUIST, *An operator-integration-factor splitting method for time-dependent problems: Application to incompressible fluid flow*, J. Sci. Comput., **5** : 263–292, 1990.
15. Y. MADAY, D. MEIRON, A. PATERA, and E.M. RONQUIST, *Analysis of iterative methods for the steady and unsteady Stokes problem: application to spectral element discretizations*, SIAM J. Sci. Comput. **14**(2) : 310–337, 1993.
16. E.M. RONQUIST, *A domain decomposition method for elliptic boundary value problems: Application to unsteady incompressible fluid flow*, in the Proceedings of 5th Conference on Domain Decomposition Methods for Partial Differential Equations, D.E. Keyes et al. [eds.], pp.545–557, 1991.

17. J. SZUMBARSKI, P. OLSZEWSKI, A. STYCZEK, J. ROKICKI, Z. MALOTA, and K. WAWRUCH, *Computations of an Unsteady Viscous Flow in a Three Dimensional System of Ducts*, J. Theoretical Appl. Mech., **42**(1)—Part 1, and (4)—Part 2, 2004.
 18. A. QUARTERONI, F. SALERI, and A. VENEZIANI, *Analysis of the Yosida method for the incompressible Navier-Stokes equations*, J. de Mathematiques Pures et Appliques, **78**: 473–503, 1999.
 19. W. COUZY, *Spectral Element Discretization of the Unsteady Navier-Stokes Equations and Its Iterative Solution on Parallel Computers*, Ph.D. Thesis, Ecole Polytechnique Federale De Lausanne, No 1380, 1995.
 20. *Lecture notes of the Summer School on the Modelling of the Cardiovascular System*, (org. A. Quarteroni), EPFL, Lausanne, 25–30 August 2003.
 21. A. QUARTERONI and L. FORMAGGIA, *Mathematical Modelling and Numerical Simulation of the Cardiovascular System*, MOX Rep. 1, 2002.
 22. A. VENEZIANI and C. VERGARA, *Flow Rate Defective Boundary Conditions in Haemodynamics Simulations*, MOX Rep. 35, 2003.
 23. P. GERVASIO, F. SALERI, and A. VENEZIANI, *Algebraic Fractional Step Schemes with spectral methods for the Incompressible Navier-Stokes Equations*, MOX. Rep. 61, 2005.
 24. L. FORMAGGIA, J.F. GERBEAU, F. NOBILE, and A. QUARTERONI, *Numerical treatment of defective boundary conditions for the Navier-Stokes equations*, EPFL, Departement de Mathematiques, Preprint 20, 2000.
 25. *Fluent 6.2 User's Guide*, Fluent Inc., 2005.
-

Contributed Papers

Biological and Physiological Mechanisms of the Hair Preservative Effect of Scalp Cooling in Chemotherapy-Induced Hair Loss

F.E.M. JANSSEN, G.M.J. VAN LEEUWEN,
and A.A. VAN STEENHOVEN

Technische Universiteit Eindhoven
PO Box 513, 5600 MB Eindhoven, The Netherlands
f.e.m.janssen@tue.nl

Hair loss is a feared side-effect of chemotherapy treatment. It may be prevented by cooling the scalp during administration of cytostatics. The supposed mechanism is that by cooling the scalp, both temperature and perfusion (blood flow) are diminished, affecting drug supply and drug effect in the hair follicle. However, the exact contribution of both temperature and perfusion to the hair preservative effect of scalp cooling is unknown.

Aim of this study is to develop a biological and physiological model of scalp cooling, and to identify the important aspects in scalp cooling. For this, sub models for heat transfer, medicine transport and cell damage are being developed. To tune these models, dedicated experiments are performed on the relationship between temperature and blood flow, and on the influence of temperature and chemotherapy concentration on hair follicle damage.

With the complete model, it will be possible to improve current day scalp cooling treatment.

1. Introduction

When chemotherapy is used as a cancer treatment, partial or complete hair loss does often occur. This causes psychological stress [1], and it is one of the most feared side effects of cancer therapy [2]. By cooling the scalp during chemotherapy treatment this hair loss can be reduced or even prevented [3].

There are two mechanisms that assumedly explain the hair preservative effect of scalp cooling [4]. The first is reduced blood flow to the subcutaneous tissue during cooling, which reduces the amount of drugs being de-

livered to the hair follicle. The other mechanism is a reduced subcutaneous cell metabolism in response to the hypothermia, making hair follicles less susceptible to drug damage.

However, the effect of scalp cooling varies strongly [5] which can partly be attributed to a lack of insight in the precise temperature dependence of these mechanisms. Another important aspect is that it is uncertain whether local variations in skin temperature and blood flow exist during cooling.

In this study, a computer model is being developed to describe all aspects of scalp cooling. The model includes different numerical models to describe drug transport, heat transfer and hair follicle damage and experiments are conducted to improve numerical relations in those models. With the complete model, it will be possible to assess crucial parameters in the design and user protocol of scalp cooling.

2. Experiments on Blood Flow and Temperature

One of the main points of interest in this study is the interplay between temperature and perfusion. In literature, the well known Q_{10} relation of thermal physiology is used to model variations in metabolism (M) and subsequent responses in blood flow (W_B) due to changes in temperature [6, 7]:

$$\begin{aligned} M &= M_0 \cdot Q_{10}^{\frac{(T-T_0)}{10^\circ\text{C}}} \\ W_B &= W_{B,0} \cdot Q_{10}^{\frac{(T-T_0)}{10^\circ\text{C}}} \end{aligned} \quad (2.1)$$

with values for Q_{10} ranging from 2.0 to 3.0 [6]. However, these values have not been verified for cooling of the human scalp. Even the validity of these functions needs to be assessed.

Therefore, experiments are being performed to investigate the relationship between scalp temperature and scalp blood flow. A laser doppler probe (407, Perimed UK Ltd) and a J-type thermocouple are placed on the scalp skin (frontal skull, slightly off-center to the right). A cold cap system (Paxman Coolers Ltd UK) is used without pre-cooling to cool the skin with a slow rate of approximately $0.1^\circ\text{C}/\text{min}$. Total time of cooling is about 120 minutes.

A result of a preliminary experiment on blood flow and temperature is shown in Figure 1. In this figure, relative perfusion $W_B/W_{B,0}$ is plotted against the temperature difference $\Delta T = T_{\text{sk}} - T_{\text{sk},0}$. Because of the definition of $W_{B,0}$, the graph necessarily includes $\Delta T = 0$, $W_B/W_{B,0} = 1$.

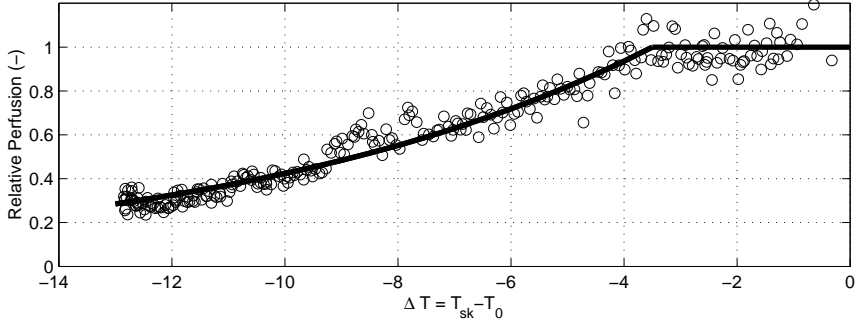


FIGURE 1. Preliminary experiment on the relationship between temperature and perfusion. Relative perfusion and temperature of the skin are shown during cooling of the skin. The solid line denotes a Q_{10} value of 3.75 with a threshold of 3.5°C.

Perfusion drops down to 28% for a temperature drop of 13°C, which is in agreement with findings of Bülow [4]. Using Eq. (2.1), this would correspond to a Q_{10} value of 2.65.

However, it is striking to see that during the first 3 to 4 degrees of cooling, there is no change in perfusion. This would indicate there is a negative threshold value for changes in blood flow. A fit through the graph yielded a threshold value of 3.5°C, and a Q_{10} value of 3.75.

As stated earlier, these results are from one preliminary experiment. Further experiments are needed to establish the relation and individual variation for the temperature dependence of perfusion.

3. Heat Transfer Model

A numerical model has been made to describe heat transfer in the head during cooling [8]. The head and cold cap are both approximated by spherical elements representing brain, skull, fat, skin, hair and cold cap (Fig. 2). Heat transport in the head is modelled using Pennes' well-known "bio-heat transfer" equation:

$$\rho c \frac{\partial T}{\partial t} = \nabla \cdot (k \nabla T) + W_B(T_A - T) + M$$

in which ρ , c and k are the tissue density, specific heat and thermal conductivity, respectively. T is the local tissue temperature and T_A the temperature of the blood in the main arteries supplying the scalp, here assumed to be

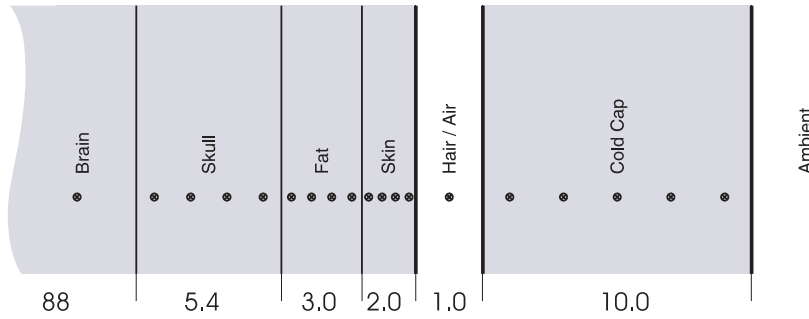


FIGURE 2. Schematic representation of the heat transfer model and placement of the nodes. Dimensions of the model are shown in millimeters.

constant and set to 37°C. Values of these properties used in our standard head model are shown in Table 1.

TABLE 1. Thermophysical tissue parameters used in the standard head model.

	d [mm]	k [W/(mK)]	Q [W/m³]	$W_{b,0}$ [kg/(m³s)]
Brain	88.0	0.5	8800	8.5
Skull	5.4	1.0	130	0.15
Fat	3.0	0.2	130	0.2
Skin	2.0	0.384	500	1.5
Hair	2.5	0.026	0	0
Cold Cap	10.0	0.5	0	120

W_B and M are the blood perfusion rate and the metabolic heat production in the tissue, respectively, which are both functions of temperature. Temperature dependent blood flow is modelled using the Q_{10} -threshold function as found in the preliminary experiment:

$$W_B = \begin{cases} W_{b,0} & \text{if } T \geq (T_0 - 3.5); \\ W_{b,0} \cdot 3.75^{\frac{(T-(T_0-3.5))}{10}} & \text{if } T < (T_0 - 3.5). \end{cases} \quad (3.1)$$

At the interface between two different layers, a special numerical method is used to ensure that both temperature and heat flux are continuous across the interface boundaries.

Boundary conditions for the model include convective heat transfer (q_C'') and radiative heat transfer (q_R'') to the surroundings:

$$\begin{aligned} q_C'' &= h(T - T_{\text{amb}}), \\ q_R'' &= \sigma(T^4 - T_{\text{amb}}^4). \end{aligned}$$

In these equations, h is the heat transfer coefficient appropriate for free convection ($h = 4 \text{ W}/(\text{m}^2\text{K})$) and σ is the Stefan Boltzmann constant ($\sigma = 5.669 \times 10^{-8} \text{ W}/(\text{m}^2\text{K}^4)$). Ambient temperature (T_{amb}) is set to 20°C.

The cold cap has a thickness of 10 mm and uses a thermal conductivity of 0.5 W/(mK). The coolant in the cap has an estimated mass flow of 0.17 kg/s. This value is adjusted to a flow of 120 kg/(m³s), such that it can be used in the Pennes equation. Coolant temperature is set to -8°C.

A parameter study was performed with the heat transfer model. Simulation of a scalp cooling procedure consisted of two steps. First, the temperature without a cold cap was calculated keeping metabolism and perfusion constant. The resulting temperature profile was used as the reference temperature profile (T_0) for temperature dependent metabolism (Eq. 2.1) and blood flow (Eq. 3.1). Then, a cold cap was added to the model and the steady state solution was calculated.

The base model shows a minimum skin temperature of 18.3°C and a relative blood flow of 18%. The results of the parameter study will be compared to the result of the standard model. Results are shown in Table 2.

TABLE 2. Change in minimum skin temperature and relative blood flow during cooling with a cold cap as a result of different parameter values. $\Delta T = T_{\min} - T_{\min,\text{standard}}$, so a negative value means a colder skin than in the standard analysis. Blood flow values are given in percentages of blood flow before cooling. Blood flow in the standard analysis was reduced to 18%.

property / scaling factor	$\times 0.5$	$\times 2.0$	$\times 0.5$	$\times 2.0$
	ΔT [K]	ΔT [K]	W_B [%]	W_B [%]
d_{fat}	3.1	-5	28	9.7
d_{skin}	0.3	-0.2	20	18
d_{hair}	-8.2	3.5	6.4	30
k_{fat}	-3.5	1.5	12	23
k_{hair}	3.4	-2.7	29	13

From this table, it is clear that thickness and thermal conductivity of both the fat layer and the hair layer are the most important parameters that influence skin temperature and perfusion. Changing the hair layer thickness from 1 mm to 2 mm increases temperature by 3.5°C, while changing it from 1 mm to 0.5 mm decreases temperature by 8.2°C. In the first case the perfusion is almost five times the perfusion of the second case.

For the clinic, this means that a good control of the thermal resistance of the hair layer is essential. It should be kept as low as possible to ensure good cooling, without exceeding the limits of thermal comfort for the patient.

4. Physiologically Based Pharmacokinetic Model

To relate drug dosage to toxic effects with the aim to evaluate the effect of scalp cooling, it is first of all necessary to predict the exact concentration of cytotoxic drugs in the hair follicle. For this, Physiologically Based Pharmacokinetic (PBPK) models are useful tools [10]. They divide the body into compartments that represent individual organs and tissue groupings. Physiologic and biochemical constants are used to model transport, clearance and metabolism of drugs with a set of differential equations for the mass balance in each compartment (Fig. 3).

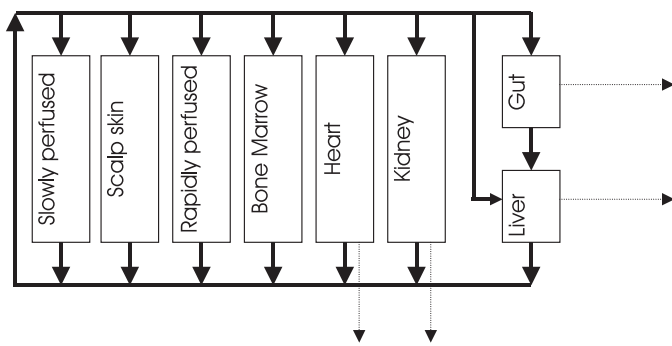


FIGURE 3. Schematic representation of a physiologically based Pharmacokinetic model for DOX. →: blood flow; - ->: metabolic or excretory pathways.

An eight-compartment flow limited model is used [11], incorporating tissue-specific metabolism and biliary and urinary elimination. For each compartment, a generic mass balance equation is used:

$$\frac{dA_i}{dt} = W_{B_i}(C_A - C_{V_i}) - \frac{dA_{E,M_i}}{dt}$$

where A_i is the amount of drug in the compartment in [moles], W_{B_i} is the blood flow through the compartment in [l/s], and C_A and C_{V_i} are the arterial and venous blood concentrations in [moles/m³]. A_{E,M_i} denotes the amount of drugs that are being excreted or metabolized in the tissue in [moles], showing

either linear kinetics:

$$\frac{dA_{E,M_i}}{dt} = K_{\text{MET}} \cdot C_{V_i} \cdot V_i$$

or saturable chemical-specific binding kinetics (i.e. Michaelis–Menten Kinetics):

$$\frac{dA_{E,M_i}}{dt} = \frac{V_{\text{MAX}} \cdot C_{V_i}}{K_M + C_{V_i}}$$

Here, K_{MET} is a first order metabolic rate constant [s^{-1}], V_i denotes the volume of the i^{th} compartment in [m^3], V_{MAX} is the maximum rate of activity in [moles/s], and K_M denotes a Michaelis' constant in [moles/ m^3].

The amount of drugs in the blood compartment is calculated using another mass balance.

$$\frac{dA_B}{dt} = \sum_i W_{B_i} C_{V_i} - \sum_i W_{B_i} C_A$$

We use the cytostatic Doxorubicin (DOX) in our model, since it is commonly used, it causes hair loss, and biochemical and biophysical properties of this drug are available [11]. This drug binds to plasma proteins in the blood, and only free drug concentration is available for uptake in the tissues. Free DOX concentration in the arterial blood is calculated as:

$$C_A = \frac{A_B}{V_B} \cdot (1 - F_B) \quad (4.1)$$

with V_B the volume of the blood compartment in [m^3], and F_B the fraction of DOX bound to plasma proteins, typically 0.7.

Doxorubicin is also able to bind to specific macromolecules in tissues (e.g. DNA), also showing Michaelis–Menten Kinetics. To compensate for this, the venous return concentration is calculated as:

$$C_{V_i} = \frac{A_i}{V_i} - \frac{T_{\text{DNA}} \cdot C_{V_i}}{K_{\text{DNA}} + C_{V_i}}$$

in which T_{DNA} is the tissue-specific DNA binding capacity for DOX in [moles/ m^3].

Temperature dependent blood flow obtained by the heat transfer model is used in the PBPK model as input parameter. The model then calculates the drug concentration in the hair follicle compartment. Finally, a statistical model is needed to be able to assess the amount of hair damage and to predict whether hair loss will occur.

5. Experiments on Hair Follicle Damage

In a study on Doxorubicin handling by kidney epithelial tissue, Decorti shows that Doxorubicin uptake is temperature dependent [13]. At 37°C, drug uptake in the kidney cells in one hour is 7 times higher than at 4°C. We would like to investigate these effects for drug uptake in the hair follicle using temperatures that are relevant for scalp cooling. But not only drug uptake, also hair follicle damage should be analyzed.

To gain more insight into the importance of both reduced drug supply and reduced drug actions, *in vitro* experiments will be conducted on the influence of both temperature and drug concentration on drug uptake and hair follicle damage. In this study, hair follicle damage is defined as the amount of anti-tumor protein p53 produced in the hair follicle. This protein is produced by hair follicles when damaged by cytotoxic drugs and is always present in chemotherapy-induced hair loss [12].

A preliminary protocol defines 4 different regimes to be studied, making combinations of either high (32–34°C) or low temperature (20–22°C) and low or high drug concentration. These low and high drug concentrations will be determined by the PBPK model with or without cooling, respectively. In addition, 2 control groups will be studied where drug concentration is zero. With these experiments, we hope to determine the relative importance of the two mechanisms to which the prevention of hair loss are attributed.

6. Results and Outlook

The aim of this study is to develop a biological and physiological model of scalp cooling, in order to identify the important aspects in scalp cooling. For this, numerical models for heat transfer, medicine transport and cell damage are being developed. Important aspect in this study is the mutual relationship between temperature and perfusion, since it is needed for the heat transfer model and to simulate medicine transport in the human body.

In a preliminary experiment, we investigated this relationship. The results show a negative threshold for relative perfusion (3.5°C), and subsequent the fitted Q_{10} value ($Q_{10} = 3.75$) is greater than any value cited in literature ($2 < Q_{10} < 3$). However, neglecting the threshold behavior and using Eq. (2.1), the perfusion reduction corresponds to a Q_{10} value of 2.65. This shows that further experiments are needed to investigate this threshold behavior and to establish the relation for the temperature dependence of perfusion.

Our heat transfer model shows that important parameters are the thermal resistances of both the fat and hair layer [9]. During cooling, the base model shows a skin temperature of 18°C and a factor 5 decrease in perfusion. Changing the thickness of the hair layer yields skin temperatures ranging from 22°C to 10°C, and perfusion may be reduced by a factor 3 to 15 from normal. Changes in the fat layer thickness, and changes in thermal conductivity of both fat and hair layer show similar results. This large variation in perfusion reduction shows that temperature should be as low as possible, yet still comfortable for the patients, to ensure that the amount of drugs delivered to the hair follicles is as low as possible.

The heat transfer model provides the necessary perfusion data for a Physiological Based Pharmacokinetic (PBPK) model. Using relative perfusion and temperatures of the scalp skin, the total amount of drugs that are delivered to the hair follicles can be calculated. A statistical model is needed to determine the resulting damage inflicted to the hair follicle. For this, experiments are to be conducted.

The fact that DOX uptake in kidney cells decreases with lower temperatures [13], independent of perfusion, poses an interesting starting point for further examination. In the near future, hair follicle experiments are to be conducted, to investigate the influence of drug uptake and hair follicle damage at relevant temperatures. Also, the influence of extracellular concentrations will be studied.

After experimental establishment of some of the primitive relations that are part of the chain of events preventing hair loss, the combination of submodels will result in a complete model that can help in optimizing scalp cooling for hair loss prevention.

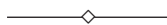
Acknowledgement

The authors would like to acknowledge the work and support of Dr. W.P.M. Breed. This research was sponsored by SOBU, an administrative cooperation between Tilburg University and the Eindhoven University of Technology.

References

1. P. KATSIMBRI, A. BAMIAS, and N. PAVLIDIS, *Prevention of chemotherapy-induced alopecia using an effective scalp cooling system*, Eur. J. Cancer, **36**: 766–771, 2000.

2. T.F. CASH, *The psychology of hair loss and its implications for patient care*, Clin. Dermatol., **19**: 161–166, 2001.
3. C. PROTIERE, K. EVANS, J. CAMERLO, M.P. D'INGRADO, G. MACQUART-MOULIN, P. VIENS, D. MARANINCHI, and D. GENRE, *Efficacy and tolerance of a scalp-cooling system for prevention of hair loss and the experience of breast cancer patients treated by adjuvant chemotherapy*, Support. Care Cancer, **10**: 529–537, 2002.
4. J. BÜLOW, L. FRIBERG, O. GAARDSTING, and M. HANSEN *Frontal subcutaneous blood flow, and epi- and subcutaneous temperatures during scalp cooling in normal man*, Scand. J. Clin. Lab. Invest., **45**: 505–508, 1985.
5. E.G. GREVELMAN and W.P.M. BREED, *Prevention of chemotherapy-induced hair loss by scalp cooling*, Ann. Oncol., **16**: 352–358, 2005.
6. B.H. DENNIS, R.C. EBERHART, G.S. DULIKRAVICH, and S.W. RADONS, *Finite-element simulation of cooling of realistic 3-D human head and neck*, J. Biomech. Eng., **125**: 832–840, 2003.
7. D. FIALA, K.J. LOMAS and M. STOHRE *A computer model of human thermoregulation for a wide range of environmental conditions: the passive system*, J. Appl. Phys., **87**: 1957–1972, 1999.
8. F.E.M. JANSSEN, G.M.J. VAN LEEUWEN, and A.A. VAN STEENHOVEN, *Numerical simulation of scalp cooling to prevent chemotherapy-induced alopecia*, Proceedings of the ASME-ZSIS International Thermal Science Seminar II, 2004.
9. F.E.M. JANSSEN, G.M.J. VAN LEEUWEN, and A.A. VAN STEENHOVEN, *Modelling of temperature and perfusion during scalp cooling*, Phys. Med. Biol., in press, 2005.
10. F.P. THEIL, T.W. GUENTERT, S. HADDAD, and P. POULIN, *Utility of physiologically based pharmacokinetic models to drug development and rational drug discovery candidate selection*, Tox. Letters., **138**: 29–49, 2003.
11. D.L. GUSTAFSON, J.C. RASTATTER, T. COLOMBO, and M.E. LONG, *Doxorubicin pharmacokinetics: Macromolecule binding, metabolism, and excretion in the context of a physiologic model*, J. Pharm. Sci., **91**: 1488–1501, 2002.
12. V.A. BOTCHKAREV, E.A. KOMAROVA, F. SIEBENHAAR, N.V. BOTCHKAREVA, P.G. KOMAROV, M. MAURER, B.A. GILCHREST, and A.V. GUDKOV *p53 is essential for chemotherapy-induced hair loss*, Cancer Res., **18**: 5002–5006, 2000.
13. G. DECORTI, I. PELOSO, D. FAVARIN, F. BARTOLI KLUGMANN, L. CANDUSSIO, E. CRIVELLATO, F. MALLARDI, and L. BALDINI, *Handling of Doxorubicin by the LLC-PK₁ Kidney Epithelial Cell Line*, J. Pharmacol. Exp. Ther., **286**: 525–530, 1998.



Propagation of a Solute Wave in a Curved Vessel

G. PONTRELLI¹⁾ and A. TATONE²⁾

¹⁾*Istituto per le Applicazioni del Calcolo, CNR
Viale del Policlinico 137, 00161 Roma, Italy
g.pontrelli@iac.cnr.it*

²⁾*DISAT, Facoltà di Ingegneria, Università dell’Aquila,
67040 Monteluco di Roio (AQ), Italy
tatone@ing.univaq.it*

Mass transport and diffusion processes of a substance dissolved in the blood are studied. A linearization procedure over the steady state solution is carried out and an asymptotic analysis is used to study the influence of a small curvature with respect to the straight tube. Numerical results show the characteristics of the long wave propagation and the role played by the curvature on the solute distribution.

Key words: *Wave propagation, solute dynamics, numerical methods.*

1. Introduction

Mass transfer and diffusion phenomena inside the arterial lumen and through the vascular wall are of great importance for physiological functions, such as oxygenation, nourishment of tissues and metabolic drainage processes. Some mathematical models coupling 3D flow and solute dynamics have been developed in recent years [1–4]. They are defined in a finite arterial segment of arbitrary shape, where an inflow solute distribution is provided [1, 2]. Some of them consider also absorption and exchange through the vascular tissues [3]. All these models provide the local concentration pattern and are useful to understand the relationship between the local flow pattern, the nourishing of arterial tissues and possible pathologies derived when such a process is altered [4].

It is known that geometrical effects, such as curvature, will strongly affect the flow pattern and consequently the concentration of gases and substances dissolved in the blood [5]. It is worth to investigate how, and to what extent, the geometry and the haemodynamic factors are responsible for anomalous accumulation and altered absorption of substances on the arterial wall, leading to atherosclerotic lesions and degenerative processes [6].

In the present paper, a perturbation approach is used to model the mass transport and diffusion process inside a straight or moderately curved artery, similarly to the work in [7]. It is described by the advection-diffusion equation and a Robin interface condition is imposed at the boundary to model a solute exchange through the wall, with the flow field given. For most substances such a process is convection dominated, due to a low diffusion coefficient [5]. Being interested in propagative phenomena, we consider the solute dynamics inside the vascular tissue negligible, and the so called *free-wall* model is used [4].

Induced by the periodicity of respiratory, hormonal and feeding acts, the concentration of a substance in blood is subject both to an oscillation in time and to a spatial variation along the vessel, sustained by the fluid motion [5, 6]. For example, the pulsatile insulin release in the blood stream is induced by the oscillation in glycolysis and generates a wave of period 5–10 min. [8]. In general, the wave period is strongly dependent on the substance considered. As a consequence, for any substance, we look for the propagation characteristics, in relation with the medium diffusivity and wall permeability properties. The aim of this study is to characterize the solute propagation in the blood flow and to provide the local distribution of concentration that can be affected by geometrical factors, such as the curvature.

The layout of this paper is as follows: in Sec. 2 the mathematical problem is stated in its general formulation as a convection-diffusion equation and its coupling with fluid dynamics is shown. For simplicity, the diffusivity and the wall permeability coefficients are assumed constants. Hence, a linearization procedure over a steady state solution is accomplished and a splitting of the concentration variable from the fluid dynamical field is achieved. A wave type solution in a torus is sought for the unsteady component (Sec. 3) and a perturbation method is used to separate the dominant component in a straight tube from the part due to a possible small curvature (Sec. 4). Finally, in Sec. 5 some numerical experiments show the characteristics of the wave propagation in a straight and in a bended artery and the influence of geometrical factors on the solute distribution.

2. The Advection-diffusion Problem

The motion of blood in a vessel is modelled by the flow of a newtonian viscous fluid in an elastic tube. Different substances are dissolved in blood, transported through the stream and possibly exchanged through the arterial wall [5, 6]. For simplicity, the presence of one solute only is considered and let us denote by c its concentration. Because of both diffusive and convective phenomena, c satisfies the following advection-diffusion equation [1]:

$$\frac{\partial c}{\partial t} + \mathbf{v} \cdot \nabla c - \mu \Delta c = 0 \quad (2.1)$$

with \mathbf{v} the fluid velocity, $\mu > 0$ a diffusivity coefficient. A possible exchange of solute through the wall is expressed by:

$$(\mu \nabla c) \cdot \mathbf{n} + \sigma c = \sigma c_{\text{ext}} \quad (2.2)$$

where $\sigma \geq 0$ is the wall permeability and c_{ext} is a concentration external to the vessel (if the wall is impermeable, $\sigma = 0$). In the following, we will be interested in the concentration dynamics in the lumen only. Therefore the present model does not account for any possible external variations of concentration, and c_{ext} is considered constant. Strictly speaking, μ and σ do depend on the flow field and on the temperature [1, 2] but, for simplicity, let us assume them as constant. Due to the small value of μ , for most substances the problem is highly convection dominated in large arteries.

In principle, fluid and solute dynamics are coupled processes and influence reciprocally. However in this model the solute is regarded as a passive scalar: it is simply advected by the blood flow in the lumen, any feedback effect on the fluid viscosity and density being neglected. As a consequence, we split the flow from the solute dynamics: the fluid velocity \mathbf{v} is computed beforehand, and Eqs. (2.1)–(2.2) are subsequently solved.

Problem (2.1)–(2.2) is usually defined in an arterial segment with proximal and distal boundary conditions assigned, together with an initial condition. By standard arguments for parabolic problems, it can be proved that, under appropriate regularity assumptions on the coefficients and on the velocity field, the above boundary value problem is mathematically well posed [4, 9]. However, since a special case will be studied here, the definition of proximal/distal boundary conditions will be again addressed in Sec. 3.

Let us decompose the variables \mathbf{v} and c as sum of a steady state part (denoted by a bar) and an unsteady component (denoted by a circumflex)

accent):

$$\mathbf{v} = \bar{\mathbf{v}} + \hat{\mathbf{v}}, \quad c = \bar{c} + \hat{c} \quad (2.3)$$

and let us assume the unsteady parts $\hat{\mathbf{v}}$ and \hat{c} (and $\nabla\hat{\mathbf{v}}$ and $\nabla\hat{c}$ as well) are *small* enough with respect to the steady ones such that the nonlinear term $\mathbf{v} \cdot \nabla c$ in Eqs. (2.1) can be linearized as:

$$(\bar{\mathbf{v}} + \hat{\mathbf{v}}) \cdot (\nabla \bar{c} + \nabla \hat{c}) \approx \bar{\mathbf{v}} \cdot \nabla \bar{c} + \bar{\mathbf{v}} \cdot \nabla \hat{c} + \hat{\mathbf{v}} \cdot \nabla \bar{c} \quad (2.4)$$

neglecting the higher order terms. In other words, small fluctuations of velocity and concentration are superimposed to a steady solution.

It is easy to verify that:

$$\bar{c} = \begin{cases} c_{\text{ext}} & \text{if } \sigma \neq 0, \\ \text{const} & \text{if } \sigma = 0 \end{cases} \quad (2.5)$$

satisfies the following boundary value problem:

$$\begin{aligned} \bar{\mathbf{v}} \cdot \nabla \bar{c} - \mu \Delta \bar{c} &= 0 \\ \mu \nabla \bar{c} \cdot \mathbf{n} + \sigma \bar{c} &= \sigma c_{\text{ext}} \quad \text{at the wall} \end{aligned} \quad (2.6)$$

where \bar{c} equals the constant value as in Eq. (2.5) at any boundary other than the wall. This corresponds to the fact that, for a time interval long enough, the solute pervades the whole tube and, in the limit, it reaches a uniform concentration.

3. Wave Solution

By Eqs. (2.4) and (2.6), the unsteady solution satisfies the following equation:

$$\frac{\partial \hat{c}}{\partial t} + \bar{\mathbf{v}} \cdot \nabla \hat{c} + \hat{\mathbf{v}} \cdot \nabla \bar{c} - \mu \Delta \hat{c} = 0 \quad (3.1)$$

with a homogeneous boundary condition at the wall:

$$\mu \nabla \hat{c} \cdot \mathbf{n} + \sigma \hat{c} = 0. \quad (3.2)$$

Because of Eq. (2.5), the homogeneous boundary value problem (3.1)–(3.2) depends only on the steady fluid velocity $\bar{\mathbf{v}}$ and is independent of the unsteady flow field $\hat{\mathbf{v}}$. This proves that the small wall deformation, which is demonstrated of much importance in vascular dynamics [7], is irrelevant in the solute motion.

We are going now to define a precise domain and a specific form for the solution of the problem (3.1)–(3.2). Let us consider a *long* tube of circular cross section of radius a , having the shape of a torus with small curvature $1/R$.

For the following analysis, it is convenient to work out the equations in a toroidal coordinate system (r, θ, ψ) . The axial coordinate $z = R\theta$ is introduced to avoid degeneracy when $R \rightarrow \infty$ (straight tube).

The problem is now rewritten in nondimensional form by the following substitutions:

$$r \rightarrow \frac{r}{a}, \quad z \rightarrow \frac{z}{a}, \quad t \rightarrow \frac{Vt}{a}, \quad \mathbf{v} \rightarrow \frac{\mathbf{v}}{V}$$

where V is a characteristic velocity. Without loss of generality, the concentration is considered dimensionless.

Denoting by:

$$\text{Pe} = \frac{aV}{\mu} \quad (\text{P\'eclet number}), \quad \text{Sh} = \frac{a\sigma}{\mu} \quad (\text{Sherwood number})$$

two characteristic numbers, the governing Eqs. (3.1)–(3.2) become:

$$\begin{aligned} \frac{\partial \hat{c}}{\partial t} + \bar{\mathbf{v}} \cdot \nabla \hat{c} - \frac{1}{\text{Pe}} \nabla^2 \hat{c} &= 0, \\ \nabla \hat{c} \cdot \mathbf{n} + \text{Sh} \hat{c} &= 0. \end{aligned} \tag{3.3}$$

The physiological and metabolic functions of living beings are typically periodic and an intermittent release of substances (i.e. oxygen, hormones, nutrients, waste products) in the blood is carried out by several organs and glands. For example, respiratory and digestive acts have a period ranging, according to the species, from seconds to hours. It is realistic to assume that, for each substance, there exists a pulsatile source of solute concentration that, advected by the fluid, propagates downstream. As the blood flow is essentially unidirectional, the unsteady component \hat{c} is sought in the form of an harmonic longitudinal travelling wave:

$$\hat{c} = \tilde{c}(r, \psi) e^{i(\omega t - kz)} \tag{3.4}$$

with ω a nondimensional circular frequency ($\omega \rightarrow \omega a/V$) and k the nondimensional wave number ($k \rightarrow ka$). Consequently, the nondimensional wave speed is $\omega/\text{Re}(k)$ and the nondimensional wavelength is $1/\text{Re}(k)$. Because of the explicit dependence on z and t in the waveform Eq. (3.4), neither proximal and distal boundary conditions, nor an initial condition are required.

For the following analysis, it is worth to express the amplitude of the wave (3.4) in terms of a *mass per unit length* defined by:

$$Q := \int_0^1 \tilde{c}(r)rdr \quad (3.5)$$

Concentration wave (3.4) has no direct relation with the pressure wave generated by the heart beat and transmitted by the fluid through the vessel distensibility. In physiological cases, ω is generally very low ($\omega \ll 1$).

4. Asymptotic Analysis

All arteries are affected by a small or moderate degree of curvature. A perturbation method is used to study the influence of a small curvature with respect to the straight case. As the curvature parameter $\varepsilon = a/R$ is assumed to be small ($\ll 1$), the amplitude in Eq. (3.4) is expanded as a power series of ε over an axisymmetric solution $c_0(r)$:

$$\tilde{c}(r, \psi) = c_0(r) + \varepsilon c_1(r, \psi) + \varepsilon^2 c_2(r, \psi) + \dots \quad (4.1)$$

The fluid steady velocity $\bar{\mathbf{v}}$ undergoes a similar expansion over $\bar{\mathbf{v}}_0$:

$$\bar{\mathbf{v}}(r, \psi) = \bar{\mathbf{v}}_0(r) + \varepsilon \bar{\mathbf{v}}_1(r, \psi) + \varepsilon^2 \bar{\mathbf{v}}_2(r, \psi) + \dots \quad (4.2)$$

with $\bar{\mathbf{v}}_0$ is the Poiseuille velocity and $\bar{\mathbf{v}}_1$ is the first order velocity for a moderately curved tube [11]. Therefore one has:

$$\bar{\mathbf{v}} \cdot \nabla \tilde{c} = (\bar{\mathbf{v}}_0 + \varepsilon \bar{\mathbf{v}}_1) \cdot (\nabla c_0 + \varepsilon \nabla c_1) = \bar{\mathbf{v}}_0 \cdot \nabla c_0 + \varepsilon (\bar{\mathbf{v}}_1 \cdot \nabla c_0 + \bar{\mathbf{v}}_0 \cdot \nabla c_1) + \varepsilon^2 \dots \quad (4.3)$$

Expression (3.4) and expansions (4.1)–(4.3) are substituted in Eqs. (3.3), and terms of the same power of ε , up to the first order, are equated.

0-th order solution

The amplitude of concentration in a straight tube is governed by the following linear equation:

$$i\omega c_0 + \bar{\mathbf{v}}_0 \cdot \nabla c_0 - \frac{1}{Pe} \nabla^2 c_0 = 0. \quad (4.4)$$

Letting $\omega_P = \omega_{\text{Pe}}$ (*scaled frequency*) and $k_P = k_{\text{Pe}}$ (*scaled wavenumber*), Eq. (4.4) is rewritten in scalar notations as:

$$\frac{d^2 c_0}{dr^2} + \frac{1}{r} \frac{dc_0}{dr} + i(k_P \bar{w}_0 - \omega_P) c_0 = 0 \quad (4.5)$$

where all terms containing k^2 have been neglected, since large wavelengths are considered in the present application, and

$$\bar{w}_0(r) = 1 - r^2$$

is the Poiseuille axial velocity profile, nondimensionalized by scaling with V .

The boundary conditions associated with the Eq. (4.5) are:

$$\frac{dc_0}{dr} = 0 \quad \text{at } r = 0 \quad (\text{symmetry condition}), \quad (4.6)$$

$$\frac{dc_0}{dr} + \text{Sh} c_0 = 0 \quad \text{at } r = 1. \quad (4.7)$$

For a given frequency ω_P , the Sturm-Liouville eigenvalue problem (4.5)–(4.7) is solved to obtain the wave number k_P which corresponds to an admissible c -wave solution in a straight tube.

Through a variable transformation, we obtain the general integral of Eq. (4.5) written in terms of two constants A and B :

$$c_0(r) = \exp\left(-\frac{G}{2}r^2\right) \left[A\mathcal{L}\left(H - \frac{1}{2}, Gr^2\right) + B\mathcal{U}\left(\frac{1}{2} - H, 1, Gr^2\right) \right] r \quad (4.8)$$

with \mathcal{L} the Laguerre function and \mathcal{U} the Tricomi confluent hypergeometric function with complex argument [10] and with:

$$G = (ik_P)^{\frac{1}{2}}, \quad H = \frac{(ik_P)^{\frac{1}{2}}}{4} \left(1 - \frac{\omega_P}{k_P}\right).$$

A boundedness condition at $r = 0$ implies $B = 0$, and through the boundary condition (4.7), we obtain the *frequency equation*:

$$\left(\sqrt{k_P} + i^{\frac{3}{2}} \text{Sh}\right) \mathcal{L}\left(H - \frac{1}{2}, G\right) + 2\sqrt{k_P} \mathcal{L}_g\left(H - \frac{3}{2}, 1, G\right) = 0 \quad (4.9)$$

where \mathcal{L}_g is the generalized Laguerre function. It gives the set of wavenumbers k_P correspondent to a given frequency ω_P . Finally, replacing in Eq. (4.8), one has:

$$c_0(r) = A \exp\left(-\frac{(ik_P)^{\frac{1}{2}}}{2} r^2\right) \mathcal{L}\left(\frac{(ik_P)^{\frac{1}{2}}}{4} \left(1 - \frac{\omega_P}{k_P}\right) - \frac{1}{2}, (ik_P)^{\frac{1}{2}} r^2\right) r. \quad (4.10)$$

The constant A is determined by using Eq. (3.5).

1st order solution

The correction due to a small curvature is described by the first order linear problem:

$$i\omega c_1 + \bar{\mathbf{v}}_0 \cdot \nabla c_1 - \frac{1}{Pe} \nabla^2 c_1 = -\bar{\mathbf{v}}_1 \cdot \nabla c_0.$$

By letting:

$$c_1(r, \psi) = \check{c}_1(r) \sin \psi, \quad \check{c}_1 \rightarrow c_1 \quad (4.11)$$

we obtain the non homogeneous problem:

$$\begin{aligned} \frac{\partial^2 c_1}{\partial r^2} + \frac{1}{r} \frac{\partial c_1}{\partial r} - \frac{c_1}{r^2} + i(k_P \bar{w}_0 - \omega_P) c_1 \\ = ik_P (r \bar{w}_0 - w_d) c_0 + (Pe u_d - 1) \frac{dc_0}{dr} \end{aligned} \quad (4.12)$$

with the boundary conditions:

$$c_1 = 0 \quad \text{at } r = 0, \quad (4.13)$$

$$\frac{dc_1}{dr} + \text{Sh} c_1 = 0 \quad \text{at } r = 1. \quad (4.14)$$

where u_d and w_d are respectively the nondimensional radial and the axial component of the steady flow in a curved tube [11]. Due to the antisymmetry of the first order solution c_1 (see Eq. (4.11)), the overall mass flux conservation of $c_0 + \varepsilon c_1$ in the half-section $(r, \psi) \in [0, 1] \times [-\pi/2, \pi/2]$ is guaranteed.

Note that the Péclet number appears at the right hand side of Eq. (4.12) as coefficient of u_d . The solution turns out to be strongly dependent on it, because it magnifies the role of secondary flow. Such effect exists as long as a transverse flow—induced by the curvature—is present, and grows with Pe .

5. Numerical Results and Discussion

The frequency Eq. (4.9) is solved numerically with a Newton type method by searching the complex roots k_P corresponding to a given ω_P . Because of the large wavelength, only the smallest root is selected. Results show that both wavelength and attenuation reduce with increasing ω_P and the effect of wall permeability is present only for small frequencies.

The curve connecting the pairs $(\omega_P, \omega_P/\text{Re}(k_P))$ for $\omega_P \in [10^{-3}, 10^5]$ at varying Sh is shown in Fig. 1 (dispersion curve). It turns out that the wave

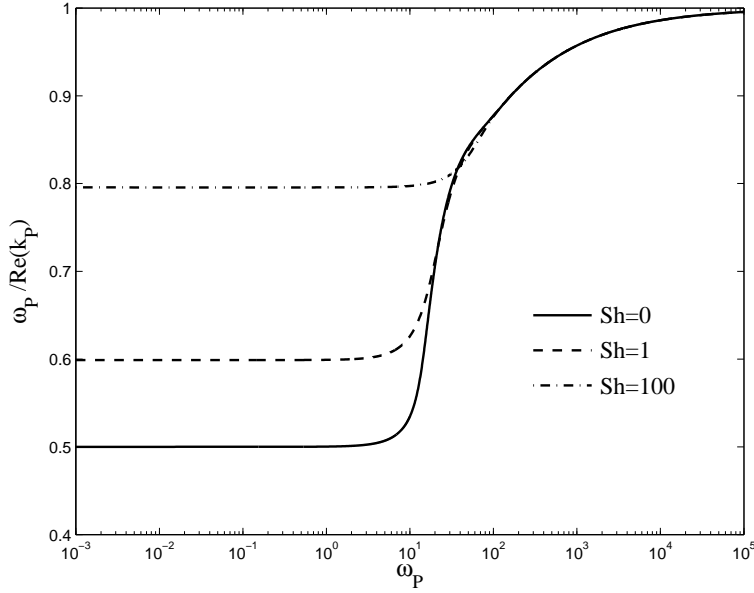


FIGURE 1. Dispersion curves for three different mass transfer coefficients Sh . The wave speed tends to the same asymptotic value for relatively high frequencies and exhibits a variation with Sh only at very low frequencies. In a range of typical frequencies ($10 \leq \omega_P \leq 100$) the speed undergoes a sudden raise.

speed tends to the value 1 (independent of Sh), for relatively large values of the frequency. On the other hand, at very small frequencies the wave speed is rapidly decreasing tending to a finite limit as $\omega_P \rightarrow 0$. Such limit is $1/2$ for $Sh = 0$ and increases with Sh . A critical frequency separates two regimes for each value of Sh : a layer where the velocity undergoes a sudden raise from a larger range where the velocity stays almost constant (Fig. 1).

The exact solution c_0 of the Eqs. (4.5)–(4.7) is given by Eq. (4.10). The boundary value problem (4.12)–(4.14) is then solved numerically with a collocation method using a cubic spline approximating function [12].

Once the analytical 0-th order solution is evaluated and the 1-st order problem solved numerically, the full wave solution is reassembled (see Eqs. (2.3), (3.4) and (4.1)) as:

$$c = \bar{c} + \tilde{c}e^{i(\omega t - kz)} = \bar{c} + (c_0 + \varepsilon c_1 \sin \psi)e^{i(\omega t - kz)}.$$

The physical problem depends on a number of parameters, each of them may vary in a quite wide range, and there is a variety of different limiting cases. In

the present work we will focus the attention on the influence of the solution c on the diffusivity—parametrized by Pe and on the wall permeability—parametrized by Sh . These two parameters are varied in a convenient interval to describe a number of substances dissolved in blood and different medium properties. Other parameters are fixed as:

$$a = 0.5 \text{ cm}, \quad V = 24 \text{ cm s}^{-1}, \quad Q = 0.01.$$

Concentration amplitudes c_0 for three typical values of ω_P are shown in Fig. 2. Approximately flat concentration profiles at low ω_P , are replaced by more oscillating fronts, with a possible undershooting, at higher ω_P . At relatively higher ω_P , the concentration flux occurs in the core of the vessel and is independent of Sh . The influence of curvature is small at low Pe , but becomes relevant at higher Pe , with a more pronounced oscillating profile (Fig. 3). At the high Péclet numbers under consideration ($\approx 10^5$), a noticeable difference with respect to a straight tube appears even for a curvature ratio small as $\varepsilon = 10^{-4}$. The first order solution c_1 is of few orders of magnitude higher than c_0 , and their ratio grows with Pe . A significant result is the

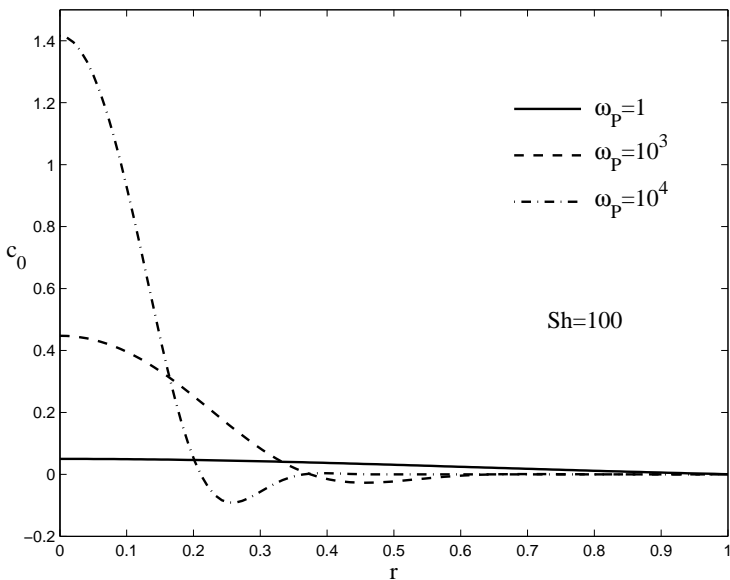


FIGURE 2. Concentration profiles along the horizontal half-diameter ($\psi = \pi/2$) of the cross section $z = 0$ at $t = 0$, for three values of ω_P . Differences with Sh are shown less pronounced and a core flux is evident at higher ω_P .

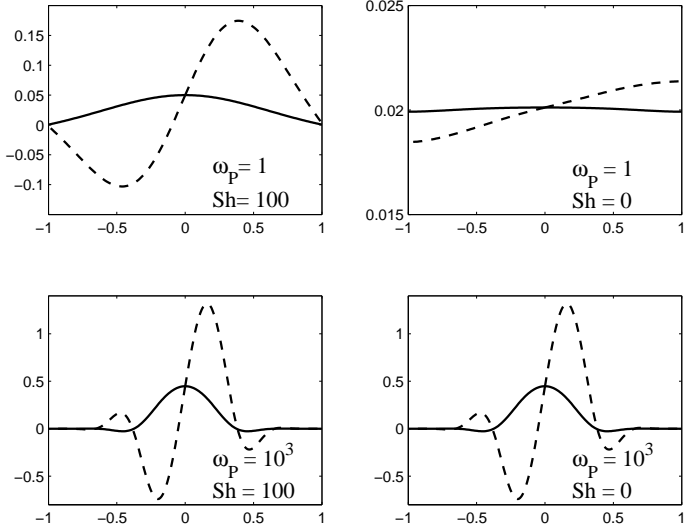


FIGURE 3. Concentration profiles along the horizontal diameter ($\psi = \pm\pi/2$) of the cross section $z = 0$ at $t = 0$ for $Pe = 10^5$. Plots highlight the combined effects of the wall permeability Sh (left-right) and of the wave frequency ω_P (top-bottom) in the case of a straight tube (continuous line) and of a slightly curved tube with $\varepsilon = 10^{-4}$ (dashed line). For such value of Pe , the solution is extremely sensitive to the curvature and, at low frequencies, even to Sh .

skewness of the c profiles: the maximum peak of concentration flux is shifted towards the outer bend and increases in magnitude. Consequently a wall flux reduction at the inner wall of the curvature is reported. This is in correlation with clinical observations of atherosclerotic lesions at the inner wall of arterial bends. The effect of the wall permeability on the concentration waveform is shown to be frequency dependent.

Acknowledgement

The authors are grateful to M. Prosi and P. Zunino for the stimulating discussions and helpful comments.

References

1. G. RAPPITSCH, K. PERKTOLD and E. PERNKOPF, *Numerical modelling of shear-dependent mass transfer in large arteries*, Int. J. Num. Meth. Fluids, **25**: 847–857, 1997.

2. G. KARNER, K. PERKTOLD, H.P. ZEHENTNER and M. PROSI, *Mass transport in large arteries and through the arterial wall*, in: Intra and Extracorporeal Cardiovascular Fluid Dynamics, Adv. Fluid Mech., P. Verdonck and K. Perktold [Eds.] WIT press, Southampton, pp.209–247, 2000.
 3. M. PROSI, K. PERKTOLD, Z. DING and M.H. FRIEDMAN, *Influence of curvature dynamics on pulsatile coronary artery flow in a realistic bifurcation model*, J. Biomech., **37**:1767–1775, 2004.
 4. A. QUARTERONI, A. VENEZIANI and P. ZUNINO, *Mathematical and numerical modeling of solute dynamics in blood flow and arterial walls*, SIAM, J. Num. Anal., **39**(5):1488–1511, 2002.
 5. J.A. MOORE and C.R. ETHIER, *Oxygen mass transfer calculations in large arteries*, J. Biomech. Eng., **119**:469–475, 1997.
 6. D.K. STANGEBY and C.R. ETHIER, *Computational analysis of coupled blood-wall arterial LDL transport*, ASME J. Biomech. Eng., **124**:1–8, 2002.
 7. G. PONTRELLI and A. TATONE, *Wave propagation in a fluid flowing through a curved thin-walled elastic tube*, submitted to Europ. J. Mech., 2005.
 8. M.G. PEDERSEN, R. BERTRAM and A. SHERMAN, *Intra- and inter-islet synchronization of metabolically driven insulin secretion*, Biophys. J. BioFAST, doi:10.1529/biophysj.104.055681, April 15, 2005.
 9. A. QUARTERONI and A. VALLI, *Numerical approximation of partial differential equations*, Springer Series in Comp. Math. 23, Springer-Verlag, Berlin, 1997.
 10. M. ABRAMOWITZ and I.A. STEGUN [eds.], *Handbook of mathematical functions*, Washington DC, National Bureau of Standards, 1972.
 11. W.R. DEAN, *Note on the motion of fluid in a curved pipe*, Phil. Mag., **4**:208–223, 1927.
 12. J.D. PRYCE, *Numerical solution of Sturm-Liouville problems*, Monographs on Numerical Analysis, Oxford University Press, Oxford, 1993.
-

Ultrasonic Doppler Measurement of the Attenuation, Scattering and Blood Hematocrit in the Human Artery

WOJCIECH SECOMSKI¹⁾, ANDRZEJ NOWICKI¹⁾,
and PIERO TORTOLI²⁾

¹⁾*Department of Ultrasound,
Institute of Fundamental Technological Research,
Polish Academy of Sciences, Warsaw, Poland*

²⁾*Electronics and Telecommunications Department,
University of Florence, Italy*

The goal of this work was to develop a clinically applicable method for non-invasive acoustic determination of hematocrit *in vivo* based on the Doppler Ultrasound.

The value of hematocrit (HCT) was determined from the pulse-echo measurements of acoustic attenuation at 20 MHz. The measurements in blood *in vivo* were implemented using 128 gate pulse Doppler flowmeter. The Doppler signal was recorded in the brachial artery and attenuation coefficients were calculated from the appropriate ratios between the received echo amplitudes.

The method proposed appears to be promising for *in vivo* determination of hematocrit, as 5% error is adequate to monitor changes at patients in shock or during dialysis.

Key words: *ultrasound, Doppler, blood, hematocrit*

1. Introduction

At present the only noninvasive method for estimating the blood hematocrit is based on the measurement of speed of sound [7] or near infrared spectroscopy [13] and is mainly used during patient's dialysis. Other applications include patients in the posttraumatic shock, open-heart surgery and anemia. We propose a novel approach to solve this problem. The instrumentation developed is based on the measurement of absorption of ultrasonic

wave in blood independently of the overall attenuation outside the blood vessel. The instrument consists of a 128 gate pulsed Doppler operating at 20 MHz and DSP signal-processing unit.

Time gating of the receiver makes it possible to record echoes returning from a specific depth. The delay of the receiving gate in relation to the transmitted impulse is directly proportional to the distance between the measured volume and transducer surface. Approximately speaking, the measurement volume has the form of a cylinder whose axis overlaps with the symmetry axis of the ultrasound transducer. The cylinder length depends on the duration of the switched-on receiver gate, while the cylinder diameter equals the diameter of the ultrasound beam. Using higher ultrasound frequencies makes it possible to reduce the measurement volume, both its length and diameter.

2. Ultrasonic Attenuation in Blood

When a wave propagates through a medium, its energy is reduced as a function of distance. The energy may be diverted by scattering or absorbed by the medium and converted to heat. The pressure p of a plane wave propagating in the z direction is given by equation:

$$p = p_0 e^{-\alpha z} \quad (2.1)$$

where p_0 is the pressure at $z = 0$ and α is the pressure attenuation coefficient. The total coefficient α is a sum of the attenuation coefficients α_i caused by independent energy losses in the medium:

$$\alpha = \sum_i \alpha_i. \quad (2.2)$$

The blood consists of plasma in which are suspended blood cells, mostly red, erythrocytes. Thus the total attenuation coefficient α in blood can be expressed as:

$$\alpha = \alpha_1 + \alpha_2 + \alpha_3 \quad (2.3)$$

where α_1 is an attenuation coefficient caused by acoustical absorption in blood cells, α_2 relates to absorption in plasma and α_3 is caused by scattering on the cell-plasma boundaries. Total ultrasonic attenuation in blood depends on frequency and is equal to [6]:

$$\alpha = \alpha_0 f^{1.2} \quad (2.4)$$

where $\alpha_0 = 0.021 \text{ Np/cm} = 0.18 \text{ dB/cm}$ [3, 6] and f is the ultrasonic frequency, in MHz. Other authors published $\alpha_0 = 0.014 \dots 0.018 \text{ Np/cm} = 0.12 \dots 0.16 \text{ dB/cm}$ and frequency exponent is equal to $1.19 \dots 1.23$, [5].

To estimate relation between attenuation coefficient α and hematocrit HCT, ratios between coefficients $\alpha_1 \dots \alpha_3$ must be found. Coefficient α_3 is related to the acoustical scattering on the red blood cells only. Those cells consist more than 99% of all blood cells in quantity and volume. For the ultrasonic frequencies $f = 2 \dots 20 \text{ MHz}$, used for medical diagnostics, wavelength is equal to $\lambda = 750 \dots 75 \mu\text{m}$. Average size of the red blood cell $d = 8 \mu\text{m}$ is much less than ultrasonic wavelength. The mismatches in density and compressibility between the cell and the plasma are fairly small. In that case the Born approximation is valid. With the above assumptions, the Green's function approach gives the differential scattering cross-section $\sigma_d(\gamma)$ [12]:

$$\sigma_d(\gamma) = \frac{V_c^2 \pi^2}{\lambda_0^4} \left[\frac{\kappa_e - \kappa_o}{\kappa_o} + \frac{\rho_e - \rho_o}{\rho_e} \cos \gamma \right]^2 \text{ cm}^2/\text{sr} \quad (2.5)$$

where V_c is the volume of the red blood cell, λ_0 is an acoustical wavelength, κ_e , ρ_e and κ_o , ρ_o are the compressibility and mass density of the red blood cell and surrounding plasma, respectively, γ is the angle between the incident and the scattered wave vectors. For the human blood $V_c = 87 \mu\text{m}^3$ called mean corpuscular volume (MCV), $\kappa_e = 34.1 \times 10^{-7} \text{ cm/N}$; $\kappa_o = 40.9 \times 10^{-7} \text{ cm/N}$; $\rho_e = 1.092 \text{ g/cm}^3$; $\rho_o = 1.021 \text{ g/cm}^3$ [11, 12].

The angular scattering coefficient $\sigma_s(\gamma)$ is given by:

$$\sigma_s(\gamma) = \sigma_d(\gamma)(N_c/\Omega)W \text{ 1/cm} \cdot \text{sr} \quad (2.6)$$

where N_c is the total number of the red blood cells in the insonified volume Ω . For the human $N_c/\Omega = 5 \times 10^6 \text{ 1/mm}^3$ [9]. W is the packing factor and can be viewed as a measure of orderliness in the spatial cells arrangement. There is non-linear dependence of W versus hematocrit HCT with maximum at $\text{HCT} \cong 25\%$ [11]. This model is valid for not aggregated blood cells. However aggregation occurs for $\text{HCT} > 25\%$ and increase of scattering coefficient is compensated by decrease of packing factor W .

The total scattering σ can be expressed as:

$$\sigma = \int_{4\pi} \sigma_s(\gamma) d\gamma \quad (2.7)$$

where $d\gamma$ is the differential solid angle.

Thus, from Eqs. (2.5), (2.6), (2.7), for the human blood, the total scattering is given by:

$$\begin{aligned}\sigma &= \frac{V_c^2 \pi^2 N_c N}{\Omega \lambda_0^4} \int_{4\pi} \left[\frac{\kappa_e - \kappa_o}{\kappa_o} + \frac{\rho_e - \rho_o}{\rho_e} \cos \gamma \right]^2 d\gamma \\ &= \frac{3.7352 \times 10^{-10}}{\lambda_0^4} \int_{4\pi} [-0.1663 + 0.0650 \cos \gamma]^2 d\gamma \\ &= \frac{3.7352 \times 10^{-10}}{\lambda_0^4} \times 0.3669 = \frac{1.3704 \times 10^{-10}}{\lambda_0^4}. \quad (2.8)\end{aligned}$$

The scattering attenuation coefficient α_3 , in dB/cm, calculated from equation (2.8) is equal to:

$$\alpha_3 = -10 \log(1 - \sigma(f)) = -10 \log(1 - 2.7070 \times 10^{-7} f^4) \quad (2.9)$$

where f is the ultrasonic frequency in MHz.

The frequency dependence of the ultrasonic attenuation coefficient α and the scattering attenuation coefficient α_3 are presented in Fig. 1 and in Table 1. Even for the highest frequency $f = 20$ MHz, the scattering coefficient α_3 is at least two orders less than total scattering coefficient α and may be neglected. Then ultrasonic attenuation in blood is caused only by acoustical absorption

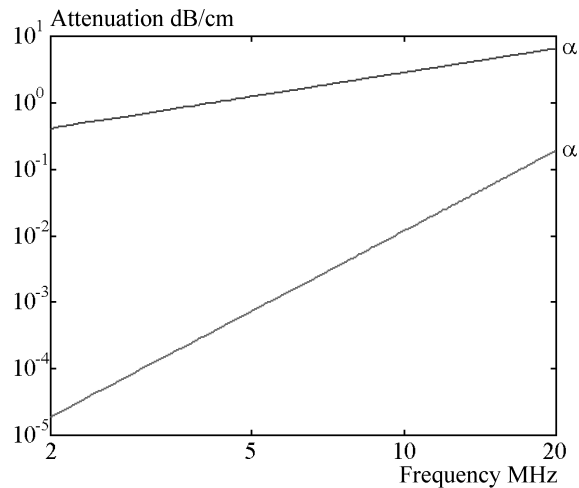


FIGURE 1. Total attenuation coefficient of the human blood α and scattering attenuation coefficient α_3 for frequencies $f = 2 \dots 20$ MHz. Calculated from equations (2.4) and (2.9).

TABLE 1. Calculated and measured values of the total attenuation and scattering attenuation coefficient in blood.

Frequency	2 MHz	5 MHz	10 MHz	20 MHz
Attenuation coefficient α calculated from (4) (dB/cm)	0.41	1.24	2.85	6.55
Attenuation coefficient α measured [2] (dB/cm)	0.4	1.3	3.0	—
Backscattering coefficient $\sigma_s(\gamma = \pi)$ calculated from (6) (1/cm·sr)	6.31×10^{-7}	2.47×10^{-5}	3.95×10^{-4}	6.31×10^{-3}
Backscattering coefficient $\sigma_s(\gamma = \pi)$ measured [11] (1/cm·sr)	—	2.0×10^{-5}	5.4×10^{-4}	—
Total scattering σ calculated from (8) (1/cm)	4.33×10^{-6}	1.69×10^{-4}	2.71×10^{-3}	4.33×10^{-2}
Scattering coefficient α_3 calculated from (9) (dB/cm)	1.88×10^{-5}	7.35×10^{-4}	1.18×10^{-2}	1.92×10^{-1}

in the blood cells and plasma:

$$\alpha = \alpha_1 + \alpha_2. \quad (2.10)$$

The size of the red blood cells is at least one order smaller than length of ultrasonic wave. Absorption depends on the total volume of plasma and the sum of the cells volume. The attenuation coefficient α can be expressed as:

$$\alpha = \frac{V_K}{V} \alpha_K + \frac{V_O}{V} \alpha_O \quad (2.11)$$

where α_K , V_K and α_O , V_O are the absorption coefficient and volume of the red blood cell and plasma, respectively. V is a sum of V_K and V_O . The hematocrit HCT value is given by equation:

$$\text{HCT} = \frac{V_K}{V}. \quad (2.12)$$

Equations (2.10) and (2.11) yield:

$$\alpha = \text{HCT}\alpha_K + (1 - \text{HCT})\alpha_O \quad (2.13)$$

or:

$$\alpha = \alpha_O + \text{HCT}(\alpha_K - \alpha_O). \quad (2.14)$$

Those equations present linear relation of the attenuation coefficient to the hematocrit.

3. Doppler Attenuation Measurement

The attenuation was measured in-vitro from the spectrum of the Doppler signal. In Fig. 2 the initial measurement system is shown. It provides for a measurement of flow velocity at two different depths. In practical terms, this means using two receivers, in which the gate delay has a constant difference, corresponding to the constant distance between measurement volumes Q_1 and Q_2 . The power of the backscattered Doppler signal from the first and the second gate was determined from equations (2.1) and (2.2), respectively,

$$P_{Q1} = P_T T \eta_1, \quad (3.1)$$

$$P_{Q2} = P_T T \eta_2 e^{-4\alpha z} \quad (3.2)$$

where P_T denotes the transmitted acoustic power, T is equal to total loss of the signal between the transducer and the gate Q_1 , η_1 and η_2 denotes the backscattering coefficients of red blood cells in the gates Q_1 and Q_2 respectively, α is equal to the total acoustic attenuation and z the axial distance between the two gates (see Fig. 2).

The backscattering coefficient depends on hematocrit, cell aggregation and concentration of roleaux [8]. The cell aggregation changes with spatial shear rate, acceleration and turbulences [4]. The backscattering coefficient depends on the angle between the flow direction and the transducer axis [1].

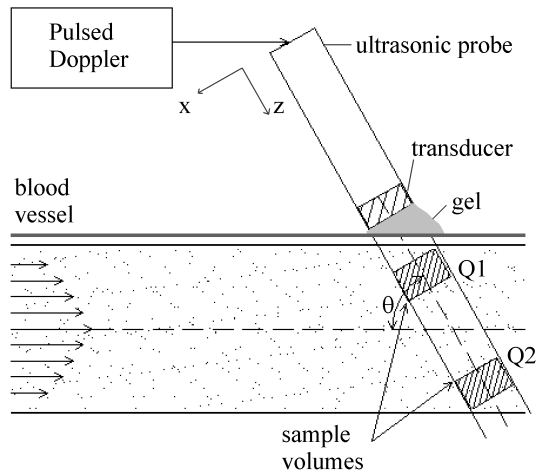


FIGURE 2. The principle of operation of the initial, two gate Doppler hematocrit meter

When the gates (sample volumes) are positioned symmetrically to the center of the vessel, it can be assumed, that:

$$\eta_1 = \eta_2. \quad (3.3)$$

Then, from (3.1) and (3.2) attenuation coefficient can be determined as:

$$\alpha = \frac{\ln(P_{Q1}/P_{Q2})}{4z}. \quad (3.4)$$

The hematocrit value based on pulse-echo measurements and Eq. (2.14) can be then expressed as [10]:

$$HCT = 11.2(\alpha - 3.66). \quad (3.5)$$

As mentioned earlier, 20 MHz Doppler signal was chosen to maximize the sensitivity of the hematocrit meter. The 3 mm diameter, 20 MHz transducer was made of Lithium Niobate crystal and special attention was paid to ensure symmetric distribution of the generated field.

4. Measurements in-vitro

To further examine the Doppler approach, a multigate system with 128 gates was constructed. The tested porcine blood of various hematocrit flew within a plexiglas tube of internal diameter equal to 6.4 mm. A peristaltic pump forced either continuous flow with constant velocity 15 cm/s or pulsatile flow with cyclic velocity variation between -16 cm/s and +68 cm/s. The distance between the axis of the tube and the transducer surface was 4.0 mm. In this way, the sampling volumes were located symmetrically. The value of hematocrit was determined from the ratios of the power Doppler spectra from the two sets of measurements corresponding to laminar and pulsatile flow. The porcine blood assays ranging from 3%...72% HCT. For each hematocrit sample 100 sets of Doppler spectra were recorded, each set being related to all of 128 gates across the vessel. After the spectra were acquired, the data were processed using MatLab™ software (The MathWorks, Natick, MA, USA). For each spectrum recorded in each gate, the power of the flow signal was calculated and Doppler power profile DPP (the distribution of the Doppler power across the vessel diameter) was obtained. The DPP data were used to calculate the value of hematocrit. The averaged linear regression was calculated from the DPP curve. The slope of the regression line

divided by 2 is equal to the attenuation coefficient. The DPP data were used to calculate the value of hematocrit. Next, all measurements were averaged to yield the final value of hematocrit. The results are presented in Fig. 3.

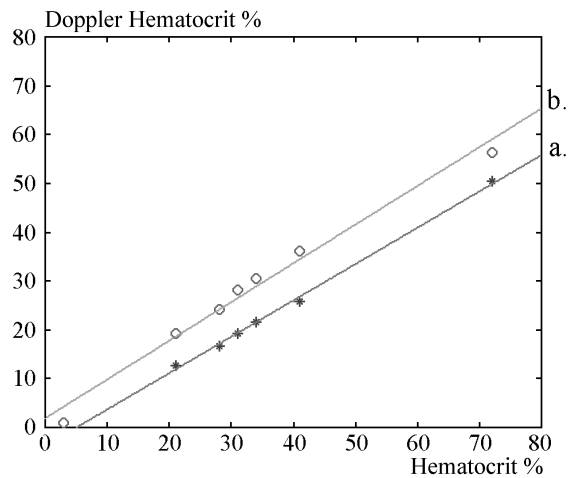


FIGURE 3. Comparison of the results obtained using conventional hematocrit centrifuge and multigate Doppler method for porcine blood; a. constant velocity blood flow; b. pulsatile flow

The correlation coefficient was $R = 0.999$ for continuous flow and $R = 0.992$ for pulsatile flow. The standard deviation was $SD = 0.065 \text{ dB/cm}$ and $SD = 0.239 \text{ dB/cm}$ respectively. The absolute accuracy of Doppler measurements were $\pm 15\%$ HCT for continuous flow and $\pm 4.9\%$ HCT for pulsatile flow.

5. Measurements in-vivo

In vivo measurements of hematocrit were performed on radial artery in 9 volunteers. The hematocrit values varying from 36.4% to 47.4%. For each volunteer 250 sets of Doppler spectra were recorded, each set being related to all of 128 gates across the vessel. The recording was done over a period of 2.5 s; that corresponded to 2 heart cycles. After the spectra were acquired, the data were processed and Doppler power versus depth was calculated. The hematocrit value in vivo was calculated from the Eq. (3.5). The results are presented in Fig. 4.

The correlation coefficient was $R = 0.986$, $n = 9$. The absolute accuracy of Doppler in-vivo measurements in brachial artery were not more than

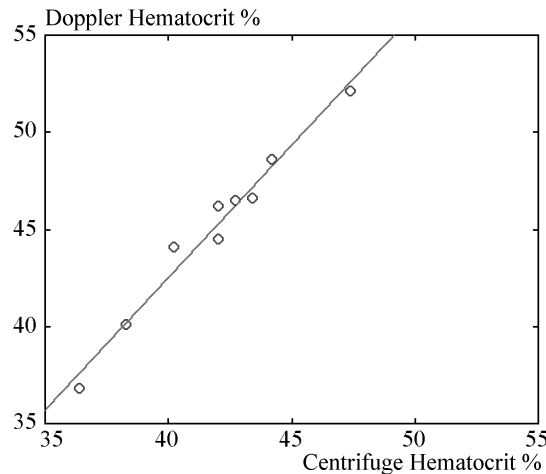


FIGURE 4. Comparison of the results obtained using centrifuge and multigate Doppler method *in vivo* in the brachial artery.

4.7% HCT. The determined error was always positive, the Doppler measurement was always overestimated.

6. Summary

The goal of this work was to develop a clinically applicable method for non-invasive acoustic determination of hematocrit *in vivo* based on the Doppler Ultrasound.

The value of hematocrit (HCT) was determined from the pulse-echo measurements of acoustic attenuation at 20 MHz. The measurements in blood *in vivo* were implemented using 128-gate, 20 MHz pulse Doppler flowmeter. The Doppler signal was recorded in the brachial artery and attenuation coefficients were calculated from the appropriate ratios between the received echo amplitudes.

The attenuation coefficient of ultrasonic wave *in vitro* was determined from the measurements of porcine blood samples with hematocrit varying between 3% and 72%. The *in vitro* experiments indicated that the attenuation coefficient increased linearly with hematocrit. The correlation coefficient was $R = 0.999$ for the continuous blood flow and $R = 0.992$ for pulsatile flow. The *in vivo* measurements were performed in the brachial artery in 9 volunteers. The absolute accuracy of *in vivo* measurements was determined to be within $\pm 5\%$ HCT.

The method proposed appears to be promising for in vivo determination of hematocrit as 5% error is adequate to monitor changes at patients in shock or during dialysis. The multigate system largely simplifies the placement of an ultrasonic probing beam in the center of the blood vessel. Current work focuses on enhancing the method's applicability to arbitrary selected vessels and reducing the HCT measurement error to well below 5%.

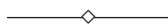
Acknowledgements

The Polish State Committee for Scientific Research grant 5 T07 B03 225 (KBN) supported this work.

References

1. L. ALLARD, G. CLOUTIER, and L-G. DURAND, *Effect of the insonification angle on the Doppler backscattered power under red blood cell aggregation conditions*, IEEE Trans. Ultrason. Ferr., **43**(2):211–219, 1996.
2. E. CARSTENSEN, K. LI, and H. SCHWAN, *Determination of the Acoustic Properties of Blood and its Components*, J. Acoust. Soc. Am., **25**(2):286–289, 1953.
3. S. CHARM and G. KURLAND, *Blood Rheology: Cardiovascular Fluid Dynamics*, D. Bergel [ed.], Academic Press, London and New York 1972.
4. G. CLOUTIER, Z. QUIN, L. DURAND, and B. TEH, *Power Doppler Ultrasound Evaluation of the Shear Rate and Shear Stress Dependencies of Red Blood Cell Aggregation*, IEEE Trans. Biomed. Eng., **43**:441–450, 1996.
5. F. DUCK, *Physical Properties of Tissue, A Comprehensive Reference Book*, Academic Press, London, New York 1990.
6. L. FILIPCZYŃSKI, R. HERCZYŃSKI, A. NOWICKI, and T. POWAŁOWSKI, *Przepływy krwi, hemodynamika i ultradźwiękowe dopplerowskie metody pomiarowe* (Blood flow, haemodynamics, and ultrasonic doppler measurement methods) [in Polish] PWN, Warszawa, 1980.
7. C. JOHNER, P.W. CHAMNEY, D. SCHNEDITZ, and M. KRAMER, *Evaluation of an ultrasonic blood volume monitor*, Nephrol. Dial. Transplant., **13**(8):2098–2103, 1998.
8. B. LIM and R. COBBOLD, *On the relation between aggregation, packing and the backscattered ultrasound signal for whole blood*, Ultrasound Med. Biol., **25**(9):1395–1405, 1999.
9. S. PAWEŁSKI and S. MAJ, *Normy i kliniczna interpretacja badań diagnostycznych w medycynie wewnętrznej* (Guidelines and clinical interpretation of diagnostic measurements in medicine) [in Polish], PZWL Warszawa 1981

10. W. SECOMSKI, A. NOWICKI, F. GUIDI, P. TORTOLI, and P.A. LEWIN, *Non-invasive, in-vivo measurements of hematocrit*, J. Ultras. Med., **22**(4) : 375–384, 2003.
11. K. SHUNG, R. SIGELMANN, and J. REID, *Scattering of ultrasound by blood*, IEEE Trans. Biomed. Eng., **BME-23**(6) : 460–467, 1976.
12. K. SHUNG, and G. THIEME, *Ultrasonic scattering in biological tissues* CRC Press, Boca Raton 1993.
13. S.B. ZHANG, B.R. SOLLER, S. KAUR, K. PERRAS, and T.J. VANDER SALM, *Investigation of noninvasive in vivo blood hematocrit measurement using NIR reflectance spectroscopy and partial least-squares regression*, Appl. Spectroscopy, **54**(2) : 294–299, 2000.



Patient Temperature in Cardiac Surgery—Model Development and Experiments

N.M.W. SEVERENS^{1,2)}, W.D. VAN MARKEN LICHTENBELT³⁾
G.M.J. VAN LEEUWEN¹⁾, A.A. VAN STEENHOVEN¹⁾
and B.A.J.M. DE MOL²⁾

¹⁾ *Technische Universiteit Eindhoven*
PO Box 513, 5600 MB Eindhoven, The Netherlands
n.m.w.severens@tue.nl

²⁾ *Academic Medical Center*
PO BOX 22660, 1100 DD Amsterdam, The Netherlands

³⁾ *Maastricht University*
PO BOX 616, 6200 MD Maastricht, The Netherlands

During cardiac surgery the body is cooled by means of the heart lung machine in order to protect vital organs like heart and brain. Afterwards the body is rewarmed followed by decoupling of the heart lung machine. However, due to unnatural distribution of body heat (relatively cold periphery) often an undesirable drop of core temperature occurs. This 'afterdrop' adversely affects recovery. This article details about the development of a mathematical model to understand the heat transfer processes in the body during surgery. With the numerical model we can mimic the temperature distribution in a human body during and after cardiac surgery. Measurement data is being collected that can be used as input data in the model and for validation of the model. In this way we get more insight into the occurrence and prevention of afterdrop.

1. Introduction

For over four decades, whole body hypothermia has been widely used to reduce metabolic demand and protect vital organs during open heart surgery. During cardiac surgery with cardiopulmonary bypass—the majority of car-

diac surgical interventions—cooling is performed by means of the heart lung machine (HLM). The procedure consists of six distinct phases as detailed below and shown in Fig.1.

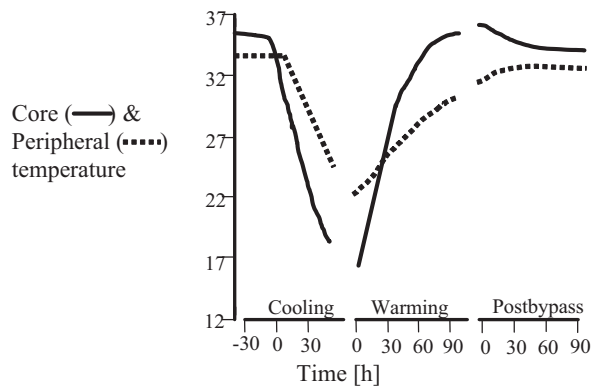


FIGURE 1. Core and peripheral temperatures during and after deep cardiopulmonary bypass. Adapted from Rajek [9].

1. The patient is anaesthetized. Due to anaesthetics the patient's metabolic rate is lowered and the threshold for vasoconstriction shifts to lower core temperatures. Furthermore the anaesthetics often contain vasodilatators. This leads to a lowering of the core temperature of approximately 2°C (not shown in Fig.1) [6].
2. The first stage of the actual surgery: the thorax is opened.
3. The body is connected to a HLM whereby the blood is circulated through the machine. Blood from the HLM enters the body through a tube inserted in the aorta. The oxygenator of the HLM contains a simple heat-exchanger in which the heat exchanging fluid is water. In this stage the patient is cooled further by adjusting the temperature in the heat exchanger.
4. The main cardiac surgical procedure takes place during which the body is kept at a constant low temperature. The temperature during surgery depends on the surgical intervention e.g. for aorta valve replacements and coronary artery bypass grafts 30°C is a common temperature, whilst during surgery on the aortic arch the patient is cooled to 16–18°C.

5. On nearing completion of the surgical procedure the body is warmed at a steady rate by adjusting the water temperature of the heat exchanger. Rewarming must not take place too rapidly in order to prevent cell damage. Core body parts (thorax and brain) react faster on rewarming than peripheral parts (arms and legs).
6. Once the core organs have reached the target temperature the patient is disconnected from the HLM and the temperature of the body is allowed to self equilibrate. This often results in a phenomenon known as afterdrop: a decrease in the temperature of the core organs. The afterdrop effect is considered to be a result of the large temperature difference between the core and peripheral regions at the moment of decoupling [11].

Patients who experience a large afterdrop need longer to recover and may experience more post-operative complications [8] than patients who are not hypothermic after surgery. Clinicians try to prevent or at least minimize the afterdrop effect as much as possible. Often forced-air heating blankets that are draped over the patients legs are used in the rewarming phase. In this way the temperature gradient between the core and the periphery decreases.

For the prevention of the afterdrop effect more knowledge about heat transfer in the anaesthetized human body during cardiac surgery is needed. We are building a numerical thermal model of the patient that can be used by a clinician to determine the optimal warming protocol in order to avoid afterdrop.

2. Whole Body Model

2.1. General Model

The computational model that is being developed is based on descriptions of Fiala [2, 3] who developed a thermal model for predicting human thermal and regulatory responses. We extended the model in such a way that it is also applicable to cardiac surgery.

The numerical model approximates the geometry of the human body with a sphere (head) and cylindrical elements, see Fig. 2. Each element consists of different tissue layers (bone, muscle, fat, skin). The tissue layers consist of one or more nodes. The temperature at the tissue nodes are calculated by

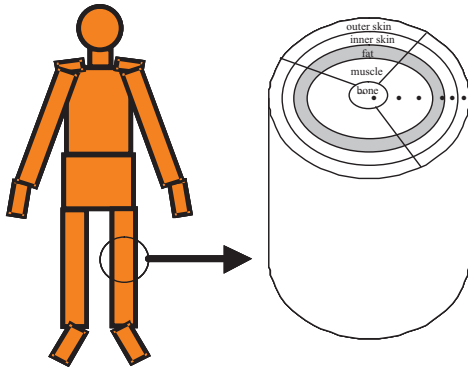


FIGURE 2. Schematic drawing of the human body model. On the right side a detail picture is given of the tissue layers in the leg.

solving the Pennes bioheat [7] equation for each time step:

$$\begin{aligned} \rho c \frac{\partial T}{\partial t} &= \nabla k \cdot \nabla T + \rho_b c_b w_b (T_a - T) + q_m & (2.1) \\ \text{storage} &= \text{conduction} + \text{convection} + \text{heat production} \end{aligned}$$

with ρ tissue density, c specific heat, T_a local arterial blood temperature, T tissue temperature, t time, k thermal conductivity, w volumetric blood perfusion rate [$\frac{\text{m}^3 \text{blood}}{\text{m}^3 \cdot \text{s}}$], q_m metabolic heat production and subscript b denoting blood properties. The partial derivatives with respect to radius were approximated by using a central difference method. On the interface between two adjoining tissue layers, boundary conditions are used that impose continuity of temperature and heat flux across the interface.

The arterial blood temperature in the human model is calculated by assuming that the returning venous blood is mixed in a virtual mixing vessel. The temperature of the mixed venous blood is the new arterial temperature. For some elements counter current heat exchange (CCX) between arteries and veins takes place. Local temperature T_a is in that case the arterial temperature after CCX.

The heart lung machine is implemented in the model in such a way that the temperature of the arterial blood that enters the body can be prescribed. This temperature is used instead of the mixing vessel temperature of the venous blood.

Autonomous thermoregulation by the body occurs in four ways: vasodilatation, vasoconstriction, shivering and sweating. Thermoregulation is described in the model by implementing control equations based on regression analysis of Fiala [3]. Fiala derived equations that give a description how the human body adapts to changes in the environment so as to maintain its normal temperature. These thermoregulatory responses are determined by the deviation of core temperature and average skin temperature from their neutral values: $\Delta T_i = T_i - T_{i,\text{neutral}}$. The control equation for e.g. vasoconstriction (C_s [-]) reads:

$$C_s = 35[\tanh(0.3\Delta T_{sk,m} + 1) - 1]\Delta T_{sk,m} + 3.9\Delta T_{sk,m} \frac{dT_{sk,m}}{dt}$$

where $T_{sk,m}$ is the mean skin temperature. C_s has a minimum value of 0. A similar type of equation can be used to describe vasodilatation (D_l [W/K]). Because of the hypothermic situation in cardiac surgery vasodilatation will not occur ($D_l = 0$). Vasodilatation and vasoconstriction affect the volumetric perfusion of the inner skin layer, but not the blood flow in the other tissue types. Defining $\beta_i = \rho_b c_b w_b$ the expression for tissue blood flow is of the following form:

$$\beta_i = f \times 2^{\frac{T_i - T_{i,0}}{10^\circ C}} \quad (2.2)$$

with

$$f = \frac{\beta_{0,i} + a_{dl,i} D_l / V_i}{1 + a_{cs,i} C_s e^{-D_l/50}} \quad \text{for inner skin layer} \quad (2.3)$$

$$f = 1 \quad \text{for other tissue}$$

in which $a_{dl,i}$ and $a_{cs,i}$ are the distribution factor of vasodilatation and vasoconstriction respectively and V_i is the volume [m^3] of segment i . Equation (2.2) is based on the Q10-criterium as first mentioned by Stolwijk [12]: a 10 $^\circ C$ temperature decrease will halve the blood flow.

For shivering (Sh [W]) a similar type of control equation as for vasoconstriction has been developed. Shivering leads to extra metabolism in muscle tissue according to:

$$q_{i,\text{Sh}} = a_{sh,i} \text{Sh} / V_i \quad (2.4)$$

which must be included in q_m in Eq. (2.1). In Eq. (2.4) $a_{sh,i}$ is the distribution factor for shivering. The shivering induced perfusion in muscle tissue is given by [5]:

$$\beta_{i,\text{Sh}} = 0.932 q_{i,\text{Sh}}. \quad (2.5)$$

The coefficient 0.932 in Eq. (2.5) is estimated on the basis of the amount of oxygen that blood needs to supply for extra work in muscle tissue [1].

2.2. Adaptation for Anesthesia

Additionally adaptations are made that modify the thermoregulation equations for a situation where the patient is anaesthetized. Sessler [10] showed that thermoregulatory thresholds in anaesthetized subjects differ from unaesthetized subjects. During general anaesthesia the thresholds for vasoconstriction and nonshivering thermogenesis change from $\approx 36.7^{\circ}\text{C}$ to $\approx 34.5^{\circ}\text{C}$. Similarly, the thresholds for active vasodilatation and sweating increase $\approx 1^{\circ}\text{C}$. Shivering rarely occurs during anesthesia and even if it is triggered it is most time prohibited by muscle relaxants.

Van Leeuwen [5] implemented anesthesia parameters that take into account the lowering of the vasoconstriction and shivering thresholds. Temperature shift parameters are introduced to describe the threshold change for thermoregulatory responses during anaesthesia e.g.: $\Delta T_{cs,ca} = \Delta T_{cs,ca}$, where ca is a measure for the level of anaesthesia and $\Delta T_{cs,ca}$ is the shift in vasoconstriction threshold at the specific anaesthesia level. The parameters ΔT_{cs} and ΔT_{sh} are fixed input parameters. The values that are used for these parameters in the preliminary simulation given in paragraph 2.3 are -4°C and -5°C respectively.

Some phases during surgery may exist in which the effects of anaesthetics wear off. This is taken into account by adjusting the magnitude of ca where the normalized value of ca is between 0 and 1. The washout of the anaesthetic parameter ca is modelled as follows:

$$\frac{dca}{dt} = \frac{ca_{in} - ca(t)}{\tau_1} - \frac{ca(t)}{\tau_2} \quad (2.6)$$

in which ca_{in} is the supply of anaesthetics, and τ_1 and τ_2 time constants describing the average diffusion and decay.

The control equation for vasoconstriction under anesthesia has become:

$$\begin{aligned} Cs = & 35[\tanh(0.3(\Delta T_{sk,m} - \Delta T_{cs,ca}) + 1) - 1](\Delta T_{sk,m} - \Delta T_{cs,ca}) \\ & + 3.9(\Delta T_{sk,m} - \Delta T_{cs,ca}) \frac{dT_{sk,m}}{dt} - ca \times Av. \end{aligned}$$

In practice administration of anaesthetics is accompanied by a loss of vascular tone and an increase in peripheral blood flow. This is modelled by adding

the negative term $ca \times Av$ in the control equation for vasoconstriction. The vasotone parameter Av was set to 80 [5].

During cardiac surgery muscle relaxants are administered to the patient that prohibit shivering. Towards the end of the intervention the administered dose muscle relaxants can decline. The control equation for shivering then reads:

$$\begin{aligned} Sh = & 10[\tanh(0.5(\Delta T_{sk,m} - \Delta T_{sh,ca}) + 3.6) - 1](\Delta T_{sk,m} - \Delta T_{sh,ca}) \\ & - 28(\Delta T_{hy} - \Delta T_{sh,ca}) + 1.7(\Delta T_{sk,m} - \Delta T_{sh,ca}) \frac{dT_{sk,m}}{dt} - 30 \quad (2.7) \end{aligned}$$

where T_{hy} the hypothalamus/core temperature. Furthermore administration of anaesthetics lowers the metabolic rate. This effect was modelled by adjusting the heat production term in (2.1) in the following way:

$$q_m = q_m(1 - ca \times q_{ca}) + q_{Sh}$$

where q_{ca} is set to 0.15 Wm^{-3} for the standard anatomy.

2.3. Example: Cardiac Surgery

With the current model we simulated a complete cardiac surgical procedure with characteristics as in Table 1. In the simulation shivering is impaired during the first two phases. During the second last and last phase ($t = 160$ – 270 min.) we assume that shivering is re-establishing according to (2.6) and (2.7). Also vasomotion is returning to a normal level.

TABLE 1. Characteristics of simulation of the surgical procedure.

Time [min]	Simulation
0–70	Supply anaesthetics: $ca = 1$, $T_\infty = 18^\circ\text{C}$, shivering prohibited
70–160	Cooling patient till 30°C , $ca = 1$, shivering prohibited
160–210	Rewarming till 37°C , using heating blanket, $ca = 0$
210	Decoupling from heart lung machine, using heating blanket, $ca = 0$

In Fig. 3 preliminary results of core and peripheral temperatures are shown during cardiac surgery. This result shows the main temperature characteristics as also observed in Fig. 1, such as the slower reaction of the periphery compared to the core to the arterial blood temperature changes prescribed by the HLM and the characteristic afterdrop after decoupling the

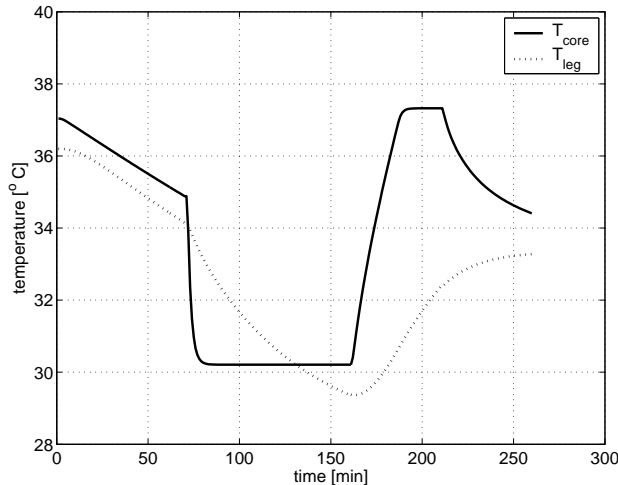


FIGURE 3. Core and peripheral temperature simulations of a cardiac surgery. The solid line gives the core (brain) temperature and the dashed line gives the temperature of the periphery *viz.* muscle layer in the leg.

HLM. Uncertainties in the model exist about the moment shivering actually starts and the chosen values in the vasomotion relations during surgery. Clinical data is now being collected to validate and refine the control equations—vasodilatation, vasoconstriction and shivering—of patients that undergo open heart surgery.

3. Experimental Methods

With approval from the Medical Ethical Committee of the Academic Medical Center of Amsterdam we are studying 16 patients undergoing aorta valve replacement. The aim of the study is to find a relation between different cooling/rewarming procedures and the core-periphery gradient with corresponding changes in perfusion. The study results will be used to deduct relations of thermoregulation—changes in perfusion by vasomotion—of cardiac patients during anesthesia that can be used in the numerical model.

3.1. Protocol

We enroll only patients aged 60–80 years. Patients are cooled during cardiopulmonary bypass to a minimum nasopharyngeal temperature of 30°C. They are rewarmed on completion of surgery to a nasopharyngeal tempera-

ture of 37–37.5°C and a rectal temperature of minimally 36.3°C. The ingoing blood temperature is maximum 4°C warmer than the temperature that leaves the patient's body. The flow rate of the heart lung machine is set to approximately 2.4 L/min per m² body surface.

A schematic overview of the experimental setup at the operating theater is depicted in Fig. 4. The same setup is used at the intensive care unit, with the exception of the heart lung machine. Eight patients will be covered with forced-air warming blankets during the rewarming phase and the other eight patients are rewarmed without using heating blankets. After disconnecting the HLM, patients are transferred to the intensive care unit where they are covered by standard draping.

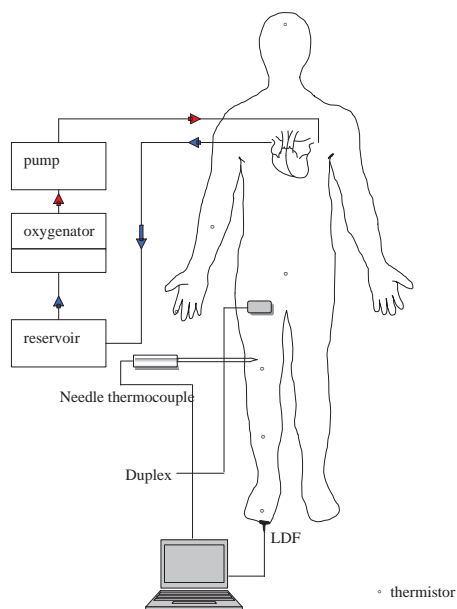


FIGURE 4. Setup in operating theater. The patient is connected to a heart lung machine that consists of: a reservoir, an oxygenator with heat exchanger and a pump. All used measurement techniques are shown at the measurement position: wireless thermistors (iButtons) depicted by \circ , needle thermocouple in the upper thigh, Laser Doppler Flowmetry on the big toe, Duplex measurements in the femoral artery.

3.2. Methods

Before surgery the patients's body characteristics are measured: length, weight, length of the thigh and lower leg, circumference of the mid-upper thigh, mid-lower thigh, mid-upper calf and mid-lower calf.

Data is collected during surgery and the first six hours at the intensive care unit. Blood pressure and heart rate are recorded every minute. Core temperatures are measured from the nasopharynx. Temperatures in the rectum and in the pulmonary artery are measured once per minute. Leg tissue temperature is determined using needle thermocouples (Physitemp Instruments Inc.) with three sensors at 8-, 18-, and 38-mm. The needles are inserted perpendicular to the skin surface slightly lateral from the anterior midupper right thigh. Mean skin temperature according to the seven-point system of Hardy/Dubois [4] is determined by performing measurements with wireless thermistors (iButton) at the forehead, lower arm, finger tip, foot dorsum, lower leg, upper leg and abdomen. In order to measure thermoregulatory changes skin perfusion is measured by Laser Doppler Flowmetry (Perimed) on the right big toe. The many arteriovenous shunts under the toe show very strong responses to temperature. The calf-minus-toe skin-surface gradient is also used as an indicator for vasoconstriction and vasodilation [6]. Blood supply to the leg is measured by Duplex-measurements in the right femoral artery. Diameter and centerline velocity in the artery are measured at four defined points in time.

4. Outlook

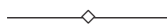
Measurements have started in the surgery room and intensive care unit. The resulting data will be used for further development of the model. Furthermore the heat loss from the opened thorax during cardiac surgery will be studied what must eventually lead to adjustment of the thorax cylinder in the whole body model.

Acknowledgement

We are fortunate that in building our own model we could build on the model developed by dr. Fiala, now at De Montfort University (UK).

References

1. R.F. BURTON, *Physiology by Numbers; an encouragement to quantitative thinking*, 2nd ed. Cambridge UK: Cambridge University Press, 2000.
2. D. FIALA, K.J. LOMAS, and M. STOHRER, *A computer model of human thermoregulation for a wide range of environmental conditions: the passive system*, J. Appl. Physiol., **87**(5):1957–1972, 1999.
3. D. FIALA, K.J. LOMAS, and M. STOHRER, *Computer prediction of human thermoregulatory and temperature responses to a wide range of environmental conditions*, Int. J. Biometeorol., **45**:143–159, 2001.
4. J.D. HARDY and E.F. DUBOIS, *The technic of measuring radiation and convection*, J. Nutr., **15**:461–475, 1938.
5. G.M.J. VAN LEEUWEN, F.E.M. JANSSEN, W.D. VAN MARKEN-LICHTENBELT, B.A.J.M. DE MOL, and A.A. VAN STEENHOVEN, *Modelling patient temperature for improved thermal management during surgery*, Proceedings of The ASME-ZSIS International Thermal Science Seminar II, Bled, Slovenia, pp.362–368, 2004.
6. T. MATSUKAWA, D.I. SESSLER, A.M. SESSLER, M.B.A. SCHROEDER, M. OZAKI, A. KURZ, and C. CHENG, *Heat flow and distribution during induction of general anesthesia*, Anesthesiology, **82**:662–673, 1995.
7. H.H. PENNES, *Analysis of tissue and arterial blood temperatures in the resting human forearm*, J. Appl. Phys., **1**(2):93–122, 1948.
8. K.H. POLDERMAN, *Application of therapeutic hypothermia in the intensive care unit: opportunities and pitfalls of a promising treatment modality-Part 2: Practical aspects and side affects*, Intensive Care Med, **30**:757–769, 2004.
9. A. RAJEK, R. LENHARDT, D.I. SESSLER, M. GRABENWÖGER, J. KASTNER, P. MARES, U. JANTSCH, and E. GRUBER, *Tissue heat content and distribution during and after cardiopulmonary bypass at 17°C*, Anesth. Analg., **88**:1220–1225, 1999.
10. D.I. SESSLER, *Deliberate mild hypothermia*, Neurosur. Anesthesiology, **7**(1):38–46, 1995.
11. D.I. SESSLER, *Perioperative heat balance*, Anesthesiology, **92**:587–596, 2000.
12. J.A.J. STOLWIJK, *A mathematical model of physiological temperature regulation in man*, NASA CR-1855, 1971.



Vascular Model of Heat Transfer in Perfused Tissue

MACIEJ STAŃCZYK

*Institute of Fundamental Technological Research
Polish Academy of Sciences
ul. Świętokrzyska 21, 00-049 Warsaw, Poland
mstan@ippt.gov.pl*

The vascular model of the bio-heat transfer for soft living tissues is described, along with its numerical implementation. Main concepts of the method are discussed and the proposed approach to the number of problems is described in detail. These include: description and generation of the tissue vasculature, tissue and blood domain discretization, method for calculation of temperatures in the coupled tissue-blood system and its numerical aspects.

Algorithms implemented in the computer programs are described and example results are presented. Various aspects of numerical and practical nature are discussed, and the conclusions are indicated with examples and comparisons of generated structures and results.

The most important assumptions made are highlighted and the possibilities of extending the presented method are indicated. Finally, the direction of further research and possibilities created by the presented method are discussed.

Key words: *bioheat equations, soft tissue modelling, vascular models*

1. Introduction

Transport of heat in living biological tissues is a very complex phenomenon. The tissue is invariably an inhomogeneous, anisotropic material and a scene for various processes influencing the heat balance. The muscle contraction is the most notable example of heat-generating process. Also there is a plethora of transport processes concerning various body fluids. These fluids convect heat between domains of the tissue and supplement the conductive mode of heat transfer.

The influence of the circulating fluid on the heat balance is most prominent in the case of soft tissue perfused with blood. The blood flows through the vessels forming a circulatory system. The heart supplies the pressure driving the blood through the branching system of vessels that get smaller and smaller in size, until they reach the level of capillaries. At that point the blood drains into the small venous vessel that drain into larger and larger vessels ultimately bringing the blood to the heart to complete the circulation.

There are numerous refinements and exceptions to the simple picture sketched above, but it is realistic enough to serve as a basis for the further considerations of the influence of blood flow on the heat transfer in tissue. The temperature of the blood as it traverses the vessels of subsequent generations is schematically depicted in Fig. 1. The most important conclusion from this figure is the fact that the temperature of the blood is significantly different from that of the tissue only when the blood is in relatively large vessels. The thermal equilibration between the tissue and the blood vessels becomes an increasingly quicker process with the decreasing vessel diameter. This fact is even more pronounced in the data presented in Table 1. In this table the basic characteristic data for different generations of vessels are given along with the *thermal equilibration length* defined as the vessel length required for the difference of temperature between the blood (in the vessel) and the surrounding tissue to drop by the factor of e.

TABLE 1. Properties of different generations of blood vessels, after [7]; x_{eq} —thermal equilibration length.

vessel	% vascular volume	avg. radius [μm]	avg. length [mm]	x_{eq} [mm]
aorta	3.30	5 000	380	190 000
large artery	6.59	1 500	200	4 000
arterial branch	5.49	500	90	300
terminal art. branch	0.55	300	8	80
arteriole	2.75	10	2	0.005
capillary	6.59	4	1.2	0.0002
venula	12.09	15	1.6	0.002
terminal vein	3.30	750	10	100
venous branch	29.67	1 200	90	300
large vein	24.18	3 000	200	5 000
vena cava	5.49	6 250	380	190 000

The facts presented in Fig. 1 and Table 1 are sometimes simplified in order to create a specific models of heat transfer. The Pennes equation assumes

that no heat transfer between blood vessels and tissue takes place until the level of capillaries is reached, the heat exchange being immediate and complete at that level (x_{eq} is large for large vessels because of their large heat content). Conversely, the Wulff model of directed perfusion assumes that blood is equilibrated thermally with tissue all the time ($x_{eq} = 0$).

The models of heat transfer in perfused tissue (bio-heat equations) available in literature can be basically divided in two classes, the continuum models and the vascular models. The brief description of these is presented in the following.

1.1. Continuum Models

The continuum models describe the perfused tissue without regarding individual blood vessels, by means of a single tissue temperature. The bio-heat equation describes the balance of energy in terms of that temperature, taking into account the blood flow via additional source terms or effective conductivity. We now review three most important continuum models.

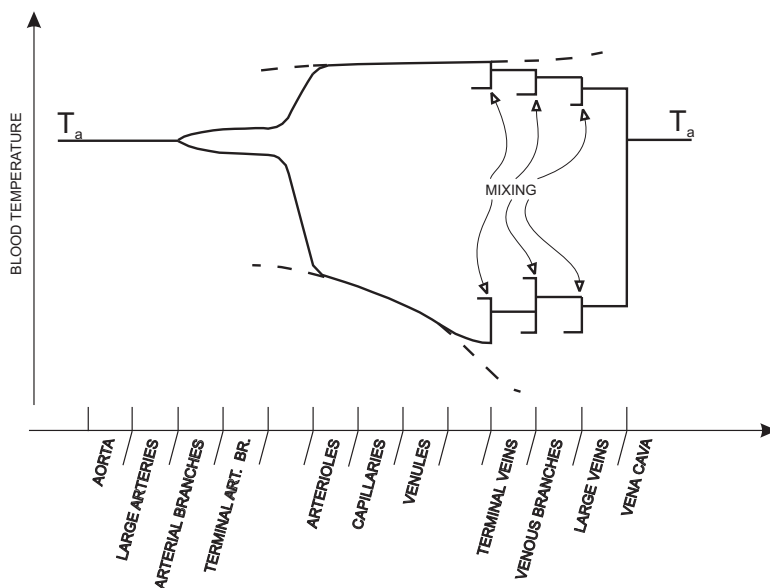


FIGURE 1. The temperature of the blood as it traverses the generations of blood vessels. The blood reaches two portions of tissue: colder than aorta blood temperature and hotter than aorta blood temperature. These two tissue temperatures are schematically indicated by the dashed line, after [7].

1.1.1. Pennes model. The Pennes model has been postulated by Harry Pennes in 1948 as a result of series of experiments aimed at measuring the temperature profile in a resting human forearm, [9]. To explain the measurement results, Pennes assumed that the essential site of blood-tissue heat exchange are capillary vessels. The blood was supposed to reach these vessels at the so-called arterial supply temperature T_a , and leave them at venous return temperature, which was postulated by Pennes to be equal to local tissue temperature. In the most common form, the Pennes equation also assumes that material is isotropic and material constants are independent of temperature

$$\rho c \frac{\partial T}{\partial t} = \lambda \nabla^2 T + w_{bl} c_{bl} (T_a - T) + q_m \quad (1.1)$$

where ρ and c denote tissue density and specific heat respectively, λ is tissue conductivity, w_{bl} and c_{bl} are blood perfusion rate and specific heat respectively while q_m is the volumetric heat source (of metabolical origin).

The most important parameter in the Pennes equation is the perfusion rate, expressed in kg_{blood} per m³_{tissue} per second. It is characteristic for the given type of tissue and varies in the considerable range.

There is a vast amount of literature concerning the Pennes equation. For a detailed review the reader is referred to [12] and the references therein. The Pennes equation is undoubtedly the most popular model of bio-heat transfer and, without question, the simplest. Yet it often yields better agreement with experiments than the more elaborate models. Final remark of this brief introduction of Pennes equation: fifty years after the publication of the original paper by Pennes, Eugene Wissler critically assessed the original work of Pennes and his experimental results, [18]. Wissler concludes that the procedure adopted by Pennes was faulty and his conclusions—unfounded. Therefore it would seem that the model called by many simply “the bio-heat equation” was arrived at by chance.

1.1.2. Wulff model of directed perfusion. In 1974 Wulff raised several critical objections to the Pennes model, [19]. The most important ones were that thermal equilibration in the pre-capillary vessels should not be neglected, and that the possibly directed character of the blood flow should be taken into account.

Wulff postulated that the flow of the blood through the tissue region should be modelled in terms of the Darcy velocity \mathbf{U} . He also assumed that

the blood is always at the local tissue temperature. Resulting model is the usual heat conduction equation with an advective term:

$$\rho c \frac{\partial T}{\partial t} = \lambda \nabla^2 T - \rho_{\text{bl}} c_{\text{bl}} \mathbf{U} \cdot \nabla T + q_m.$$

The Wulff model is not nearly as popular as Pennes equation. The assumption of instantaneous equilibration is clearly not satisfied for every vessel, cf. Fig. 1. Also blood flow is not always unidirectional, in fact this is almost never the case, and vessels most often form countercurrent pairs. For further discussion of the Wulff model the reader is referred to [12].

1.1.3. Effective conductivity models. This class of models lumps all the effects of the blood flow into an effective conductivity coefficient of the tissue. Some models assume simply that this effective tissue conductivity is proportional to first or second power of the perfusion-like parameter characterizing blood flow. The theoretical foundation for this class of models has been provided by Weinbaum and Jiji in 1985.

In the model presented in [15] they assumed that all the vessels, important to bio-heat transfer, take form of counter-current artery-vein pairs and there exists a dominant direction \mathbf{m} of these pairs at every point in the tissue. They also assumed that the dominant mode of heat transfer is incomplete counter-current exchange between the vessels in the pair, and the local tissue temperature can be approximated by blood average temperature. These, and a number of other assumptions served to derive the following equation:

$$\rho c \frac{\partial T}{\partial t} = \nabla(\boldsymbol{\lambda}_{\text{eff}} \nabla T) + q_m - \frac{\pi^2 n r^2 \lambda_{\text{bl}}^2}{4\sigma\lambda} \text{Pe}^2 (\mathbf{m} \cdot \nabla T) \text{div } \mathbf{m}$$

where n is a number density of vessel pairs in the tissue, r is the radius of a single vessel, σ is a constant shape coefficient of heat transfer and Pe is the Péclet number of blood flow in the vessel. For a detailed derivation of the equation and definition of the quantities involved, the reader is referred to the original paper [15]. The quantity $\boldsymbol{\lambda}_{\text{eff}}$ is the effective conductivity tensor and is defined by

$$\boldsymbol{\lambda}_{\text{eff}} = \lambda \left(\mathbf{I} + \frac{n\pi^2 r^2 \lambda_{\text{bl}} \text{Pe}}{4\sigma\lambda} \mathbf{m} \otimes \mathbf{m} \right)$$

where \otimes denotes tensor product.

The introduction of Weinbaum-Jiji model has initiated a long-lasting discussion about the validity of the most important assumptions used. In their later paper, Weinbaum and Jiji suggest that the areas of applicability of their model are restricted to a range of vessel diameters and proposed a suitable criterion, [16], see also [6]. For more complete review of the objections raised against the Weinbaum-Jiji model and the remedies proposed, the reader is referred to [12].

1.2. Vascular Models

Vascular models describe the process of heat transfer between the blood in vessels, characterized by blood temperature and the tissue characterized by the tissue temperature. No assumption is made *a priori* concerning the possible equality of these two temperatures. Therefore the full range of the thermal equilibration regimes, as depicted in the Fig. 1, can be reproduced. This means however that the model needs to include the detailed information about the structure of the circulatory system within the region of interest and needs to keep track of all the blood temperatures throughout this system in order to calculate the tissue temperature.

This high level of complexity results also in high computational power needed to perform calculations on such models. In fact, the vascular model presented by Brinck and Werner in [5] could only be formulated and solved for very small region of tissue. For this reason the vascular models are not common in the literature and the only one attempt of actual calculation, known to the present author is the one presented in [5].

However, in addition to tissue temperature, it allows one to calculate all the blood temperatures and model various physiological phenomena such as vasodilation and vasoconstriction, blood viscosity changes etc. in the most straightforward manner.

The actual formulation of the vascular model developed by the author and its numerical implementation is the main topic of the present paper.

2. Method

We develop an implementation of the vascular model for calculating heat exchange in vascularized, living tissue, under prescribed heat loading conditions. The model contains a description of the complex blood circulation system occupying the tissue region of interest. It is assumed that the blood

travels through vessels that form a *tree-like structure*. The tree consists of a number of interconnected *segments*. Each segment is composed of two *vessels* lying in the counter-current arrangement. One of the vessels is the feeding vessel (artery), the other is the draining vessel (vein). Such an arrangement is found in a majority of blood vessels, [15]. The exceptions are the largest vessels (aorta and vena cava) and capillaries. When the tissue domain of interest does not contain the largest vessels (and this is the case in peripheral circulation, which is most interesting here), the former exception does not apply. Furthermore, as was shown in the preceding section, in usual thermal loading conditions, the temperature equilibration between the blood vessels and the surrounding tissue, takes place long before the blood reaches capillaries. It is hypothesized here, that this will hold true, even in the most extreme thermal loading scenarios.

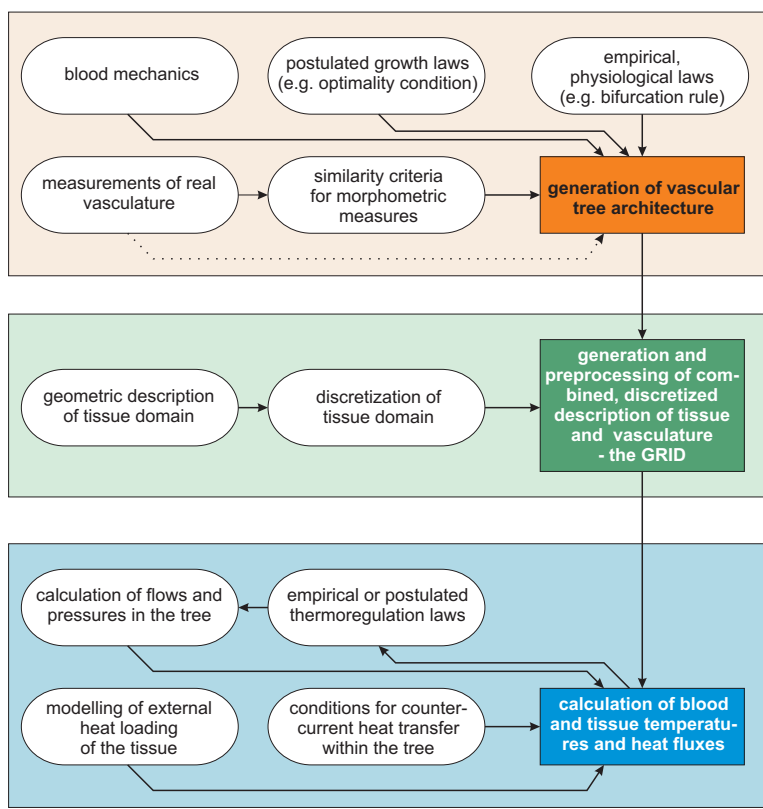


FIGURE 2. The three basic steps employed in the presented method. They are implemented in the three independent computer programs.

If we furthermore assume, that the capillaries and other smallest vessels are isotropic in their spatial arrangement, it becomes clear that the vascular model needs to include detailed description of the architecture of only those vessels that are not in the thermal equilibrium with tissue. Depending on the severity of the thermal loading to which the tissue region is subjected, different levels of detail will be needed (in the presence of steep gradients of tissue temperature, the temperatures in small arterioles and venules need to be calculated, whereas if the tissue temperature is more uniform, these temperatures may be safely assumed equal to tissue temperature).

The architecture of the realistic vascular system is reconstructed according to a number of rules. Then the tissue domain, in which the vascular tree is embedded is discretized and the relation between this discretization and the description of vasculature is established. Finally the heat exchange in various pre-defined scenarios can be calculated. In Fig. 2, the basic steps of the method are depicted.

3. Tree Generation

Generation of the vascular tree is performed by means of the algorithm based on the one presented in [10]. It aims at generation of the hydraulically balanced tree, which obeys additional *bifurcation rule*, and which minimizes the volume of blood needed to vascularize the given domain. The algorithm is a sequential one and consists of extending the existing tree branch after branch. Before we pass to the description of the algorithm let us introduce the relevant notions.

3.1. Notations

vessel—a single conduit embedded in the domain of interest (be it two- or three-dimensional), characterized by the starting and ending point, which determine the local axis of the vessel. The flow of blood in the model can take place through the vessels only. The vessel is the simplest, one-dimensional domain. Several scalar fields are defined on the vessel: vessel radius, blood velocity (measured in the direction of the local axis of the vessel) and temperature. In the method described in the present paper, both the blood velocity and vessel radius are assumed constant along the vessel.

segment—a pair of vessels, characterized by common starting and ending points, identical radii and opposite blood flow velocities. The segment is the basic building block of the vascular tree and it serves to model a counter-current artery-vein vessel pair. The vessel with positive velocity is referred to as *artery* or the *feeding vessel*, while the vessel with negative velocity is the *vein* (the draining vessel).

connected segments—two or more segments, arranged spatially in such a way, that the end-point of one of them (the *parent segment*) is the start-point of all the others (the *daughter segments*). In the presented model it is assumed, that the blood leaving the artery of the parent segment enters the arteries of the daughter segments, also the blood leaving the veins of the daughter segments is collected in the vein of the parent segment.

bifurcation—the point, where two (or more) segments meet. The bifurcation is the end-point of one parent segment and start-point of one or more daughter segments (the bifurcation can be also called the *junction*.)

terminal segment—the segment which has no daughter segments. In the model it is assumed that the blood leaving the artery of the terminal segment enters directly the draining vessel of that segment (the vein). The temperature of this blood is assumed to change to the local tissue temperature upon entering the vein of the terminal segment. Terminal segments are designed to model the ultimate blood-tissue equilibration process in the capillaries.

root segment—the segment which has no parent segment. The temperature of the blood entering the feeding vessel of the root segment and its flow (or pressure) are prescribed boundary conditions to the model, while the temperature of the blood leaving the draining vessel of the root segment is one of the most important results from the model.

vascular tree—a system of interconnected segments, stemming from one root segment and bifurcating through a number of generations. The sequence of bifurcations ends at the terminal segments. In the presented method the generated vascular tree is initially (i.e. before it is processed for further calculations) a binary tree i.e. each non-terminal vessel has exactly two daughter vessels.

subtree—a tree formed by all descendant segments of a particular parent segment.

mesh—a discretization of tissue domain of interest into appropriate elements (for further use in finite differences, finite elements or other methods).

grid—a combined and mutually compatible discretizations of the tissue domain (the mesh) and of the vascular tree into appropriate elements and interconnected segments, supplemented with additional membership information; suitable for further calculation of coupled tissue and blood temperatures. The notion of grid is explained in detail in Sec. 4.

3.2. Generation Algorithm

The generation algorithm employed is based on the one introduced in [10]. The modifications introduced by the present author will be indicated at the end of the presentation.

It is assumed that the tissue receives the nutrients from the blood on the capillary level, which corresponds to the terminal segment in the presented model. It is furthermore assumed that exists an elementary quantity of tissue (terminal area in 2D setting or terminal volume in 3D setting), whose demand is satisfied by prescribed, elementary blood flow Q_{term} through the single terminal segment. The generation consists basically of the following steps:

1. scale the tissue region of interest until it has the elementary area or volume,
2. plant the single root terminal vessel with the start point on the boundary and end point inside this scaled region,
3. scale the tissue region, so its area/volume can accommodate one more terminal area/volume; the region needs now one more terminal segment to satisfy its demands,
4. add a new terminal segment to the tree,
5. check if a desired tissue region size/tree complexity has been attained, if not—proceed to the step (3).

Each time, before step (3) is entered, and at the end of the whole procedure, the tree complies with all the assumptions. All steps of the above algorithm, except the step (4) are simple and require no further explanations.

Step (4)—the procedure of adding the new terminal segment to the tree—is executed by means of the following algorithm:

- (4.1) find a satisfactory location for the end point of prospective, new terminal segment,
- (4.2) find the best segment to act as a parent segment to the new terminal,
- (4.3) create the new terminal segment temporarily connecting the arbitrary point on the parent segment (the present implementation uses the point in the geometric center of the parent segment) with the end-point chosen in step (4.1),
- (4.4) adjust segment radii throughout the tree to adjust the hydraulic resistance to the increased blood flow, and optimize the location of the bifurcation point based on minimization of corresponding blood volume.

We begin the detailed description of these steps with explanation of step (4.3) and (4.4). The disturbed order of the presentation is motivated by the fact that some of the preceding steps can be easily described in terms of the functionality of these steps.

3.2.1. Adding a new terminal segment to the vascular tree. The method presented in [10] (and adopted here) assumes that there are two laws, governing the sizes of the blood vessels in the vascular tree. The first is that the hydraulic balance must be achieved, i.e. the flow and pressure at the end point of each terminal vessel must be the same. This means that the ratio of total hydraulic resistances of two subtrees in the tree is inversely proportional to the ratio of the number of terminal segments in those subtrees. The hydraulic resistance of the single vessel is calculated according to the Hagen-Poiseulle law:

$$R = \frac{8\nu L}{\pi r^4}$$

where ν is blood viscosity, L is the length of the segment and r is its radius. The hydraulic resistance of the binary subtree, where the segment S is a root segment is:

$$R(S) = \begin{cases} \frac{8\nu L(S)}{\pi r^4(S)} & \text{if } S \text{ is a terminal segment,} \\ \frac{8\nu L(S)}{\pi r^4(S)} + \frac{R(S_L)R(S_R)}{R(S_R)+R(S_L)} & \end{cases}$$

where the notation S_L and S_R has been used to denote both daughter segments of the segment S .

The second law governing the growth of the modeled vascular tree is the bifurcation law. It is an empirical, physiological law, [10]

$$r^\gamma(S) = r^\gamma(S_L) + r^\gamma(S_R) \quad (3.1)$$

where γ is the prescribed *bifurcation exponent*, which is assumed to be 2.7 [10].

Equation (3.1) is known in the literature as the Murray's law. It is based on the hypothesis that the bifurcations in the vasculature are designed in such a way as to minimize the pumping power required and metabolic energy expense to drive and maintain the system [11]. It has also been proved that, this condition is equivalent to ensuring that the wall shear stress is homogeneous throughout the vascular system, [11, 13]. This latter fact is important because it gives clue to the mechanism of growth of blood vessels.

Value of the exponent γ obtained by means of theoretical study is three. Its derivation is based on several assumptions, among others of laminar blood flow obeying the Hagen-Poiseuille law and constant blood viscosity. Estimation of the γ exponent for the cases where these assumptions are relaxed yields only slight decrease in its value [11].

The optimality condition used as a starting point for construction of the transport systems (where fluid, heat, or other media is transported) underlies the so-called constructal theory, developed by A. Bejan in late 1990's [3]. While it is based on universal concepts, the constructal theory finds applications in the modelling of vascular systems [4]. The theoretical considerations of optimality lead to numerous quantitative scaling laws which are satisfied by the actual living organisms in surprisingly wide range of scales [17].

In the presented model both the hydraulic balance law and bifurcation rule are sufficient to determine vessel radii throughout the tree. The process of updating the radii after the new terminal segment is added will be from now on called *balancing of the tree*. Numerical implementation of this procedure is greatly facilitated by using the *bifurcation ratios* (e.g. ratios of segment radius to the radius of parent segment) instead of the actual radii. The whole subtree described by the bifurcation ratios can be scaled very easily.

The location of the start point of the new vessel is then optimized. As we recall it is first set to be an arbitrary point along the parent segment of the newly inserted terminal segment (midpoint of this segment in the implementation developed by the present author). The optimization aims at establishing the start point of the new segment, that minimizes the overall blood volume in the tree. The optimization procedure is described here in

a 2D setting. If we denote the blood volume in the entire tree as a function of start point of a new segment as $\mathcal{B}(x, y)$ the optimization proceeds as follows:

- (i) estimate the size of the spatial step of the optimization Δl by taking it to be the smallest of the following numbers: 30% length of the new segment, 30% length of its sibling and difference in their lengths (provided it is nonzero),
- (ii) calculate $\mathcal{B}(x, y)$, $\mathcal{B}(x + \Delta l, y)$ and $\mathcal{B}(x, y + \Delta l)$ (should any of these points be outside the tissue domain, then the sign of Δl is reversed),
- (iii) the start point of the new segment is then moved in the direction of lowering \mathcal{B} , the spatial step is reduced and the procedure starting at step (ii) is repeated until \mathcal{B} does not change significantly with each new iteration or maximum iteration number is exceeded.

It is worth noticing, that each evaluation of the function $\mathcal{B}(x, y)$ requires that the tree is rebalanced, ensuring that bifurcation rule holds and the hydraulic balance is preserved throughout the tree.

3.2.2. Determining the location of end point of new terminal segment. We return presently to the description of algorithm for adding the new terminal vessel into the tree (step 4 of the generation algorithm). Step (4.1) of that procedure consists of finding the location for the prospective new terminal segment. To this end a semi-random procedure is employed. It can be briefly described as follows:

- (i) choose a random location P inside the region of interest,
- (ii) calculate the minimum distance between P and every segment in the tree,
- (iii) if the above-calculated distance falls below a prescribed threshold ϵ_R the procedure is repeated from step (i); if the number of repetitions exceeds a prescribed threshold, then ϵ_R is lowered by a constant ratio and the sequence is started afresh,
- (iv) if the prospective location is sufficiently distant to each segment in the tree, it is accepted.

It should be remarked that the presented algorithm offers several possibilities for further improvements and extensions. These can be exploited to enable modelling of the features of real biological tissues. Let us describe two such potential directions of improvement.

The vasculature in living tissue is seldom homogenous on a large scale. Fatty tissue is relatively poorly vascularized, the blood circulation system of muscles is more developed and some internal organs have very complex and dense vascularity (e.g. liver or kidney). The possible way to model these inhomogeneities is to prescribe a nonhomogeneous probability density function which favours areas of higher tissue perfusion during the procedure of selection of an end point of the prospective new terminal vessel. The threshold ϵ_R can also be assigned different values for different tissues.

The other idea is to allow the threshold ϵ_R to be function of spatial variable. In this way, in certain areas, smaller distances between the segments would be allowed, while, in others, larger clearance between segments would have to be preserved.

3.2.3. Determining the parent segment for the new terminal segment. To complete the description procedure we now describe the algorithm for selecting the parent segment of the new terminal segment. It is the most time-consuming and—at the same time—probably the simplest part of the segment addition algorithm. The new terminal segment is added to each existing tree segment as its daughter segment in a manner described in Sec. 3.2.1. The total tree blood volume is calculated and the new terminal segment is removed. Finally the segment yielding the lowest blood volume is selected to be the parent for a new terminal segment.

It is worth noticing that each action of adding of the terminal segment involves numerous iterations of geometric optimization of the start point location procedure and the segment removal from the tree requires rebalancing of the tree. Furthermore, the selection algorithm slows down dramatically, as the number of segments in the tree increases.

For these reasons, the present author has proposed an improvement to the above-described procedure (which, in its general form, has been described in [10]). Instead of verifying suitability of every segment in the tree in the role of parent segment of the new terminal, only the one closest to the new terminal end point is tried, as well as only those others, whose distance to this point does not exceed twice the distance to the closest one. Then, the usual

procedure selects the one that yields the lowest blood volume in the tree. This improvement will be called the *preselection* in the following discussion.

The preselection narrows the search considerably and the procedure does not slow down very much with increasing number of segments in the tree. The reason for this behaviour is that, for any given point there is usually the same number of segments that are within twice the distance to the one closest to this point.

3.3. Example Results of Tree Generation

The described algorithm has been implemented in the form of the *grower* program. In the present version the program handles only two-dimensional, rectangular tissue regions. However, in principle, there are no significant obstacles to extending the functionality to other, convex 2D domains. The present author believes also, contrary to the opinion expressed by authors of [10], that the extension of the presented algorithm to nonconvex and three-dimensional domains is also possible.

3.3.1. Influence of geometric optimization and effectiveness of pre-selection procedure. Figure 3 presents the 101- and 301-terminal trees generated with optimization of the new terminal start-point (geometric optimization) turned on and off. In the non-optimized trees, not only the new segment is always inserted in the midpoint of the parent segment, but also the process of selecting the parent segment is conducted by means of comparison of the blood volumes in various non-optimized potential new trees. The results clearly do not resemble vascular trees. However, one must bear in mind that the geometrical optimization is the most time-consuming element of the algorithm. In Table 2 the times of tree generation with optimization turned on and off are compared for two trees (101 and 301 terminal segments). As one can see, including optimization slows the generation process considerably.

TABLE 2. Time (in seconds) of generation of 100 and 300 new terminals in the 2D vascular tree consisting initially of one segment. The generated trees are presented in Fig. 3.

number of terminals	no optimization	optimization	no optimization preselection	optimization preselection
	no preselection	no preselection		preselection
100	4	121	<1	6
300	193	4773	5	86

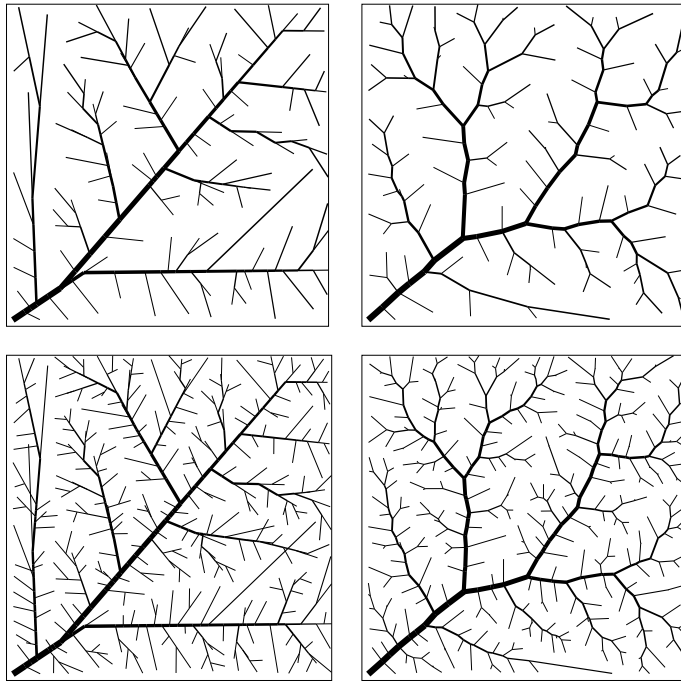


FIGURE 3. The trees generated with geometric optimization turned off (left) and on (right). Top: trees containing 101 terminal segments, bottom: trees with 301 terminal segments.

Table 2 gives also some idea about the effectiveness of the innovation introduced by the present author to the parent segment selection algorithm (preselection). Since the number of the potential possibilities to verify, in each segment addition step, does not grow significantly with the tree complexity, the preselection gives much smaller generation times, when compared to the full search. The generation rate does not drop so dramatically when the preselection method is used, which enables one to generate larger trees, such as the one presented in Fig. 4. The generation time of this tree was below sixty hours on 3 GHz PC. Without the preselection procedure, the generation of this tree would not be possible.

Also it should be remarked that the comparison of total blood volume in the generated trees was found to yield exactly the same value for trees generated with and without the preselection algorithm. It confirms the assumption that none of the potential parent vessels eliminated by preselection would have been selected by the full search procedure. For example the 301-terminal tree depicted in Fig. 3, bottom, right contains 32.2923 mm^3 of

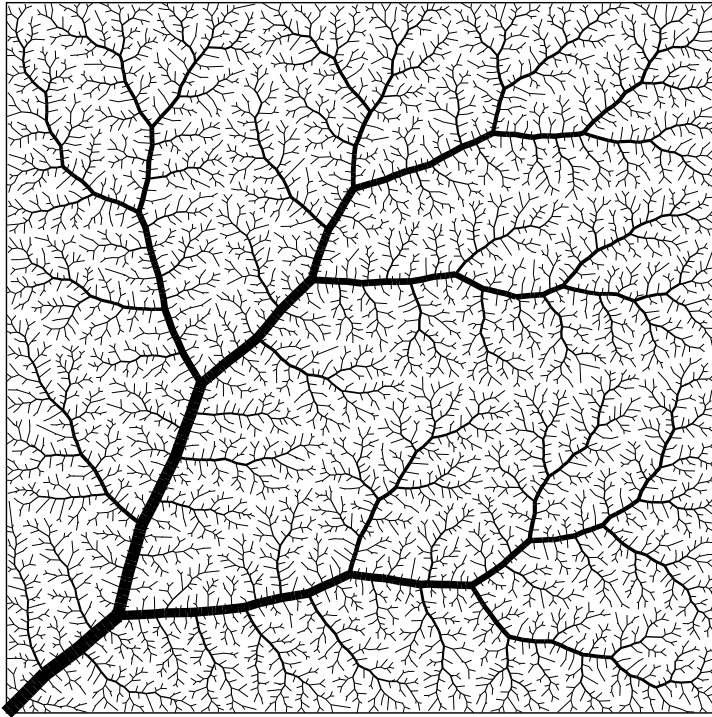


FIGURE 4. The tree containing 6000 terminal segments, generated using the geometric optimization and preselection procedures. The generation time was below 60 hours on 3 GHz PC.

blood and is generated during well over one hour by full search procedure. The preselection yields exactly the same volume, after almost one and a half of a minute. The verification of the blood volumes between the two methods was not tried for larger trees because the time necessary for a full search becomes excessive¹⁾.

3.3.2. Influence of the bifurcation exponent. The bifurcation exponent γ , introduced in Eq. (3.1) is a purely empirical parameter, estimated to be equal 2.7 for normal circulation system. However, it can be varied in the relatively wide range, yielding distorted vascular trees. Comparison of a number of results obtained for various values of γ are depicted in Fig. 5.

¹⁾As the tree generation involves a random element, one would expect that the volumes of two 301-terminal trees would never be precisely equal. However quasi-random procedure employed in the actual implementation uses a random number generator that yields always the same sequence of pseudo-random numbers, which facilitates comparisons.

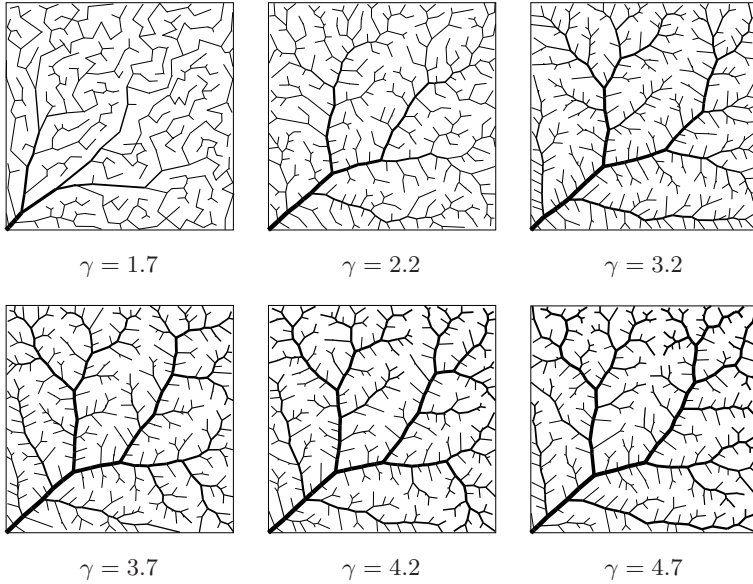


FIGURE 5. The 301-terminal trees generated using various non-standard values of the bifurcation exponent γ . The corresponding tree, generated with $\gamma = 2.7$ is depicted in Fig. 3, bottom, right.

4. Mesh and Grid Creation

Once the description of the vascular tree embedded in the tissue region of interest is available, the next step is to create discretization (mesh) of the tissue matrix and develop such spatial discretization of the vascular tree, that would be compatible with that mesh, i.e. that would facilitate the calculation of the coupled tissue and blood temperature problems. In practice, the mesh of the tissue domain has to be created and then the vascular tree is subdivided in such a way, that each tree segment can be assigned to a single element of tissue discretization (e.g. finite element). Usually, the tree is no longer a binary tree after such subdivision (parent segments are created, that have a single daughter segment).

A tissue domain mesh can be created by any method. It would probably be advantageous to devise method for simultaneous tissue domain mesh creation and vascular tree subdivision. That would allow one to control the size of the resulting tree segments and tissue elements. In the implementation employed in the `grower` program a simpler technique is adopted. The 2D rectangular tissue domain is subdivided into a prescribed number of elements and then, the vascular tree is subdivided.

The subdivided vascular tree and meshed tissue domain are called the *grid* in the following text. Each segment in the grid is embedded entirely in a single tissue domain element, and each element is assigned a list of segments embedded in it. In this way, the subsequent calculation of the heat exchange between the vascular tree and the tissue domain is greatly facilitated.

Apart from establishing a direct relation between the tissue domain and the vascular tree, the process of creating the grid allows one to calculate a number of parameters. These are:

- the number of segments per element,
- the number of terminal segments per element,
- blood fraction in the element.

Distribution of these parameters, calculated for the sparse grid, is depicted in the Fig. 6. The shades of gray in the figure are used to denote the absolute value of the blood fraction (white= 100%, black= 0%) or, for other parameters, the value relative to the maximum attained in the grid (white=maximum, black=0).

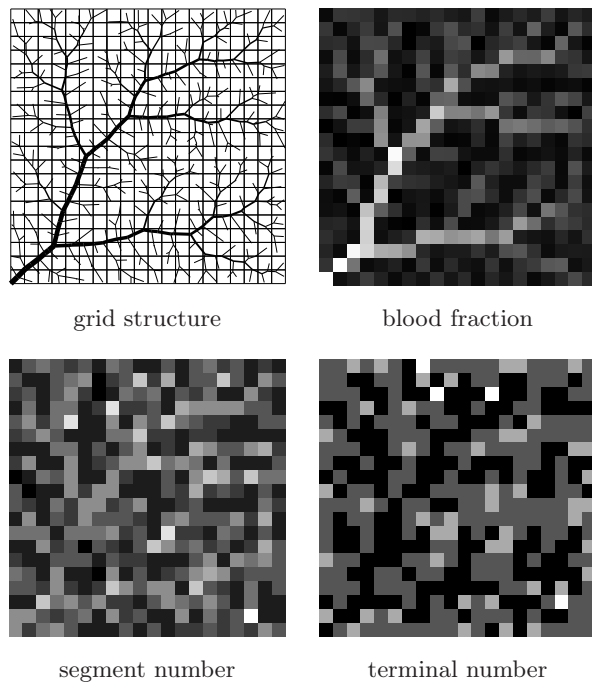


FIGURE 6. The grid created out of 301-terminal tree and a 20×20 mesh.

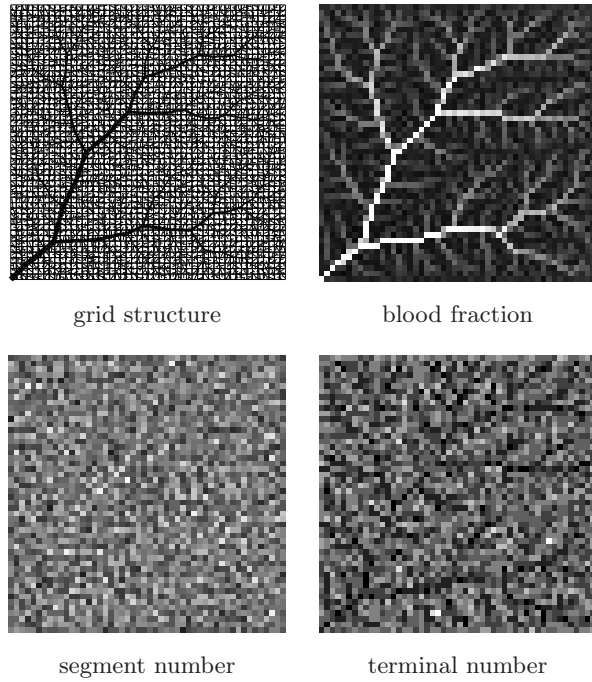


FIGURE 7. The grid created out of 7201-terminal tree and a 50×50 mesh.

The tree in Fig. 6 features 301 terminal segments and the number of segments before subdivision was 601 (the number of segments in any binary tree is twice the number of its terminals minus one). The tree was subjected to further division to match the tissue region mesh of 20×20 elements. After the subdivision the number of segments was 1137.

The example of a relatively complex grid is presented in the Fig. 7. The initial number of terminals was 7201 (14 401 segments) and, after division suitable for 50×50 mesh of tissue domain, the number of segments increased to 20 894.

5. Blood Temperature Calculations

5.1. Introduction

In the present section the geometrical model of the vasculature and tissue, whose generation and preparation has been described in the preceding sections, is used for calculation of the blood and tissue temperatures and heat fluxes.

As we recall, the vascular system is described by means of the complex tree of simple blood vessel pairs (segments). The tree is embedded in the surrounding tissue. A single vessel pair consists of artery and vein of circular cross-sections, lying in countercurrent arrangement. Apart from geometrical data, such as vessel radius r (common to both vessels and assumed constant throughout the length of the vessel), starting and ending points, the pair is characterized by the two temperatures (of arterial and venous blood): $T_a(s)$ and $T_v(s)$ respectively, that are dependent on the axial coordinate of the pair s , and by the blood velocity, that is assumed constant throughout the vessel. The tissue temperature along the vessel is denoted $T_t(s)$. Figure 8 depicts the single segment.

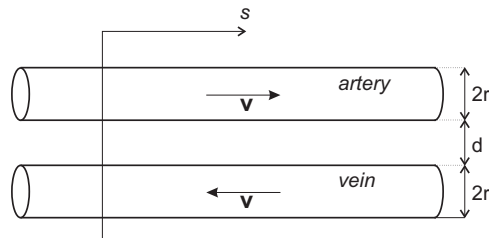


FIGURE 8. Primitive building block of vascular tree: countercurrent vessel pair segment

The condition of constant blood velocity along each segment corresponds to the assumption that no mass transfer takes place through the vessel walls. It may seem that this assumption excludes the phenomenon of the so-called large vessel bleed-off from considerations using the presented method. In fact, the present model allows very small vessels to branch off the large ones, and the flow through these very small vessels can be regarded as the model of bleed-off effect. In the opinion of the author, it is a valid, albeit numerically expensive, method of modelling the large-vessel bleed-off effect.

In the presented method, employed in the `f1ower` program (bottom in Fig. 1), the vessels are treated as one-dimensional entities immersed in the space of higher dimension (two or three). Therefore, whenever reference is made to vessel (arterial/venous) temperature, it is understood that the mixing-cup temperature is meant. The spatial variable for the vessel (axial coordinate) is denoted s .

5.2. Single Vessel Equilibrium

The considerations similar to those presented here can be found in [2, 1]. Let us consider the energy balance equation for the single vessel, embedded in medium, subject to heat flux along its length as depicted in Fig. 9.

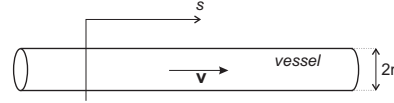


FIGURE 9. Single vessel embedded in medium

The energy balance equation reads:

$$\pi r^2 \frac{\partial E(s)}{\partial t} = 2\pi r q_w(s) - \pi r^2 \frac{\partial q(s)}{\partial s} - \pi r^2 \rho_{bl} c_{bl} v \frac{\partial T(s)}{\partial s} \quad (5.1)$$

where $q_w(s)$ denotes the heat flux received through the vessel wall, $q(s)$ is the conduction heat flux in the vessel and ρ_{bl} and c_{bl} are the density and specific heat of the fluid (blood) respectively.

In most physiological situations, the axial conduction in the blood can be neglected, also the internal energy of the blood can be expressed in terms of the temperature. Also the heat exchange through the vessel wall can be described by $\bar{q}_w(s) = 2\pi r q_w(s)$, a quantity of heat exchanged by the unit length of the vessel in unit time.

$$\rho_{bl} c_{bl} \frac{\partial T(s)}{\partial t} = \frac{1}{\pi r^2} \bar{q}_w(s) - \rho_{bl} c_{bl} v \frac{\partial T(s)}{\partial s} \quad (5.2)$$

The heat flux received by the unit length of the vessel wall at s can be conceptually divided into two portions: the one received from the counter-current vessel q_{cc} and the one received from the surrounding tissue q_t . The former is proportional to the temperature difference between the vessels and to the conductivity of the tissue. The latter is proportional to the temperature difference between the vessel and the tissue and the conductivity of the tissue. Formally one has:

$$\bar{q}_{cc} = \bar{\sigma}_{cc} \lambda_t (T_{cc}(s) - T(s)), \quad (5.3)$$

$$\bar{q}_t = \bar{\sigma}_t \lambda_t (T_t(s) - T(s)), \quad (5.4)$$

$$\bar{q}_w = \bar{q}_{cc} + \bar{q}_t. \quad (5.5)$$

Here $\bar{\sigma}_{cc}$ and $\bar{\sigma}_t$ are constant, dimensionless, shape coefficients for heat conduction between the vessels and between the vessel and the tissue respectively. They are assumed to depend on the geometry of the system only (vessel radius and spacing between vessels). A number of dimensional shape factors, determined for various geometries are given in [8]. For two parallel cylinders of diameters D_1 and D_2 , lying a distance w apart (w is measured axis-to-axis) Incropera and DeWitt propose the following expression for the shape factor:

$$\bar{\sigma} = \frac{2\pi}{\cosh^{-1}\left(\frac{4w^2 - D_1^2 - D_2^2}{2D_1 D_2}\right)}.$$

For the cylinders of the same diameter $D_1 = D_2 = D$ lying two diameters apart $w = 2D$ one has:

$$\bar{\sigma} = \frac{2\pi}{\cosh^{-1}(7)} = \frac{2\pi}{\ln(7 + \sqrt{48})} \approx 2.3855.$$

For convenience of notation, we introduce shape coefficients per unit cross-sectional area of the vessel:

$$\sigma_{cc} = \frac{\bar{\sigma}_{cc}}{\pi r^2}; \quad \sigma_t = \frac{\bar{\sigma}_t}{\pi r^2}.$$

5.3. Equilibrium of the Vessel Pair

We assume that the s -axis (axis of the vessel) is oriented in the direction of the blood flow in the artery and opposite to the flow in vein. We then have for the artery (for convenience, the dependence on s is not indicated):

$$\rho_{bl} c_{bl} \frac{\partial T_a}{\partial t} = \sigma_{cc} \lambda_t (T_v - T_a) + \sigma_t \lambda_t (T_t - T_a) - \rho_{bl} c_{bl} v \frac{\partial T_a}{\partial s}. \quad (5.6)$$

The corresponding equation for the vein is:

$$\rho_{bl} c_{bl} \frac{\partial T_v}{\partial t} = \sigma_{cc} \lambda_t (T_a - T_v) + \sigma_t \lambda_t (T_t - T_v) + \rho_{bl} c_{bl} v \frac{\partial T_v}{\partial s}. \quad (5.7)$$

The heat transported into tissue from the unit length of the vessel pair is therefore:

$$q_l = -\sigma_t \lambda_t ((T_t - T_a) + (T_t - T_v)) = 2\sigma_t \lambda_t \left(\frac{T_a + T_v}{2} - T_t \right). \quad (5.8)$$

5.4. Numerical Formulation

We now reformulate the heat transfer problem in the framework of finite differences. Since each vessel pair segment is connected on one side to the parent segment, and on the other, it feeds one or two daughter segments it is convenient to consider a single vessel pair segment to be basic unit of the discretization. In the following derivations we denote the length of the segment by L , the time step of the simulation by Δt ; the values at the start and end of the segment are denoted by superscript s and e . Spatial derivatives are calculated by forward-difference for vein and by backward-difference for artery. The reason for this choice is clarified below. The temperature gradients in both vessels of the pair are approximated to be constant throughout the segment.

5.4.1. Explicit Method In the explicit formulation all heat flow rates are calculated using the blood temperature values at the beginning of the time step. This method is significantly cheaper numerically, although it imposes severe limitation on the size of time step used. The artery and vein temperatures in segments are calculated sequentially, in the selected order.

Equation (5.6), yields the following algebraic equation for the end-segment temperature of arterial blood:

$$\begin{aligned} T_a^e(t + \Delta t) &= T_a^e(t) \\ &+ \Delta t \left(\frac{\lambda_t}{\rho_{bl}c_{bl}} (\sigma_{cc}(T_v^e(t) - T_a^e(t)) + \sigma_t(T_t^e(t) - T_a^e(t))) - v \frac{T_a^e(t) - T_a^s(t)}{L} \right). \end{aligned} \quad (5.9)$$

Similarly, equation (5.7), yields the following algebraic equation for the start-segment temperature of venous blood:

$$\begin{aligned} T_v^s(t + \Delta t) &= T_v^s(t) \\ &+ \Delta t \left(\frac{\lambda_t}{\rho_{bl}c_{bl}} (\sigma_{cc}(T_a^s(t) - T_v^s(t)) + \sigma_t(T_t^s(t) - T_v^s(t))) + v \frac{T_v^e(t) - T_v^s(t)}{L} \right). \end{aligned} \quad (5.10)$$

The chosen method for spatial gradient approximation requires that additional equations for the start-segment artery temperature and end-segment vein temperature are specified to complete the formulation. These equations

are simply *the mixing conditions* expressing the fact, that there is no accumulation of energy at the junctions between segments. The mixing condition for artery expresses the fact that the blood entering daughter vessels has the end-segment arterial temperature of the parent segment:

$$T_a^s(t + \Delta t) = \begin{cases} T_{\text{supply}} & \text{for root segment,} \\ \mathcal{P}(T_a^e(t + \Delta t)) & \text{for non-root segment.} \end{cases} \quad (5.11)$$

Here T_{supply} is the prescribed arterial supply temperature, i.e. the temperature of the blood entering the arterial circulation in the considered tissue region; the operator \mathcal{P} returns value of its argument for the parent of the considered segment (i.e. while $T_a^s(t)$ denotes the segment start-point arterial temperature at time t , $\mathcal{P}(T_a^s(t))$ denotes the segment start-point arterial temperature of the parent of the present segment at time t). We recall that there is only one segment (root segment) in the vascular tree that has no parent segment.

The mixing condition for venous blood expresses the fact that the end-segment temperature of the venous blood can be calculated as a result of mixing of two venous blood flows from the daughter segments:

$$T_v^e(t + \Delta t) = \begin{cases} T_t & \text{for terminal segment,} \\ \frac{1}{vr^2} \sum_{i=0}^d \mathcal{D}_i(vr^2 T_v^s(t + \Delta t)) & \text{for non-terminal segment.} \end{cases} \quad (5.12)$$

Here we denote by d the number of daughter segments to the considered segment and introduce the operator \mathcal{D}_i that refers to the variables of the i th daughter segment of the considered segment. This operator is analogous to \mathcal{P} . We recall that the segments having no daughter segments are referred to as *terminal segments*. In the model it is assumed that the blood in terminal segments is in thermal equilibrium with surrounding tissue and therefore any blood draining into venular vessels of those segments is at the local tissue temperature.

For stability of the presented numerical scheme for the artery (5.9), the following condition must hold:

$$\Delta t < \left(\frac{\lambda_t}{\rho_{bl} c_{bl}} (\sigma_{cc} + \sigma_t) + \frac{v}{L} \right)^{-1}. \quad (5.13)$$

It can be readily verified that the formulation for vein (5.10) yields an identical criterion. Since the first term in the parenthesis on the r.h.s. of (5.13)

is of several orders of magnitude smaller than the second term, one can infer that the condition pertinent to the blood advection determines stability.

Unfortunately, the brief inspection of the grid creation method described in the Sec. 4 shows that the vascular tree segments can get arbitrarily small in the course of subdivision. There are two kinds of situations, where such unusually short vessels arise. They are schematically depicted in Fig. 10.

Due to these anomalous tree segments the direct application of the explicit method is untenable. The calculation of the shortest segment length for the sparse grid in Fig. 6 and dense grid in Fig. 7 yielded the lengths of the order of 10^{-6} and 10^{-9} m respectively. Calculation of the maximum time step ensuring stability of the numerical formulation, according to Eq. (5.13) resulted in times of the order 10^{-10} and 10^{-13} s respectively. Clearly these values are too small for simulation.

Three solutions to this problem can be proposed:

- preconditioning of the grid prior to calculations (see middle rectangle in Fig. 2); The shortest vessel segments can be eliminated by appropriate repositioning of the nodes of the tissue region mesh and—possibly—by slight corrections of the shape of the tree. Using the latter method, one needs to ensure that the hydraulic balance and the bifurcation rule are not violated, also the changes of the shape of the tree have to be very small so that the optimality ensured by the growth algorithm is not disturbed much. These two approaches are illustrated in Fig. 11. The

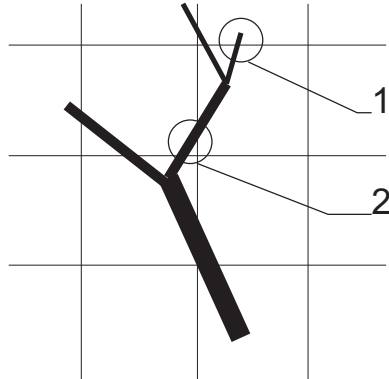


FIGURE 10. Two kinds of situation, where arbitrarily short segments arise in subdivision during the creation of the grid: 1. segment traverses the mesh element boundary with its end-point very close to this boundary; 2. segment traverses the mesh element very close to its corner.

drawback of this method is the fact that the appropriate algorithm for repositioning the tissue region mesh nodes seems to be rather difficult to devise.

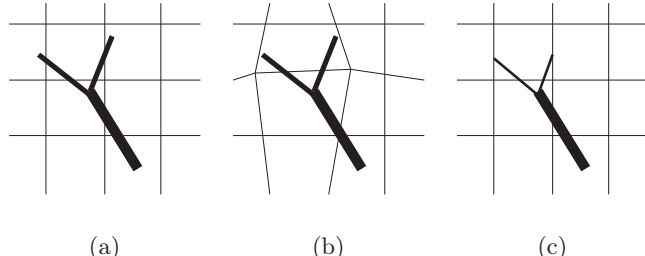


FIGURE 11. Two ways of improving an initial grid (a), which contains two very short terminal segments. In (b) the tissue region mesh is deformed and in (c) the vascular tree is truncated, the vessel radii being adjusted to obey the bifurcation rule and hydraulic balance law.

- omitting the shortest segments in the numerical formulation; If the shortest segment is the only daughter segment of its parent or is a parent to only one daughter segment (most of the shortest segments are expected to fall in that category), then it can be treated together with its parent (daughter) segment as a single segment in the numerical scheme. All heat exchanged with the tissue elements would be distributed between the tissue elements surrounding the segments according to the lengths ratio of the segments. This situation is schematically depicted in Fig. 12.
- application of the numerical scheme that imposes no limit (such as Eq. (5.13)) on the time step used, e.g. implicit finite differences method. This method will be discussed in the next subsection.

5.4.2. Implicit method. In the implicit method, the artery and vein temperatures in segments are calculated simultaneously. The tissue temperatures are still calculated separately so heat flow rates are calculated on the basis of the blood temperatures at the end of the current step and current (start of the step) tissue temperatures. The method requires solving the appropriate system of equations, whose size is determined by the number of segments. It is unconditionally stable, so a time step size larger than the one used in explicit formulation may be selected.

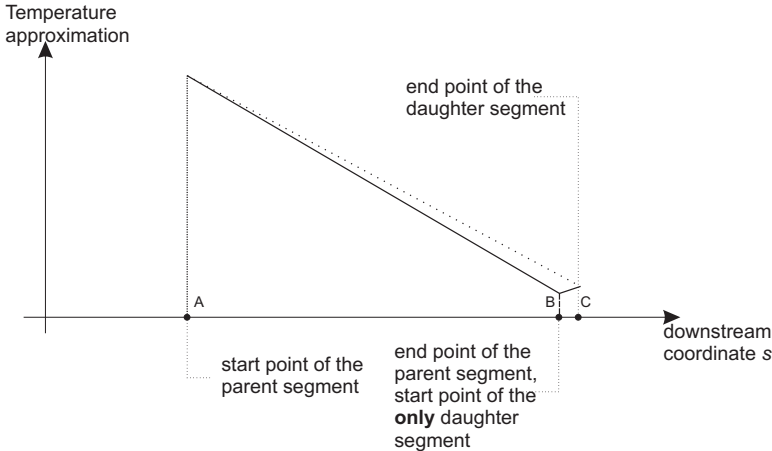


FIGURE 12. In the numerical scheme, treating the parent-single daughter succession of segments as a single segment means that the intermediate node will be omitted and the approximation of the temperature will be the one denoted with dotted line as opposed to the example of original one (solid line). In this example, the parent segment AB lies within the element I of tissue domain mesh, while its only daughter vessel—in the element II. The heat exchanged by the combined segment AC with the tissue is split between the elements I and II in proportion to the lengths AB and BC. Temperatures at nodes A, B, and C are set arbitrarily in this example.

Equation (5.6), yields the following algebraic equation for the end-segment temperature of arterial blood:

$$\begin{aligned} T_a^e(t + \Delta t) \left(1 + \Delta t \left(\frac{\lambda_t \sigma_{cc}}{\rho_{bl} c_{bl}} + \frac{v}{L} \right) \right) - T_v^e(t + \Delta t) \left(\frac{\lambda_t \sigma_{cc} \Delta t}{\rho_{bl} c_{bl}} \right) \\ - T_a^s(t + \Delta t) \frac{v \Delta t}{L} = T_a^e(t) + \frac{\lambda_t \sigma_t \Delta t}{\rho_{bl} c_{bl}} (T_t^e(t) - T_a^e(t)). \quad (5.14) \end{aligned}$$

Similarly, equation (5.7), yields the following algebraic equation for the start-segment temperature of venous blood:

$$\begin{aligned} T_v^s(t + \Delta t) \left(1 + \Delta t \left(\frac{\lambda_t \sigma_{cc}}{\rho_{bl} c_{bl}} + \frac{v}{L} \right) \right) - T_a^s(t + \Delta t) \frac{\lambda_t \sigma_{cc} \Delta t}{\rho_{bl} c_{bl}} \\ - T_v^e(t + \Delta t) \frac{v \Delta t}{L} = T_v^s(t) + \frac{\lambda_t \sigma_t \Delta t}{\rho_{bl} c_{bl}} (T_t^s(t) - T_v^s(t)). \quad (5.15) \end{aligned}$$

Equations (5.11) and (5.12) hold also in the case of the implicit method.

5.4.3. Summary The pair of equations (5.9) and (5.10), or (5.14) and (5.15), along with (5.11), and (5.12) enable the calculation of arterial and venous temperatures at time $t + \Delta t$. The tissue temperature is calculated independently, by means of the suitable numerical procedure for integration of nonstationary heat conduction equation. Each segment of the vascular tree embedded in the tissue provides local line heat source of intensity described by Eq. (5.8). Furthermore, each terminal segment provides point heat source of intensity

$$q_{\text{term}} = \pi r^2 \rho_{\text{bl}} c_{\text{bl}} v (T_a^e - T_v^e), \quad (5.16)$$

located at its end-point. It should be noted that the vascular tree embedded in the tissue domain of interest, should be sufficiently complex (the vasculature should be modeled to a sufficient level of detail), so that the blood reaching terminal vessels is in thermal equilibrium with tissue and q_{term} is small. In real organisms the artery-vein connection takes place at the level of capillaries, where the blood is in full equilibrium with the tissue, even on the most extreme thermal loadings. In most cases, the temperature equilibrating takes place several branching generations earlier, cf. [7].

5.4.4. Implementation of the Implicit Method In order to implement the above-mentioned finite difference scheme an appropriate numbering is adopted. Each tree segment is assigned a number i being an integer multiple of 3, so that the segments are indexed with the numbers $0, 3, 6, \dots$. The following degrees of freedom are then introduced for each segment:

number	meaning
0	T_a^e
1	T_v^s
2	T_v^e

The global number of the degree of freedom is then obtained by adding the local number of the degree of freedom to the segment number. For example the end-of-segment venous temperature in the segment 21 (that is the eighth segment) will be denoted θ^{23} (21 for segment and 2 for T_v^e).

The start-of-segment arterial temperature need not to be treated as an unknown variable, since, by Eq. (5.11) it can be replaced by appropriate parent segment temperature, therefore we have three temperature degrees of freedom per segment.

Before the matrix form of the implicit method is derived we introduce some convenient notations:

$$\alpha = \frac{\lambda_t \Delta t}{\rho_{bl} c_{bl}}, \quad \beta^n = \frac{v(n) \Delta t}{L(n)}$$

where the variable n denotes the segment number, e.g. $v(n)$ is the blood velocity in the n th segment. Furthermore, by $T_t^{n,s}$ we denote tissue temperature at the location of start-point of the n -th segment while by $T_t^{n,e}$ we denote tissue temperature at the location of end-point of the n -th segment.

The global matrix for nodal temperature calculation is constructed by inserting three equations for every segment in the tree. That is, for every segment n we proceed as follows:

1. if the segment n is a root segment:

- (a) enter the following equation no. n into the constructed system:

$$\begin{aligned} \theta^n(t + \Delta t)(1 + \alpha\sigma_{cc} + \beta^n) - \theta^{n+2}(t + \Delta t)\alpha\sigma_{cc} \\ = \theta^n(t)(1 - \alpha\sigma_t) + \alpha\sigma_t T_t^{n,e}(t) + T_{\text{supply}}\beta^n, \end{aligned}$$

- (b) enter the following equation no. $n+1$ into the constructed system:

$$\begin{aligned} \theta^{n+1}(t + \Delta t)(1 + \alpha\sigma_{cc} + \beta^n) - \theta^{n+2}(t + \Delta t)\beta^n \\ = \theta^{n+1}(t)(1 - \alpha\sigma_t) + \alpha\sigma_t T_t^{n,s}(t) + T_{\text{supply}}\alpha\sigma_{cc}, \end{aligned}$$

2. if the segment n is not a root segment:

- (a) determine the number m of the parent segment of n ,

- (b) enter the following equation no. n into the constructed system:

$$\begin{aligned} \theta^n(t + \Delta t)(1 + \alpha\sigma_{cc} + \beta^n) - \theta^{n+2}(t + \Delta t)\alpha\sigma_{cc} - \theta^m(t + \Delta t)\beta^n \\ = \theta^n(t)(1 - \alpha\sigma_t) + \alpha\sigma_t T_t^{n,e}(t), \end{aligned}$$

- (c) enter the following equation no. $n+1$ into the constructed system:

$$\begin{aligned} \theta^{n+1}(t + \Delta t)(1 + \alpha\sigma_{cc} + \beta^n) - \theta^m(t + \Delta t)\alpha\sigma_{cc} - \theta^{n+2}(t + \Delta t)\beta^n \\ = \theta^{n+1}(t)(1 - \alpha\sigma_t) + \alpha\sigma_t T_t^{n,s}(t), \end{aligned}$$

3. determine numbers of the daughter segments p and o (or just p if there is only one daughter segment),

4. if there are no daughter segments (n is a terminal segment) enter the following equation no. $n + 2$ into the constructed system,

$$\theta^{n+2}(t + \Delta t) = T_t^{n,e}(t)$$

5. if there is one daughter segment p of the segment n enter the following equation no. $n + 2$ into the constructed system

$$\theta^{n+2}(t + \Delta t) - \theta^{p+1}(t + \Delta t) = 0,$$

6. if there are two daughter segments p and o of the segment n enter the following equation no. $n + 2$ into the constructed system

$$v(n)r^2(n)\theta^{n+2}(t + \Delta t) - v(p)r^2(p)\theta^{p+1}(t + \Delta t) - v(o)r^2(o)\theta^{o+1}(t + \Delta t) = 0.$$

In the resulting set of equations the equation having the same number k as some segment corresponds to Eq. (5.14) for that segment, equation with number $k + 1$ corresponds to Eq. (5.15) for that segment and equation numbered $k + 2$ corresponds to the mixing condition Eq. (5.12) for that segment. Temperature continuity condition for that segment Eq. (5.11) is already used in the formulation (three temperature DOFs per segment instead of four).

6. Tissue Temperature Calculations

For the calculations of tissue temperature the usual Fourier-Kirchhoff conduction equation is used:

$$\rho_t c_t \phi_t \frac{\partial T_t}{\partial t} = \lambda_t \nabla^2 T_t + q_m + q_{bl}. \quad (6.1)$$

Here q_m is a constant metabolic volumetric heat source, while ϕ_t is the local volumetric tissue fraction and q_{bl} is the net heat exchanged by the tissue with the blood vessels per tissue element volume. Its calculation procedure is described in the following.

Equation (6.1) is solved numerically using the finite element method for discretization in space and finite difference method for time discretization. The vascular tree model is subdivided as described in Sec. 4, so that each segment of the tree is contained in a single tissue element. In other words, each tissue element k can be assigned a set of n_k tree segments located inside it and a set of m_k terminals located inside it (obviously $n_k \geq m_k$). It is

pointed out that the tissue fraction ϕ_t can be readily calculated (see Figs. 6 and 7) and remains constant in time (unless one takes the thermoregulation effects into account).

The blood-flow-related volumetric heat source q_{bl} is calculated for each element and is subdivided in two components:

$$q_{\text{bl}}^{(k)} = \frac{1}{V^{(k)}} \left(\hat{q}_l^{(k)} + \hat{q}_{\text{term}}^{(k)} \right). \quad (6.2)$$

Here $V^{(k)}$ is the volume of the k th element, $\hat{q}_l^{(k)}$ is the heat conducted from the walls of all vessels embedded in the k th element to the tissue matrix (see Eq. (5.8)), and $\hat{q}_{\text{term}}^{(k)}$ is the heat transported at the tips of all the terminal vessels embedded in the k th element to the tissue matrix (this heat accounts for the possible temperature difference between arterial end-of-terminal temperature and the end-of-terminal venous temperature, see Eq. (5.16)). The first term in parentheses in Eq. (6.2) is calculated as follows (see Eq. (5.8)):

$$\hat{q}_l^{(k)} = 2\sigma_t \lambda_t \sum_{i=1}^{n_k} \int_{\text{start}(i)}^{\text{end}(i)} \left(\frac{T_a(l) + T_v(l)}{2} - T_t(l) \right) dl \quad (6.3)$$

where $\text{start}(i)$ and $\text{end}(i)$ denote the starting and ending point of the i th segment contained within the considered element, l being the local coordinate of the segment.

The second term in parentheses in Eq. (6.2) is obtained (see Eq. (5.16)):

$$\hat{q}_{\text{term}}^{(k)} = \pi \rho_{\text{bl}} c_{\text{bl}} \sum_{i=1}^{m_k} r^2(i) v(i) (T_a^e - T_t). \quad (6.4)$$

In the course of numerical calculations all temperatures on the r.h.s. of Eqs. (6.3, 6.4) are taken from the previous time step (explicit formulation).

7. Example Results—Steady-state Temperature Distribution

The presented method was implemented in a computer program and used in a number of example simulations. Here we pass to the description of the selected results. The simulations were done on the moderately dense grid consisting a vascular tree comprising of 301 terminals (601 segments, 1137 segments after tree meshing) and 20×20 tissue mesh (441 nodes). The linear dimension of the region was 22.31 mm. The setup is depicted in Fig. 13.

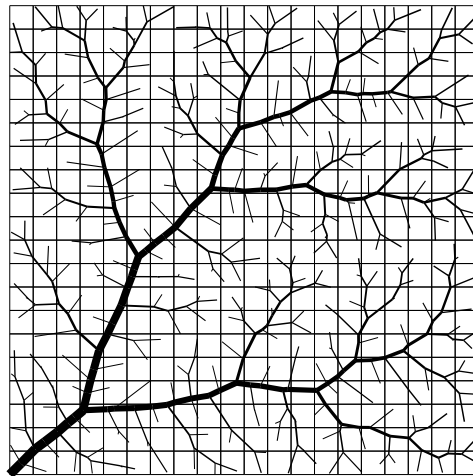


FIGURE 13. Vascular tree model and tissue mesh used in the calculations

Since no thermoregulatory loop was introduced (blood flow is independent of temperature), the hydraulic calculations were performed just once, at the beginning of the simulation.

For the simulation adiabatic boundary conditions were assumed on lower, left and right boundaries of the tissue region. The top boundary was maintained at 25°C. The initial tissue temperature was assumed to be 25°C. The blood feeding the system via arterial vessel of the root segment was kept at 37°C. Obviously, the return blood temperature in the root was calculated by the model. The metabolic heat generation rate was set to be 7000 W/m³.

The steady-state was obtained by computing subsequent steps of time-transient simulation until temperatures did no longer change.

Figure 14 displays the calculated temperature of the blood particle as it traverses the region of interest, starting in the arterial vessel of the root segment, making its way to the most distant terminal in the tree, and, after entering the venous circulation, returning to the draining vessel of the root segment. The scale on the horizontal axis is in arbitrary units (1 corresponds to the width (height) of the square domain of interest).

The data in Fig. 14 have clear physical interpretation. The warm blood, perfusing cool region of tissue gets cooler as it flows through arterial part of the tree. The temperature variations are continuous. At the furthest point of the selected circulation loop (at the end of the terminal vessel) the blood attains the local body temperature, which happens to be 25.25°C (the terminal

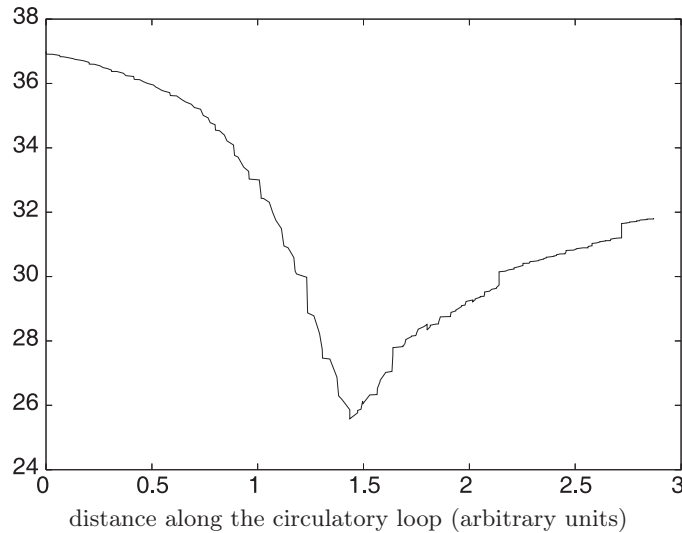


FIGURE 14. Blood temperature along the circulation path feeding the terminal most distant to the root segment; Horizontal axis corresponds to the length (in arbitrary units) along that path.

lies close to the isothermal outer boundary, kept at 25°C). The blood then enters the venous circulation and travels towards the root. On its way it is rewarmed by the counter-current artery and its temperature rises. The process is discontinuous in this case as the blood streams mix in every junction. Finally the root segment is reached, the return venous temperature being ca. 31.8°C.

Since the temperature in the venous tree is discontinuous through the branchings, the vessel-to-vessel heat flow and consequently the slope of the arterial temperature curve can also be expected to be discontinuous. Indeed—careful inspection of Fig. 14 reveals that there are no discontinuities on the arterial side, although the slope is sometimes very high. Summarizing: the temperature curve of the arterial circulation continuous but nonsmooth due to discontinuous vessel-to-vessel heat flux. The vessel-to-vessel flux is, in turn, discontinuous due to venous blood temperature jumps at branchings where mixing takes place. This feature of the model is a consequence of assumption that blood mixing in the branchings of the venous circulation is immediate.

It is noteworthy that the rough scheme in Fig. 1 and the calculated results of the model, presented in Fig. 14 are similar.

The steady-state averaged temperature distribution in the vertical direction is presented in Fig. 15.

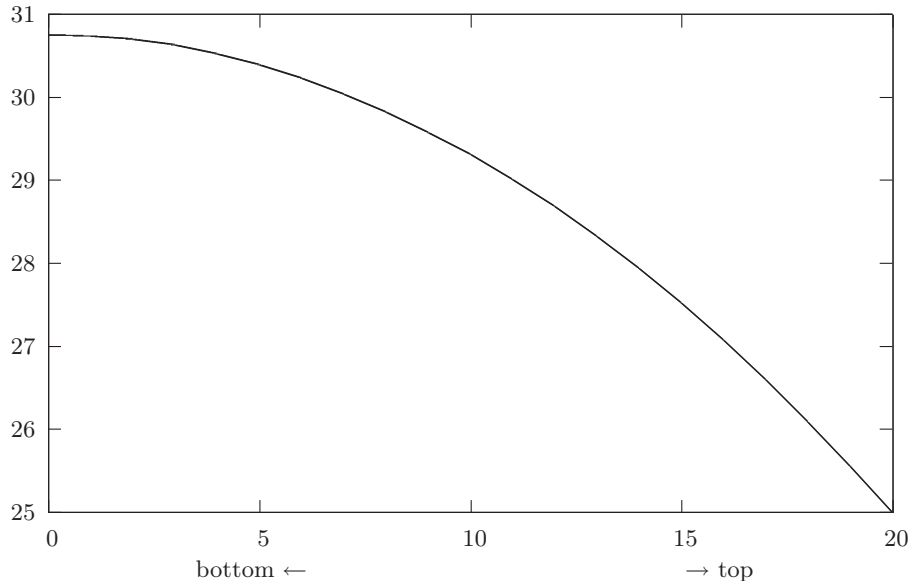


FIGURE 15. Horizontally-averaged tissue temperature profile.

8. Conclusions

The presented method allows one to take account of the impact of countercurrent blood flow through the vascular tree of prescribed geometry on the heat transfer in soft tissue. It uses three independent temperatures: arterial blood temperature, venous blood temperature, and tissue temperature. Therefore, no simplifying assumptions regarding the relation between these are needed (in contrast to e.g. model presented in [15]). This advantage is attained at the expense of model complication and numerical cost of the calculations.

Possibly the most serious limitation of the presented results is the fact that they were obtained with a 2D implementation. Extension to fully three-dimensional case is required if clinically-relevant calculations are to be attempted. It should be pointed out that the method is not intrinsically two-dimensional and the 2D implementation developed to obtain results presented here was chosen on the basis of its simplicity and clarity of presentation.

The presented method is well suited to the investigation of thermoregulation phenomena. It is known that, among other mechanisms of thermoreg-

ulation, the vasodilation and vasoconstriction plays a prominent role. For that purpose the model needs to be supplemented with the additional law relating the relative vessel radius to the local temperature. The pressure/flow calculation is then performed at every step of time-transient analysis.

Nonhomogeneously-perfused tissues can be described by the presented model as well. The vascular tree generation algorithm can be adjusted to yield small vessel density in some tissue regions (e.g. adipose tissue) and large vessel density in the others, for example by introducing a spatial variation of probability density for growing a new terminal. It should be remarked however that for clinically-applicable simulations of effect of large vessels on local hyperthermia, use of real, measured vessel geometry would probably be better [14].

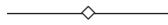
Acknowledgement

The presented work was financially supported by the Ministry of Science and Information Technology (Poland), grant No. 4 T11F 003 25.

References

1. J.W. BAISH, P.S. AYYASWAMY, and K.R. FOSTER, *Small-scale temperature fluctuations in perfused tissue during local hyperthermia*, J. Biomech. Eng. **108**: 246–250, 1986
2. J.W. BAISH, P.S. AYYASWAMY, and K.R. FOSTER, *Heat transport mechanisms in vascular tissues: a model comparison*, J. Biomech. Eng. **108**: 324–331, 1986
3. A. BEJAN, *From heat transfer principles to shape and structure in nature: constructal theory*, J. Heat Transfer, **122**: 430–449, 2000
4. A. BEJAN, *The tree of convective heat streams: its thermal insulation function and the predicted 3/4-power relation between body heat loss and body size*, J. Heat Mass Transfer, **44**: 699–704, 2001
5. H. BRINCK and J. WERNER, *Estimation of the thermal effect of blood flow in a branching countercurrent network using a three-dimensional vascular model*, J. Biomech. Eng. **116**: 324–330, 1994
6. C.K. CHARNY, S. WEINBAUM, and R.L. LEVIN, *An evaluation of the Weinbaum-Jiji bioheat equation for normal and hyperthermic conditions*, J. Biomech. Eng. **112**: 80–87, 1990
7. M.M. CHEN and K.R. HOLMES, *Microvascular contributions in tissue heat transfer*, Annals New York Acad. Sci. **335**: 137–154, 1980

8. F.D. INCROPERA and D.P. DEWITT, *Fundamentals of Heat and Mass Transfer 4th. ed.* John Wiley&Sons New York, Chichester, Brisbane, Toronto, Singapore 1996
9. H.H. PENNES, *Analysis of tissue and arterial blood temperatures in the resting human forearm*, J. Appl. Physiology 1:93–122, 1948
10. W. SCHREINER and P.F. BUXTBAUM, *Computer-optimization of vascular trees*, IEEE Trans. BME 40(5):482–491, 1993
11. T.F. SHERMAN, *On connecting large vessels to small: the meaning of Murray's law*, J. Gen. Physiol., 78:431–453, 1981
12. M. STAŃCZYK and J.J. TELEGA, *Modelling of heat transfer in biomechanics—a review. Part I. Soft tissues*, Acta Bioengng. Biomech. 4(1):31–61, 2002
13. L.A. TABER, S. NG, A.M. QUESNEL, J. WHATMAN and C.J. CARMEN, *Investigating Murray's law in the chick embryo*, J. Biomech., 34:121–124, 2001
14. G.M.J. VAN LEEUWEN and A.A. VAN STEENHOVEN, *Heat Transfer in Humans—Local and Whole-Body*, Abimed Lecture Notes 6, Blood Flow Modelling and Diagnostics, T.A. Kowalewski [ed.], Warsaw 2005.
15. S. WEINBAUM and L.M. JIJI, *A new simplified bioheat equation for the effect of blood flow on local average tissue temperature*, J. Biomech. Eng. 107:131–139, 1985
16. S. WEINBAUM, L.M. JIJI, and D.E. LEMONS, *The bleed-off perfusion term in the Weinbaum-Jiji bioheat equation*, J. Biomech. Eng. 114:539–544, 1992
17. G.B. WEST, *The origin of universal scaling laws in biology*, Physica A, 263:104–113.
18. E.H. WISSSLER, *Pennes' 1948 paper revisited*, J. Appl. Physiology 85(1):35–41, 1998
19. W. WULFF, *The energy conservation equation for living tissue*, IEEE Trans. BME 21(6):494–495, 1974



Estimation of Wall Shear Stress Using a Multi-Branched Model of the Human Arterial System

PAVEL V. STROEV¹⁾, JASON J. BEECH-BRANDT¹⁾,
SALIKH S. ZAKIROV²⁾ PETER R. HOSKINS³⁾
WILLIAM J. EASSON¹⁾

¹⁾*School of Engineering and Electronics,
The University of Edinburgh, Edinburgh, EH9 3JL, Scotland
Pavel.Stroev@ed.ac.uk*

²⁾*Intel, 14 Bolshoy Savvinsky, Moscow, 119435, Russia*

³⁾*Medical Physics Section, The University of Edinburgh,
Chancellors Building, 49 Little France Crescent, Edinburgh,
EH16 4SB, Scotland*

Simulation of wall shear stress (WSS) is of interest in studies, which attempt to identify the effect of alterations in the geometry and physical properties of the circulation on WSS and on the potential for disease development. Computational fluid dynamics and finite element simulations are computationally demanding, and only model a small section of the arterial system. An alternative approach is the use of a multi-branched model to provide estimates of WSS in different regions throughout the arterial tree.

In the present paper the arterial system was represented by a multi-branched model. Velocity profiles occurring in fully developed pulsatile flow were obtained using Womersley's theory. Mean and peak WSS were calculated in different arteries. Simulations for aging and atherosclerosis were also carried out.

The 1D multi-branched model is easy to implement and it is not computationally demanding. It may be used for detailed quantitative analysis of the velocity profiles obtained by assigning specific values to the various portions of the model of the human arterial tree. It may therefore be a useful tool to estimate WSS in arteries, allowing the effect of alteration of model parameters on WSS to be investigated.

Key words: *Transmission line, systemic circulation, shear rate*

1. Introduction

It is now generally agreed that mechanical and hemodynamic factors are responsible for the development of arterial diseases. It was demonstrated in a number of studies that atherosclerotic plaque is initiated in regions of low or oscillating wall shear stress (WSS) [5, 14, 27]. Simulation of WSS is of interest in studies which attempt to identify the effect of alterations in the geometry and physical properties of the circulation on WSS and on the potential for disease development. Having bifurcations and curved vessels in a complex 3D arterial system leads to complex flow patterns, in which there are commonly secondary flow motions, and in some vessels, such as the carotid, regions of flow recirculation. The usual approach that has been taken in flow simulation is the use of computational fluid dynamics (CFD) [24, 21, 22] and finite element modelling (FEM) [23]. These methods can provide detailed 3D images showing the time varying WSS patterns in particular arteries. However, such simulations are computationally demanding, and only model a small section of the arterial tree.

In this study we used a multi-branched configuration proposed by Avolio [1] reflecting the layout of the human arterial tree. Validation studies of other models based on the same concept [20, 13] have demonstrated a good agreement with experiments and proved to be very robust. The model is an analogue of the uniform transmission line in electrical engineering, which is based on linear theory, thus allowing use of spectral techniques.

We present a simulation, which enables us to explore the effects of various changes in model design, such as the effect of altering characteristics of the arteries and downstream resistance, and to simulate various pathological and physiological conditions. The aim of this study is to obtain such profiles to see whether they give physically realistic estimates of WSS at the different points of the system.

2. Method

WSS, by definition, is $\mu(\nabla\mathbf{u} + \nabla\mathbf{u}^T)$, where μ is dynamic viscosity, and $\nabla\mathbf{u}$ is the velocity gradient (T denotes transposition). For axial flow, WSS becomes $\mu\frac{\partial w}{\partial r}|_{r=R}$, where R is the radius of the vessel, and $w(r, t)$ is axial velocity being a function of radius r and time t .

We used Womersley's solution for fully developed pulsatile flow in a straight circular cylinder to obtain velocity profiles as a function of flow rate [23]

rather than pressure gradient [25]. If the inlet length for the k^{th} tube is no less than $0.06R_k \text{Re}$, where $\text{Re} = 2R_k v / \nu$ is Reynolds number, v being average flow velocity, and ν —kinematic viscosity, the radial and circumferential components of velocity and pressure can be overlooked as negligible, pressure varies linearly with axial position, and the axial velocity becomes a function of t and r only [6].

Given the flow rate as the function of time $Q(t)$, in the frequency domain we have the Fourier representation

$$Q(t) = \sum_{n=0}^N B_n e^{in\omega t}$$

where N is the number of harmonics, B_n are the coefficients of the Fourier series and ω is the circular frequency.

Now we can find the Womersley velocity profiles:

$$w(r, t) = \frac{2B_0}{\pi R_k^2} \left[1 - \left(\frac{r}{R_k} \right)^2 \right] + \sum_{n=1}^N \left\{ \frac{B_n}{\pi R_k^2} \left[\frac{1 - \frac{J_0(\alpha_n \frac{r}{R_k} i^{3/2})}{J_0(\alpha_n i^{3/2})}}{1 - \frac{2J_1(\alpha_n i^{3/2})}{\alpha_n i^{3/2} J_0(\alpha_n i^{3/2})}} \right] \right\} e^{in\omega t}$$

where $\alpha_n = R_k \sqrt{\frac{n\omega}{\nu}}$ is the Womersley number, R_k being the radius of the k^{th} artery and ν —kinematic viscosity; J_0 and J_1 are Bessel functions of the first kind of order 0 and 1 respectively.

For the k^{th} vessel of the system, the transfer function relates the distal pressure P_{dk} to the proximal pressure P_{pk} as

$$\frac{P_{dk}}{P_{pk}} = \frac{1 + \Gamma_k}{e^{\gamma_k l_k} + \Gamma_k e^{-\gamma_k l_k}} \quad (2.1)$$

where l_k is the length of the k^{th} vessel, Γ_k is the reflection coefficient, and γ_k is the propagation constant for the k^{th} artery. The reflection coefficient is expressed as

$$\Gamma_k = \frac{Z_{Tk} - Z_{0k}}{Z_{Tk} + Z_{0k}} \quad (2.2)$$

where Z_{Tk} is the terminal impedance and Z_{0k} is the characteristic impedance of the k^{th} segment of the system, which is expressed as

$$Z_{0k} = \frac{\rho c_{0k}}{\pi R_k^2 \sqrt{1 - \sigma^2}} (1 - F_{10k})^{-1/2} e^{i\phi_k/2}$$

where ρ is density of blood, and the pulse wave velocity for the k^{th} tube is defined by the Moens-Korteweg equation as

$$c_{0k} = \sqrt{\frac{E_k h_k}{2\rho R_k}}$$

where E_k is the value of elastic modulus and h_k is wall thickness of the k^{th} artery, σ is the Poisson ratio, and the Womersley function F_{10k} is defined by

$$F_{10k} = \frac{2J_1(\alpha_k i^{3/2})}{\alpha_k i^{3/2} J_0(\alpha_k i^{3/2})}.$$

The phase difference ϕ between the applied force and the resulting displacement is expressed as $\phi = \phi_0(1 - e^{-2\omega})$, where ϕ_0 is an asymptotic value.

The propagation constant is expressed as

$$\gamma_k = \frac{i\omega}{c_{0k}} \sqrt{\frac{1 - \sigma^2}{1 - F_{10k}}} e^{-i\phi_k/2}$$

and the input impedance of the k^{th} segment is expressed as

$$Z_{ik} = Z_{0k} \frac{1 + \Gamma_k e^{-2\gamma_k l_k}}{1 - \Gamma_k e^{-2\gamma_k l_k}}. \quad (2.3)$$

If the k^{th} vessel is not a terminal one, there are n vessels branching out of it. In this case,

$$\frac{1}{Z_{Tk}} = \sum_{p=1}^n \frac{1}{Z_{ip}} \quad (2.4)$$

where Z_{ip} is input impedance of the p^{th} vessel branching out of the k^{th} vessel.

We assumed all the terminal vessels of the branching structure to be terminated in windkessels with resistance R_k and capacitance C_k [16, 12, 13]. If the k^{th} vessel is a terminal one,

$$Z_{Tk} = Z_{0k} + \frac{1}{\frac{1}{R_k} + i\omega C_k}. \quad (2.5)$$

Terminal impedances of the peripheral branches are obtained using Eq. (2.5). Then their input impedances are worked out with Eq. (2.3). Wherever branching takes place, Eq. (2.4) is used to work out the terminal impedance of the upstream vessel once input impedances of all the downstream vessels

are known. Working backwards towards the origin of the system, the input impedance of every sub-system is obtained. The terminal impedance of the upstream vessel is taken as the input impedance to the downstream subsystem of the vessels and the reflection coefficients are worked out using Eq. (2.2). Equation (2.1) gives the transfer functions—the complex numbers with moduli giving the amount of amplification or attenuation of a particular frequency traveled along the vessel and phase giving the time lag. This gives us pressure waves and, as input impedances are known, flow waves in every artery are also obtained.

2.1. Anatomical Data

Vascular dimensions and elastic constants were taken from [1], except for the upper limbs. It was pointed out in [13] that use of the data given in [1] produced a relatively slow average pulse wave velocity, so corrected data for the upper limbs were introduced in that work and were used in our model also. The values for resistance R and compliance C of the windkessels representing distal terminations were taken from [16]. The flow waveform at the aortic root, which was taken as the input signal to the model, is shown in Fig. 1.

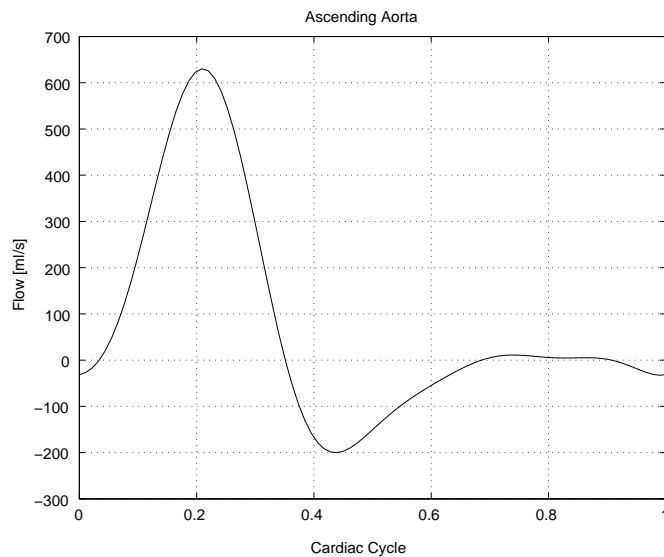


FIGURE 1. Flow rate at the aortic root—input signal to the model

In order to be able to compare the results for the healthy arteries before going on to simulating disease, the following parameters were taken as in [1]: wall viscoelasticity ϕ_0 was taken as 15° , blood viscosity $\mu = 0.004 \text{ Pa s}$, blood density $\rho = 1050 \text{ kg/m}^3$, and Poisson ratio $\sigma = 0.5$.

2.2. Simulations

As a demonstration of the model's capability, the following physiological and clinical conditions have been simulated: age-related changes in the elastic properties of the arterial wall and focal atherosclerosis.

The stiffness of arterial segments is known to increase with advancing age [15, 11]. Regional differences in distensibility were noted by many researchers [4, 17], with distensibility being less in abdominal aorta than in thoracic aorta. In the systemic arteries pulse wave velocity shows a greater increase with age in the aorta than in peripheral arteries [2, 10], so we doubled the stiffness of the aorta and used factor 1.5 for all the other arteries to simulate aging.

In simulation of focal atherosclerosis the length of stenosis was somewhat arbitrarily taken as 0.7 cm in the middle of the femoral artery (12.7 cm long). The decrease of the vessel diameter was taken as 80% (severe stenosis). The plaque was taken to be 10 times stiffer than healthy arterial wall. Flow rate and WSS were calculated for both healthy and stenosed artery at the sites A and B shown in Fig. 2.

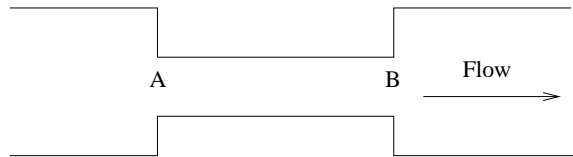


FIGURE 2. Model of the stenosed artery. Flow rate and WSS were estimated at the points A and B.

3. Results

During the simulations flow rate and WSS have been estimated for some major arteries: brachial, carotid, radial, thoracic aorta, abdominal aorta, common iliac, femoral, popliteal and tibial artery. Peak and average WSS predicted from our model are shown in Table 1.

TABLE 1. Peak and average flow [ml/s] and WSS [Pa] in the arteries.

Artery	Peak Flow	Mean Flow	Peak WSS	Mean WSS
Brachial	10.83	5.32	3.75	1.52
Common carotid	10.76	6.514	1.45	0.65
Radial	3.08	1.618	4.01	2.02
Thoracic aorta	172.4	25.12	3.58	0.14
Abdominal aorta	75.18	13.86	4.69	0.38
Common iliac	23.98	6.05	1.74	0.22
Femoral	9.20	2.53	4.16	0.93
Popliteal	7.91	2.54	5.69	1.6

3.1. Aging

The effects of non-uniform increase of arterial stiffness on blood flow rate and WSS in common carotid artery are shown in Fig. 3.

With advancing age, the reflected wave arrives earlier during ejection and the amplitude of the reflected wave increases causing a decrease in mean volume flow and mean WSS in common carotid artery. When aortic stiffness was doubled and factor 1.5 was used for all the other arteries, we noted 6% decrease in mean volume flow and mean WSS. High frequency oscillations become slightly damped due to the non-uniform increase of arterial stiffness.

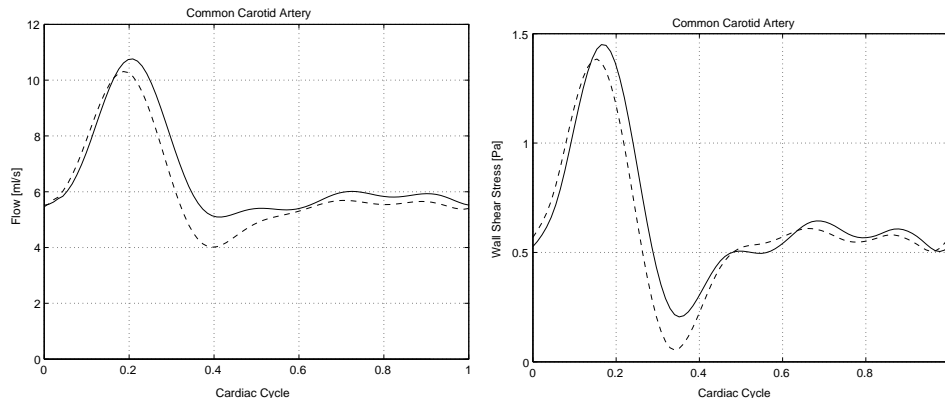


FIGURE 3. Flow rate and WSS in common carotid artery of a younger person (solid line) and those of an older person (broken line).

3.2. Focal Atherosclerosis

Flow rates and WSS in the stenosed femoral artery are shown on Fig. 4 by the solid lines just before the stenosis (site A on Fig. 2) and by the broken lines immediately after it at the site B.

On Fig. 5, the flow rate and WSS in the healthy femoral artery are shown. Solid and broken lines show flow rates and WSS at the same points along the artery. It can be seen that in the case of the stenosed artery phase shift is much more pronounced and the flow wave is attenuated.

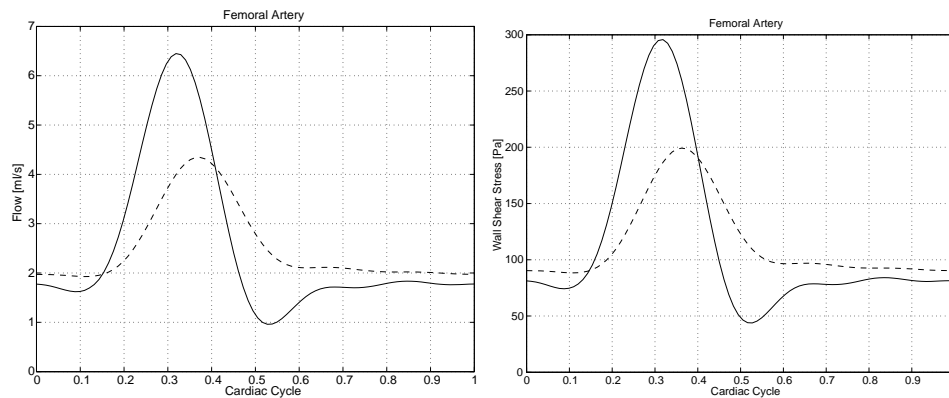


FIGURE 4. Flow rate and WSS in stenosed femoral artery at the points A (solid line) and B (broken line) shown on figure 2.

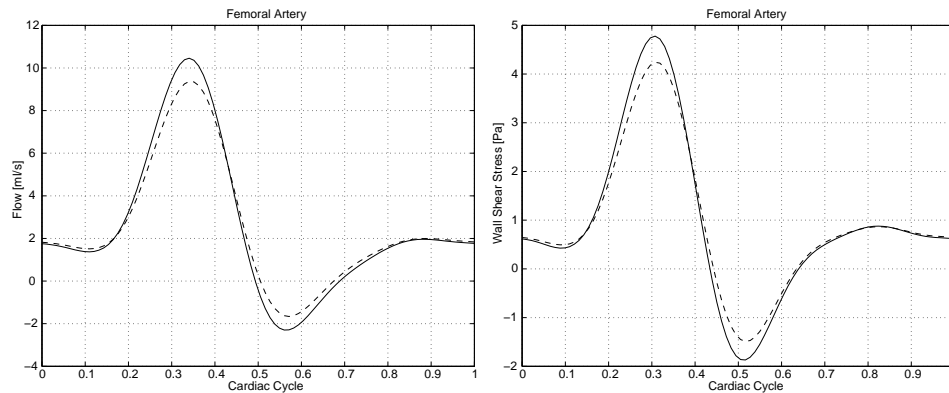


FIGURE 5. Flow rate and WSS in healthy femoral artery at the points A (solid line) and B (broken line) shown on figure 2.

4. Discussion

This study investigates the effects of arterial properties and their interaction with flow wave propagation in the human arterial tree. A distributed model represents the layout of the larger arteries in the systemic circulation. Windkessels represent the lumped or effective properties of the terminations making it possible to account for the effects of altered arterial tone and the capacitance of the small arterioles. In our work, the velocity profiles occurring in fully developed pulsatile flow in the model of the systemic arterial circulation taking account of presence of multiple reflection sites due to branching and tapering were used [20], so physically realistic estimates can be expected.

Local geometry is known to be the main factor determining WSS patterns in the arteries [7]. However, such local differences do not explain the difference in WSS between relatively straight segments in different parts of the arterial tree. The model described in this work can be used to obtain estimates of flow rate and WSS in such segments, as it is reasonable to assume fully developed flow there.

Our estimates for WSS are different to the measurements of wall shear rate reported by Wu et al. [26], who suggested a non-uniform distribution of WSS throughout the arterial system and found that superficial femoral artery had the lowest mean and peak WSS (see Table 2).

TABLE 2. Mean WSS [Pa] in the arteries ($\mu = 0.004 \text{ Pas}$).

Artery	WSS measured by Wu et al.	WSS predicted using the data by Wu et al.
Brachial	0.49 ± 0.25	0.42
Common carotid	0.83 ± 0.15	1.043
Femoral	0.33 ± 0.15	0.306

This can be explained once the difference between the diameters of the arteries in our model and their work is taken into account. When the mean diameters reported in [26] were used in our model, good agreement was found between the simulation and the measurements: the values for WSS in common carotid artery were found to be within 20% of each other, for mean WSS in femoral artery they were found to be within 7% of each other, and for mean WSS in brachial artery they were found to be within 14% of each other (no other parameters had been changed). This shows that flow and dia-

meter changes have significant influence on WSS values, which is consistent with the findings of Box et al. [3].

It is well known that arteries adapt to long-term increases or decreases in WSS, so if the flow rate is altered from its physiologic state for a long period, the arterial diameter changes to recover the physiologic range of shear in the range 1–2 Pa [28, 9, 8]. In our work remodelling of the artery walls was not taken into account. Our model predicts non-uniform distribution of WSS in the arterial tree. However, we cannot definitely state whether it is the case or simply a result of using the model parameters, which are incorrect. More work is required to validate the model parameters.

Limitations of our model due to its linearity were extensively discussed earlier [1, 13, 18]. It was reported that nonlinearities present in the arterial system were in the order of 5–10% within physiological range of frequencies and pressures in the arterial system [19]. In this study we did not attempt to account for non-linear effects because fully developed flow was assumed to take place in the points of interest.

The methods used in our study can be employed to estimate WSS and oscillatory shear index [26] in order to determine which arteries are prone to disease in two ways:

1. Getting the velocity profiles as a function of flow rate rather than pressure gradient has an advantage: the flow waveforms recorded during conventional ultrasound diagnostics may be used as the input signal to estimate WSS at the points where the measurements are taken.
2. When the flow waveform from a particular artery is not available (or practically difficult to obtain), it can be synthesized with the aid of the model.

5. Conclusion

The 1D multi-branched model is easy to implement and it is not computationally demanding. In this work we used it to carry out a detailed quantitative analysis of the velocity profiles obtained by assigning specific values to the various distal portions of the multi-branched model of the human arterial tree. It has been shown that they have given physically realistic estimates of WSS at the different points of the system. It may therefore be a useful tool to estimate WSS in arteries, allowing the effect of alteration of model parameters on WSS to be investigated.

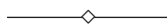
Acknowledgement

The authors would like to thank Prof. A. Avolio for his help. This study was funded by the Overseas Research Students Awards Scheme and EPSRC, whose generous support is gratefully acknowledged.

References

1. A. AVOLIO, *Multi-branched Model of the Human Arterial System*, Medical and Biological Engineering and Computing, **18**: 709–718, 1980.
2. A. AVOLIO, D. FA-QUAN, L. WEI-QIANG, L. YAO-FEI, H. ZHEN-JONG, X. LIAN-FEN, and M. O'ROURKE, *Effects of aging on arterial distensibility in populations with high and low prevalence of hypertension: comparison between urban and rural communities in China*, Circulation, **71** : 202–210, 1985.
3. F. BOX, R. VAN DER GEEST, M. RUTTEN, and J. REIBER, *The influence of flow, vessel diameter, and non-Newtonian blood viscosity on the wall shear stress in a carotid bifurcation model for unsteady flow*, Investigative Radiology, **40**(5) : 277–294, 2005.
4. H. BUTCHER and W. NEWTON, *The influence of age, atherosclerosis and homotransplantation upon the elastic properties of major human arteries*, Annals of Surgery, **148** : 1–20, 1958.
5. C. CARO, *Alterations of arterial hemodynamics associated with risk factors for atherosclerosis and induced by pharmacological or physiologic means: implications for the development/management of atherosclerosis*, [in:] Hosoda, Yaginuma, Sugawara et al. [eds.] Recent Progress in Cardiovascular Mechanics, pp. 197–213, Switzerland, Harwood Academic Publishers, 1994.
6. C. CARO, T. PEDLEY, R. SCHROTER, and W. SEED, *The mechanics of the circulation*, p.53, Oxford University Press, 1978.
7. M. FRIEDMAN, O. DETERS, F. MARK, C. BARGERON, and G. HUTCHINS, *Arterial geometry affects hemodynamics—potential risk factor for atherosclerosis*, Atherosclerosis, **46** : 225–231, 1983.
8. D. GIDDENS, C. ZARINS, and S. GLAGOV, *The role of fluid mechanics in the localization and detection of atherosclerosis*, J. Biomech. Eng., **115** : 588–594, 1993.
9. S. GLAGOV, C. ZARINS, D. GIDDENS, and D. KU, *Hemodynamics and atherosclerosis: insights and perspectives gained from studies of human arteries*, Archives of Pathology Laboratory Medicine, **112** : 1018–1031, 1988.
10. S. GREENWALD, A. CARTER, and C. BERRY, *Effect of age on the in vitro reflection coefficient of the aortoiliac bifurcation in humans*, Circulation, **82** : 114–123, 1990.
11. T. IMURA, K. YAMAMOTO, K. KANAMORI, T. MIKAMI, and H. YASUDA, *Noninvasive ultrasonic measurement of the elastic properties of the human abdominal aorta*, Cardiovascular Research, **20** : 208–214, 1986.
12. M. KARAMANOGLU, E. GALLAGHER, A. AVOLIO, and M., O'ROURKE, *Functional origin of reflected pressure waves in a multibranched model of the human arterial system*, American Journal of Physiology, **267** : H1681–H1688, 1994.

-
13. M. KARAMANOGLU, E. GALLAGHER, A. AVOLIO, and M. O'ROURKE, *Pressure wave propagation in a multibranched model of the human upper limb*, American Journal of Physiology, **269**: H1363–H1369, 1995.
 14. D. KU, D. GIDDENS, C. ZARINS, and S. GLAGOV, *Pulsatile flow and atherosclerosis in the human carotid bifurcation*, Arteriosclerosis, **5**: 293–302, 1985.
 15. B. LEAROYD and M. TAYLOR, *Alterations with age in the visco-elastic properties of human arterial walls*, Circulation Research, **18**: 278–292, 1966.
 16. Z. LIU, F. SHEN, and F. YIN, *Impedance of arterial system simulated by viscoelastic T tubes terminated in windkessels*, American J. Physiology, **256**: H1087–H1099, 1989.
 17. T. NAKASHIMA, and J. TANIKAWA, *A study of human aortic distensibility with relation to atherosclerosis and aging*, Angiology, **22**: 477–490, 1971.
 18. W. NICHOLS, M. O'ROURKE [eds.], *McDonald's blood flow in arteries. Theoretical, experimental and clinical principles*, 4thed., pp.104, 223–224, 240–242, Arnold 1998.
 19. F. PYTHOUD, N. STERGIOPULOS, and J. MEISTER, *Separation of arterial pressure' waves into their forward and backward running components*, Journal of Biomechanical Engineering, **118**: 295–301, 1996.
 20. P. SEGERS and P. VERDONCK, *Role of tapering in aortic wave reflection: hydraulic and mathematical model study*, Journal of Biomechanics, **33**: 299–306, 2000.
 21. D. STEINMAN, *Image-based computational fluid dynamics modelling in realistic arterial geometries*, Annals of Biomedical Engineering, **30**: 483–497, 2002.
 22. D. STEINMAN, D. VORP, C. ETHIER, *Computational modeling of arterial biomechanics: Insights into pathogenesis and treatment of vascular disease*, Journal of Vascular Surgery, **37**(5) : 1118–1128, 2003.
 23. C. TAYLOR, T. HUGHES, and C. ZARINS, *Finite element modeling of blood flow in arteries*, Comp. Methods in Appl. Mechanics and Engineering, **158**: 155–196, 1998.
 24. D. VORP, D. STEINMAN, and C. ETHIER, *Computational modeling of arterial biomechanics*, Computing in Science and Engineering, **3**(5) : 51–64, 2001.
 25. J. WOMERSLEY, *Method for the calculation of velocity, rate of flow and viscous drag in arteries when the pressure gradient is known*, J. Physiology, **127**: 553–563, 1955.
 26. S. WU, S. RINGGAARD, S. OYRE, M. HANSEN, S. RASMUS, and E. PEDERSEN, *Wall shear rates differ between the normal carotid, femoral, and brachial arteries: an in vivo MRI study*, Journal of Magnetic Resonance Imaging, **19**(2) : 188–193, 2004.
 27. C. ZARINS, D. GIDDENS, B. BHARADVAJ, V. SOTTIURAI, R. MABON, and S. GLAGOV, *Carotid bifurcation: quantitative correlation of plaque localization with flow velocity profiles and wall shear stress*, Circulation Research, **53**: 502–514, 1983.
 28. C. ZARINS, M. ZATINA, D. GIDDENS, D. KU, and S. GLAGOV, *Shear stress regulations of artery lumen diameter in experimental atherogenesis*, Journal of Vascular Surgery, **5** : 413–420, 1987.



The Effect of Suspended Microspheres on Viscosity of Blood

EVGENY YU. TARAN and OLGA O. MELNYK

*Faculty of Mechanics and Mathematics
Kyiv Taras Shevchenko National University
taran@univ.kiev.ua*

The expression and numerical values for effective shear viscosity of a dilute suspension of spherical microparticles in blood are obtained. If blood reveals properties of a polar fluid during hydrodynamic interaction with suspended particles, then the Cowin polar fluid should be used for the rheological modeling of blood. The above-mentioned statement is true even in the cases of blood flow in large blood vessels or in channels of different devices, in which blood, in the absence of suspended spherical particles, behaves as the Newtonian fluid.

Key words: *dilute suspension, suspension in blood, suspended microspheres, Cowin polar fluid, suspension effective viscosity*

1. Introduction

A dilute suspension in blood of rigid microspheres of the same size possessing zero buoyancy is considered in this paper.

Suspensions in blood can arise [1] on addition of particles of contrast agents for the purposes of X-ray visualization of blood vessels, on addition of particles of medical substances with the aim of delivery of drugs to affected organs and so on.

Suspension in blood also arise outside of the human body, for example, on addition of polymeric beads containing a fine magnetic colloid encapsulated in the inner core of the polymeric matrix [1] for the improvement of biochemical/biomedical analyses of blood. Suspensions in blood arise too in devices for dialysis of blood.

While solving medical problems through the use of suspensions in blood, the possible consequences of biomechanical intervention into the human body

should be remembered. In particular, it is necessary to study the influence of the addition of suspended particles on the viscosity of blood. In this paper, the simplest – spherical – form of suspended particles is considered, and also the analytical expression and numerical values for the effective viscosity of a dilute suspension of microspheres in blood as a suspension carrier fluid are obtained.

2. The Rheological Model of Blood as the Carrier Fluid of a Suspension

We assume in this paper that the radius of the suspended particles is significantly larger than the characteristic size of blood microstructure elements—red blood cells, platelets and white blood cells. This allows one to consider the interaction of blood with suspended particles as a hydrodynamic interaction of a liquid continuum with bodies suspended in it.

As usual in suspension rheology, the flow of the carrier fluid of the suspension—blood—around the suspended particles is considered within the Stokes approximation.

While choosing the continual rheological model of blood it is necessary to be knowledgeable about the rheological peculiarities of blood in gradient flows, its structural features, and also how the structure of blood influences its behaviour as a liquid medium.

In accordance with [2], blood behaves differently depending on the characteristic size of the flow region. Particularly, in large vessels it behaves as the Newtonian fluid and in small vessels its behaviour is non-Newtonian.

The total volume of red blood cells is approximately 50 times more than the total volume of other formed elements of blood—platelets and white blood cells [2], therefore the rheological behaviour of blood is determined by the concentration and mechanical properties of red blood cells only [2].

As in any concentrated suspension, the high concentration of red blood cells—approximately 46% in human blood causes neighboring red blood cells to change the spinning of each other in gradient flows of blood. Therefore, each red blood cell's own angular velocity in gradient flows of blood differs from the regional angular velocity of the elementary blood volume that they occupy. This fact explains the choice of the Cowin polar fluid [5] in the present paper, as in papers [3, 4], for rheological modeling of blood.

The phenomenological rheological model of the Cowin polar fluid [5] is one of the structural continuum models [6]. In order to account for the influ-

ence of the elements of fluid microstructure on the stress state in the fluid, it is assumed in the Cowin model [5] that the fluid particles, found in an elementary volume which is moving with the translational velocity v_i and rotating with the regional angular velocity $\omega_k = \frac{1}{2}\varepsilon_{klr}v_{r,l}$, may rotate furthermore with the angular velocity Ω_k around the center of the elementary volume. This means that the particles of the medium may have their own angular characteristics that differ from the angular velocity of the elementary volume as a whole. It is also assumed that a force couple is acting between the fluid particles. In this case, the effect of one part of the fluid on another part adjacent to it is characterised not only by the surface forces (viscous stresses) but also surface momentums (couple stresses). The rheological equations of state of the Cowin polar fluid are

$$\tau_{ij} = -p\delta_{ij} + 2\mu d_{ij} - 2kH_{ij}, \quad (2.1)$$

$$\Lambda_{ij} = \alpha\delta_{ij}\Psi_{rr} + (\beta + \gamma)\Psi_{ij} + (\beta - \gamma)\Psi_{ji}, \quad (2.2)$$

where τ_{ij} is the viscous stress tensor; Λ_{ij} is the couple stress tensor; d_{ij} is the strain rate tensor, $d_{ij} = 1/2(v_{i,j} + v_{j,i})$; $v_{i,j}$ is the velocity gradient tensor; $H_{ij} = \varepsilon_{mij}(\Omega_m - \omega_m)$; ε_{mij} is the Levi-Civita tensor; Ψ_{ij} is the gradient of the fluid particles' own angular velocity Ω_m , $\Psi_{ij} = \Omega_{i,j}$; μ , k , α , β , γ are rheological constants; the comma in the indices denotes differentiation in the direction of the axis denoted by the index which follows the comma.

Considering the elementary flows in the papers [5, 7], it was obtained that the effective viscosity of the Cowin polar fluid (Eqs. (2.1), (2.2)) does not depend on the flow's kinematic characteristics, but is determined only by the flow's geometry and the rheological constants of the model defined by Eqs. (2.1), (2.2). So, the effective viscosity of the polar fluid (Eqs. (2.1), (2.2)) in the Couette flow is defined by the formula

$$\mu_a^{(0)} = \frac{\mu}{1 - (N_0 l_0 / h) \tanh(N_0 l_0 / h)}, \quad (2.3)$$

where h is one-half of the width of the channel in the Couette flow; N_0 and l_0 are determined by the formulas

$$N_0 = \sqrt{\frac{k}{\mu + k}}, \quad l_0 = \sqrt{\frac{\beta + \gamma}{\mu}},$$

$\tanh z$ is the hyperbolic tangent.

According to [5], the parameters N_0 and l_0 vary within the limits $0 \leq N_0 \leq 1$, $l_0 \geq 0$. At $N_0 = 0$, the rheological model of a polar fluid becomes a rheological model of the Newtonian fluid with the viscosity μ [5]. From Eq. (2.3), in this case, it is determined that $\mu_a^{(0)} = \mu$.

The parameter l_0 , which has a dimension of length, is linked, according to [5], with the characteristic size of the microstructure elements of real microstructure fluids that are modeled by the polar fluid (Eqs. (2.1), (2.2)). The analysis of Eq. (2.3) shows that, while $0 < N_0 \leq 1$, the influence of the rotational viscosity k of the polar fluid on the effective viscosity $\mu_a^{(0)}$ only takes place at finite values of $2h/l_0$, i.e. in relatively narrow channels of the Couette flow of the polar fluid. In the opposite case, i.e. at $h/l_0 \rightarrow \infty$, the influence of rotational viscosity k of the polar fluid (Eqs. (2.1), (2.2)) on its effective viscosity $\mu_a^{(0)}$ is absent; in this case, it follows from Eq. (2.3) that $\mu_a^{(0)} = \mu$, i.e. the polar fluid (Eqs. (2.1), (2.2)) behaves as the Newtonian fluid with the viscosity μ . This analysis demonstrates the similarity of rheological behaviour of the Cowin polar fluid at $0 < N_0 \leq 1$ in narrow and wide channels and the rheological behaviour of blood in small and large blood vessels respectively.

The constitutive equations (2.1), (2.2) of the Cowin polar fluid were used in the papers [3, 4] for the rheological modeling of blood. The comparison in [4] of the velocity profiles of the polar fluid and blood in the Poiseuille flows, with the use of experimental data obtained in [8] allowed to obtain the values of parameters N_0 , l_0 of the Cowin polar fluid for the rheological modeling of blood at the different haematocrit values C_b (Table 1).

3. The Effective Viscosity of a Dilute Suspension of Beads in Blood

The study of a dilute suspension of beads of the same radius possessing zero buoyancy in the Cowin polar fluid (Eqs. (2.1), (2.2)) in [9] allowed to obtain the expression for the effective viscosity μ_a of such suspension:

$$\mu_a = \mu (1 + 2.5cF(N_0; 2a/l_0)) \quad (3.1)$$

where c is the volume concentration of suspended beads, a is the radius of suspended beads;

$$F(N_0, 2a/l_0) = \frac{3N_0 K_{3/2}((2a/l_0)N_0)}{(2a/l_0) K_{5/2}((2a/l_0)N_0)}. \quad (3.2)$$

In Eq. (3.2) $K_{3/2}(z)$ and $K_{5/2}(z)$ are the functions of MacDonald of half-integer order.

The effective viscosity μ_a defined by Eqs. (3.1), (3.2) was obtained in [9] using the assumptions of the Einsteinian theory [10] of dilute suspensions:

1. rigid spherical suspended particles have the same dimensions;
2. the diameter d of suspended spherical particles is much smaller than the characteristic dimension \bar{l} of the suspension macroflow region but is much greater than the characteristic dimension l of microstructural elements of the carrier fluid

$$l \ll d \ll \bar{l};$$

3. no-slip condition is fulfilled on the surface of the suspended particles;
4. the motion of the suspension's carrier fluid with respect to the suspended particles is slow;
5. the volume concentration of suspended particles is small; the suspension is assumed to be diluted;
6. suspended particles possess zero buoyancy.

The use of Eqs. (2.1), (2.2) in this paper for rheological modeling of blood as a suspension carrier fluid requires the fulfillment of the assumptions 1–6 for the considered suspension of spherical particles in blood.

The assumptions 1, 2, 4–6 are not specific, they can be used for a suspension in blood as well as for a suspension with a low-molecular carrier fluid. But the fulfillment of condition 3 for a suspension in blood is not evident, since blood as a carrier fluid of the suspension is itself a suspension of its formed elements. But in spite of that, according to [4], no-slip condition for blood is also fulfilled. The comparison in [4] of different boundary conditions on the surface flowed around by blood, that was modeled by the Cowin polar fluid (Eqs. (2.1), (2.2)), showed that the results of theoretical calculations and experiments have the best coincidence at the fulfillment of no-slip condition.

The functions of MacDonald of half-integer order $K_{3/2}(z)$ and $K_{5/2}(z)$ are expressed in terms of elementary functions [11]. It allows us to obtain the

effective viscosity μ_a of the considered dilute suspension in blood defined by Eqs. (3.1), (3.2) in a form suitable for analysis and calculations

$$\mu_a = \mu \left(1 + \frac{5}{2} c \frac{N_0^2 (2a/l_0)^2 + 3N_0 (2a/l_0) + 3}{N_0^2 ((2a/l_0)^2 - 3) + 3N_0 (2a/l_0) (1 - N_0^2) + 3} \right). \quad (3.3)$$

The evaluation of parameters N_0 and l_0 of the polar fluid (Eqs. (2.1), (2.2)) in [4] while modeling blood flows allows to investigate the influence of the polar properties of blood on the effective viscosity of a dilute suspension of beads in it using Eq. (3.3).

First of all, according to Eq. (3.3), in the limiting case $c = 0$, i.e. in the absence of suspended particles in the suspension, the carrier fluid—blood—modeled by a polar fluid behaves as the Newtonian fluid with the viscosity μ . Such a result corresponds with real behaviour of blood in large blood vessels [2]. This means that Eq. (3.3) determines the effective viscosity of a dilute suspension of beads in blood precisely in large blood vessels.

Secondly, the analysis of Eq. (3.3) also reveals that the increase of a/l_0 leads to the disappearance of the influence of rotational viscosity of blood k at $0 < N_0 \leq 1$ on the suspension's effective viscosity. In such a limiting case, Eq. (3.3) takes the form

$$\mu_a = \mu (1 + 2, 5c),$$

i.e. the effective viscosity of a dilute suspension of beads in blood is determined by the Einstein formula [10].

It is obvious from Eq. (3.3) that the influence of the rotational viscosity k of blood as a carrier fluid of the considered suspension on the effective suspension viscosity μ_a is revealed at finite values of the ratio $2a/l_0$, i.e. at a comparatively small size of suspended spherical particles.

The equation (3.3) is used in the paper for finding the numerical values of the characteristic viscosity

$$[\mu_a] = \frac{\mu_a - \mu}{\mu c}$$

of the suspension. The results of the calculation of $[\mu_a]$ for the considered suspension in blood at the different values of radius a of suspended particles and haematocrit values C_b of blood as a carrier fluid of the suspension are given in Table 1.

The columns 1–4 of Table 1 for the characteristic viscosity $[\mu_a]$ of the suspension correspond to the four values of radius a of suspended particles:

TABLE 1. Numerical values of the characteristic viscosity $[\mu_a]$ of dilute suspension of beads in blood.

$C_b, \%$	N_0	$l_0 \times 10^6 \text{ m}$	$[\mu_a]$			
			1	2	3	4
5	0.5021	8.475	2.8385	2.8071	2.7808	2.7586
10	0.5316	12.968	2.9952	2.9543	2.9193	2.8891
20	0.5501	16.597	3.1111	3.0649	3.0246	2.9893
30	0.5547	20.526	3.1963	3.1492	3.1072	3.0699
40	0.5569	23.462	3.2486	3.2019	3.1599	3.1219

$a = 3.5 \times 10^{-5} \text{ m}$, $4 \times 10^{-5} \text{ m}$, $4.5 \times 10^{-5} \text{ m}$, $5 \times 10^{-5} \text{ m}$. Such values of radius a of suspended spherical particles are significantly greater than the effective radius of red blood cells, which ranges from $2.56 \times 10^{-6} \text{ m}$ to $2.88 \times 10^{-6} \text{ m}$ considering that the red blood cells' volume ranges from $70 \mu\text{m}^3$ to $100 \mu\text{m}^3$ [2]. Such a choice of radius of suspended spherical particles ensures correctness of using the Einstein theory [10] to rheological study of dilute suspension in blood.

4. Conclusions

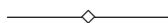
The analysis of the analytical expression for the effective viscosity μ_a of a dilute suspension of beads in blood (Eq. (3.3)) and the numerical values for the characteristic viscosity $[\mu_a]$ of the considered suspension shows that blood with suspended beads 70–100 microns in diameter reveals its non-Newtonian, i.e. polar, properties even in those gradient flows in which blood behaves as the Newtonian fluid in the absence of suspended particles. Among such flows are blood flows in middle-sized and large vessels or in channels of most apparatuses outside the human body.

The obtained numerical values of the characteristic viscosity $[\mu_a]$ of the considered suspension also show that taking into account the polar properties of blood as a carrier fluid of the suspension leads to the increase of the suspension's characteristic viscosity in comparison with a dilute suspension with the Newtonian model of blood. In particular, the characteristic viscosity $[\mu_a]$ is increased from the well known Einstein value 2.5 [10] for a dilute suspension of beads with the Newtonian carrier fluid to the values listed in Table 1, which were obtained in the present paper while modeling blood as a carrier fluid of the suspension by the Cowin polar fluid (Eqs. (2.1), (2.2)) for different values of haematocrit values C_b and different values of radius a of the suspended beads.

The studies carried out in the present paper expand the range of uses of the Cowin polar fluid as a rheological model of blood. The Cowin polar fluid should be used to model blood as a carrier fluid of a dilute suspension of rigid microspheres even in middle-sized and large blood vessels or in channels of most apparatuses in cases when blood exhibits properties of the polar fluid while interacting with suspended particles.

References

1. U. HÄFELY, W. SCHÜTT, J. TELLER and M. ZBOROWSKI [eds.], *Scientific and clinical applications of magnetic carriers*, Plenum Press, New York 1997.
2. V. A. LEVTOV, S. A. REGIRER, and N. KH. SHADRINA *Rheology of blood*, Meditsina, Moscow, 1982 [in Russian].
3. T. ARIMAN, M.A. TURK, and N.D. SYLVESTER, *The steady and pulsatile flow of blood*, J. Appl. Mech. Trans. ASME., **41**(1):1–7, 1974.
4. P. CHATURANI and D. BISWAS, *A comparative study of Poiseuille flow of a polar fluid under various boundary conditions with applications to blood flow*, Rheol. Acta, **23**(4):435–445, 1984.
5. S.C. COWIN, *The theory of polar fluids*, Adv. Appl. Mech., **14**:279–347, 1974.
6. T. ARIMAN, M.A. TURK and N.D. SYLVESTER, *Microcontinuum fluid mechanics—a review*, Int. J. Engng. Sci., **11**(8) 905–930, 1973.
7. T. SAWADA and T. TANAHASHI, *Fundamental steady flow of polar fluids*, Bull. JSME., **24**(196):1778–1786, 1981.
8. G. BUGLIARELLO and J. SEVILLA, *Velocity distribution and other characteristics of steady and pulsatile blood flows in fine glass tubes*, Biorheol., **7**:85–107, 1970.
9. M.E. ERDOGAN and N. KADIOGLU, *The viscosity of a polar fluid with suspensions*, Rheol. Acta., **10**(3):378–381, 1971.
10. A. EINSTEIN, *Eine neue Bestimmung der Moleküldimensionen*, Ann. Physik., **19**:289–306, 1906.
11. A.F. NIKIFOROV and V.B. UVAROV, *The special functions of mathematical physics*, Nauka, Moscow, 1984 [in Russian].



Already appeared in the ABIOMED *Lecture Notes* series:

1. J. MIZRAHI, *Muscle/Bone Interactions in the Musculo-Skeletal System*
 2. A. NOWICKI and J. LITNIEWSKI (Eds.), *Proceedings of the Workshop on Ultrasound in Biomeasurements, Diagnostics and Therapy*
 3. J. PIEKARSKI (Ed.), *Tissue Remodelling*
 4. S. SIDEMAN, *Insight into the Heart: Cardiac Energetics*
 5. T. LEKSZYCKI and P. MAŁDYK(Eds.), *Biomaterials in Orthopaedic Practice*

INSTITUTE OF FUNDAMENTAL TECHNOLOGICAL RESEARCH

publishes the following periodicals:

ARCHIVES OF MECHANICS — bimonthly (in English)

ARCHIVES OF ACOUSTICS — quarterly (in English)

ARCHIVES OF CIVIL ENGINEERING — quarterly (in English)

ENGINEERING TRANSACTIONS — quarterly (in English)

COMPUTER ASSISTED MECHANICS AND ENGINEERING SCIENCES

— quarterly (in English)

JOURNAL OF TECHNICAL PHYSICS — quarterly (in English)

Subscription orders for all journals published by IFTR may be sent directly to:

Editorial Office

Institute of Fundamental Technological Research

Institute of Fundamental
Świetokrzyska 21, p. 508

00-049 Warszawa, POLAND